

NDOT Research Report

Report No: NV-RDT-06-007

A Study of Fiber Reinforced Plastics for Seismic Bridge Restrainers

January 2005

Prepared by Research Division
Nevada Department of Transportation
1263 South Stewart Street
Carson City, Nevada 89712



This work was sponsored by the Nevada Department of Transportation. The contents of this report reflect the views of the authors, who are responsible for the facts and the accuracy of the data presented herein. The contents do not necessarily reflect the official views or policies of the State of Nevada at the time of publication. This report does not constitute a standard, specification, or regulation.

TECHNICAL REPORT DOCUMENTATION PAGE

Report No. NV-RDT-06-007	2. Government Accession No.	3. Recipient's Catalog No.	
4. Title and Subtitle A Study of Fiber Reinforced Plastics for Seismic Bridge Restrainers	5. Report Date January 2005		
	6. Performing Organization Code		
7. Author(s) Johnson R., Saiidi M., Maragakis M.	8. Performing Organization Report No. CCEER-05-02		
9. Performing Organization Name and Address Center of Civil Engineering Earthquake Research Department of Civil Engineering/258 University of Nevada Reno, NV 89557	10. Work Unit No.		
	11. Contract or Grant No. P821-03-803		
12. Sponsoring Agency Name and Address Nevada Department of Transportation Research Division 1263 South Stewart Carson City, NV 89712	13. Type or Report and Period Covered		
	14. Sponsoring Agency Code NDOT		
15. Supplementary Notes			
16. Abstract Easily installed and inspected fiber reinforced plastic (FRP) as an alternative to steel for restrainer construction to reduce bridge hinge movements during earthquakes was examined. Glass, carbon, and hybrid (glass/carbon) restrainers were constructed and dynamically tested in the large-scale structures laboratory. Work included: (1) Tensile tests on FRP strips and on FRP/concrete bond versus loading rate; (2) FRP restrainer development, including dynamic testing; (3) Shake table data analysis and comparisons of FRP, steel, and SMA Restrainer performance; (4) Development of a FRP restrainer design method. Findings confirm FRP restrainer potential for future implementation to structures. Results include: (1) FRP strength is strain-rate insensitive; (2) FRP/concrete bond strength is a function of concrete shear strength and is strain rate sensitive; (3) Flexible restrainer construction and restrainer/concrete bond methods are demonstrated; (4) A simplified FRP restrainer design method, more realistic than AASHTO, and that considers bridge structure dynamic characteristics, is proposed.			
17. Key Words fiber reinforced plastic, bridge hinge movements, FRP, SMA, FRP strength, shake table	18. Distribution Statement Unrestricted. This document is available through the National Technical Information Service, Springfield, VA 21161		
19. Security Classif. (of this report) Unclassified	20. Security Classif. (of this page) Unclassified	21. No. Of Pages 292	22. Price

Report No. CCEER-05-02

**A STUDY OF FIBER REINFORCED PLASTICS
FOR SEISMIC BRIDGE RESTRAINERS**

R. Johnson, M. Saidi, M. Maragakis

Prepared for

**National Cooperative Highway Research Program's Innovations
Deserving Exploratory Analysis Project
and
Nevada Department of Transportation**

**Center of Civil Engineering Earthquake Research
Department of Civil Engineering/258
University of Nevada
Reno, Nevada 89557**

January 2005

ACKNOWLEDGEMENTS

This study was funded by the National Cooperative Highway Research Program's Innovations Deserving Exploratory Analysis project (NCHRP-IDEA) and co-funded by the Nevada Department of Transportation (NDOT). However, the opinions, findings, and conclusions presented in this document are those of the authors and do not necessarily represent the views of NCHRP or NDOT.

The author wishes to express their appreciation to the advisory board for this study; Dr. Saad El-Azazy (CALTRANS), and members; Dr. Allaoua Kartoum (CALTRANS), Mr. Harry Capers (NJDOT), and Mr. Troy Martin (NDOT). Thanks are due to Dr. Shen-Yi Luo for sharing his original work on flexible composites. Special thanks are due to Dr. Patrick LaPlace, Dr. Ian Buckle, Mr. Paul Lucas, Mr. Robert Nelson and Mr. Nathan Johnson of the Civil Engineering Department for their help and support.

The report is based on an M.S.C.E. thesis by the first author, supervised by the other authors.

ABSTRACT

Easily installed and inspected fiber reinforced plastic (FRP) as an alternative to steel for restrainer construction to reduce bridge hinge movements during earthquakes was examined. Glass, carbon, and hybrid (glass/carbon) restrainers were constructed and dynamically tested in the large-scale structures laboratory. Work included: (1) Tensile tests on FRP strips and on FRP/concrete bond versus loading rate; (2) FRP restrainer development, including dynamic testing; (3) Shake table data analysis and comparisons of FRP, steel, and SMA restrainer performance; (4) Development of a FRP restrainer design method. Findings confirm FRP restrainer potential for future implementation to structures. Results include: (1) FRP strength is strain-rate insensitive; (2) FRP/concrete bond strength is a function of concrete shear strength and is strain rate sensitive; (3) Flexible restrainer construction and restrainer/concrete bond methods are demonstrated; (4) A simplified FRP restrainer design method, more realistic than AASHTO, and that considers bridge structure dynamic characteristics, is proposed.

TABLE OF CONTENTS

ACKNOWLEDGEMENTS.....	i
ABSTRACT.....	ii
TABLE OF CONTENTS.....	iii
LIST OF TABLES.....	viii
LIST OF FIGURES.....	x
1 INTRODUCTION	
1.1 General Perspective.....	1
1.2 Previous Studies.....	2
1.2.1 FRP Under Cyclic Loading.....	2
1.2.2 Recent Studies on Dynamic Performance of Restrainers	3
1.3 Objectives and Scope.....	5
2 MATERIAL STUDIES	
2.1 Introduction.....	6
2.2 Introduction to Strain Rate Effect.....	6
2.3 Test Protocol.....	7
2.4 Material Test Set-Up and Instrumentation.....	7
2.5 Plain Fabric Tensile Tests.....	8
2.5.1 Glass Fabric Test Results.....	8
2.5.1.a Stress-Strain Relationship.....	9
2.5.2 Carbon Fabric Test Results.....	9
2.5.2.a Stress-Strain Relationship.....	10

2.6	Flexible Composites.....	10
2.6.1	SYLGARD 184 Silicone Elastomer.....	11
2.6.2	Vacuum Box.....	11
2.6.3	Elastomer Coating Process.....	12
2.7	Elastomer Coated Fabric Tensile Tests.....	14
2.7.1	Glass Test Results.....	14
2.7.2	Carbon Test Results.....	15
2.7.3	Comparison of Failure Modes.....	16
2.8	FRP-Concrete Bond Strength.....	16
2.8.1	Specimen Design.....	17
2.8.2	Bond Test Set-Up.....	19
2.8.3	Interfacial Bond Test Results.....	19
2.8.3.a	Force-Displacement and Stress-Strain Relationship.....	21
2.9	Concluding Remarks.....	21
3	FRP RESTRAINERS	
3.1	Introduction.....	22
3.2	Restrainer Design Method.....	22
3.2.1	Demand.....	23
3.2.2	Flexible FRP Capacity.....	24
3.2.3	FRP/Concrete Bond Capacity.....	25
3.3	Restrainer Designer.....	26
3.3.1	GFRP.....	27

3.3.2	CFRP.....	28
3.3.3	Hybrid (Glass and Carbon).....	29
3.4	Restrainer Fabrication.....	30
4	EXPERIMENTAL PROGRAM	
4.1	Introduction.....	33
4.2	Test Specimen.....	33
4.3	Test Parameters.....	33
4.3.1	Restrainer Slack.....	34
4.3.2	Earthquake Motion.....	34
4.3.3	Frame Period Ratio (T_1/T_2).....	34
4.4	Data Acquisition Equipment and Instrumentation.....	34
4.5	Test Schedule.....	35
5	FRP RESTRAINER TEST RESULTS	
5.1	Introduction.....	37
5.2	GFRP.....	37
5.2.1	Response Histories.....	37
5.3	CFRP.....	38
5.3.1	Response Histories.....	39
5.4	CGFRP (Hybrid).....	40
5.4.1	Series 3-1 to 3-6.....	41
5.4.1.a	Response Histories.....	41
5.4.2	Series 3-1S and 3-2S.....	42
5.4.2.a	Response Histories.....	42

5.4.3	Series 3-1T and 3-2T.....	42
5.4.3.a	Response Histories.....	43
5.5	Concluding Remarks.....	43
6	COMPARISONS OF RESPONSE OF FRP RESTRAINERS WITH STEEL AND SMA RESTRAINERS	
6.1	Introduction.....	45
6.2	GFRP, CFRP, CGFRP Comparisons.....	45
6.2.1	Response Histories.....	46
6.3	Comparisons of CGFRP Restrainer Response for Different Motions.....	46
6.3.1	Response Histories.....	47
6.4	Comparison of Response for Different Restrainer Types.....	47
6.4.1	Response Histories.....	48
7	RESTRAINER DESIGN APPROACH	
7.1	Introduction.....	49
7.2	Existing Restrainer Design Procedures.....	49
7.2.1	CALTRANS.....	49
7.2.2	AASHTO.....	50
7.2.3	Trochalakis et. al. (1997).....	50
7.2.4	DesRoches and Fenves (1997).....	50
7.3	New Restrainer Design Method (2004).....	50
7.4	Examples.....	51
7.4.1	AASHTO.....	52

7.4.2	New Restrainer Design Method.....	52
7.5	Design of Attachment.....	53
7.6	Concluding Remarks.....	54
8	SUMMARY AND CONCLUSIONS	
8.1	Summary.....	56
8.2	Conclusions.....	57
8.3	Recommendations for Further Work.....	58
	REFERENCES.....	60
	TABLES.....	64
	FIGURES.....	94
	APPENDIX A: LIST OF CCEER PUBLICATIONS.....	258

LIST OF TABLES

CHAPTER 2

2.1	Composite and Dry Fiber Properties.....	64
2.2	Glass Fabric Strip Material Tests.....	65
2.3	Carbon Fabric Strip Material Tests.....	66
2.4	Properties of Sylgard 184 Silicone.....	67
2.5	Properties of Acrylite Plus.....	67
2.6	Stress Calculations from FRP Tensile Tests (Glass) (SI Unit: MPa).....	68
2.6.a	Stress Calculations from FRP Tensile Tests (Glass)..... (US Unit: ksi)	69
2.7	Calculated Tensile Modulus and Stiffness (Glass).....	70
2.8	Stress Calculations from FRP Tensile Tests (Carbon) (SI Unit: MPa).....	71
2.8.a	Stress Calculations from FRP Tensile Tests (Carbon) (US Unit: ksi).....	72
2.9	Calculated Tensile Modulus and Stiffness (Carbon).....	73
2.10	Dr. Teng’s Model to Determine Effective Bond Length.....	74
2.11	Comparisons of 3 Sets of Fiberglass Tensile Tests (Plain Fabric, Coated Fabric, Interfacial Bond) (SI Unit: MPa).....	75
2.11.a	Comparisons of 3 Sets of Fiberglass Tensile Tests (Plain Fabric, Coated Fabric, Interfacial Bond) (US Unit: ksi)	76
2.12	Comparisons of 3 Sets of Carbon Tensile Tests (Plain Fabric, Coated Fabric, Interfacial Bond (SI Unit: MPa)).....	77
2.12.a	Comparisons of 3 Sets of Carbon Tensile Tests (Plain Fabric, Coated Fabric, Interfacial Bond (US Unit: ksi)).....	78

CHAPTER 3

3.1	Force Demand used in FRP Restrainer Design (SI Unit: kN)	79
3.1.a	Force Demand used in FRP Restrainer Design (US Unit: kip)	80
3.2	Average Measured Flexible FRP Strength.....	81
3.3	Design Width of Flexible Composite.....	81
3.4	Capacity of Flexible FRP with Design Width.....	81

3.5	New Effective Lengths for Bonded Portion of GFRP Restrainer.....	82
3.6	New Effective Lengths for Bonded Portion of CFRP Restrainer.....	82
3.7	Effective Bond Lengths for Bonded Portion of Hybrid Restrainer.....	82
CHAPTER 4		
4.1	Frame Properties and Dimensions.....	83
4.2	Channels of Data Acquisition System.....	84
4.3	Test Protocol for FRP Restrainer Tests.....	85
CHAPTER 5		
5.1	Observations During Testing of GFRP Restrainers.....	86
5.2	Maximum Specimen Responses, Determined During GFRP Restrainer Shake Table Tests.....	87
5.3	Observations During Testing of CFRP Restrainers.....	88
5.4	Maximum Specimen Response, Determined During CFRP Restrainer Shake Table Tests.....	89
5.5	Observations During Testing of CGFRP Restrainers.....	90
5.6	Maximum Specimen Response, Determined During CGFRP Restrainer Shake Table Tests.....	91
CHAPTER 6		
6.1	Total Force vs. Maximum Displacement for Different Cable Types, From Shake Table Tests (SI Unit: kN).....	92
6.1.a	Total Force vs. Maximum Displacement for Different Cable Types, From Shake Table Tests (US Unit: kip).....	93

LIST OF FIGURES

CHAPTER 2

2.1	Yield Stress of Steel vs. Strain Rate.....	94
2.2	Steel Coupon Pulled at Static Strain Rate.....	95
2.3	Steel Coupon Pulled at Dynamic Strain Rate.....	95
2.4	Strain Rate History for Steel Restrainer Shake Table Test, PGA = 0.15g.....	96
2.5	Strain Rate History for SMA Restrainer Shake Table Test, PGA = 0.15g.....	96
2.6	Material Tensile Tests Using MTS Load Frame.....	97
2.7	Close-Up of carbon Fabric Strip Tensile Tests.....	97
2.8	Glass Fabric Strips with Ends Marked for Epoxy Application	98
2.9	Dipping Ends of Fabric Strips into Resin.....	98
2.10	Typical Failure Mode of Fiberglass Strips.....	98
2.11	Typical Failure Mode of Carbon Fabric Strips.....	98
2.12	Stress-Strain Relationship for Glass FRP Strip #1 @ 167 $\mu\epsilon$ /sec.....	99
2.13	Stress-Strain Relationship for Glass FRP Strip #2 @ 167 $\mu\epsilon$ /sec.....	99
2.14	Stress-Strain Relationship for Glass FRP Strip #3 @ 167 $\mu\epsilon$ /sec.....	99
2.15	Stress-Strain Relationship for Glass FRP Strip #4 @ 1000 $\mu\epsilon$ /sec.....	100
2.16	Stress-Strain Relationship for Glass FRP Strip #5 @ 1000 $\mu\epsilon$ /sec.....	100
2.17	Stress-Strain Relationship for Glass FRP Strip #6 @ 1000 $\mu\epsilon$ /sec.....	100
2.18	Stress-Strain Relationship for Glass FRP Strip #7 @ 5000 $\mu\epsilon$ /sec.....	101
2.19	Stress-Strain Relationship for Glass FRP Strip #8 @ 5000 $\mu\epsilon$ /sec.....	101
2.20	Stress-Strain Relationship for Glass FRP Strip #9 @ 5000 $\mu\epsilon$ /sec.....	101
2.21	Stress-Strain Relationship for Glass FRP Strip #10 @ 10000 $\mu\epsilon$ /sec.....	102
2.22	Stress-Strain Relationship for Glass FRP Strip #11 @ 10000 $\mu\epsilon$ /sec.....	102
2.23	Stress-Strain Relationship for Glass FRP Strip #12 @ 10000 $\mu\epsilon$ /sec.....	102

2.24	Stress-Strain Relationship for Glass FRP Strip #13 @ 50000 $\mu\epsilon/\text{sec}$	103
2.25	Stress-Strain Relationship for Glass FRP Strip #14 @ 50000 $\mu\epsilon/\text{sec}$	103
2.26	Stress-Strain Relationship for Glass FRP Strip #15 @ 50000 $\mu\epsilon/\text{sec}$	103
2.27	Stress-Strain Relationship for Glass FRP Strip #19 @ 50000 $\mu\epsilon/\text{sec}$	104
2.28	Stress-Strain Relationship for Glass FRP Strip #20 @ 50000 $\mu\epsilon/\text{sec}$	104
2.29	Stress-Strain Relationship for Glass FRP Strip #21 @ 50000 $\mu\epsilon/\text{sec}$	104
2.30	Stress-Strain Relationship for Glass FRP Strip #16 @ 100000 $\mu\epsilon/\text{sec}$	105
2.31	Stress-Strain Relationship for Glass FRP Strip #17 @ 100000 $\mu\epsilon/\text{sec}$	105
2.32	Stress-Strain Relationship for Glass FRP Strip #18 @ 100000 $\mu\epsilon/\text{sec}$	105
2.33	Stress-Strain Relationship for Carbon FRP Strip #1 @ 167 $\mu\epsilon/\text{sec}$	106
2.34	Stress-Strain Relationship for Carbon FRP Strip #2 @ 167 $\mu\epsilon/\text{sec}$	106
2.35	Stress-Strain Relationship for Carbon FRP Strip #3 @ 167 $\mu\epsilon/\text{sec}$	106
2.36	Stress-Strain Relationship for Carbon FRP Strip #4 @ 167 $\mu\epsilon/\text{sec}$	107
2.37	Stress-Strain Relationship for Carbon FRP Strip #5 @ 1000 $\mu\epsilon/\text{sec}$	108
2.38	Stress-Strain Relationship for Carbon FRP Strip #6 @ 1000 $\mu\epsilon/\text{sec}$	108
2.39	Stress-Strain Relationship for Carbon FRP Strip #7 @ 1000 $\mu\epsilon/\text{sec}$	108
2.40	Stress-Strain Relationship for Carbon FRP Strip #8 @ 5000 $\mu\epsilon/\text{sec}$	109
2.41	Stress-Strain Relationship for Carbon FRP Strip #9 @ 5000 $\mu\epsilon/\text{sec}$	109
2.42	Stress-Strain Relationship for Carbon FRP Strip #10 @ 5000 $\mu\epsilon/\text{sec}$	109
2.43	Stress-Strain Relationship for Carbon FRP Strip #11 @ 10000 $\mu\epsilon/\text{sec}$	110
2.44	Stress-Strain Relationship for Carbon FRP Strip #12 @ 10000 $\mu\epsilon/\text{sec}$	110
2.45	Stress-Strain Relationship for Carbon FRP Strip #13 @ 10000 $\mu\epsilon/\text{sec}$	110

2.46	Stress-Strain Relationship for Carbon FRP Strip #14 @ 50000 $\mu\epsilon$ /sec.....	111
2.47	Stress-Strain Relationship for Carbon FRP Strip #15 @ 50000 $\mu\epsilon$ /sec.....	111
2.48	Stress-Strain Relationship for Carbon FRP Strip #16 @ 50000 $\mu\epsilon$ /sec.....	111
2.49	Stress-Strain Relationship for Carbon FRP Strip #17 @ 100000 $\mu\epsilon$ /sec.....	112
2.50	Stress-Strain Relationship for Carbon FRP Strip #18 @ 100000 $\mu\epsilon$ /sec.....	112
2.51	Stress-Strain Relationship for Carbon FRP Strip #19 @ 100000 $\mu\epsilon$ /sec.....	112
2.52	Components of Clear Acrylic Vacuum Box.....	113
2.53	Vacuum Box Construction.....	114
2.54	Epoxy Coating Process.....	115
2.55	Elastomer Coating Process.....	115
2.56	Force vs. Displacement, Elastomer Coated Glass Strip #1 ...	116
2.57	Stress vs. Strain, Elastomer Coated Glass Strip #1.....	116
2.58	Force vs. Displacement, Elastomer Coated Glass Strip #2...	117
2.59	Stress vs. Strain, Elastomer Coated Glass Strip #2.....	117
2.60	Force vs. Displacement, Elastomer Coated Glass Strip #3...	118
2.61	Stress vs. Strain, Elastomer Coated Glass Strip #3.....	118
2.62	Force vs. Displacement, Elastomer Coated Glass Strip #4...	119
2.63	Stress vs. Strain, Elastomer Coated Glass Strip #4.....	119
2.64	Force vs. Displacement, Elastomer Coated Glass Strip #5...	120
2.65	Stress vs. Strain, Elastomer Coated Glass Strip #5.....	120
2.66	Force vs. Displacement, Elastomer Coated Glass Strip #6...	121
2.67	Stress vs. Strain, Elastomer Coated Glass Strip #6.....	121
2.68	Force vs. Displacement, Elastomer Coated Glass Strip #7...	122
2.69	Stress vs. Strain, Elastomer Coated Glass Strip #7.....	122
2.70	Force vs. Displacement, Elastomer Coated Glass Strip #8...	123
2.71	Stress vs. Strain, Elastomer Coated Glass Strip #8.....	123
2.72	Force vs. Displacement, Elastomer Coated Glass Strip #9...	124
2.73	Stress vs. Strain, Elastomer Coated Glass Strip #9.....	124
2.74	Force vs. Displacement, Elastomer Coated Glass Strip #10	125
2.75	Stress vs. Strain, Elastomer Coated Glass Strip #10.....	125
2.76	Force vs. Displacement, Elastomer Coated Glass Strip #11	126
2.77	Stress vs. Strain, Elastomer Coated Glass Strip #11.....	126
2.78	Force vs. Displacement, Elastomer Coated Glass Strip #12	127
2.79	Stress vs. Strain, Elastomer Coated Glass Strip #12.....	127
2.80	Force vs. Displacement, Elastomer Coated Glass Strip #13	128
2.81	Stress vs. Strain, Elastomer Coated Glass Strip #13.....	128
2.82	Force vs. Displacement, Elastomer Coated Glass Strip #14..	129
2.83	Stress vs. Strain, Elastomer Coated Glass Strip #14.....	129
2.84	Force vs. Displacement, Elastomer Coated Glass Strip #15..	130

2.85	Stress vs. Strain, Elastomer Coated Glass Strip #15.....	130
2.86	Force vs. Displacement, Elastomer Coated Glass Strip #16....	131
2.87	Stress vs. Strain, Elastomer Coated Glass Strip #16.....	131
2.88	Force vs. Displacement, Elastomer Coated Glass Strip #17...	132
2.89	Stress vs. Strain, Elastomer Coated Glass Strip #17.....	132
2.90	Force vs. Displacement, Elastomer Coated Glass Strip #18....	133
2.91	Stress vs. Strain, Elastomer Coated Glass Strip #18.....	133
2.92	Force vs. Displacement, Elastomer Coated Glass Strip #19.....	134
2.93	Stress vs. Strain, Elastomer Coated Glass Strip #19.....	134
2.94	Force vs. Displacement, Elastomer Coated Glass Strip #20....	135
2.95	Stress vs. Strain, Elastomer Coated Glass Strip #20.....	135
2.96	Force vs. Displacement, Elastomer Coated Glass Strip #21....	136
2.97	Stress vs. Strain, Elastomer Coated Glass Strip #21.....	136
2.98	Force vs. Displacement, Elastomer Coated Glass Strip #22....	137
2.99	Stress vs. Strain, Elastomer Coated Glass Strip #22.....	137
2.100	Force vs. Displacement, Elastomer Coated Carbon Strip #2 ...	138
2.101	Stress vs. Strain, Elastomer Coated Carbon Strip #2.....	138
2.102	Force vs. Displacement, Elastomer Coated Carbon Strip #3.....	139
2.103	Stress vs. Strain, Elastomer Coated Carbon Strip #3.....	139
2.104	Force vs. Displacement, Elastomer Coated Carbon Strip #4.....	140
2.105	Stress vs. Strain, Elastomer Coated Carbon Strip #4.....	140
2.106	Force vs. Displacement, Elastomer Coated Carbon Strip 5.....	141
2.107	Stress vs. Strain, Elastomer Coated Carbon Strip #5.....	141
2.108	Force vs. Displacement, Elastomer Coated Carbon Strip ...	142
2.109	Stress vs. Strain, Elastomer Coated Carbon Strip #6.....	142
2.110	Force vs. Displacement, Elastomer Coated Carbon Strip	143
2.111	Stress vs. Strain, Elastomer Coated Carbon Strip #7.....	143
2.112	Force vs. Displacement, Elastomer Coated Carbon Strip	144
2.113	Stress vs. Strain, Elastomer Coated Carbon Strip #8.....	144
2.114	Force vs. Displacement, Elastomer Coated Carbon Strip	145
2.115	Stress vs. Strain, Elastomer Coated Carbon Strip #9.....	145
2.116	Force vs. Displacement, Elastomer Coated Carbon Strip	146
2.117	Stress vs. Strain, Elastomer Coated Carbon Strip #10.....	146
2.118	Force vs. Displacement, Elastomer Coated Carbon Strip #11...	147
2.119	Stress vs. Strain, Elastomer Coated Carbon Strip #11.....	147
2.120	Force vs. Displacement, Elastomer Coated Carbon Strip #12....	148
2.121	Stress vs. Strain, Elastomer Coated Carbon Strip #12.....	148
2.122	Force vs. Displacement, Elastomer Coated Carbon Strip #13...	149
2.123	Stress vs. Strain, Elastomer Coated Carbon Strip #13.....	149
2.124	Force vs. Displacement, Elastomer Coated Carbon Strip #14....	150
2.125	Stress vs. Strain, Elastomer Coated Carbon Strip #14.....	150
2.126	Force vs. Displacement, Elastomer Coated Carbon Strip #15....	151
2.127	Stress vs. Strain, Elastomer Coated Carbon Strip #15.....	151
2.128	Force vs. Displacement, Elastomer Coated Carbon Strip #16....	152
2.129	Stress vs. Strain, Elastomer Coated Carbon Strip #16.....	152

2.130	Force vs. Displacement, Elastomer Coated Carbon Strip #17.....	153
2.131	Stress vs. Strain, Elastomer Coated Carbon Strip #17.....	153
2.132	Force vs. Displacement, Elastomer Coated Carbon Strip #18.....	154
2.133	Stress vs. Strain, Elastomer Coated Carbon Strip #18.....	154
2.134	Force vs. Displacement, Elastomer Coated Carbon Strip #19.....	155
2.135	Stress vs. Strain, Elastomer Coated Carbon Strip #19.....	155
2.136	Force vs. Displacement, Elastomer Coated Carbon Strip #20.....	156
2.137	Stress vs. Strain, Elastomer Coated Carbon Strip #20.....	156
2.138	Comparisons of Tensile Failure Mode for .a Elastomer Coated Glass Strips and .b Uncoated Glass Strips.....	157
2.139	Comparisons of Tensile Failure Mode for .a Elastomer Coated Carbon Strips and .b Uncoated Carbon Strips.....	158
2.140	Strength Ratio vs. Strain Rate for Elastomer Coated Glass Strips.....	159
2.141	Strength Ratio vs. Strain Rate for Elastomer Coated Carbon Strips.....	159
2.142	Single Lap Test.....	160
2.143	Concrete Blocks Used in FRP/Concrete Bond Tests.....	161
2.144	FRP/Concrete Bond Tests on MTS Load Frame.....	162
2.145	Glass and Carbon Strips for Bond Tests.....	163
2.146	Beam Preparation for FRP/Concrete Bond Tests.....	164
2.147	FRP/Concrete Bond Test Specimen Construction.....	165
2.148	Tensile Tests on Interfacial Bond Between FRP and Concrete.....	166
2.149.a	Strength Ratios for GFRP/Concrete Bond.....	167
2.149.b	Strength Ratios for CFRP/Concrete Bond.....	167
2.150	Best Line Fit of Strength Ratios vs. Strain Rate for FRP/Concrete Bond.....	168
2.151	Bond Failure During Tensile Tests	169
2.152	Close-Up of Bond Failure.....	169
2.153	Force vs. Bond Slip for GFRP/Concrete Bond #1	170
2.154	Average Bond Stress vs. Bond Strain, GFRP/Concrete Bond#1	170
2.155	Force vs. Bond Slip for GFRP/Concrete Bond #2.....	171
2.156	Average Bond Stress vs. Bond Strain, GFRP/Concrete Bond#2.....	171
2.157	Force vs. Bond Slip for GFRP/Concrete Bond #4.....	172
2.158	Average Bond Stress vs. Bond Strain, GFRP/Concrete Bond#4	172
2.159	Force vs. Bond Slip for GFRP/Concrete Bond #5.....	173

2.160	Average Bond Stress vs. Bond Strain, GFRP/Concrete Bond#5.....	173
2.161	Force vs. Bond Slip for GFRP/Concrete Bond #6.....	174
2.162	Average Bond Stress vs. Bond Strain, GFRP/Concrete Bond #6.....	174
2.163	Force vs. Bond Slip for GFRP/Concrete Bond #7.....	175
2.164	Average Bond Stress vs. Bond Strain, GFRP/Concrete Bond#7.....	175
2.165	Force vs. Bond Slip for GFRP/Concrete Bond #7.....	176
2.166	Average Bond Stress vs. Bond Strain, GFRP/Concrete Bond#9.....	176
2.167	Force vs. Bond Slip for GFRP/Concrete Bond #10.....	177
2.168	Average Bond Stress vs. Bond Strain,GFRP/Concrete Bond#10.....	177
2.169	Force vs. Bond Slip for GFRP/Concrete Bond #11.....	178
2.170	Average Bond Stress vs. Bond Strain,GFRP/Concrete Bond#11.....	178
2.171	Force vs. Bond Slip for GFRP/Concrete Bond #12.....	179
2.172	Average Bond Stress vs. Bond Strain GFRP/Concrete Bond#12	179
2.173	Force vs. Bond Slip for GFRP/Concrete Bond #13.....	180
2.174	Average Bond Stress vs. Bond Strain GFRP/Concrete Bond#13.....	180
2.175	Force vs. Bond Slip for GFRP/Concrete Bond #14.....	181
2.176	Average Bond Stress vs. Bond Strain,GFRP/Concrete Bond#14.....	181
2.177	Force vs. Bond Slip for GFRP/Concrete Bond#15...	182
2.178	Average Bond Stress vs. Bond Strain,GFRP/Concrete Bond#15.....	182
2.179	Force vs. Bond Slip for GFRP/Concrete Bond#16.....	183
2.180	Average Bond Stress vs. Bond Strain,GFRP/Concrete Bond#16.....	183
2.181	Force vs. Bond Slip for GFRP/Concrete Bond#17.....	184
2.182	Average Bond Stress vs. Bond Strain,GFRP/Concrete Bond#17.....	184
2.183	Force vs. Bond Slip for GFRP/Concrete Bond#18.....	185
2.184	Average Bond Stress vs. Bond Strain,GFRP/Concrete Bond#18.....	185
2.185	Force vs. Bond Slip for GFRP/Concrete Bond#19.....	186
2.186	Average Bond Stress vs. Bond Strain,GFRP/Concrete Bond#19.....	186
2.187	Force vs. Bond Slip for GFRP/Concrete Bond#20.....	187
2.188	Average Bond Stress vs. Bond Strain,GFRP/Concrete Bond#20.....	187
2.189	Force vs. Bond Slip for CFRP/Concrete Bond #1.....	188

2.190	Average Bond Stress vs. Bond Strain, CFRP/Concrete Bond#1.....	188
2.191	Force vs. Bond Slip for CFRP/Concrete Bond #2.....	189
2.192	Average Bond Stress vs. Bond Strain, CFRP/Concrete Bond#2.....	189
2.193	Force vs. Bond Slip for CFRP/Concrete Bond #3.....	190
2.194	Average Bond Stress vs. Bond Strain, CFRP/Concrete Bond#3.....	190
2.195	Force vs. Bond Slip for CFRP/Concrete Bond #4.....	191
2.196	Average Bond Stress vs. Bond Strain, CFRP/Concrete Bond#4.....	191
2.197	Force vs. Bond Slip for CFRP/Concrete Bond #5.....	192
2.198	Average Bond Stress vs. Bond Strain, CFRP/Concrete Bond#5.....	192
2.199	Force vs. Bond Slip for CFRP/Concrete Bond #6.....	193
2.200	Average Bond Stress vs. Bond Strain, CFRP/Concrete Bond#6.....	193
2.201	Force vs. Bond Slip for CFRP/Concrete Bond #7.....	194
2.202	Average Bond Stress vs. Bond Strain, CFRP/Concrete Bond#7.....	194
2.203	Force vs. Bond Slip for CFRP/Concrete Bond #8.....	195
2.204	Average Bond Stress vs. Bond Strain, CFRP/Concrete Bond#8.....	195
2.205	Force vs. Bond Slip for CFRP/Concrete Bond #9.....	196
2.206	Average Bond Stress vs. Bond Strain, CFRP/Concrete Bond#9.....	196
2.207	Force vs. Bond Slip for CFRP/Concrete Bond #10.....	197
2.208	Average Bond Stress vs. Bond Strain,CFRP/Concrete Bond#10.....	197
2.209	Force vs. Bond Slip for CFRP/Concrete Bond #11.....	198
2.210	Average Bond Stress vs. Bond Strain,CFRP/Concrete Bond#11.....	198
2.211	Force vs. Bond Slip for CFRP/Concrete Bond#12.....	199
2.212	Average Bond Stress vs. Bond Strain,CFRP/Concrete Bond#12.....	199
2.213	Force vs. Bond Slip for CFRP/Concrete Bond#13.....	200
2.214	Average Bond Stress vs. Bond Strain,CFRP/Concrete Bond#13.....	200
2.215	Force vs. Bond Slip for CFRP/Concrete Bond#14.....	201
2.216	Average Bond Stress vs. Bond Strain,CFRP/Concrete Bond#14.....	201
2.217	Force vs. Bond Slip for CFRP/Concrete Bond #15.....	202
2.218	Average Bond Stress vs. Bond Strain,CFRP/Concrete Bond#15.....	202
2.219	Force vs. Bond Slip for CFRP/Concrete Bond#16.....	203

2.220	Average Bond Stress vs. Bond Strain,CFRP/Concrete Bond#16.....	203
2.221	Force vs. Bond Slip for CFRP/Concrete Bond#18.....	204
2.222	Average Bond Stress vs. Bond Strain,CFRP/Concrete Bond#18.....	204
2.223	Force vs. Bond Slip for CFRP/Concrete Bond#19.....	205
2.224	Average Bond Stress vs. Bond Strain,CFRP/Concrete Bond#19.....	205
2.225	Force vs. Bond Slip for CFRP/Concrete Bond#20.....	206
2.226	Average Bond Stress vs. Bond Strain,CFRP/Concrete Bond#20.....	206

CHAPTER 3

3.1	Chen and Teng's Bond Strength Model for Plate to Concrete.....	207
3.2	Illustration of Unidirectional Section of the FRP Restrainer.....	207
3.3	Calculation of Effective Bond Length and Bond Capacity for GFRP Prior to Increase in Plate Size.....	208
3.4	Calculation of Effective Length and Bond Capacity of 3 layers of GFRP (Unidirectional and 45° and 135°)....	209
3.5	Calculation of Effective Length and Bond Capacity of FRP Plate with Two Layers Angled Laminate (45° and 135°).....	209
3.6	Effective Bond Areas for GFRP Restrainer.....	210
3.7	Area of GFRP Restrainer Bonded to Blocks is Double the Effective Bond Area.....	211
3.8	Dimensions of GFRP Restrainer.....	212
3.9	Calculation of Effective Length and Bond Capacity for CFRP Prior to Increase in Plate Size.....	213
3.10	Calculation of Effective Length and Bond Capacity of 3 Layers of CFRP (unidirectional, and 45° and 135°).....	214
3.11	Calculation of Effective Length and Bond Capacity of CFRP Plate with Two Layers of Angled Laminate 45° and 135°).....	214
3.12	Effective Bond Areas for CFRP Restrainer.....	215
3.13	Area of CFRP Restrainer Bonded to Blocks is Double The Effective Bond.....	216
3.14	Dimensions of CFRP Restrainer.....	217
3.15	Coating Unidirectional Segment of Hybrid Restrainer with SYLGARD 184 Silicone Elastomer.....	218
3.16	Bond Length Formulation for Angled Glass Epoxy Laminate Portion of FRP Plate.....	219
3.17	Bond Length Formulation for Angled and Unidirectional Glass Epoxy Laminate Portion of FRP Plate.....	219

3.18	Bond Length Formulation for Angled Glass and Unidirectional Carbon Epoxy Laminate Portion of FRP...	219
3.19	Components of Hybrid Restrainer Plate, (1) Angled Glass, (2) Unidirectional and Angled Glass, (3) Unidirectional Carbon and Angled Glass.....	220
3.20	Effective Bond Areas for Hybrid Restrainer.....	221
3.21	Area of Hybrid Restrainer Bonded to Blocks is Double the Effective Bond Area.....	222
3.22	Dimensions of Hybrid Restrainer.....	223
3.23	Epoxy Coating Process.....	224
3.24	Elastomer Coating Process.....	224
3.25	Assembling FRP Restrainers.....	225
3.26	Attaching FRP Restrainers to Shake Table Specimen...	226

CHAPTER 4

4.1	Test set-up for FRP bridge restrainer shake table Experiments.....	227
4.2	FRP restrainer test set-up.....	228
4.3	Caltrans ATC32E vs. artificial motion input into shake table.....	229
4.4	Instrumentation for GFRP restrainer tests.....	230
4.5	Instrumentation for CFRP restrainer tests.....	231
4.6	Instrumentation for hybrid FRP restrainer tests.....	232

CHAPTER 5

5.1	GFRP restrainer shake table tests.....	233
5.2	CFRP restrainer shake table tests.....	233
5.3	CGFRP restrainer shake table tests.....	233
5.4	Effect of Earthquake Motion on GFRP Restrainers.....	234
5.5.a	Acceleration History GFRP Restrainer Test, PGA = 0.05g ATC32E.....	235
5.5.b	Displacement History GFRP Restrainer Test, PGA = 0.05g ATC32E.....	235
5.5.c	Force History GFRP Restrainer Test, PGA = 0.05g ATC32E.....	235
5.6.a	Acceleration History GFRP Restrainer Test, PGA = 0.1g ATC32E.....	236
5.6.b	Displacement History GFRP Restrainer Test, PGA = 0.1g ATC32E.....	236
5.6.c	Force History GFRP Restrainer Test, PGA = 0.1g ATC32E.....	236
5.7.a	Acceleration History GFRP Restrainer Test, PGA = 0.15g ATC32E.....	237
5.7.b	Displacement History GFRP Restrainer Test, PGA = 0.15g ATC32E.....	237

5.7.c	Force History GFRP Restrainer Test, PGA = 0.15g ATC32E.....	237
5.8.a	Acceleration History GFRP Restrainer Test, PGA = 0.2g ATC32E.....	238
5.8.b	Displacement History GFRP Restrainer Test, PGA = 0.2g ATC32E.....	238
5.8.c	Force History GFRP Restrainer Test, PGA = 0.2g ATC32E.....	238
5.9.a	Acceleration History GFRP Restrainer Test, PGA = 0.25g ATC32E.....	239
5.9.b	Displacement History GFRP Restrainer Test, PGA = 0.25g ATC32E.....	239
5.9.c	Force History GFRP Restrainer Test, PGA = 0.25g ATC32E.....	239
5.10.a	Acceleration History GFRP Restrainer Test, PGA = 0.3g ATC32E.....	240
5.10.b	Displacement History GFRP Restrainer Test, PGA = 0.3g ATC32E.....	240
5.10.c	Force History GFRP Restrainer Test, PGA = 0.3g ATC32E.....	240
5.11	Effect of Earthquake Motion on CFRP Restrainers.....	241
5.12	Rupture of South-Side CFRP Restrainer (Top to Bottom).....	242
5.13.a	Acceleration History CFRP Restrainer Test, PGA = 0.05g, ATC32E.....	243
5.13.b	Displacement History CFRP Restrainer Test, PGA = 0.05g, ATC32E.....	243
5.14.c	Force History, CFRP Restrainer Test, PGA = 0.05g, ATC32E.....	243
5.14.a	Acceleration History CFRP Restrainer Test, PGA = 0.1g, ATC32E.....	244
5.14.b	Displacement History CFRP Restrainer Test, PGA = 0.1g, ATC32E.....	244
5.14.c	Force History, CFRP Restrainer Test, PGA = 0.1g, ATC32E.....	244
5.15.a	Acceleration History CFRP Restrainer Test, PGA = 0.15g, ATC32E.....	245
5.15.b	Displacement History CFRP Restrainer Test, PGA = 0.15g, ATC32E.....	245
5.15.c	Force History, CFRP Restrainer Test, PGA = 0.15g, ATC32E.....	245
5.16.a	Acceleration History CFRP Restrainer Test, PGA = 0.2g, ATC32E.....	246
5.16.b	Displacement History CFRP Restrainer Test, PGA = 0.2g, ATC32E.....	246

5.16.c	Force History, CFRP Restrainer Test, PGA = 0.2g, ATC32E.....	246
5.17	Effect of Earthquake Motion on CGFRP Restrainers, Unidirectional Motion, ATC32E.....	247
5.18.a	Acceleration History Hybrid (long) Restrainer Test, PGA = 0.05g, ATC32E.....	248
5.18.b	Displacement History Hybrid (long) Restrainer Test, PGA = 0.05g, ATC32E.....	248
5.18.c	Force History Hybrid (long) Restrainer Test, PGA = 0.05g, ATC32E.....	248
5.19.a	Acceleration History Hybrid (long) Restrainer Test, PGA = 0.1g, ATC32E.....	249
5.19.b	Displacement History Hybrid (long) Restrainer Test, PGA = 0.1g, ATC32E.....	249
5.19.c	Force History Hybrid (long) Restrainer Test, PGA = 0.1g, ATC32E.....	249
5.20.a	Acceleration History Hybrid (long) Restrainer Test, PGA = 0.15g, ATC32E.....	250
5.20.b	Displacement History Hybrid (long) Restrainer Test, PGA = 0.15g, ATC32E.....	250
5.20.c	Force History Hybrid (long) Restrainer Test, PGA = 0.15g, ATC32E.....	250
5.21.a	Acceleration History Hybrid (long) Restrainer Test, PGA = 0.2g, ATC32E.....	251
5.21.b	Displacement History Hybrid (long) Restrainer Test, PGA = 0.2g, ATC32E.....	251
5.21.c	Force History Hybrid (long) Restrainer Test, PGA = 0.2g, ATC32E.....	251
5.22.a	Acceleration History Hybrid (long) Restrainer Test, PGA = 0.25g, ATC32E.....	252
5.22.b	Displacement History Hybrid (long) Restrainer Test, PGA = 0.25g, ATC32E.....	252
5.22.c	Force History Hybrid (long) Restrainer Test, PGA = 0.25g, ATC32E.....	252
5.23.a	Acceleration History Hybrid (long) Restrainer Test, PGA = 0.3g, ATC32E.....	253
5.23.b	Displacement History Hybrid (long) Restrainer Test, PGA = 0.3g, ATC32E.....	253
5.23.c	Force History Hybrid (long) Restrainer Test, PGA = 0.3g, ATC32E.....	253
5.24	Effect of Near Fault Earthquake Motion, Sylmar, on CGFRP Restrainers.....	254
5.25.a	Acceleration History Hybrid (long) Restrainer Test, PGA = 0.15g, Sylmar.....	255

5.25.b	Displacement History Hybrid (long) Restrainer Test, PGA = 0.15g, Sylmar.....	255
5.25.c	Force History Hybrid (long) Restrainer Test, PGA = 0.15g, Sylmar.....	255
5.26.a	Acceleration History Hybrid (long) Restrainer Test, PGA = 0.3g, Sylmar.....	256
5.26.b	Displacement History Hybrid (long) Restrainer Test, PGA = 0.3g, Sylmar.....	256
5.26.c	Force History Hybrid (long) Restrainer Test, PGA = 0.3g, Sylmar.....	256
5.27	Effect of Earthquake Motion on CGFRP Restrainers Transverse Motion, ACT32E.....	257
5.28	Close Up of Debonding of FRP Plate from Transverse Motion at a PGA of 0.05g and 0.1g, ATC32E.....	258
5.29.a	Displacement History Hybrid(trans) Restrainer Test PGA = 0.05, ATC32E.....	259
5.29.b	Displacement History Hybrid(trans) Restrainer Test PGA = 0.05g. ATC32E. Restrainer Elongation Readings Taken in the Longitudinal Direction.....	259
5.30.a	Displacement History Hybrid(trans) Restrainer Test PGA = 0.1g, ATC32E.....	260
5.30.b	Displacement History Hybrid(trans) Restrainer Test, PGA = 0.1g, ATC32E. Restrainer Elongation Readings Taken in the Longitudinal Direction.....	262
5.31	Tyfo Fibrwrap Anchors.....	261

CHAPTER 6

6.1.a	Block Acceleration Histories, ATC32E, PGA = 0.05g.....	262
6.1.b	FRP Restrainer Elongation Histories, ATC32E, PGA = 0.05g.....	262
6.1.c	FRP Total Restrainer Force Histories, ATC32E, PGA = 0.05g.....	262
6.2.a	Block Acceleration Histories, ATC32E, PGA = 0.1g.....	263
6.2.b	FRP Restrainer Elongation Histories, ATC32E, PGA = 0.1g.....	263
6.2.c	FRP Total Restrainer Force Histories, ATC32E, PGA = 0.1g.....	263
6.3.a	Block Acceleration Histories, Case 1, PGA = 0.15g.....	264
6.3.b	FRP Restrainer Elongation Histories, Case 1, PGA = 0.15g.....	264
6.3.c	FRP Total Restrainer Force Histories, Case 1, PGA = 0.15g.....	264
6.4.a	Block Acceleration Histories, Case 2, PGA = 0.2g.....	265

6.4.b	FRP Restrainer Elongation Histories, Case 2, PGA = 0.2g.....	265
6.4.c	FRP Total Restrainer Force Histories, Case 2, PGA = 0.2g.....	265
6.5.a	Block Acceleration Histories, ATC32E, PGA = 0.15g.....	266
6.5.b	FRP Restrainer Elongation Histories, ACT32E, PGA = 0.15g.....	266
6.5.c	FRP Total Restrainer Force Histories, ACT32E, PGA = 0.15g.....	266
6.6.a	Block Acceleration Histories, ATC32E, PGA = 0.3g.....	267
6.6.b	FRP Restrainer Elongation Histories, ACT32E, PGA = 0.3g.....	267
6.6.c	FRP Total Restrainer Force Histories, ACT32E, PGA = 0.3g.....	267
6.7	Earthquake Spectra from CGFRP Restrainer Shake Table Tests ACT32E vs Sylmar, Case 1.....	268
6.8.a	Acceleration History, CGFRP Restrainer Tests, PGA = 0.15.....	269
6.8.b	Restrainer Elongation History, CGFRP Restrainer Tests, PGA = 0.15g.....	269
6.8.c	Total Restrainer Force History, CGFRP Restrainer Tests, PGA = 0.15g.....	269
6.9.a	Acceleration History, CGFRP Restrainer Tests, PGA = 0.3g.....	270
6.9.b	Restrainer Elongation History, CGFRP Restrainer Tests, PGA = 0.3g.....	270
6.9.c	Total Restrainer Force History, CGFRP Restrainer Tests, PGA = 0.2g.....	270
6.10	Earthquake Spectras from Steel, SMA and GFRP Restrainer Shake Table Tests, Case 1.....	271
6.11	Earthquake Spectras from Steel, SMA and GFRP Restrainer Shake Table Tests, Case 2.....	272
6.12	Maximum Elongation of Different Restrainer Types, Case 1.....	273
6.13	Maximum Elongation of Different Restrainer Types, Case 2.....	273
6.14.a	Block Acceleration Histories from Comparable GFRP, Steel and SMA Restrainer Tests, Case 1.....	274
6.14.b	Block Acceleration Histories from Comparable GRFP, Steel, and SMA Restrainer Tests, Case 2.....	274
6.15.a	Relative Hinge Movement Histories from Comparable GFRP, Steel, and SMA Restrainer Tests, Case 1.....	275
6.15.b	Relative Hinge Movement Histories from Comparable GFRP, Steel, and SMA Restrainer Tests, Case 2.....	275

6.16.a	Total Restrainer Force Histories from Comparable GFRP, Steel, and SMA Restrainer Tests, Case 1.....	276
6.16.b	Total Restrainer Force Histories from Comparable GFRP, Steel, and SMA Restrainer Tests, Case 2.....	276

CHAPTER 7

7.1	2 DOF of system Converted to Single DOF System with FRP Restrainer.....	277
7.2	Equilibrium of Forces for System with FRP Restrainer.....	277
7.3	Design Response Spectrum used for Design Procedures...	278
7.4	Design Dimensions for CFRP Restrainer.....	279

CHAPTER 1

INTRODUCTION

1.1 General Perspective

Multi-frame bridges are common in the construction of medium and long bridges. The necessity of inhibiting longitudinal displacement in the in-span hinge region of these bridges initiated the seismic restrainer design retrofit program in California after the San Fernando earthquake in 1971. This retrofit program included the installation of restrainers at hinges and bearings to limit the longitudinal movement and keep the structure tied together during the severe shaking of earthquakes.

The main purpose of restrainers is to prevent spans from falling off their supports during the maximum credible earthquake. The most common type of restrainers in the United States is the cable restrainer. The cable restrainers used in California are made of high-strength steel. These steel cables are anchored to the diaphragms or webs of concrete bridges or to the bottom flange of steel girders (Vlassis et al 2000). Past tests were conducted at the University of Nevada, Reno (UNR) to explore the use of shape memory alloy restraining device to address shortcomings of traditional steel restrainers (Johnson et al 2004). The research conducted in this project involves the testing, manufacture and design procedure for a bridge restrainer made with another alternative material, fiber reinforced plastics (FRP).

FRP is a material familiar in civil engineering as a means of externally increasing the strength of structures. The interest in fiber composites for construction applications is growing very rapidly. The flexibility and high strength of FRP fabric makes it an intriguing material. These qualities of high tensile strength, low weight and flexibility also make it a material worth investigating as a possible alternative to steel in seismic restrainers. Using FRP as a material for seismic bridge restrainers is a new and innovative idea. Beneficial aspects of FRP restrainers compared to steel restrainers are: (1) Installation of conventional restrainers is intrusive, requiring drilling of concrete, whereas, FRP restrainers are epoxied directly onto the outside of the bridge after minimal surface preparation; (2) In many cases conventional restrainers are hidden, making them hard to inspect, whereas, FRP restrainers are visible; (3) Unlike conventional restrainers, FRP restrainers do not require an attachment system; (4) Availability of the material and economical manufacturing translates into low costs. FRP restrainers offer ease of installation and inspection, in addition to having high strength. This project examines the feasibility of using FRP restrainers as a viable option to steel restrainers for the seismic retrofit of bridges.

1.2 Previous Studies

The section provides a review of both previous work pertaining to cyclic loading of FRP and previous studies of restrainers. Past research on cyclic or rapid strain rate effect on FRP was investigated because restrainers are subjected to dynamic cyclic loading and information about FRP dynamic response would be relevant. No literature was found on the effect of dynamic loading on performance of FRP. Previous studies on the seismic performance of bridge restrainers were also studied to establish both the shortcomings and design parameters for in-span hinge cable restrainers. Because FRP restrainers only take tensile forces, they can be compared to traditional cable bridge restrainers.

1.2.1 FRP Under Cyclic Loading

Bizindavyi et al. 2003

An experimental study was conducted on bonded FRP-to-concrete joints under cyclic loading. Single lap tests were done to determine the failure modes after repeated, up to 2.0×10^6 cycles. The specimens were subjected to low amplitude loading frequency. The researchers found that for specimen with equivalent effective bond area, a length beyond the effective bond length resulted in lower maximum slip. They also found that narrower bond widths exhibited higher values of slip than those having larger widths when subjected to repeated cycles of loading. It was observed that the shorter the bonded area, the higher the bond stress intensity and the shorter the fatigue life of the connection.

Tan et al. 2003

Direct tensile tests were conducted at the National University of Singapore to determine the interfacial bond strength of continuous fiber sheets bonded to concrete. Single lap tests were performed on specimens under cyclic loading. These tensile tests were performed at a slow rate of 0.1 mm/min (6.56×10^{-5} in/sec). It was found that bond resistance increased with bond length and concrete strength. It was also found that bond width had a significant effect on the fatigue bond resistance, with wider bond width leading to better resistance. Debonding was initiated by shear failure in the concrete near the joint. Once shear cracks began to appear, the failure zone propagated very rapidly resulting in total debonding, with a shattered thin layer of concrete still bonded to the FRP.

Zhao and Cho 2004

This paper investigated the impact induced damage initiation and propagation in laminated composite shell under low-velocity impact. The damage propagation with composite plate and shell proceeded differently. As the contact force built up, the damage propagated at the outer layer first and then progressed into inner layers in the composite shell. In a composite plate, the damage was found to initiate in the bottom layer and proceed to the inner layers. The damage modes were matrix cracking, fiber breakage, and delamination.

Colak 2004

In this study, the mechanical behavior of PBXW-128 and PBXN-110 polymer cylindrical specimens under uniaxial compression were investigated. Both of these polymers were in the inert form. The experiments at room temperature were conducted at three different strain rates, 10^{-4} , 10^{-2} , and $10^0/s$. These tests concluded that the stress-strain response of these polymers was insensitive to strain rate.

1.2.2 Recent Studies on Dynamic Performance of Restrainers

Since the San Fernando earthquake in California in 1971, two major design procedures have been used in the U.S. They include the force based AASHTO method and the displacement based equivalent static procedure used by CALTRANS. Since the late 1980's, research in bridge restrainer design and analysis increased with many important studies; Selna et al., 1989, Saiidi et al., 1992, Yang et al., 1994, Trochalakis et al., 1996, Fenves and DesRoches, 1996, Hudgings et al., 1997, and Randall et al., 1998. Japanese code for restrainers is similar to the AASHTO restrainer design procedure. It is force based and does not consider relative displacement between the bridge frames (DesRoches and Fenves 2001). This section includes a review of new developments and important recent work related to the application of seismic restrainers.

Vlassis et al. 2000

The main objectives of this study were to investigate the pounding between adjacent bridge spans at in-span hinges, to evaluate the performance and efficiency of seismic restrainers in inhibiting relative displacements across the hinges, and to assess the effects of restrainer gap. Cable restrainers were used to connect the specimen consisting of two box girder reinforced concrete blocks representative of adjacent bridge spans. The experimental results concluded that impact between adjacent spans during out-of-phase motion produce larger than expected accelerations levels, that restrainers were capable of reducing hinge relative displacements, and that a zero restrainer gap resulted in significantly higher restrainer forces compared to cases with slack.

Shinozuka et al. 2000

This study determined the effectiveness of damper/restrainers. The damper/restrainer consisted of a nonlinear viscous damper and an elastic spring connected in parallel. A finite element analysis of this numerical simulation study determined that damper restrainers were highly effective in reducing both relative hinge displacements and impact forces due to pounding expansion joints.

DesRoches et al. 2000

This work involved both a new restrainer design procedure using modal analysis to determine the response of tension-only in-span hinge restrainers of a multiple-frame bridge and examined the factors affecting the response of intermediate hinges. The restrainer design method was only valid for hinges and not for abutments. A simplified version of this design method is discussed in Chapter 7. The conclusions of this study determined that maximum hinge displacement is a function of frame period ratio, frame target displacement ductility, and characteristics of the ground motion. This study also concluded that pounding increased relative hinge displacement in out-of-phase frames but decreased hinge displacement in in-phase frames. A new design method was developed and found to be more rational than the current AASHTO and Caltrans methods. Modal analysis was incorporated into the design method to account for the dynamic characteristics of the adjacent bridge frames.

Watanabe, G., and Kawashima, K. 2004

This research was on the effectiveness of cable-restrainers for mitigating rotation of skewed bridge subjected to strong ground shaking. Skewed bridges show very unique structural response as a result of pounding between frames during earthquake motion because of their rotational response. This research found that by providing restrainers that limit displacement, thus controlling separation between adjacent decks, rotation of the decks during earthquake motion is effectively mitigated.

Saiidi et al. 2004

The main objectives of this study were to investigate the effect of some important parameters on the behavior of multiple-frame bridges retrofitted with steel cable restrainers subjected to longitudinal earthquake motion. This study found that the most critical case of restrainer slack is when the initial slack is equal to zero, resulting in higher forces. Ground motions for soft soil type were used, resulting in higher spectral accelerations for period ratios between adjacent bridge frames of less than 0.7.

Maragakis, E. et al. 2004

Shape memory alloy (SMA) bridge restrainers were tested on a representative in-span hinge of a multi-span bridge to determine their performance. The tests were conducted at UNR, in cooperation with Georgia Institute of Technology. Another objective of this study was to compare the performance of SMA to steel restrainers. The SMA restrainers showed promise as restraining devices to limit hinge displacement in bridges and the ability to dissipate energy. Under equivalent loading, the SMA restrainers produced both smaller relative displacement and lower maximum block accelerations than the steel restrainers.

The above studies demonstrated the effectiveness of mostly steel restrainers and provided design tools that may be generally applied to different restrainer types.

The studies also revealed that restrainers made from shape memory alloys have the potential of being at least as effective as steel restrainers.

1.3 Objectives and Scope

The objective of this study was to determine the feasibility of developing and testing a bridge restrainer made of FRP. To accomplish these objectives, material tests and bond tests were conducted, followed by development and shake table testing of three restrainer types. A new restrainer design method was developed and is illustrated through an example in Chapter 7.

This four-part project included:

- Material tests on uncoated and elastomer coated glass and carbon strips
- FRP/concrete bond tests to determine the mode of failure and bond strength between FRP and concrete
- Design of an FRP bridge restrainer
- Developing a tentative design procedure for FRP restrainers

The material tests and bond tests were conducted at various strain rates, from static to dynamic, to determine if there is an apparent strain rate effect for composite lamina. Strain rate effect, or the possible effect of changing strength with increase of strain rate, is of interest in restrainer design because of the dynamic nature of earthquake movement. The strain rate could potentially affect both the FRP strength properties and bond to concrete. The mode of failure of the bond between FRP and concrete was also of interest in this study. Past studies on FRP/concrete strength and failure modes have been conducted but no studies could be found that also incorporated the effect of various strain rates.

Results from the material tests, led to the development of an FRP restrainer. FRP restrainer dimensions were calculated based on both current material tests and data collected during past SMA and steel restrainer tests. Three types of FRP restrainers were manufactured. They consist of glass (GFRP), carbon (CFRP), and a hybrid (GCFRP), consisting of glass and carbon composite laminate.

An identical test set-up was used for the steel, SMA and FRP restrainer tests to allow comparison among these three restrainer types. Previous steel and SMA restrainer tests, conducted at the UNR large-scale structures lab, provided the test protocol used in the FRP restrainer shake table tests. The primary focus was on the performance of FRP restrainers under longitudinal motions, but limited tests were conducted using transverse motions. Several current design procedures were investigated to determine their applicability to FRP restrainer design. A new simple force-based method was developed for restrainer design and is illustrated through an example.

CHAPTER 2

MATERIAL STUDIES

2.1. Introduction

Material tests at various strain rates were performed on the glass and carbon fiber reinforced polymer (FRP) fabrics used in the restrainer experiments. Tensile tests were carried out on fabric strips to obtain the ultimate fabric strength. Following tensile tests on uncoated (dry) fabrics, the necessity of a coating became apparent to ensure composite action among fibers. An elastomer material was chosen to coat the fabrics and ensure better strength performance. The tensile test results were analyzed to determine the effect of strain rate on FRP. The last set of material tests were conducted to determine the strain rate effect on the interfacial bond strength between externally bonded FRP fabrics and concrete. The results from these tests were analyzed to determine bond strength and failure mode at different strain rates. This chapter describes the specimens, the testing procedure, and the results.

2.2 Introduction to Strain Rate Effect

Past studies have concluded that stress-strain properties are a function of loading rate. A significant increase in strength has been generally observed at higher strain rates. These effects may be especially noteworthy for blast loading and near fault earthquakes, which have high velocities that will result in high strain rates (Saiidi 2004). Several studies have been reported on steel and concrete subjected to dynamic strain rates from about 10^4 to about 10^9 microstrains/second ($\mu\epsilon/\text{sec}$). Past research has shown that at high strain rates, there is an effect on steel and concrete properties. At $50000 \mu\epsilon/\text{sec}$, concrete compressive strength increases by approximately 25%. Peak load and the area under the load-deflection diagram increase with the rate of straining (Kulkarni and Shah 1998). In steel, loading at a high rate results in f_y increasing by 10 to 20 percent (Paulay and Priestley 1992). Figure 2-1 shows an example of strength increase in steel with an increase of strain rate (Handwerker 2003). The reason for this increase of strength with higher strain rates is believed to be from the extremely localized yielding due to enhanced bond among the molecules at high rates. Internal friction or slippage does not have time to occur under high strain rate. Figure 2-2 and 2-3 show a close-up of the failure mode of a steel coupon subjected to tensile tests at low strain rate of $167 \mu\epsilon/\text{sec}$, Fig. 2-2, and high strain rate of $100000 \mu\epsilon/\text{sec}$, Fig. 2-3. The steel specimen subjected to a slow rate shows a relatively smooth failure surface. In Fig. 2-3, the higher strain rate during tensile tests resulted in a more irregular failure plane. This irregularity is a consequence of insufficient time for the load to distribute to other parts of the section during tensile tests under high strain rates (Dusicka 2004).

Strain rate effect of FRP was of interest due to the dynamic nature of earthquake loading that was to be applied in the FRP restrainer tests. Data from earlier steel and shape memory alloy (SMA) tests conducted on shake tables in the large-scale structures laboratory at the University of Nevada, Reno, were analyzed. The data revealed restrainer strain rates in excess of 100,000 $\mu\epsilon/\text{sec}$. Both of these restrainers were subjected to the Applied Technology Council record ATC32E ground motion in the longitudinal direction (Caltrans 2001). The ground acceleration used in these two shake table tests had a PGA of 0.15g. Figure 2-4 shows the strain rate history for a steel restrainer (Camargo-Sanchez et al. 2004). In 2003, SMA restrainers of equivalent stiffness to the steel restrainers were tested on a shake table. The SMA restrainer tests show strain rates in excess of 200,000 $\mu\epsilon/\text{sec}$ [use consistent form of units- either spell out or use abbreviation. Figure 2-5 illustrates the data for high amplitude rates. It can be noted that strain rates in excess of 100,000 $\mu\epsilon/\text{sec}$ occurred in seven instances. The maximum strain rates revealed in Fig. 2-4 and 2-5 determined the target strain rates that were used in the FRP tensile tests.

2.3 Test Protocol

A test protocol was developed to assess 25.4 mm (1 in) wide, 305 mm (12 in) long glass and carbon fabric strips in an MTS load frame tensile testing machine at various strain rates. The maximum strain rate that could be applied was 100000 $\mu\epsilon/\text{sec}$. At least three samples per rate were tested in accordance with ASTM standards D3039. According to the test method, “a thin flat strip of material having a constant rectangular cross section is mounted in the grips of a mechanical testing machine and monotonically loaded in tension. The ultimate strength of the material can be determined from the maximum load carried before failure.” A standard head displacement rate of 2 mm/min (167 $\mu\epsilon/\text{sec}$) was suggested for a constant static rate. Constant dynamic rates of 1000, 5000, 10000, 50000, and 100000 $\mu\epsilon/\text{sec}$ were used in the tests.

2.4 Material Test Set-Up and Instrumentation

Flex Test IIM Controllers ran the MTS load frame seen in Fig. 2-6. National Instruments and Flex Test IIM Controllers ran the data acquisition system. The specimens were inserted approximately 51.4 mm (2 in) on both ends into the grip jaws of the load frame. The grip surfaces on the wedge-action grips were lightly serrated and every effort was made to prevent premature failure due to misalignment of the strips. An input displacement rate, i.e. inches/second, was fed into the controller. This rate was then converted to strain rate by dividing the input rate by the gage length. This resulted in the input displacement rates of 167, 1000, 5000, 10000, 50000, 100000 $\mu\epsilon/\text{sec}$. The strain response was determined from reading laser targets placed on the strips. The laser strips, seen in Fig. 2-7, were placed on the center portion of the strips approximately 51.4 mm

(2 in) apart. These targets were read by the data acquisition system to determine the strain.

2.5 Plain Fabric Tensile Tests

Ordinary glass and carbon fabric, provided by the Fyfe Corp., was chosen for the tensile tests with the aim of producing a restrainer with common materials. The glass fabric was a Tyfo SEH-51A fabric. It is a unidirectional glass fabric normally used as a reinforcing fabric in a fiberwrap system. The glass material is oriented in the 0° direction with additional yellow glass cross fibers at 90°. The carbon fabric was a Tyfo SCH-41. It is a unidirectional carbon fabric with glass veil backing for added fabric stability during installation. The carbon material is oriented in the 0° direction. As with the glass fabric, the SCH-41 is normally used as a reinforcing fabric in a composite system (Fyfe Co. 2003). Table 2-1 displays the plain and laminate composite fabric properties for both the glass (GFRP) and carbon (CFRP) as reported by the supplier. The GFRP laminate has an elongation at break of 2.2 percent and design strength of 460 MPa (66.7 ksi) in the primary direction. The CFRP laminate has a design composite strength of 745 MPa (108 ksi) and a 1.2 percent elongation until break. The laminate thicknesses of GFRP and CFRP are 1.3 mm. (0.05 in.) and 1.0 mm. (0.04 in.), respectively. The measured properties are in accordance with ASTM D3039 and ASTM C1557-03

An example of the first series of material tests, seen in Fig. 2-7, consisted of strips of uncoated glass and carbon fabric pulled on the MTS load frame to determine failure mode, strength, elongation at break, and strain rate effect. Figure 2-8 and 2-9 show the marked ends that were used for guides while dipping the extremities of the strips in resin prior to testing. Upon cure, the Tyfo S resin and fabric created the composite ends necessary to produce a successful gripping action in the load frame. This resulted in a 203 mm. (8 in.) long and 25.4 mm. (1 in.) wide effective portion of plain fabric outside of the grips to be loaded in tension until failure.

2.5.1 Glass Fabric Test Results

In the first set of tests glass fabric strips were tested at the static rate (167 $\mu\epsilon/\text{sec}$) and five constant dynamic rates (1000 $\mu\epsilon/\text{sec}$ – 100000 $\mu\epsilon/\text{sec}$). Table 2-2 shows the results from these tensile tests. In accordance with the ASTM standards, at least three specimens per rate were tested. As seen in the right column of Table 2-2, the failure of the uncoated glass strips was quite sudden and explosive, particularly at the higher strain rates. According to the manufacturer, the design ultimate tensile strength in the primary direction for fiberglass composite (Table 2-1) is 460 MPa (66.7 ksi). The average measured value for tensile strength of the uncoated glass strips was approximately 266 MPa (38.6 ksi). This 42% reduction in strength, from the design composite tensile

strength, was the result of the absence of load sharing among the fibers. The fiberglass acted more as individual fibers than as a unit. There also appeared to be a pattern of failure occurring at the edges. Figure 2-10 and 2-11 show the typical failure modes of the glass and carbon strips, respectively. Note that the failure occurred in the outer edges of the glass strip.

2.5.1.a. Stress-Strain Relationship

Figures 2-12 through 2-32 illustrate the measured stress strain relationship for the 21 uncoated glass strips tested under various strain rates. At small strains the results are erratic because the strips were not completely tight. Also, a small amount of noise can be seen in these graphs, possibly due to small laser tape slippage. The graphs show a linear stress-strain relationship up to failure. The manufacturer's specified elongation at break of 2.2% for the fiberglass, seen in Table 2-1, is generally consistent with the results of the measured strains at the peak stresses (Figs. 2-12 through 2-32). As stated earlier, the average maximum strength is approximately 42 percent below the design strength. The measured strength below 200 MPa (29 ksi), seen in Fig. 2-16 and 2-27, is a result of misalignment of the fabric strips upon insertion in the MTS load frame. Upon examination of the stress-strain results at various strain rates (167, 1000, 5000, 10000, 50000, 100000 $\mu\text{E}/\text{sec}$), there does not appear to be a clear increase of strength with strain rate. This will be discussed later in this chapter.

2.5.2 Carbon Fabric Test Results

The results from the plain carbon strip tensile tests are listed in Table 2-3. The test protocol used for the glass strip tests was repeated for the carbon tensile tests. The same range of strain rates were used, 167 to 100000 $\mu\text{E}/\text{sec}$. Unlike the glass strips, the carbon strips did not fail in an explosive manner. According to Fyfe Co, the manufacturer, the design tensile strength for a strip of carbon composite in the primary direction is 745 MPa (108 ksi). The average measured tensile strength for the carbon strips was approximately 516 MPa (74.8 ksi). This was 31% lower than the expected composite strength. The reduction in strength in the glass was 42%. This improvement of strength comparison for carbon fabric, from the design to the measured tensile strength, appears to be from the system holding the longitudinal threads together. In the glass material, cross fibers of yellow glass hold the glass material into the composition of a fabric. In the carbon material, the longitudinal carbon fibers are held together in an interlocking system. This interlocking system, seen in Fig. 2-10, resulted in better stress distribution across the fibers and appeared to reduce the edge effect seen in the tensile failure of the glass strips. It appears that the geometrical structure of the fabric has a significant influence on its tensile strength.

2.5.2.a. Stress-Strain Relationship

The stress-strain relationship of the uncoated carbon strips is illustrated in Figures 2-33 through 2-51. As with the glass strips, the linearity of this material is observable in these graphs. A clear trend in strength change with increase of strain rate (strain rate effect) is not demonstrated in these stress-strain relationships, or in the data listed in Table 2-3. As seen in Table 2-1, the manufacturer's specified elongation at break for carbon is 1.2 percent. These diagrams verify this strain at maximum stress for this material. As with the glass stress-strain graphs, a slight amount of noise from the slippage of laser targets during the tensile tests is visible. A minimum strength of 441 MPa (64 ksi) is seen in seventeen of these nineteen diagrams. A lower strength appears in Fig. 2-34 and Fig. 2-46 as a result of possible misalignment of the carbon strips in the MTS load frame grips.

2.6. Flexible Composites

The poor strength performance and failure mode seen in the above tensile tests on plain glass and carbon strips confirmed the necessity for a composite action among fibers to fully mobilize the entire width. The word *composite material* signifies that two or more materials are combined on a macroscopic scale to form a useful third material. While the long fibers of the glass and carbon in the fabric are inherently much stiffer and stronger than the same material in bulk form, composite action is crucial in enabling the constituents for proper load distribution among the fibers. The fact that this is on a macroscopic scale vs. a microscopic scale signifies that the components of the different materials can be seen with the naked eye (Jones 1999). Stiff composites are commonly seen in civil engineering as a replacement for traditional materials or as an element in strengthening columns. For application as a bridge restraining device, a flexible composite action was required. It was necessary for the portion of the restrainer in the hinge area to provide high tensile strength while being sufficiently flexible to buckle under compression without building up significant stresses.

A coating system developed by Dr. Luo, a professor of the Mechanical Engineering Department at the University of Nevada Reno, was used to prepare flexible composites (Lu 1993, Luo 1988, Mitra 1995). The flexible composite was produced with textile fabrics and SYLGARD 184 silicone elastomer, a product of Dow Chemical. "Fabric reinforced flexible composites, such as rubber-coated fabrics, can undergo relatively large deformation. They have very good formability while retaining high strength. There are many applications such as inflatable structures, air-bag material, etc. (Luo and Mitra 1999)." These characteristics of flexible composites also make them ideal as material for bridge restrainers.

2.6.1. SYLGARD 184 Silicone Elastomer

SYLGARD 184 is a silicone that cures to a flexible elastomer. It is commonly used as an encapsulate for electrical components because of its good dielectric properties. SYLGARD 184 also has elongation of up to 100%, stability over a wide temperature range (-55C to 200C), repairability, good fatigue resistance and adhesion properties, and low shrinkage and retraction (DOW Corning 2004). It is these former qualities that make SYLGARD 184 a desirable component in a flexible composite used in a civil engineering application. Properties of SYLGARD 184 silicone elastomer are listed in Table 2-4.

SYLGARD 184 is supplied in two parts, a base and curing agent, mixed in a ratio of 10 parts base to one part curing agent, by weight. Cure is evidenced by a gradual increase in viscosity, followed by gelation and conversion to a solid elastomer. At 25 C, the pot life of SYLGARD 184 silicone elastomer is 2 hours. The viscosity of SYLGARD 184-elastomer, base, and curing agent can be lowered by the addition of 200 fluid, 50cST. Quantities of 10 percent or less will have little or no effect on the physical qualities. DOW Corning 1200 RTV Prime Coat is recommended to coat material prior to application of SYLGARD 184 elastomer to promote adhesion. For best results, the prime coat should be used within 2 hours of elastomer coating.

Air bubbles are usually present following mixing of SYLGARD 184 silicone elastomer base and curing agent. Vacuum de-airing is recommended. The elastomer should be vacuumed in a container with at least four times the liquid volume to allow for expansion of material. In the present study, the mixture was first vacuumed in a glass container using a vacuum of 635 mm to 737 mm (25 in to 29 in) of mercury. Following this initial evacuation of air, the material was coated with the vacuumed SYLGARD 184 and placed in a vacuum box constructed in the University of Nevada, Reno Large Scale Structures Lab. This coated fabric was again vacuumed to remove excess air from the mixture and promote thorough covering of the fabric. The vacuum was continued until the liquid expanded and settled to its original volume and bubbling subsided. This second vacuuming took approximately 30 minutes because the addition of the 200 fluid helped reduce the viscosity and decrease the time needed to vacuum the system.

2.6.2. Vacuum Box

Construction of a vacuum box was necessary to vacuum the flexible composite. It was desirable to observe the de-airing process. Thus Acrylite Plus, a clear acrylic, was the material of choice for the box. Properties of Acrylite Plus are listed in Table 2-5. These properties were used to calculate the box dimensions required to meet the strength demands and deflection capacity necessary to introduce the 30% vacuum from 101 kPa to 80 kPa (14.7 psi to 11.6 psi)

recommended by Dow Chemical. The sides of the box were analyzed using the plates theory (Timoshenko 1976). The restrainer dimensions determined the required top and bottom box dimensions of 610 mm. by 914 mm. (2 ft. by 3 ft.). A minimum top and bottom thickness of 25.4 mm (1.25 in) and minimum side thickness of 3 mm. (0.1 in) were required. The final vacuum box dimensions are seen in Fig. 2-52.

Construction of the vacuum box can be seen in Fig. 2-53. Weld-on, a welding chemical that melts the plastic pieces together, was used (Fig. 2-53 (b)). A fine line of weld-on was needed in the joints to form an airtight box. The top of the box seen in Fig. 2-53 (c) was formed with additional 6X6 mm² plastic strips melted onto the top piece to develop a self-sealing top. The completed vacuum system seen in Fig. 2-53 (d) consists of a thick glass bowl and lid used to vacuum the air introduced into the elastomer during mixing of the two-part base and curing agent. A small vacuum flow (0.0283 m³ (1 ft³) per minute) is sufficient for the first part of the vacuuming process. This first step takes between 10-15 minutes to de-air the SYLGARD 184, depending on its viscosity. The completed vacuum box seen in Fig. 2-13 (d) was used to vacuum the elastomer through the fabric. The second part of the vacuum process requires a larger vacuum pump, at least 5 cubic feet (SI) per minute, to de-air the composite before the elastomer becomes too viscous. The stronger pump is also needed to remove large air bubbles that may become trapped under the fabric. As stated earlier, this step takes between 20 - 30 minutes.

2.6.3. Elastomer Coating Process

Making the elastomer-coated strips for tensile tests involved a two-step process. Figure 2-54 and 2-55 show these two steps. The ends of the fabric had to be coated with resin to make a stiff composite required for the grips in the MTS load frame. This epoxy coating process, seen in Fig. 2-54, involved first painting resin onto the end portions of the fabric, Fig. 2-54 (a). Then excess resin was squeezed from the fabric, Fig 2-54 (b), to prevent excessive wicking of the epoxy into the middle section that would later be coated with elastomer. After the ends of the fabric had cured into a stiff composite, the middle section of the material was coated with elastomer. A step-by-step procedure for this process follows:

1. Cut fabric into required sections
2. Apply epoxy to the ends (last 51 mm (2 in)) of fabric. This will take approximately 3 days to dry
3. Apply Dow Corning 1200 prime coat to fabric. SYLGARD 184 will not normally bond to clean, nonporous surfaces such as metal or glass. A primer coat is required to ensure adhesion to these surfaces. This application should be put on at least 15 minutes and no more than 8 hours (best if 1 to 2 hours) before elastomer application to assure bonding between elastomer and fabric

4. Attach fabric, with dry epoxied ends, to Plexiglas sheet that is approximately 51 mm (2 in) longer than the ends of the fabric in the non-epoxied direction, and 76 mm (3 in) shorter than the fabric in the epoxied direction. When the fabric is placed on the sheet 38 mm (1.5 in) of epoxied ends from each side will overhang the sheet.
5. Clamp the fabric onto the Plexiglas sheet by sandwiching the fabric between metal strips. This will create a well in which to pour the elastomer.
4. To ensure that the well is leak proof, apply a thin strip of weather stripping between the composite material and the metal strips that are forming the well. Additional caulking may be used.
5. SYLGARD 184 silicone elastomer is supplied in two parts, a lot-matched base and curing agent, mixed in a ratio of 10 parts base to one part curing agent, by weight. For best curing results, glassware or tined cans and glass or metal stirring implements should be used.
6. Measure the accurate amount of elastomer base and curing agent (10 to 1). Mix with a smooth action that will minimize the introduction of excess air. Use a prewarmed bowl to help slow the mixture from becoming viscous too quickly.
7. Vacuum the elastomer mixture in a container with at least four times the liquid volume to allow for expansion of the material. When the pressure of the vacuum is down to 600 mm of mercury (1 atmosphere = 760 mm Hg) the air bubbles in the resin will be enlarged and elevate to the surface. For best results alternate atmospheric pressure with this reduced pressure. This process will take about ½ hour.
8. Clean and degrease all application surfaces using a solvent to remove all oils and surface contaminants. Dry and remove all solvent before application.
9. Pour approximately half of the elastomer mixture into the well and vacuum a few times.
10. Pour the remaining elastomer onto fabric that has been placed in the curing container. When practical pouring should be done under a vacuum, particularly for material with fine voids.
11. Use vacuum grease and caulking around the edges of the vacuum box to ensure a good vacuum.
12. A vacuum pump connected to the vacuum box should work continuously to provide a vacuum environment, which can eliminate any remaining air from the composite. A vibrational table will help wet all of the fibers.
13. After the elastomer is fairly stable, approximately 2-3 hours, smooth the top with a back and forth motion with a straight edge across the top of the frame.
14. A few minutes after the smoothing process, cover the top of the material with a sheet of Teflon or polyurethane to ensure a clean surface. This material picks up all floating particles, such as dust, during the curing process.

15. For best results in the curing process to better bond the fiber and matrix and reduce the air bubbles, cure at room temperature for 24 hours, then put it in an oven at 65C for another 24 hours.
16. Remove lamina from frame after it has cured. The metal should easily remove from the elastomer; remove anything else with a sharp knife.
17. A thin film should be placed on top of the lamina sheet before cutting. The film attached to the samples is peeled off just prior to testing in order to protect the surface of the specimens.

The final step in this process was to cut the completed fabric into 25.4 mm. (1 in.) wide, 305 mm. (12 in.) long pieces.

2.7. Elastomer Coated Fabric Tensile Tests

The second series of tensile tests for the elastomer coated fiberglass, Tyfo SEH-51A, and elastomer-coated carbon, Tyfo SCH-41; fabric strips had an identical test set-up and protocol as the first series of tests. A minimum of three specimens per strain rate for each fabric type was tested in accordance with ASTM standards. As in the earlier tests on the uncoated fabric strips, the MTS load frame was used to determine tensile strength. The expectation of the flexible composite fabric strip tests was to achieve a higher strength, closer to the manufacturers design strength for the glass and carbon composites.

A strong mechanical interaction between elastomer and fabric occur in the initial stage of tensile testing. The matrix material resists rearrangement of the fabric. The elastic modulus of elastomer is lower than the fabric and the composite is “soft” at this stage. Then, the geometrical arrangement of the fabric becomes stable and the fibers carry most of the load.

The manufacture and analysis of GFRP and CFRP bridge restrainers was the ultimate goal of this project. It was necessary to know the stiffness of the elastomer coated glass and carbon fabric to calculate restrainer force in the future experiments. The stiffness and modulus of elasticity of these coated strips were calculated from data collected in the tensile tests.

2.7.1. Glass Test Results

Figures 2-56 through 2-99 illustrate the force-displacement and stress-strain relationship of the glass elastomer coated strips subjected to tension. The stiffness of the material was calculated from the force-displacement diagram and the modulus of elasticity was found from the stress-strain diagram. Figure 2-99(a) shows the typical failure mode for the SYLGARD elastomer coated glass strips subjected to tension. The pattern of edge failure seen in the uncoated strips is also evident in the glass flexible composite strips. The strength of these glass-coated strips was fairly close to the maximum stress achieved in the uncoated glass strips. As stated earlier, the expectation in coating the strips was to increase the strength of this material by composite action. The geometric arrangement of the glass in these 25.4 mm. (1 in.) strips was more influential

than the flexible composite action in determining the strengths of these strips. Table 2-6 shows the average strength of both the uncoated (A) and coated fabric (B) strips under tensile loading. The right column of Table 2-6 shows the average ratios of strength of the coated vs. uncoated strips under various strain rates. It is evident that the elastomer did not affect the strength performance. A small amount of flexible composite action as a consequence from a “soft” initial stage and later “stiff” stage is seen in a few of the force-displacement and stress-strain relationship of these strips. Figures 2-56, 2-60, 2-62, 2-64 are examples of the initial “soft stage” resulting from the lower stiffness of the elastomer. It is seen in these figures, that after this initial stage, the system becomes stable and the fibers carry most of the load resulting in a stiffer system. As in the earlier uncoated glass strip tests, there does not appear to be a consistent trend of increasing strength with increase of strain rate.

Table 2-7 shows the stiffness and tensile modulus calculated for the coated glass fabric strips tensile tests. The calculated average stiffness for the elastomer-coated fiberglass is 9.0 kN/mm (51 kip/in) while the calculated tensile modulus is 16982 MPa (2462 ksi). This is below the manufacturers design tensile modulus of 20900 MPa (3030 ksi) which may be a result of the great influence of the geometric system of the fabric resulting from cross fibers connecting the unidirectional fibers for the 25.4 mm. (1 in.) strips. The low strength seen in this structure of connecting the fibers may be mitigated in a wider strip of fabric. Also note that the specified laminate properties are for epoxy-coated fibers and not for elastomer-coated fibers. The lower modulus of the elastomer may allow for a larger shear lag that would prevent the full participation of all the fibers in resisting the loads.

2.7.2. Carbon Test Results

The second set of elastomer coated fabric tensile tests involved carbon fabric strips covered with SYLGARD 184. Figures 2-100 Fig. 2-137 illustrate the individual strip force-displacement and stress-strain relationships. The edge failure seen in the flexible composite glass strips was not evident in the elastomer-coated strips. Figure 2-137(a) shows the typical mode of failure seen in the flexible CFRP strips. This figure illustrates that composite action between the carbon fibers resulted in rupture along the width of the strip, and not predominantly along the edge. As in the coated glass strip tests, the stiffness of the material and tensile modulus were calculated from these diagrams. The initial “soft” stage and consequent “stiff” stage of these flexible composite strips is evident in these diagrams. Figure 2-100 and 2-101 are typical of this phenomenon of an initial soft, followed by a stiff stage, associated with flexible composites.

Table 2-8 displays the tensile strength achieved, per strain rate, for both the coated and uncoated carbon fabric strips. There is a clear increase of

approximately 40% in the strength because of the elastomer coating. This is a result of the flexible composite action that is not evident in the coated glass strips. It appears that the difference between the strength results for the coated glass and carbon strips is the glass veil backing added for stability, and the more complex system connecting the unidirectional carbon fibers in addition to the effectiveness of the elastomer in distributing the load across the section. Table 2-8 shows the increased strength because of the coating but it also reveals clearly that the strength does not appear to be sensitive to strain rate.

The results of the stiffness and tensile modulus calculated from Fig. 2-100 to Fig. 2-137 are listed in Table 2-9. The measured average tensile modulus of 63000 MPa (9100 ksi) is above the manufacturer's design value for SCH-41 (carbon) composite. This is confirmation that, in the case of the elastomer coated carbon, forces are distributed across the fibers.

2.7.3. Comparison of Failure Modes

Comparisons of the tensile failure mode for the glass and carbon strips are shown in Fig. 2-138 and Fig. 2-139. These strips are viewed from low to high dynamic rate (left to right). The glass strips in Figure 2-138 show the great influence of the fabric structure in the way that these strips have failed in tension. The plain fabric strips, witnessed in Fig. 2-138 (b) have failed in an explosive manner while the elastomer coated strips seen in 2-138 (a) have failed more as a unit. They achieved similar tensile strength because the fabric structure had a great influence. The failure mode of the carbon strips, seen in Fig. 2-139 shows the edge effect expected in failure, but the improved system of unifying the unilateral fibers allowed the elastomer coated strip seen in Fig. 2-139 (a) to achieve design strength.

There is no clear evidence of a strain rate effect for either coated or uncoated fabric. Figures 2-140 and Fig. 2-141 reveal the strength ratio to strain rate relationship for the glass coated and carbon coated fabric strips subjected to tensile tests. There is significant scatter in the data in these two diagrams. The change in strength with strain rate is within scatter in the data. Internal slippage does not have time to occur in homogeneous materials at high strain rate, thus giving them higher strength. Unlike homogeneous materials, slippage of fibers does occur under all strain rates in FRP materials and hence no strain rate effect is seen.

2.8. FRP-Concrete Bond Strength

Debonding failures are often brittle and occur with little or no visible warning. Studies have shown that decreasing the shear stiffness of adhesives, increasing FRP stiffness, and increasing concrete strength all play a role in bond behavior. When properly prepared, the bond strength is greater than the shearing strength of the concrete to which the FRP is attached. The objects of these single lap

pullout tests were to verify that the minimum and often controlling factor of bond strength is related to the compressive strength of the concrete, to examine modes of failure and determine if a strain rate had an effect on bond strength. Tests were conducted to determine the effect of loading rate on bond strength between FRP and concrete. These tests consisted of both glass and carbon strips bonded to concrete blocks, assessed at static to dynamic strain rates (167, 1000, 5000, 10000, 50000, 100000 $\mu\epsilon/\text{sec}$). FRP is generally bonded to concrete by way of adhesives. Experimental and theoretical work exists on the bond strength between FRP and concrete. All design recommendations concerning debonding failures are based on the assumption that the interfacial strength depends on the concrete strength rather than the adhesive strength. This is because present day resins are so strong that interfacial failures occur in the concrete. The bond strength cannot always increase with an increase in the bond length and the ultimate tensile strength of the FRP plate may never be reached however long the bond length is. Effective bond length is the length beyond which any increase in bond length cannot increase the bond strength. However, for external use, a longer bond length can improve the apparent ductility of the bond area (Teng et al. 2001, Tan 2003, Nakaba et al. 2001, Kamel 2000). Teng et al. developed a model combining fracture mechanics analysis with experimental evidence (Teng et al 2001). According to this model, the effective bond length is:

$$L_e = ((E_p * t_p) / (f'_c)^{0.5})^{0.5} \quad ,\text{mm} \quad (\text{Eq. 2-1})$$

In which,

E_p = modulus of elasticity of FRP plate ,MPa
 t_p = thickness of FRP plate ,mm
 f'_c = concrete compressive strength ,MPa

where L_e is proportional to the square root of the modulus of elasticity and thickness of the FRP plate and inversely proportional to the square of the square root of the compressive strength of the concrete. In this study, the model by Teng et al. was used to determine the maximum FRP plate length that would be used in the interfacial bond tests.

2.8.1. Specimen Design

A series of single lap pullout tests (Fig. 2-142) were performed to determine bond failure, bond strength, and strain rate effect. Thirty-nine concrete beams with dimensions of 286 mm x 76 mm x 76 mm (11.25 in x 3 in x 3 in) were fabricated. Type I Portland cement concrete was used to make the beams. The 28-day concrete cylinder compressive strength was 36 MPa (5200 psi). The crushed granites had a nominal maximum aggregate size of 10 mm and the sand had 30% of fines passing through a 60 μm sieve. The program PCA column (PCA Col 2005) was utilized to determine reinforcement requirements for the beams. Figure 2-143 shows a diagram of the concrete beams used in the bond tests.

Two #3 bars were included to increase flexural and tensile capacity and 12.7mm (0.5in) all-threads were embedded in the concrete for connection to a steel plate. The all-threads in the beams were bolted through steel plates to the MTS load frame to provide a rigid attachment for the tensile tests. This can be seen in the upper portion of Fig. 2-144.

Twenty 25.4 mm (1 in) wide strips of glass and twenty strips of carbon fabrics were prepared with a middle 203 mm (8 in) section coated with SYLGARD 184 elastomer. The two ends of the strips were coated with epoxy resin to duplicate the end segments of the restrainers. One end of the strips would be attached into the grips of the load frame and the other stiff end of the composite was used as an FRP plate to attach to the concrete beams. The glass and carbon strips are shown in Fig. 2-145 prior to attachment to the beams. The effective bond length was calculated to determine the minimal desired length to be attached to the beams using Eq. 2-1. The bond strength was found from Eq. 2-2:

$$P_u = 0.427 \cdot \beta_p \cdot \beta_L \cdot (f'_c)^{0.5} \cdot b_p \cdot L_e \quad ,N \quad (\text{Eq. 2-2})$$

In which,

β_p = width coefficient defined by:

$$\left(\frac{2-b_p/b_c}{1+b_p/b_c} \right)^{0.5}$$

b_p/b_c = width ratio of bonded plate to concrete member ,unitless

β_L = bond length coefficient defined by:

$$1 \quad \text{if } L \geq L_e$$

$$\sin(\pi L / (2L_e)) \quad \text{if } L < L_e$$

f'_c = concrete compressive strength (5200 psi for the beams), MPa

b_p = width of plate ,mm

L_e = effective bond length, mm

The effective length to be used was determined by the bond strength method illustrated in Table 2-10. A nominal bond length of 69 mm (2.7 in) and 76 mm (3 in) was used for the GFRP and CFRP strips, respectively. Dr. Teng's formulation for bond strength (eq. 2-2) verified that this nominal bond length would ensure bond failure in the GFRP and CFRP tests. Bond failure was desired to study both mode of failure and measured bond strength.

The bond of FRP to the concrete substrate is of critical importance. There must be proper surface preparation of the beams. The method used to bond the FRP laminate to the concrete beams consisted of in-place bonding and curing of the GFRP and CFRP strips directly on the concrete. Figures 2-146 and 2-147 illustrate the sequence of the required tasks as listed below:

1. Grind surface of concrete beams to an amplitude of 1.6 mm (1/16 in)
2. Vacuum beams to remove concrete dust
3. Air Blast beams to remove remaining dust

4. Prepare a mixture of fix-all concrete patching compound to fill any large holes
5. Dampen concrete beams but do not leave standing water in voids
6. Carefully fill in holes with patching compound and smooth with a trowel
7. With a damp cloth, remove any excess fix-all from the surface of the beams to ensure the proper concrete strength for the bonded area.
8. Allow for the patching compound to dry for 2 hours.
9. After patching compound is dry, apply epoxy to the composite portion of 25.4 mm (1 in) wide elastomer coated strips to middle 1/3 of beams
10. Use the length of composite plate determined above for the FRP/concrete interface
11. Place polyurethane squares on top of each epoxied block, cover with rubber pads and steel plates until dry, at least 3 days.
12. After strips have dried on blocks, remove plastic, and plates.

Figures 2-146(a) and Fig. 2-146(b) show the sanding of the blocks and subsequent vacuuming to remove all concrete dust. After the FRP plates were bonded to the beams, Fig. 2-147(a), they were covered with polyurethane, a material that will not adhere to the resin. Then weights were placed over the epoxied FRP plates, Fig. 2-147(b), until they have cured to ensure an even layer of resin.

2.8.2. Bond Test Set-Up

The bond test set-up, seen in Fig. 2-148(a) and Fig. 2-148(b), consisted of a series of single lap pull tests. Twenty concrete beams with externally bond GFRP plates were first tested, followed by twenty concrete beams with externally bonded CFRP plates. The middle 203 mm (8 in) portion of the FRP strip that was not attached to either the grips or bonded to the beams was coated with elastomer. A 279 mm x 102 mm x 12.7 mm (11 in x 4 in x 0.5 in) steel plate was anchored to the concrete beams to attach the beams to the grips in the testing machine. Laser targets were attached to exterior of the bonded area to measure deformation. Figure 2-148 illustrates a bond specimen with the lower portion of the composite strip and upper portion of the steel plate gripped by the MTS load frame. The setup provide for direct bond test without creating any significant eccentricity. The test protocol used in the strip tests (Sec. 2.5 and 2.7) was repeated in the bond tests. A minimum of three specimens per strain rate (167, 1000, 5000, 10000, 50000, 100000 $\mu\epsilon$ /sec) for each of the glass and carbon FRP/concrete bond were tested until failure.

2.8.3. Interfacial Bond Test Results

Table 2-11 and 2-12 show results of all three sets of tensile tests (plain fabric, elastomer coated fabric, and interfacial bond). The tensile strength of the concrete beams was approximately 3.7 MPa (540 psi) when calculated from the equation, $7.5 * (5200 \text{ psi})^{(0.5)}$. To calculate measured bond strength for the forty

samples, the measured force was divided by effective bond area. The effective bond area was 1935 mm² (3 in²) for CFRP specimens and 1742 mm² (2.7 in²) for GFRP specimens. The right hand column of Table 2-11 shows that at a static rate of 167 με/sec, the average bond strength at failure for the GFRP was 3.7 MPa (540 psi). In Table 2-12, the average maximum strength for CFRP/concrete bond is approximately 4.1 MPa (590 psi). The fact that these strengths are close confirms that concrete strength does control FRP/concrete interfacial bond strength. It is also observed in the right hand columns of Tables 2-11 and 2-12 that strain rate has an effect on the bond performance. Figures 2-149(a) and 2-149(b) illustrate dynamic to static strength ratios as a function of strain rate for the GFRP and CFRP/concrete bond tests, respectively. When compared to the strength ratio vs. strain rate diagrams for elastomer coated fabric strips, the effect of strain rate on strength for bond becomes evident. This is because bond is controlled by f_c and f_c is known to increase with increase of strain rate. Because the bond strength is controlled by concrete properties as opposed to the fiber type, the data for all the bond tests were combined and an equation for the best fit line was determined (Fig. 2-150): At a concrete compressive strength of 5200 psi, the ratio of dynamic strength/static strength in FRP/concrete bond was found to increase with 0.052Ln (strain rate) + 0.736. The relationship of the square root of f_c to bond strength results in the formulation of Equation 2-3. In this “Johnson/Saiidi” equation of effective interfacial tensile bond strength between FRP and concrete, the square root of f_c is divided by the square root of 5200 psi (the 28-day compressive strength of the concrete beams used in the bond experiments).

$$f_{y\text{bond}} = [0.052\text{Ln}(\epsilon) + 0.736] * (f'_c)^{(0.5)} / (5200)^{(0.5)} \quad (\text{Eq. 2-3})$$

In which,

ε = microstrains/second

f_c = concrete compressive strength ,psi

According to Eq. 2-3 at a strain rate of 50000 με/sec the bond strength will increase by 30%. Tests of concrete samples have shown that at 50000 με/sec the compressive strength of concrete, f_c, increases by approximately 24 percent (Paulay and Priestley 1992). Because bond strength is proportional to the square root of f_c, the result of Eq. 2-3 agrees with past research on strain rate effect on concrete compressive strength.

Figures 2-151 and 2-152 show the typical modes of failure in the bond tests. The debonding at the interface between the concrete and the GFRP plate in Fig. 2-151 is typical of the individual bond tests. It should be noticed that a thin layer of concrete adheres to the FRP. This can be seen in the close-up of the GFRP/concrete bond failure in Fig. 2-152. A layer of concrete was debonded with the glass strip. The thickest section of concrete is at the far edge of the strip.

Most specimens failed by shear failure initiated in the concrete near the edge of the concrete beam. This failure zone spread very quickly resulting in a sudden brittle debonding.

2.8.3.a. Force-Displacement and Stress-Strain Relationships

The measured force vs. bond slip and average bond stress vs. bond strain for different specimens are shown in Fig. 2-153 to 2-226. Unlike the linear stress strain relationship seen in the fabric tests, the best line fit for the bond relationships is a second order equation. In a few instances, such as that seen in Fig. 2-165 and 2-166, a parabolic relationship resembling that of concrete is apparent. These force-displacement and stress strain curves verify the important role of concrete in bond strength. There does appear to be a strong relationship of stiffness of the fabric to ultimate bond slip or bond strain. The average bond strain for the GFRP/concrete tests was 0.63 percent while the average bond strain for the CFRP/concrete tensile tests was 0.31%. This is because of the higher modulus of elasticity of CFRP.

2.9. Concluding Remarks

1. Tensile strength of carbon flexible composite is equivalent to manufacturers design strength for carbon composite.
2. There is an edge effect in the failure mode seen in the tensile tests.
3. Tensile strength of uncoated and coated glass strips is approximately equal. There is clear evidence that geometric arrangement of the fabric is critical to achieve design strength. This may be a result of reduced edge effect by a better system of unifying the unidirectional fibers of the fabric.
4. The controlling factor in FRP/concrete interfacial bond is the compressive strength of the concrete.
5. Maximum bond strain is dependent on both the stiffness of the fabric and on the strength of concrete.
6. Effective bond length is the length beyond which any increase in bond length cannot increase the bond strength. However, for external use, a longer bond length can improve the ductility of the failure process. Bond failures are often brittle and occur with little or no visible warning.
7. There is no apparent strain rate effect in either coated or uncoated fabric. This is because unlike homogeneous materials, there is internal slippage of the fibers at high strain rates.
8. There is a clear increase in bond strength as strain rate increases. This is because bond is controlled by concrete compressive strength, f'_c , and f'_c is known to increase with increase of strain rate.

CHAPTER 3

FRP RESTRAINERS

3.1 Introduction

The feasibility of using FRP as a bridge restraining device is a new concept. The ease of application, stiffness, availability of the material, and economical manufacturing of this product makes it deserving of investigation. Results from the previous glass and carbon material tests and past steel and SMA restrainer experiments were used in design of FRP restrainers. Three restrainer types were fabricated and tested under dynamic loading. These restrainers consisted of GFRP, CFRP and a set of hybrid restrainers made of glass and carbon fibers. A GFRP restrainer has the advantage of maximum elongation until break (2.2%). A CFRP restrainer has greater rupture strength, and a hybrid composite restrainer has the potential of producing a system that is non-linear. This chapter presents background information about the design of the restrainers, the design process, and the installation of the restrainers.

3.2 Restrainer Design Method

The premise for the design of the restrainers was force based. Because FRP is a linear material, the restrainers were designed to remain elastic. A maximum restrainer force of 17.8 kN (4 kip) per side was measured during earlier shake table testing of steel and SMA restrainers during shake table tests under the design earthquake of 0.7 times ATC32E. This restrainer demand was used in the FRP restrainer designs. A factor of safety of 2 was implemented to ensure elastic performance. Past research of bridge components strengthened using CFRP have indicated that in many cases strengthened specimens failed after the composites reached 50 to 65% of the rupture strength of the laminates (Brena et al 2003 and Xiao et al 1997), and hence a factor of safety of 2 was believed to be reasonable.

The FRP restrainers are a two-component system. The area of the restrainer in the hinge region is flexible to allow movement in compression and tension while undergoing cyclic, dynamic motions. The restrainer ends are a stiff composite plate bonded and cured onto the concrete bridge specimen. The middle section of the restrainer in the hinge area is a flexible composite of fabric coated with SYLGARD 184 elastomer. Failure in bond is undesirable because bond failures

are often brittle and occur with little or no visible warning. The FRP restrainers were designed so if failure did occur, it would be in the flexible segment and not in the interfacial bond between concrete and FRP. The FRP/concrete bond was designed to have greater capacity than the flexible composite. An FRP plate, twice the size of the effective bond area, was used to ensure that bond failure would not occur. Research has shown that the longer the bond length, the larger the number of cycles to failure (Tan 2003). Research on the effects of adverse environmental conditions on strength capacity of externally bonded CFRP shows that the most significant reduction (33%) in strength was due to long-term exposure to 100% humidity. Less severe to the delamination process was dry heat, alkalinity, freezing and thawing, and salinity (Grace 2004). This long-term strength degradation of FRP/concrete bond from harmful weather conditions was taken into account in design of the restrainers. The bond tests on flexible glass and carbon strips bonded to concrete beams indicated that the bond strength between FRP and concrete is controlled by the tensile strength of concrete. In calculating the bond length, the compressive strength of the concrete in the bridge blocks was divided by two as an added factor of safety.

The average measured flexible FRP strength for the glass and carbon flexible composite was taken from the results of the coated fabric material tests (Chapter 2). These tensile test results of 230 MPa (33.3 ksi) for the flexible glass composite and 717 MPa (104 ksi) for the carbon flexible composite at rupture determined the fabric width necessary for sufficient strength capacity.

In designing FRP restrainers, three parameters need to be considered: (1) demand on restrainer from earthquake motion, (2) capacity of the flexible laminate, and (3) capacity of FRP/concrete bond. The restrainer demand was based on the highest restrainer force at maximum earthquake acceleration measured during the earlier steel and SMA restrainer experiments. The basic flexible composite capacity was taken as the average measured flexible FRP strength determined during the tensile tests of the elastomer-coated strips. Capacity of the FRP/concrete bond was based on Teng's formula for effective bond length.

3.2.1 Demand

- Determine maximum force requirement for the individual restrainers from data from previous steel and SMA restrainer shake table tests (Sanchez-Camargo et al 2004, Johnson et al 2004). The maximum measured force per restrainer in the SMA experiments was 19 kN (4.2 kip). The maximum total force from steel restrainer tests was 36 kN (8.1 kip). The single steel restrainer was centered inside the concrete cell. The FRP restrainers are similar to the SMA restrainers, in that they are attached to the sides of the blocks.

- The stiffness is an important aspect in the restrainers because the ultimate elongation must be less than the seat width to prevent collapse. FRP is a linear material and the total elongation for glass and carbon are 2.2 and 1.2 percent respectively. The portion of the restrainer that is unrestrained is approximately 254 mm (10 in). Consequently, the ultimate elongation in the glass and carbon restrainers would be 5.6 mm and 3.0 mm (0.22 in and 0.12 in) before failure. Therefore, in this material, the stiffness element was not used as the primary design criteria

Table 3-1 shows the maximum measured restrainer forces during shake table tests of steel cable restrainers in 2000 and SMA cable restrainers in 2003. The SMA restrainer was designed with equal stiffness to the steel restrainer to ensure comparable test results between the two cable types (Johnson et al 2003). All three restrainer types (steel, SMA and FRP) had a nominal slack of approximately 12.7mm (0.5 in). The test set-up in all three restrainers was identical, with a period ratio of 0.6 between concrete blocks representative of an in-span region of a box girder bridge. The total maximum restrainer force measured for the steel and SMA cable restrainers during dynamic tests was equivalent, at approximately 35 kN (8 kip). The largest single SMA restrainer force of 19 kN (4.2 kip) was utilized for the FRP restrainer force based design.

3.2.2 Flexible FRP Capacity

There were several options for determining strength capacity for the flexible composite segment of the FRP restrainer. They include:

- Manufacturer's specified strength of composite material
- Lowest measured ultimate force (from tensile tests)
- Average measured strength (from tensile tests) \leq specified
- Average measured ultimate stress— σ (tensile test results)

Using the lowest measured tensile strength may be overly conservative, particular when a separate factor of safety is also used. The manufacturers design strength in the primary direction for glass and carbon composite was considered, but was not used. Although the UNR results for strength agreed with those of the manufacturer for the carbon fibers, the results for glass composite strength did not agree. Table 3-2 shows the measured average tensile strength for glass and carbon flexible laminates. Those test results show an average measured tensile strength of 717 MPa (104 ksi) vs. the manufacturer's design strength of 745 MPa (108 ksi) for carbon composite; whereas, in the glass composite strips, the measured strength was one half of the manufacturers design strength, or 230 MPa (33 ksi) vs. 460 MPa (66.7 ksi). It was decided to base the capacity of the flexible composite portion of the FRP restrainer on the average measured strength.

A factor of safety of 2 was utilized in the capacity design of the flexible laminate. Figure 2-139 (b) demonstrates the reduction of tensile strength results for coated

and uncoated carbon and glass as a result of edge effect. This edge effect strength reduction is pronounced in the 25.4 mm (1 in) FRP strips but may not be quite as dominant in a wider strip of composite. To minimize the strength reduction due to edge effect, an arbitrary minimum width of 76 mm (3 in) was used in the restrainer design.

Table 3-3 shows the design width for the flexible portion of the glass and carbon restrainers. The width was calculated using a FOS of 2, times the force demand, divided by the average tensile capacity for a 25.4 mm. (1 in.) wide strip of flexible composite. The calculated width, in inches, was then rounded up to the next whole number, subject to the minimum width of 76 mm. (3 in.). The final design width to be used for the flexible composite portion of the restrainer in the hinge area of the blocks was 152 mm (6 in) for the glass and 76 mm (3 in) for the carbon restrainer. Flexible composite capacity for glass and carbon was recalculated using the design width of 152 mm (6 in) (glass) and 76 mm (3 in) (carbon). Table 3-4 shows the calculated capacity for the flexible FRP. The final design capacity of the flexible GFRP was 45 kN (10 kip) while the capacity calculated for the CFRP was higher, at 56 kN (12.5 kip).

3.2.3 FRP/Concrete Bond Capacity

Teng's bond strength model (Teng et al 2001) was implemented in the design of the Interfacial bond between the FRP composite plate and the concrete of the blocks. Most past studies have acknowledged that bond strength does not increase beyond a certain bond length. These investigations do not take into account effective bond length. Teng and Chen proposed a bond strength model that incorporates effective length, fracture mechanics, experimental evidence, and provides accurate predictions. The basic assumptions of the model are:

- Ultimate bond strength is related to $(f'_c)^{(0.5)}$
- τ_f , defined as maximum bond shear stress, is approximated by the tensile strength of concrete which can be related to the compressive strength of concrete by $(f'_c)^{(0.5)}$
- A linearly decreasing shear-slip model, seen in Fig. 3-1, may be used because for FRP-to-concrete joints, the typical slip values are $\delta_1 = 0.02$ mm at peak shear and $\delta_f = 0.2$ mm at failure, that is, δ_1 is small compared with δ_f .
- Typical value for δ_f is about 0.2 mm, therefore the effective bond length can be approximated by:

$$L_e = (E_p \cdot t_p / (f'_c)^{(0.5)}) \quad , \text{mm} \quad (\text{Eq. 3-1})$$

- A simple ultimate bond strength model based on a linearly decreasing shear-slip model and test data is used.

$$P_u = 0.427 \cdot \beta_p \cdot \beta_L \cdot (f'_c)^{(0.5)} \cdot b_p \cdot L_e \quad , \text{N} \quad (\text{Eq. 3-2})$$

$$\beta_L = 1 \text{ if } L \geq L_e$$

$$\beta_L = \sin(\pi \cdot L / (2 \cdot L_e)) \text{ if } L < L_e$$

where β_p and L_e are in mm and f'_c is in MPa

$$E_p = \text{tensile modulus of FRP plate} \quad , \text{MPa}$$

$$\beta_p = ((2-b_p/b_c)/(1+b_p/b_c))^{(0.5)}$$

b_p = width of bonded plate ,mm

b_c = width of concrete member on same plane as bonded plate ,mm

*Note: b_p/b_c ratio has significant effect on the ultimate bond strength. A smaller b_p compared with b_c may result in a higher shear stress at the interface at failure due to a nonuniform stress distribution across the width of the concrete member.

- Stress in the bonded plate at failure:

$$\sigma_{db} = 0.427\beta_p\beta_L(E_p (f'_c)^{(0.5)}/t_p)^{(0.5)} \quad , \text{MPa}$$

$$= 0.4\beta_p\beta_L(E_p (f_{cu})^{(0.5)}/t_p)^{(0.5)}$$

where the cube compressive strength $f_{cu} = 1.25f'_c$

- Ratio of the stress in the plate at bond failure to the plate tensile strength:

$$\sigma_{db}/f_p = 0.427\beta_p\beta_L/E_p\varepsilon_p(E_p (f'_c)^{(0.5)}/t_p)^{(0.5)}$$

$$= 0.427\beta_p\beta_L/\varepsilon_p((f'_c)^{(0.5)}/E_p t_p)^{(0.5)}$$

f_p = ultimate strength of FRP plate ,MPa

ε_p = ultimate strain in FRP plate

Chen and Teng design recommendations for conservative ultimate strength is:

- Coefficient of 0.427 was reduced to 0.315 to reduce it to the 95th percentile
- $\gamma_b = 1.25$ (partial safety factor for bond strength) Safety factor is to achieve a consistent level of safety margin for both debonding and FRP tensile strength.

3.3 Restrainer Design

The restrainer design methodology was used to design the glass, carbon, and hybrid FRP bridge restrainers. The glass restrainer was designed and tested first, followed by the carbon and hybrid restrainer. The initial stage of construction of the restrainers began with the fabrication of the unidirectional piece of the restrainer, or the portion of the restrainer that contained the flexible composite section. This was a two-step process. It consisted of first coating the ends of a strip of fabric with resin. The ends were cured for approximately three days. Then, the middle 10 inches of the strip was coated with SYLGARD 184 elastomer. This resulted in unidirectional strip of fabric with stiff FRP composite ends and a flexible composite center. An example of this is seen in Fig. 3-2. The edges of the stiff composite section of the unidirectional piece are dashed. The sequence of this two-step process is a result of the material properties of the resin and elastomer. It was desirable to provide a small overlap of the stiff and flexible coatings to reduce stress concentration. The only way to achieve this was

to coat a small section of the stiff composite with elastomer. The elastomer is capable of adhering to the stiff composite but the resin is unable to stick to the elastomer.

In the initial stage of restrainer bond strength design, Teng's model was used to determine if the restrainer segment would provide sufficient bond strength. However, the width and thickness of the restrainer was found to be insufficient. Enlarging the ends of the restrainer was necessary to produce the necessary bond capacity. The plate enlargement was determined by doubling the effective bond area, as determined in Teng's model. The FRP plate enlargement consisted of two pieces of 45 and 135-degree fabric bonded onto the ends of the restrainer segment consisting of both flexible and stiff composite. The completed bond area of the FRP restrainer met the requirement for adequate bond capacity.

3.3.1 GFRP

Figure 3-3 shows the computation for effective bond length and bond capacity of the composite lamina in the primary direction. Concrete strength was taken as the 28-day compressive strength (44.8 MPa) of a recent block repair material. The calculated bond capacity of 26 kN (6 kip) was determined to be less than the calculated capacity of the flexible glass composite lamina (44 kN (10 kip)). Thus, the computed effective bond length of 68 mm (2.7 in) would provide a capacity that was less than the target value. Hence the thickness and area of the bonded segments were increased. The additional portion of FRP plate consisted of GFRP at 45 and 135 degrees. This additional segment of the plate was determined to contribute $(\cos 45^\circ)^2$ or 1.41 times the tensile strength of the strip in primary tensile strength direction. Two formulations of bond strength were calculated to determine effective length and approximate bond strength for the enlarged FRP plate size. The first, seen in Fig 3-4, calculates the new bond capacity and effective length for the rectangular portion of plate that would now consist of one layer of unidirectional laminate and two layers of angled FRP. The angled layers of glass epoxy were chosen as 45 and 135-degree sections to aid in improved distribution of forces from the FRP plate to the concrete box. With the addition of the angled laminate, Fig. 3-4 shows an increased bond length and improved bond capacity. An additional calculation was made for the portion of the enlarged FRP plate outside of the rectangular section. Figure 3-5 demonstrates the new effective length for this angled portion of the bonded area. At this point in the restrainer design, effective length was used to determine effective bond area. The new effective length for this enlarged FRP plate is illustrated in Table 3.5. In the primary restrainer direction, the new effective length is 99 mm (3.9 in) and in the angled direction, the effective bond length is 76 mm (3 in). From this effective length a bond area was calculated. This area is multiplied by the tensile strength of concrete to achieve an estimate for bond capacity that is more conservative than Teng's bond capacity formula.

Figure 3-6 illustrates a diagram of the effective areas for the bonded portions of the GFRP restrainer. The primary direction of the force is in the x direction. The fabric in this direction is considered to be used to its full capacity. The horizontal component of the inclined laminate was used. Calculations for this area are seen at the bottom of Fig. 3-6. The resulting effective bond area was 45800 mm² (71 in²) for the GFRP restrainers. The compressive strength of concrete used in this calculation was $f_c = 44.8$ MPa (6500 psi). The resulting bond capacity of the effective area was calculated using the effective area times the tensile strength of concrete divided by 2, or $((71 \text{ in}^2) * (7.5 / 2(\text{FOS})) * (f_c)^{(0.5)})$. The bond capacity of the GFRP plates was determined to be 93 kN (21 kip), which was greater than the 45 kN (10 kip) capacity of the flexible glass composite. The plate size was doubled beyond the effective area for added factor of safety. Figure 3-7 and 3-8 show the final GFRP restrainer design, with the flexible composite in the center and the stiff composite plates on the ends. These two components, flexible and stiff composite, create an integrated restrainer with outside dimensions of 406 mm (16 in) by 775 mm (30.5 in).

3.3.2 CFRP

Figure 3-9 shows the computation for effective bond length and bond capacity for the CFRP restrainer. Concrete strength was taken as 38 MPa (5500 psi), which is a conservative estimate of the concrete block strength. The earlier calculations for required flexible composite width predetermined the 76 mm (3 in) used as the FRP plate width. The computed effective bond length of 102 mm (4.0 in), as well as the other physical properties of the carbon composite lamina, resulted in deficient bond capacity. The FRP plate size and thickness were increased to provide for bond capacity of at least 55.6 kN (12.5 kip). As in the GFRP restrainer, the additional portion of FRP plate consisted of CFRP at 45 and 135 degrees. Two formulations of bond strength were calculated to determine effective length and approximate bond strength for the enlarged FRP plate size. The first, seen in Fig. 3-10, calculates the new bond capacity and effective length for the rectangular portion of plate that would now consist of one layer of unidirectional laminate and two layers of angled FRP. With the addition of the angled laminate, Fig. 3-10 shows an increased bond length and improved bond capacity. An additional calculation was made for the portion of the enlarged FRP plate outside of the rectangular section. Figure 3-11 demonstrates the new effective length for this angled portion of the bonded area. At this point in the restrainer design, effective length was used to determine effective bond area. The new effective length for this enlarged FRP plate is shown in Table 3.5. In the primary restrainer direction, the new effective length is 155 mm (6.1 in) and in the angled direction, the effective bond length is 119 mm (4.7 in). From this effective length a bond area was calculated.

Figure 3-12 illustrates the effective areas for the bonded portions of the CFRP restrainer. The primary direction of the force is in the x direction. The fabric in

this direction is considered to be used to its full capacity. The calculations for the bonded area are similar to those of GFRP (Fig. 3-12). The effective bond area was of 42400 mm² (66 in²) for the CFRP restrainers.

Bond strength of the CFRP plates was calculated using the tensile strength of concrete and a FOS of 2. The resulting bond capacity of the effective area was calculated using the effective area times the tensile strength of concrete divided by 2, or $((66 \text{ in}^2) * (7.5 / 2(\text{FOS})) * (5500)^{(0.5)})$. Bond capacity of the CFRP plates was determined to be 80kN (18 kips), which was greater than the 56 kN (12.5 kip) capacity of the flexible carbon composite. Figure 3-14 shows the final CFRP restrainer design. The effective length is extended to double its calculated distance and the resulting restrainer dimensions are seen in Figure 3-8. It can be observed that the effective bond area for the CFRP restrainer is larger than that of the GFRP restrainer but the capacity of the GFRP/concrete bond is larger. This is due to the strong relationship between concrete strength and bond capacity.

3.3.3 Hybrid (Glass and Carbon)

The hybrid restrainer design was similar to the previous restrainer models. The distinct difference between the hybrid restrainer and the other two restrainer types is the unidirectional segment bridging the two FRP plates. This portion of the hybrid restrainer consisted of a unidirectional composite laminate of both glass and carbon fabric. Figure 3-15 shows the center part of this segment being coated with SYLGARD 184 silicone elastomer prior to enlarging the stiff composite ends that form the FRP plates. A 50.8 mm (2 in) wide strip of carbon fabric was centered on a 152 mm (6 in) wide strip of glass fabric. As with the other unidirectional strips, the first step in the hybrid restrainer construction consisted of first coating the ends of the fabric with Tyfo S epoxy to form a stiff laminate. The second step in this process is seen in Fig. 3-15. The middle section that will form the flexible composite is then coated with elastomer to form the portion of the restrainer in the hinge area. Capacity of the flexible composite segment of the restrainer was calculated using results from the glass and carbon flexible lamina material tests (Chapter 2). The formulation, seen below, resulted in a hybrid flexible composite capacity of 80 kN (18 kip).

$$\text{Flexible hybrid capacity} = (6\text{in} * 1.67\text{kip/in} + 2\text{in} * 4.16\text{kip/in})$$

Basic calculations for bond length, seen in Fig. 3-16 through Fig. 3-18, were performed. From previous GFRP and CFRP restrainer design calculations, bond capacity of the unidirectional composite lamina, without the addition of larger end plates, was known to be deficient and was not checked until the final design step. Three distinct calculations for bond length were conducted. These consisted of three plate components seen in Fig. 3-19. They include the effective bond length of the angled (45 and 135 degree) glass/epoxy composite laminate (Segment 1), effective bond length of the unidirectional and angled glass composite (Segment

2), and the effective bond length of the angled glass and unidirectional carbon and glass composite laminate (Segment 3). Figure 3-16 demonstrates the calculated effective bond length for Fig.3-19(1). Figure 3-17 shows the effective bond length for the segment of the hybrid FRP plate seen in Fig. 3-19(2) and Fig. 3-18 gives the calculated effective bond length for the portion of the plate seen in Fig. 3-19(3). The effective bond lengths for these three components of the hybrid plate are illustrated in Table 3-7. The effective lengths for these different components range from 79 mm (3.1 in) for the angled (45 and 135 degree) glass to 145 mm (5.7 in) for the portion of the plate that consists of the glass/carbon epoxy laminate. From this effective length a bond area was calculated.

Figure 3-20 illustrates a diagram of the effective bond areas for the bonded portions of the hybrid restrainer. Calculations for this area are seen at the bottom of Fig. 3-20. The effective bond area was 45900 mm² (71 in²) for the hybrid restrainers.

Bond strength of the hybrid plates was calculated using the tensile strength of concrete and a FOS of 2. The resulting bond capacity of the effective area was calculated using the effective area times the tensile strength of concrete divided by 2, or $((71 \text{ in}^2) * (7.5 / 2(\text{FOS})) * (5500)^{(0.5)})$. Bond capacity of the hybrid composite plates was determined to be 89kN (20 kip), which was greater than the 80 kN (18 kip) capacity of the flexible hybrid composite. Figure 3-21 and 3-22 show the final hybrid restrainer design, with the flexible composite in the center and the stiff composite plates on the ends.

3.4 Restrainer Fabrication

Fabric pieces of a predetermined size were cut with a common rotary blade found in fabric shops. This creates clean-cut surfaces. The glass and carbon fabric used in these restrainers is unidirectional and cut surfaces parallel to the fibers are crucial to achieve optimal strength. Two sizes of fabric were cut per restrainer. One strip of fabric became the unidirectional pieces connecting the elastomer-coated portion of the restrainer to the bonded FRP plates. Four 45 degree rectangular pieces of fabric developed into the FRP plates that were bonded onto either side of the in-span hinge area of the blocks.

The next step in restrainer production, seen in Fig. 3-23(a), consisted of painting epoxy onto the unidirectional piece of fabric. Epoxy resin, Tyfo-S, was used as both the matrix for the FRP and as the bonding adhesive between the FRP and the concrete. The required fabric width for this portion of the restrainer was 76 mm (3 in) for the carbon restrainer and 152 mm (6 in) for the glass restrainer. Upon completion, this large piece was cut into the two unidirectional pieces that formed the middle section of the restrainers. The epoxy was painted up to a predetermined section of the unidirectional strip. Steps from the elastomer coating process in Chapter 2 were followed in this part of the restrainer

fabrication. Pressing excess epoxy from the fabric, seen in Fig 3-23(b), is very important. The resin tends to wick up into the material. Squeezing excess resin from the fabric permits a more defined line between the stiff and flexible composite.

Figure 3-24(a) illustrates pouring the vacuumed elastomer over the middle portion of the unidirectional piece. This produced the flexible portion of the restrainer. It is preferable to coat the fabric with a minimal amount of elastomer to produce a thoroughly coated but pliable flexible composite. The final step in the elastomer coating process, discussed in Chapter 2, is to vacuum air from the material covered with SYLGARD 184. This unidirectional segment of the restrainer was now complete. It was cut into 2 equal sections in approximately 3 to 5 days, upon cure of the elastomer. Polyurethane was used to wrap the elastomer-coated portion of the restrainer before the next step in the fabrication process.

Fig. 3-25(a) illustrates arranging the fabric that forms the FRP composite plate. The flexible composite, wrapped in polyurethane, is seen in the middle of the image. The resin coated ends of the strip were placed between the 45 and 135 degree pieces of fabric that form the FRP plates. Epoxy was painted onto the three layers of fabric and covered with polyurethane, seen in Fig. 3-25(b). After the matrix of fabric and resin cured, the sheeting was removed. Figure 3-25(c) shows excess epoxy being trimmed from an FRP plate. A plate surface devoid of irregularities was desired to form a strong bond between FRP plate and concrete. The finished restrainer was attached to the vertical surface of the blocks with epoxy. The consistency of resin is too thin for vertical application. Therefore, for this experiment a thickener was used. Figure 3-25(d) shows the epoxy being thickened with cab-o-sil, which is submicron silica. It is a synthetic, amorphous untreated fumed silicon dioxide. Because of its inert nature, it has been used in food such as ketchup as well as in shampoo. It has extremely fine particle size, is pure white and free flowing. A volume of Cabosil contains about 94% dead air space, with a density of 2.3 lb/ft³. During the cure cycle, epoxies tend to run off and vertical surfaces become resin starved. Cabosil prevents this runoff and holds the liquid resin in place until the curing agent takes over and hardens. Typically, Cabosil is added at a 1 to 7 percent proportion based on the weight of the resin. A 50/50 volume ratio of resin to Cabosil produces a toothpaste like resin consistency. This was the approximate ratio used in the restrainer experiments. The addition of Cabosil has no effect on such properties as pot life and cure time. It only affects strength to the degree that there may be entrapped air but thorough mixing can reduce this.

A completed FRP restrainer is seen in Fig. 3-25(e). Figure 3-26 illustrates the ease of affixing the FRP restrainer to the shake table specimen. The attachment consisted of (a) sanding the blocks, (b) airblasting the blocks to remove excess concrete dust, (c) and attaching the restrainer to the specimen with thickened

resin. Figure 3-26(d) shows the FRP plate being compressed onto the blocks. Clamping the FRP onto the blocks not only secured it in place until the resin was sufficiently stiffened, but also ensured an even layer of epoxy between the blocks and the plate. In approximately three days, the resin had cured and the clamps were removed. Prior to shake table tests, an additional layer of resin was applied to the bonded area, Fig 3-26(e), to form a final epoxy coating.

CHAPTER 4

EXPERIMENTAL PROGRAM

4.1 Introduction

The experimental set-up used in the FRP bridge restrainer shake table tests, instrumentation, and test protocols are described in this chapter. The testing program had been established in previous restrainer experiments conducted at the large-scale structures laboratory at the University of Nevada, Reno. Keeping the testing program the same as those of previous restrainer studies, enabled comparisons among the performance of steel and SMA cable restrainers (Vlassis et al 2000, Johnson et al 2004, Camargo et al 2004) to that of the FRP restrainers. The measured data for FRP restrainers and comparison with other restrainer types are presented in subsequent chapters.

4.2 Test Specimen

These experiments were performed on one of the 50-ton capacity biaxial shake tables in the large-scale structures lab at UNR. The test blocks and the supporting bearings, seen in Figs. 4-1 and 4-2, were by Vlassis et al. 2000. Dimensions of the blocks were based on superstructure dimensions of representative CALTRANS bridges. Each block represents one bridge frame consisting of superstructure and columns. Block properties and dimensions are given in Table 4-1. The compressive strength of the concrete cells is 37.9 MPa (5500 psi). The specimen consists of a light, 94 kN (21.1 kip), (A) and heavy, 125 kN (28 kip), (B) block. The difference in weight between the two blocks was accomplished with the addition of lead bricks placed inside Block B. Two sets of elastomeric pads were used. They simulate the stiffness of the bridge substructure. Four pads were bolted onto the underside of the individual blocks. Elastomeric bearing properties can be viewed in Table 4-1. Bearings A, attached to Block A, has a combined stiffness of 910 kN/m (5.2 kip/in). Bearings B, affixed to Block B, are the softer of the bearings, with a combined stiffness of 473 kN (2.7 kip/in). The ratio of periods between the two blocks was determined by the mass of the blocks and the stiffness of the pads. The specimen was lifted into position with a 25-ton crane, and anchored onto the shake table.

4.3 Test Parameters

Parameters from the previous steel and SMA cable restrainer experiments conducted at the same facility provided the criteria for the restrainer slack, earthquake motion, and period ratio between blocks used in the FRP restrainer

tests. These parameters resulted in the most critical scenario of frequent block impact and restrainer engagement in the former restrainer tests.

4.3.1 Restrainer Slack

An approximate restrainer slack of 12.7 mm (0.5 in) was provided during the bonding of the FRP restrainers to the sides of the blocks. The restrainer slack was accomplished by levering open the 12.7 mm (0.5 in) gap in the blocks with a 25.4-mm (1-in) thick piece of steel prior to restrainer installation. Upon cure of the resin bonding the restrainers to the blocks, the steel piece was removed, resulting in the 12.7 mm (0.5 in) slack in the FRP restrainers.

Zero slack accounts for thermal contractions that result in the cable stretching during extreme cold weather. For this reason, bridge restrainers are typically installed with a slack to reduce restrainer forces.

4.3.2 Earthquake Motions

The response spectra ATC32E (Caltrans 1999 Seismic Design Criteria) was used to develop a synthetic input ground motion that was used in shake table earthquake simulations. ATC32E is based on the ARS curve for soil type, E, and peak acceleration of $0.36g \pm 0.25$. Soil type E is classified as a soft soil with shear wave velocity of less than 180 m/s. MatLab software was used to compare the spectra for the synthetic motion to that of the design spectra. Figure 4-3 shows the target vs. the achieved ARS curve. It also illustrates the spectra for shake table motions normalized to 0.05g to 0.3g. Tests were performed in increments of 0.05g, from a PGA of 0.05g to 0.3g. The tests were limited to a PGA of 0.3g because of the extremely large bearing displacements at this acceleration, which exceeded the design displacement of the bearing.

4.3.3 Frame Period Ratio (T_1/T_2)

This parameter is the ratio of the vibration period of the stiffer block (A) over the period of the softer block (B). This period ratio of 0.6 was used for all of the test runs. It was accomplished with a combination of block mass and stiffness provided by the elastomeric pads. The relatively small period ratio used in these restrainer tests resulted in large out-of-phase motion between the frames. Table 4-1 lists the system properties of the individual block periods, which resulted in the ratio of 0.6. The period ratio of 0.6 is a realistic ratio for many of the existing actual bridges.

4.4 Data Acquisition Equipment and Instrumentation

National Instruments PX1 8186 data acquisition system was used to collect the experimental data. This system has a variety of features for accurately capturing

dynamic data. The sampling rate was 100 Hz (0.01 sec). The data was filtered using analog low pass filters equaling 100 Hz. The data acquisition system allows for a timed sample and generates output files that can be transferred to an Excel spreadsheet for analysis.

Novotechnik LWG-225 linear extensometers were used to measure the relative hinge displacement. One transducer was used on top and two were used on each side of the hinge region. Unimeasure PA-40, 40-inch string extensometers were used to measure absolute displacement between the blocks and a fixed frame surrounding the specimen. The string extensometers were also used to measure absolute displacement between the shake table and the fixed frame. Crossbow CXLOZLF1 $\pm 2g$ accelerometers were placed on the block and table to measure the acceleration of both the specimen and table. Table 4-2 displays the 24 channels of input that were utilized during the restrainer tests. During the first FRP restrainer tests, three transducers, three accelerometers, and nine string extensometers measured the relative displacement, acceleration, and absolute displacement of the specimen. Figure 4-4 illustrates the instrumentation used during the GFRP shake table tests. Additional instrumentation was added for the later tests to capture movement in the transverse direction. Figures 4-5 and 4-6 show the instrumentation used during the CFRP and hybrid restrainer tests. The transducers on Gap 1 and 3 were removed during the hybrid restrainer tests conducted in the transverse direction to prevent damage to the transducers.

4.5 Test Schedule

The FRP restrainer tests were conducted on June 29 (GFRP), July 20 (CFRP), and August 11, 2004 (hybrid). The staggering of the restrainer test schedules allowed time for data analysis between constructions of the various restrainer types. The ATC32E-compatible synthetic record was used as the input earthquake motion for the GFRP and CFRP restrainer shake table tests. Unidirectional motion in the Y, or east-west, direction was used for all tests. Additional shake table tests in the transverse; north south; direction and an earthquake motion simulating the 1994 Northridge- SYLMAR were utilized for the hybrid restrainer tests. The ATC 32E motion contains many high-amplitude acceleration peaks that cause impact between the concrete blocks. The additional spectrum and motion were introduced during the last restrainer tests in hope of acquiring supplementary knowledge of FRP restrainer performance under a recorded earthquake motion as opposed to a synthetic one.

The test protocol from the FRP restrainer tests is listed in Table 4-3. The peak ground motion was increased from 0.05g to a maximum of 0.3g throughout the shake table tests. The maximum peak ground acceleration of 0.3g was determined by the design displacement of the elastomeric pads attached between the blocks and the shake table. In the GFRP restrainer tests, a PGA of 0.3g was achieved because the restrainers retained their integrity throughout the

tests and the excessive displacement of the elastomeric pads controlled the maximum PGA of 0.3g. For the CFRP restrainer tests, one of the restrainers ruptured during motion 2-4 with a PGA of 0.2g (Table 4-3) and the testing was stopped. The hybrid FRP restrainers did not rupture during the tests of longitudinal movement. A maximum peak ground acceleration of 0.3g was achieved for both the ground motion produced by ATC32E and that of the Sylmar ground motion. For the hybrid restrainer, two tests were performed to examine performance in the transverse direction (perpendicular to the restrainers). The ATC32E was used as the input motion used in the additional tests in the transverse direction. Testing was continued until the restrainers debonded.

Restrainer slack on the north side of the blocks was approximately 13 mm (0.5 in) while the slack of the south restrainer was around 10 mm (0.4 in). This difference in slack on the two sides of the blocks was a result of irregularities in block construction and placement. The difference in slack was consistent throughout the shake table tests of the FRP restrainers. This resulted in the restrainer on the south side engaging before the north side restrainer. This is not inconsistent with restrainer performance of actual bridges.

CHAPTER 5

FRP RESTRAINER TEST RESULTS

5.1 Introduction

Shake table tests were carried out on the GFRP, CFRP and CGFRP (hybrid) restrainers to determine their dynamic performance (Fig. 5-1 to Fig. 5-3). An identical shake table and specimen set-up was used for all three types of FRP restrainers. Block acceleration and restrainer elongation histories were measured every 0.01 seconds during dynamic tests. This provided the data necessary to produce acceleration and displacement histories for the FRP restrainers. Termination of the dynamic tests was either a result of restrainer failure or excessive displacement of the bearings that simulated substructure stiffness. The estimated restrainer force histories are also discussed in this chapter.

5.2 GFRP

Shake table tests for the GFRP restrainers consisted of ATC32E unidirectional earthquake motion. Increasing incremental activity, from a PGA of 0.05g to 0.3g, provided frequent restrainer engagement and block impact. The observed performance of the GFRP restrainers during these motions is illustrated in Table 5-1 and Fig. 5-4. At a peak table acceleration of 0.05g, 0.1g, and 0.15g (Fig. 5-4(a)), no damage was observed in either the north or south side restrainers. At 0.2g (Fig. 5-4(b) and Fig. 5-4(e)), fiber failure was seen on the bottom edge of the hinge area of both the north and south restrainers. This was similar to what was seen in the tensile tests on elastomer coated glass fabric strips. The outer damage remained small through a PGA of 0.25g (Fig. 5-4(c) and Fig. 5-4(f)). As a consequence of earlier and more frequent restrainer engagement, the south restrainer had more observable damage at this peak ground acceleration. At a peak ground acceleration of 0.3g (Fig. 5-4(d) and Fig. 5-4(g)), a slight amount of debonding was seen at the hinge area, at the interface of the FRP plates and the concrete blocks. Figure 5-4(d) and Fig. 5-4(g) illustrate the maximum damage witnessed at the end of the GFRP restrainer shake table tests. This minor damage to the restrainers and slight reduction in bond area was not considered to affect the integrity of the GFRP restrainers. The tests ended due to excessive displacement of the elastomeric pads.

5.2.1 Response Histories

The measured block acceleration, restrainer deformation, and restrainer force histories for different motions are shown in Fig. 5-5 through Fig. 5-10. The instrumentation used to determine the acceleration and displacement for the

GFRP restrainer experiments was shown in Fig. 4-4. Accelerometers attached to the center top of blocks A (Atopacc) and B (Btopacc) measured magnitude of the block acceleration. Relative displacement between blocks A and B was measured directly with displacement transducers located between the hinge area on the north side (GAP1) and south side (GAP3) of the blocks. Restrainer elongation was calculated by subtracting the displacement at restrainer engagement from the relative displacement. GFRP restrainer force was calculated by multiplying the GFRP restrainer stiffness (40 kN/mm (233 kip/in)) by restrainer elongation.

Table 5-2 displays the maximum specimen response determined during the GFRP restrainer shake table tests. The maximum restrainer elongation occurred in the GFRP restrainers on the south side of the blocks. The response histories reveal a small relative displacement between concrete blocks and a large maximum restrainer force. Block B measured the greatest block accelerations. The accelerations ranged from 0.75g measured at a peak ground acceleration of 0.05g to a block acceleration of 2.66g measured at a PGA of 0.3g.

Table 5-2 shows that under dynamic motion, the largest restrainer elongation measured for each incremental test ranged from 3.86 mm (0.152 in) measured at a PGA of 0.05g to 9.14 mm (0.360 in) measured at a peak ground acceleration of 0.3g. This GFRP restrainer elongation of 9.14 mm (0.36 in) exceeded the expected maximum elongation. The manufacturers design elongation at failure is 2.2%. With a flexible composite hinge length of 267 mm (10.5 in), the projected maximum restrainer elongation was 5.9 mm (0.23 in). This maximum elongation, above that of the manufacturers design specifications, may have either been a result of bond slippage, though none was apparent.

The restrainer forces listed in Table 5-2 is a summation of the calculated force in both the south and north side restrainers. Under earthquake motion, these GFRP restrainer forces were calculated at 208 kN (46.7 kips) for a PGA of 0.05g to a maximum total force of 372 kN (83.6 kips) at a PGA of 0.3g. These forces were far in excess of the maximum total restrainer forces of 36 kN (8 kips) seen in the earlier steel and SMA restrainer tests performed at UNR.

5.3 CFRP

The second set of shake table tests consisted of testing CFRP restrainers subjected to ATC32E unidirectional earthquake motion. Successive ground motion records with a PGA of 0.05g to 0.2g were applied. The observed performance of the CFRP restrainers for different runs is summarized in Table 5-3 and Fig. 5-11. At a peak ground acceleration of 0.05g, 0.1g, and 0.15g (Fig. 5-11(a), (b), (c), (e), (f), (g)), no damage was observed in either the north or south side restrainers. At a peak ground acceleration of 0.2g (Fig. 5-12(d) and Fig. 5-12(h)), the south restrainer fractured. This failure occurred in a sudden rupture of

the flexible CFRP in the hinge area of the specimen. Close-ups of the rupture of the south side restrainer captured from video images are shown in Fig. 5-12. The images clearly show that the fracture occurred at once in the upper half of the restrainer and then propagated. Unlike the failure of GFRP restrainer, the failure was not a localized fracture at the edge.

Following the rupture of the south restrainer, large rotational movement of the blocks was observed due to the loss of symmetry. This rotation resulted in debonding within the plate of the still intact north restrainer, between the unidirectional portion of the restrainer and the CFRP bonded to the blocks (Fig. 5-11(d)). This debonding led to a change in restrainer design for the hybrid restrainer. In the GFRP and CFRP restrainer fabrication, the elastomer-coated portion of the restrainer was epoxied directly above the 45 and 135-degree fabric sheets forming the FRP plates. The design change involved sandwiching the unidirectional portion of the restrainer in between the angled fabric to prevent premature debonding within the plate.

5.3.1 Response Histories

The block response histories for the CFRP restrainers are seen in Fig. 5-13 through Fig. 5-16. The instrumentation used to determine the acceleration and displacement for the CFRP restrainer experiments was shown in Fig. 4-5. Two supplementary accelerometers were attached to the center bottom of blocks A and B (ABottomacc and BBottomacc). Four additional accelerometers attached to the north and south side of the blocks (ANacc, BNacc, ASacc, BSacc) measured acceleration on the east and west side of the hinge area. Relative displacement between blocks A and B was measured with displacement transducers located between the hinge area on the north side (GAP1), middle (GAP2), and south side (GAP3) of the blocks. Restrainer elongation was calculated directly. This was accomplished by zeroing the instrumentation concurrent with restrainer engagement. Unimeasure string potentiometers were attached from the shake table to a fixed frame to capture absolute displacement in both the x and y direction (TABLE DISP X and TABLE DISP Y). CFRP restrainer force was calculated by multiplying the flexible CFRP stiffness (62 kN/mm (356 kip/in)) of the 76 mm (3 in) wide, 267 mm (10.5 in) strip by restrainer elongation.

Table 5-4 displays the maximum specimen response determined during the CFRP restrainer shake table test data. The response histories reveal a smaller relative displacement and larger maximum restrainer force than was seen in the GFRP restrainer tests. This is because of the higher stiffness of CFRP restrainers. The maximum block accelerations ranged from 0.88g measured at a peak ground acceleration of 0.05g to a maximum of 2.67g measured at restrainer failure.

Table 5-4 shows the maximum CFRP restrainer elongation of 4.29 mm (0.169 in) measured on the north side of the specimen at a PGA of 0.2g. The maximum restrainer elongation in the south restrainer measured 3.63 mm (0.143 in.) at a PGA of 0.15g. During this run, the integrity of the south restrainer appeared to have been compromised even though failure was not observed until a PGA of 0.2g (Fig. 5-13). This was apparent in the drop of force seen between a PGA of 0.15g and 0.2g. The maximum restrainer elongation was in excess of the manufacturers design elongation at break of 1.2%. With a flexible composite hinge length of 267 mm (10.5 in), the projected maximum restrainer elongation at failure was 3.2 mm (0.13 in). This rupture occurred early in the last test. At a PGA of 0.2g, the south restrainer failed and the north restrainer picked up the additional force due to the excessive block rotation. This resulted in large transverse motion and a maximum measured restrainer elongation of 4.29 mm (0.169 in) in the north side restrainer.

The rupture of the south side CFRP, restrainer seen in Fig. 5-12, was captured with a 640x480 resolution monochrome machine vision camera. The frames, seen in Fig. 5-12, were extracted from an Audio Video Interleave (AVI) and saved as a bitmap image. AVI is a Microsoft-specified format for saving audio and or video clips. You can play the files through the Media Player in Windows or through many popular browser plug-in multimedia players.

Total restrainer forces are listed in Table 5-4. At a PGA of 0.05g, 0.1g, 0.15g, and 0.2g, the calculated CFRP restrainer forces were 164 kN (36.8 kips), 297 kN (66.8 kips), 401 (90.1 kips), and 308 kN (69.2 kips), respectively. The maximum total force of 401 kN occurred at a PGA of 0.15g. After this run, the north side restrainer sustained all of the forces. The maximum restrainer forces seen in the CFRP restrainers were slightly larger than those calculated for the GFRP restrainers.

5.4 CGFRP (Hybrid)

Three sets of tests were performed on the CGFRP restrainers. The first and second sets of tests (Series 3-1 to 3-6, Table 5-5) consisted of tests in the longitudinal direction of the blocks (parallel to the restrainers). The synthetic earthquake motion, ATC 32E was applied in the first set of hybrid restrainer tests. In the second set of CGFRP restrainer tests (Series 3-1S, 3-2S, Table 5-5) the 1994 Sylmar record was applied. The objective of the second set of tests was to compare specimen response under both the synthetic and a recorded ground motion. The third set of tests (Series 3-1T, 3-2T, Table 5-5) involved ground motion ATC32E applied in the transverse direction of the blocks (perpendicular to the restrainers). The enhanced performance of the hybrid restrainers allowed for these additional shake table tests. As in the earlier GFRP and CFRP restrainer tests, the table acceleration was increased in successive runs.

Table 5-5 illustrates the observed performance of all three sets of CGFRP tests. The instrumentation used during the CGFRP restrainer tests was displayed in Fig. 4-6. There was no change in the location or type of instrumentation used in the GFRP and CGFRP tests. The displacement transducers on either side of the north and south gap had to be removed during tests in the transverse direction to prevent instrument damage.

5.4.1 Series 3-1 to 3-6

No significant restrainer damage was observed in the first set of hybrid restrainer tests. Small restrainer damage was observed on the upper edge of the carbon strip in the hinge area at a PGA of 0.25g (Series 3-5) on the north side of the specimen. This is illustrated in Fig. 5-17(e). At a PGA of 0.3g (Series 3-6), Fig. 5-17(f) displays a small elongation of this tear. No damage was observed in the south restrainer during test Series 3-1 to 3-6. As in the GFRP restrainer tests, this series of tests ended due large bearing displacements.

5.4.1. a Response Histories

The stiffness of the flexible CGFRP (82 kN/mm (470 kip/in)) was higher than that of the GFRP and CGFRP. The hybrid restrainer response histories reveal small relative displacement between concrete blocks and a large maximum restrainer force. Table 5-6 displays the maximum specimen response determined during all three series of CGFRP restrainer shake table tests. Figures 5-20 through 5-25 and Table 5-6 show restrainer elongation less than that seen in the GFRP and CFRP tests due to the increased hybrid restrainer stiffness. This resulted in large maximum restrainer forces. These forces were more than 1.4 times those estimated for the previous tests. Block accelerations witnessed in the hybrid restrainer tests are comparable to those seen in the GFRP and CFRP restrainer experiments. These accelerations range from 0.81g under a PGA of 0.05g to 2.67g at a PGA of 0.3g.

Table 5-6 shows that under dynamic motion, the largest restrainer elongation measured for each test ranged from 1.63 mm (0.064 in) measured at a PGA of 0.05g to 3.71 mm (0.146 in) measured at a peak ground acceleration of 0.3g. The CGFRP restrainer, with a stiffness twice that of the GFRP restrainer, had a maximum elongation of 3.71 mm (0.146 in), approximately 2.5 times less than that seen in the GFRP restrainer tests.

The restrainer forces for Series 3-1 to 3-6 are listed in Table 5-6. The maximum forces ranged from 134 kN to 579 kN (30.1 kips to 130.1 kips). The force histories for the CGFRP restrainers, seen in Fig. 5-18(c) through Fig. 5-23(c), show frequent restrainer engagement. This is revealed in the peaks of maximum force seen in the graphs. As stated earlier, the synthetic earthquake motion, ATC32E, provided frequent restrainer engagement.

5.4.2 Series 3-1S and 3-2S

The Sylmar earthquake record was used in Series 3-1S and 3-2S. One quarter, 0.15g, and one half, 0.3g, scaled versions of the Sylmar acceleration records were used. This provided comparable peak ground acceleration of ATC32E and Sylmar to judge the performance of the hybrid restrainers under different motions. Figure 5-24 shows the effect of SYLMAR on the CGFRP restrainers. At a PGA of 0.15g, no additional damage was seen on either the north or south restrainers. Small fiber damage, Fig. 5-24(d), was observed in the top of the south restrainer at a PGA of 0.3g. Table 5-6 shows that at equal PGAs, similar forces were estimated for the restrainer subjected to the two earthquake motions.

5.4.2.a Response Histories

Acceleration, restrainer elongation, and force histories for the SYLMAR tests are shown in Fig. 5-25 and Fig. 5-26. These histories reveal an interesting difference between the responses of the hybrid restrainers subjected to the two earthquake motions. The acceleration peaks seen in Fig. 5-20(a) and Fig 5-25(a) illustrate this difference. These graphs show the increased frequency of impact that occurs under the synthetic earthquake motion, ATC32E. At a PGA of 0.3g, similar results were seen in Fig 5-23(a) and Fig. 5-26(a). These differences resulted in more demanding shake table tests for those restrainers subjected to ATC32E. The hybrid restrainers remained intact through these first two sets of SYLMAR tests.

5.4.3 Series 3-1T and 3-2T

The CGFRP restrainers were subjected to motion in the transverse direction for Series 3-1T and 3-2T. Note that the two blocks were not restrained against relative transverse motion except for the restrainers that were intended to serve as longitudinal restrainers. Ordinarily bridges are equipped with transverse shear keys to eliminate significant transverse displacements. Most of the information obtained in these tests was based on observation because the model was not instrumented to measure transverse movements. Because ATC32E was judged to be a more demanding motion than SYLMAR, it was used in these tests. Two motions, one with a PGA of 0.05g, and the other with a PGA of 0.1g, were applied (Table 5-5). During the latter test there was a bond failure, thus preventing further testing. No additional damage was seen in the restrainers themselves. Figure 5-27 shows the effect of the transverse motion. The bond failure at the interior edge of the bonded plates is illustrated in Fig. 5-27. At a PGA of 0.05g, the failure is observed as the outlined area in both Fig. 5-27(a) and Fig. 5-27(c). Fig. 5-27(b) and Fig 5-27(d) show an increasing unbonded area of the FRP plates. A close-up of the debonding is seen in Fig. 5-28. At a PGA of 0.05g, the transverse motion initiated separation of the interior of the plates from

the portion of the restrainer affixed to the blocks. Ultimate bond failure of the restrainers occurred from further unbonding at a PGA of 0.1g. Figure 5-28 shows more extensive debonding on the west side of the north restrainer and the east side of the south restrainer. This was a result from the additional rotation introduced into the blocks during these tests of 3-1T and 3-2T.

5.4.3. a Response Histories

Figure 5-29 and Fig 5-30 illustrate the relative displacement histories between blocks A and block B in the transverse direction and restrainer elongation histories in the longitudinal direction. Table 5-6 displays the maximum longitudinal restrainer elongation at peak ground acceleration of 0.05 and 0.1g. At a PGA of 0.05g, restrainer elongation was 1.7 mm (0.067 in), but at 0.1g, the restrainer lengthened by 7.5 mm (0.307 in). The maximum elongation seen in the CGFRP restrainer tests was in keeping with the expected elongation designated by the manufacturer. Large translation in the transverse direction resulted in relative displacement between blocks in the excess of 83 mm (3.28 in) at restrainer failure. This measured data does not record the rotation seen during test series 3-1T and 3-2T.

5.5 Concluding Remarks

Engagement of FRP bridge restrainers during dynamic motion resulted in high restrainer forces and low relative displacements between blocks. The CFRP restrainer ruptured at a peak ground acceleration of 0.2g after reaching a maximum restrainer force of 401 kN (90 kip) and restrainer elongation of 4.3 mm (0.17 in). The glass restrainer was still intact at a PGA of 0.3g. The GFRP restrainer tests were terminated due to large elastomeric pad displacements. The maximum restrainer force achieved in the GFRP restrainer tests was 372 kN (84 kip) with a maximum restrainer elongation of 9.14 mm (0.36 in).

The hybrid restrainer was strong and ductile enough to allow three series of tests. The first involved the same synthetic earthquake motion, ATC 32E, and direction, similar to those of the GFRP and CFRP restrainer tests. The hybrid restrainer performed very well under this motion, with a maximum restrainer force of 579 kN (130 kip) and maximum elongation of 3.71 mm (0.146 in) at a PGA of 0.3g. No restrainer damage was observed at the end of the first series of tests. The second set of CGFRP restrainer tests involved longitudinal motion but with a real recorded earthquake motion, SYLMAR. The SYLMAR motion did result in comparable forces and restrainer elongation to those seen in the first series of tests but it resulted in less frequent restrainer engagement and block impact. Because ATC32E proved to be a more demanding earthquake motion, it was input into the shake table for the third set of CGFRP restrainer tests to explore the effect of transverse earthquakes on restrainers that are designed for longitudinal motions. At a PGA of 0.05g, the FRP plates of the restrainers began

to unbond from the concrete blocks at the inner edge of the plates. The third set of hybrid restrainer tests ended at a PGA of 0.1g due to very large displacement of the base isolators in the transverse direction. Large FRP/concrete separation (Fig. 5-28) was seen.

Direct measurement of restrainer force was not achievable during the FRP restrainer tests. Fiber optics incorporated into the restrainer would allow for direct measurement of restrainer force and may be used in future studies.

Motion in the transverse direction resulted in bond failure between the FRP plate of the restrainers and the concrete of the blocks. This is an unlikely scenario in an actual bridge, because bridges typically are equipped with transverse shear keys that prevent significant transverse relative displacements at hinges. To improve on bond and to resist transverse movement after potential failure of shear keys, FRP anchors may be used. An example anchor manufactured by the Fyfe Company is shown in Fig. 5-31. The anchors are composed of high-strength fibers embedded in a thickened Tyfo epoxy matrix (Fyfe Co. 2004). They increase bond strength and durability. Prior to bonding of the plates, anchor locations should be predrilled. The anchor penetrates the first layer of the plate and is splayed out and sandwiched by the second layer of the outer plate. Use of this system would require some design changes in the restrainers.

CHAPTER 6

COMPARISONS OF RESPONSE OF FRP RESTRAINERS WITH STEEL AND SMA RESTRAINERS

6.1 Introduction

This chapter compares the measured response of the GFRP, CFRP, and CGFRP restrainers. Additional response comparisons were made between CGFRP restrainers subjected to the synthetic motion, ATC32E, and the Sylmar motions. To evaluate the relative merit of different restrainer types, selected measured FRP restrainer data were compared with those of steel and SMA restrainers. Because the measured data for different FRP restrainer types were similar, the results for GFRP restrainers were assumed to represent the FRP restrainer responses and were used in this part of the study.

6.2 GFRP, CFRP, CGFRP Comparisons

The measured response histories for the GFRP, CFRP, and CGFRP restrainers are compared in this section for all of the earthquake runs discussed in previous chapters. These runs are seen in Table 6-1. Table 6-1 illustrates the maximum restrainer force and elongation determined from previous UNR shake table tests for different types of cable, or tension only, hinge restrainers. Two distinct cases were of particular interest. Case 1, involves the parameters of study discussed in Chapter 4, with peak ground accelerations of 0.15g. Case 2 is identical to Case 1, with the exception of a PGA of 0.2g. Under Case 1, the steel, SMA, GFRP, CFRP, CGFRP (using ATC32E and Sylmar earthquake motion) cable restrainers are compared. At 0.15g, failure did not occur in any of the restrainers. Under Case 2, at a PGA of 0.2g, failure was seen in both the steel and CFRP restrainers. Both the carbon and steel restrainers failed in rupture.

Due to the failure of the CFRP restrainers at a PGA of 0.2g (Case 2), only the response for the glass and hybrid restrainers are compared for runs with a PGA of 0.25 and 0.3g. The block acceleration histories are compared for Block B, the softer of the two blocks, because it produced the highest block accelerations. The elongation histories for the south restrainer are compared for the runs mentioned above. South restrainer elongation was slightly larger than north restrainer elongation. This was a consequence of the smaller initial slack that existed in the restrainer on the south side of the blocks, resulting in earlier restrainer engagement.

6.2.1 Response Histories

Figures 6-1 through Fig. 6-6 illustrate the response histories for the glass, carbon, and hybrid bridge restrainers. Positive accelerations indicate block movement in the east direction, while negative accelerations denote accelerations in the west direction. The block acceleration histories show that FRP restrainer type does not generally appear to have an effect on the maximum block acceleration. The peak acceleration does vary among tests with increasing peak ground acceleration. The maximum block accelerations ranged between 0.8g at a PGA of 0.05g to 2.5g at a PGA of 0.2g. The restrainer type affects the acceleration waveforms. The restrainer stiffness varies among different restrainer types. As a result the overall dynamic properties of the test model are changed, thus affecting the block accelerations.

Figure 6-1(b) through Fig. 6-4(b) illustrates restrainer elongation histories for the GFRP, CFRP, and hybrid restrainers. The least elongation is seen in the CGFRP restrainers and the largest restrainer lengthening is seen in the GFRP restrainers. This is expected due to the greater stiffness of the CGFRP restrainers (82 kN/mm vs. 40 kN/mm) vs. that of the GFRP restrainers. The rupture of the south CFRP restrainer is marked in Fig. 6-4(b). Figures 6-5(b) and Fig. 6-6(b) show that the maximum GFRP restrainer elongation was three times that of the CGFRP restrainer, although the stiffness of the GFRP restrainer is one half that of the CGFRP restrainer. The glass portion of the CGFRP restrainer is capable of the maximum elongation seen in the GFRP restrainers; this points out the greater potential of the hybrid restrainer to remain intact during earthquake motions.

Figures 6-1(c) through Fig. 6-6(c) demonstrates the calculated total force histories for the FRP restrainers. These graphs mirror the elongation histories seen in Fig. 6-1(b) through 6-6(b). This is because the FRP restrainer forces were found as the product of the restrainer elongation and the restrainer stiffness.

6.3 Comparison of CGFRP Restrainer Response for Different Motions

CGFRP restrainer response subjected to ATC32E and Sylmar earthquake records is compared. As stated in Chapter 5, ATC32E is a synthetic motion chosen to input into the shake table in previous restrainer tests because it placed high demands on the restrainer models. The ATC32E has a relatively large number of high-amplitude pulses compared to the number that is typical of recorded earthquakes. An overlay of earthquake spectra for ATC32E and Sylmar, both normalized to PGA of 0.15g, is shown in Fig. 6-7. The figure illustrates the higher response of ATC-32E record over the period of interest in these tests, 0.6 sec and 1 sec. It can be observed, that at a structural period of

1.75 sec, these spectra intersect and minimal differences are seen for longer periods.

6.3.1 Response Histories

Figures 6-8 and 6-9 illustrate the response histories from the CGFRP restrainer tests at a PGA of 0.15g and 0.3g. The block acceleration, restrainer elongation, and total restrainer force histories under both records are compared. The acceleration peaks seen in the figures show the frequency of the block impact and restrainer engagement. These figures demonstrate the higher number of block impacts measured in the shake table input with the ATC32E earthquake motion. The restrainer elongation histories from the hybrid restrainer tests verify the increased demand felt by the restrainers when subjected to the synthetic motion. Figure 6-8(b) shows that under Case 1, the restrainers experienced slightly larger elongation twice during the Sylmar tests, but the lower frequency of impact resulted in no observable restrainer damage during these tests. The calculated force histories for both Case 1 and Case 2 can be observed in Fig. 6-8(c) and Fig. 6-9(c).

6.4 Comparisons of Response for Different Restrainer Types

The large discrepancy between restrainer force and maximum elongation of the FRP and other restrainer types can be noted in Table 6-1. For Case 2, the largest measured total restrainer force of 36 kN (8.1 kips) for the steel restrainers can be compared to the largest calculated total restrainer force of 390 kN (87 kips) for the CGFRP restrainer. In Case 1, the maximum elongation of the steel cable restrainer was 38 mm (1.5 in.), compared to the maximum GFRP restrainer elongation of 3.58 mm (0.141 in.).

Limited previous tests, conducted at UNR, to determine the performance of steel and SMA restrainers under dynamic movement have concluded that SMA is superior to steel in reducing relative displacement in the hinge area of bridges (Johnson et al. 2004). The maximum displacement for blocks restrained by SMA restrainers was less than half that of the blocks restrained by steel restrainers. To compare FRP restrainer histories to that of steel and SMA restrainers, the GFRP response was chosen, as being representative of FRP restrainer responses. An overlay of the equivalent earthquake spectra for these three restrainer types is seen in Fig. 6-10 and Fig. 6-11. Restrainer elongation is greater in GFRP than the CFRP and CGFRP restrainers, but compared to the steel and SMA restrainers, the differences among the elongation of different FRP restrainer types were minimal (Table 6-1). This is demonstrated in Fig. 6-12 and Fig. 6-13. Figure 6-12 shows the higher maximum displacement observed in the steel and SMA restrainers compared to the maximum restrainer elongation measured in the glass, carbon and hybrid restrainers under Case 1. Figure 6-13 illustrates a similar trend in Case 2.

6.4.1 Response Histories

Figures 6-14 through Fig. 6-16 show the block acceleration, relative hinge movement, and total restrainer force histories from the GFRP, steel, and SMA restrainer shake table tests. Case 1 and Case 2 (Table 6-1) are used for these comparisons. Fig. 6-14(a) and Fig. 6-14(b) illustrate the differences in the magnitude of block acceleration measured during these tests. The largest block accelerations were measured during the steel restrainer tests. The peaks, representing the impacts, are greatly reduced in those blocks being restrained by the SMA or the FRP restrainers. This reduction in acceleration would result in less damage to the structure during an earthquake.

The relative hinge movement histories in Fig. 6-15(a) and Fig. 6-15(b) demonstrate the small displacement measured during the GFRP restrainer tests. The lower portion of the graph in Fig. 6-15(a) represents the hinge gap closure and block impact. The portion of the y-axis from the point of impact to the zero point represents the measured gap between the blocks. It can be observed that the block gap during the steel restrainer tests was close to 25.4 mm (1 in) while the block gap during the SMA and GFRP restrainer tests was 12.7 mm (0.5 in). The darkened horizontal line showing restrainer engagement in Fig 6-15(b) shows the approximately 12.7 mm (0.5 in) restrainer slack that was present in all three types of restrainers. The relative hinge movement of the blocks being restrained by the GFRP restrainers is barely visible above this line. These relative hinge movement histories reveal the superior ability of GFRP restrainers in reducing displacement.

Previous studies on restrainers (Saiidi, et al. 1996, Camargo-Sanchez et al. 2004 and Vlassis et al. 2000) have determined that no gap between blocks results in higher restrainer forces. This difference in block gap between the steel and SMA restrainer (12.7 mm (0.5 in)), and GFRP restrainer (25.4 mm (1 in)) tests does not appear relevant in the comparable total force history cases seen in Fig. 6-16. The measured steel and SMA restrainer forces are far less than the restrainer forces calculated during the GFRP restrainer tests. This is a result of the elastic behavior of FRP. The maximum forces calculated in the GFRP restrainers were approximately ten times those measured in the steel and SMA restrainers.

CHAPTER 7

RESTRAINER DESIGN APPROACH

7.1 Introduction

This chapter discusses different design procedures for hinge restrainers and presents a new design procedure for FRP restrainers subjected to longitudinal earthquake motions. Several simple current methods are reviewed. The use of one existing and the proposed new design method for FRP restrainer design is demonstrated through a design example.

7.2 Existing Restrainer Design Procedures

Several seismic restrainer design methods are available (CALTRANS 1990, AASHTO 1996, DesRoches and Fenves 1997, Saiidi et al. 2001, Trochalakis et al. 1995). After the 1971 San Fernando earthquake, CALTRANS developed a simple method and chose steel cable restrainers to connect adjacent frames to prevent unseating or collapse of contiguous bridge spans. Subsequent to the introduction of this program by CALTRANS, many states throughout the U. S. began their own seismic restrainer retrofit programs, using either cable or rod restrainers (Saiidi et al. 1992). The CALTRANS method has undergone several changes. One of the earlier CALTRANS methods is currently recommended by AASHTO. This section provides an overview of the more common and relatively simple methods and introduces a new simple method.

7.2.1 CALTRANS

The CALTRANS restrainer design procedure can be applied using hand calculations. The method considers limiting the displacement of the stiffer of the two frames adjacent to the hinge area. The number of the restrainers required to limit the restrainer deformation to the available seat width is determined assuming that the restrainers are rigidly anchored at the far end. The restrainers are designed to remain elastic at the allowable hinge displacement. Following the 1989 Loma Prieta and subsequent 1994 Northridge earthquake, several investigators (Saiidi et al 1993, Moehle 1995) studied the structural impact of strong motion on bridges and found a few cases where the restrainers had failed under excessive longitudinal movement of adjacent frames. This led to reexamination of the design and performance of bridge restrainers. The CALTRANS restrainer design procedure was found to be conservative during in-phase motion of adjacent frames and not conservative enough in the case of out-of-phase movement (Yang et al. 1994). The CALTRANS method involves several steps that account for hinge gap closure, abutment participation, etc. (CALTRANS 1990) presents the method and a design example.

7.2.2. AASHTO

The AASHTO design procedure for bridge restrainers is a very simple method (AASHTO 1996). It requires a longitudinal linkage force between frames that is equal to the design ground acceleration coefficient times the weight of the lighter of the two adjoining frames. The AASHTO design method does not take into account either the relative displacement between frames or the vibration periods of the frames.

7.2.3 Trochalakis et al. (1997)

This design method is a modification to the CALTRANS procedure. The two methods differ, in that the maximum unrestrained hinge displacement, D_{eq} , is estimated by taking one half of the average displacement of the unrestrained frames and multiplying this by ratio of the fundamental periods of the softer and stiffer frames to determine equivalent unrestrained displacement. The Trochalakis method bases the equation of D_{eq} on regression analysis of a large number of cases. The Trochalakis method provides a more accurate way of determining restrainer demand than the CALTRANS method.

7.2.4 DesRoches and Fenves (1997)

DesRoches and Fenves evaluated the CALTRANS and AASHTO restrainer design procedures and developed a method for restrainers at in-span hinges. They proposed an iterative restrainer design procedure. Their procedure “represents the dynamic characteristics and out-of-phase motion of adjacent bridge frames, including the inelastic behavior of frames. Two-degree of freedom modal analysis is performed to determine the relative hinge displacement using the complete quadratic combination (CQC) rule” (DesRoches et al. 2001). Each iteration consists of a 2-DOF modal analysis followed by the use of an updated estimate of restrainer stiffness. A simplified version of the DesRoches design procedure was developed that does not require iteration. The simplified DesRoches procedure is based on restrainer stiffness being a function of the frame stiffness, initial hinge displacement, target displacement, and target ductility of the frames.

7.3 New Restrainer Design Method (2004)

A new simple method was developed for design of seismic restrainers. It is a force-based design procedure, although it includes a displacement check to ensure that unseating is prevented. The basic assumption in the proposed method is that FRP restrainers rigidly connect the two adjacent segments of the bridge. The linkage of the two bridge frames reduces the two-degree-of-freedom system of the bridge frames to a single-degree-of-freedom system (Fig. 7-1). This conversion of a 2 DOF to a 1 DOF system makes this new method a quick,

simple, and conservative design procedure. Compared with the AASHTO method, the proposed approach is more realistic because it accounts for the dynamic characteristics of the bridge, without introducing significant complication.

With the combined mass (m), and stiffness (k), the fundamental period of the system is calculated. Then, with the period, acceleration is determined from the response spectrum. Using the acceleration and the combined mass and stiffness, the displacement of the combined system is determined. The restrainer force is calculated by considering the free-body diagram of either one of the frames (Fig. 7-2)

7.4 Examples

Design examples are presented to demonstrate the application of two simple methods: the methods by AASHTO, and that proposed in the present study. The following examples use CFRP with a design strength of 745 MPa (108 ksi) and a design tensile modulus of 61.5 GPa (8.9E3 ksi). Maximum elongation at rupture or yield for this material is 1.2 percent. Assume a 610 mm (2 ft) length for flexible portion of restrainer in hinge area. The bridge in this example is assumed to be located in San Francisco. The effective stiffnesses for the bridge are based on a displacement ductility of the bridge frames of $\mu=4$. The two frames have weights of 22.3 MN (5000 kips), and stiffnesses $K_1 = 357$ kN/mm (2040 kips/in) and $K_2 = 179$ kN/mm (1020 kips/in), respectively. The restrainers are designed for a seismic loading based on the NEHRP design spectrum (Fig. 7-3) for a return period earthquake of 475 years and the site is assumed to be on stiff soil. For the proposed restrainer design method, the period of the structure is taken into account, so the following acceleration and displacement are calculated from the NEHRP map:

$$S_1 = 0.6, F_v = 1.5, S_{D1} = 0.9, S_s = 1.5, F_a = 1, S_{DS} = 0.6$$

S_1 = 1-second period spectral acceleration on
Class B rock from the 1996 USGS
national ground motion maps

F_v = site coefficient for long-period portion of
design response spectrum curve

S_{D1} = design earthquake response spectral
acceleration at 1-second period

S_s = 0.2-second period spectral acceleration on
Class B rock from the 1996 USGS
national ground motions maps

F_a = site coefficient for short-period portion of
design response spectrum curve

S_{DS} = design earthquake response spectral
acceleration at short periods

7.4.1 AASHTO

The following steps are used in the AASHTO method:

Step 1 – Determine the design ground acceleration, S_a .

$$S_a = 0.6g$$

Step 2 – Determine the restrainer force by multiplying S_a by the lighter of the two adjacent bridge frames.

$$F_r = S_a * m_1 \quad (\text{Eq. 7-1})$$
$$F_r = 0.6g * 22.3 \text{ MN} = 13.8 \text{ MN} (3102 \text{ kip})$$

Step 3 – Design Restrainer Per Side of Bridge

$$\text{Required restrainer area} = F_r / F_{y\text{FRP}}$$
$$\text{Area} = 13.8 \text{ MN} / 745 \text{ MPa} = 18523 \text{ mm}^2 (28.71 \text{ in}^2)$$

Determine restrainer size to find dimensions of flexible composite per side, assuming a FOS of 1.5. Note that in the experimental studies a higher factor of safety was used. However, the FOS of 1.5 appears to be sufficient and yields reasonable results.

$$(\text{Area} * \text{FOS}) / 2 \text{ sides of bridge} = 18.52\text{E}3 \text{ mm}^2 * 1.5 / 2 = 13892 \text{ mm}^2 \text{ per side}$$

$$\text{Thickness of one layer of carbon composite} = 1 \text{ mm} (0.04 \text{ in})$$

$$\text{Assume width of restrainer} = 914 \text{ mm} (3 \text{ ft})$$

$$\text{Required number of composite layers} = 13892 / (914 * 1) = 15 \text{ layers per side}$$

Final Design: 15 layers of 610 mm (2 ft) x 914 mm (3 ft) CFRP per side

7.4.2 New Restrainer Design Method

The following steps are used in the new method:

Step 1 – Determine the period of vibration for the combined system.

$$T_{\text{tot}} = 2\pi * [(m_1 + m_2) / (k_1 + k_2) / \mu]^{(0.5)} \quad (\text{Eq. 7-2})$$
$$T_{\text{tot}} = 2\pi * [(2 * 22.3) / (9.81 * (357 + 179) / 4)]^{(0.5)} = 1.157 \text{ sec}$$

Step 2 – Determine the spectral acceleration, S_a , using the period of vibration of the combined system and the acceleration spectrum for the bridge.

$$S_a = S_{D1} / T_{\text{tot}} = 0.78g$$

Step 3 – Determine the displacement of the combined system

$$\Delta = [(m_1 + m_2) * S_a] / (k_1 + k_2) \quad (\text{Eq. 7-3})$$
$$\Delta = [(2 * 22.3 \text{ MN}) * 0.78g] / (179 \text{ kN/mm} + 357 \text{ kN/mm}) = 65 \text{ mm}$$

Step 4 – Determine the restrainer design force using equilibrium

$$(m_1 * S_a) + F_r = R_1 \quad (\text{Eq. 7-4})$$

$$(m_1 * S_a) + F_r = k_1 * \Delta \quad (\text{Eq. 7-5})$$

$$F_r = [k_1 * [(m_1 + m_2) * S_a] / (k_1 + k_2)] - (m_1 * S_a) \quad (\text{Eq. 7-6})$$

$$F_r = [[k_1 * (m_1 + m_2) / (k_1 + k_2)] - m_1] * S_a \quad (\text{Eq. 7-7})$$

$$F_r = [[179 * (2 * 22300) / (179 + 357)] - (22300)] * .78 = 5.78 \text{ MN (1298 kip)}$$

Step 5 – Design Restrainer Per Side of Bridge

$$\text{Required restrainer area} = F_r / F_{y\text{FRP}}$$

$$\text{Area} = 5.78 \text{ MN} / 745 \text{ MPa} = 7753 \text{ mm}^2 \text{ (12.01 in}^2\text{)}$$

Determine restrainer size to find dimensions of flexible composite per side:

Assume a FOS of 1.5

$$(\text{Area} * \text{FOS}) / 2 \text{ sides of bridge} = 7.75\text{E}3 \text{ mm}^2 * 1.5 / 2 = 5813 \text{ mm}^2 \text{ per side}$$

$$\text{Thickness of one layer of carbon composite} = 1 \text{ mm (0.04 in)}$$

$$\text{Assume width of restrainer} = 914 \text{ mm (3 ft)}$$

Final Design: 6 layers of 610 mm (2 ft) x 914 mm (3 ft) CFRP per side

Step 6 - Check for unseating

Check that restrainer elongation is less than seat width

$$\Delta_{r+s} = L_r * 1.2\% \text{ Strain} + L_s < \text{Seat Width}$$

$$\Delta_{r+s} = [(610 * .012) + 12.7] = 20.0 \text{ mm (0.79 in)} < 152 \text{ mm (6 in)}$$

$$\Delta_{r+s} = \text{Restrainer elongation} + \text{Restrainer slack}$$

$$L_r = \text{Predetermined length of flexible FRP}$$

$$L_s = \text{Restrainer slack (typically 12.7 mm)}$$

7.5 Design of Attachment

As discussed in Chapter 3, the required area of the composite plate is based on experimental data. It was determined that the most conservative estimate of strength in the bonded area is the tensile strength of concrete. A FOS of 1.5 beyond that of the flexible portion of the restrainer is incorporated into this part of the design. Two checks must be made for dimensions of the composite plate; they are area required by concrete strength and development length of composite. This design method for the bonded plate is standard, regardless of the design procedure used for the flexible portion of the restrainer.

Area of each plate required in regard to f'_c

$$\text{Assume } f'_c = 31.03 \text{ MPa (4500 psi)}$$

$$F_{\text{bonded}} = 5.78 \text{ MN} / 2 \text{ sides} * (\text{flexible FRP FOS} * \text{FOS})$$

$$= (5.78 / 2 * 1.5 * 1.5) = 6.5 \text{ MN}$$

$$\text{Minimum required area of bonded plate} = F_{\text{bonded}} / (7.5 * (f'_c)^{(0.5)})$$

$$= 6.5 \text{ MN} / (7.5 * (31.03 \text{ MPa})^{(0.5)}) = 1.56\text{E}5 \text{ mm}^2 \text{ (241.1 in}^2\text{)}$$

Equating bond length to required area in regard to f'_c

$$\text{Required bond area} = \text{Width of flexible composite} * \text{Bond Length (} L_e \text{)}$$

$$1.56\text{E}5 \text{ mm}^2 \text{ (241.1 in}^2\text{)} = 914 \text{ mm (3 ft)} * L_e$$

$$L_e = 170 \text{ mm (6.7 in)}$$

$$L_e = (E_p * t_p / (f'_c)^{0.5})^{0.5}$$

$$170\text{mm} = (61.5\text{E}3\text{MPa} * t_p / (31.03 \text{ MPa})^{0.5})^{0.5}$$

$t_p > 1\text{mm}$ (each layer of composite lamina is 1 mm)

Assume 6 layers of composite in plate to be consistent with flexible composite

Find new L_e using known t_p

$$L_e = (61.5\text{E}3\text{MPa} * 6 \text{ mm} / (31.03 \text{ MPa})^{0.5})^{0.5}$$

$$L_e = 257 \text{ mm (10.1 in)}$$

Final Dimensions of CFRP restrainer (Fig 7-4):

Flexible Portion: 6 layers of 610 mm (2 ft) x 914 mm (3 ft) CFRP per side

Bonded Portion: 6 layers of 1219 mm (4 ft) x 1219 mm (4 ft) CFRP per end per side

7.6 Concluding Remarks

A new design procedure for restrainers subjected to longitudinal earthquake motions was developed. Several design methods were studied and a force-based procedure was found to be most applicable to the uniqueness of FRP but it is also a simple formulation for other restrainer types. Like the AASHTO method, it is easily adapted for the design of FRP restrainers. The incorporation of the structural response into the formulation of the new method eliminates the deficiencies identified in the AASHTO method. The proposed new restrainer design method is more realistic because it accounts for dynamic characteristics of the bridge without being complicated. Examples of one existing and the new design method were presented

The AASHTO restrainer design method was applied to the first example. The restrainer force demand found from this calculation was 13.8 MN (3102 kip) compared to the 5.78 MN (1298 kip) restrainer demand calculated from the new proposed design method. The required restrainer size of the flexible restrainer was 610 mm (2 ft) x 914 mm (3 ft) for both the AASHTO and new method, but using the AASHTO method resulted in 15 layer restrainer thickness compared to the six layers of composite required by the proposed design method. This new method led to a smaller restrainer area. The six-layer flexible restrainer thickness obtained in the new method results in a realistic restrainer size both for manufacture and application.

Following the design example for the flexible portion of the restrainer in the hinge area, the attachment system was designed in Section 7-5. A FOS of 1.5 was incorporated into the design of the flexible restrainer, and above that, a FOS of 1.5 was incorporated into the design of the outer stiff composite plates to account for the brittle nature of bond failure (this produced a conservative FOS of 3 for the stiff composite). These bonded plates were designed using both the shear

strength of concrete and effective bond length formulations. A simple and possibly overly conservative method can be used for FRP plate design once the dimensions of the flexible restrainer are known. The plate design would consist of square dimensions determined by twice the width of the flexible portion of the restrainer, with thickness, or number of composite layers equal to that of the flexible restrainer.

CHAPTER 8

SUMMARY AND CONCLUSIONS

8.1 Summary

The primary objective of this study was to evaluate the use of fiber reinforced plastic (FRP) fabrics as restrainers in the seismic rehabilitation of highway bridges. Both carbon and glass fibers were included in the study. Multiple stages of investigation led to the development of this new type of restrainer. Stage 1 consisted of identifying suitable materials for FRP restrainer applications. A test matrix of over 40 specimens was developed to study the response of glass and carbon FRP fabrics under different loading rates along with an additional tests matrix of 40 specimens to investigate the response of bond between FRP fabric and concrete under different loading rates. Strain rate effect of FRP was of interest due to the dynamic nature of earthquake loading. Past shake table data for restrainers was evaluated to identify realistic strain rates. These strain rates consisted of one pseudo-static rate of $167 \mu\epsilon/\text{sec}$ and five high strain rates, from $1000 \mu\epsilon/\text{sec}$ to $100000 \mu\epsilon/\text{sec}$.

The results of tensile tests on uncoated FRP fabric strips revealed the necessity to coat the strips to insure composite action among fibers. The commonly used epoxy matrix was not suitable because it changes FRP to a rigid member, whereas FRP restrainers need to remain flexible so that they deform under compressive loads, thus preventing large compressive forces. A new elastomeric coating material was identified and was used to make flexible FRP elements. Tests on flexible glass and carbon strips showed that failure typically occurred at the edges of the specimens near the mid depth. Results also indicate that there is no strain rate effect on FRP.

Single lap pullout tests were designed for testing the FRP-to-concrete bond. These single lap tests showed that the minimum and often controlling factor of bond strength is related to the strength of concrete. Unlike the strip tests, bond strength was sensitive to the strain rate. This is because of the concrete strength is affected by the strain rate. The bond failure was brittle.

The second stage of this project was the development and testing of an FRP bridge restrainer under dynamic loading. To enable comparisons between previous shake table tests conducted at UNR on steel and SMA cable restrainers, an identical test set-up was used. Evaluation of data collected during the material tests and previous restrainer tests led to the restrainer design. Three types of restrainers were manufactured and tested, in the following order: GFRP,

CFRP, and a hybrid (CGFRP). Data analysis of the restrainer tests led to design modification in subsequent restrainer designs. An ATC32E compatible synthetic record was used as the input earthquake motion because in previous UNR restrainer tests it was shown to provide many high amplitude pulses, which resulted in frequent restrainer engagement. Unidirectional motion was used for all tests. Additional shake table tests in the transverse direction; and an earthquake motion simulating the 1994 Northridge-Sylmar were utilized for the hybrid restrainer tests. The peak ground motion was increased in increments of 0.05g, from 0.05g to a maximum of 0.3g. Note that even though this acceleration is relatively small, it caused large relative movements at the hinge of the unrestrained system and allow for restrainer studies under high demands. The peak ground acceleration of 0.3g was limited by the design displacement of the elastomeric pads attached to the test specimen.

The third stage of this project was analysis of the information collected during dynamic testing of the FRP restrainers. The acceleration and displacement data determined during the different FRP restrainer tests were compared. Data collected in the previous steel and SMA restrainer tests was also compared to measurements from the FRP restrainer tests. FRP restrainer elongation was small, but comparisons between FRP restrainer tests revealed larger relative displacement in the GFRP restrainer than in the CFRP and CGFRP restrainers. Calculated FRP restrainer forces were high due to the stiffness of the material. In comparable dynamic tests, FRP restrainers revealed relative displacement between hinges six to seven times less than that seen in the SMA tests and approximately 10 times less than the measured displacement from the steel restrainer tests. The largest accelerations were seen in the blocks restrained by the steel restrainers.

A new restrainer design procedure was developed in the last stage of this project. Several design methods were studied and a force-based procedure was found to be most applicable to the uniqueness of FRP but it is also a simple formulation for other restrainer types. The basic assumption in the proposed method is that FRP restrainers rigidly connect the two adjacent segments of the bridge. The linkage of the two bridge frames reduces the two-degree-of-freedom system of the bridge frames to a single-degree-of-freedom system. Compared to the AASHTO method, the proposed method is more realistic because it accounts for dynamic characteristics of the bridge without being complicated.

8.2 Conclusions

The general observations and conclusions derived from this study are outlined below:

1. All three types of FRP restrainers showed good performance during shake table tests at limiting relative hinge displacement between adjacent blocks and producing lower blocks accelerations than

traditional restrainers. FRP restrainers show promise as a seismic restraining device for bridges.

2. FRP strength was insensitive to strain rate (dynamic loading). This is because unlike homogeneous materials, there is internal slippage of the fibers and the slippage is insensitive to strain rate.
3. The method used to make a flexible restrainer using an elastomeric material and a vacuum system was effective.
4. The method used for the bond design and attachment of the restrainers was successful in achieving design bond strength.
5. The new restrainer design method produced more realistic restrainer demand than AASHTO by incorporating the uniqueness of FRP into the procedure. This new method led to a smaller restrainer area.
6. The performance of restrainers under a simulated recorded earthquake was similar to that of artificial earthquakes.
7. Transverse motion produced out-of-plane motion that can debond the restrainer. Transverse shear keys need to be sufficiently strong to prevent large transverse movement effects on FRP restrainers.
8. FRP/concrete bond strength is affected by strain rate because of its dependence to the concrete shear strength.
9. Comparisons among FRP restrainers and steel and SMA restrainers show a minimal elongation in FRP compared to that seen in the steel and SMA restrainers under an identical test set-up.

8.3 Recommendations for Further Work

Based on the testing and analysis performed in this study, the following recommendations are made with respect to future work:

1. Additional testing under bidirectional motions would provide a more realistic earthquake simulation program and would shed light on the effect of transverse motions on the longitudinal FRP restrainer performance.
2. The adequacy of nonlinear dynamic analytical modeling should be evaluated using the experimental data of the type obtained in this study.
3. Blast loading is a problem in bridge structures because of their lack of redundancy, particularly in the superstructure. Extremely large strain rates are achieved during this type of loading. Additional tests at high strain rates, in excess of 100000 $\mu\epsilon/\text{sec}$, are recommended.
4. This study analyzed the performance of FRP restrainers bonded to concrete. Additional studies should be performed to determine the performance of FRP restrainers on steel bridges.
5. In lieu of direct measurement, FRP restrainer force was calculated in this project using the stiffness and the measured displacements. FRP

restrainers with embedded optical fibers should be studied to provide a direct measure of the restrainer force.

REFERENCES

1. American Association of State Highway and Transportation Officials (AASHTO), (1996), "Standard Specifications for Highway Bridges, American Association of State Highway and Transportation Officials, Sixteenth Edition, 1996.
2. Bizindavyi, L., Neale, K. W., Erki, M. A., "Experimental Investigation of Bonded Fiber Reinforced Polymer-Concrete Joints under Cyclic Loading", *ASCE Journal of Composites for Construction*, pp 127-134, May 2003.
3. Brena, S. F., Wood, S. L. and Kreger, M. E., "Full-Scale Tests of Bridge Components Strengthened Using Carbon Fiber-Reinforced Polymer Composites", *ACI Structural Journal*, pp 775-794, Nov-Dec 2003.
4. Caltrans, Bridge Design Aids, California Department of Transportation, 1990.
5. Caltrans (California Department of Transportation), "Caltrans Seismic Design Criteria Version 1.2," Engineering Service Center, Earthquake Engineering Branch, California, December 2001.
6. Camargo-Sanchez, F., Maragakis, E. M, Saiidi, M. S., Elfass, S., "Seismic Performance of Bridge Restrainers at In-Span Hinges", Civil Engineering Department, Report N. *CCEER 04-04*, University of Nevada Reno, 2004.
7. Colak, Ozgen, "Mechanical Behavior of Polymers PBXW-128 and PBXN-110 Under Uniaxial and Multiaxial Compression at Different Strain Rates and Temperatures", *Journal of Testing and Evaluation*, Vol. 32, No. 5, pp 390-395, September 2004.
8. Dai, J., Ueda, T., "Interfacial Models for Fiber Reinforced Polymer (FRP) Sheets Externally Bonded to Concrete," Doctoral Dissertation, Division of Structural and Geotechnical Engineering, University of Hokkaido, Japan 2003.
9. DesRoches, R., and Fenves, G. L., "New Design and Analysis Procedures for Intermediate Hinges in Multiple-Frame Bridges", *EERC-97/12*, College of Engineering, University of California, Berkeley, December 1997.
10. DesRoches, R., and Fenves, G. L., "Design of Seismic Cable Hinge Restrainers for Bridges", *Journal of Structural Engineering*, pp 500-509, April 2000.

11. DesRoches, R., and Fenves, G. L., "Simplified Restrainer Design Procedure for Multiple-Frame Bridges", *Earthquake Spectra*, pp 551-567, November 2001.
12. Dow Corning, SYLGARD 184 Silicon Encapsulant Product Sheet, 2004.
13. Dusicka, P., Itani, A., and Buckle, I., "Cyclic Behavior of Shear Links and Tower Shaft Assembly of San Francisco-Oakland Bay Bridge Tower," *CCEER-02-6*, Department of Civil Engineering, University of Nevada, Reno, NV 2002.
14. Fyfe Co, "Tyfo SHE-51A Composite using Tyfo S Epoxy," *Product Details Sheet*, La Jolla, CA, 2003.
15. Fyfe Co, "Tyfo Fibrwrap Anchors", *Product Details Sheet*, La Jolla, CA 2004.
16. Grace, Nabil F., "Concrete Repair with CFRP", *Concrete International Journal*, 26, 5, pp 45-52, May 2004.
17. Handwerker, C., "NIST Research to Ensure the Integrity of Pipeline Facilities", Joint Pipeline R&D Forum, Washington, DC, December 2003.
18. Johnson, R. M., Maragakis, E. M., Saiidi, M. S., DesRoches, R., Padgett, J., "Experimental Evaluation of Seismic Performance of SMA Bridge Restrainers", *CCEER 04-2*, Department of Civil Engineering, University of Nevada, Reno, NV 2004.
19. Jones, Robert M., Mechanics of Composite Materials, 2nd Edition, Taylor and Francis, 1999.
20. Kamel AS, Elwi, AE and Cheng, JJR, "Experimental Study on the Behaviour of CFRP Sheets bonded to Concrete", *Proceedings of 3rd International Conference on Advanced Composite Materials in Bridges and Structures*, Ottawa, Ontario, Aug. 15-18, 2000, pp. 61-68
21. Kulkarni, S. M. and Shah, S. P., "Response of Reinforced Concrete Beams at High Strain Rates," *ACI Structural Journal*, 95 (6), 705-715 (1998).
22. Lu, Z., "Experimental Investigation of the Applications of Photostress Method and Fabric Flexible Composite on the Structural Safety," M. S. Thesis, University of Nevada, Reno, NV 1993.

23. Luo, S. Y., "Theoretical Modeling and Experimental Characterization of Flexible Composites under Finite Deformation," Ph.D. dissertation, University of Delaware 1988.
24. Luo, S. Y., and Mitra, A., "Finite Elastic Behavior of Flexible Fabric Composite under Biaxial Loading," *Journal of Applied Mechanics*, 66, 631-638, September 1999.
25. Moehle, J. P., "Northridge Earthquake of January 17, 1994: Reconnaissance Report, Volume 1, Highway Bridges and Traffic Management," *Earthquake Spectra*, Vol. 11, (No. 3), pp. 287-372, 1995.
26. Mitra, A., "Mechanical Behavior of Flexible Fabric Composite," Ph.D. dissertation, University of Nevada, Reno, NV 1995.
27. Nakaba, K., Kanakubo, T., Furuta, T., Yoshizawa, H., "Bond Behavior between Fiber-Reinforced Polymer Laminates and Concrete," *ACI Structural Journal*, May-June 2001.
28. Paulay, T., and Priestley, M.J.N., Seismic Design of Reinforced Concrete and Masonry Buildings, John Wiley and Sons, USA, 1992.
29. Saiidi, M. S., Advanced Concrete Class Notes, Civil Engineering Department, University of Nevada, Reno, (2004).
30. Saiidi, M., "Current Bridge Seismic Retrofit Practice in the United States," *ACI Concrete International*, Vol. 14, No. 12, December 1992, pp. 64-67).
31. Saiidi, M., Maragakis, E., Abdel-Ghaffar, S., Feng, S., and O'Connor, D. N., "Response of Bridge Hinge Restrainers During Earthquakes-Field Performance, Analysis, and Design," *CCEER-93-6*, Department of Civil Engineering, University of Nevada, Reno, 1993.
32. Saiidi, M., E. Maragakis, and S. Feng, "Parameters in Bridge Restrainer Design for Seismic Retrofit," *Journal of Structural Engineering*, ASCE, Vol. 121, No. 8, pp. 61-68, January 1996.
33. Saiidi, M., Randall, E. Maragakis, and T. Isakovic, "Seismic Restrainer Design Methods for Simply-Supported Bridges," *Journal of Bridge Engineering*, ASCE, Vol. 6, No. 5, September/October 2001, pp. 307-315
34. Shinozuka, M., Feng, M. Q., Kim, J.M., Nagashima, F., Kim, H. K., "Mitigation of Seismic Pounding Effect on Bridges Using Dynamic Restrainers," *SPIE's 7th Annual International Symposium on Smart Structures and Materials*, Newport Beach, March 6-9, 2000

35. Tan, K. H., "Effect of Cyclic Loading on FRP-Concrete Interfacial Bond Strength," *International Symposium on Latest Achievement of Technology and Research on Retrofitting Concrete Structures*, Japan Concrete Institute, July 2003.
36. Teng, J. G., Chen, J. F., Smith, S. T., Lam, L., FRP Strengthened RC Structures, John Wiley & Sons, Ltd., pp 20-27, 2001
37. Timoshenko, Theory of Plate and Shells, McGraw-Hill Book Company, New York 1976.
38. Trochalakis, P., Eberhard, M. O., and Stanton, J. F., "Evaluation and Design of Seismic Restrainers for In-Span Hinges," Report No. WA-RD 387.1, Washington State Transportation Center, Seattle, WA, August 1995.
39. Trochalakis, P., Eberhard, M. O., and Stanton, J. F., "Design of Seismic Restrainers for In-Span Hinges," *Journal of Structural Engineering*, ASCE, 123(4), pp 469-478.
40. Vlassis, A. G., Maragakis, E. M., Saiidi, M. S., "Experimental Evaluation of Seismic Performance of Bridge Restrainers", MCEER 00-0012, Department of Civil Engineering, University of Nevada, Reno, NV 2000.
41. Wantanabe, Gakuho and Kawashima, Kazuhiko, "*Effectiveness of Cable-Restainer for Mitigating Rotation of a Skewed Bridge Subjected to Strong Ground Shaking*", 13th World Conference on Earthquake Engineering, Vancouver, B.C., Canada, Paper No. 789, August 2004.
42. Xiao, Y., and Wu, H., "Compressive Behavior of Concrete Stub Columns Confined by Carbon Fiber Jackets", 13th U.S.-Japan Bridge Engineering Workshop, Japan, 1997
43. Yang, Y. S., Priestley, M. J. N., and Ricles, J., "Longitudinal Seismic Response of Bridge Frames Connected by Restrainers", *Rep. No. UCSD/SSRP-94/09*, Struct. Sys. Res. Proj., UCSD, La Jolla, CA 1994.
44. Zhao, G., and Cho, C., "On Impact Damage of Composite Shells by a Low-Velocity Projectile", *Journal of Composite Materials*, Vol 38, No. 14, pp1231-1253, 2004.

Table 2-1: Composite and Dry Fiber Properties

Fiberglass Composite		
	Design	Specified
Ultimate Tensile Strength in Primary Direction	66,720 psi (460 MPa) 0.58 kN/mm width (3.3 kip/in)	83,400 psi (575 MPa) 0.75 kN/mm width (4.3 kip/in)
Elongation at Break	2.2%	2.2%
Tensile Modulus	3.03 x 10 ⁶ psi (20.9 GPa)	3.79 x 10 ⁶ psi (26.1 GPa)
Laminate Thickness	0.05 in. (1.3 mm)	0.05 in. (1.3 mm)
Primary Fiber	Glass	
Carbon Fiber Composite		
	Design	Specified
Ultimate Tensile Strength in Primary Direction	107,950 psi (745 MPa) 0.75 kN/mm width (4.3 kip/in)	127,000 psi (876 MPa) 0.89 kN/mm width (5.1 kip/in)
Elongation at Break	1.2%	1.2%
Tensile Modulus	8.9 x 10 ⁶ psi (61.5 GPa)	10.5 x 10 ⁶ psi (72.4 GPa)
Laminate Thickness	0.04 in. (1.0 mm)	0.04 in. (1.0 mm)
Primary Fiber	Carbon	
Typical Dry Glass Fiber Properties		
Tensile Strength	470,000 psi (3.24 GPa)	
Tensile Modulus	10.5 x 10 ⁶ psi (72.4 GPa)	
Ultimate Elongation	4.50%	
Density	0.092 lbs./in. ³ (2.55 g/cm ³)	
Fiber Thickness	0.014 in. (0.36 mm)	
Typical Dry Carbon Fiber Properties		
Tensile Strength	550,000 psi (3.79 GPa)	
Tensile Modulus	33.4 x 10 ⁶ psi (230 GPa)	
Ultimate Elongation	1.70%	
Density	0.063 lbs./in. ³ (1.74 g/cm ³)	
Fiber Thickness	0.011 in. (0.28 mm)	
<p>1. Measured Properties in accordance with ASTM D3039 and ASTM C1557-03</p> <p>4. Design Properties based on Caltrans Memo to Designers and Federal Highway Specifications</p>		

**Table 2-2: Glass Fabric Strip Material Tests
MTS Load Frame Tensile Test**

Rate ($\mu\text{s}/\text{sec}$)	Strip #	Width (in)	(mm)	Area (in ²)	(mm ²)	Max Force (kips)	(kN)	Average Max Force (kips)	(kN)	Max Stress or Strength (ksi)	(MPa)	Average Strength (ksi)	(MPa)	Comments
Static Constant 167	1	1.18	30.0	0.059	38	1.83	8.14			31.0	214			sizzling sound prior to failure
	2	1.17	29.7	0.059	38	1.71	7.61			29.2	202			
	3	1.17	29.7	0.059	38	1.82	8.10	1.79	7.95	31.1	215	30.5	210	
Dynamic Constant 1000	4	1.17	29.7	0.059	38	1.66	7.36			28.3	195			
	5	1.14	29.0	0.057	37	1.41	6.27			24.7	171			fibers crooked
	6	1.13	28.7	0.057	36	1.68	7.45	1.58	7.03	29.6	204	27.6	190	
Dynamic Constant 5000	7	1.12	28.4	0.056	36	1.60	7.12			28.6	197			sudden failure
	8	1.24	31.5	0.062	40	2.02	8.97			32.5	224			
	9	1.40	35.6	0.070	45	2.03	9.03	1.88	8.37	29.0	200	30.0	207	
Dynamic Constant 10000	10	1.26	32.0	0.063	41	2.40	10.68			38.1	263			sudden failure
	11	1.16	29.5	0.058	37	2.34	10.40			40.3	278			
	12	1.16	29.5	0.058	37	2.19	9.74	2.31	10.27	37.8	260	38.7	267	
Dynamic Constant 50000	13	1.20	30.5	0.060	39	2.18	9.71			36.4	251			very sudden failure
	14	1.16	29.5	0.058	37	2.03	9.02			34.9	241			
	15	1.22	31.0	0.061	39	1.93	8.58	2.05	9.10	31.6	218	34.3	237	
Dynamic Constant 100000	19	1.18	30.0	0.059	38	1.57	7.00			26.7	184			very sudden failure
	20	1.14	29.0	0.057	37	1.96	8.70			34.3	237			
	21	1.17	29.7	0.059	38	1.95	8.69	1.83	8.13	33.4	230	31.5	217	
Dynamic Constant 100000	16	1.29	32.8	0.065	42	2.54	11.30			39.4	272			explosive instant failure
	17	1.30	33.0	0.065	42	2.58	11.46			39.6	273			
	18	1.29	32.8	0.065	42	2.40	10.68	2.51	11.15	37.2	257	38.7	267	

**Table 2-3: Carbon Fabric Strip Material Tests
MTS Load Frame Tensile Test**

Rate	Strip #	Width		Area		Max Force		Average Max Force		Max Stress or Strength		Average Strength		Comments
		(in)	(mm)	(in ²)	(mm ²)	(kips)	(kN)	(kips)	(kN)	(ksi)	(MPa)	(ksi)	(MPa)	
μsec Static Constant 167	1	0.97	24.6	0.039	25	2.64	11.73			68.0	468.8			
	2	0.97	24.6	0.039	25	1.66	7.38			42.8	295.1			
	3	0.96	24.4	0.038	25	3.40	15.12			88.5	610.2			
	4	0.96	24.4	0.038	25	2.45	10.91	2.54	11.29	63.9	440.6	65.8	453.7	
Dynamic Constant 1000	5	0.96	24.4	0.038	25	3.23	14.39			84.2	580.5			
	6	0.97	24.6	0.039	25	2.77	12.33			71.4	492.3			carbon has no quick
	7	0.97	24.6	0.039	25	2.67	11.89	2.89	12.87	68.9	475.0	74.8	516.0	
	8	0.97	24.6	0.039	25	3.30	14.66			84.9	585.4			or explosive failure
Dynamic Constant 5000	9	0.88	22.4	0.035	23	3.09	13.75			87.8	605.4			
	10	0.97	24.6	0.039	25	2.79	12.43	3.06	13.61	72.0	496.4	81.6	562.4	
	11	0.97	24.6	0.039	25	3.21	14.27			82.7	570.2			
	12	1.02	25.9	0.041	26	3.13	13.91			76.7	528.8			
Dynamic Constant 50000	13	1.04	26.4	0.042	27	2.99	13.31	3.11	13.83	71.9	495.7	77.1	531.6	
	14	1.02	25.9	0.041	26	2.66	11.82			65.1	448.8			
	15	1.09	27.7	0.044	28	3.21	14.27			73.6	507.5			
	16	0.88	22.4	0.035	23	2.53	11.26	2.80	12.45	71.9	495.7	70.2	484.0	
Dynamic Constant 100000	17	0.99	25.1	0.040	26	2.99	13.28			75.4	519.9			
	18	0.91	23.1	0.036	23	3.17	14.11			87.1	600.5			
	19	1.06	26.9	0.042	27	3.63	16.12	3.26	14.50	85.5	589.5	82.7	570.0	

Table 2-4: Properties of Sylgard 184 Silicone

	<u>English Units</u>	<u>SI Units</u>
Specific Gravity @ 25° C (g/cm)		1.05
Tensile Strength	700 psi	4.8 MPa
Tear Strength	15 psi	0.104 MPa
Elongation	100%	100%
Poisson's Ratio	0.46	0.46
Useful Temperature Range	-55 to 200 C	-131 to 392 F

Table 2-5: Properties of Acrylite Plus

	<u>English Units</u>	<u>SI Units</u>
Specific Gravity @ 25° C (g/cm)		1.16
Tensile Strength	8,900 psi	61.3 MPa
Tensile Modulus of Elasticity	350,000 psi	2410 MPa
Tensile Elongation, Yield	5%	5%
Flexural Strength	14,500 psi	99 MPa
Flexural Modulus of Elasticity	330,000 psi	2270 MPa

Figure 2-6: Stress Calculations from FRP Tensile Tests (Glass Fabric)

Test	Rate ($\mu\text{s}/\text{sec}$)	25.4 mm Fabric Strips (A)				25.4 mm Elastomer Coated Fabric Strips (B)				Average Percent Increase Strength (StrengthB/StrengthA)
		Strip #	Max Force (kN)	Max Stress or Strength (MPa)	Ave Stress (MPa)	Strip #	Max Force (kN)	Max Stress or Strength (MPa)	Ave Stress (MPa)	
Static Constant	167	1	8.14	247	241	1	7.71	233	204	0.8
		2	7.61	230		2	5.46	165		
		3	8.11	245		3	6.57	199		
Dynamic Constant	1000	4	7.36	223	213	4	7.26	220	204	1.0
		5	6.27	190		5	5.45	165		
		6	7.45	226		6	6.56	199		
Dynamic Constant	5000	7	7.12	216	254	7	7.81	237	242	1.0
		8	8.97	272		8	7.07	214		
		9	9.03	273		9	9.59	290		
Dynamic Constant	10000	10	10.69	324	311	10	6.56	199	230	0.7
		11	10.40	315		11	7.81	237		
		12	9.74	295		12	7.33	222		
Dynamic Constant	50000	13	9.71	294	261	13	7.95	241	236	0.9
		14	9.02	273		14	7.48	227		
		15	8.58	260		15	9.1	276		
Dynamic Constant	repeat 50000	16	8.70	264	338	16	6.55	198	236	0.7
		17	11.46	347		17	8.91	270		
		18	10.68	323		18	6.59	200		
Dynamic Constant	100000	19	8.69	263	338	19	9.5	288	236	0.7
		20	11.30	342		20	6.69	203		
		21	10.68	323		21	7.76	235		
Dynamic Constant	100000	22	10.68	323	338	22	7.22	219	236	0.7
		23	10.68	323		23	7.22	219		
		24	10.68	323		24	7.22	219		

Composite Gross Laminate Properties

* Note: Fyfe Co. Typical Design Value for Ultimate Tensile Strength in Primary Direction, 0.58 kN/mm width
 Typical Test Value for Ultimate Tensile Strength in Primary Direction, 0.73 kN/mm width

Figure 2-6(a): Stress Calculations from FRP Tensile Tests (Glass Fabric)

Test	Rate ($\mu\text{s. sec}$)	1" Fabric Strips (A)				1" Elastomer Coated Fabric Strips (B)				Average Percent Increase Strength (StrengthB/StrengthA)
		Strip #	Max Force (kips)	Max Stress or Strength (ksi)	Ave Stress (ksi)	Strip #	Max Force (kips)	Max Stress or Strength (ksi)	Ave Stress (ksi)	
Static Constant	167	1	1.830	31.0	30.4	1	1.733	34.7	30.4	1.0
		2	1.710	29.2		2	1.227	24.5		
		3	1.822	31.1		3	1.477	29.5		
Dynamic Constant	1000	4	1.655	28.3	27.5	4	1.633	32.7	30.2	1.1
		5	1.410	24.7		5	1.225	24.5		
		6	1.675	29.6		6	1.474	29.5		
		7				7	1.756	35.1		
		8				8	1.589	31.8		
Dynamic Constant	5000	9	1.600	28.6	30.0	9	2.155	43.1	35.9	1.2
		8	2.017	32.5		10	1.474	29.5		
		9	2.029	29.0		11	1.756	35.1		
Dynamic Constant	10000	10	2.402	38.1	38.7	12	1.647	32.9	34.1	0.9
		11	2.337	40.3		13	1.788	35.8		
		12	2.190	37.8		14	1.682	33.6		
		13	2.182	36.4		15	2.046	40.9		
Dynamic Constant	50000	14	2.027	34.9	32.9	16	1.473	29.5	35.0	1.1
		15	1.929	31.6		17	2.003	40.1		
		19	1.573	26.7		18	1.482	29.6		
	20	1.956	34.3							
	21	1.954	33.4							
	16	2.540	39.4	19		2.136	42.7			
Dynamic Constant	100000	17	2.577	39.6	38.7	20	1.505	30.1	35.0	0.9
		18	2.400	37.2		21	1.745	34.9		
						22	1.622	32.4		

Composite Gross Laminate Properties

* Note: Fyfe Co. Typical Design Value for Ultimate Tensile Strength in Primary Direction, 3.3 kip/in. width
 Typical Test Value for Ultimate Tensile Strength in Primary Direction, 4.17 kip/in. width

Table 2-7 : Calculated Tensile Modulus and Stiffness of 25.4 mm (1 in) Elastomer Coated Glass Strips, MTS Load Frame Tensile Test Results

Strip #	Strain Rate microstrains/second	Stiffness (k)		Tensile Modulus (E)	
		kN/mm	kip/in	MPa	ksi
1	167	8	46	16500	2400
2	167	12	69	17100	2500
3	167	6	34	12600	1820
4	167	7.3	42	15100	2200
Average @ 167		8.3	48	15325	2230
5	1000	10.8	62	17600	2560
6	1000	9.5	54	13500	1950
7	1000	8.7	50	14700	2100
8	1000	11.8	68	18000	2600
Average @ 1000		10.2	59	15950	2303
9	5000	13.3	76	24100	3500
10	5000	7.9	45	15500	2240
11	5000	7.5	43	15500	2250
Average @ 5000		9.6	55	18367	2663
12	10000	10.5	60	19400	2800
13	10000	9.9	57	17840	2600
14	10000	8.4	48	18300	2650
Average @ 10000		9.6	55	18513	2683
15	50000	12.1	69	22840	3300
16	50000	5.1	29	11400	1660
17	50000	10.9	63	22500	3270
18	50000	7	40	15600	2270
Average @ 50000		8.8	50	18085	2625
19	100000	9.6	55	19200	2780
20	100000	6.4	36	13300	1930
21	100000	6.2	35	14700	2130
22	100000	6.8	39	17000	2460
Average @ 100000		7.3	41	16050	2325
Total Average		9.0	51	16982	2462

Table 2-8: Stress Calculations from FRP Tensile Tests (Carbon Fabric)

Test	Rate ($\mu\text{s}/\text{sec}$)	25.4 mm Fabric Strips (A)				25.4 mm Elastomer Coated Fabric Strips (B)				Average Percent Increase Strength (StrengthB/StrengthA)
		Strip #	Max Force (kN)	Max Stress or Strength (MPa)	Ave Stress (MPa)	Strip #	Max Force (kN)	Max Stress or Strength (MPa)	Ave Stress (MPa)	
Static Constant	167	1	11.74	462	444	1	20.91	823	766	1.7
		2	7.38	291		2	19.31	760		
		3	15.12	595		3	18.59	732		
		4	10.90	429		4	18.99	748		
Dynamic Constant	1000	5	14.37	566	506	5	20.60	811	752	1.5
		6	12.32	485		6	17.66	695		
		7	11.88	468		7	19.04	750		
		8	14.68	578		8	22.60	890		
Dynamic Constant	5000	9	13.74	541	536	9	20.19	795	796	1.5
		10	12.41	489		10	17.84	702		
		11	14.28	562		11	18.59	732		
		12	13.92	548		12	19.53	769		
Dynamic Constant	10000	13	13.30	524	545	13	17.53	690	710	1.3
		14	11.83	466		14	16.50	650		
		15	14.28	562		15	18.82	741		
		16	11.25	443		16	17.26	680		
Dynamic Constant	50000	17	13.30	524	490	17	20.24	797	739	1.5
		18	14.10	555		18	17.04	671		
		19	16.15	636		19	17.08	672		
		20				20	16.24	639		
Dynamic Constant	100000	21			572	21	14.06	554	661	1.2

Composite Gross Laminate Properties

* Note: Fyfe Co. Typical Design Value for Ultimate Tensile Strength in Primary Direction, 0.75 kN/mm width
 Typical Test Value for Ultimate Tensile Strength in Primary Direction, 0.89 kN/mm width

Table 2-8(a): Stress Calculations from FRP Tensile Tests (Carbon Fabric)

Test	Rate ($\mu\text{s}/\text{sec}$)	1 in Fabric Strips (A)				1 in Elastomer Coated Fabric Strips (B)				Average Percent Increase Strength (StrengthB/StrengthA)
		Strip #	Max Force (kips)	Max Stress or Strength (ksi)	Ave Stress (ksi)	Strip #	Max Force (kips)	Max Stress or Strength (ksi)	Ave Stress (ksi)	
Static Constant	167	1	2.638	68.0		1	4.704	118		1.7
		2	1.659	42.8		2	4.344	109		
		3	3.399	88.5		3	4.18	105		
		4	2.453	63.9	66.8	4	4.27	107	109	
Dynamic Constant	1000	5	3.234	84.2		5	4.625	116		1.4
		6	2.772	71.4		6	3.972	99		
		7	2.672	68.9	74.8	7	4.28	107	107	
		8	3.295	84.9		8	5.078	127		
Dynamic Constant	5000	9	3.09	87.8		9	4.543	114		1.4
		10	2.794	72.0	81.6	10	4.01	100	114	
		11	3.208	82.7		11	4.183	105		
		12	3.128	76.7		12	4.389	110		
Dynamic Constant	10000	13	2.992	71.9		13	3.935	98		1.3
					77.1	14	3.708	93	101	
		14	2.668	65.1		15	4.231	106		
		15	3.208	73.6		16	3.88	97		
Dynamic Constant	50000	16	2.532	71.9	70.2	17	4.551	114	106	1.5
		17	2.986	75.4		18	3.832	96		
		18	3.171	87.1		19	3.842	96		
		19	3.625	85.5	82.7	20	3.65	91	91	
Dynamic Constant	100000					21	3.156	79	91	1.1

Composite Cross Laminate Properties

* Note: Fyfe Co. Typical Design Value for Ultimate Tensile Strength in Primary Direction, 4.3 kip/in. width
 Typical Test Value for Ultimate Tensile Strength in Primary Direction, 5.1 kip/in. width

Table 2-9 : Calculated Tensile Modulus and Stiffness of 25.4 mm (1 in) Elastomer Coated Carbon Strips, MTS Load Frame Tensile Test Results					
Strip #	Strain Rate microstrains/second	Stiffness (k)		Tensile Modulus (E)	
		kN/mm	kip/in	MPa	ksi
2	167	27	154	60000	8700
3	167	29	166	69000	10100
4	167	28	160	67000	9700
Average @ 167		28.0	160	65333	9500
5	1000	34	190	62000	9000
6	1000	26	150	52100	7600
7	1000	28	160	59100	8600
Average @ 1000		29.3	167	57733	8400
8	5000	39	220	81800	11900
9	5000	28	160	61000	8800
10	5000	33	190	66000	9600
Average @ 5000		33.3	190	69600	10100
11	10000	24	140	56000	8100
12	10000	28	160	65000	9400
13	10000	21	120	57000	8300
14	10000	33	190	78000	11300
Average @ 10000		26.5	153	64000	9275
15	50000	26	150	66100	9600
16	50000	26	150	69600	10100
17	50000	26	150	55700	8100
Average @ 50000		26.0	150	63800	9267
18	100000	24	140	55300	8000
19	100000	19	110	52000	7600
20	100000	19	110	60200	8700
Average @ 100000		20.7	120	55833	8100
Total Average		27.3	156	62768	9114

Table 2-10: Dr. Teng's Model to Determine Effective Bond Length

Glass		
$Le = (E_p * t_p / (f'_c)^{0.5})^{0.5}$		
Material Properties	SI	English
Tensile Modulus of FRP Plate (E_p)	20900 MPa	3.03E+03 ksi
Thickness of FRP Plate (t_p)	1.3 mm	0.05 in
Compressive Strength of Concrete (f'_c)	35.8 MPa	5.2 ksi
Effective Bond Length (L_e)	67 mm	2.7 in
Carbon		
$Le = (E_p * t_p / (f'_c)^{0.5})^{0.5}$		
Material Properties	SI	English
Tensile Modulus of FRP Plate (E_p)	61500 MPa	4.24E+03 ksi
Thickness of FRP Plate (t_p)	1 mm	0.04 in
Compressive Strength of Concrete (f'_c)	35.8 MPa	5.2 ksi
Effective Bond Length (L_e)	101 mm	4.0 in

Table 2-11: Comparisons of 3 Sets of Fiberglass Tensile Tests (Plain Fabric, Coated Fabric, Interfacial Bond)

Rate ($\mu\text{s}/\text{sec}$)	25.4 mm Fabric Strips				25.4 mm Elastomer Coated Fabric Strips				Glass Bond Tests (25.4 mm Strips)			
	Strip #	Max Force (kN)	Max Stress or Strength (MPa)	Ave Stress (MPa)	Strip #	Max Force (kN)	Max Stress or Strength (MPa)	Ave Stress (MPa)	Strip #	Max Force (kN)	Max Ave Bond Stress (Strength) (MPa)	Ave Bond Strength (MPa)
167	1	8.14	247		1	7.71	233		1	6.18	3.55	
	2	7.61	230		2	5.46	165		2	7.56	4.34	
	3	8.10	245		3	6.57	199		3	5.87	3.37	
1000				241	4	7.26	220	204				3.75
	4	7.36	223		5	5.45	165		4	6.54	3.75	
	5	6.27	190		6	6.56	199		5	6.98	4.01	
	6	7.45	226		7	7.81	237		6	8.63	4.95	
				213	8	7.07	214	204				4.24
	7	7.12	216		9	9.59	290		7	8.01	4.60	
5000	8	8.97	272		10	6.56	199		8	7.78	4.47	
	9	9.03	273	254	11	7.81	237	242	9	9.65	5.54	4.87
	10	10.68	324		12	7.33	222		10	6.09	3.50	
10000	11	10.40	315		13	7.95	241		11	8.99	5.16	
	12	9.74	295	311	14	7.48	227	230	12	7.74	4.44	4.37
	13	9.71	294		15	9.10	276		13	8.23	4.72	
50000	14	9.02	273		16	6.55	198		14	7.74	4.44	
	15	8.58	260		17	8.91	270		15	7.96	4.57	
	19	7.00	212		18	6.59	200					
repeat 50000	20	8.70	263									
	21	8.69	263	260				236				4.58
	16	11.30	342		19	9.50	288		16	8.45	4.85	
100000	17	11.46	347		20	6.69	203		17	9.07	5.21	
	18	10.68	323		21	7.76	235		18	10.45	6.00	
				338	22	7.22	219	236	19	8.27	4.75	5.20

ASTM 3039/D (Standard Test Method for Tensile Properties of Polymer Matrix Composite Materials), 3 specimens minimum

Fyfe Co. Description Sheet* Design Value SEH-51A (Glass) Composite Strength, 460 MPa

Tensile Strength of Concrete = 3.72 MPa

Table 2-11(a): Comparisons of 3 Sets of Fiberglass Tensile Tests (Plain Fabric, Coated Fabric, Interfacial Bond)

Rate ($\mu\text{s}/\text{sec}$)	1 in Fabric Strips				1 in Elastomer Coated Fabric Strips				Glass Bond Tests (1 in Strips)			
	Strip #	Max Force (kips)	Max Stress or Strength (ksi)	Ave Stress (ksi)	Strip #	Max Force (kips)	Max Stress or Strength (ksi)	Ave Stress (ksi)	Strip #	Max Force (kips)	Max Ave Bond Stress (Strength) (ksi)	Ave Bond Strength (ksi)
167	1	1.830	31.0	30.4	1	1.733	34.7	30.4	1	1.39	0.51	0.54
	2	1.710	29.2		2	1.227	24.5		2	1.70	0.63	
	3	1.822	31.1		3	1.477	29.5		3	1.32	0.49	
1000	4	1.655	28.3	30.4	4	1.633	32.7	30.2	4	1.47	0.54	0.61
	5	1.410	24.7		5	1.225	24.5		5	1.57	0.58	
	6	1.675	29.6		6	1.474	29.5		6	1.94	0.72	
	7				7	1.756	35.1					
	8				8	1.589	31.8					
	9				9	2.155	43.1					
5000	10	1.600	28.6	30.0	10	1.474	29.5	35.9	10	1.37	0.51	0.71
	8	2.017	32.5		11	1.756	35.1		11	2.02	0.75	
	9	2.029	29.0		12	1.647	32.9		12	1.74	0.64	
10000	11	2.337	40.3	38.7	13	1.788	35.8	34.1	13	1.85	0.69	0.63
	12	2.190	37.8		14	1.682	33.6		14	1.74	0.64	
	13	2.182	36.4		15	2.046	40.9		15	1.79	0.66	
50000	14	2.027	34.9	32.9	16	1.473	29.5	35.0	16	1.90	0.70	0.66
	15	1.929	31.6		17	2.003	40.1		17	2.04	0.76	
	19	1.573	26.7		18	1.482	29.6		18	2.35	0.87	
repeat 50000	20	1.956	34.3	38.7				35.0	19	1.86	0.69	0.75
	21	1.954	33.4						20	2.04	0.76	
	16	2.540	39.4		19	2.136	42.7		21	1.745	0.87	
100000	17	2.577	39.6	38.7	20	1.505	30.1	35.0	22	1.622	32.4	0.66
	18	2.400	37.2		21	1.745	34.9		23	1.86	0.69	
					22	1.622	32.4					

ASTM 3039/D (Standard Test Method for Tensile Properties of Polymer Matrix Composite Materials), 3 specimens minimum

Fyfe Co. Description Sheet* Design Value SEH-51A (Glass) Composite Strength, 66.72 ksi

Tensile Strength of Concrete = $7.5 \cdot ((5200\text{psi})^{0.5}) = .54 \text{ ksi}$

Table 2-12: Comparisons of 3 Sets of Carbon Tensile Tests (Plain Fabric, Coated Fabric, Interfacial Bond)

Rate ($\mu\text{s}/\text{sec}$)	25.4 mm Fabric Strips				25.4 mm Elastomer Coated Fabric Strips				Carbon Bond Tests (25.4 mm strips)			
	Strip #	Max Force (kN)	Max Stress or Strength (MPa)	Ave Stress (MPa)	Strip #	Max Force (kN)	Max Stress or Strength (MPa)	Ave Stress (MPa)	Strip #	Max Force (kN)	Max Ave Bond Stress (Strength) (MPa)	Ave Bond Strength (MPa)
167	1	11.73	469		1	20.92	824					
	2	7.38	295		2	19.32	761		3	8.72	4.50	
	3	15.12	610		3	18.59	732		4	6.67	3.45	
	4	10.91	441	454	4	18.99	748	766	5	8.18	4.23	4.06
1000	5	14.39	579		5	20.57	810		6	7.47	3.86	
	6	12.33	490		6	17.67	696		7	12.77	6.60	
	7	12.1	476	515	7	19.04	750	752	8	10.45	5.40	5.29
	8	14.66	586		8	22.59	889		9	9.34	4.83	
5000	9	13.74	607		9	20.21	796		10	10.85	5.61	
	10	12.43	496	563	10	17.84	702	796	11	7.65	3.95	4.80
	11	14.27	572		11	18.61	733				0.00	
	12	13.91	531		12	19.52	769		12	12.01	6.21	
10000	13	13.31	496		13	17.50	689		13	8.81	4.55	
				533	14	16.49	649	710	14	9.88	5.10	5.29
	14	11.82	448		15	18.82	741		15	8.54	4.41	
	15	14.27	510		16	17.26	679		16	7.25	3.75	
50000	16	11.26	496	485	17	20.24	797	739	17	13.34	6.89	5.02
	17	13.28	517		18	17.05	671		18	9.61	4.96	
	18	14.11	600		19	17.09	673		19	8.85	4.57	
	19	16.12	586	568	20	16.24	639	634	20	10.28	5.31	4.95
				21	14.04	553						

ASTM 3039/D (Standard Test Method for Tensile Properties of Polymer Matrix Composite Materials), 3 specimens minimum

Fyfe Co. Description Sheet* Design Value SCH-41 (Carbon) Composite Strength, 745 MPa

Tensile Strength of Concrete = 3.72 MPa

Table 2-12(a): Comparisons of 3 Sets of Carbon Tensile Tests (Plain Fabric, Coated Fabric, Interfacial Bond)

Rate ($\mu\text{s}/\text{sec}$)	1 in Fabric Strips				1 in Elastomer Coated Fabric Strips				Carbon Bond Tests (1 in strips)				
	Strip #	Max Force (kips)	Max Stress or Strength (ksi)	Ave Stress (ksi)	Strip #	Max Force (kips)	Max Stress or Strength (ksi)	Ave Stress (ksi)	Strip #	Max Force (kips)	Max Ave Bond Stress (Strength) (ksi)	Ave Bond Strength (ksi)	
167	1	2.638	68.0	65.8	1	4.704	117.6	109.4					
	2	1.659	42.8		2	4.344	108.6			3	1.96	0.65	
	3	3.399	88.5		3	4.18	104.5			4	1.50	0.50	
	4	2.453	63.9		4	4.27	106.8			5	1.84	0.61	0.59
1000	5	3.234	84.2	74.8	5	4.625	115.6	107.3					
	6	2.772	71.4		6	3.972	99.3			6	1.68	0.56	
	7	2.672	68.9		7	4.28	107.0			7	2.87	0.96	
	8	3.295	84.9		8	5.078	127.0			8	2.35	0.78	0.77
5000	9	3.09	87.8	81.6	9	4.543	113.6	113.6					
	10	2.794	72.0		10	4.01	100.3			9	2.10	0.70	
	11	3.208	82.7		11	4.183	104.6			10	2.44	0.81	
	12	3.128	76.7		12	4.389	109.7			11	1.72	0.57	0.70
10000	13	2.992	71.9	77.1	13	3.935	98.4	101.3					
	14				14	3.708	92.7			12	2.70	0.90	
	15	2.658	65.1		15	4.231	105.8			13	1.98	0.66	
	16	3.208	73.6		16	3.88	97.0			14	2.22	0.74	0.77
50000	17	2.532	71.9	70.2	17	4.551	113.8	105.5					
	18	2.986	75.4		18	3.832	95.8			15	1.92	0.64	
	19	3.171	87.1		19	3.842	96.1			16	1.63	0.54	
	20	3.625	85.5		20	3.65	91.3			17	3.00	1.00	0.73
100000	21			82.7	21	3.156	78.9	90.5					
	18				18	3.832	95.8			18	2.16	0.72	
	19				19	3.842	96.1			19	1.99	0.66	
	20				20	3.65	91.3			20	2.31	0.77	0.72

ASTM 3039/D (Standard Test Method for Tensile Properties of Polymer Matrix Composite Materials), 3 specimens minimum

Fyfe Co. Description Sheet* Design Value SCH-41 (Carbon) Composite Strength, 107.95 ksi

Tensile Strength of Concrete = $7.5 \cdot ((5200\text{psi})^{0.5}) = .54 \text{ ksi}$

Table 3-1: Force demand used in FRP restrainer design

Maximum Force and Stress on SMA and Steel Restrainers from Previous Shake Table Tests						
	Maximum Force			SMA Restrainers		Ave Max Stress
	West Side (kN)	East Side (kN)	West Side (MPa)	East Side (MPa)	Total Max Force (kN)	
84 Wire Cable	11.25	11.08	500	492	22.33	496
130 Wire Cable	16.55	18.86	475	542	35.41	508
Rod	16.10	17.75	259	283	33.85	271

Steel Restrainers	
Max Force (kN)	Max Stress (MPa)
36.2	1870

Table 3-1(a): Force demand used in FRP restrainer design

Maximum Force and Stress on SMA and Steel Restrainers from Previous Shake Table Tests						
	Maximum Force			SMA Restrainers		Ave Max Stress
	West Side (kip)	East Side (kip)	West Side (ksi)	East Side (ksi)	Total Max Force (kip)	
84 Wire Cable	2.53	2.49	72.5	71.4	5.02	71.95
130 Wire Cable	3.72	4.24	68.9	78.6	7.96	73.75
Rod	3.62	3.99	37.6	41.1	7.61	39.35

Steel Restrainers	
Max Force (kip)	Max Stress (ksi)
8.14	271

Table 3-2: Average Measured Flexible FRP Strength

Glass		Carbon	
kN/mm width	kip/in width	kN/mm width	kip/in width
0.29	1.67	0.73	4.16
MPa	ksi	MPa	ksi
230	33.3	717	104
<i>Fyfe specified design strength is 66.7 ksi (glass SHE-51A) 107.9 ksi (carbon SCH-41)</i>			

Table 3-3: Design Width of Flexible Composite

Glass		Carbon	
mm	in	mm	in
129	5.08	52	2.04
<i>round-up numbers to next whole number-in english units</i>			
152	6	76	3
<p>Width = (maximum earthquake demand * FOS / flexible composite capacity) Width required for FRP restrainers, per side with a FOS of 2 76mm (3in) minimal width required</p>			

Table 3-4: Capacity of Flexible FRP with Design Width

Glass		Carbon	
kN	kip	kN	kip
45	10	56	12.5
<i>divided by FOS of 2</i>			
22	5	28	6
<p>Capacity = design width * average strength per inch width 76mm (3in) minimal width required</p>			

Table 3-5: New Effective Lengths for Bonded Portion of GFRP Restrainer

	mm	in
Effective Length in Primary Direction	99	3.9
Effective Length in Angled Direction	76	3

Table 3-6: New Effective Lengths for Bonded Portion of CFRP Restrainer

	mm	in
Effective Length in Primary Direction	155	6.1
Effective Length in Angled Direction	119	4.7

Table 3-7: Effective Bond Lengths for Bonded Portion of Hybrid Restrainer

Effective Length, see Fig. 3-19(1)	mm	in
	79	3.1
Effective Length, see Fig. 3-19(2)	mm	in
	104	4.1
Effective Length, see Fig. 3-19(3)	mm	in
	145	5.7

Table 4-1: Frame Properties and Dimensions

Compressive Strength of Concrete	5500 psi	37.9 MPa
Top Slab Thickness	(20 cm)	7.9 in
Bottom Slab Thickness	(20 cm)	7.9 in
Diaphragm Thickness	(75 cm)	29.5 in
Web Thickness	(20 cm)	7.9 in
Seat Width	(25 cm)	10 in
Individual Block Properties	Block A	
Weight of Block	(93.9 kN)	21.1 kips
Weight of Additional Lead	0	0
Weight of Block + Additional Lead	(93.9 kN)	21.1 kips
Mass of Block + Additional Lead	(9560 kg)	655 slugs
Individual Elastomeric Bearing Properties	Bearing A	
Total Height	156 mm	6.15 in
Diameter (incl cover)	178 mm	7.0 in
Rubber Layer Thickness	6.0 mm	0.236
No Layers	12	12
Shims	3.04 mm	0.1196 in
Top and bottom Plates	25.4 mm	1.0 in
Shear Modulus G	0.627 MPa	0.091 ksi
Bearing Design Displacement	76.2 mm	3 in
System Properties	Block A	
Measured Stiffness from 4 Elastomeric Bearings	910 kN/m	5.2 kip/in
Frequency of Vibration (f)	1.55	0.97
Period of Block	0.644	1.033
T_A/T_B		0.6

Table 4-2: Channels of Data Acquisition System

Channel	Instrumentation	Units	Test				
			GFRP	CFRP	Hybrid		
					ATC32E long	Sylmar long	ATC32E transverse
1	Table Acc Y	g	X	X	X	X	X
2	Table Disp	in	X	X	X	X	X
3	AY2	in	X	X	X	X	X
4	AY1	in	X	X	X	X	X
5	AX1	in	X	X	X	X	X
6	AX4	in	X	X	X	X	X
7	BX1	in	X	X	X	X	X
8	BX4	in	X	X	X	X	X
9	BY4	in	X	X	X	X	X
10	BY3	in	X	X	X	X	X
11	B acc	g	X	X	X	X	X
12	A acc	g	X	X	X	X	X
13	GAP 1	in	X	X	X	X	
14	GAP 2	in	X	X	X	X	X
15	GAP 3	in	X	X	X	X	
17	AS acc	g		X	X	X	X
18	BS acc	g		X	X	X	X
19	A Bot acc	g		X	X	X	X
20	B Bot acc	g		X	X	X	X
21	AN acc	g		X	X	X	X
22	BN acc	g		X	X	X	X
23	Table Acc X	g		X	X	X	X
24	Table Disp X	in		X	X	X	X

Table 4-3: Test Protocol For FRP Restrainer Tests

GFRP Restrainers,

Series	Direction	Earthquake Motion	PGA (g)	Restrainer Slack	
				North (mm)	South (mm)
1-1	longitudinal	ATC32E	0.05	13	10
1-2	longitudinal	ATC32E	0.1	13	10
1-3	longitudinal	ATC32E	0.15	13	10
1-4	longitudinal	ATC32E	0.2	13	10
1-5	longitudinal	ATC32E	0.25	13	10
1-6	longitudinal	ATC32E	0.3	13	10

CFRP Restrainers

Series	Direction	Earthquake Motion	PGA (g)	Restrainer Slack	
				North (mm)	South (mm)
2-1	longitudinal	ATC32E	0.05	13	10
2-2	longitudinal	ATC32E	0.1	13	10
2-3	longitudinal	ATC32E	0.15	13	10
2-4	longitudinal	ATC32E	0.2	13	10

Hybrid (Carbon/Glass) Restrainers

Series	Direction	Earthquake Motion	PGA (g)	Restrainer Slack	
				North (mm)	South (mm)
3-1	longitudinal	ATC32E	0.05	13	10
3-2	longitudinal	ATC32E	0.1	13	10
3-3	longitudinal	ATC32E	0.15	13	10
3-4	longitudinal	ATC32E	0.2	13	10
3-5	longitudinal	ATC32E	0.25	13	10
3-6	longitudinal	ATC32E	0.3	13	10
3-1S	longitudinal	Sylmar	0.15	13	10
3-2S	longitudinal	Sylmar	0.3	13	10
3-1T	transverse	ATC32E	0.05	13	10
3-2T	transverse	ATC32E	0.1	13	10

Table 5-1: Observations During Testing of GFRP Restrainers

$T_A/T_B = 0.6$, ATC 32 Soil Type E				
Series	PGA	Restrainer Location	Restrainer Slack (in)	June 29, 2004
				Comments
1-1	0.05	North	0.5	No Visible Damage
		South	0.4	No Visible Damage
1-2	0.1	North	0.5	No Visible Damage
		South	0.4	No Visible Damage
1-3	0.15	North	0.5	No Visible Damage
		South	0.4	No Visible Damage
1-4	0.2	North	0.5	Very small fiber failure seen on bottom edge of restrainer
		South	0.4	Small fiber failure seen on bottom edge of restrainer
1-5	0.25	North	0.5	Very small fiber failure seen on bottom edge of restrainer
		South	0.4	Slight elongation of tear seen at 0.2g
1-6	0.3	North	0.5	Beginning of debonding seen at attachment of GFRP to concrete at edge of elastomer coated fabric. No increase seen in fiber failure.
		South	0.4	Beginning of debonding seen at attachment of GFRP to concrete at edge of elastomer coated fabric. Fiber failure at bottom or restrainer increases

Table 5-2: Maximum Specimen Response, Determined During GFRP Restrainer Shake Table Tests

PGA (g)	Block B Acceleration (g)	South Restrainer Elongation		Total Restrainer Force	
		(mm)	(in)	(kN)	(kip)
0.05	0.75	3.86	0.152	158	35.5
0.1	1.39	6.05	0.238	246	55.3
0.15	2.23	7.32	0.288	298	67.0
0.2	2.54	7.92	0.312	323	72.6
0.25	2.64	9.12	0.359	372	83.5
0.3	2.66	9.14	0.360	372	83.6

Table 5-3: Observations During Testing of CFRP Restrainers

$T_A/T_B = 0.6$, ATC 32 Soil Type E

Series	PGA	Restraint Location	Restraint Slack (in)	July 20, 2004	
				Comments	Comments
2-1	0.05	North	0.5	No Visible Damage	
		South	0.4	No Visible Damage	
2-2	0.1	North	0.5	No Visible Damage	
		South	0.4	No Visible Damage	
2-3	0.15	North	0.5	No Visible Damage	
		South	0.4	No Visible Damage	
2-4	0.2	North	0.5	Debonding seen between outer and inner layer of FRP plate (NE)	
		South	0.4	Fiber rupture in elastomer coated section in hinge area	

Table 5-4: Maximum Specimen Response, Determined During CFRP Restrainer Shake Table Tests

PGA (g)	Block B Acceleration (g)	Restrainer Elongation		Total Restrainer Force (kN)	Total Restrainer Force (kip)
		(mm)	(in)		
0.05	0.88	2.08	0.082	164	36.8
0.1	1.68	3.25	0.128	297	66.8
0.15	1.82	3.63	0.143	401	90.1
0.2	2.67	4.29	0.169	308	69.2

Table 5-5: Observations During Testing of CGFRP Restrainers
 $T_A/T_B = 0.6$, ATC 32 Soil Type E

Series	PGA	Restrainer Location	Restrainer Slack (in)	Motion in Longitudinal Direction	
				August 11, 2004	Comments
3-1	0.05	North	0.5	No apparent damage	
		South	0.4	No apparent damage	
3-2	0.1	North	0.5	No apparent damage	
		South	0.4	No apparent damage	
3-3	0.15	North	0.5	No apparent damage	
		South	0.4	No apparent damage	
3-4	0.2	North	0.5	No apparent damage	
		South	0.4	No apparent damage	
3-5	0.25	North	0.5	Slight edge damage on carbon strip	
		South	0.4	No apparent damage	
3-6	0.3	North	0.5	Slight edge damage on carbon strip	
		South	0.4	No apparent damage	

$T_A/T_B = 0.6$, Sylmar

Motion in Longitudinal Direction					
3-1S	0.15	North	0.5	No apparent damage	
		South	0.4	No apparent damage	
3-2S	0.3	North	0.5	No apparent damage	
		South	0.4	No apparent damage	

$T_A/T_B = 0.6$, ATC 32 Soil Type E

Motion in Transverse Direction					
3-1T	0.05	North	0.5	Slight debonding at inner edge of FRP plate	
		South	0.4	Slight debonding at inner edge of FRP plate	
3-2T	0.1	North	0.5	Increased debonding at inner edge of FRP plate	
		South	0.4	Increased debonding at inner edge of FRP plate	

Table 5-6: Maximum Specimen Response, Determined During CGFRP Restrainer Shake Table Tests						
Series	PGA (g)	Block B Acceleration longitudinal (g)	Restrainer Elongation (Long)		Total Restrainer Force (kN)	Total Restrainer Force (kip)
			(mm)	(in)		
3-1	0.05	0.81	1.63	0.064	134	30.1
3-2	0.1	1.70	1.83	0.072	279	62.8
3-3	0.15	2.12	2.36	0.093	313	70.4
3-4	0.2	2.49	2.72	0.107	390	87.7
3-5	0.25	2.58	3.25	0.128	533	119.9
3-6	0.3	2.67	3.71	0.146	579	130.1
3-1S	0.15	1.85	2.74	0.108	433	97.4
3-2S	0.3	2.44	3.33	0.131	528	118.8
			Restrainer Elongation (Long)		Relative Block Displacement (Trans)	
			(mm)	(in)	(mm)	(in)
3-1T	0.05	0.21	1.70	0.067	47.09	1.854
3-2T	0.1	0.91	7.49	0.307	83.49	3.287

Table 6-1: Total Force vs. Maximum Displacement for Different Cable Types, From Shake Table Tests

Restrainer Types	Steel Cable		SMA Cable		Glass FRP		Carbon FRP		Hybrid FRP		Hybrid FRP	
	(elastomer coated portion)		(elastomer coated portion)		(elastomer coated portion)		(elastomer coated portion)		(elastomer coated portion)		(elastomer coated portion)	
Total Stiffness	2.8 kN/mm	2.8 kN/mm	2.8 kN/mm	2.8 kN/mm	163 kN/mm	249 kN/mm	249 kN/mm	329 kN/mm	329 kN/mm	329 kN/mm	329 kN/mm	329 kN/mm
# of Restrainers	5	two 130-wire	two 130-wire	two 130-wire	2	2	2	2	2	2	2	2
Slack (in)	0.5	0.5	0.5	0.5	0.43	0.43	0.43	0.43	0.43	0.43	0.43	0.43
Earthquake Motion	ATC32E	ATC32E	ATC32E	ATC32E	ATC32E	ATC32E	ATC32E	ATC32E	ATC32E	ATC32E	Sylmar	Sylmar
PGA (g)	Max	Max	Max	Max	Max	Max	Max	Max	Max	Max	Max	Max
	Calc	Calc	Calc	Calc	Calc	Calc	Calc	Calc	Calc	Calc	Calc	Calc
	Total	Total	Total	Total	Total	Total	Total	Total	Total	Total	Total	Total
	Force (kN)	Force (kN)	Force (kN)	Force (kN)	Force (kN)	Force (kN)	Force (kN)	Force (kN)	Force (kN)	Force (kN)	Force (kN)	Force (kN)
0.05	Max	9	9.4	9	9.4	158	0.838	164	1.880	134	0.813	
	Calc											
	Total	24	17.0	245	2.743	298	3.048	279	1.702			
	Force (kN)	30	38.0	298	3.581	400	3.531	313	1.905	433	2.642	
0.1	Max	34	22.9	325	4.216	307	3.404 (Failure)	390	2.362			
	Calc											
	Total	35	28.2	369	5.258	533	3.251	579	3.531	528	3.2	
	Force (kN)	36	99.1 (Failure)	369	5.359	579	3.531	528	3.2			
0.25	Max											
	Calc											
	Total											
	Force (kN)											
0.3	Max											
	Calc											
	Total											
	Force (kN)											

* Equivalent cases are highlighted

* Stiffness of elastomer coated fabric obtained from average of static rate tensile tests of 25.4 mm strips

Table 6-1(a): Total Force vs. Maximum Displacement for Different Cable Types, From Shake Table Tests

Restrainer Types	Steel Cable		SMA Cable		Glass FRP		Carbon FRP		Hybrid FRP		Hybrid FRP	
	(elastomer coated portion)		(elastomer coated portion)		(elastomer coated portion)		(elastomer coated portion)		(elastomer coated portion)		(elastomer coated portion)	
Total Stiffness	4.0 kip/in	4.0 kip/in	4.0 kip/in	233 kip/in	356 kip/in	470 kip/in	470 kip/in	470 kip/in	470 kip/in	470 kip/in	470 kip/in	470 kip/in
# of Restrainers	5	two 130-wire	two 130-wire	2	2	2	2	2	2	2	2	2
Slack (in)	0.5	0.5	0.5	0.43	0.43	0.43	0.43	0.43	0.43	0.43	0.43	0.43
Earthquake Motion	ATC32E	ATC32E	ATC32E	ATC32E	ATC32E	ATC32E	ATC32E	ATC32E	ATC32E	ATC32E	ATC32E	Sylmar
PGA (g)	Max	Max	Max	Max	Max	Max	Max	Max	Max	Max	Max	Max
	Calc	Calc	Calc	Calc	Calc	Calc	Calc	Calc	Calc	Calc	Calc	Calc
	Total	Total	Total	Total	Total	Total	Total	Total	Total	Total	Total	Total
	Force (kip)	Force (kip)	Force (kip)	Force (kip)	Force (kip)	Force (kip)	Force (kip)	Force (kip)	Force (kip)	Force (kip)	Force (kip)	Force (kip)
0.05		2.1	0.37	35.5	0.033	36.8	0.074	30.1	0.032			
0.1		5.3	0.67	55.3	0.108	66.8	0.120	62.8	0.067			
0.15 (Case 1)	6.7	7.1	0.75	67.0	0.141	90.1	0.139	70.4	0.075	97.4	0.104	
0.2 (Case 2)	8.1	7.7	0.90	72.5	0.166	69.2	0.134 (Failure)	87.7	0.093			
0.25		7.9	1.11	83.4	0.207			119.9	0.128			
0.3				83.4	0.211			130.1	0.139	118.8	0.126	

* Equivalent cases are highlighted

* Stiffness of elastomer coated fabric obtained from average of static rate tensile tests of 1" strips

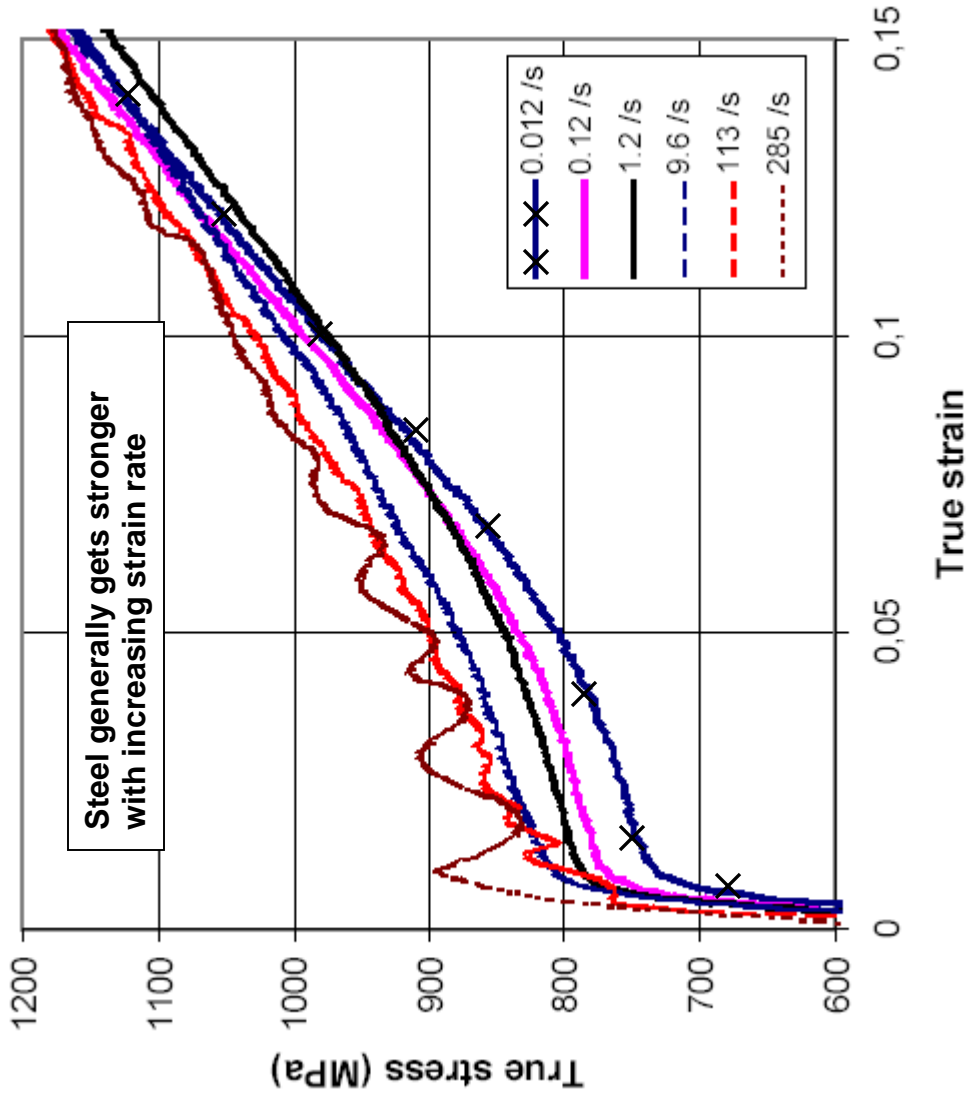


Figure 2-1: Yield Stress of Steel vs. Strain Rate

**Slow rate resulting
in wider neck and
smoother surface.**

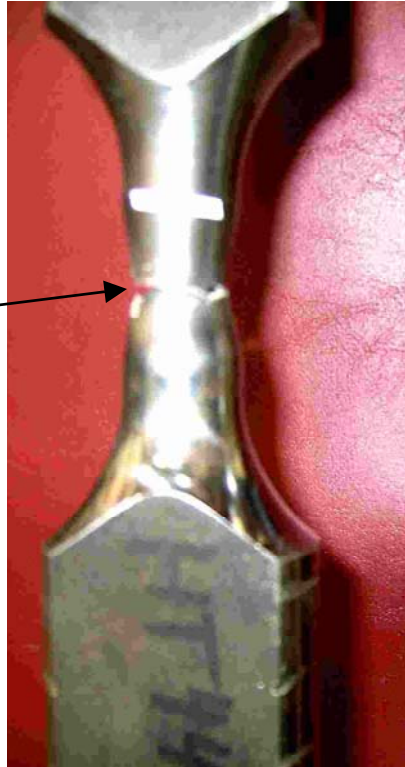


Figure 2-2: Steel Coupon Pulled at Static Strain Rate

**Dynamic rate
resulting in narrow
neck and more
irregular surface.**

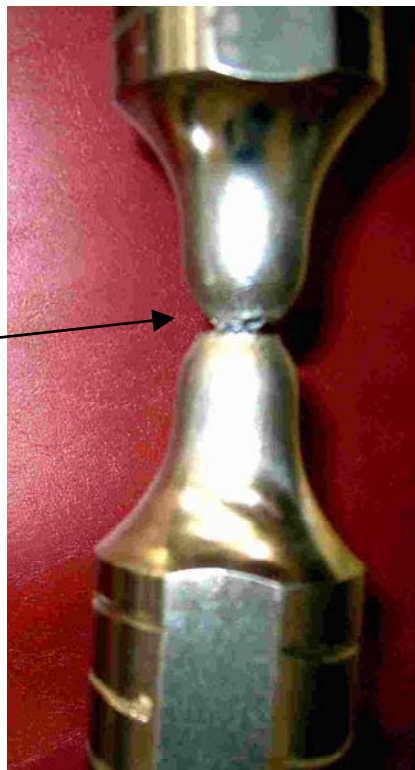


Figure 2-3: Steel Coupon Pulled at Dynamic Strain Rate

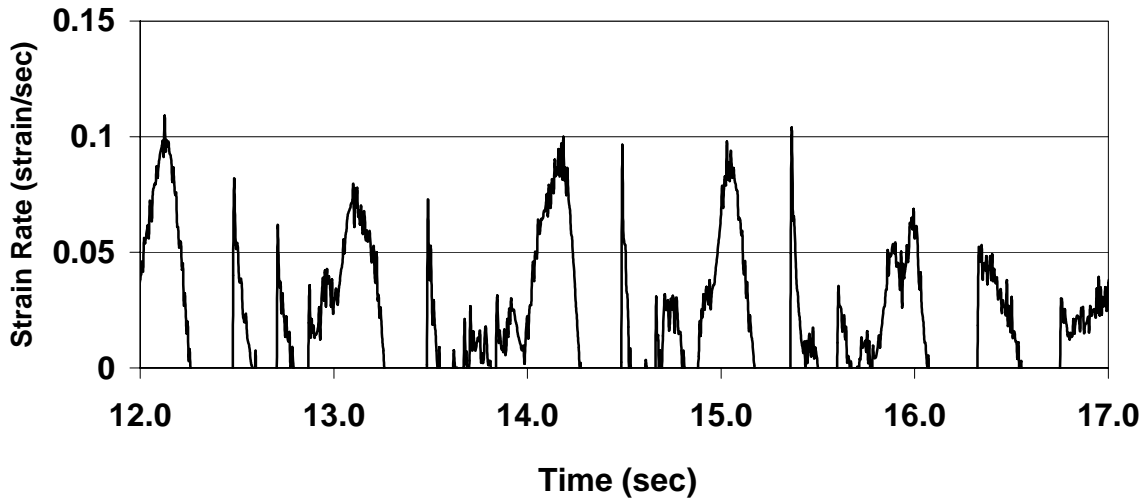


Figure 2-4: Strain Rate History for Steel Restrainer Shake Table Test,
PGA = 0.15g

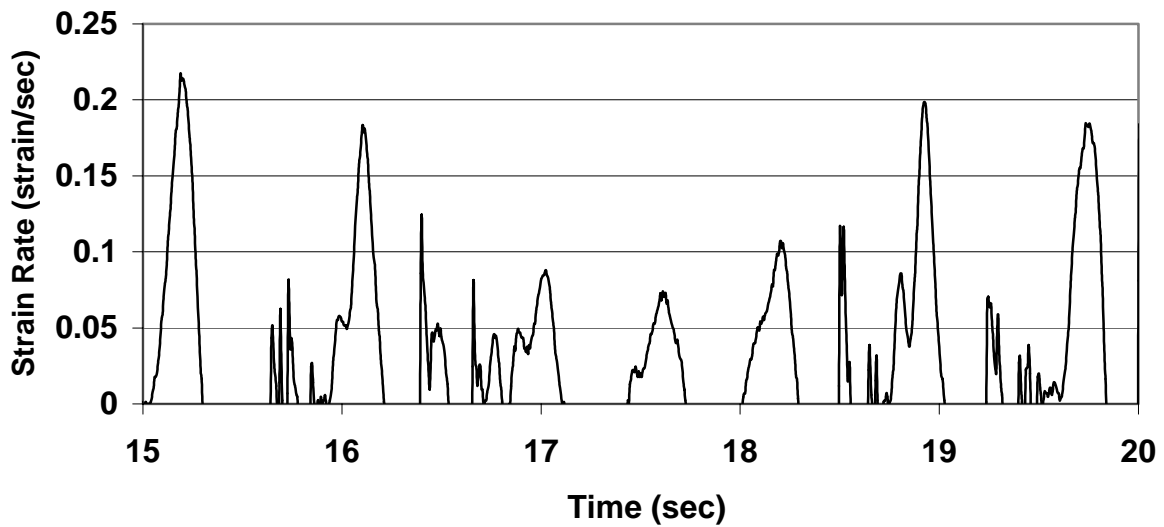


Figure 2-5: Strain Rate History for SMA Restrainer Shake Table Test,
PGA = 0.15g



Figure 2-6: Material Tensile Tests Using MTS Load Frame

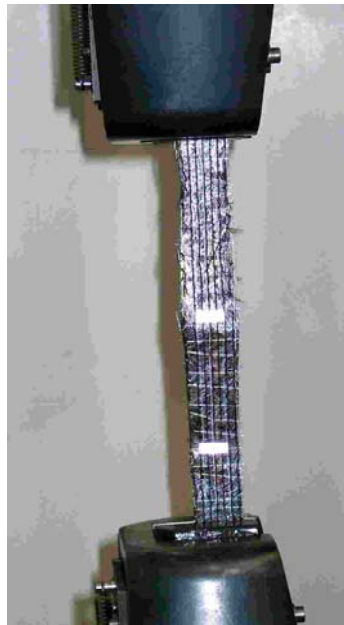


Figure 2-7: Close-Up of Carbon Fabric Strip Tensile Tests



Figure 2-8: Glass Fabric Strips with Ends Marked for Epoxy Application



Figure 2-9: Dipping Ends of Fabric Strips into Resin

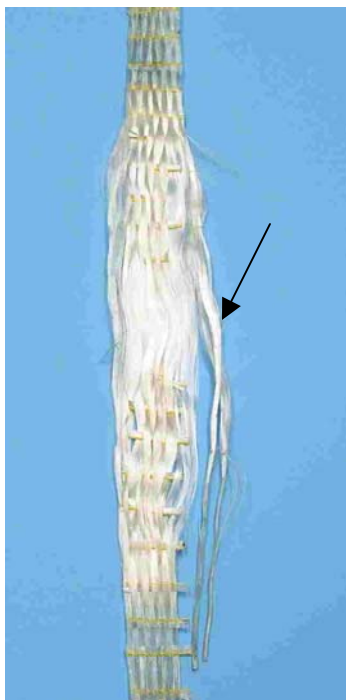


Figure 2-10: Typical Failure Mode of Fiberglass Strips



Figure 2-11: Typical Failure Mode of Carbon Fabric Strips

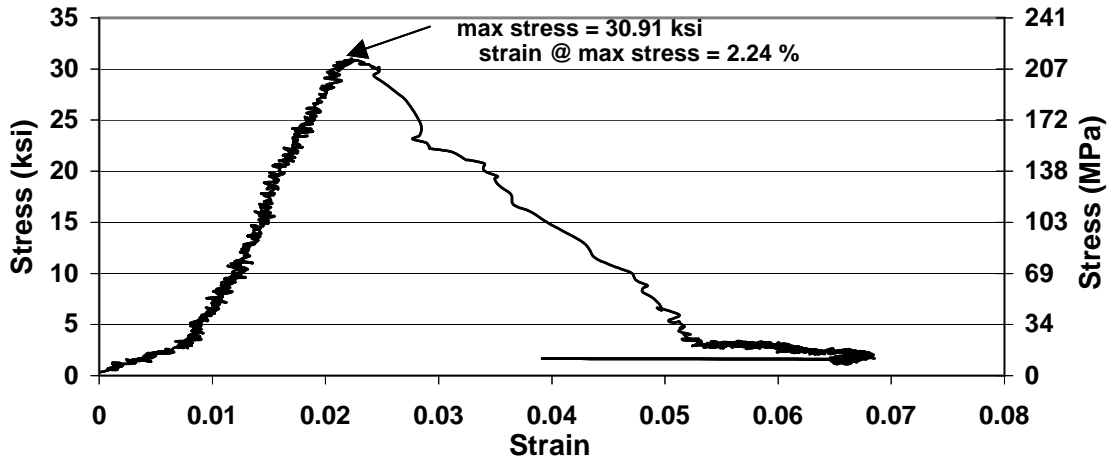


Figure 2-12: Stress-Strain Relationship for Glass FRP Strip #1 @167 μ s/sec

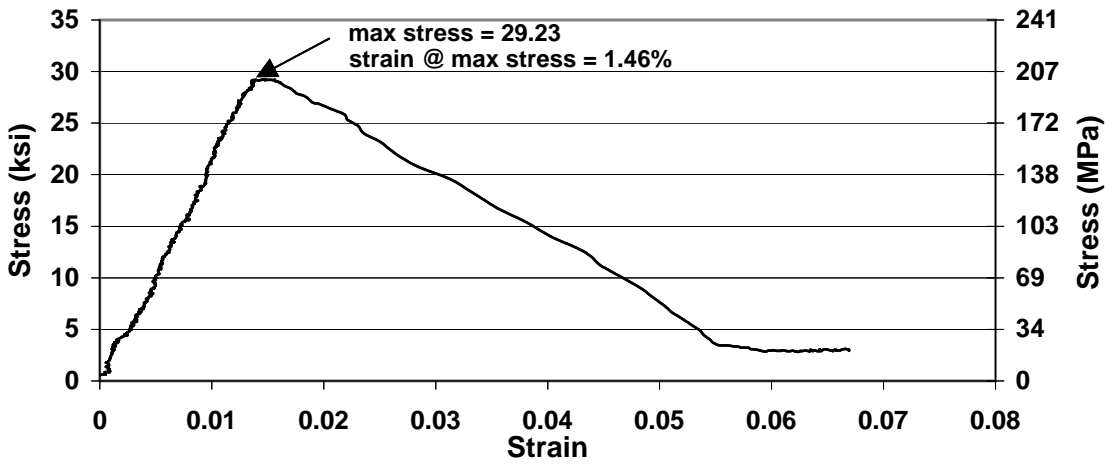


Figure 2-13: Stress-Strain Relationship for Glass FRP Strip #2 @167 μ s/sec

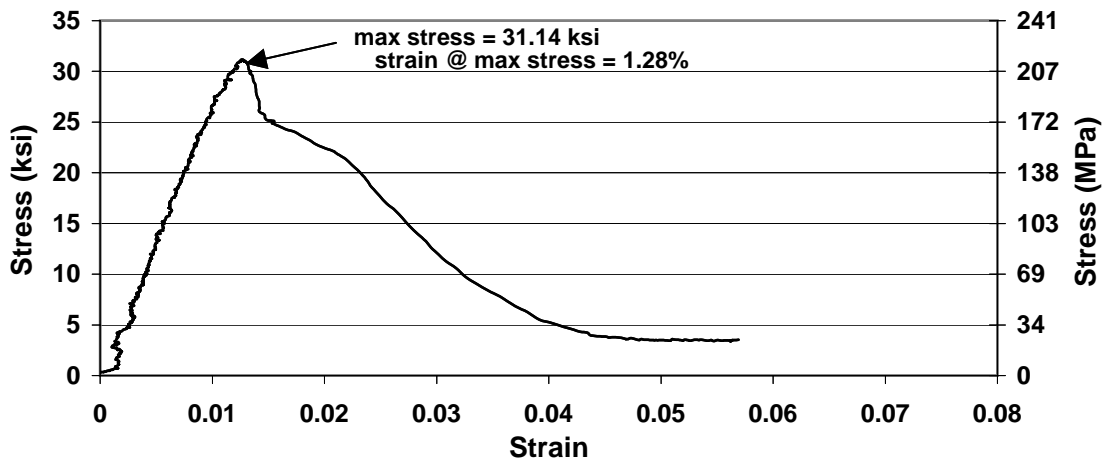


Figure 2-14: Stress-Strain Relationship for Glass FRP Strip #3 @167 μ s/sec

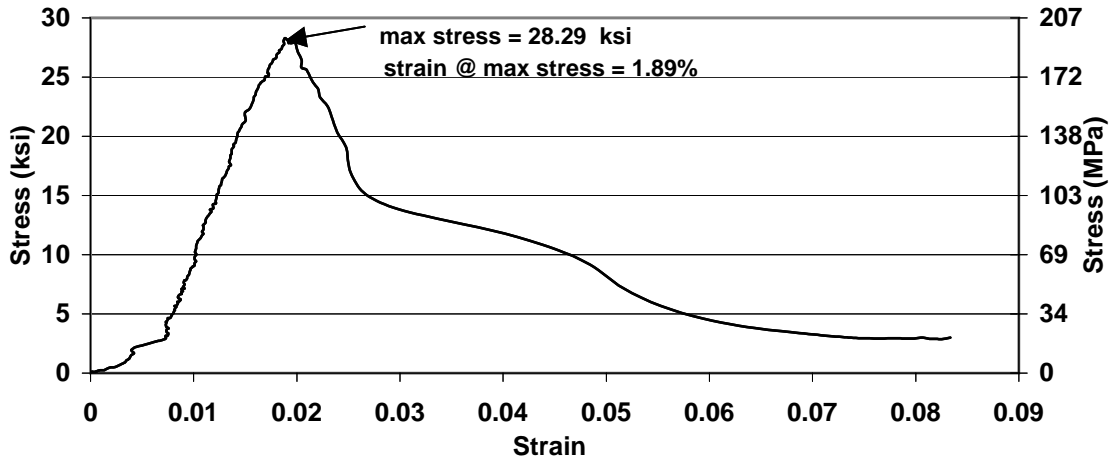


Figure 2-15: Stress-Strain Relationship for Glass FRP Strip #4 @ 1000 $\mu\text{s}/\text{sec}$

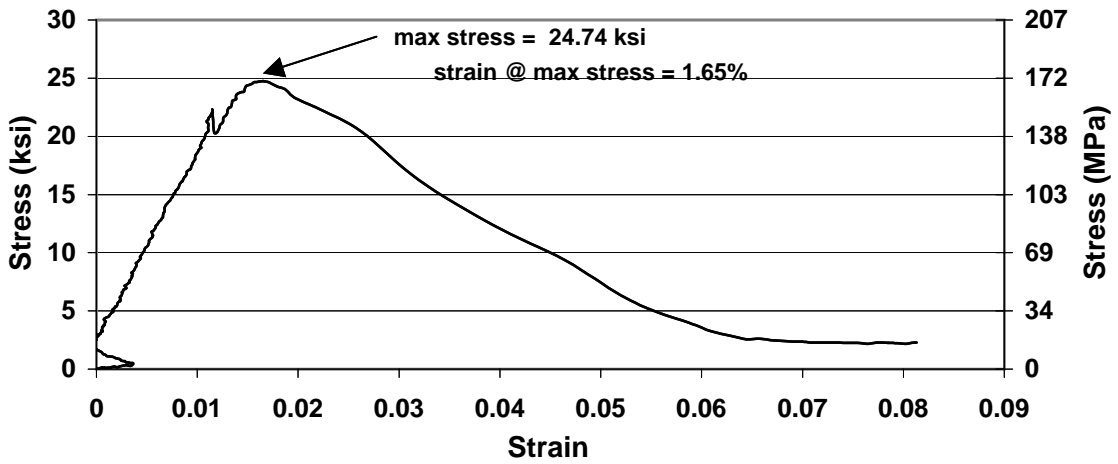


Figure 2-16: Stress-Strain Relationship for Glass FRP Strip #5 @ 1000 $\mu\text{s}/\text{sec}$
(Fibers in Strip # 5 not Perfectly Aligned)

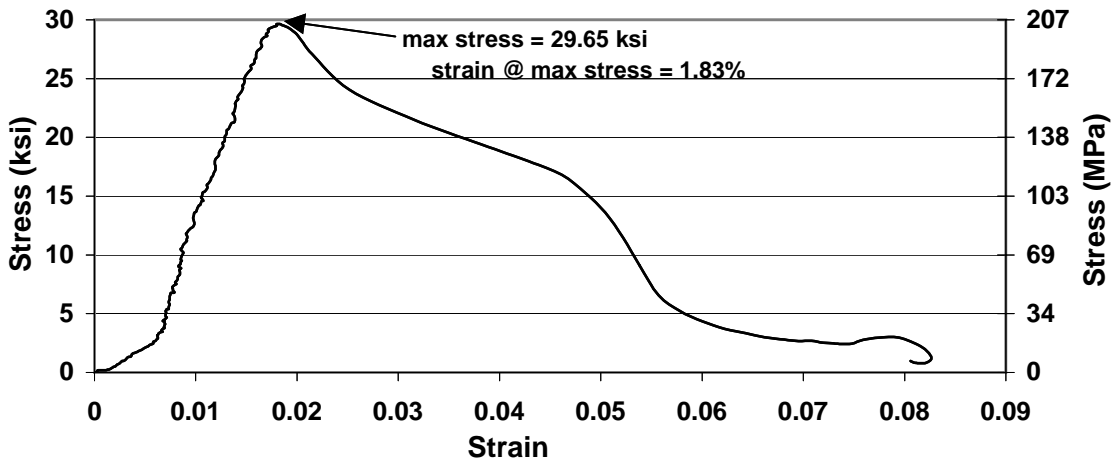


Figure 2-17: Stress-Strain Relationship for Glass FRP Strip #6 @ 1000 $\mu\text{s}/\text{sec}$

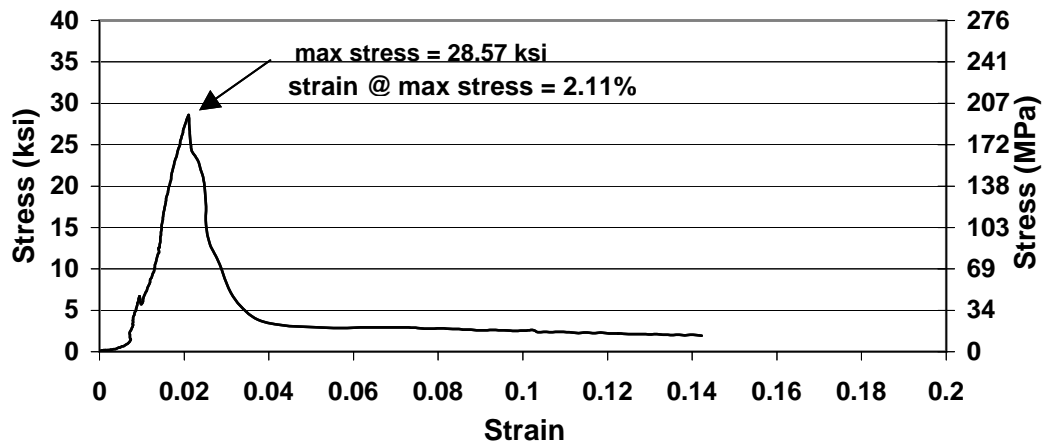


Figure 2-18: Stress-Strain Relationship for Glass FRP Strip #7 @ 5000 $\mu\text{s}/\text{sec}$

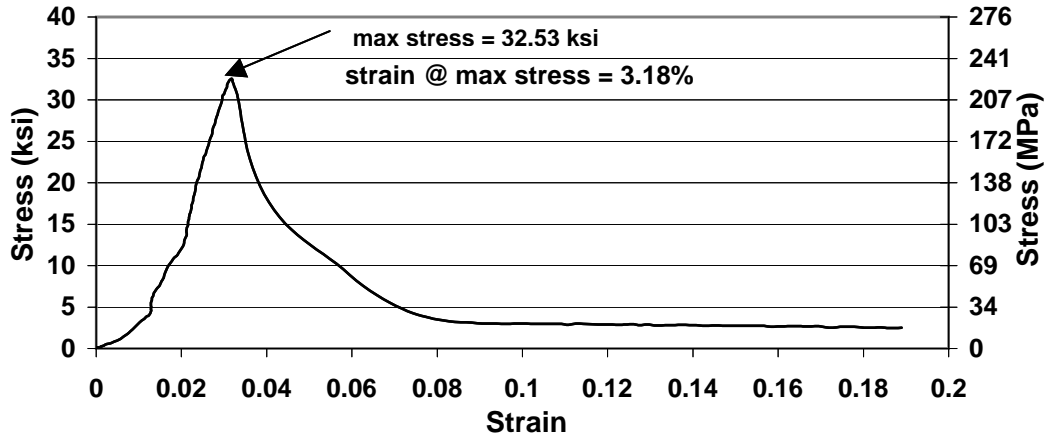


Figure 2-19: Stress-Strain Relationship for Glass FRP Strip #8 @ 5000 $\mu\text{s}/\text{sec}$

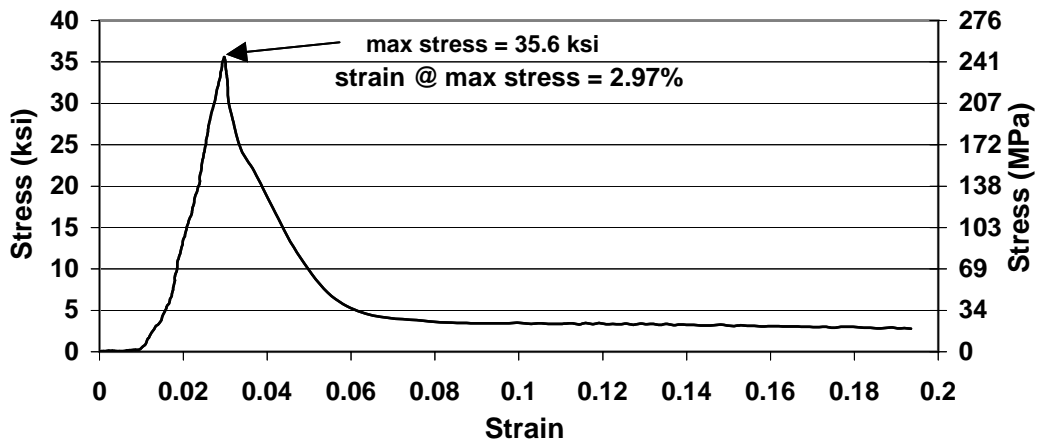


Figure 2-20: Stress-Strain Relationship for Glass FRP Strip #9 @ 5000 $\mu\text{s}/\text{sec}$

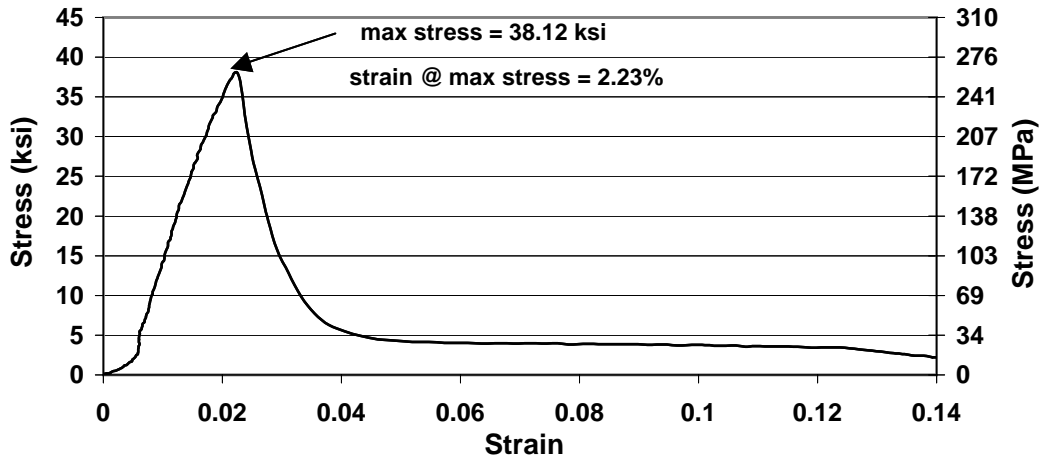


Figure 2-21: Stress-Strain Relationship for Glass FRP Strip #10 @ 10000 μ s/sec

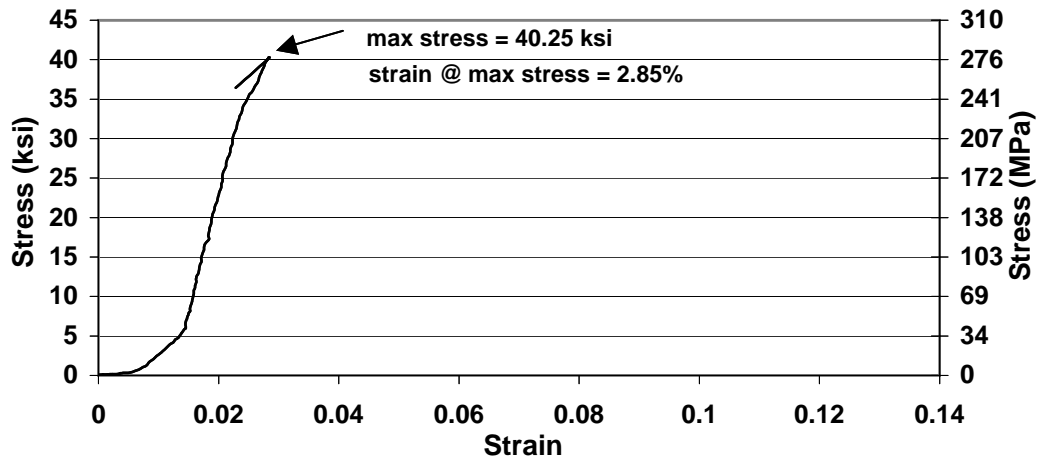


Figure 2-22: Stress-Strain Relationship for Glass FRP Strip #11 @ 10000 μ s/sec

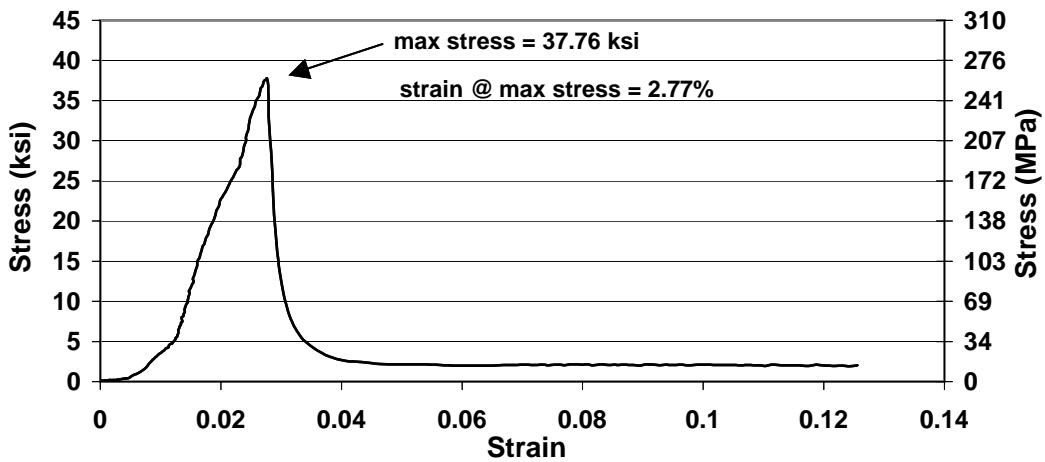


Figure 2-23: Stress-Strain Relationship for Glass FRP Strip #12 @ 10000 μ s/sec

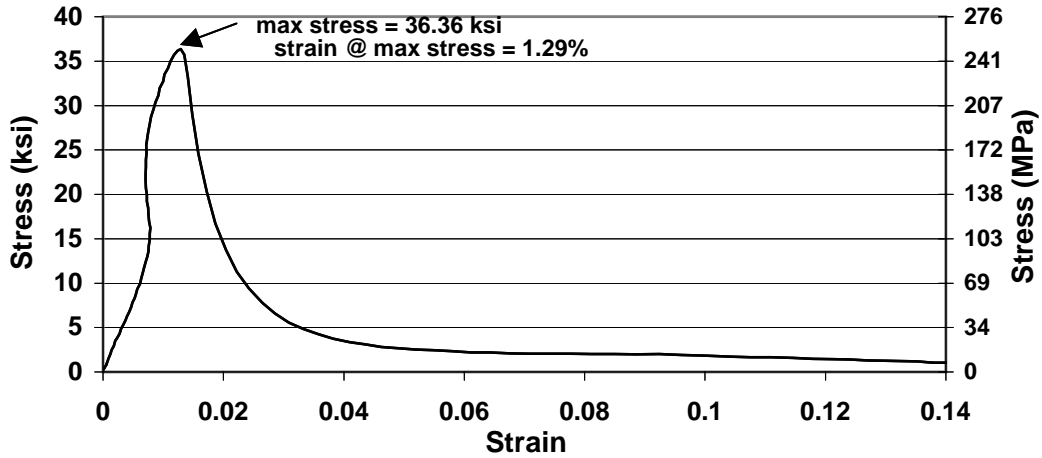


Figure 2-24: Stress-Strain Relationship for Glass FRP Strip #13 @ 50000 $\mu\text{s}/\text{sec}$

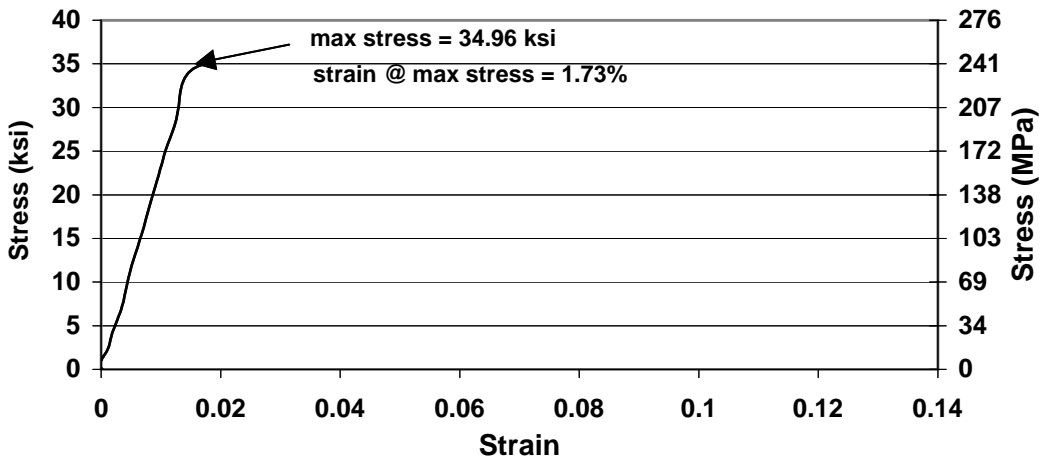


Figure 2-25: Stress-Strain Relationship for Glass FRP Strip #14 @ 50000 $\mu\text{s}/\text{sec}$

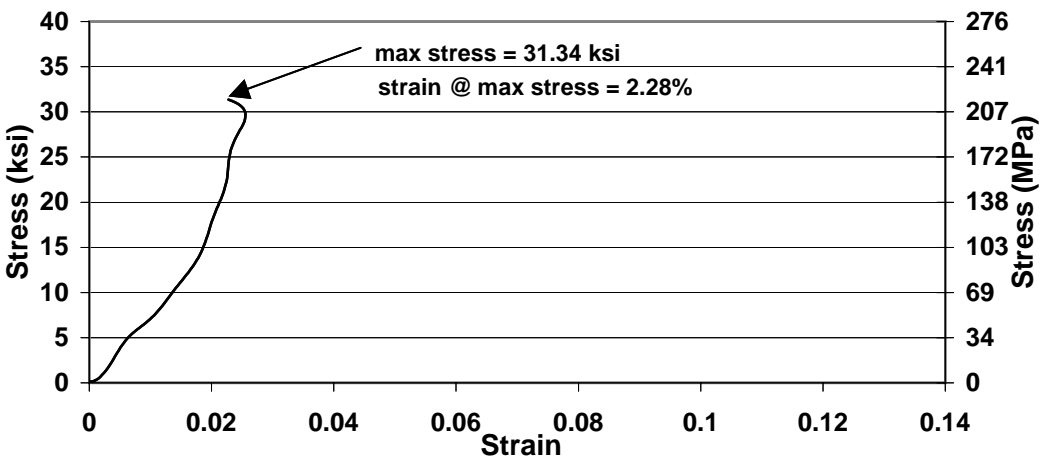


Figure 2-26: Stress-Strain Relationship for Glass FRP Strip #15 @ 50000 $\mu\text{s}/\text{sec}$

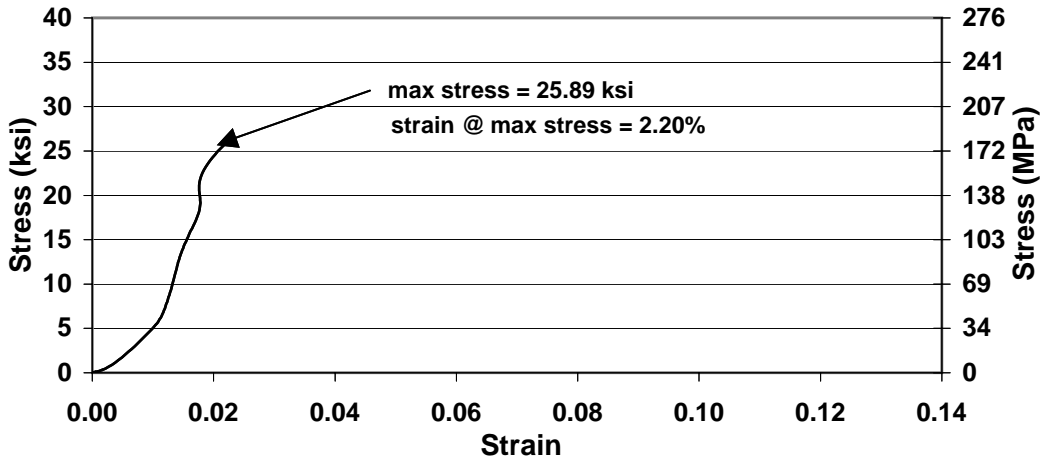


Figure 2-27: Stress-Strain Relationship for Glass FRP Strip #19 @ 50000 μ s/sec

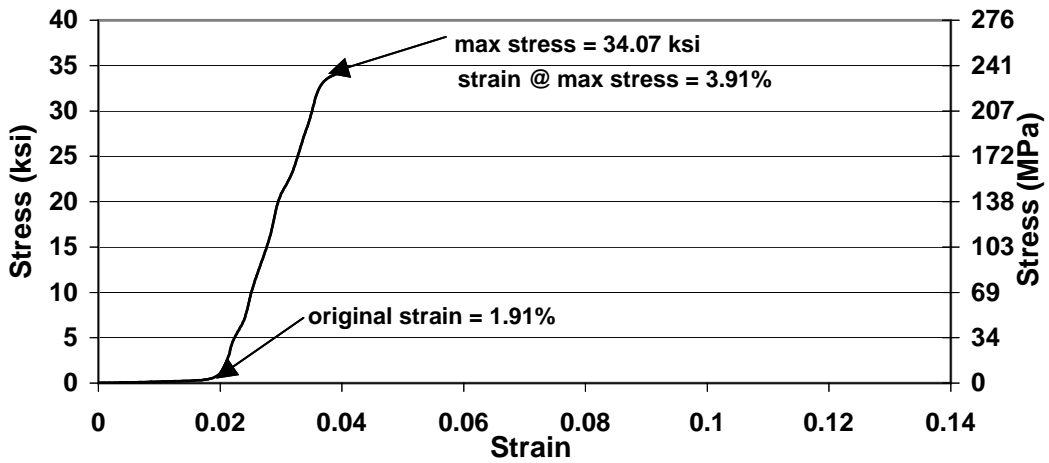


Figure 2-28: Stress-Strain Relationship for Glass FRP Strip #20 @ 50000 μ s/sec

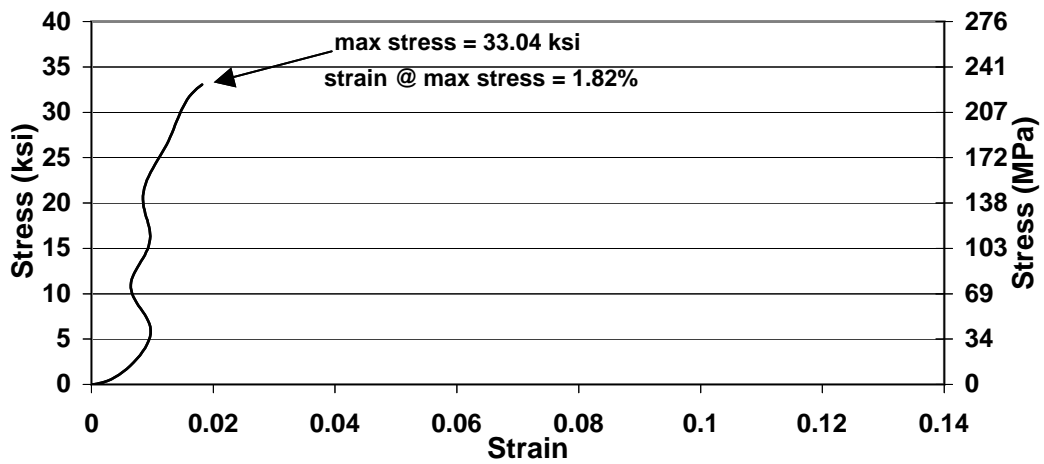


Figure 2-29: Stress-Strain Relationship for Glass FRP Strip #21 @ 50000 μ s/sec

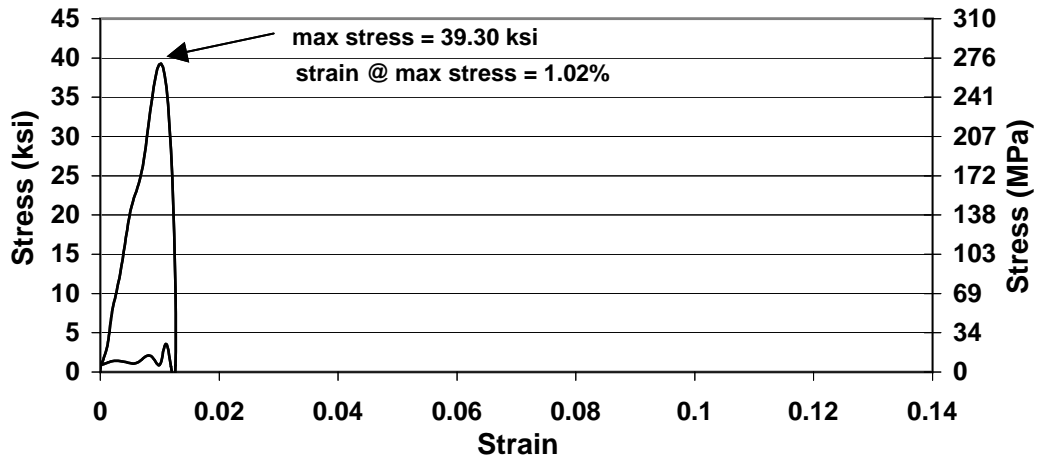


Figure 2-30: Stress-Strain Relationship for Glass FRP Strip #16 @ 100000 μ s/sec

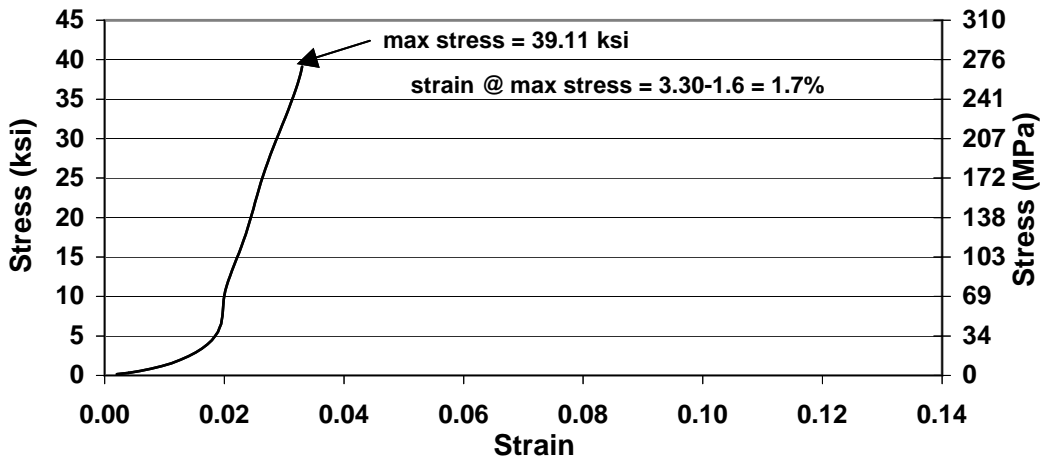


Figure 2-31: Stress-Strain Relationship for Glass FRP Strip #17 @ 100000 μ s/sec

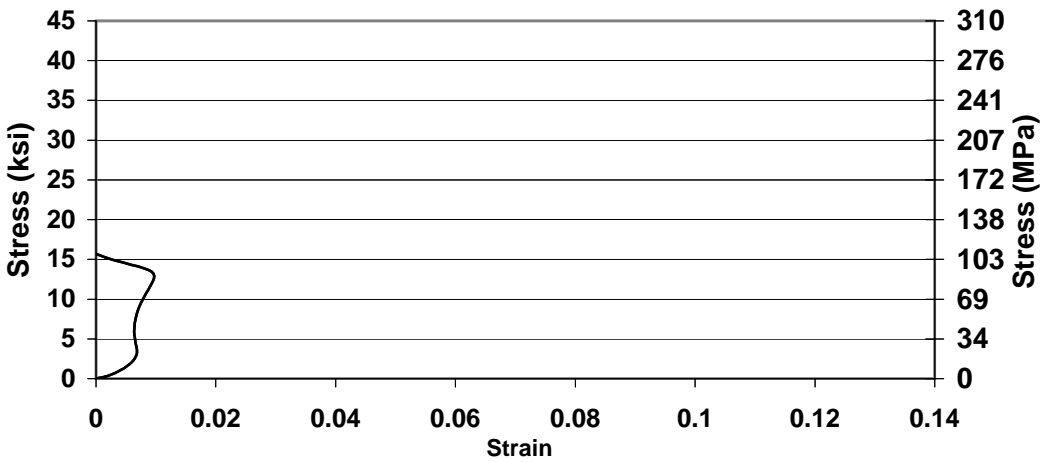


Figure 2-32: Stress-Strain Relationship for Glass FRP Strip #18 @ 100000 μ s/sec

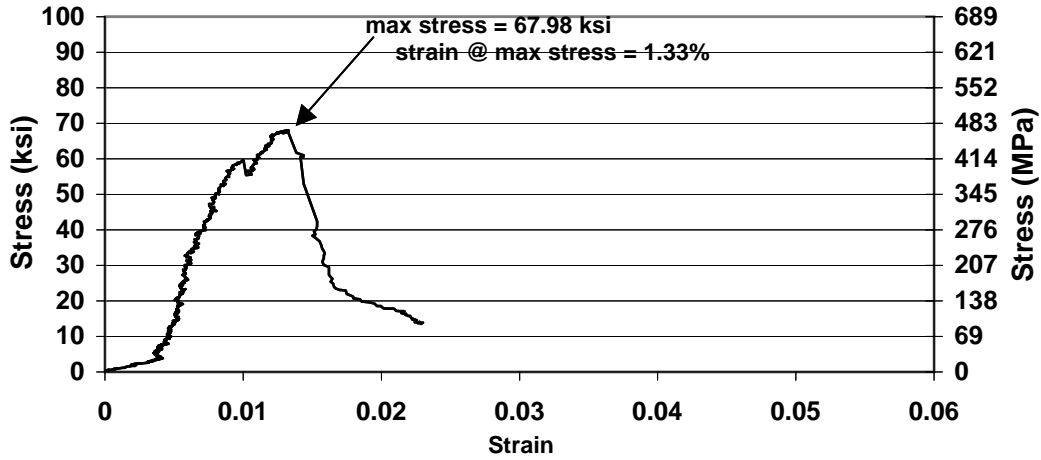


Figure 2-33: Stress-Strain Relationship for Carbon FRP Strip #1 @ 167 μ s/sec

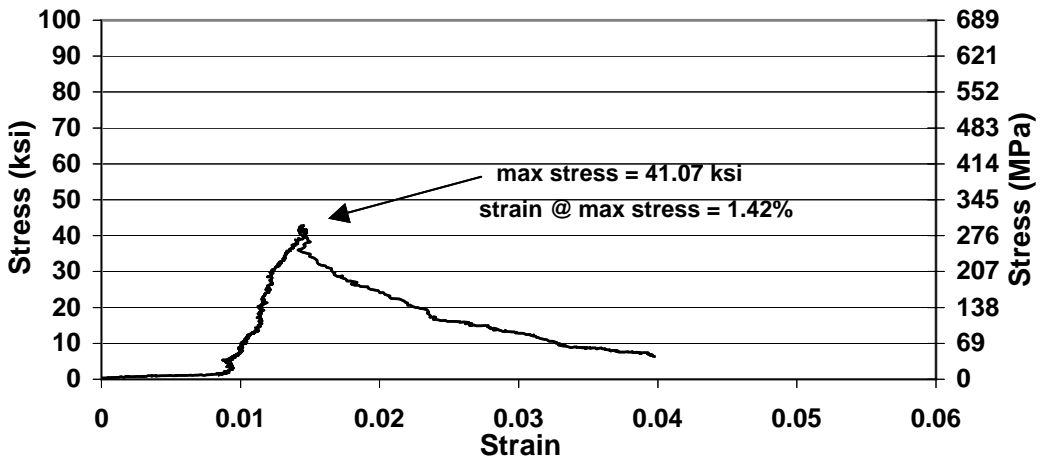


Figure 2-34: Stress-Strain Relationship for Carbon FRP Strip #2 @ 167 μ s/sec

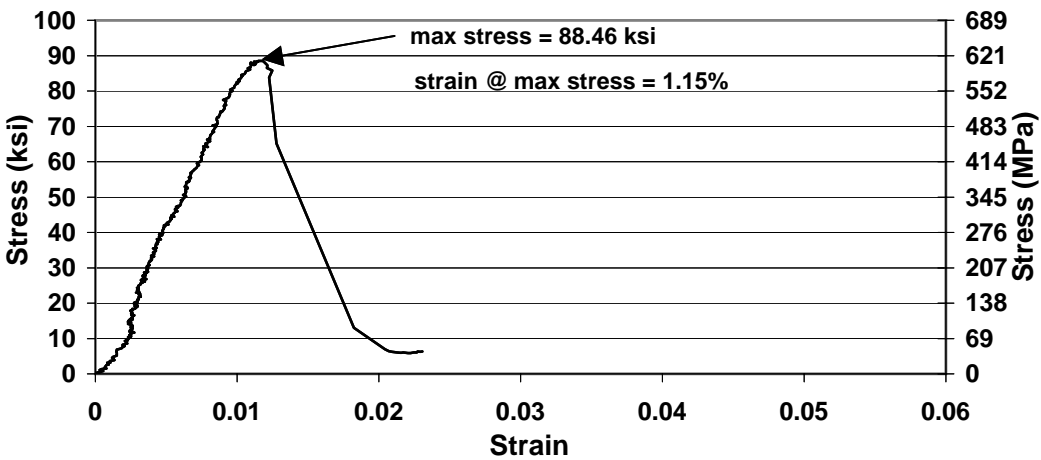


Figure 2-35: Stress-Strain Relationship for Carbon FRP Strip #3 @ 167 μ s/sec

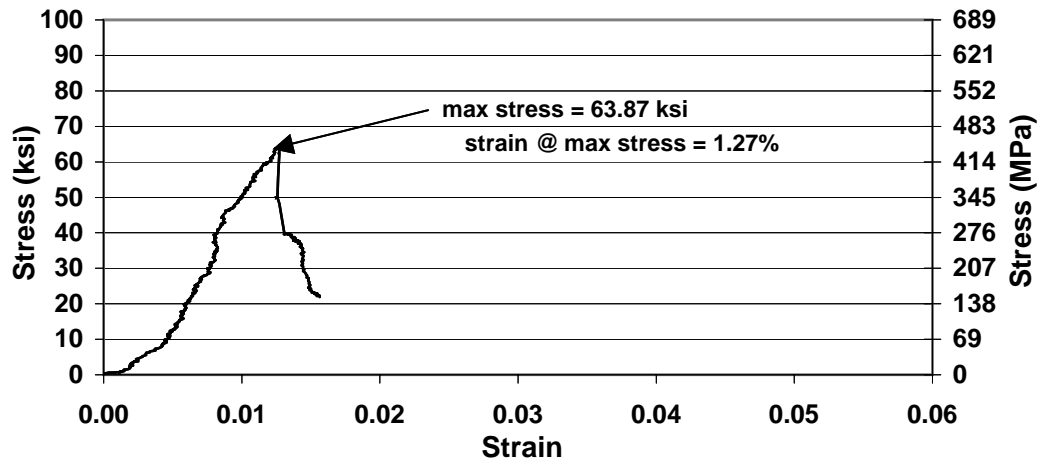


Figure 2-36: Stress-Strain Relationship for Carbon FRP Strip #4 @ 167 μ s/sec

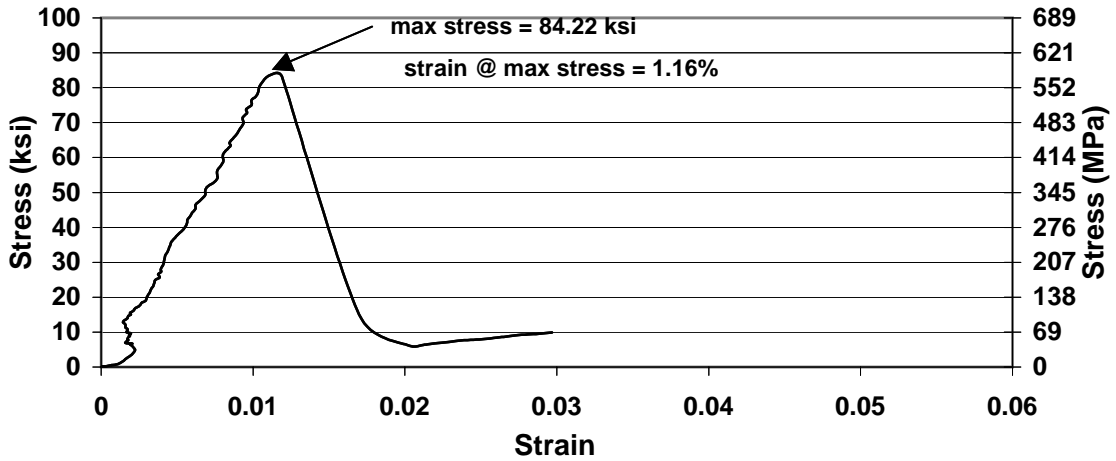


Figure 2-37: Stress-Strain Relationship for Carbon FRP Strip #5 @ 1000 μ s/sec

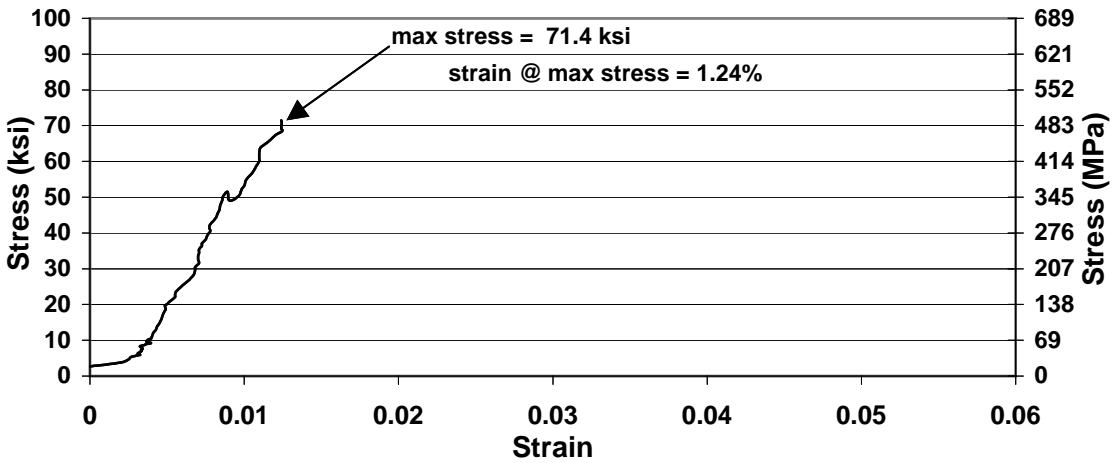


Figure 2-38: Stress-Strain Relationship for Carbon FRP Strip #6 @ 1000 μ s/sec

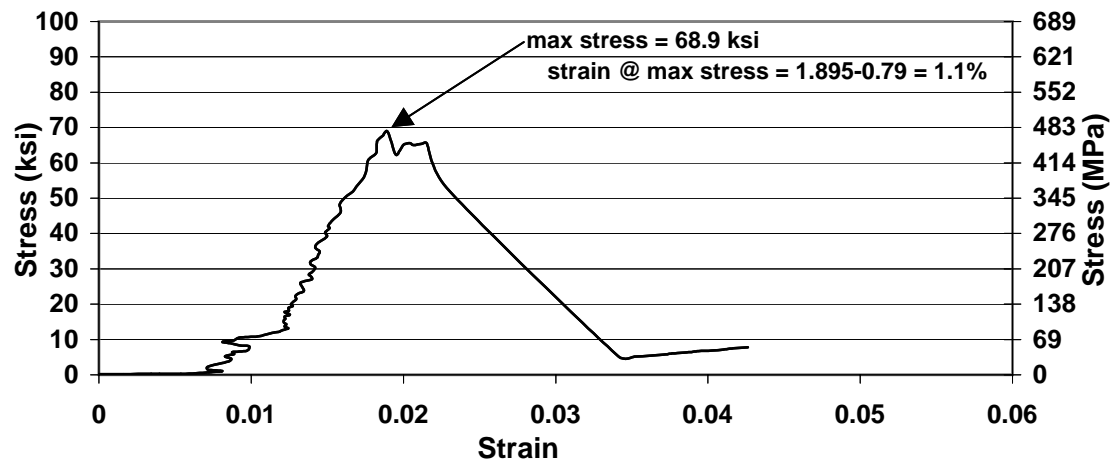


Figure 2-39: Stress-Strain Relationship for Carbon FRP Strip #7 @ 1000 μ s/sec

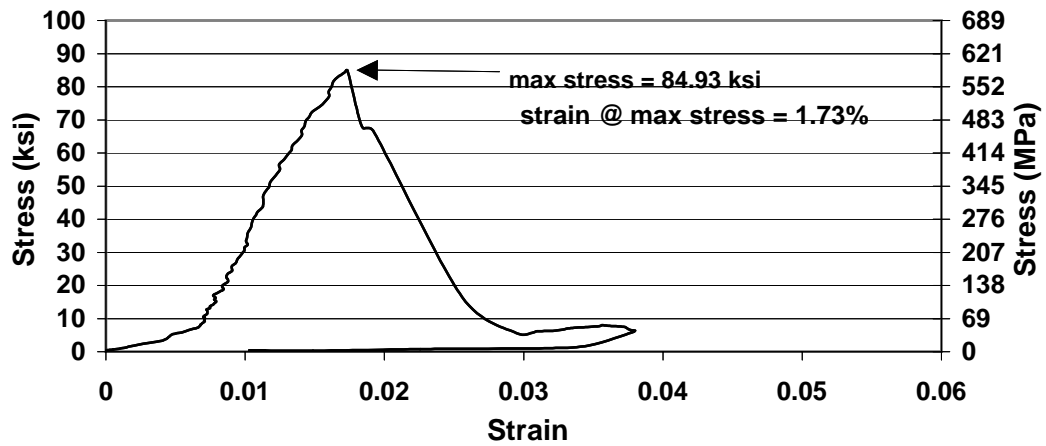


Figure 2-40: Stress-Strain Relationship for Glass FRP Strip #8 @ 5000 $\mu\text{s}/\text{sec}$

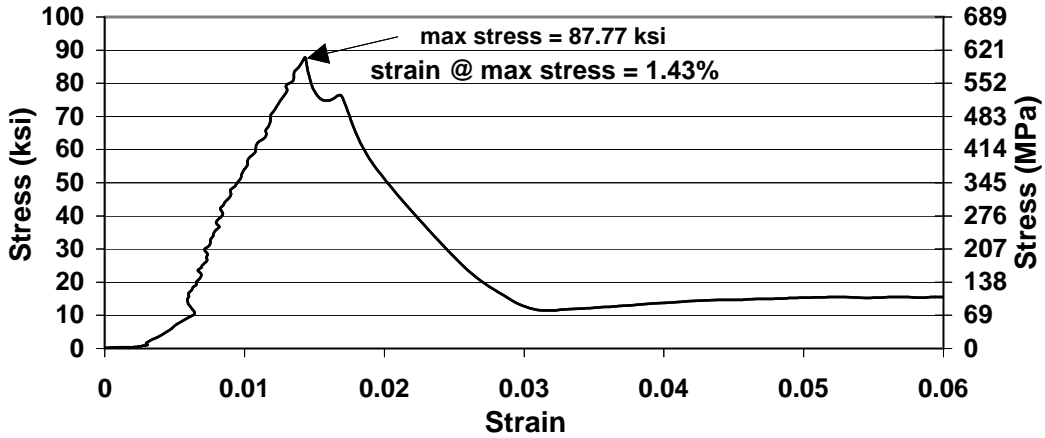


Figure 2-41: Stress-Strain Relationship for Carbon FRP Strip #9 @ 5000 $\mu\text{s}/\text{sec}$

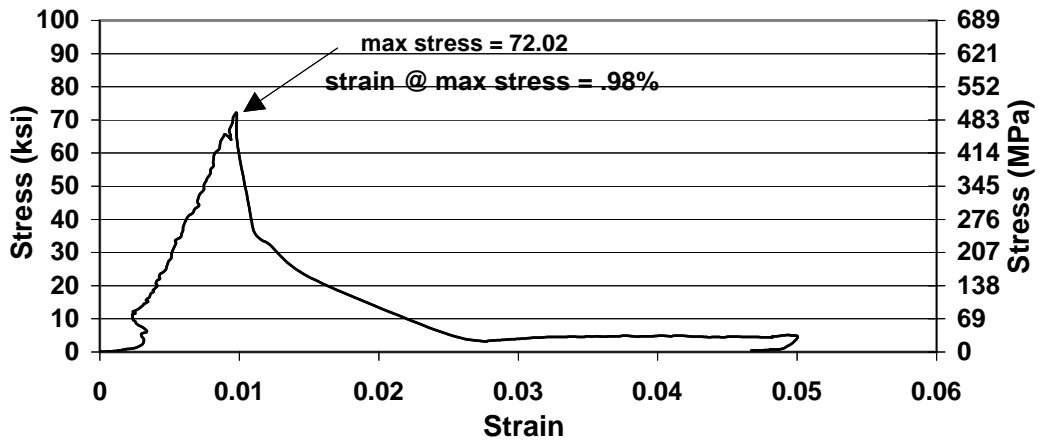


Figure 2-42: Stress-Strain Relationship for Carbon FRP Strip #10 @ 5000 $\mu\text{s}/\text{sec}$

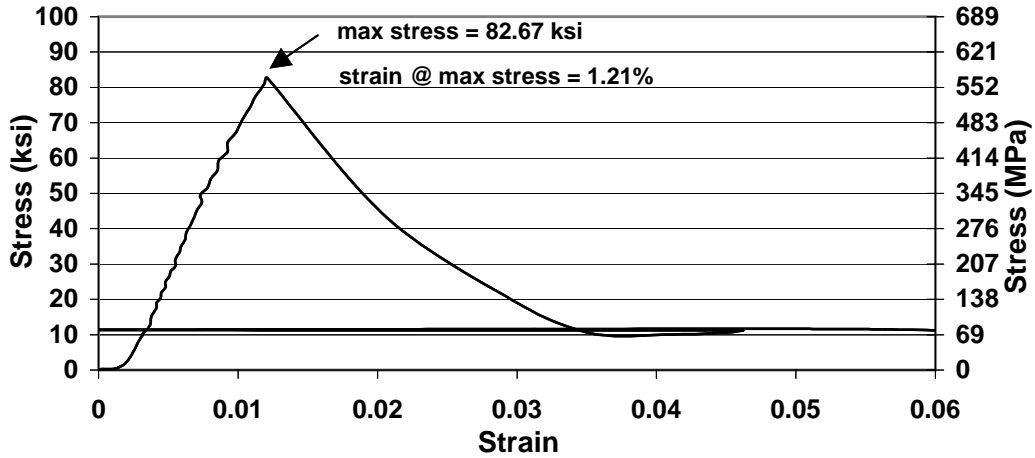


Figure 2-43: Stress-Strain Relationship for Carbon FRP Strip #11 @ 10000 $\mu\epsilon/\text{sec}$

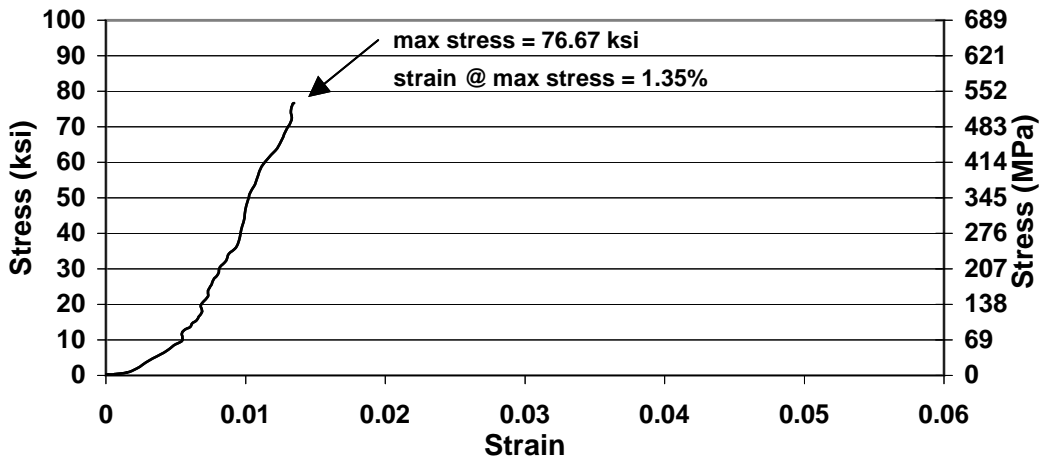


Figure 2-44: Stress-Strain Relationship for Carbon FRP Strip #12 @ 10000 $\mu\epsilon/\text{sec}$

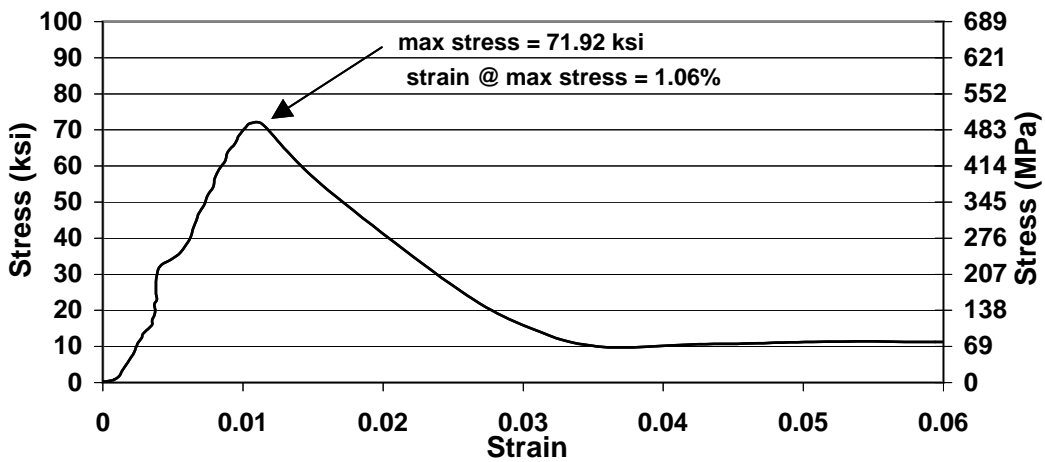


Figure 2-45: Stress-Strain Relationship for Carbon FRP Strip #13 @ 10000 $\mu\epsilon/\text{sec}$

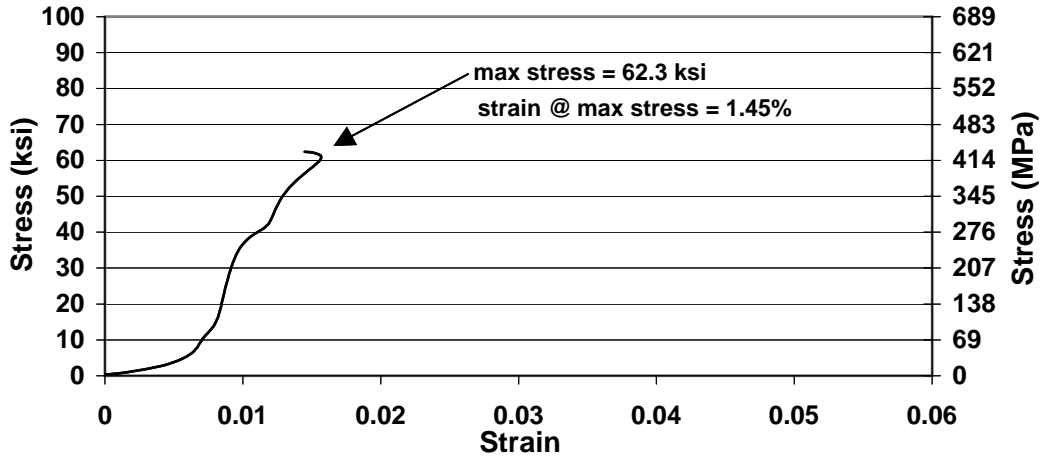


Figure 2-46: Stress-Strain Relationship for Carbon FRP Strip #14 @ 50000 $\mu\text{s}/\text{sec}$

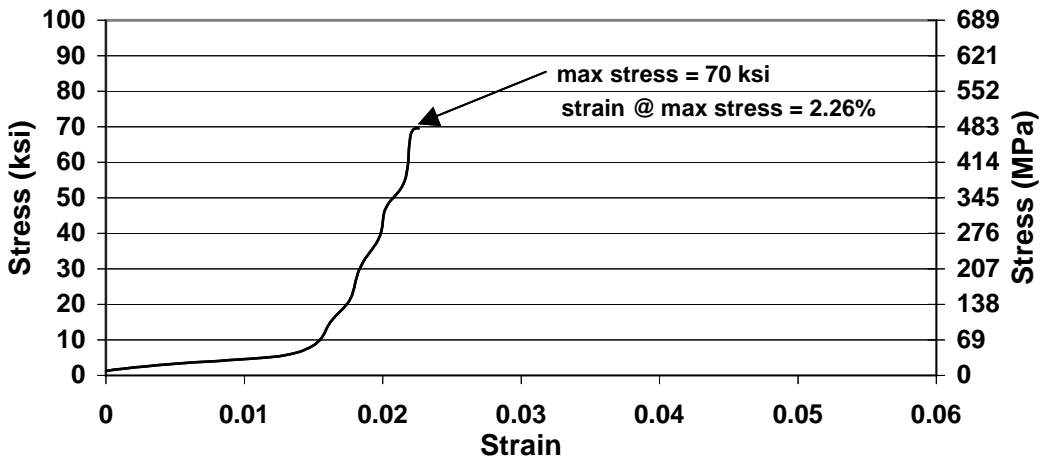


Figure 2-47: Stress-Strain Relationship for Carbon FRP Strip #15 @ 50000 $\mu\text{s}/\text{sec}$

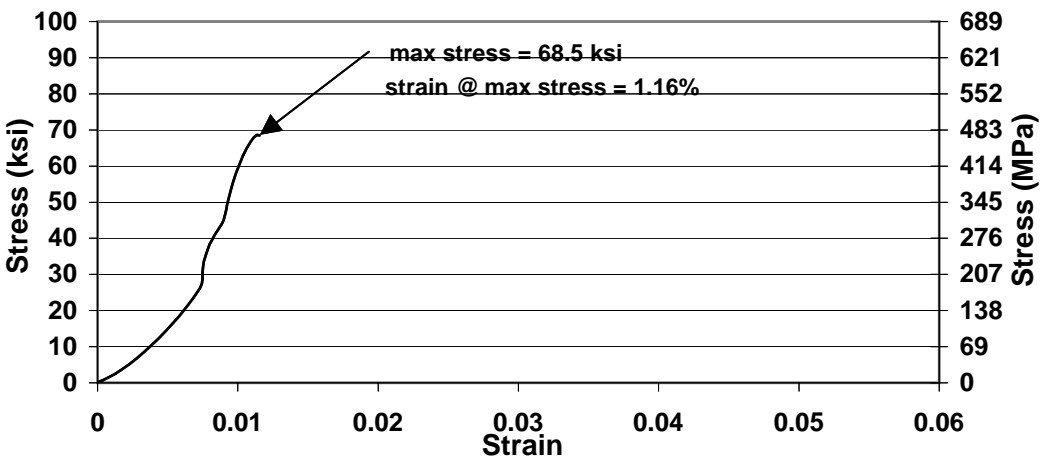


Figure 2-48: Stress-Strain Relationship for Carbon FRP Strip #16 @ 50000 $\mu\text{s}/\text{sec}$

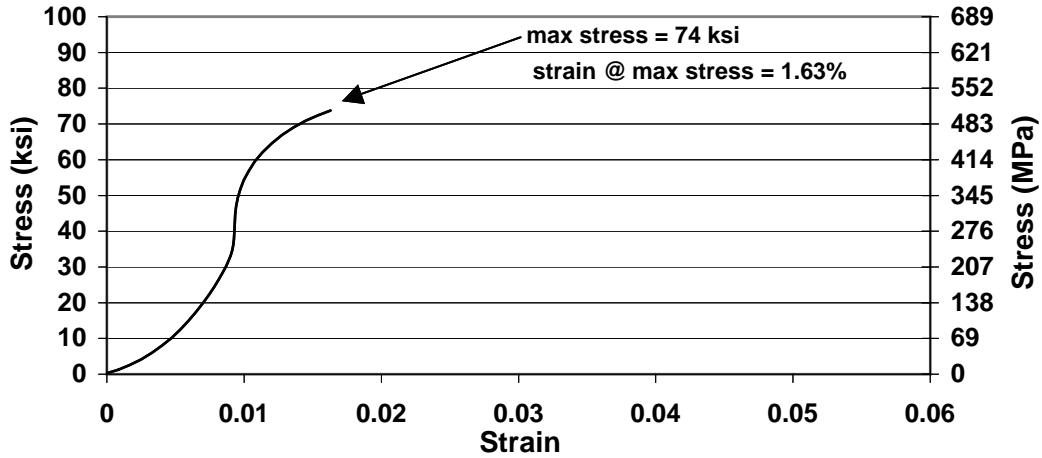


Figure 2-49: Stress-Strain Relationship for Carbon FRP Strip #17 @ 100000 $\mu\text{s}/\text{sec}$

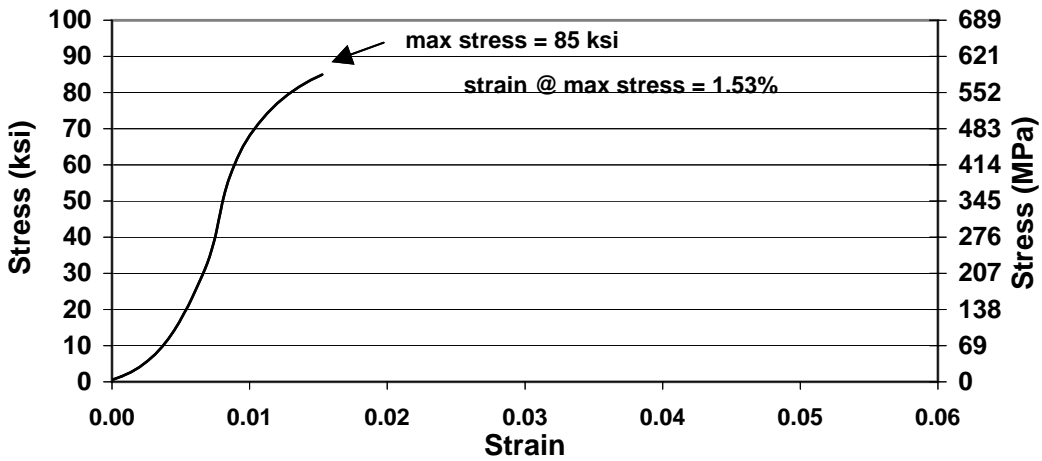


Figure 2-50: Stress-Strain Relationship for Carbon FRP Strip #18 @ 100000 $\mu\text{s}/\text{sec}$

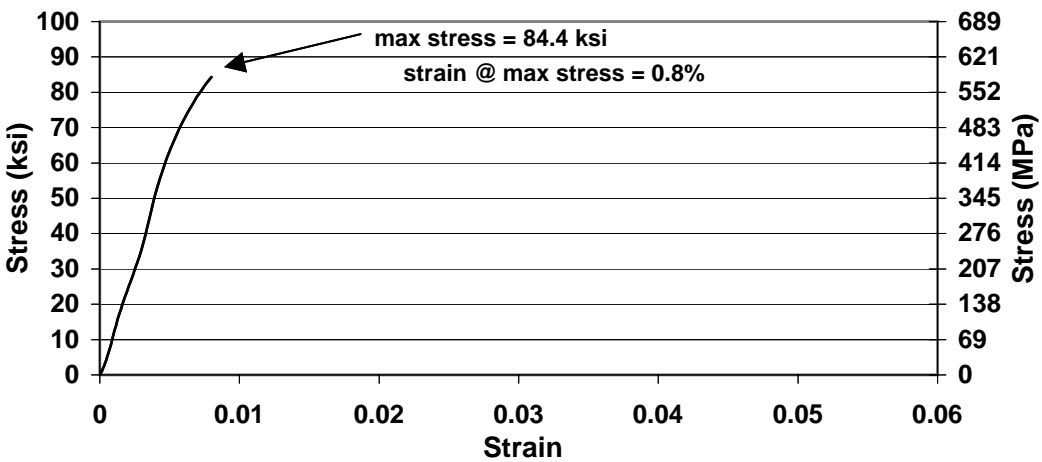


Figure 2-51: Stress-Strain Relationship for Carbon FRP Strip #19 @ 100000 $\mu\text{s}/\text{sec}$

Type B and D are Sides of the Vacuum Box, Type A is the Top of the Box, and Type C is the Base. The Pieces are Clear Acrylic Sheets.

Notes:

Type A thickness = 1.25 in

Type B thickness = 0.50 in

Type C thickness = 1.25 in

Type D thickness = 0.50 in

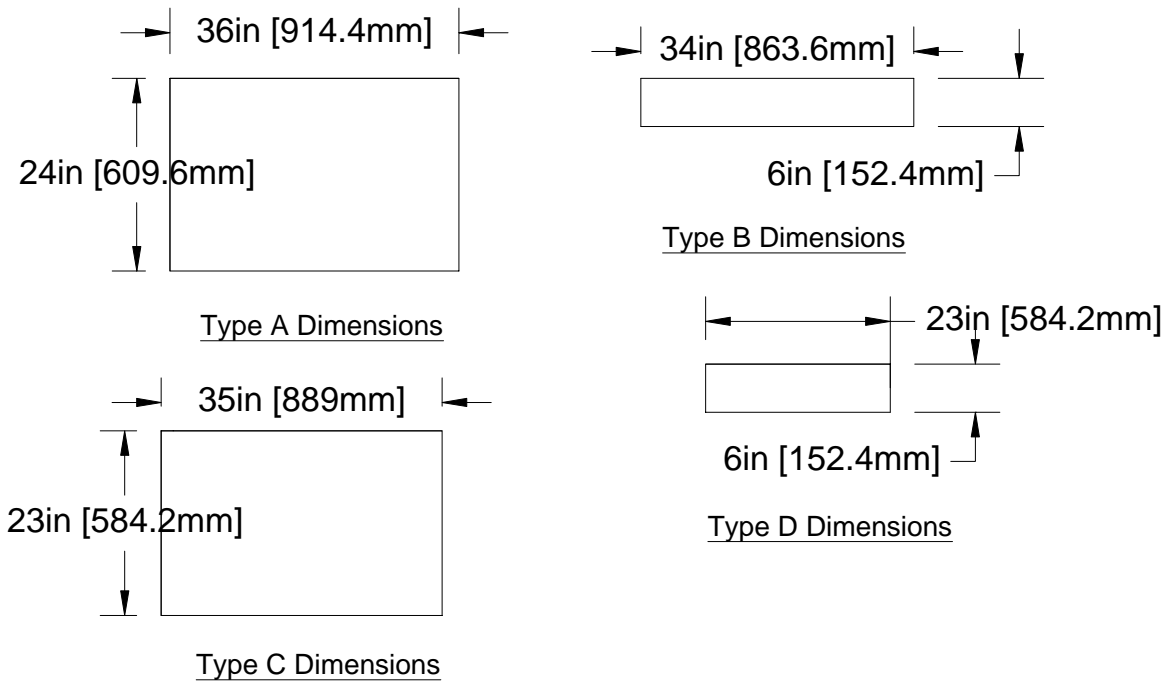


Figure 2-52: Components of Clear Acrylic Vacuum Box



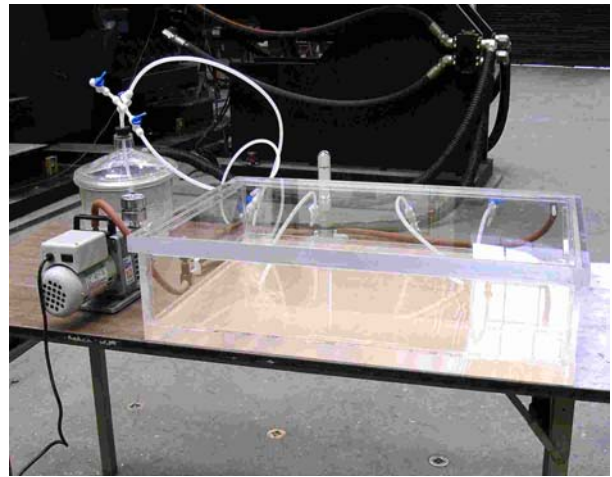
(a) Arranging Acrylite Sheets into Vacuum Box



(b) Forming Box with Weld-On

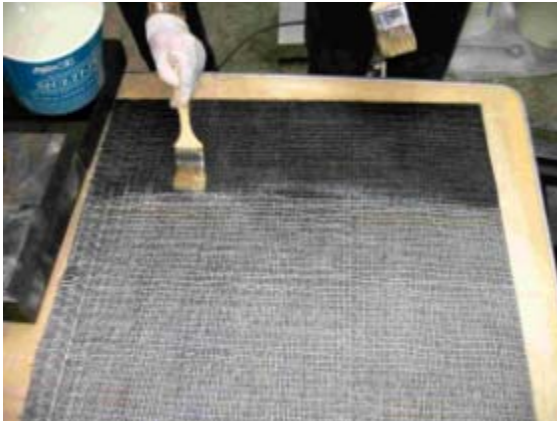


(c) Forming Self-Sealing Top



(d) Completed Vacuum Box with Pumps

Figure 2-53: Vacuum Box Construction



(a) Painting Epoxy onto Fabric

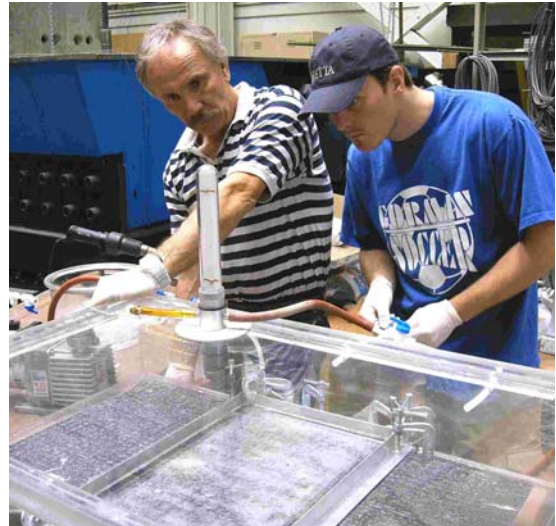


(b) Squeezing Excess Epoxy from Fabric

Figure 2-54: Epoxy Coating Process



(d) Pouring Elastomer over Fabric.



(d) Vacuuming Air from Elastomer Coated Fabric

Figure 2-55: Elastomer Coating Process

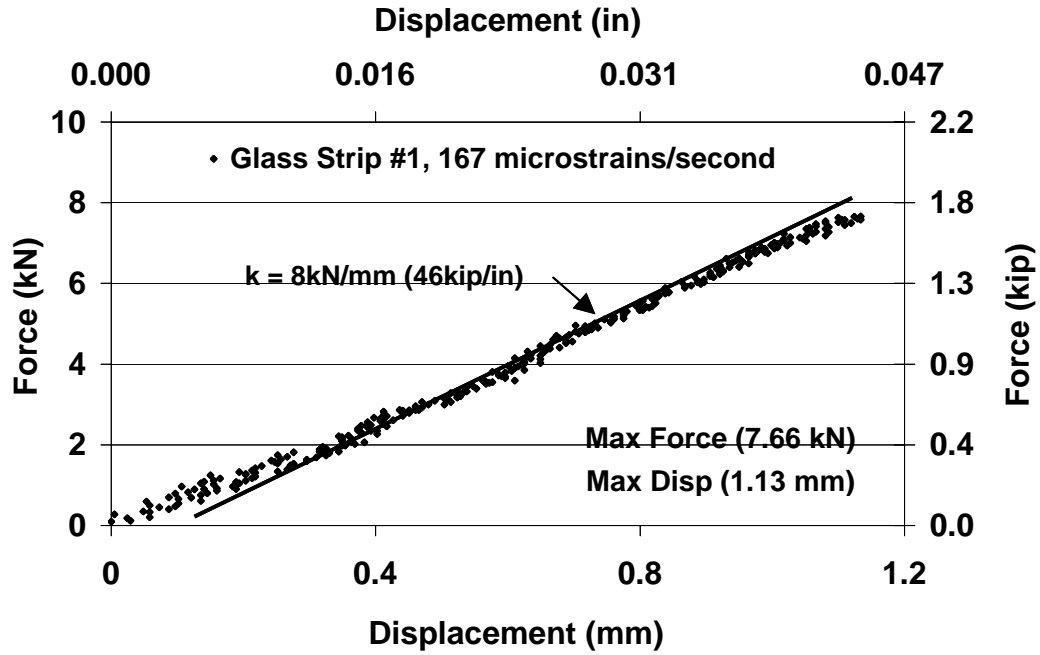


Figure: 2-56: Force vs. Displacement, Elastomer Coated Glass Strip #1

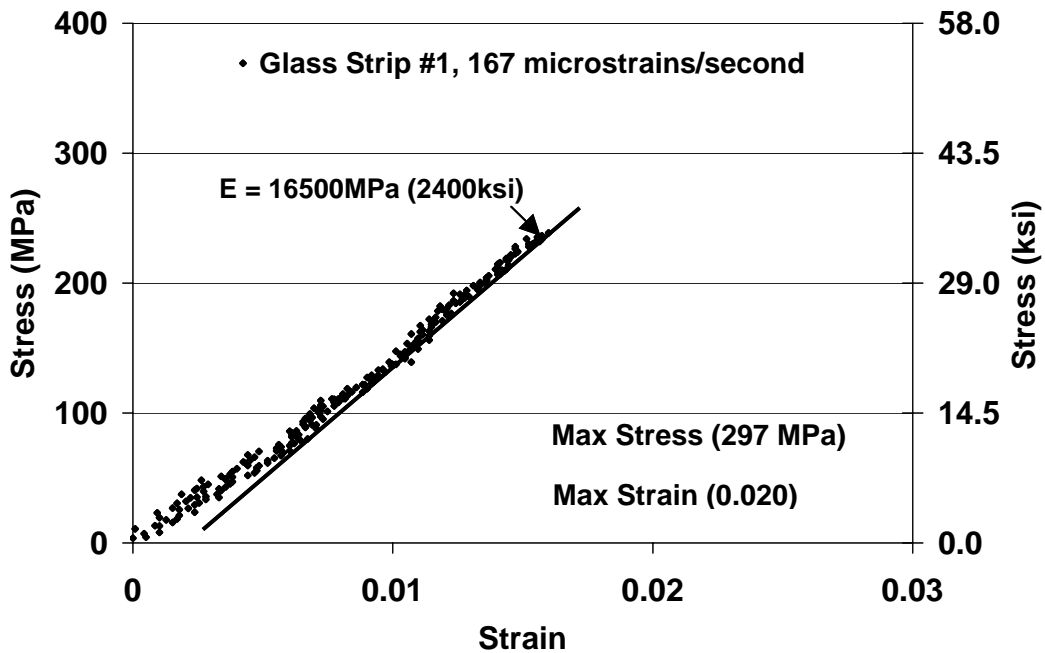


Figure:2-57: Stress vs. Strain, Elastomer Coated Glass Strip #1

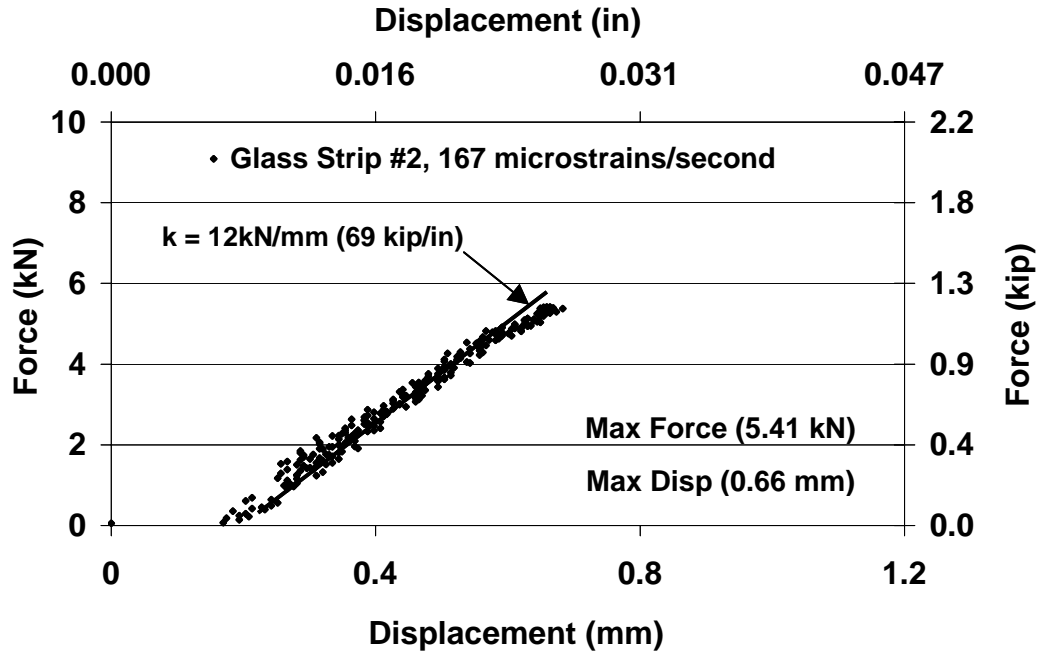


Figure: 2-58: Force vs. Displacement, Elastomer Coated Glass Strip #2

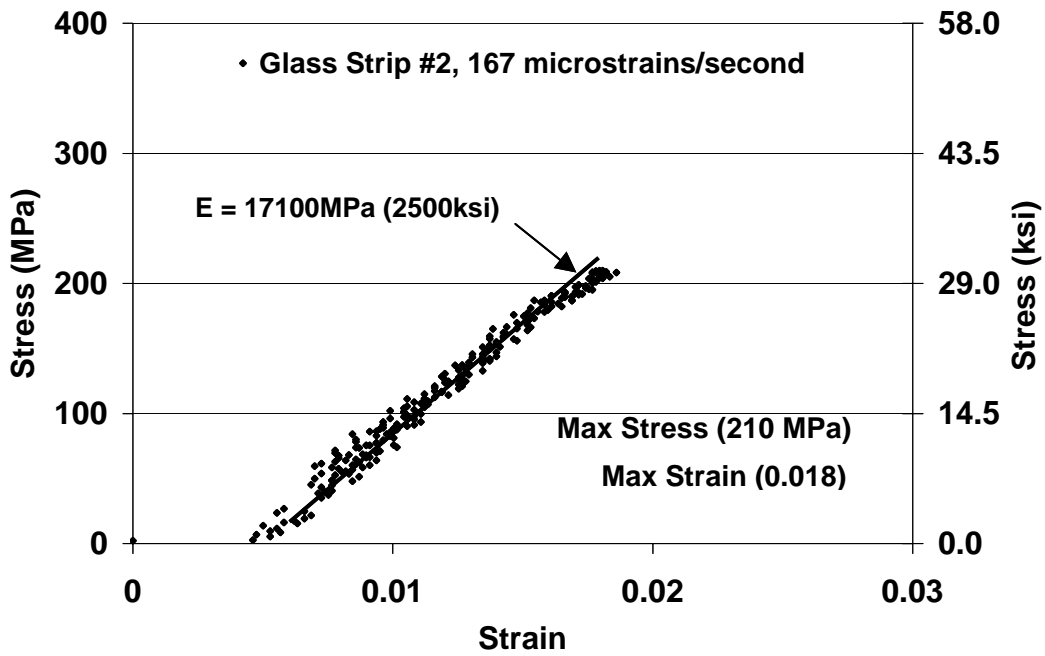


Figure:2-59: Stress vs. Strain, Elastomer Coated Glass Strip #2

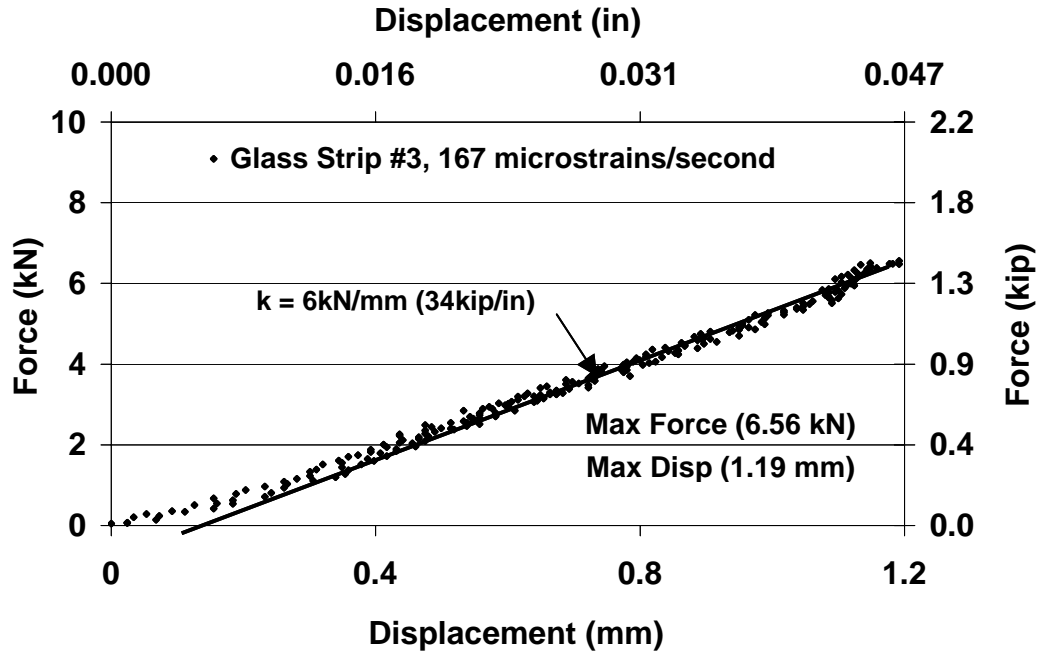


Figure 2-60: Force vs. Displacement, Elastomer Coated Glass Strip #3

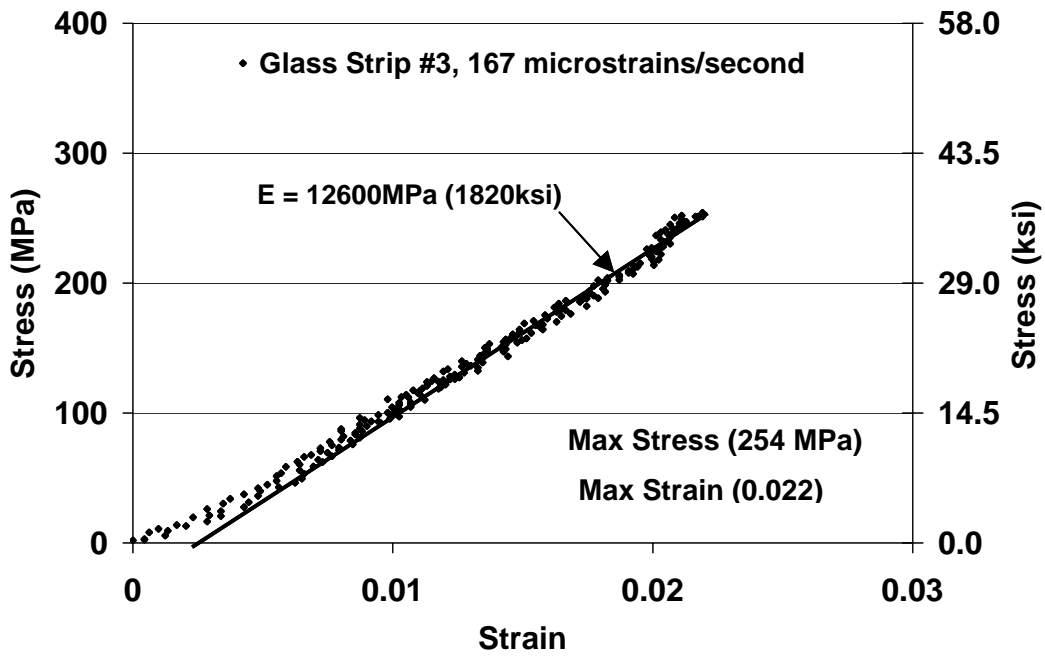


Figure 2-61: Stress vs. Strain, Elastomer Coated Glass Strip #3

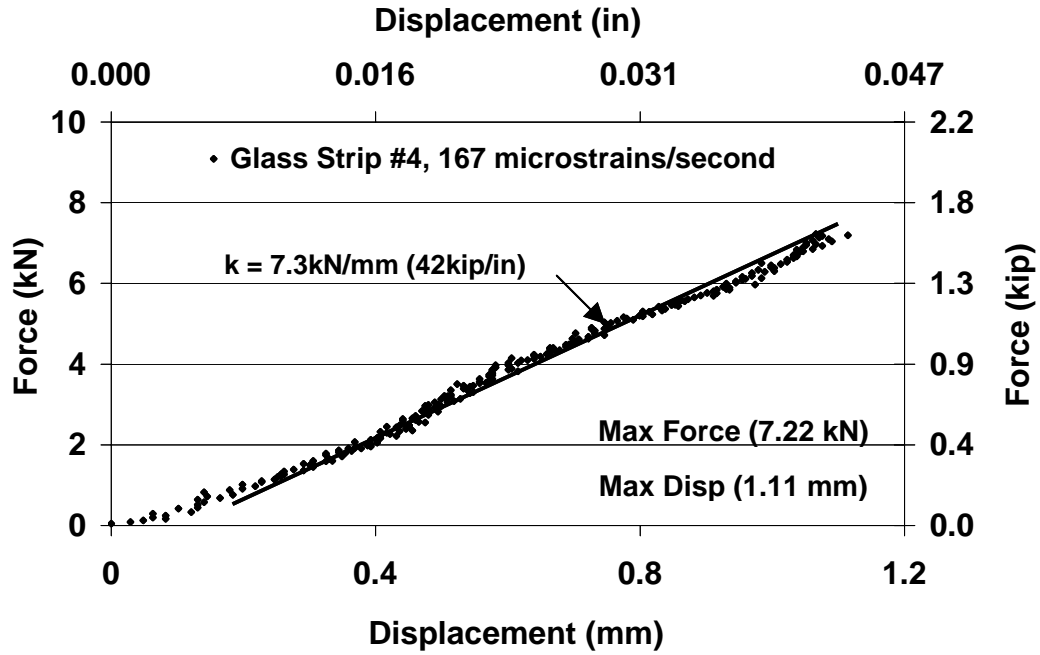


Figure 2-62: Force vs. Displacement, Elastomer Coated Glass Strip #4

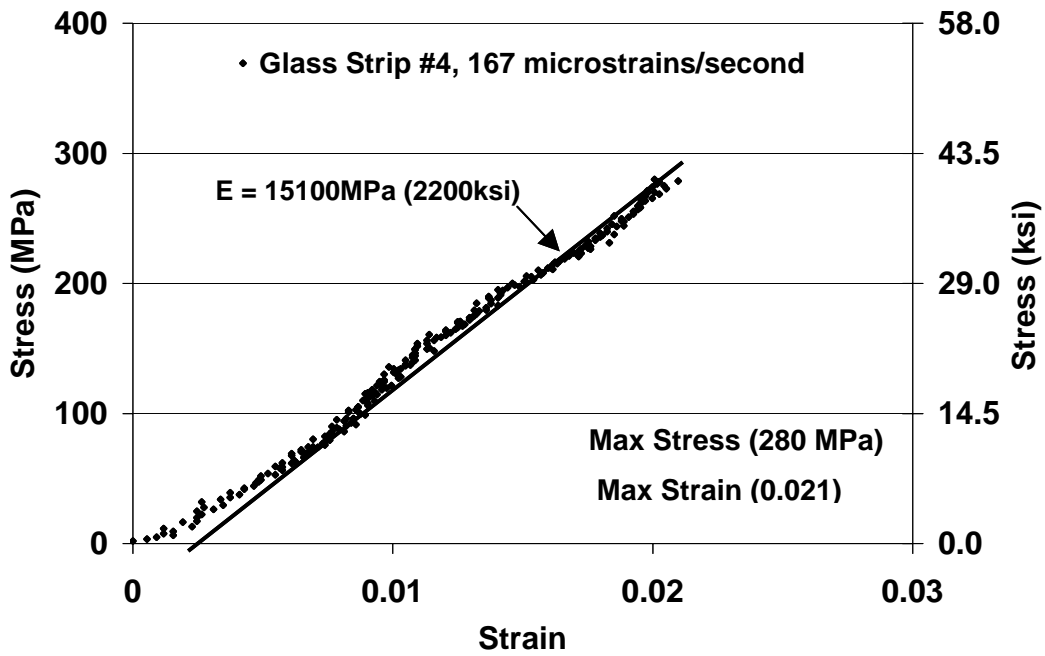


Figure 2-63: Stress vs. Strain, Elastomer Coated Glass Strip #4

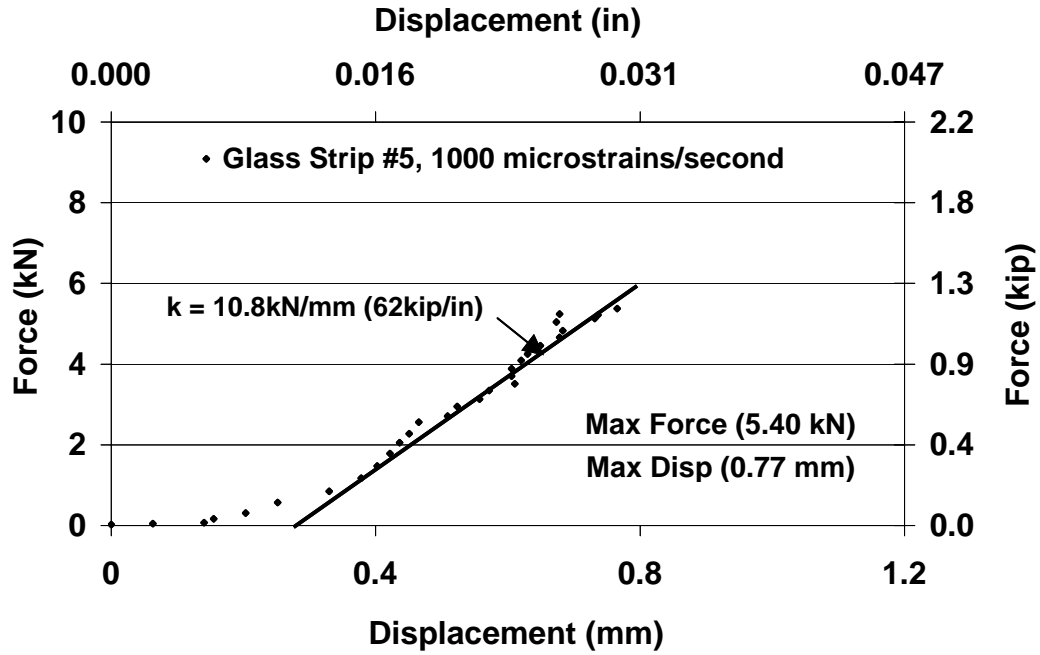


Figure 2-64: Force vs. Displacement, Elastomer Coated Glass Strip #5

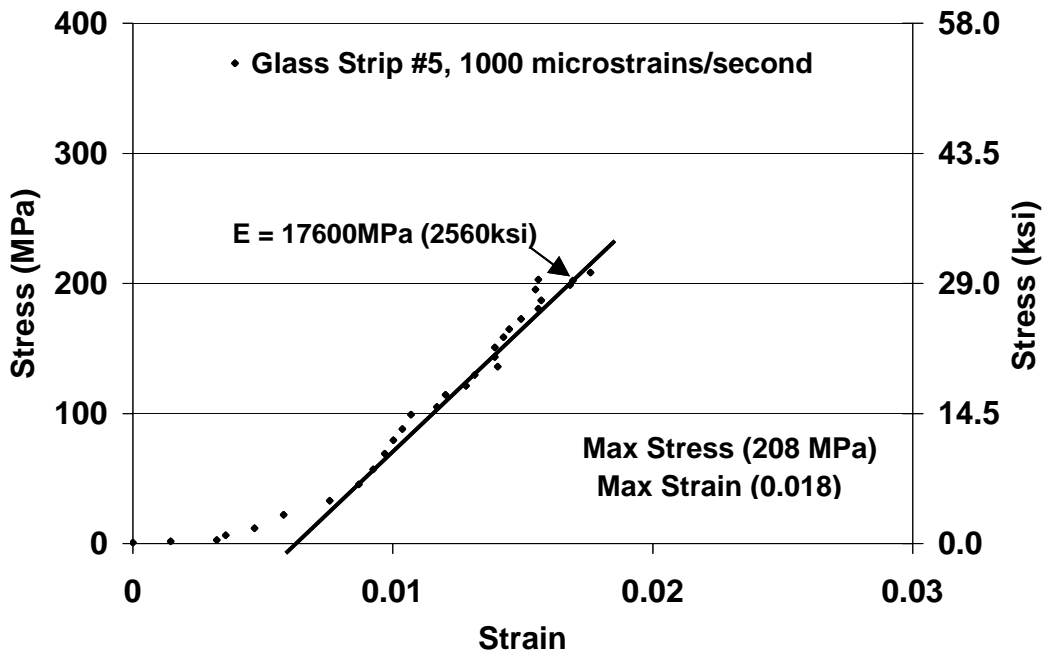


Figure 2-65: Stress vs. Strain, Elastomer Coated Glass Strip #5

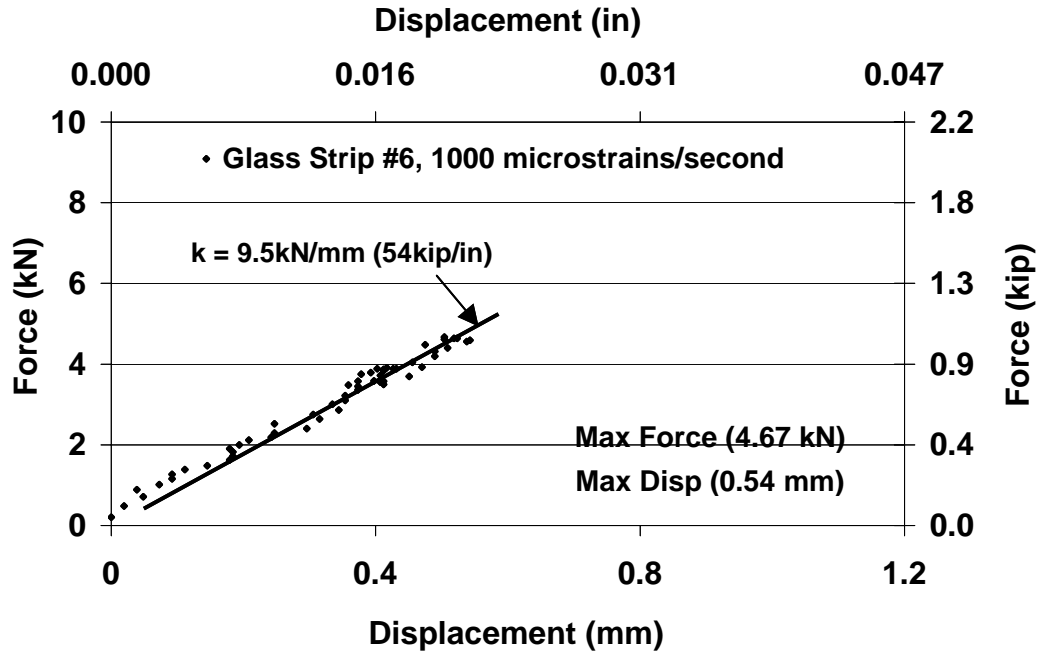


Figure 2-66: Force vs. Displacement, Elastomer Coated Glass Strip #6

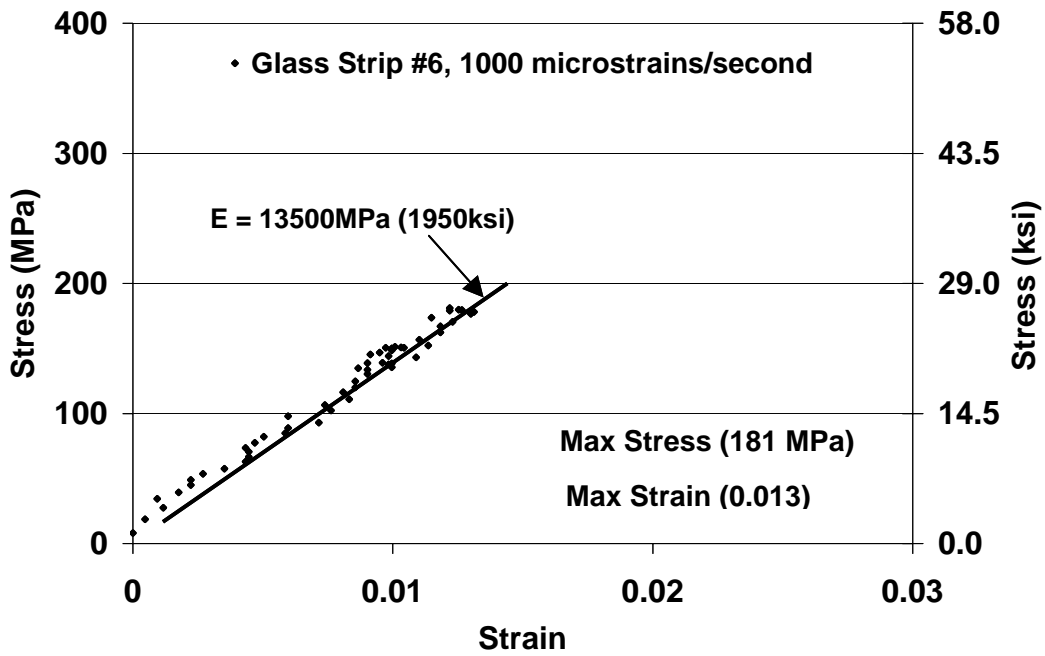


Figure 2-67: Stress vs. Strain, Elastomer Coated Glass Strip #6

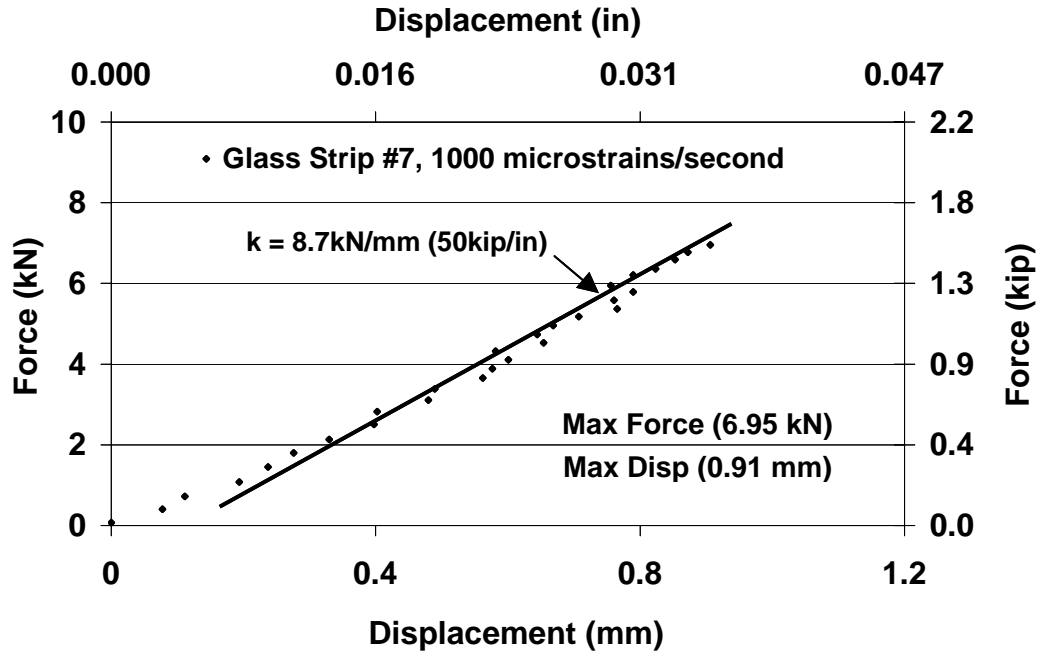


Figure 2-68: Force vs. Displacement, Elastomer Coated Glass Strip #7

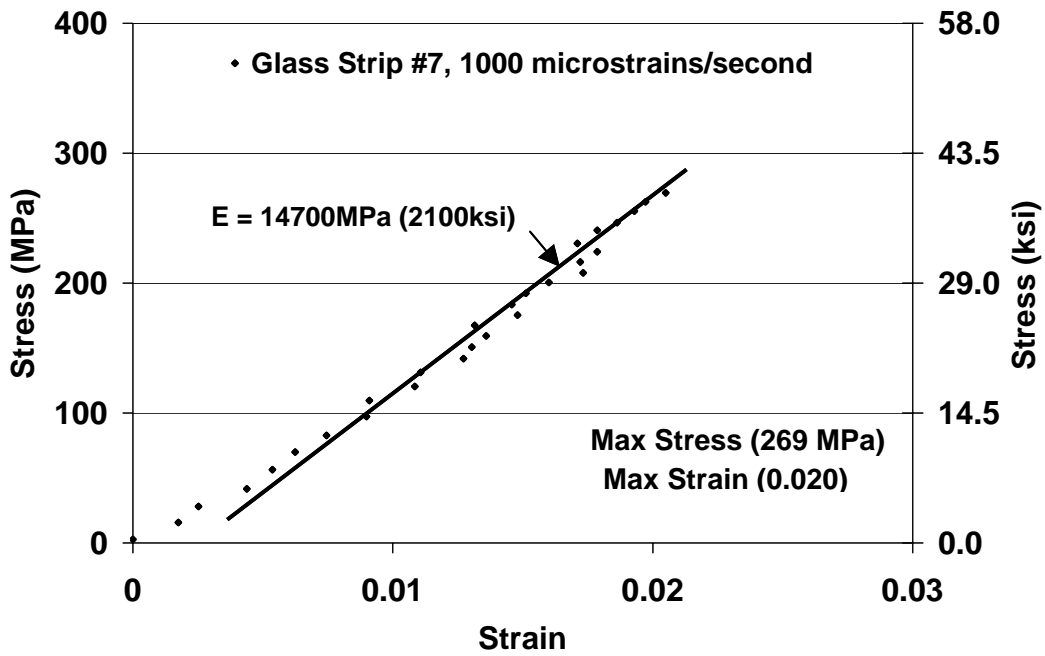


Figure 2-69: Stress vs. Strain, Elastomer Coated Glass Strip #7

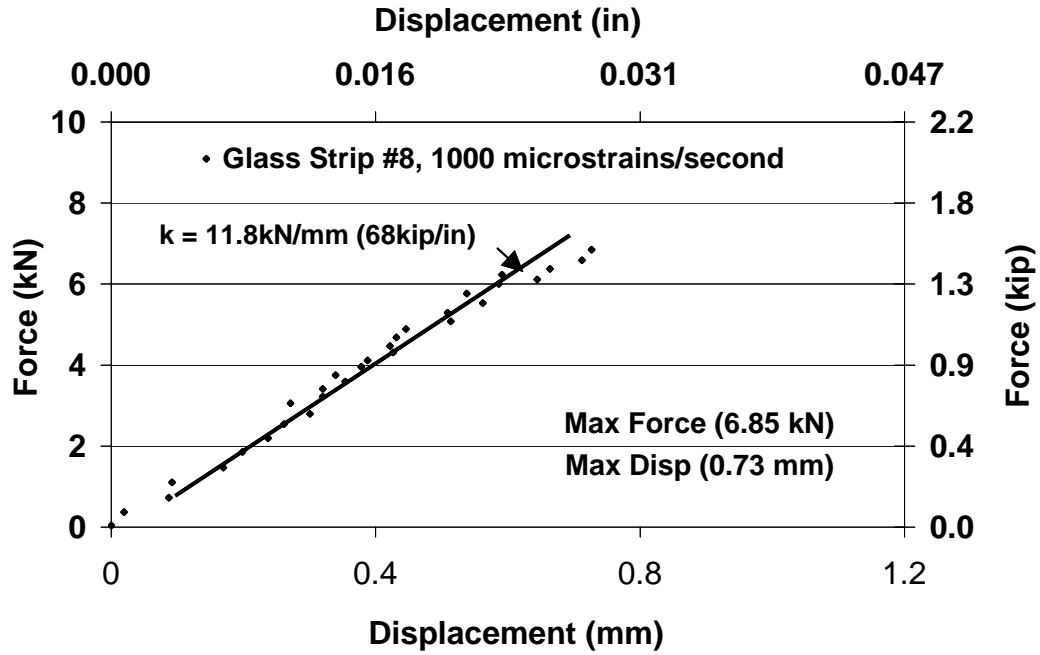


Figure 2-70: Force vs. Displacement, Elastomer Coated Glass Strip #8

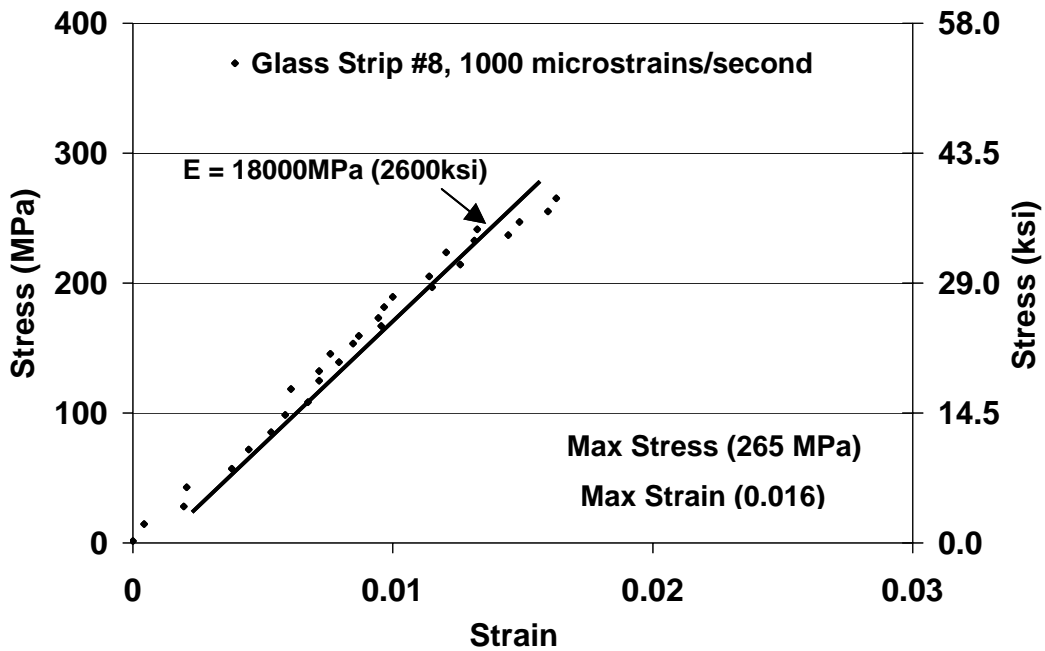


Figure 2-71: Stress vs. Strain, Elastomer Coated Glass Strip #8

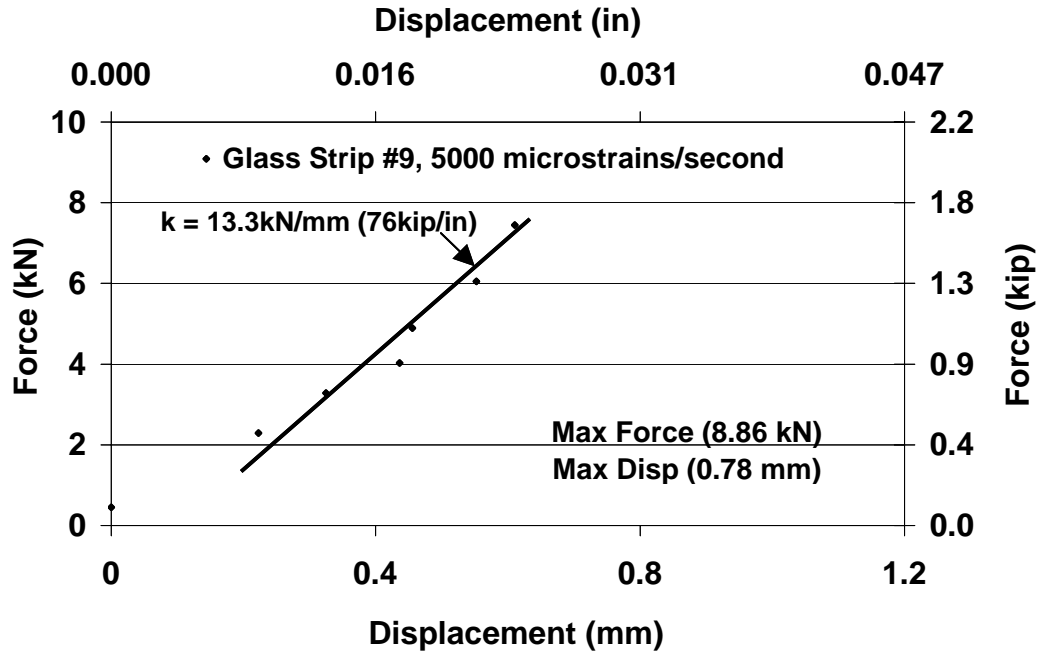


Figure 2-72: Force vs. Displacement, Elastomer Coated Glass Strip #9

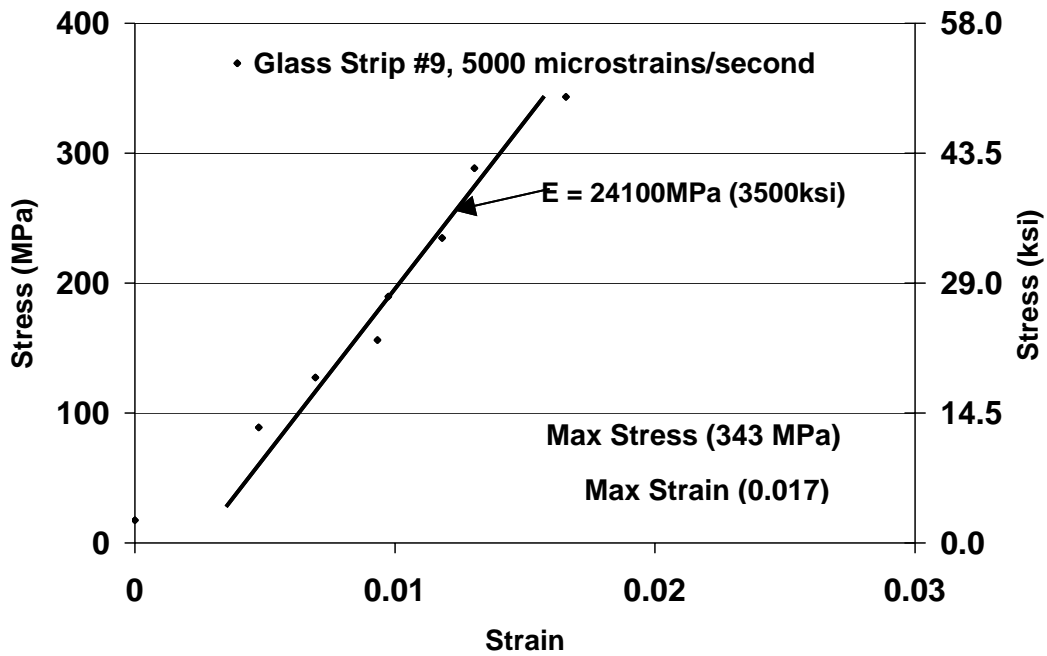


Figure 2-73: Stress vs. Strain, Elastomer Coated Glass Strip #9

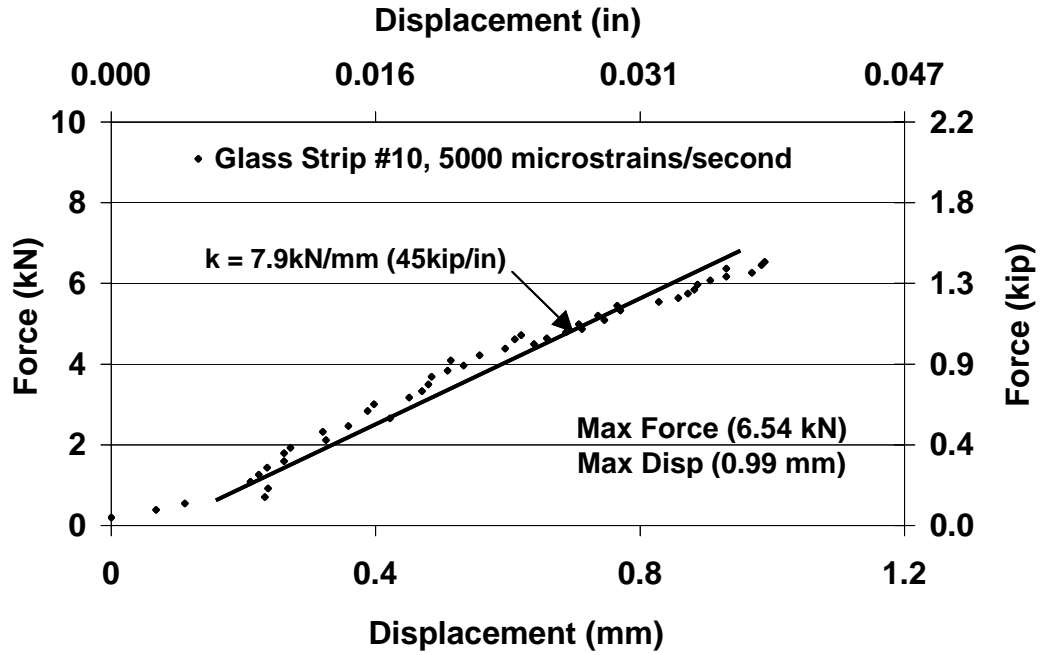


Figure 2-74: Force vs. Displacement, Elastomer Coated Glass Strip #10

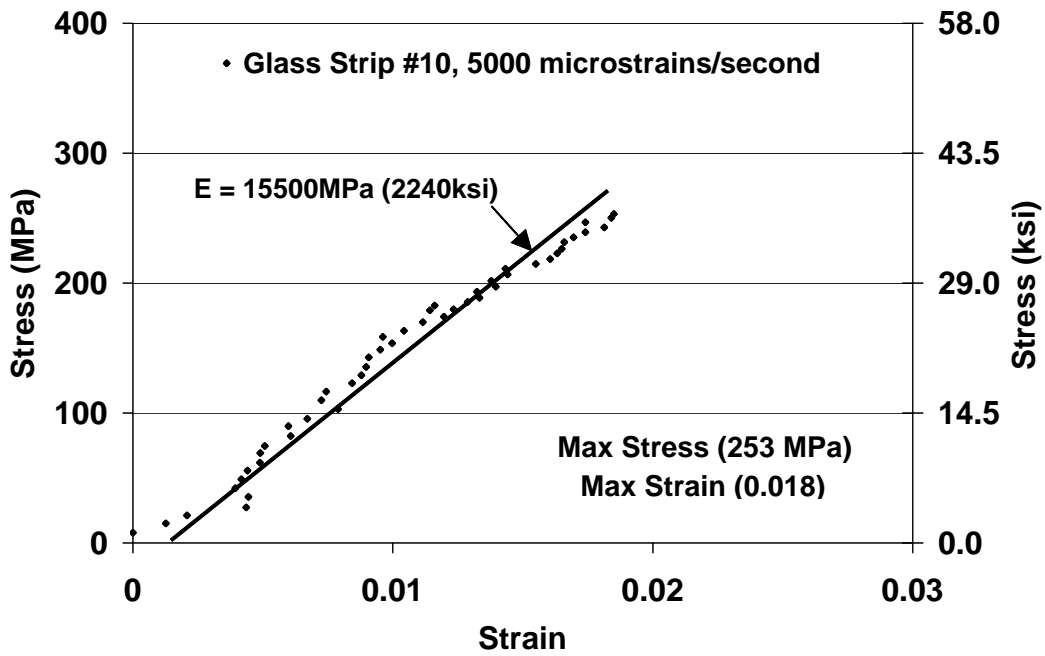


Figure 2-75: Stress vs. Strain, Elastomer Coated Glass Strip #10

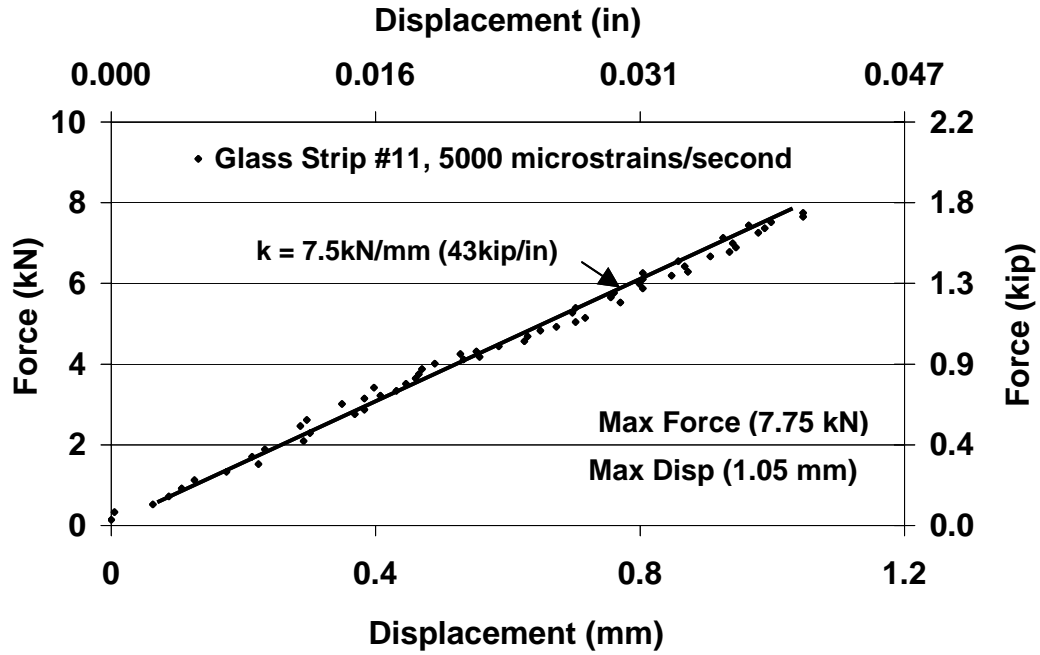


Figure 2-76: Force vs. Displacement, Elastomer Coated Glass Strip #11

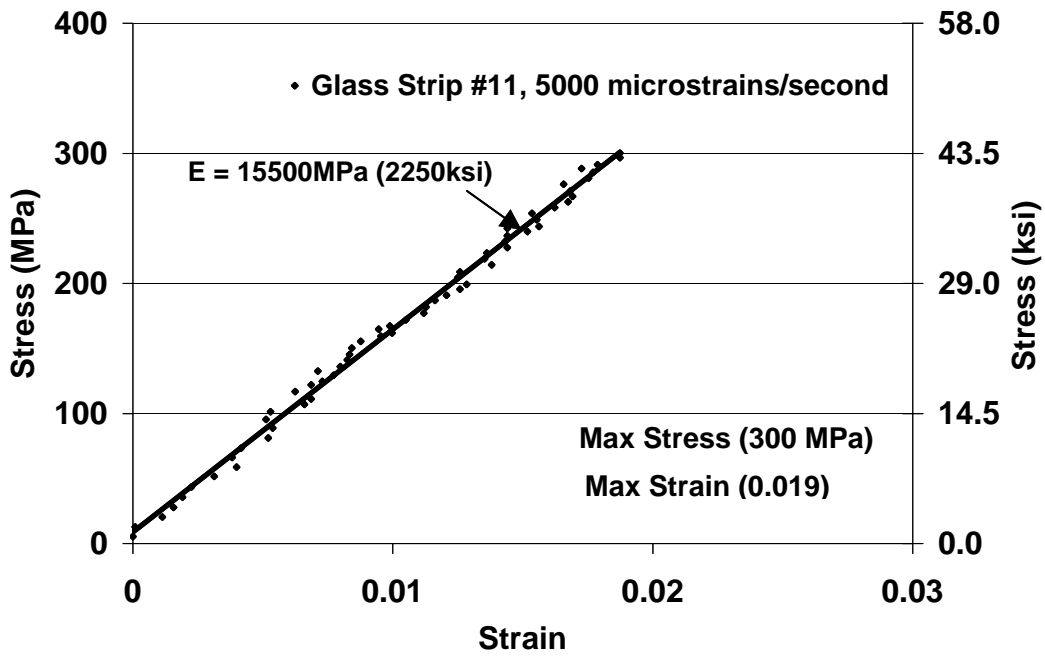


Figure 2-77: Stress vs. Strain, Elastomer Coated Glass Strip #11

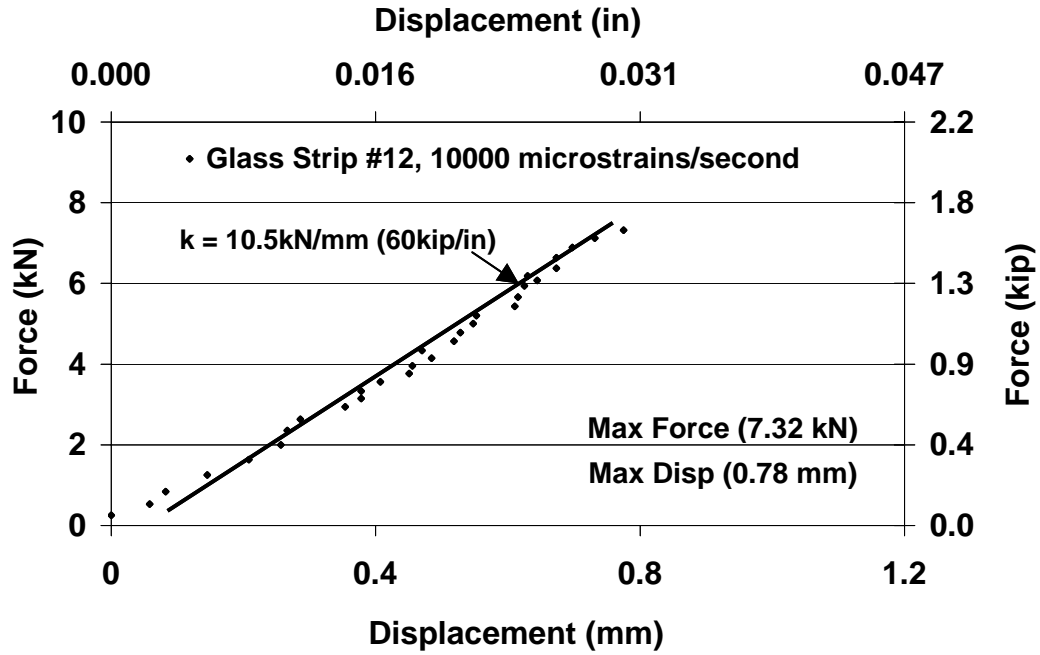


Figure 2-78: Force vs. Displacement, Elastomer Coated Glass Strip #12

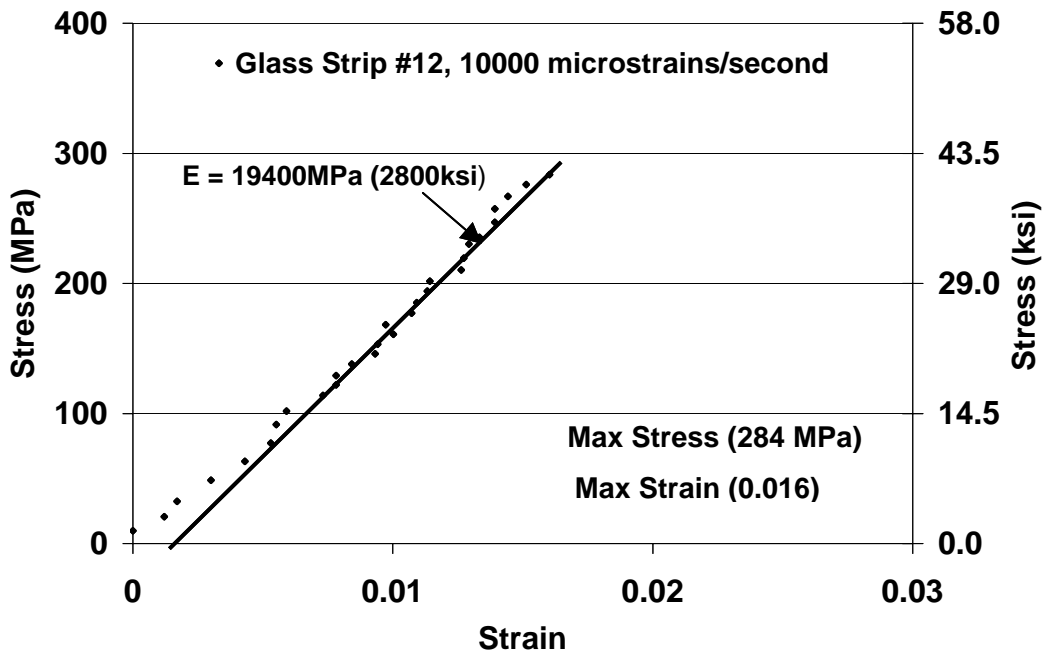


Figure 2-79: Stress vs. Strain, Elastomer Coated Glass Strip #12

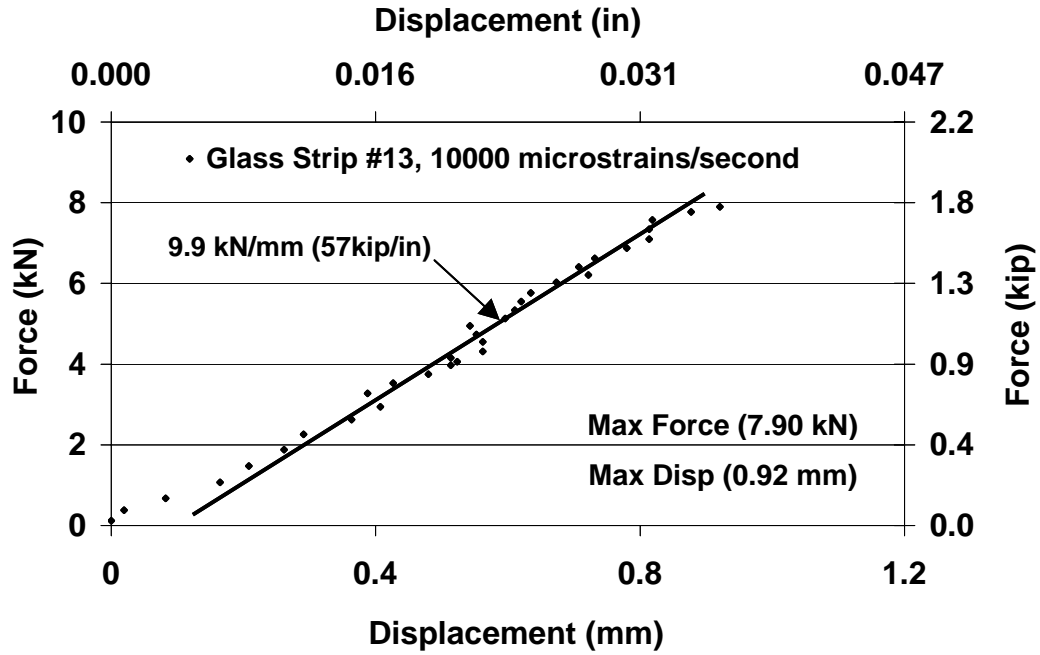


Figure 2-80: Force vs. Displacement, Elastomer Coated Glass Strip #13

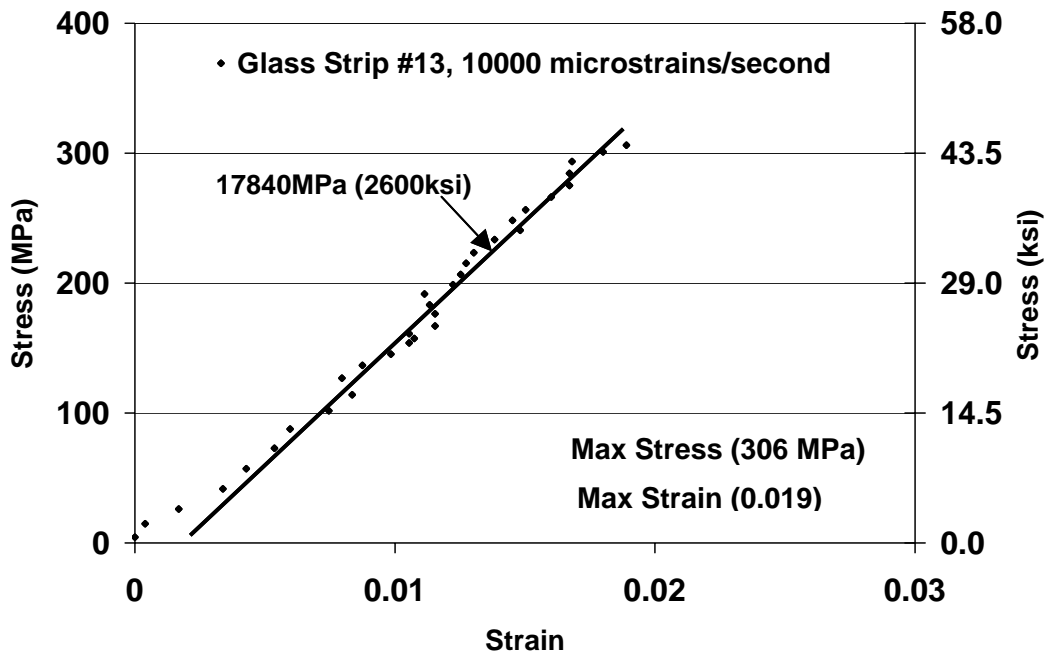


Figure 2-81: Stress vs. Strain, Elastomer Coated Glass Strip #13

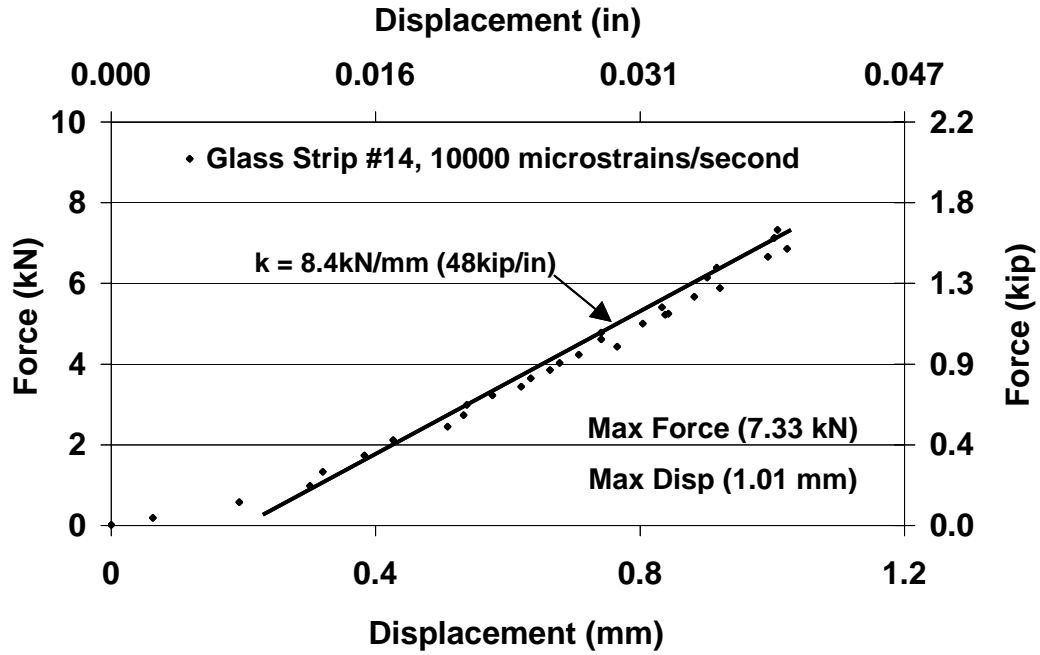


Figure 2-82: Force vs. Displacement, Elastomer Coated Glass Strip #14

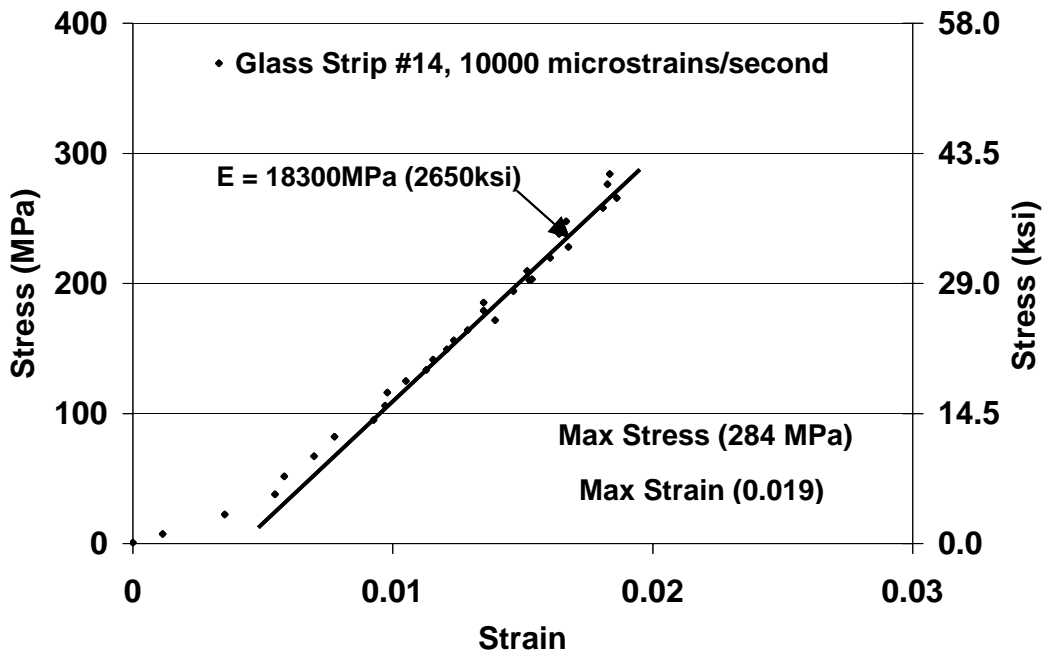


Figure 2-83: Stress vs. Strain, Elastomer Coated Glass Strip #14

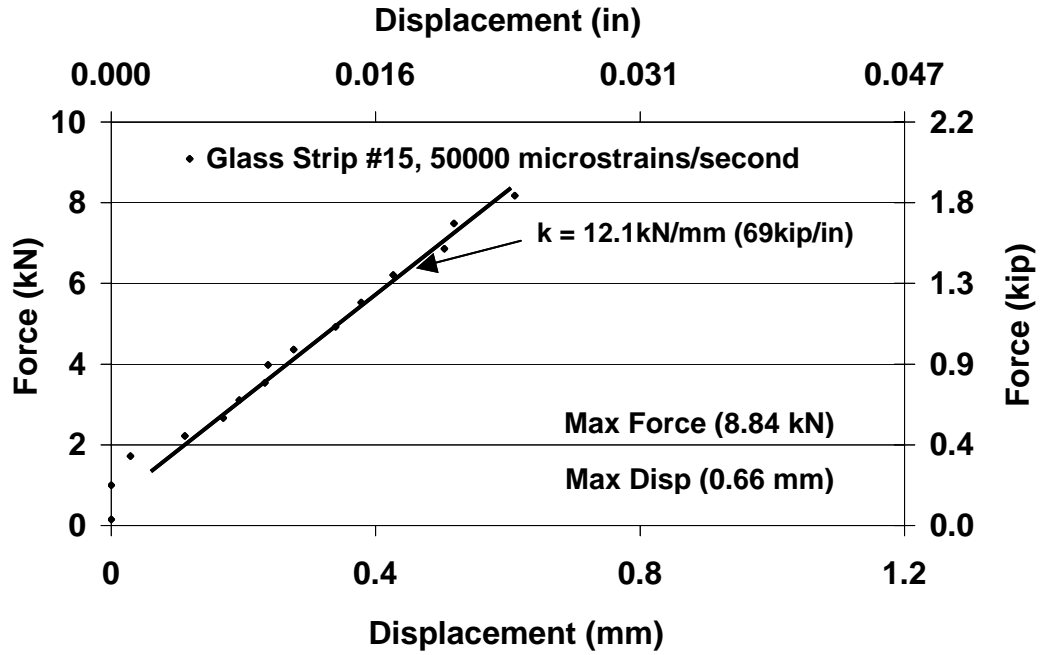


Figure 2-84: Force vs. Displacement, Elastomer Coated Glass Strip #15

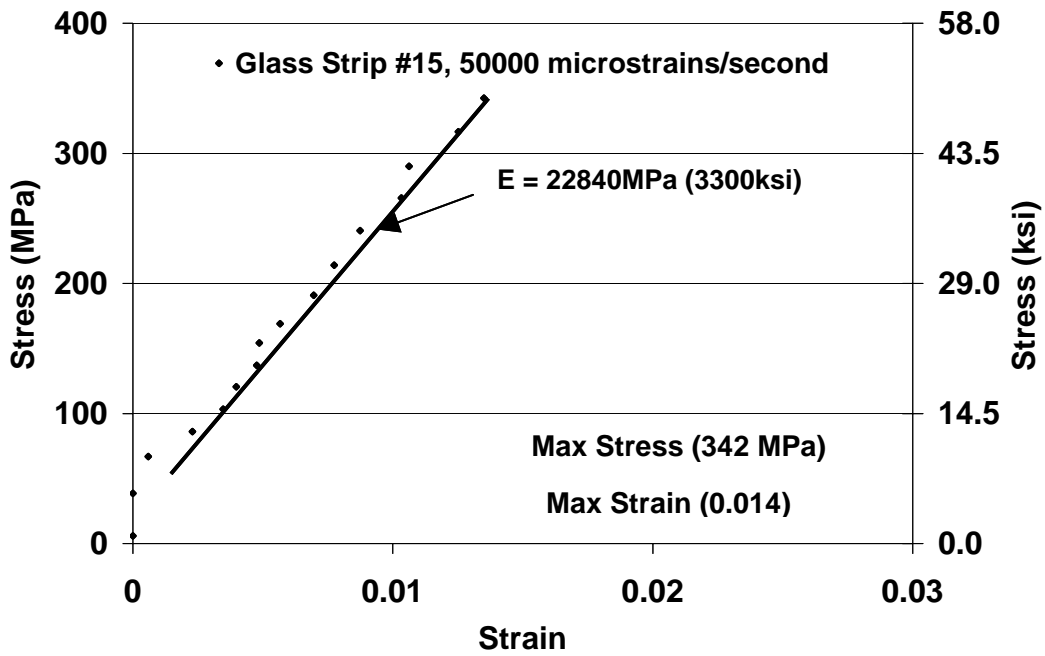


Figure 2-85: Stress vs. Strain, Elastomer Coated Glass Strip #15

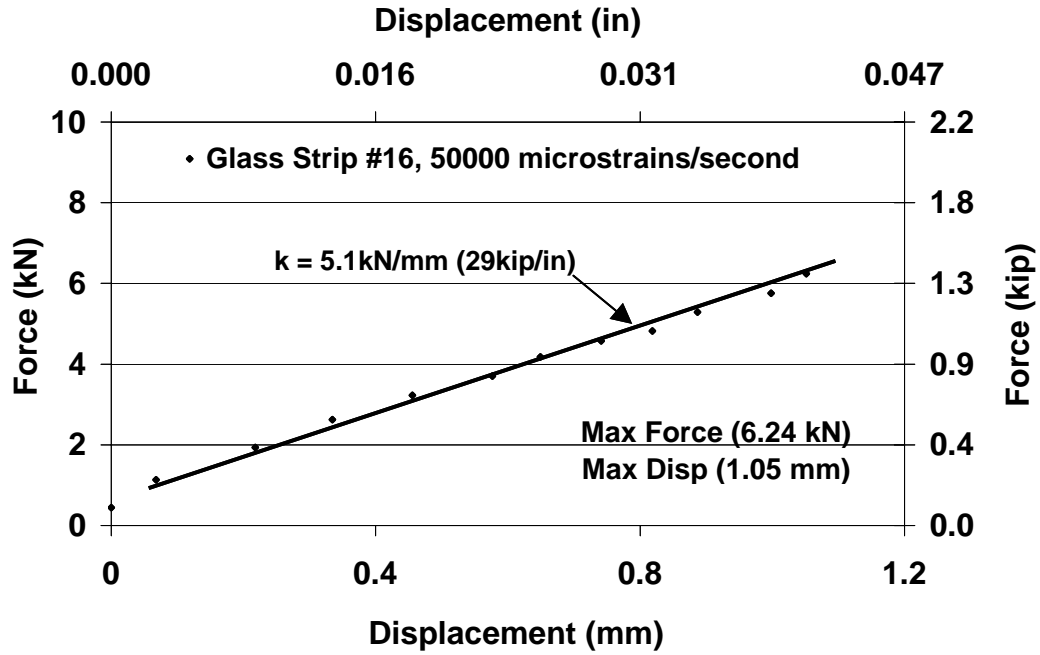


Figure 2-86: Force vs. Displacement, Elastomer Coated Glass Strip #16

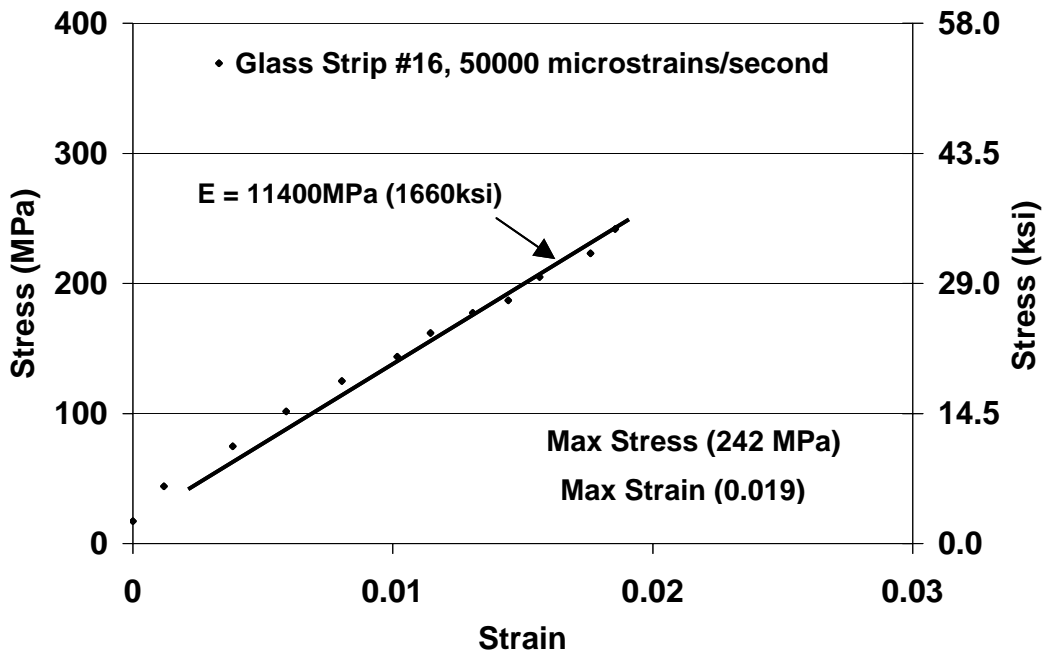


Figure 2-87: Stress vs. Strain, Elastomer Coated Glass Strip #16

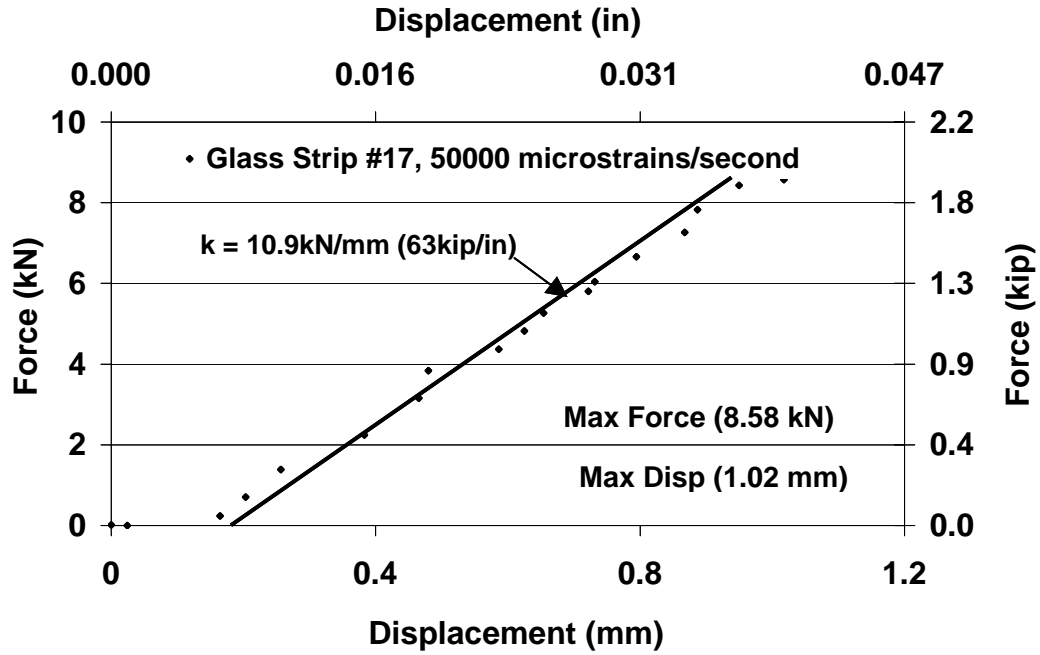


Figure 2-88: Force vs. Displacement, Elastomer Coated Glass Strip #17

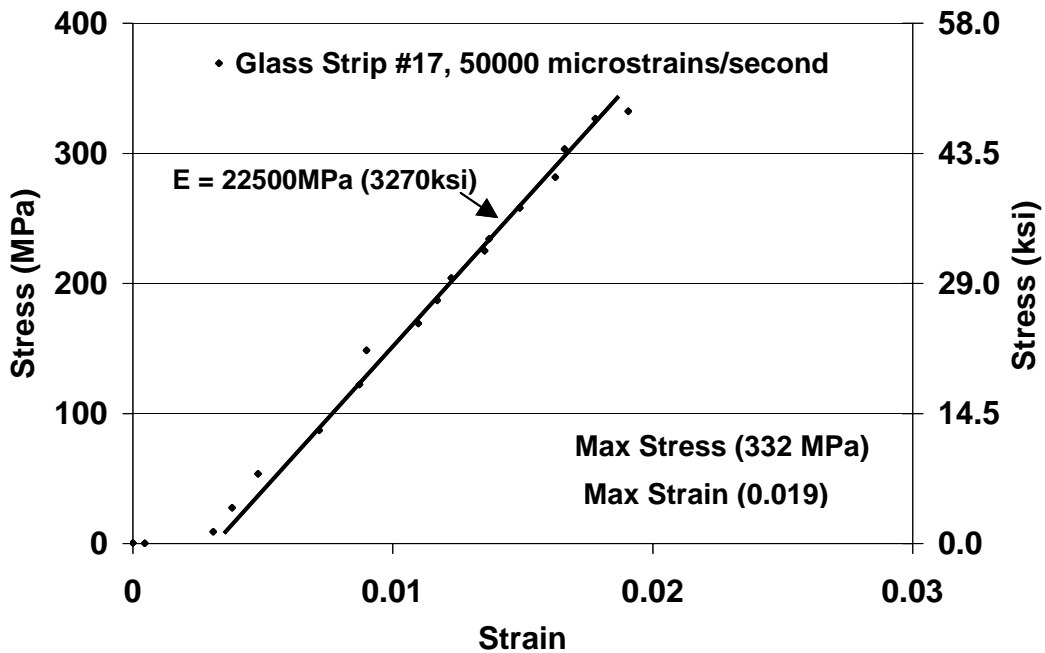


Figure 2-89: Stress vs. Strain, Elastomer Coated Glass Strip #17

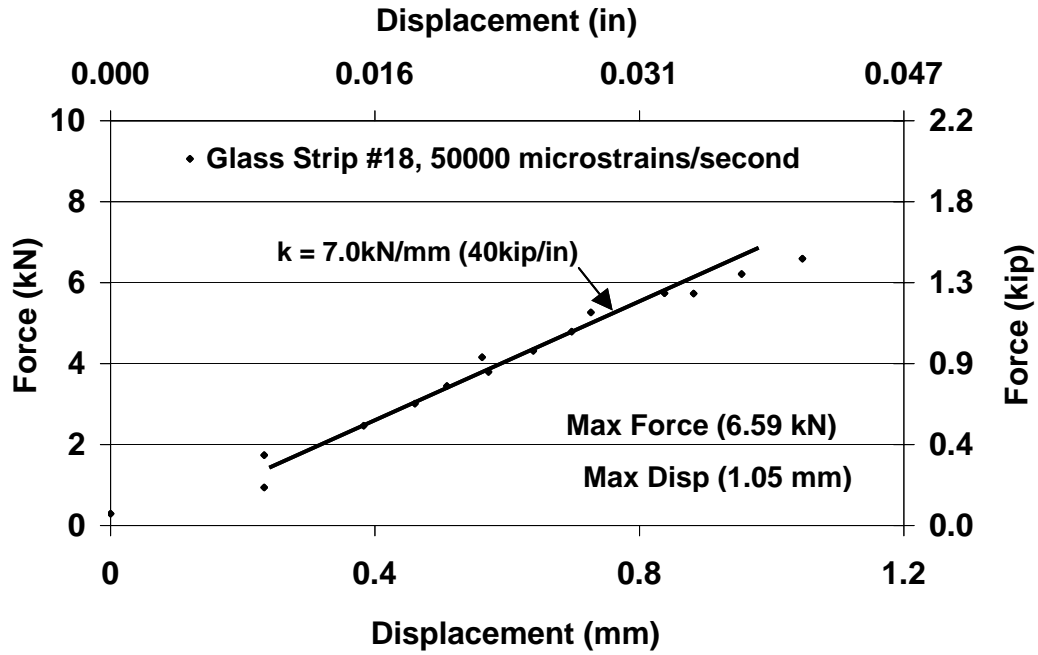


Figure 2-90: Force vs. Displacement, Elastomer Coated Glass Strip #18

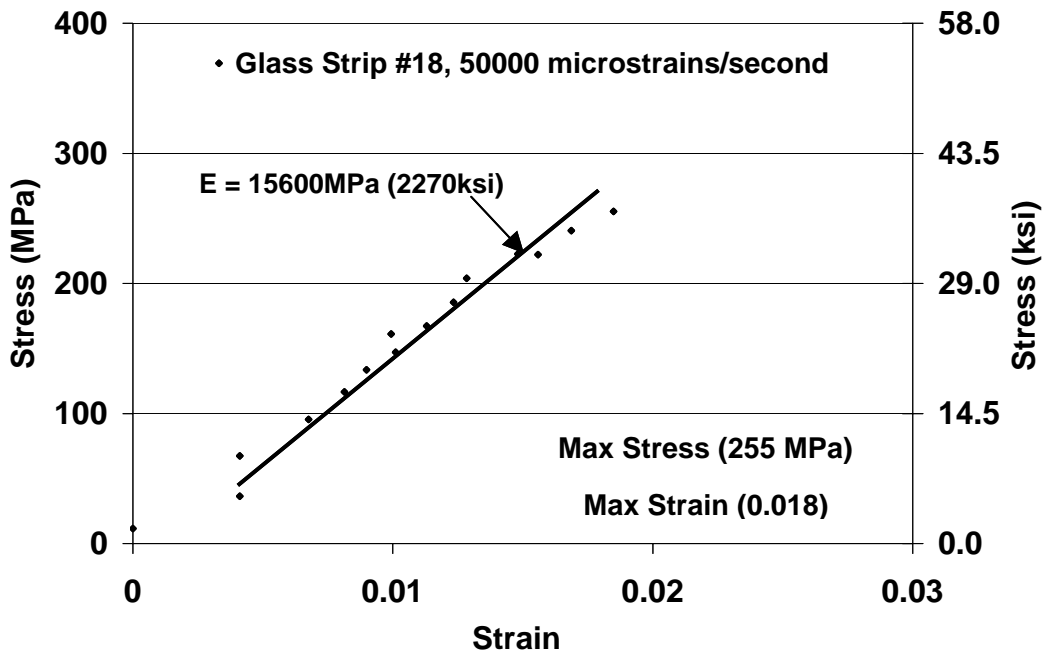


Figure 2-91: Stress vs. Strain, Elastomer Coated Glass Strip #18

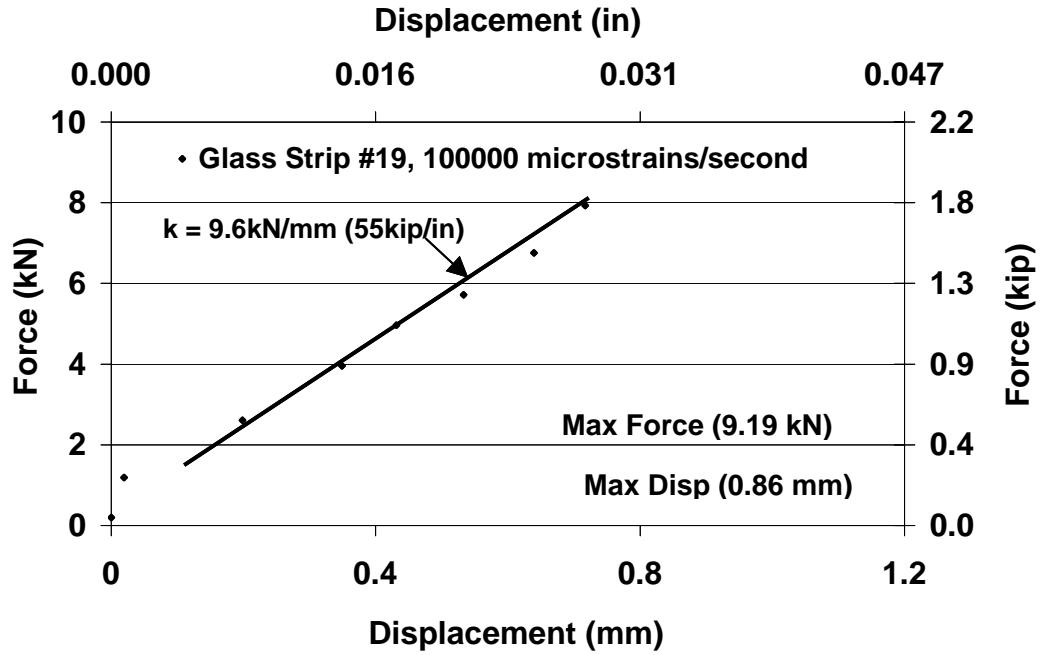


Figure 2-92: Force vs. Displacement, Elastomer Coated Glass Strip #19

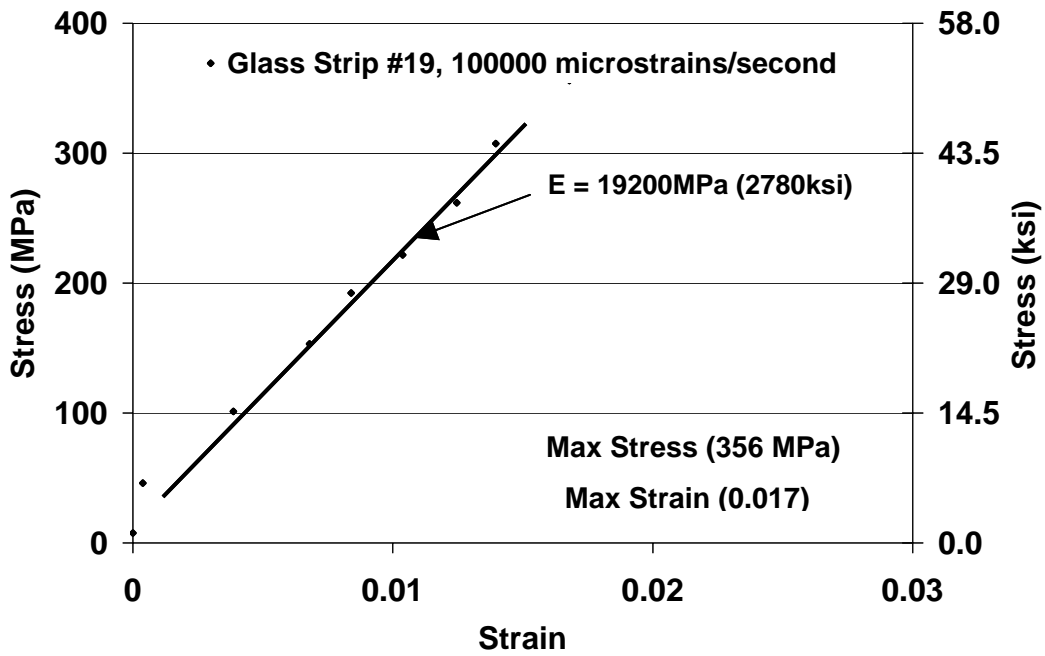


Figure 2-93: Stress vs. Strain, Elastomer Coated Glass Strip #19

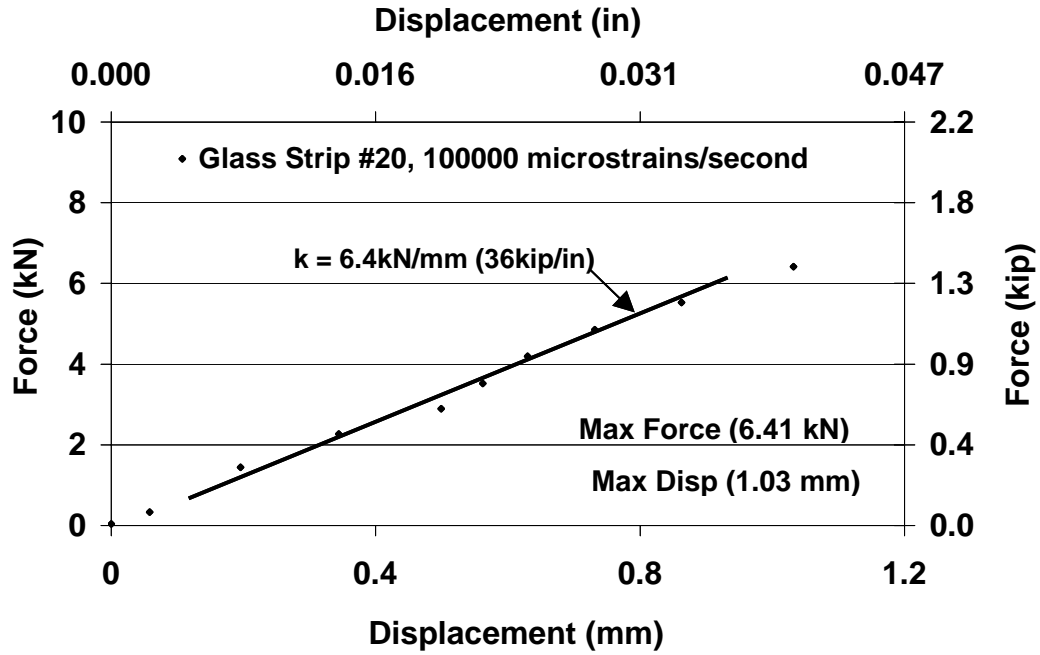


Figure 2-94: Force vs. Displacement, Elastomer Coated Glass Strip #20

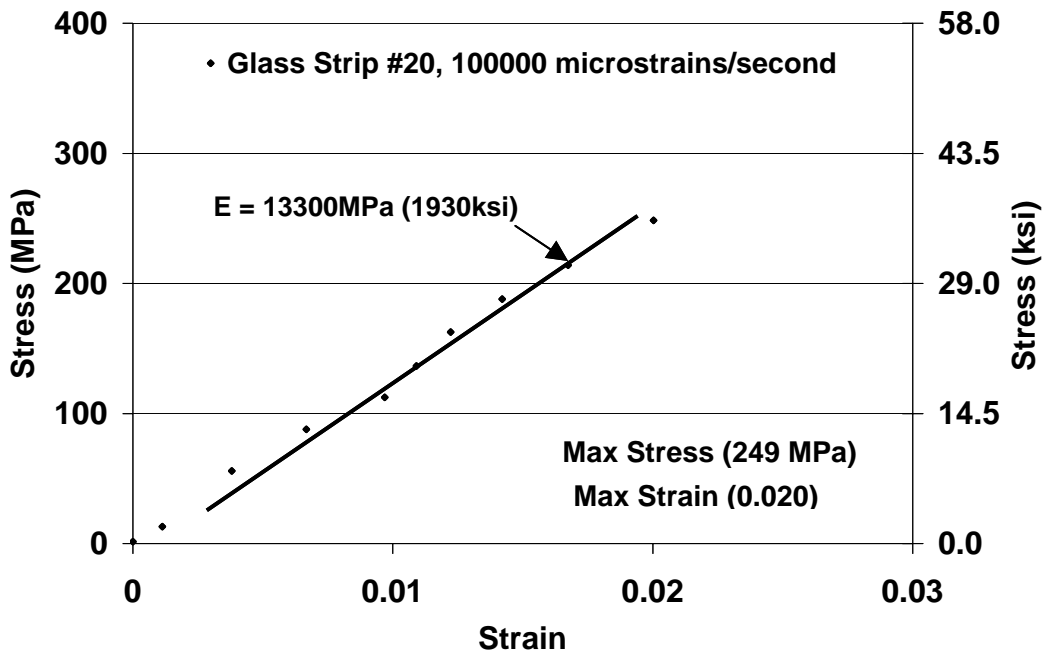


Figure 2-95: Stress vs. Strain, Elastomer Coated Glass Strip #20

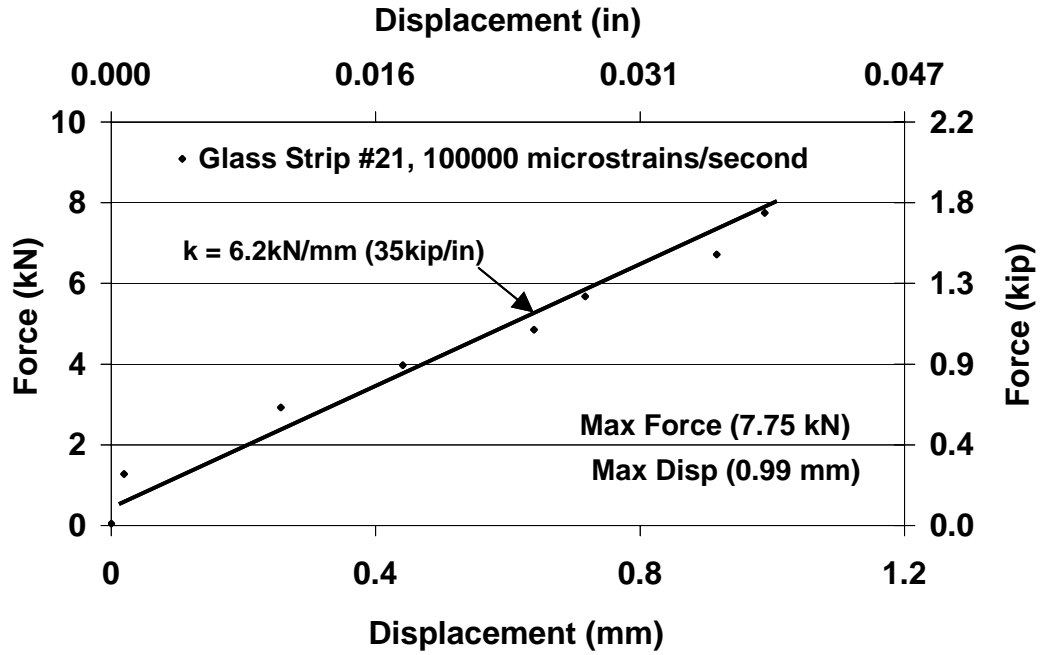


Figure 2-96: Force vs. Displacement, Elastomer Coated Glass Strip #21

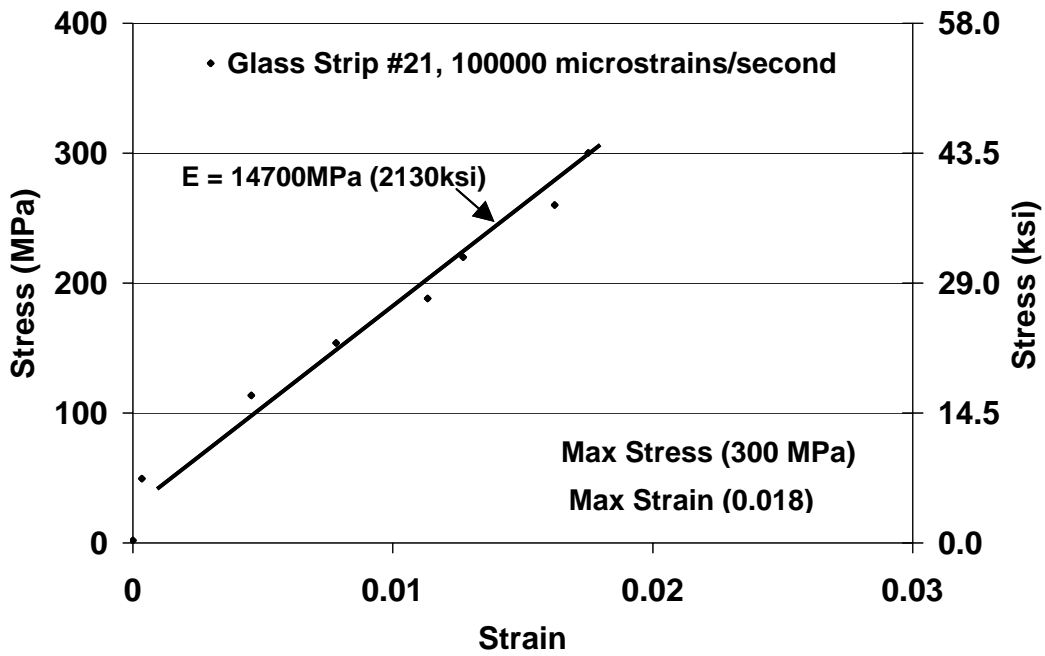


Figure 2-97: Stress vs. Strain, Elastomer Coated Glass Strip #21

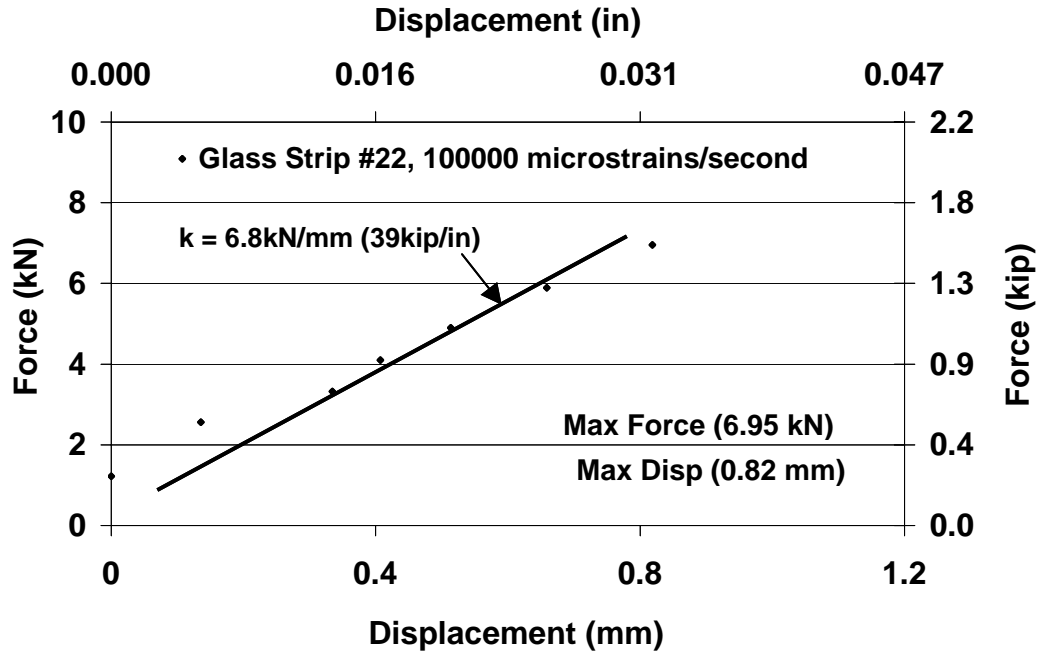


Figure 2-98: Force vs. Displacement, Elastomer Coated Glass Strip #22

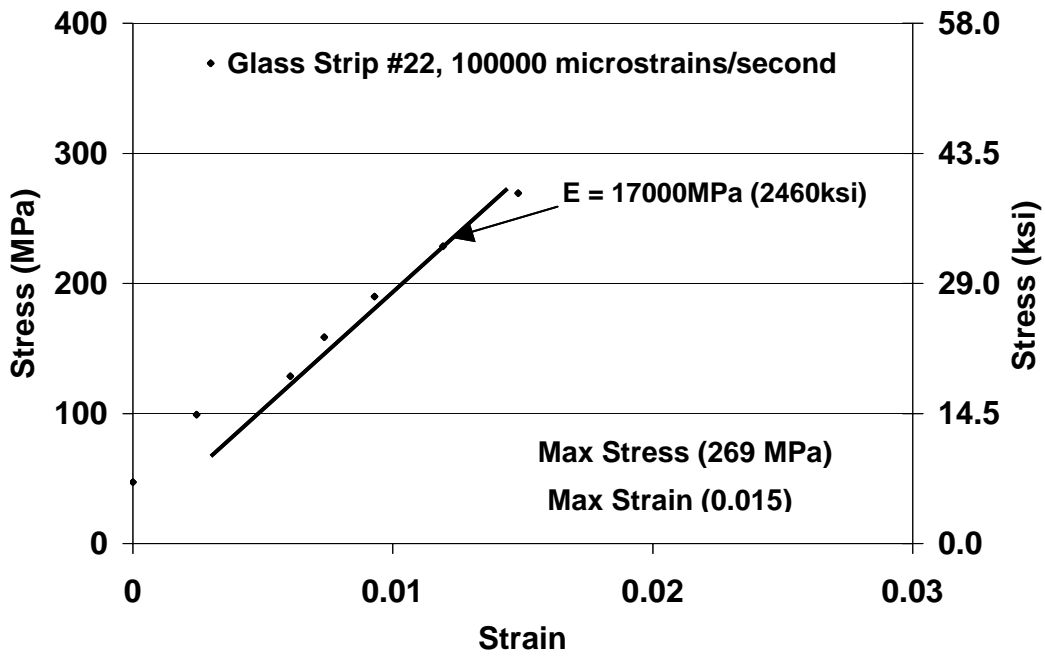


Figure 2-99: Stress vs. Strain, Elastomer Coated Glass Strip #22

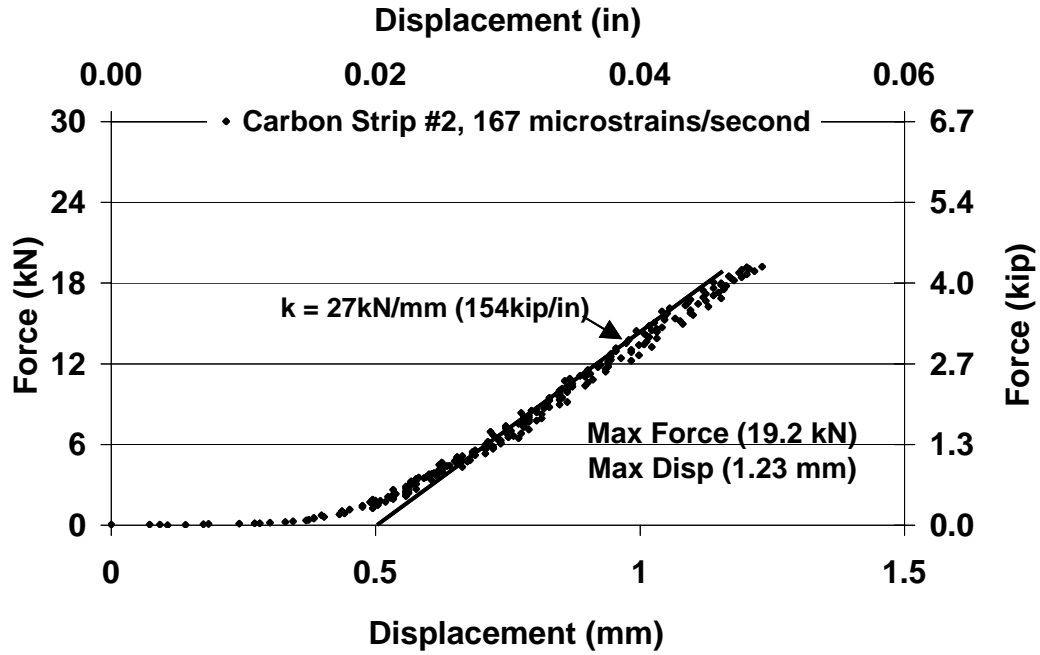


Figure 2-100: Force vs. Displacement, Elastomer Coated Carbon Strip #2

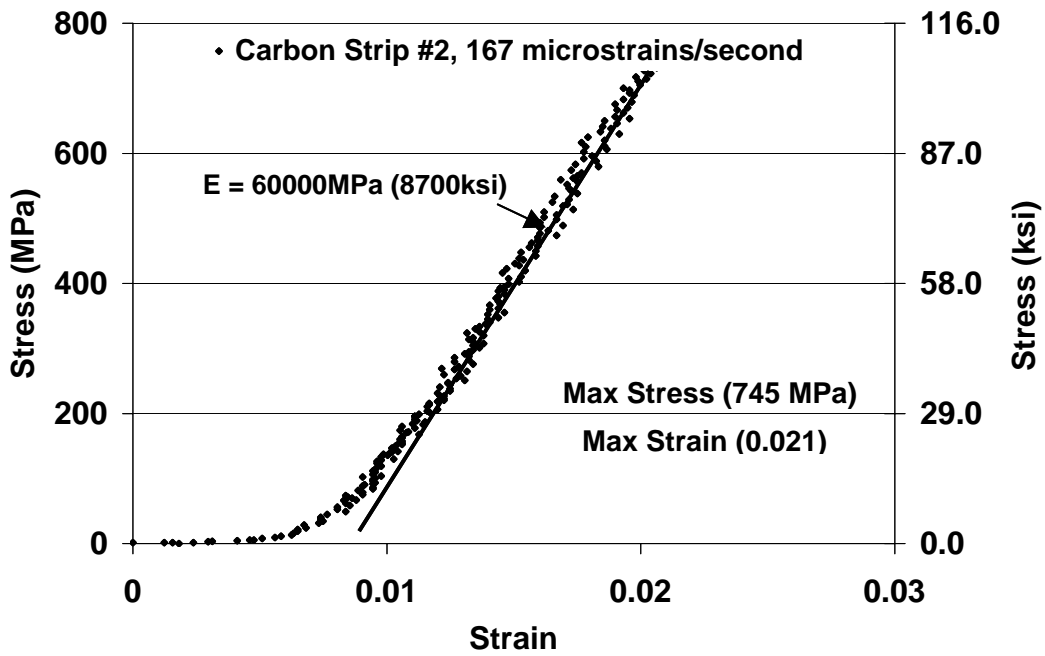


Figure 2-101: Stress vs. Strain, Elastomer Coated Carbon Strip #2

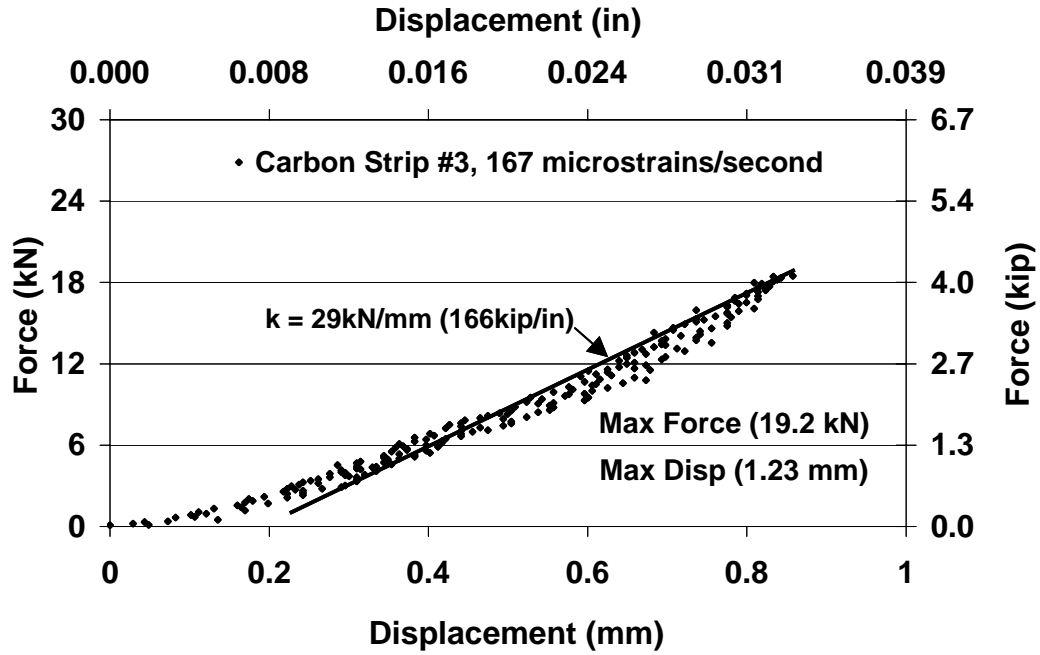


Figure 2-102: Force vs. Displacement, Elastomer Coated Carbon Strip #3

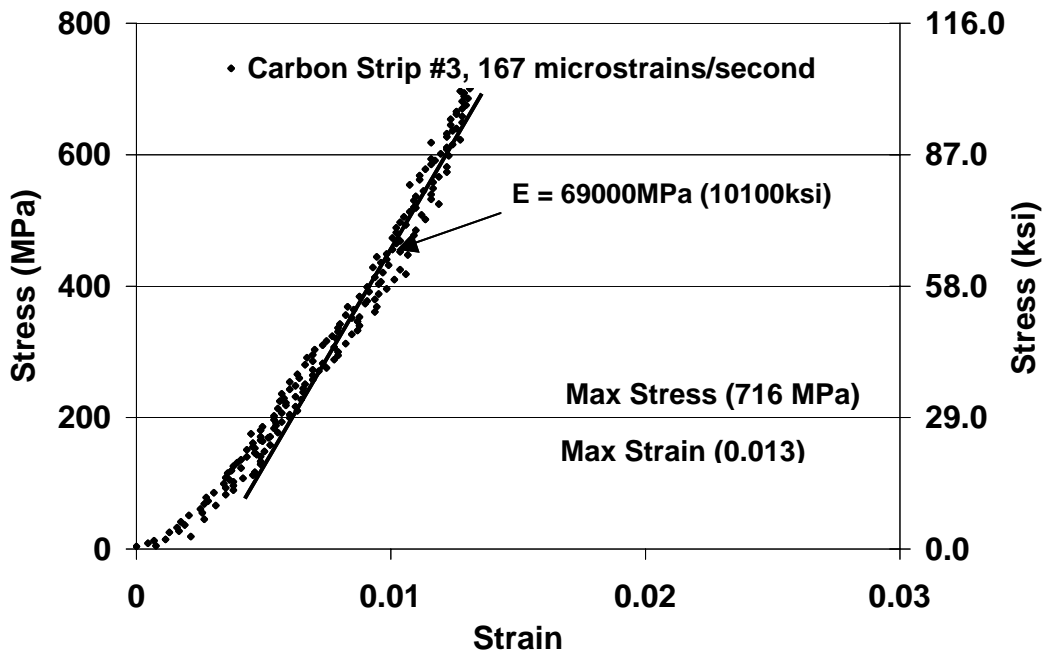


Figure 2-103: Stress vs. Strain, Elastomer Coated Carbon Strip #3

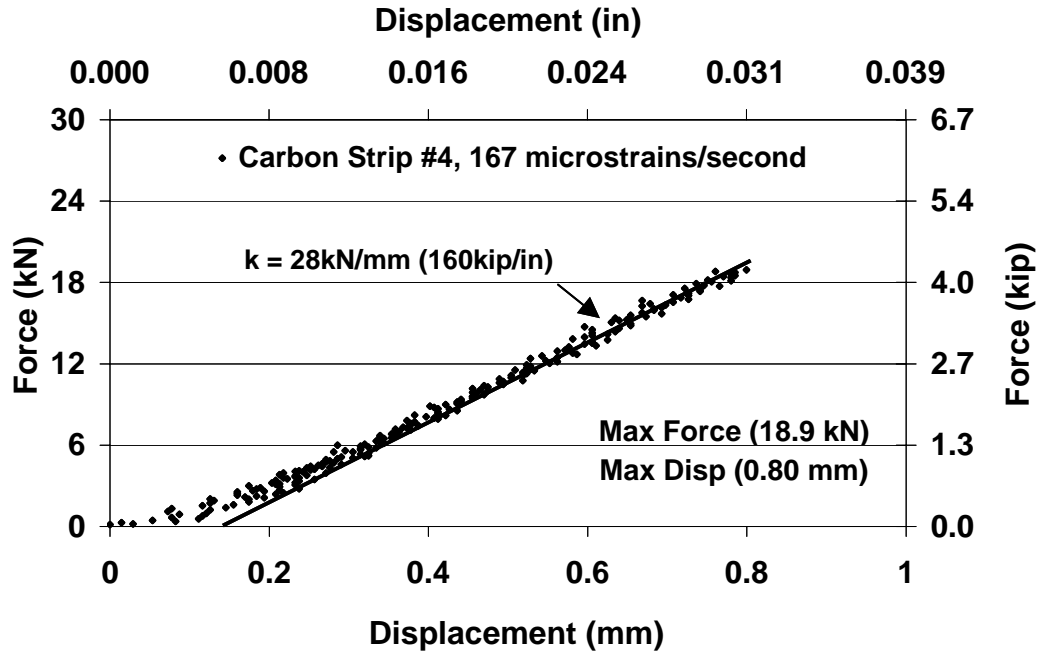


Figure 2-104: Force vs. Displacement, Elastomer Coated Carbon Strip #4

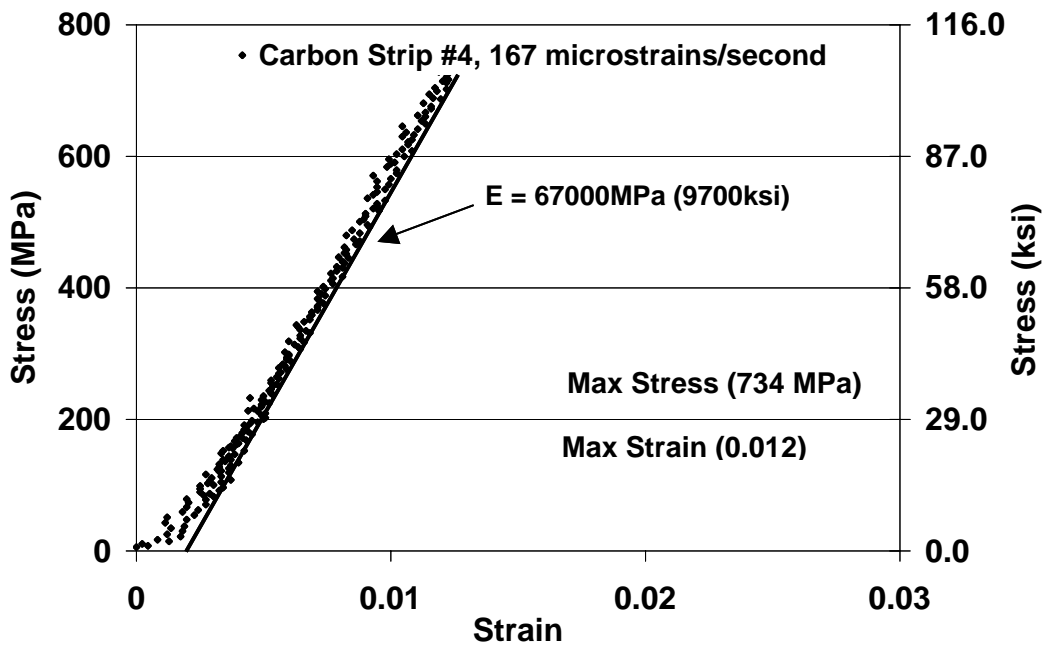


Figure 2-105: Stress vs. Strain, Elastomer Coated Carbon Strip #4

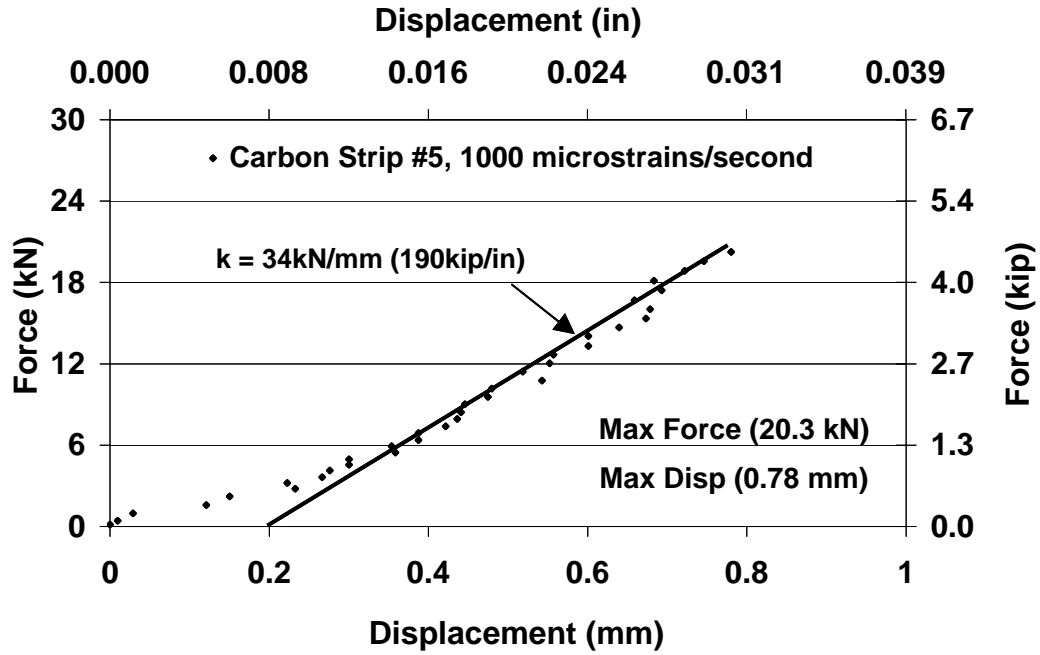


Figure 2-106: Force vs. Displacement, Elastomer Coated Carbon Strip #5

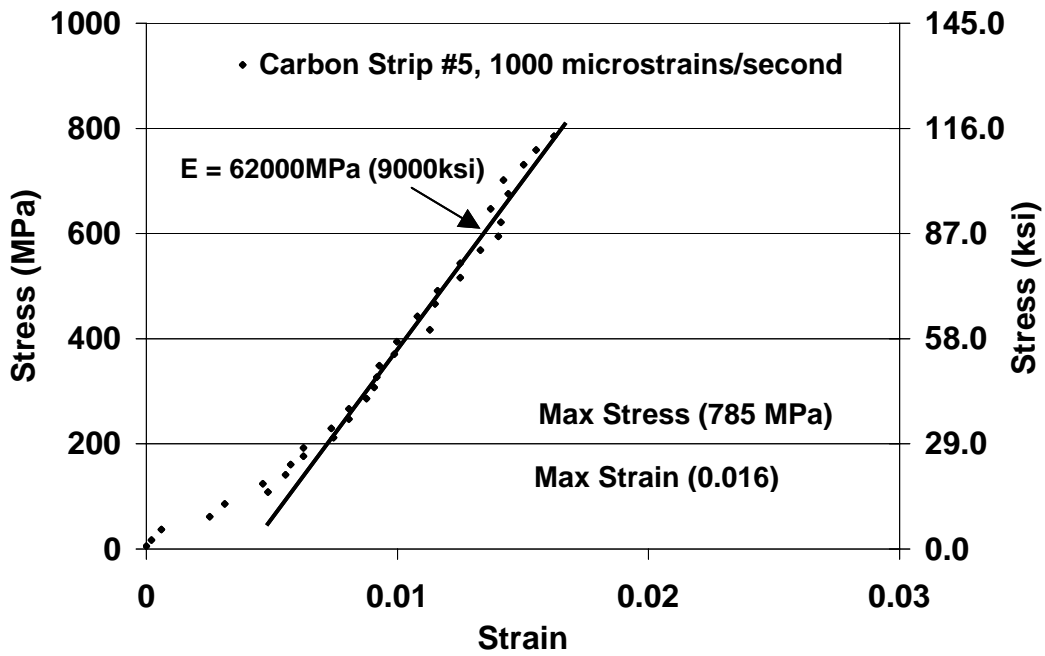


Figure 2-107: Stress vs. Strain, Elastomer Coated Carbon Strip #5

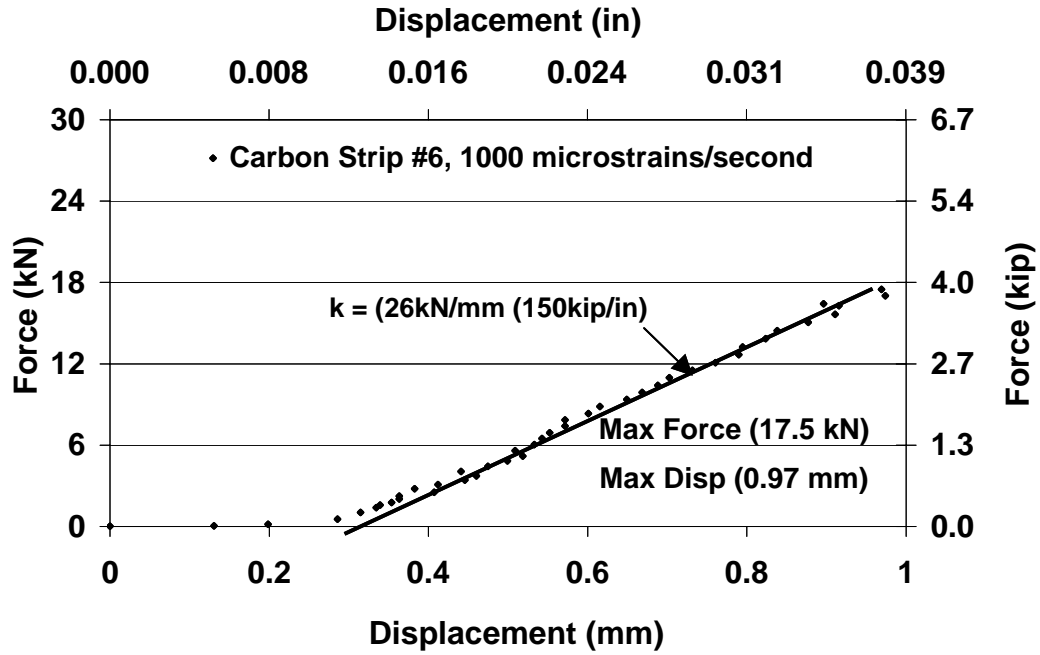


Figure 2-108: Force vs. Displacement, Elastomer Coated Carbon Strip #6

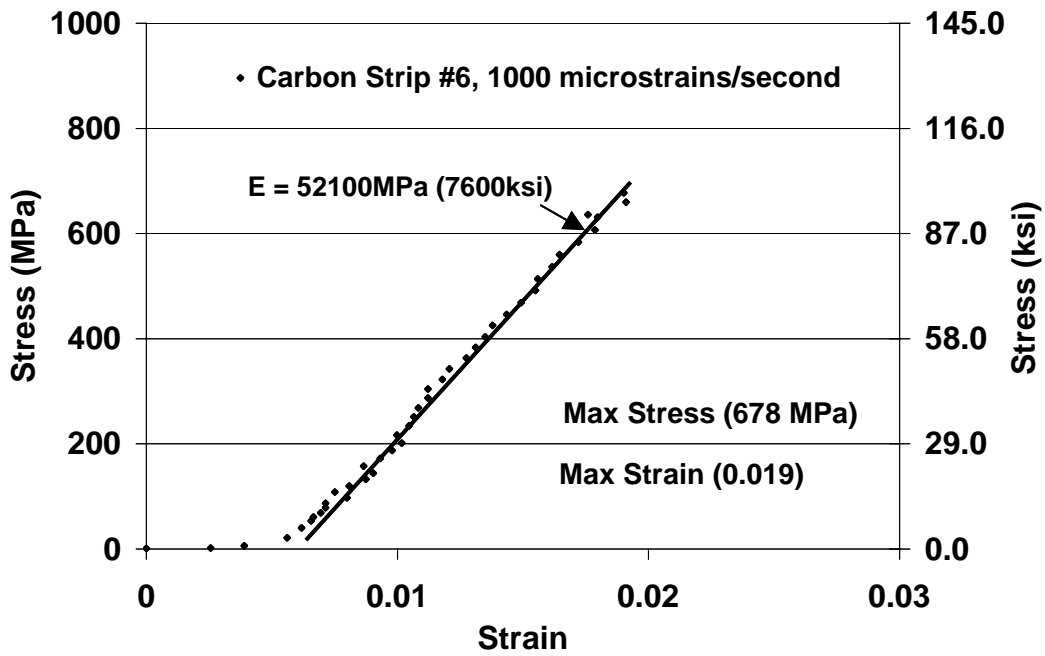


Figure 2-109: Stress vs. Strain, Elastomer Coated Carbon Strip #6

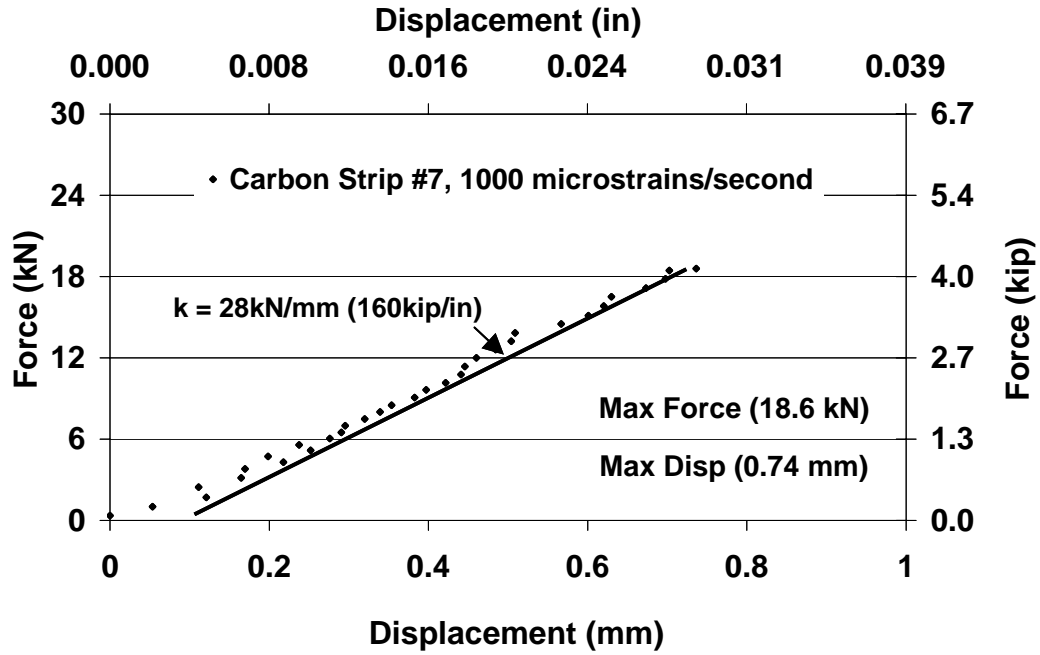


Figure 2-110: Force vs. Displacement, Elastomer Coated Carbon Strip #7

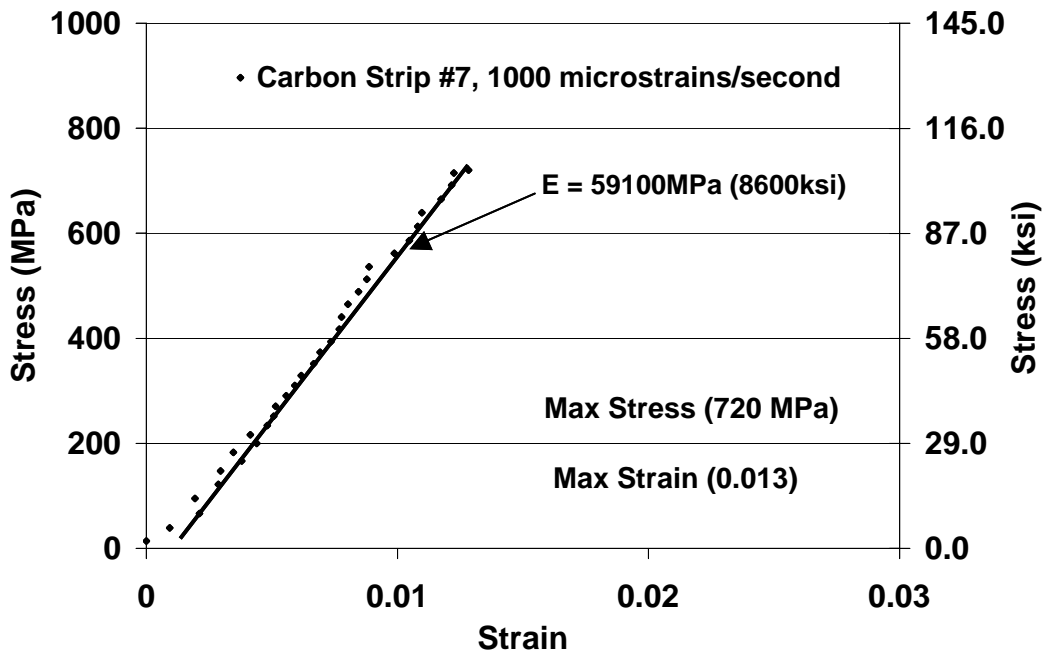


Figure 2-111: Stress vs. Strain, Elastomer Coated Carbon Strip #7

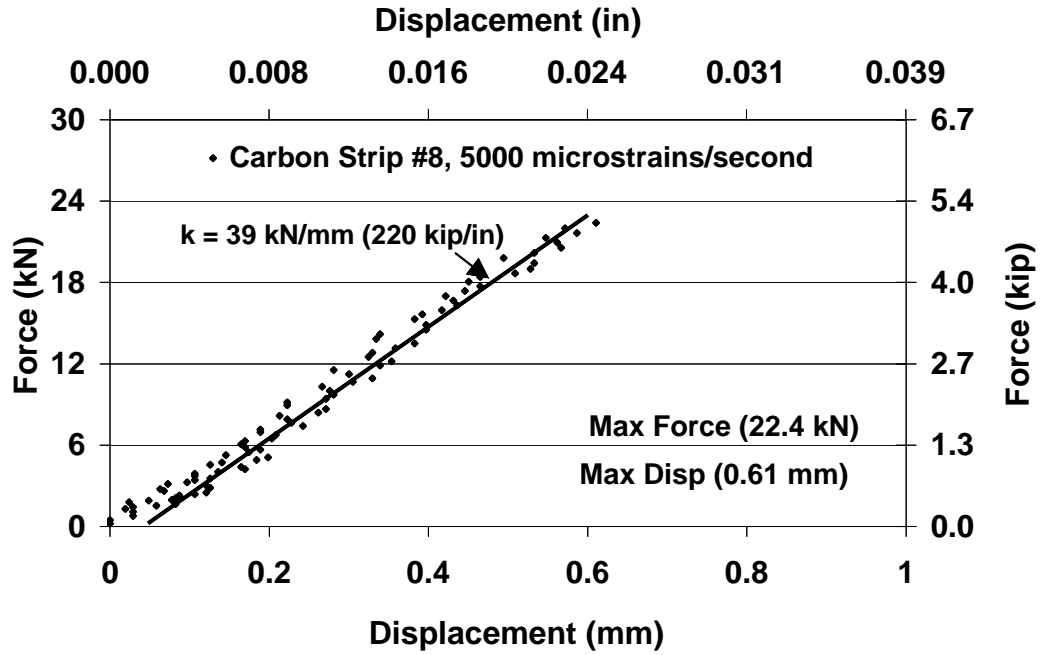


Figure 2-112: Force vs. Displacement, Elastomer Coated Carbon Strip #8

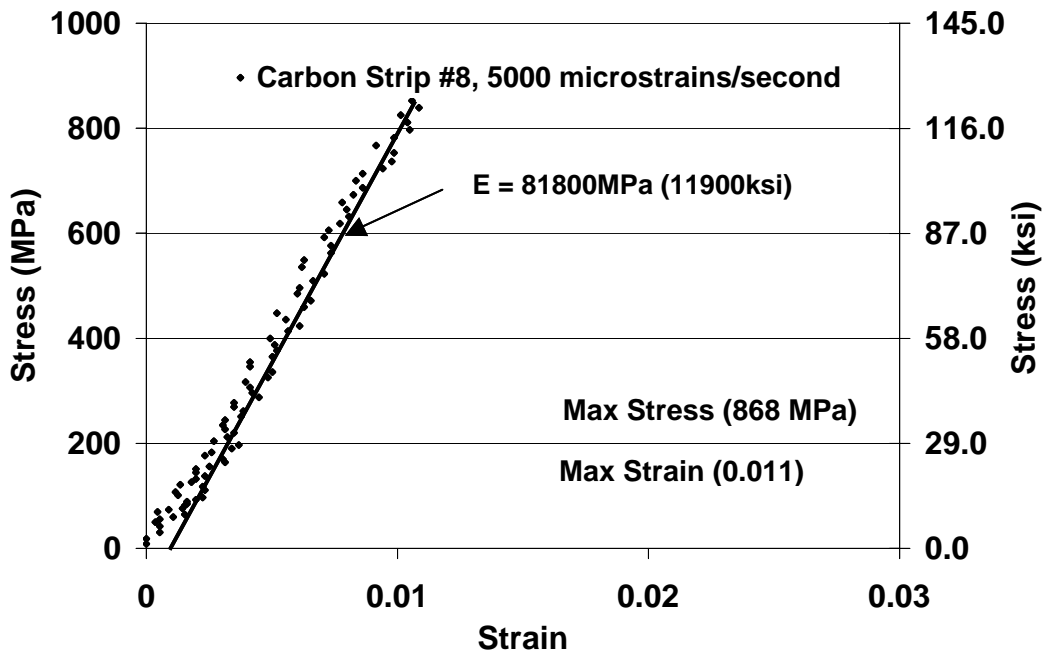


Figure 2-113: Stress vs. Strain, Elastomer Coated Carbon Strip #8

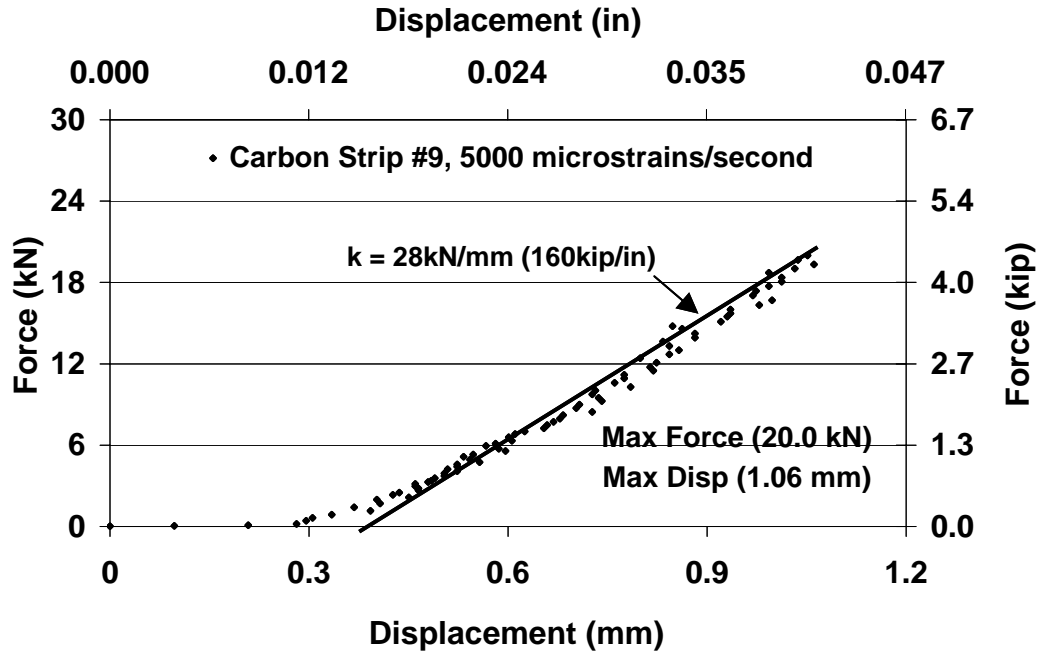


Figure 2-114: Force vs. Displacement, Elastomer Coated Carbon Strip #9

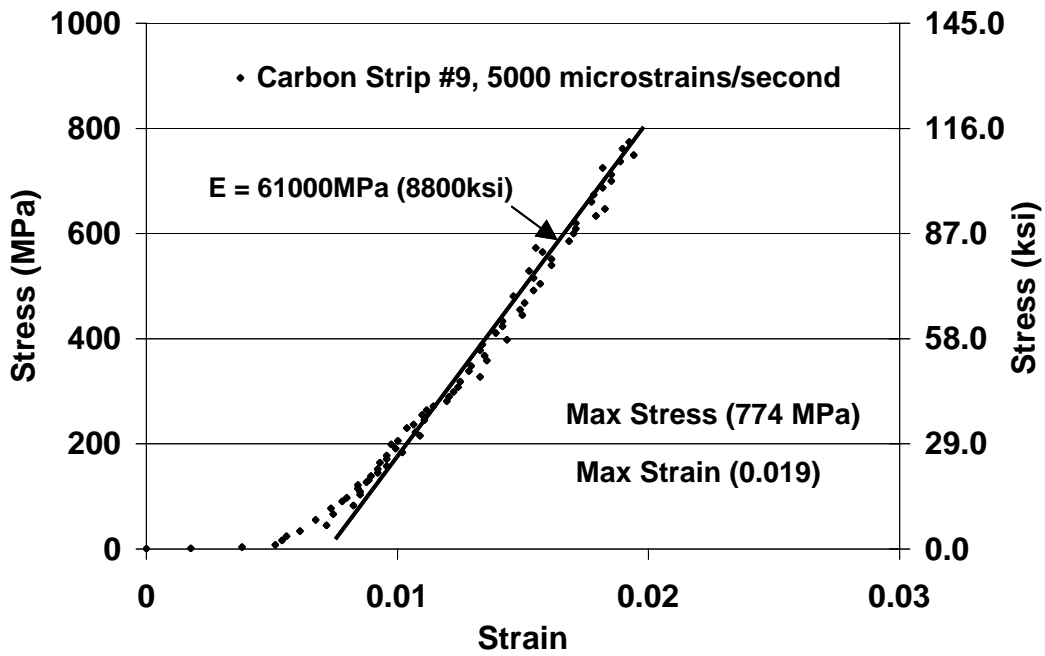


Figure 2-115: Stress vs. Strain, Elastomer Coated Carbon Strip #9

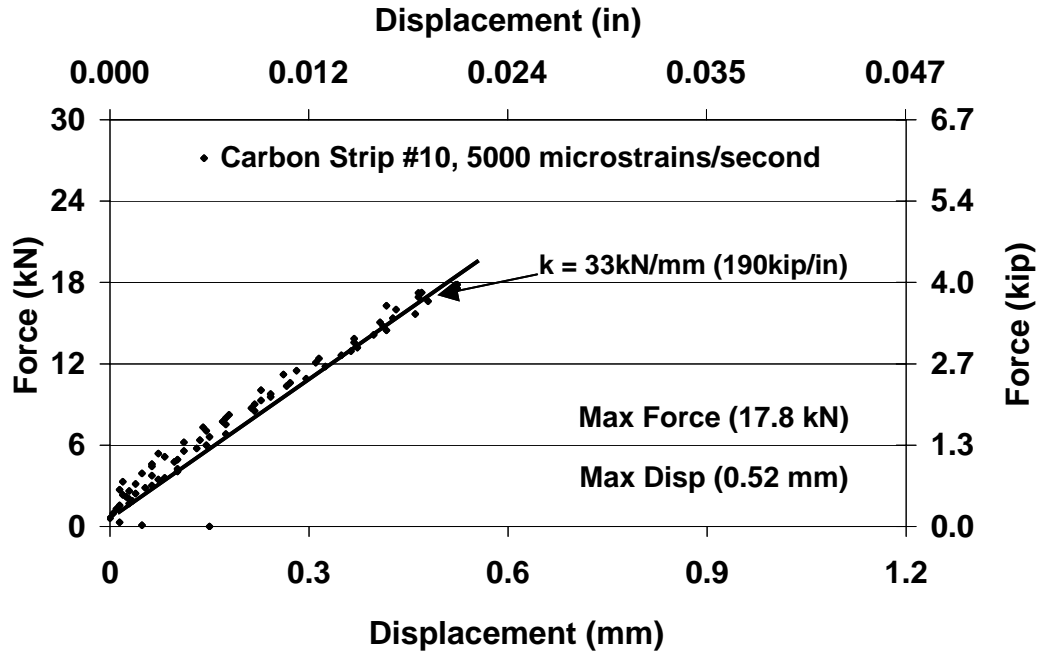


Figure 2-116: Force vs. Displacement, Elastomer Coated Carbon Strip #10

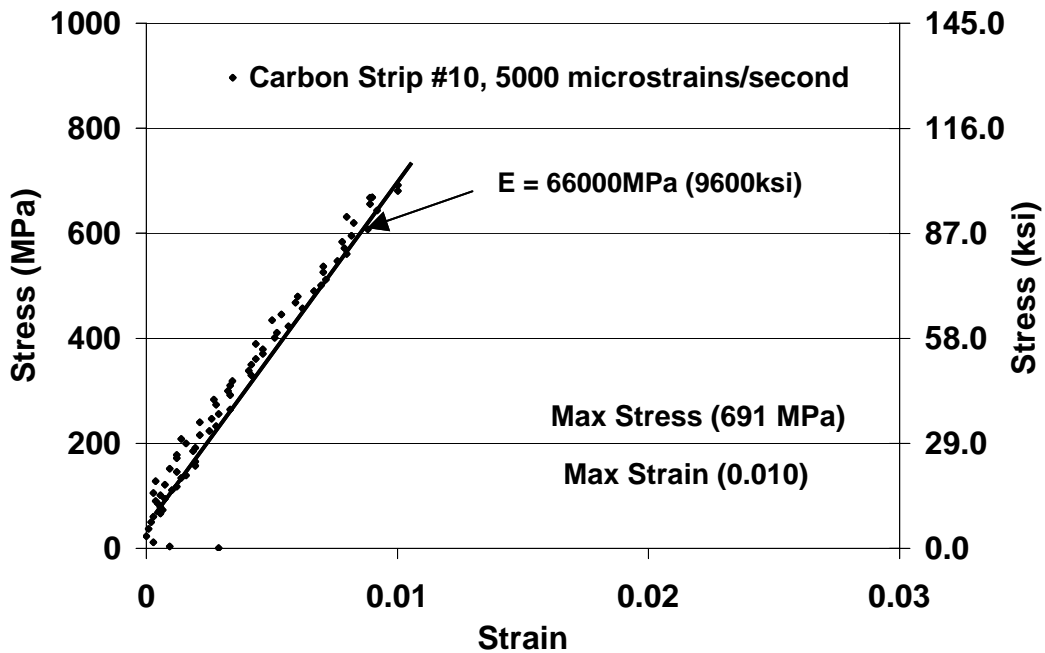


Figure 2-117: Stress vs. Strain, Elastomer Coated Carbon Strip #10

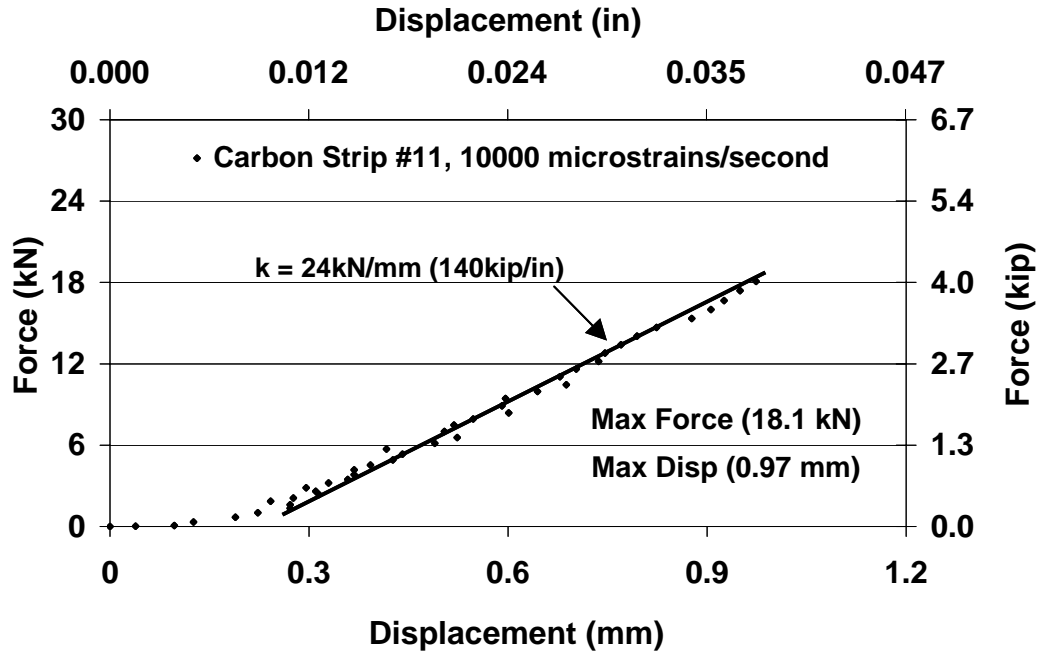


Figure 2-118: Force vs. Displacement, Elastomer Coated Carbon Strip #11

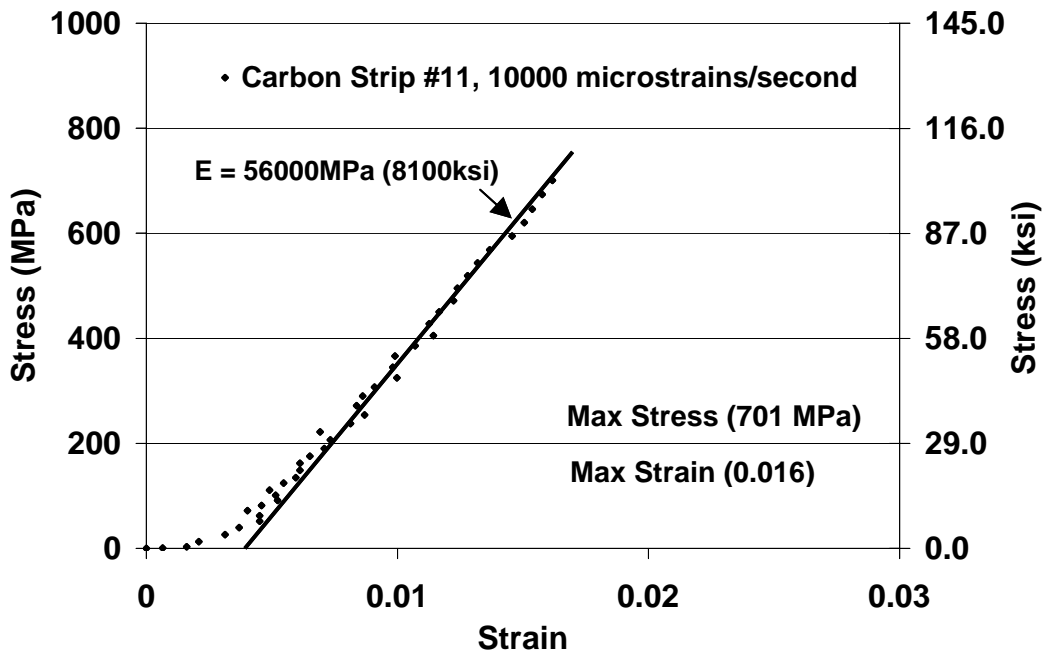


Figure 2-119: Stress vs. Strain, Elastomer Coated Carbon Strip #11

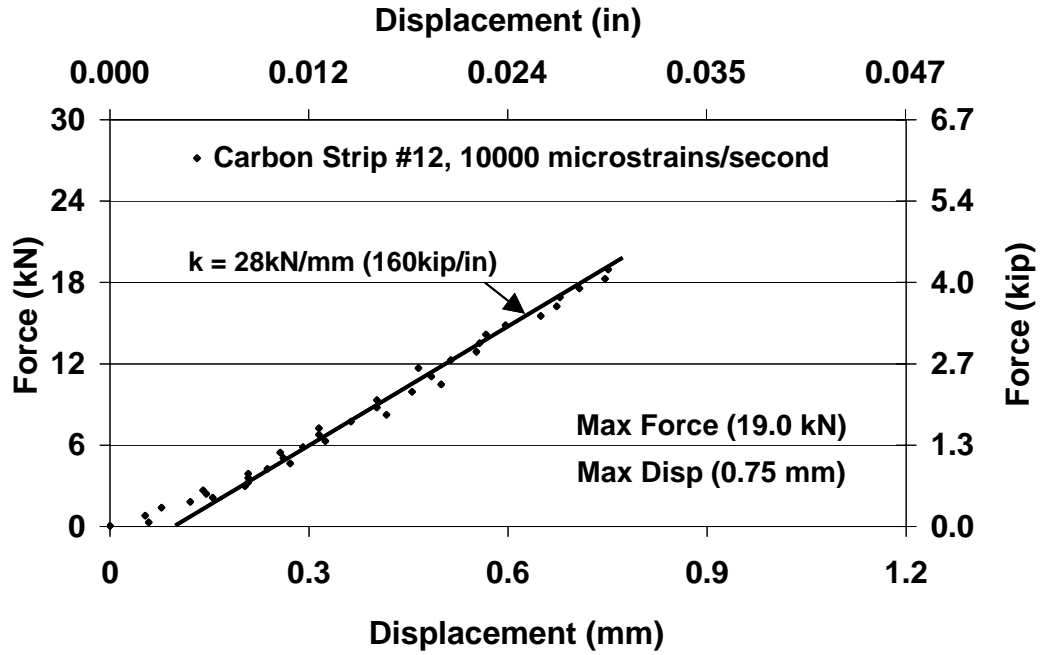


Figure 2-120: Force vs. Displacement, Elastomer Coated Carbon Strip #12

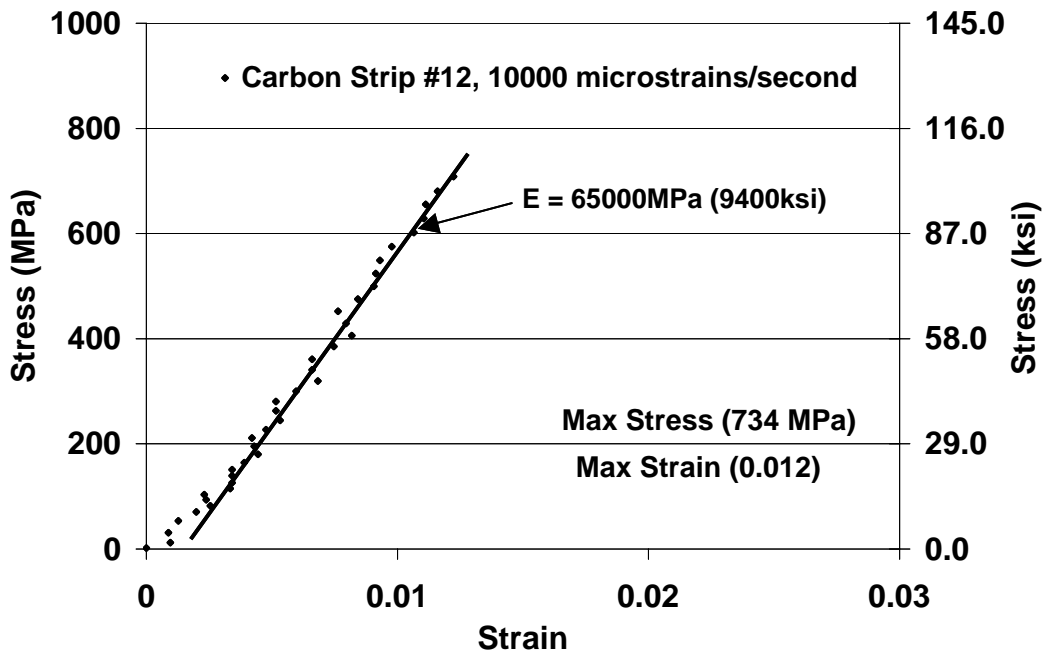


Figure 2-121: Stress vs. Strain, Elastomer Coated Carbon Strip #12

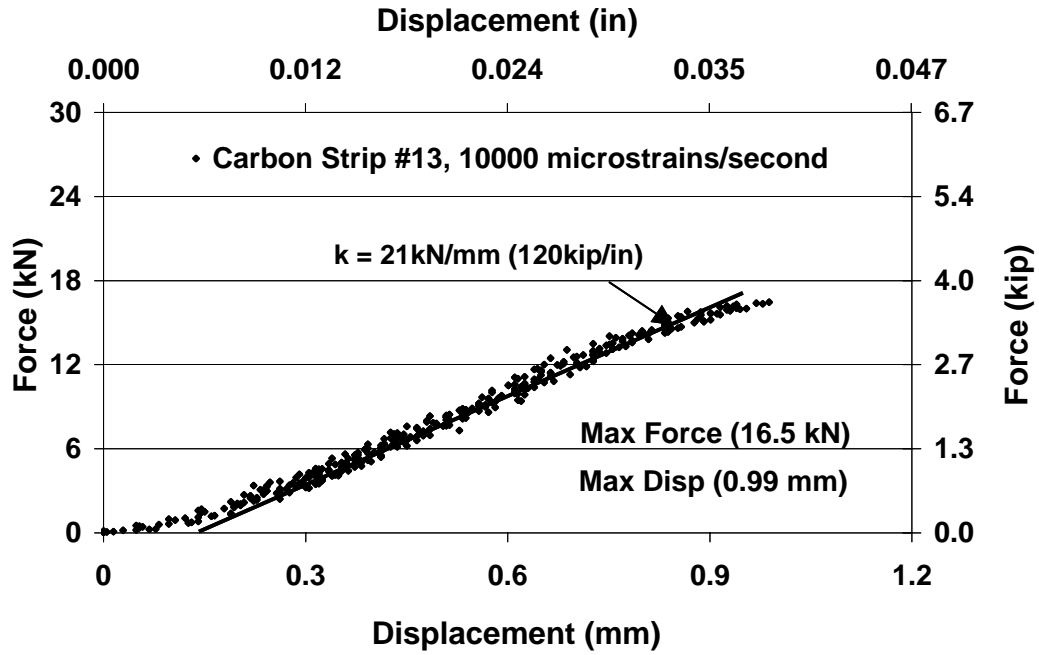


Figure 2-122: Force vs. Displacement, Elastomer Coated Carbon Strip #13

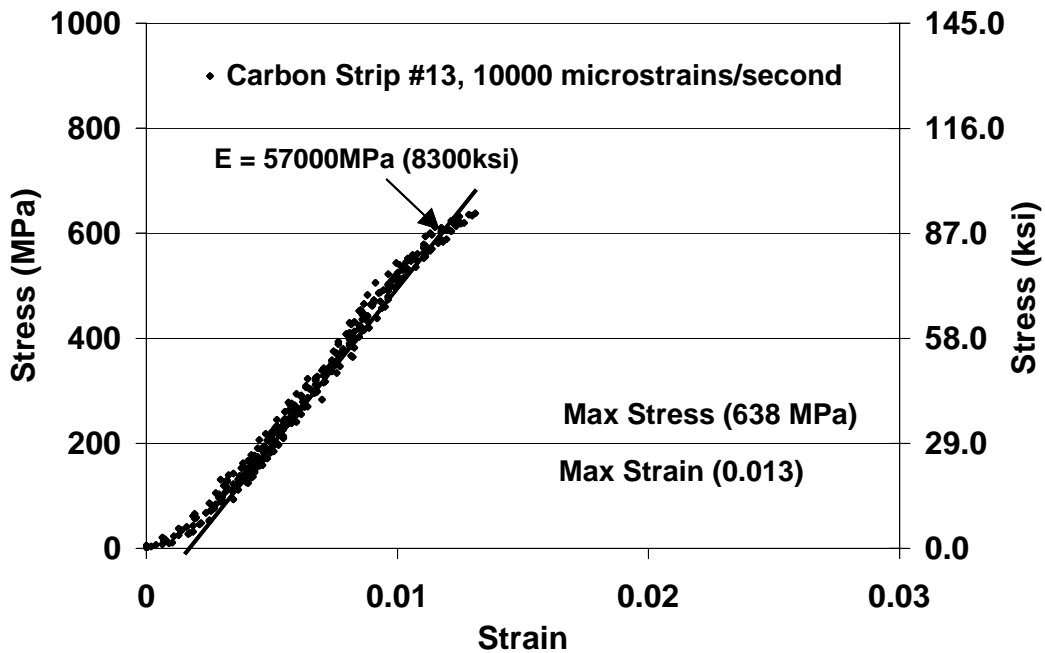


Figure 2-123: Stress vs. Strain, Elastomer Coated Carbon Strip #13

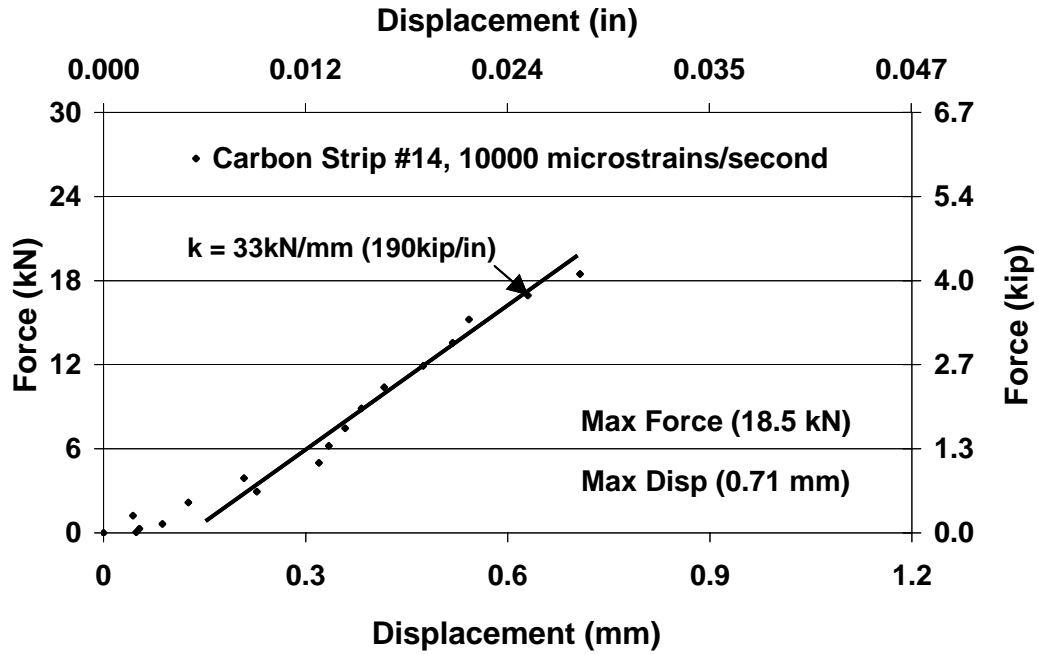


Figure 2-124: Force vs. Displacement, Elastomer Coated Carbon Strip #14

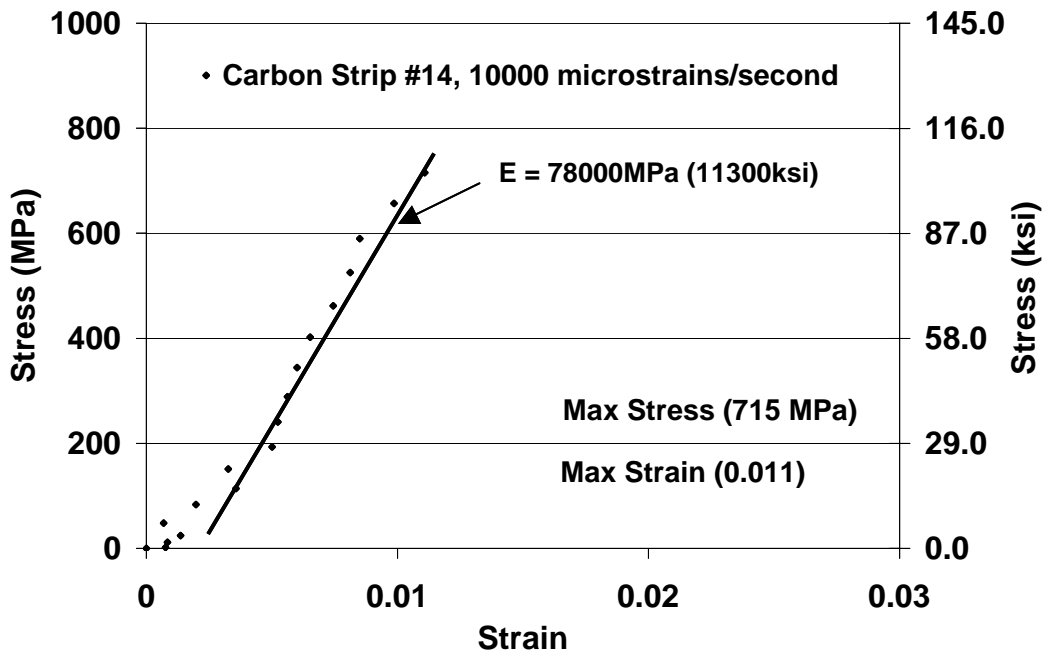


Figure 2-125: Stress vs. Strain, Elastomer Coated Carbon Strip #14

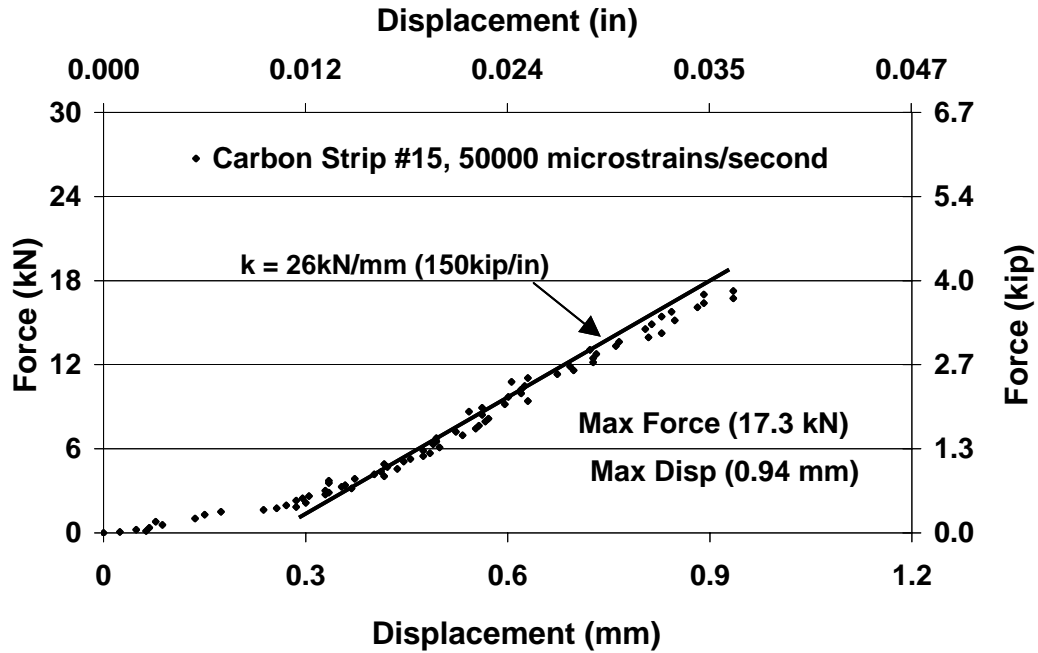


Figure 2-126: Force vs. Displacement, Elastomer Coated Carbon Strip #15

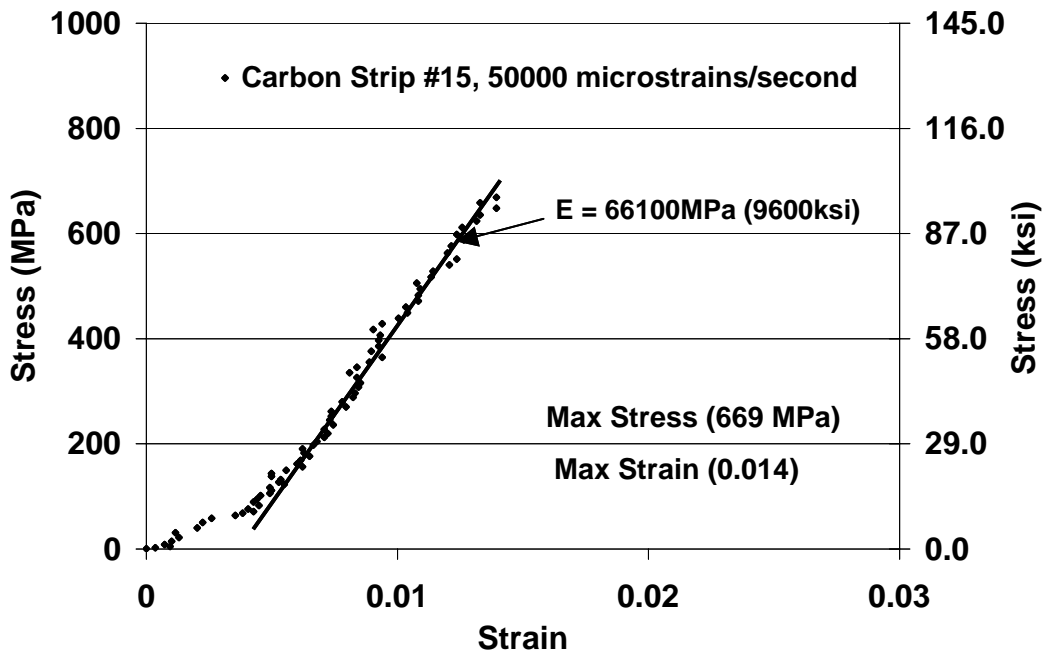


Figure 2-127: Stress vs. Strain, Elastomer Coated Carbon Strip #15

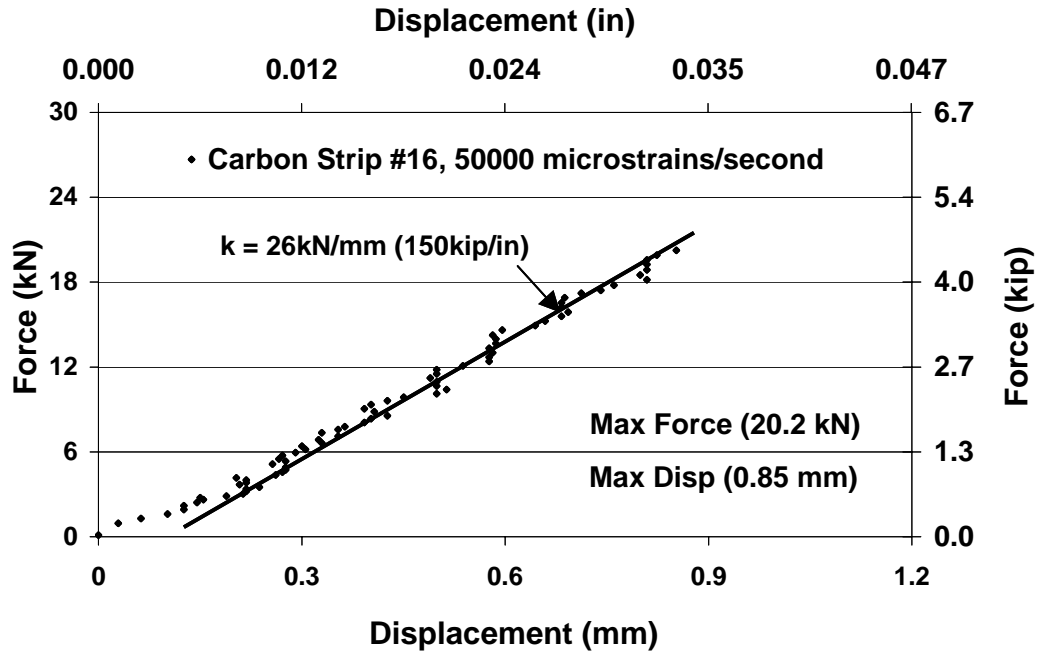


Figure 2-128: Force vs. Displacement, Elastomer Coated Carbon Strip #16

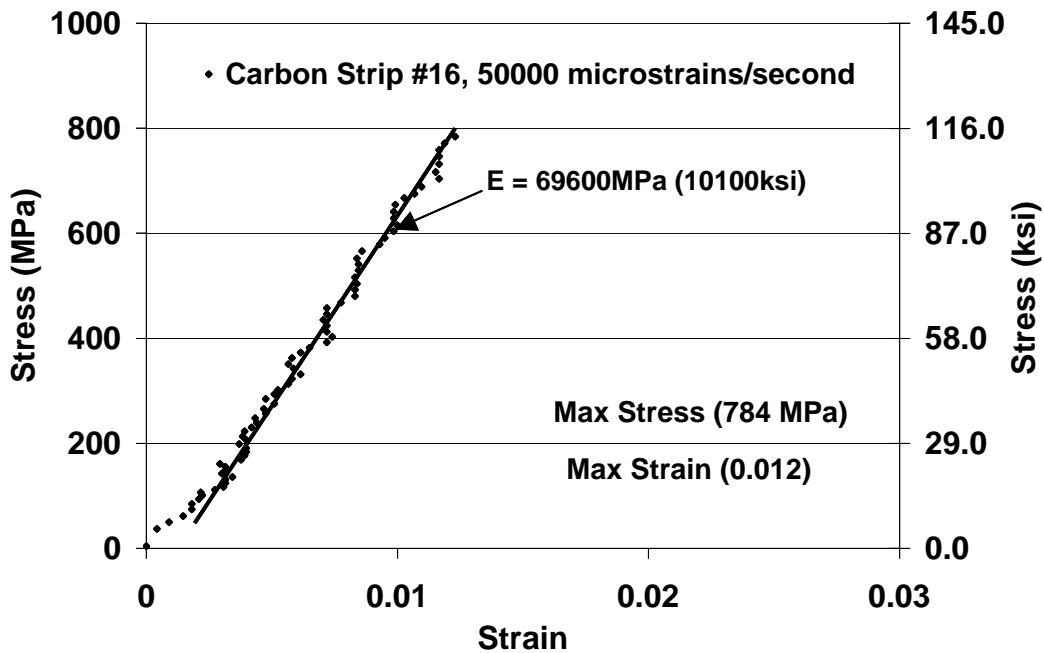


Figure 2-129: Stress vs. Strain, Elastomer Coated Carbon Strip #16

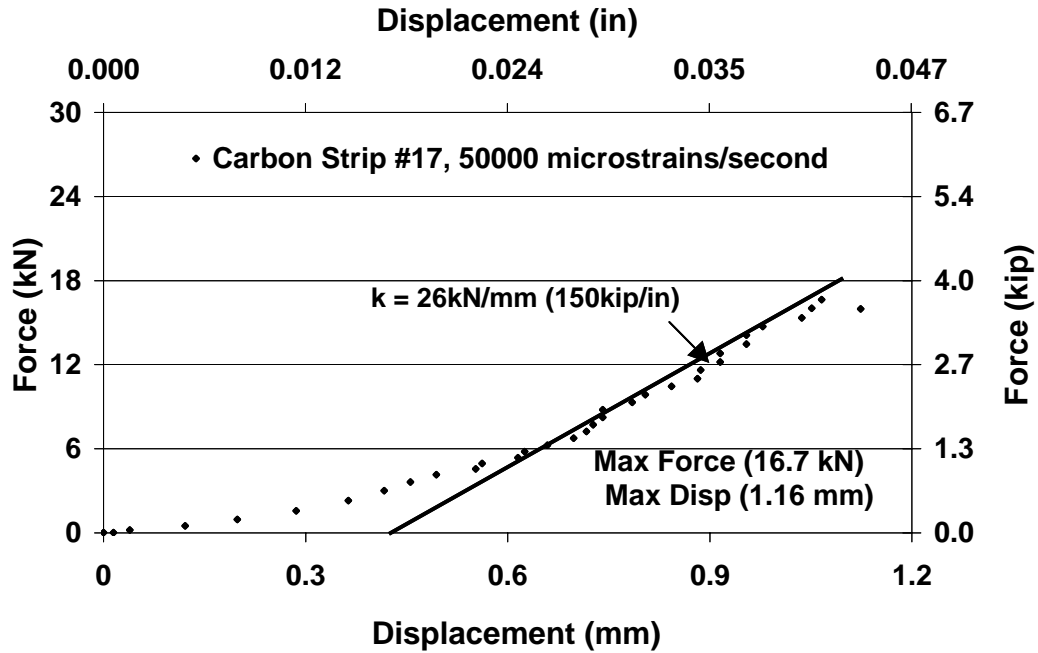


Figure 2-130: Force vs. Displacement, Elastomer Coated Carbon Strip #17

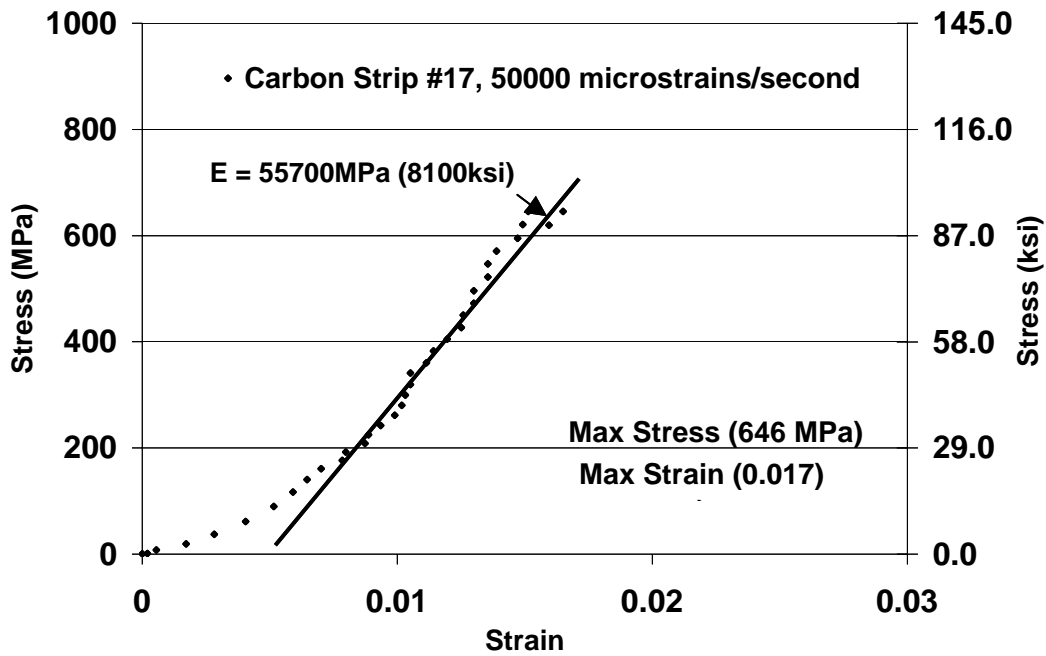


Figure 2-131: Stress vs. Strain, Elastomer Coated Carbon Strip #17

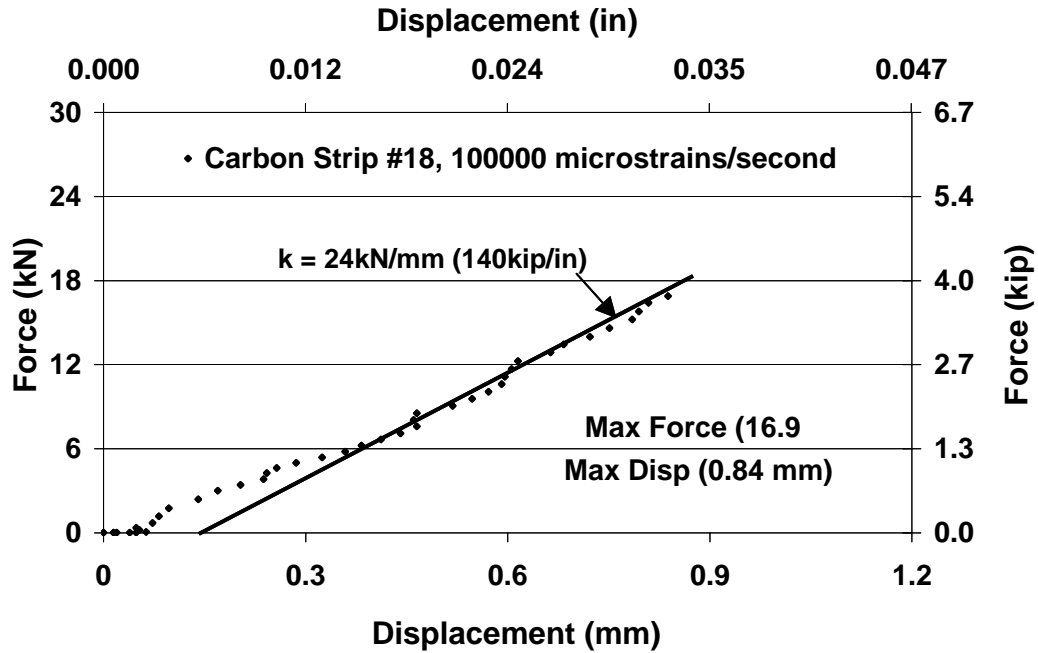


Figure 2-132: Force vs. Displacement, Elastomer Coated Carbon Strip #18

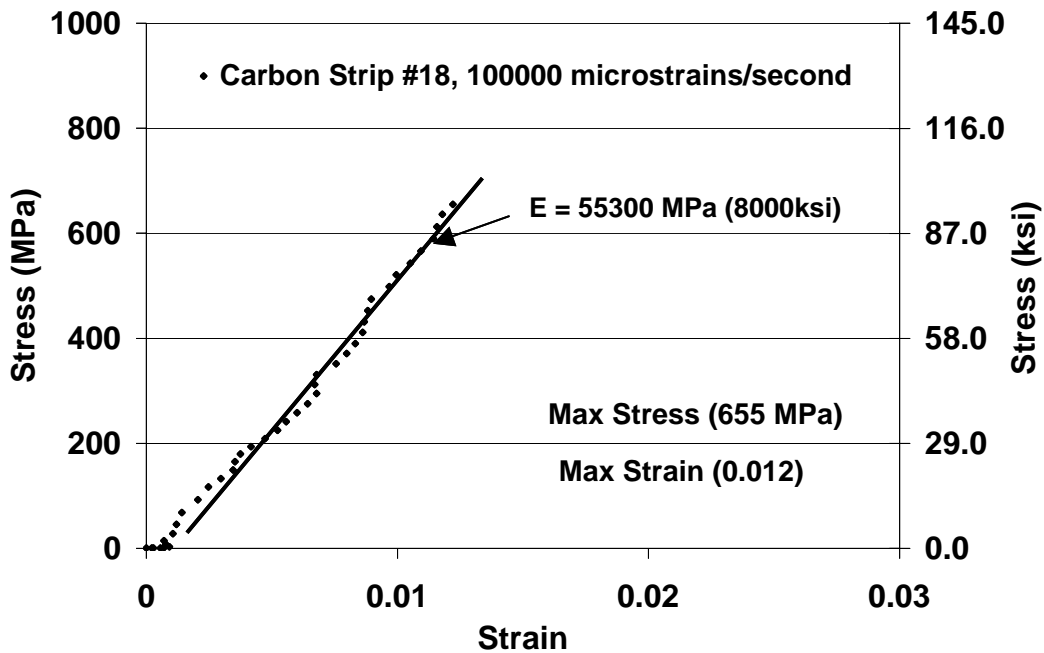


Figure 2-133: Stress vs. Strain, Elastomer Coated Carbon Strip #18

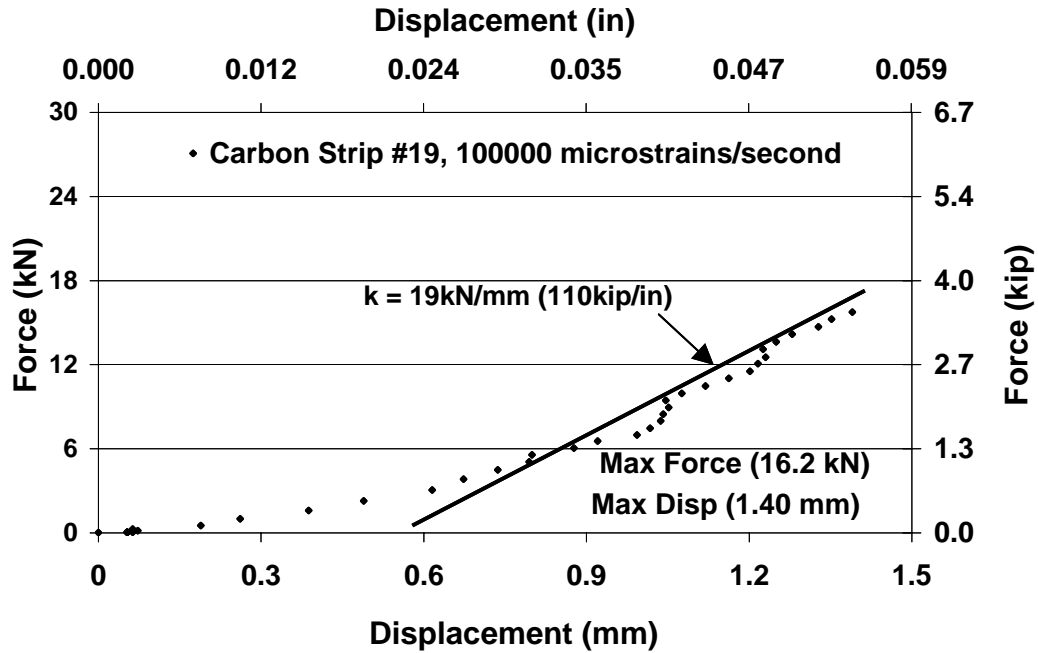


Figure 2-134: Force vs. Displacement, Elastomer Coated Carbon Strip #19

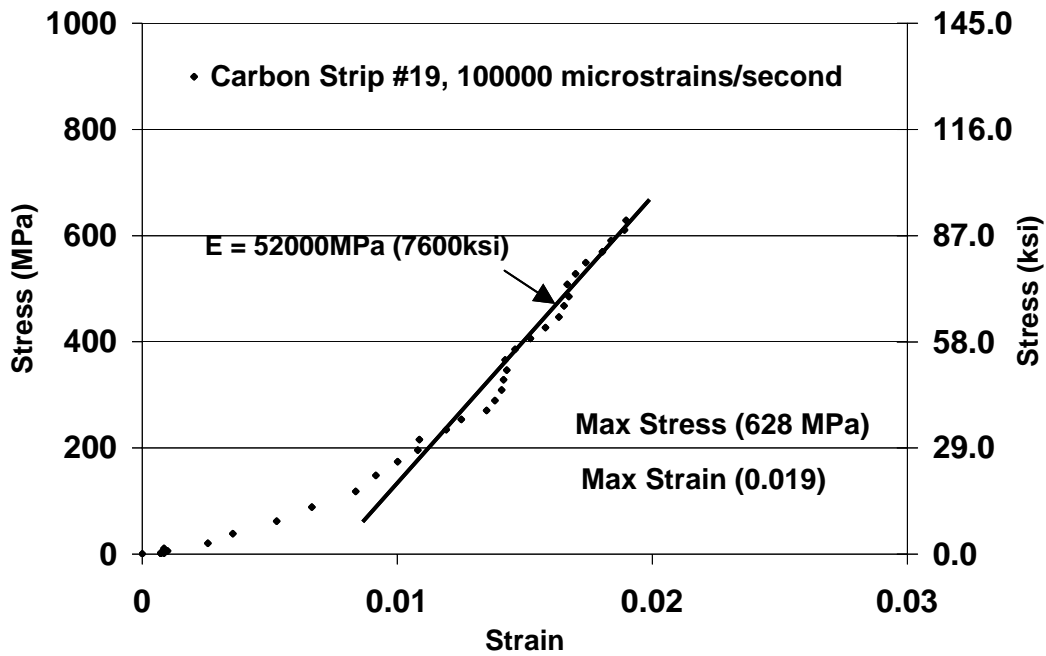


Figure 2-135: Stress vs. Strain, Elastomer Coated Carbon Strip #19

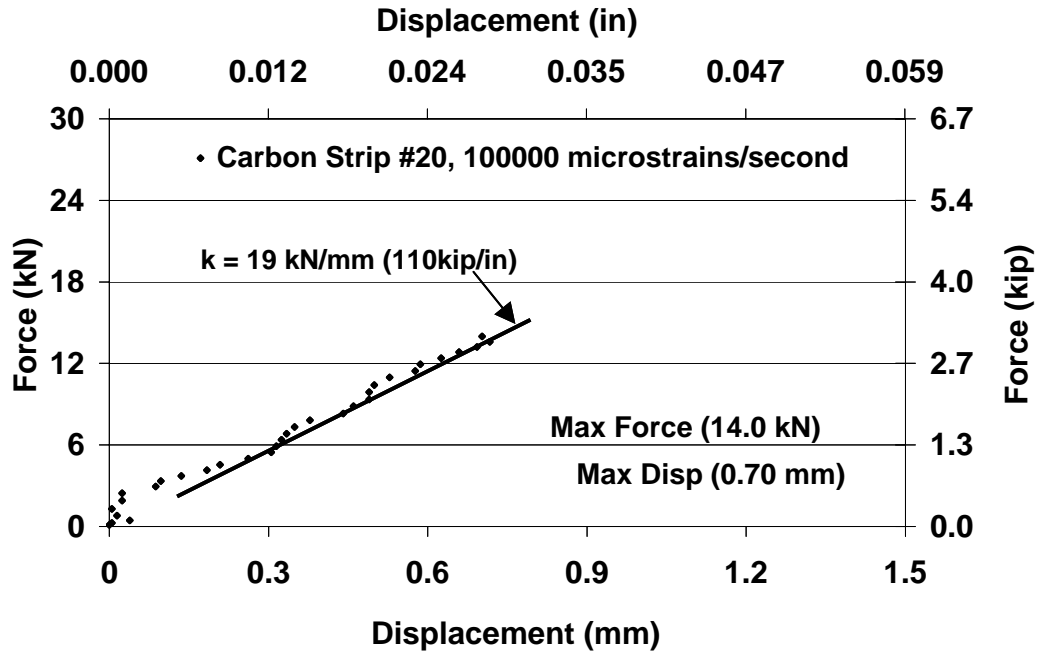


Figure 2-136: Force vs. Displacement, Elastomer Coated Carbon Strip #20

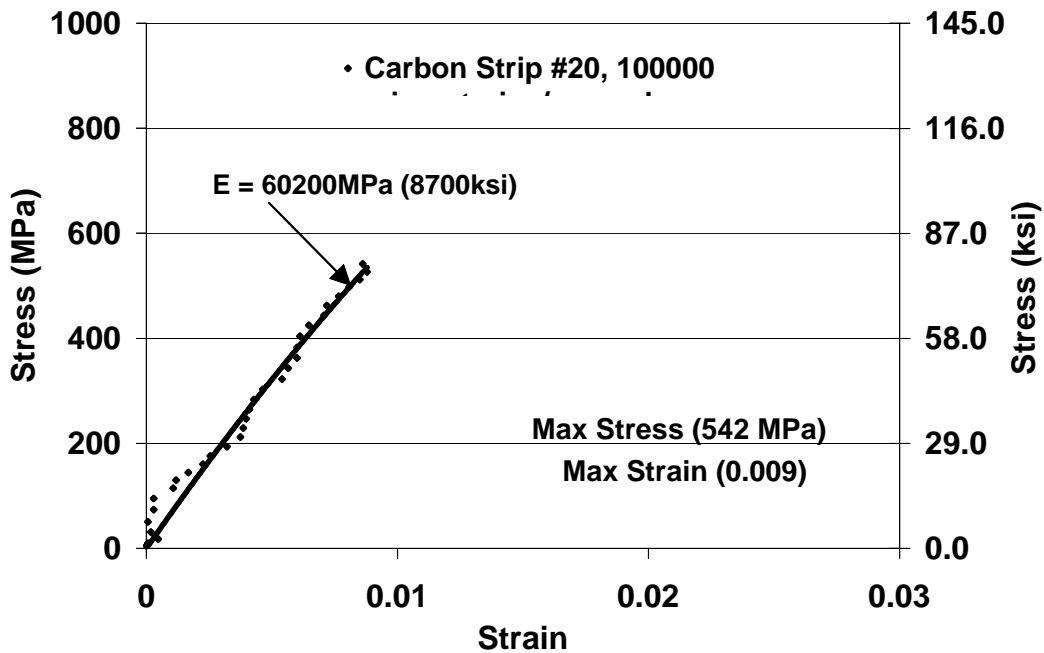
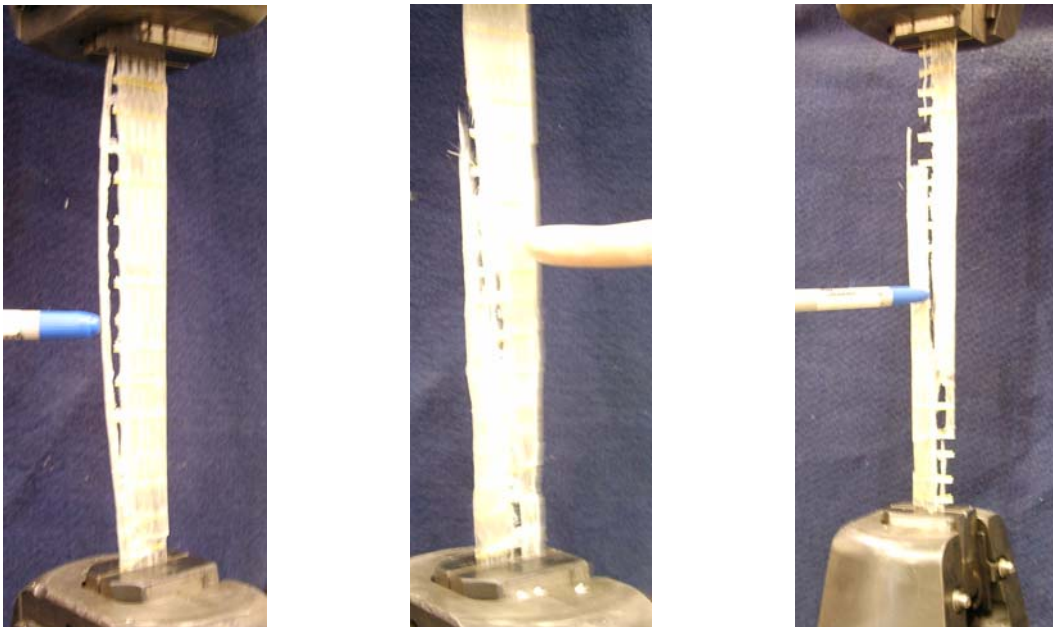
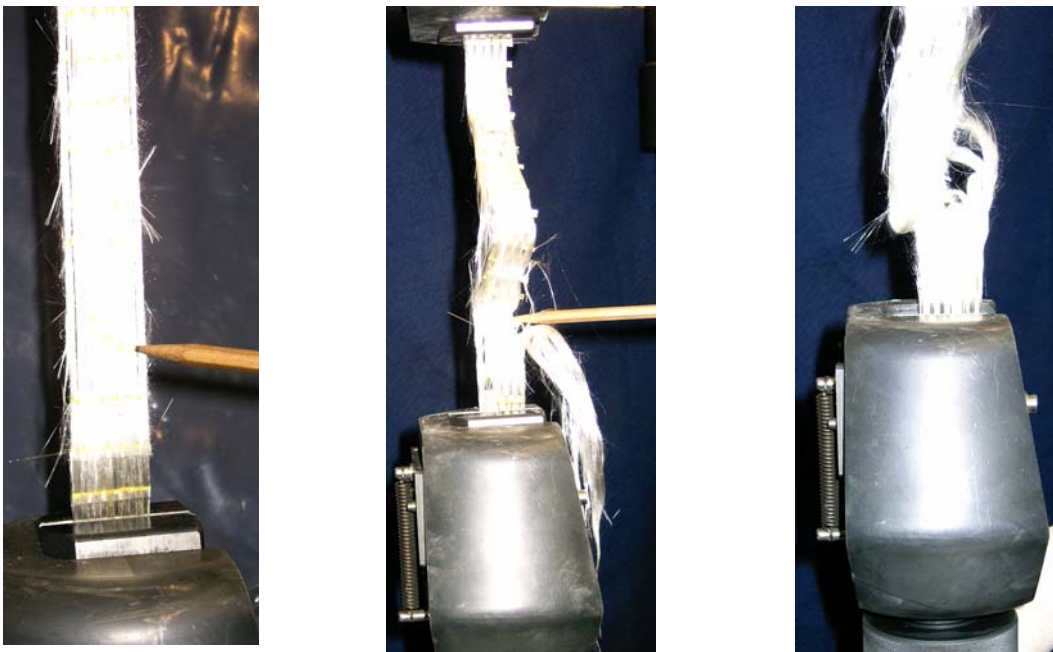


Figure 2-137: Stress vs. Strain, Elastomer Coated Carbon Strip #20

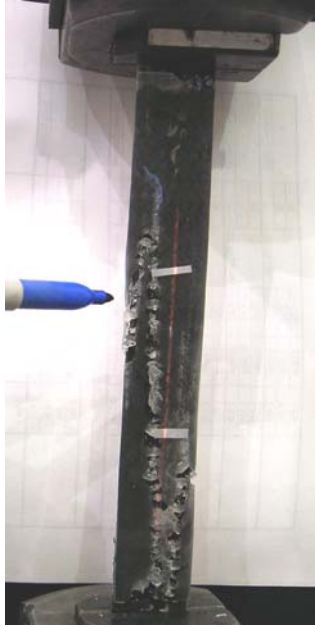


(a) Elastomer Coated Strips with Increasing Rate (Left to Right) from Low to High Dynamic Rate

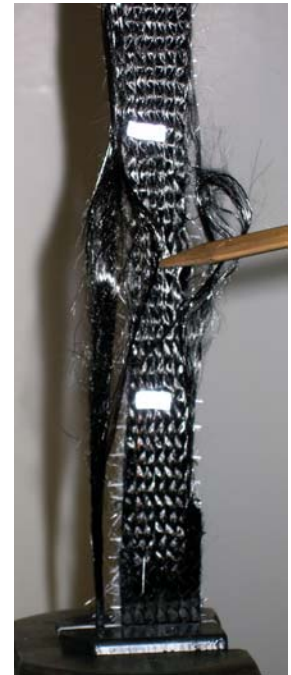
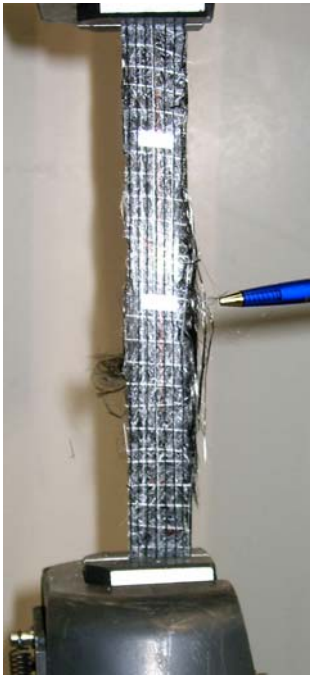


(b) Plain Fabric Strips with Increasing Rate (Left to Right) from Low to High Dynamic Rate

Figure 2-138: Comparisons of Tensile Failure Mode for (a) Elastomer Coated Glass Strips and (b) Uncoated Glass Strips



(a) Elastomer Coated Strip



(b) Plain Fabric Strips with Increasing Rate (Left to Right) from Low to High Dynamic Rate

Figure 2-139: Comparisons of Tensile Failure Mode for (a) Elastomer Coated Carbon Strips and (b) Uncoated Carbon Strips

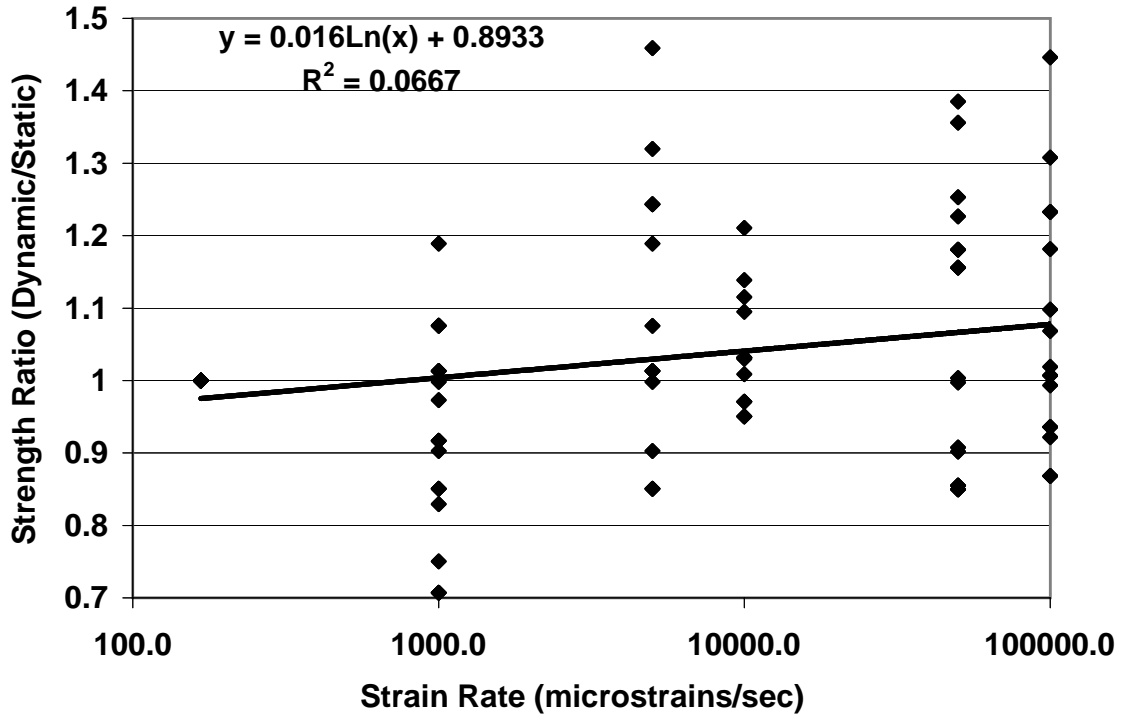


Figure 2-140: Strength ratio vs. strain rate for elastomer coated glass strips

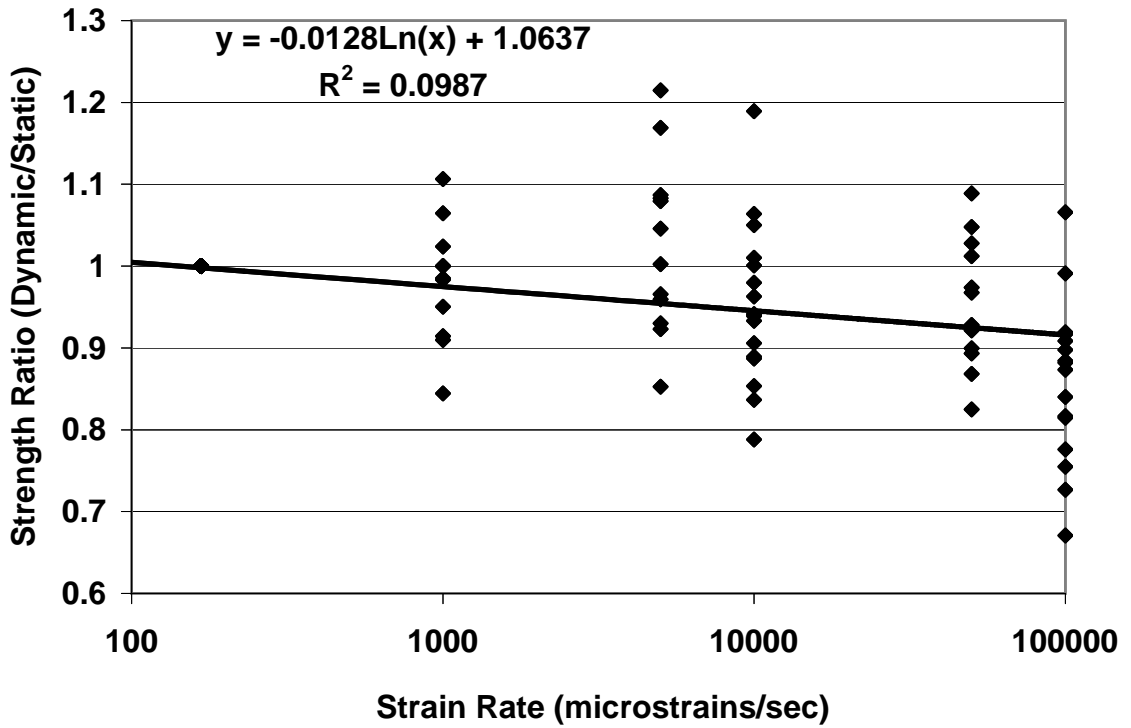


Figure 2-141: Strength ratio vs. strain rate for elastomer coated carbon strips

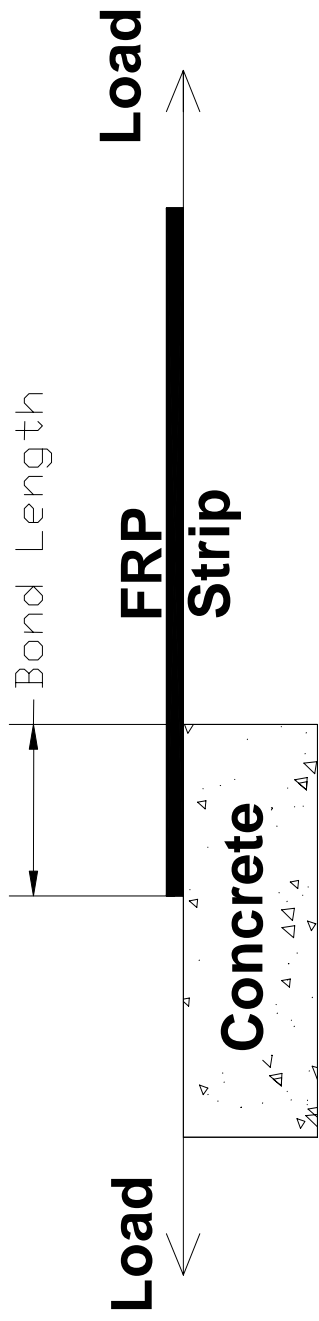
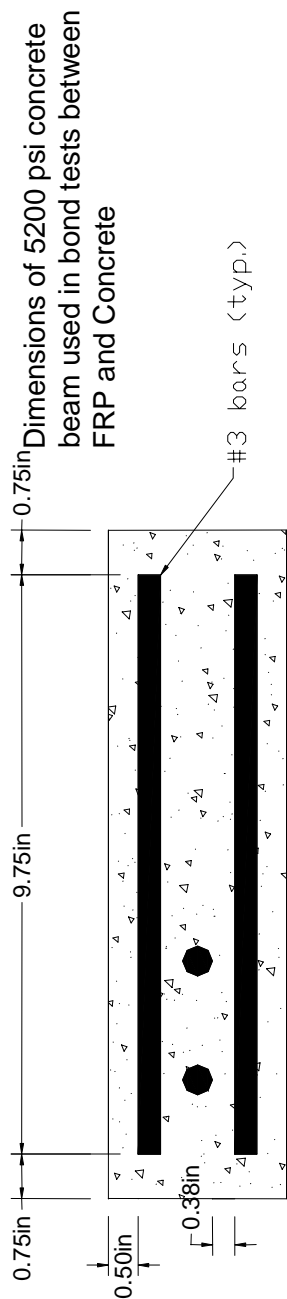
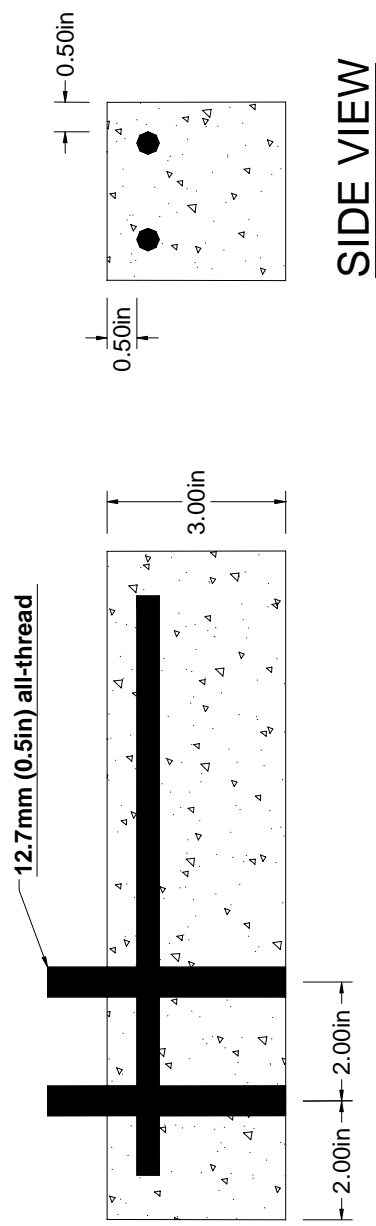


Figure 2-142: Single Lap Test



PLAN VIEW



ELEVATION

SIDE VIEW

Figure 2-143: Concrete Blocks used in FRP/Concrete Bond Tests



Figure 2-144: FRP/Concrete Bond Tests on MTS Load Frame

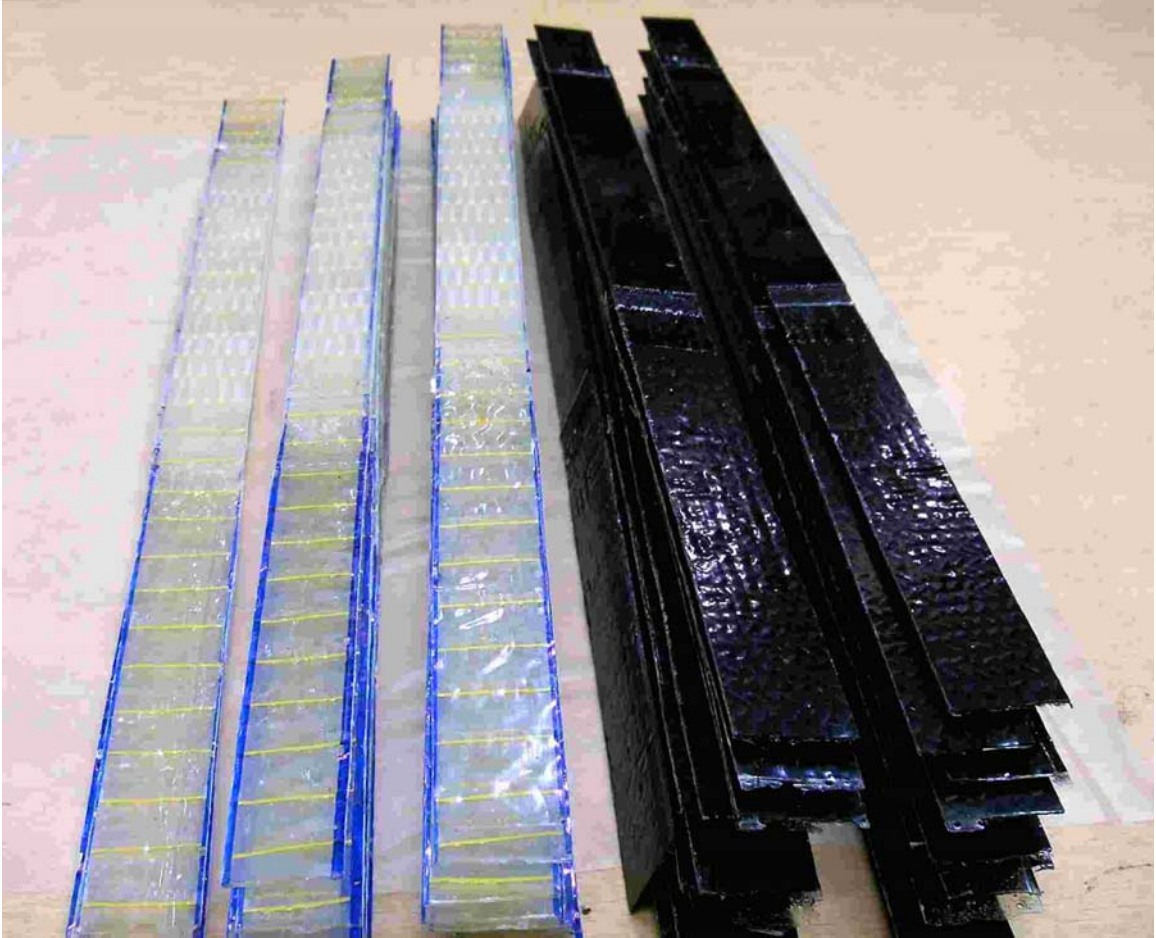
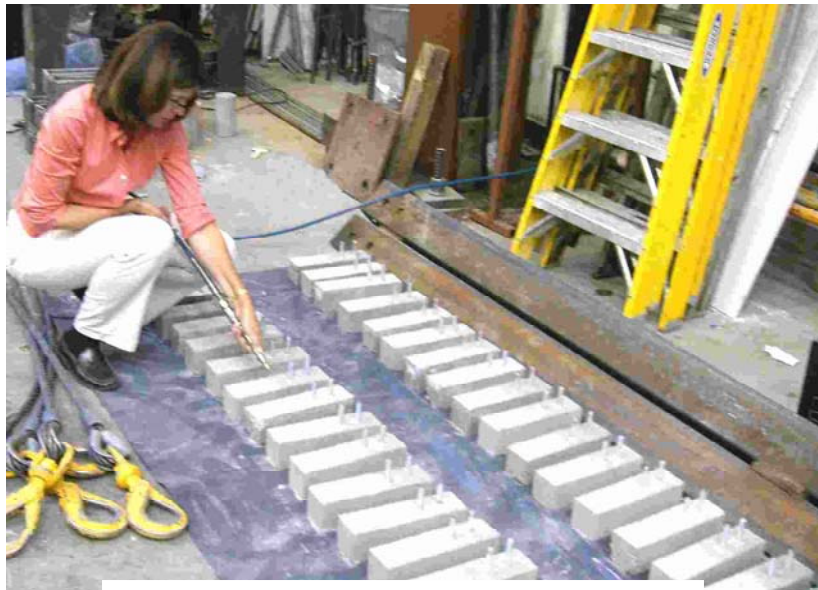


Figure 2-145: Glass and Carbon Strips for Bond Tests



(a) Sanding Blocks



(b) Vacuuming Blocks

Figure 2-146: Beam Preparation for FRP/Concrete Bond Tests



(a) Strips being Epoxied to Concrete Blocks

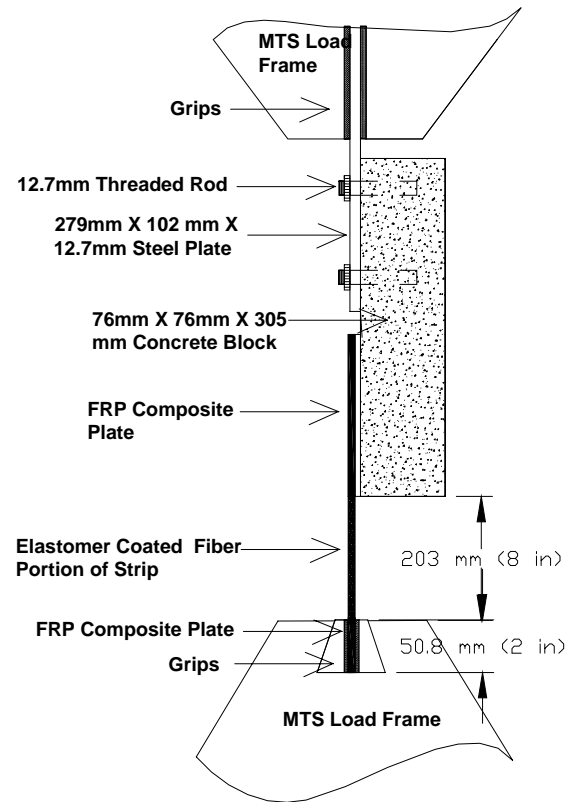


(b) Covering Bonded Strips with Polyurethane and Weights.

Figure 2-147: FRP/Concrete Bond Test Specimen Construction



(a) Bond Tests



(b) Close-up of test set-up

Figure 2-148: Tensile Tests on interfacial Bond between FRP and Concrete

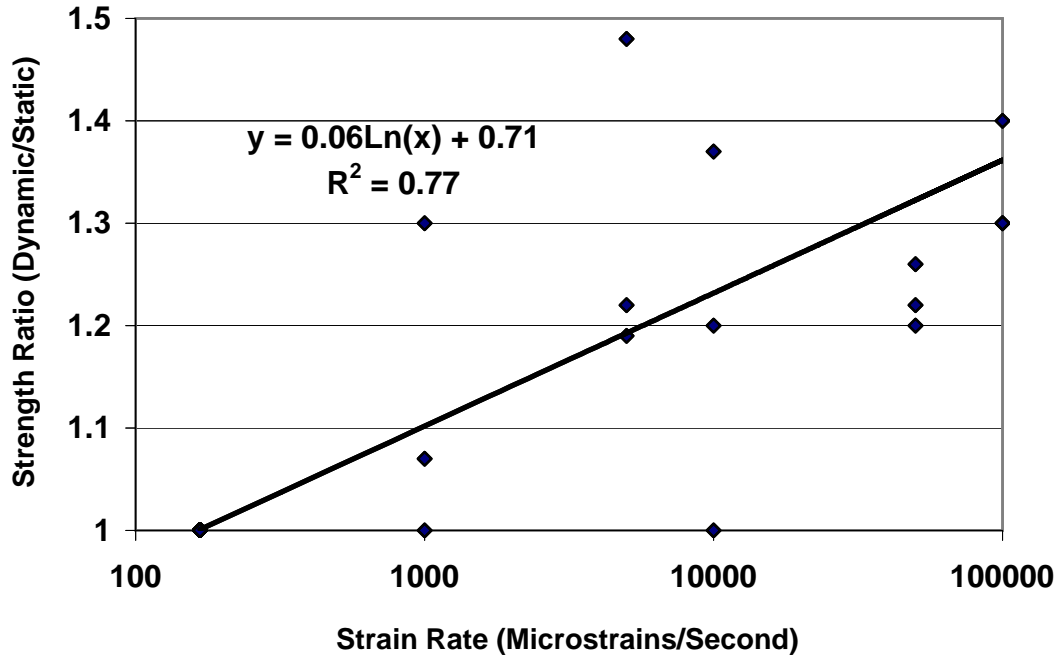


Figure 2-149(a): Strength Ratios for GFRP/Concrete Bond (Results from Tensile Tests)

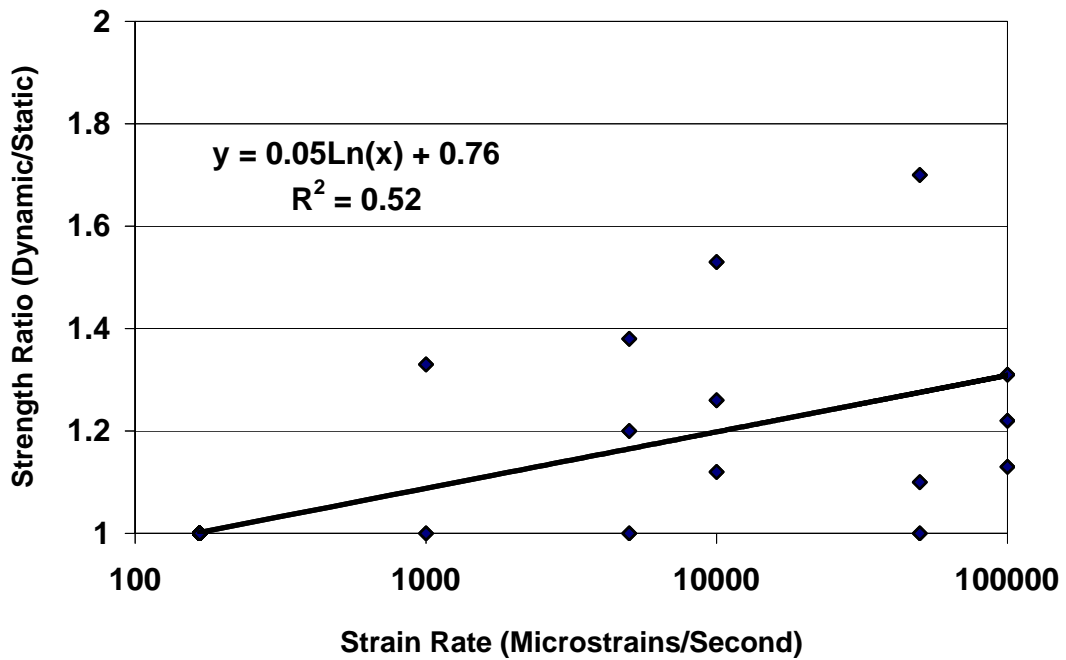


Figure 2-149(b): Strength Ratios for CFRP/Concrete Bond (Results from Tensile Tests)

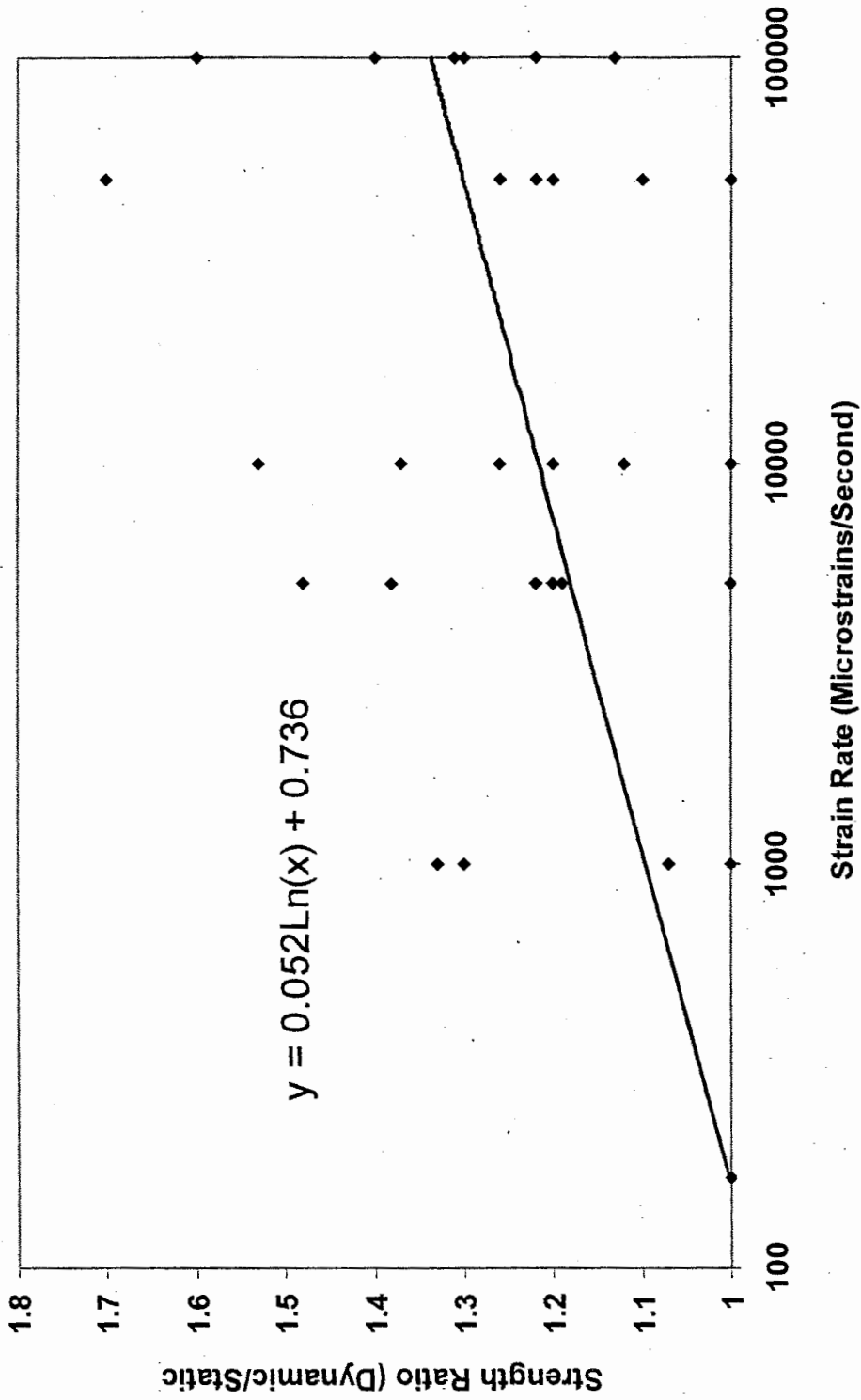


Figure 2-150: Best Line Fit of Strength Ratios vs Strain Rate for FRP/Concrete Bond



Figure 2-151: Bond Failure during Tensile Tests



Figure 2-152: Close-up of Bond Failure

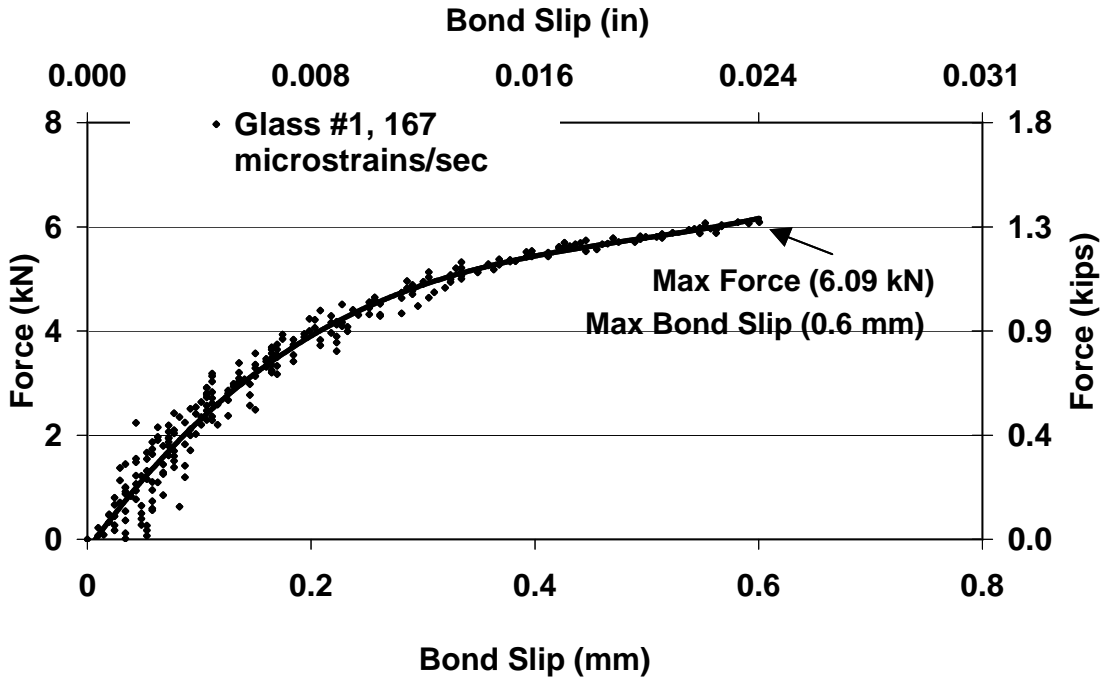


Figure 2-153: Force vs. bond slip for GFRP/concrete bond #1

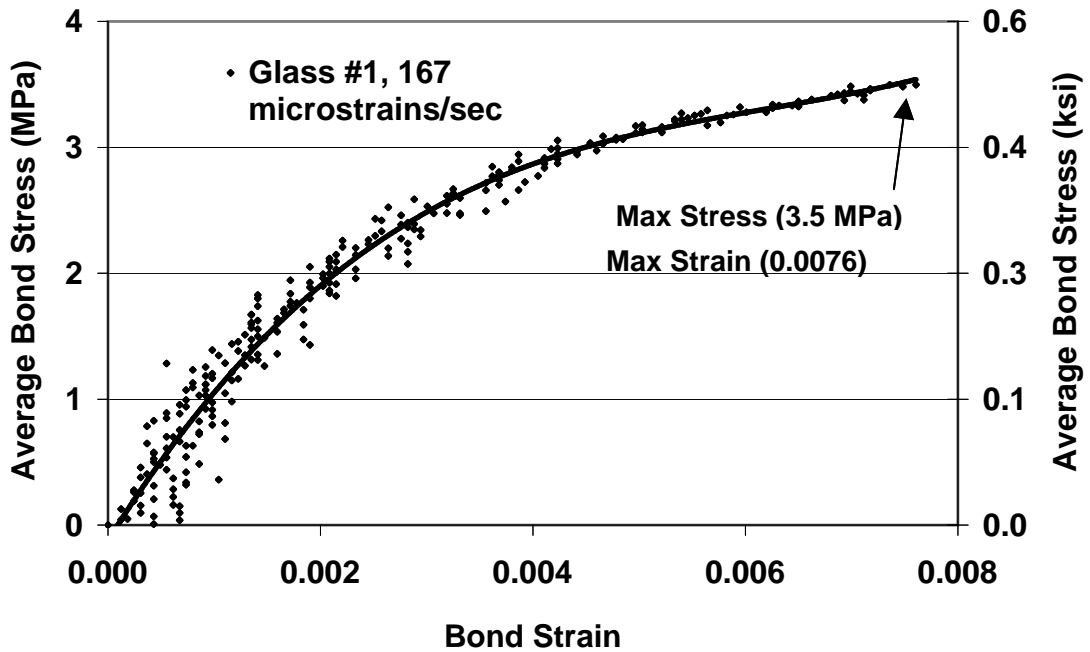


Figure 2-154: Average bond stress vs. bond strain, GFRP/concrete bond #1

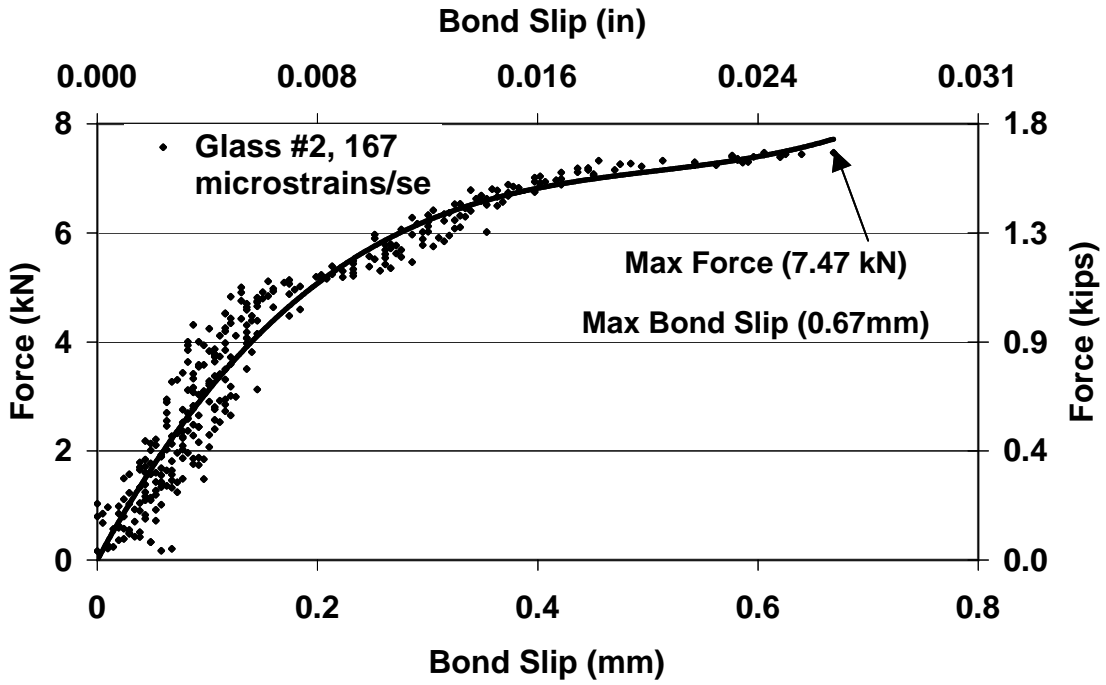


Figure 2-155: Force vs. bond slip for GFRP/concrete bond #2

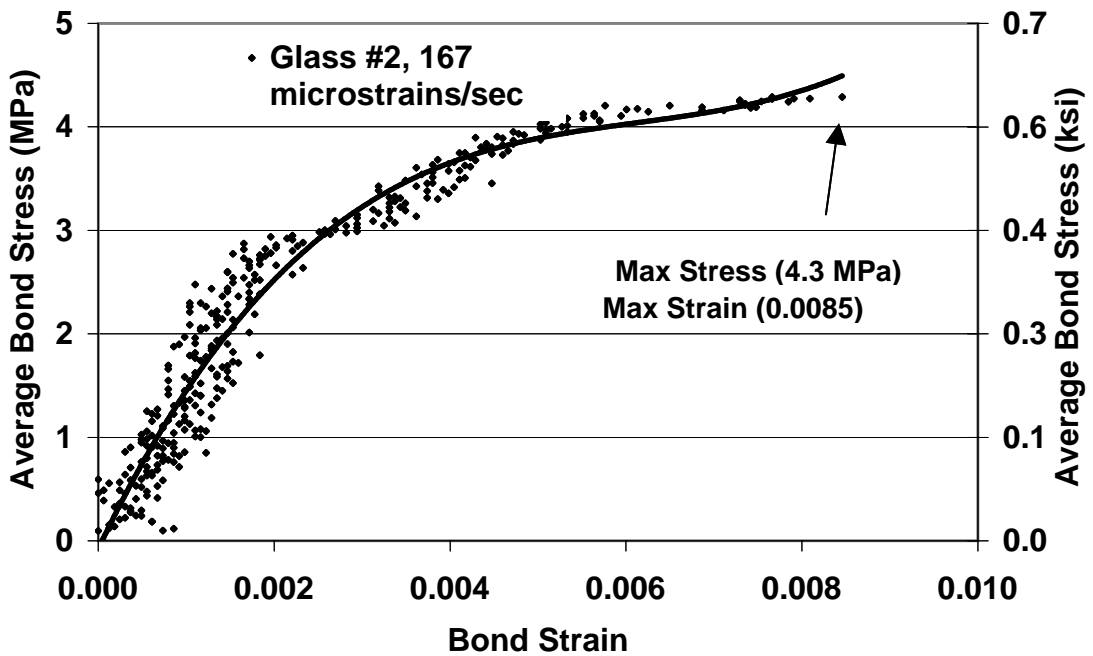


Figure 2-156: Average bond stress vs. bond strain, GFRP/concrete bond #2

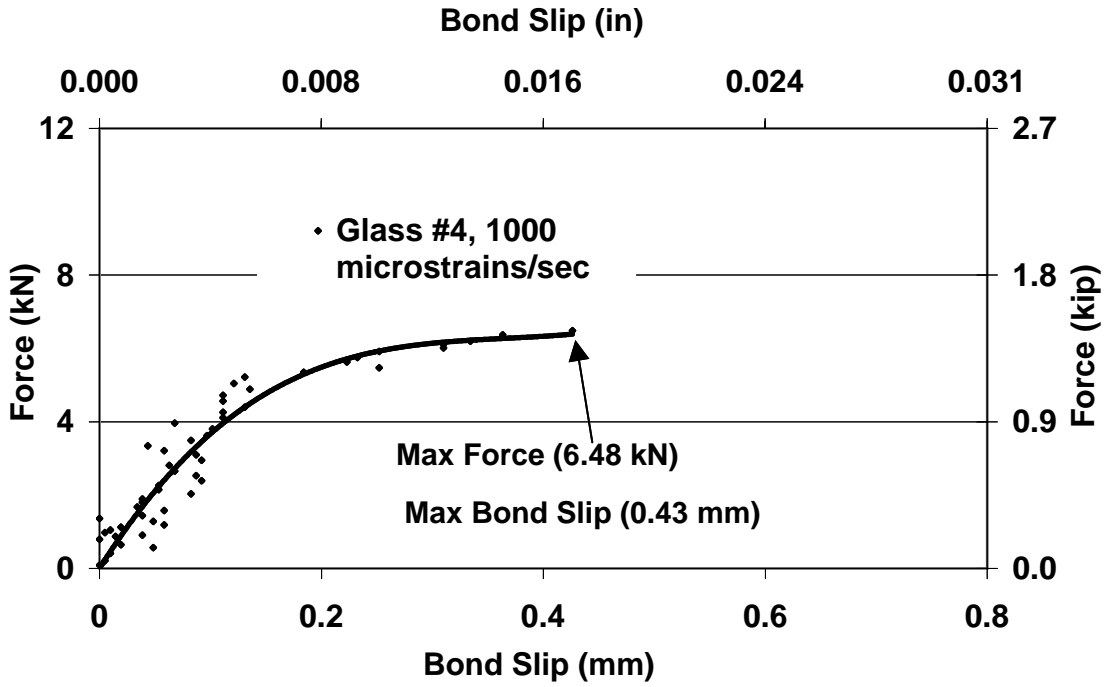


Figure 2-157: Force vs. bond slip for GFRP/concrete bond #4

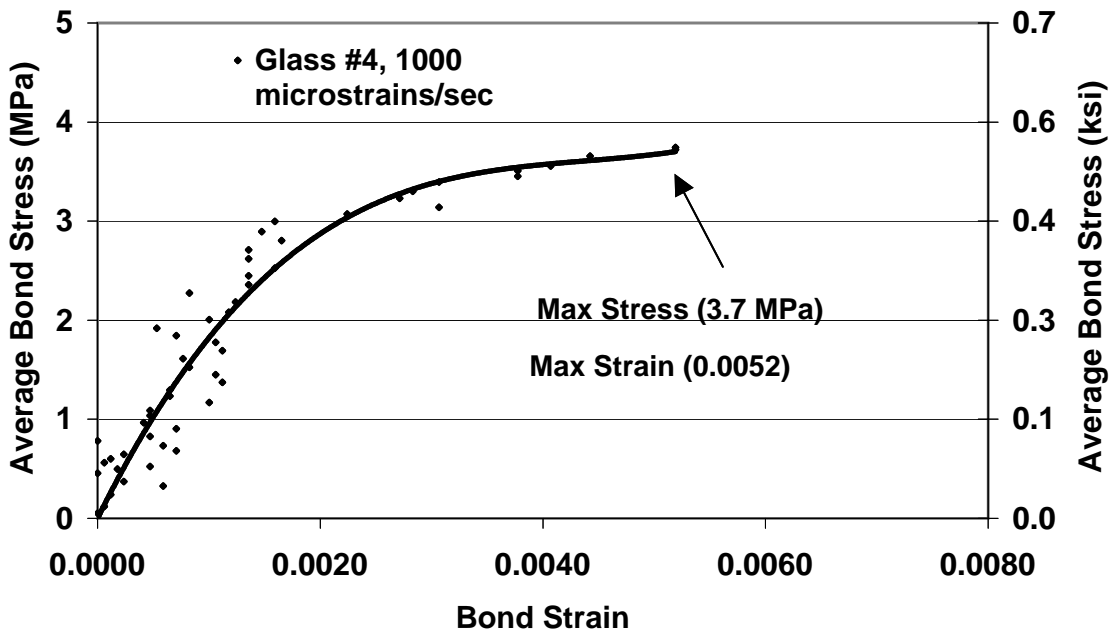


Figure 2-158: Average bond stress vs. bond strain, GFRP/concrete bond #4

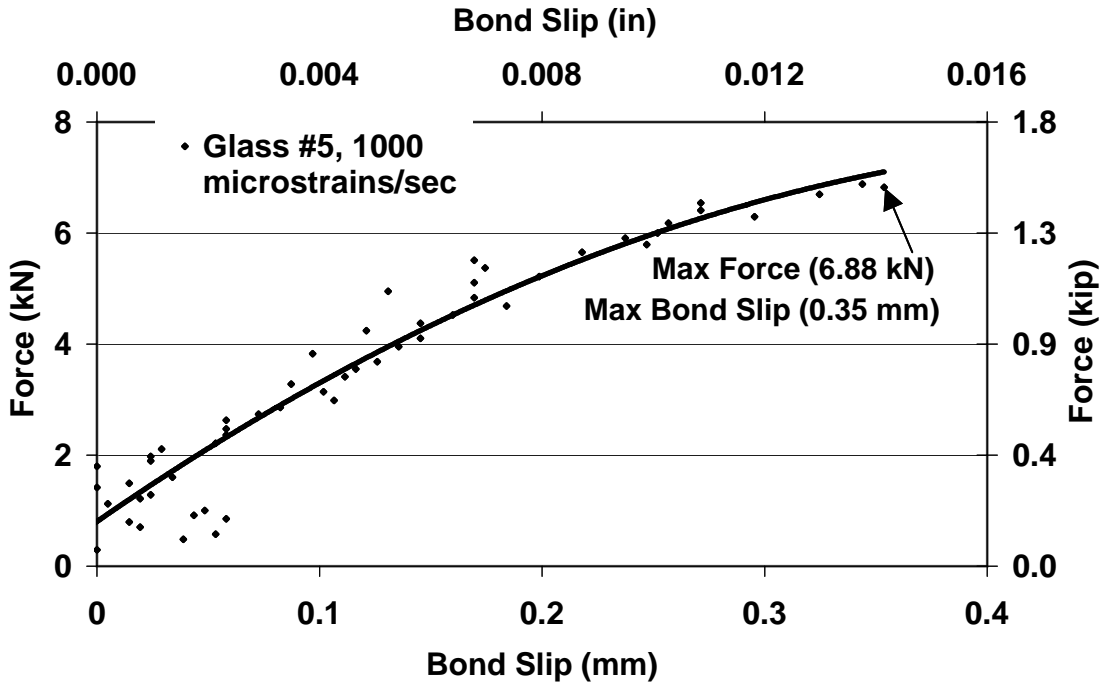


Figure 2-159: Force vs. bond slip for GFRP/concrete bond #5

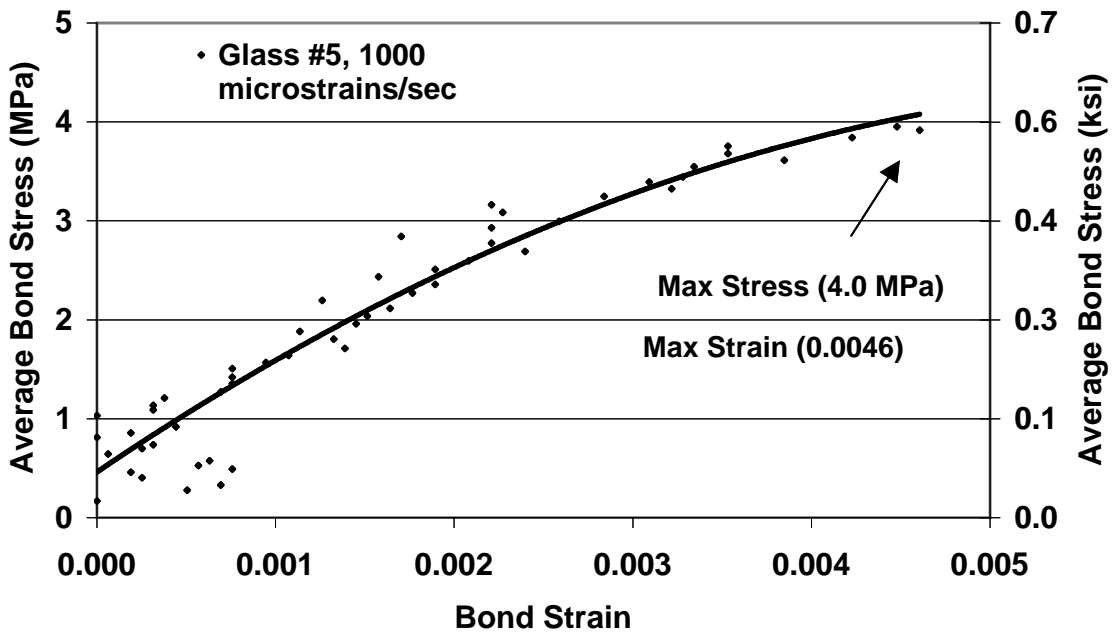


Figure 2-160: Average bond stress vs. bond strain, GFRP/concrete bond #5

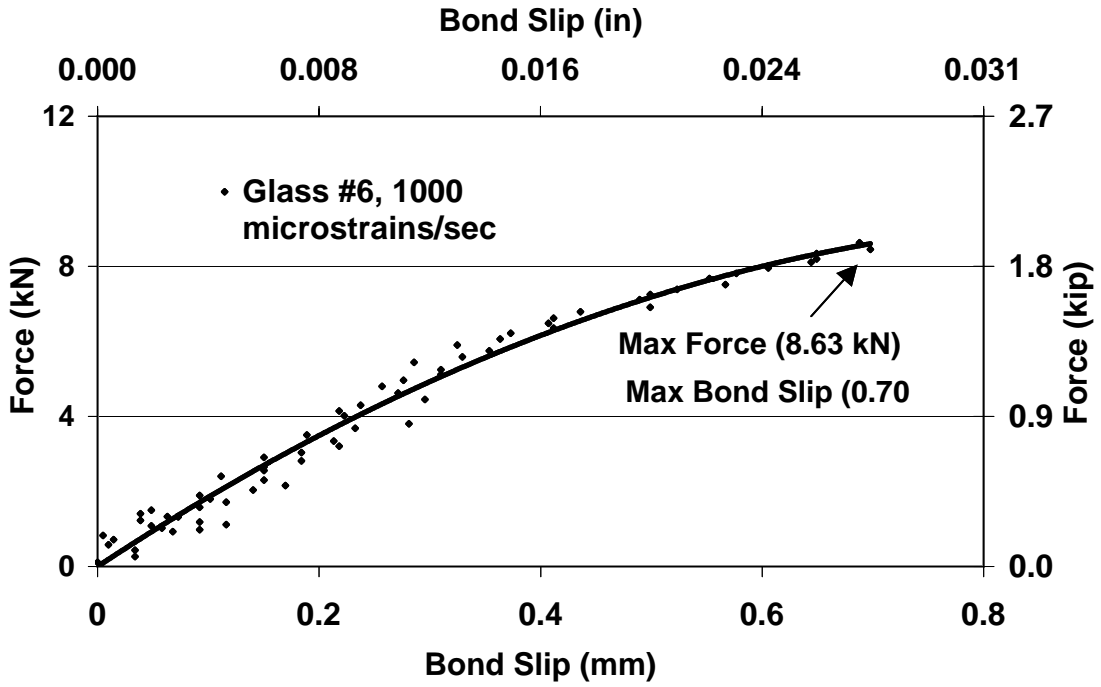


Figure 2-161: Force vs. bond slip for GFRP/concrete bond #6

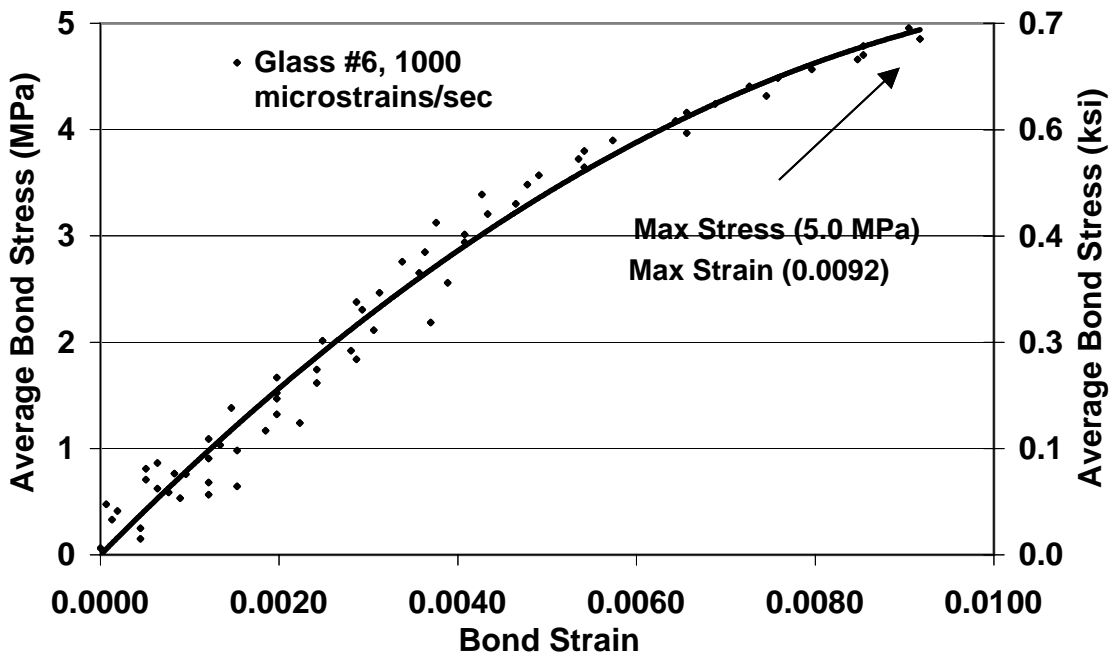


Figure 2-162: Average bond stress vs. bond strain, GFRP/concrete bond #6

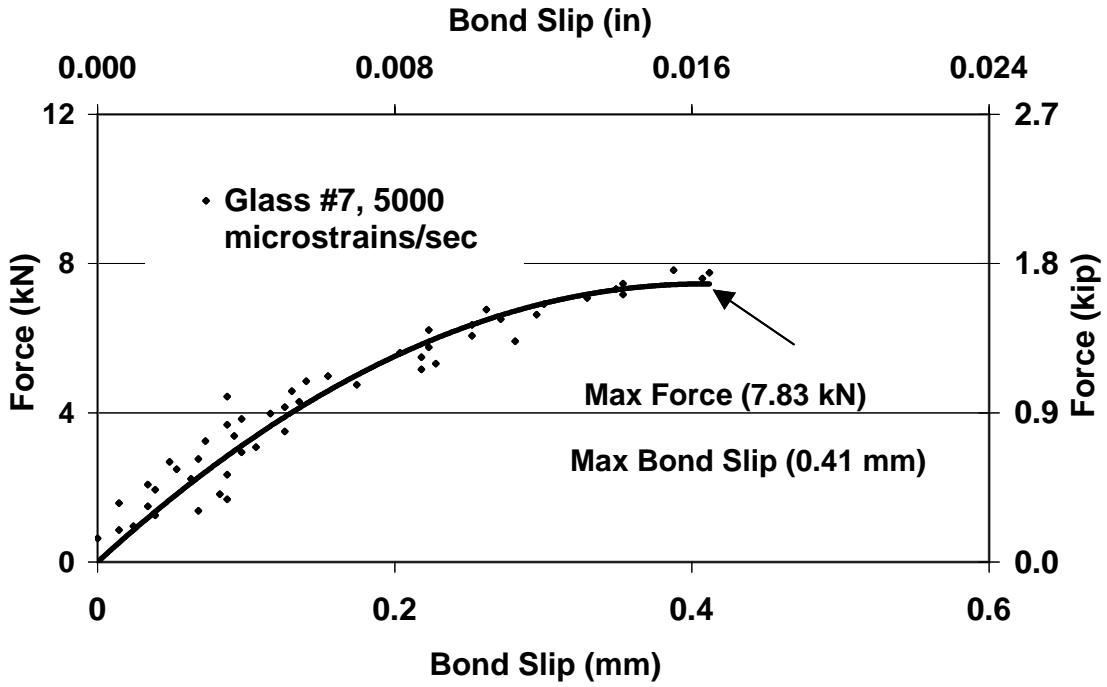


Figure 2-163: Force vs. bond slip for GFRP/concrete bond #7

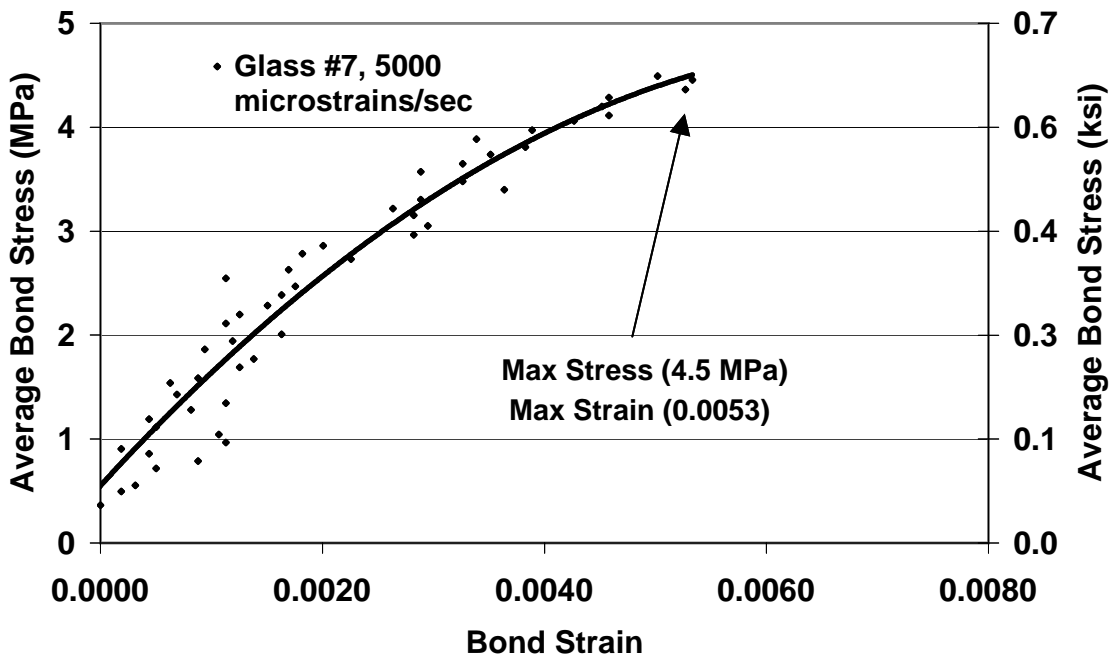


Figure 2-164: Average bond stress vs. bond strain, GFRP/concrete bond #7

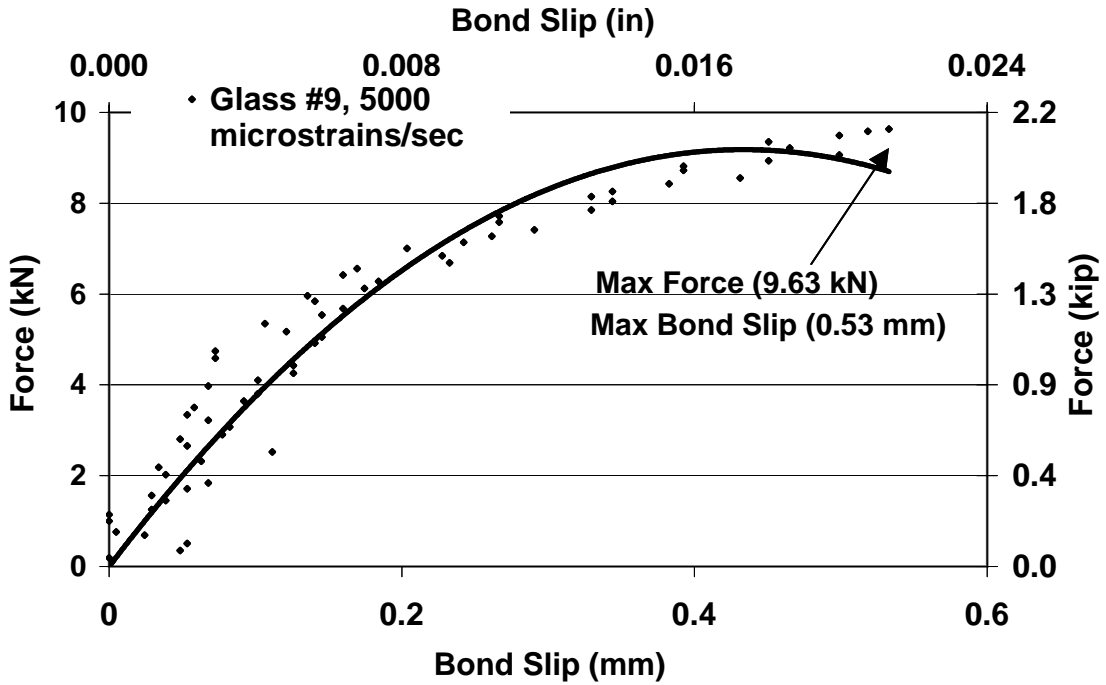


Figure 2-165: Force vs. bond slip for GFRP/concrete bond #9

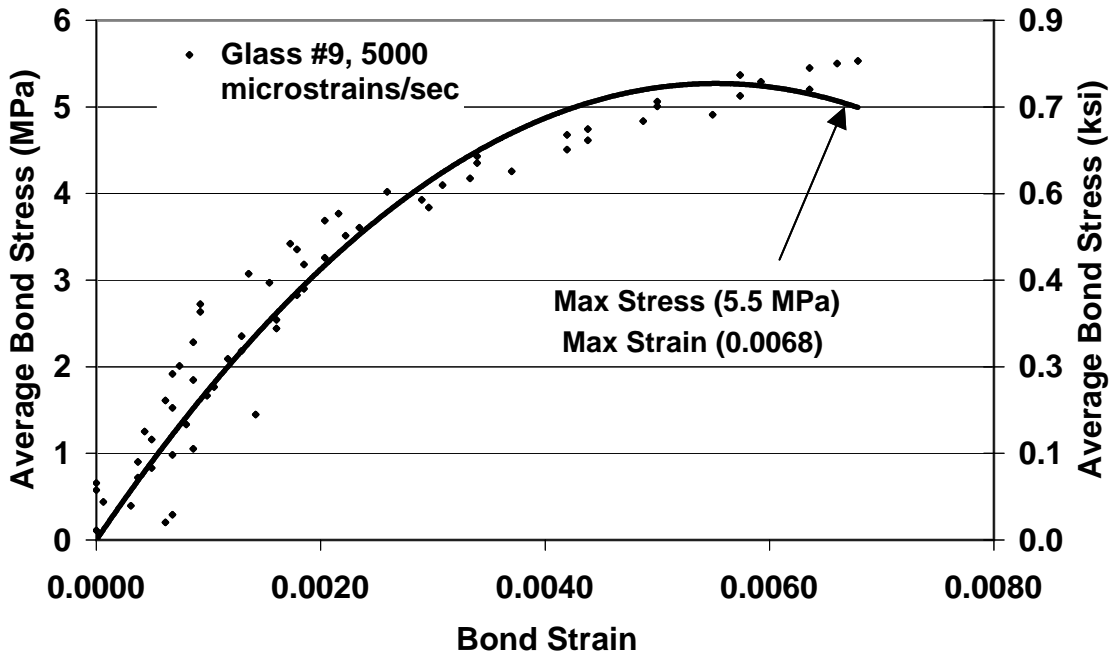


Figure 2-166: Average bond stress vs. bond strain, GFRP/concrete bond #9

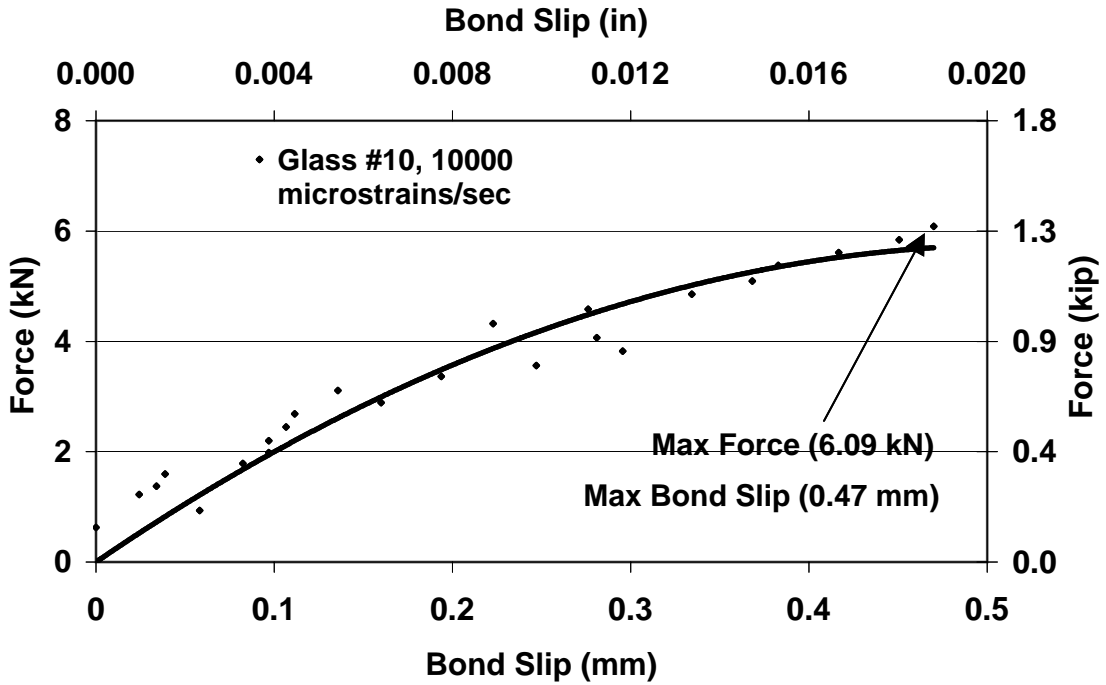


Figure 2-167: Force vs. bond slip for GFRP/concrete bond #10

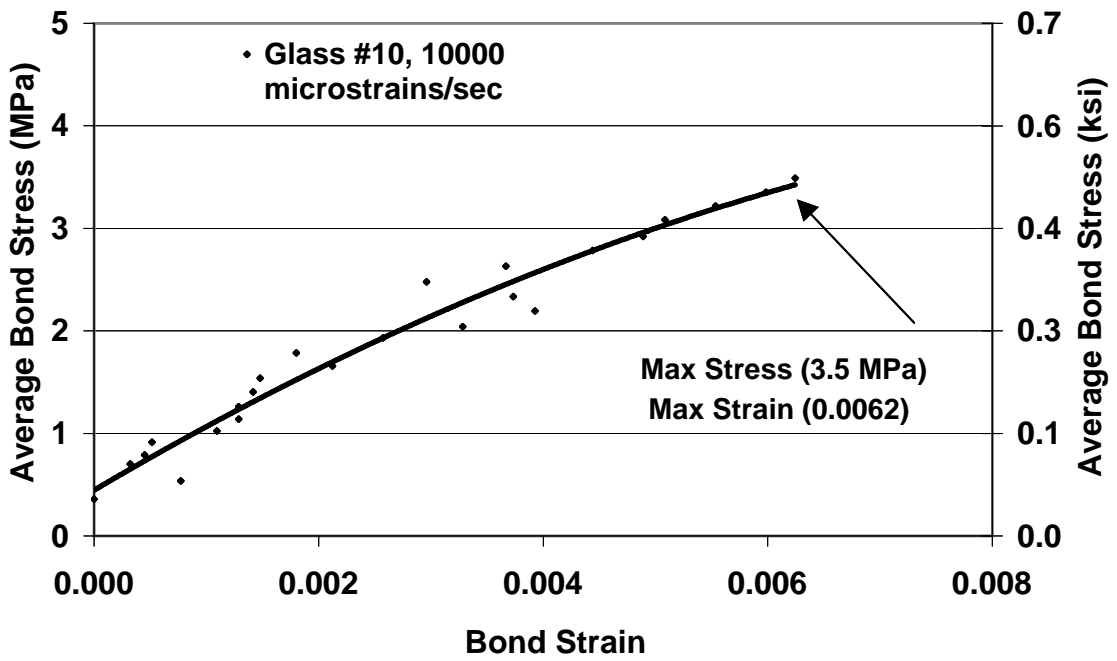


Figure 2-168: Average bond stress vs. bond strain, GFRP/concrete bond #10

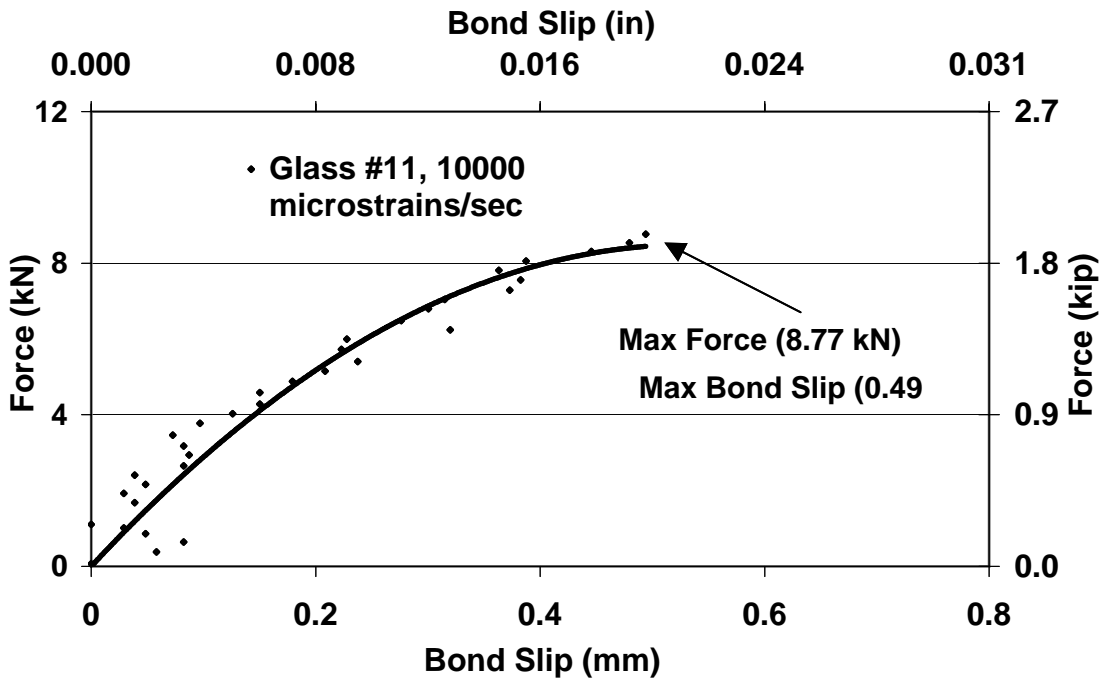


Figure 2-169: Force vs. bond slip for GFRP/concrete bond #11

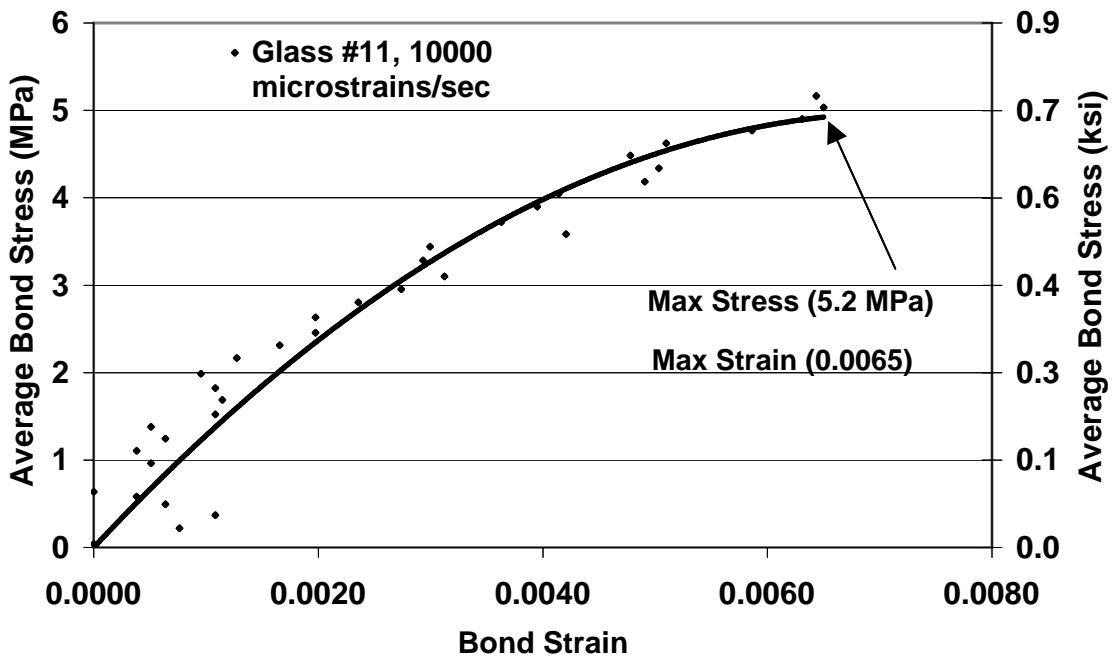


Figure 2-170: Average bond stress vs. bond strain, GFRP/concrete bond #11

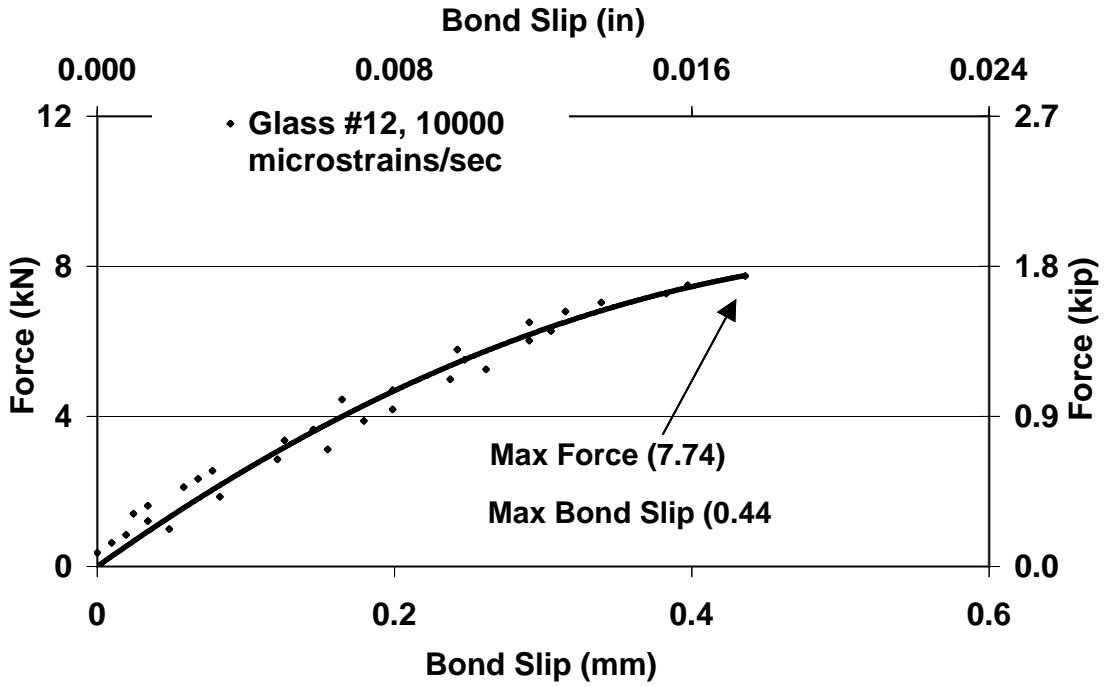


Figure 2-171: Force vs. bond slip for GFRP/concrete bond #12

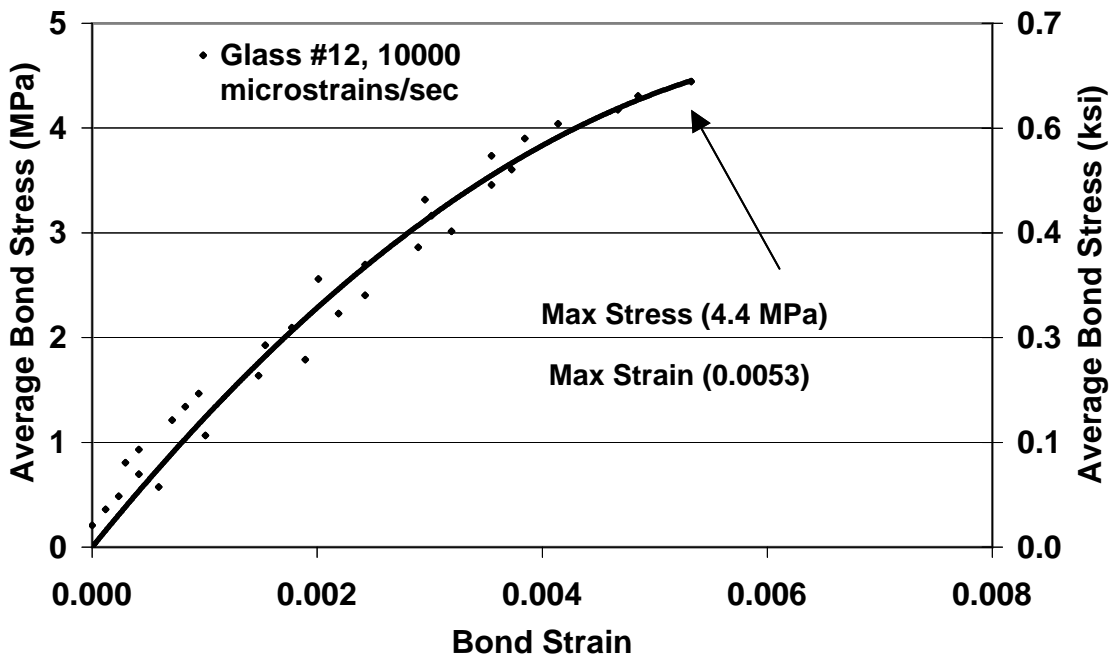


Figure 2-172: Average bond stress vs. bond strain, GFRP/concrete bond #12

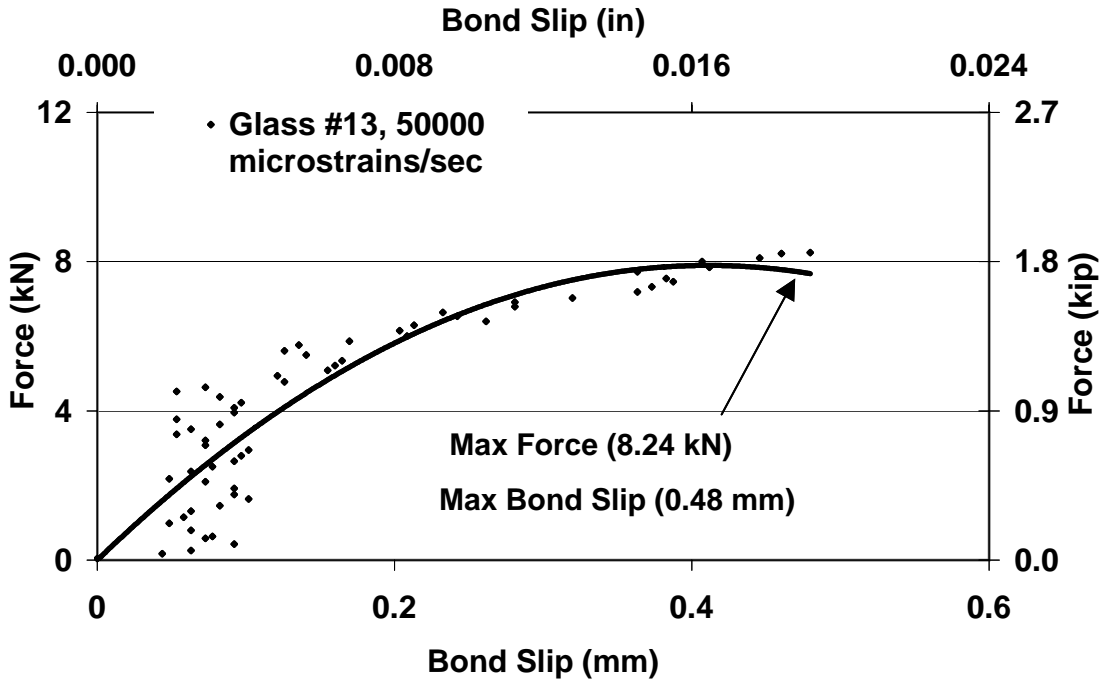


Figure 2-173: Force vs. bond slip for GFRP/concrete bond #13

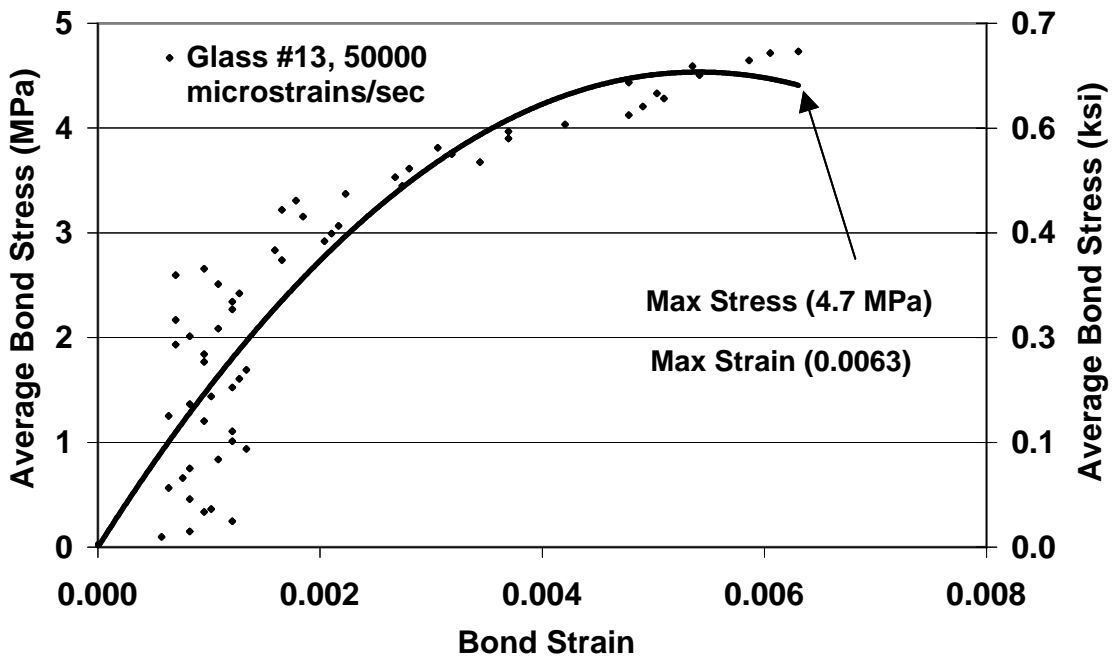


Figure 2-174: Average bond stress vs. bond strain, GFRP/concrete bond #13

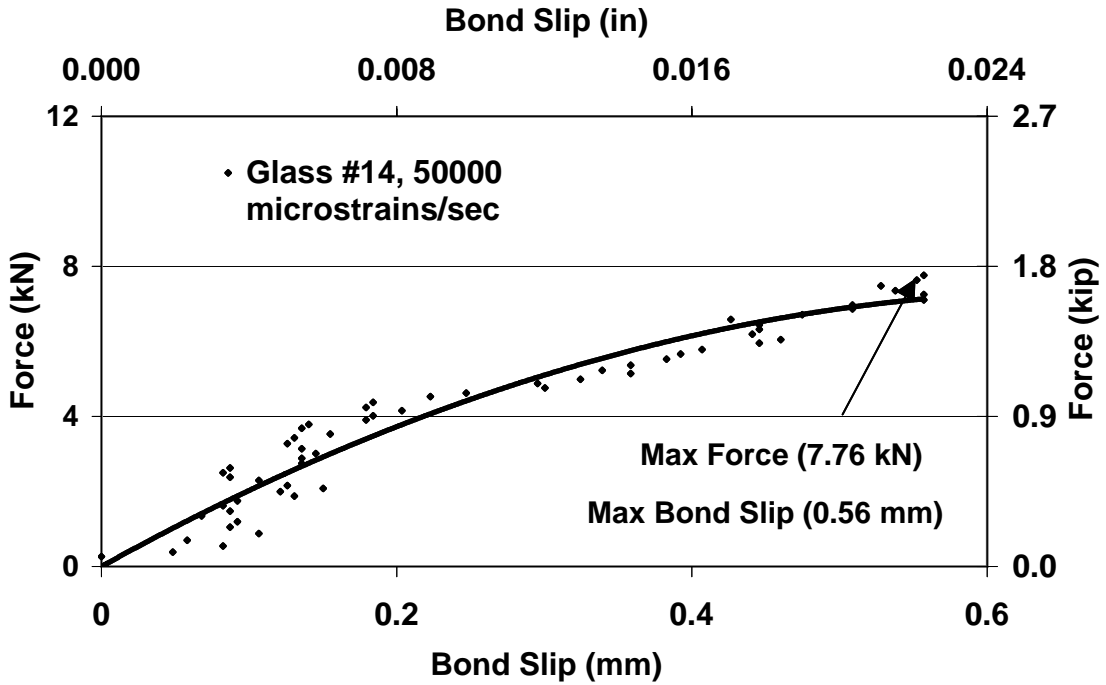


Figure 2-175: Force vs. bond slip for GFRP/concrete bond #14

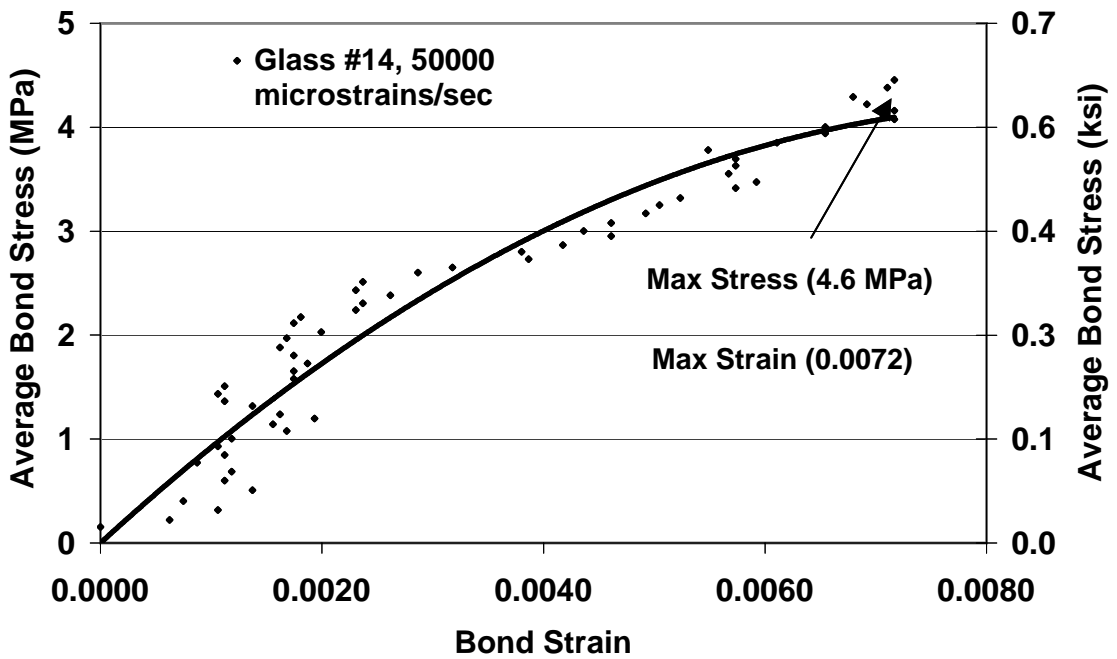


Figure 2-176: Average bond stress vs. bond strain, GFRP/concrete bond #14

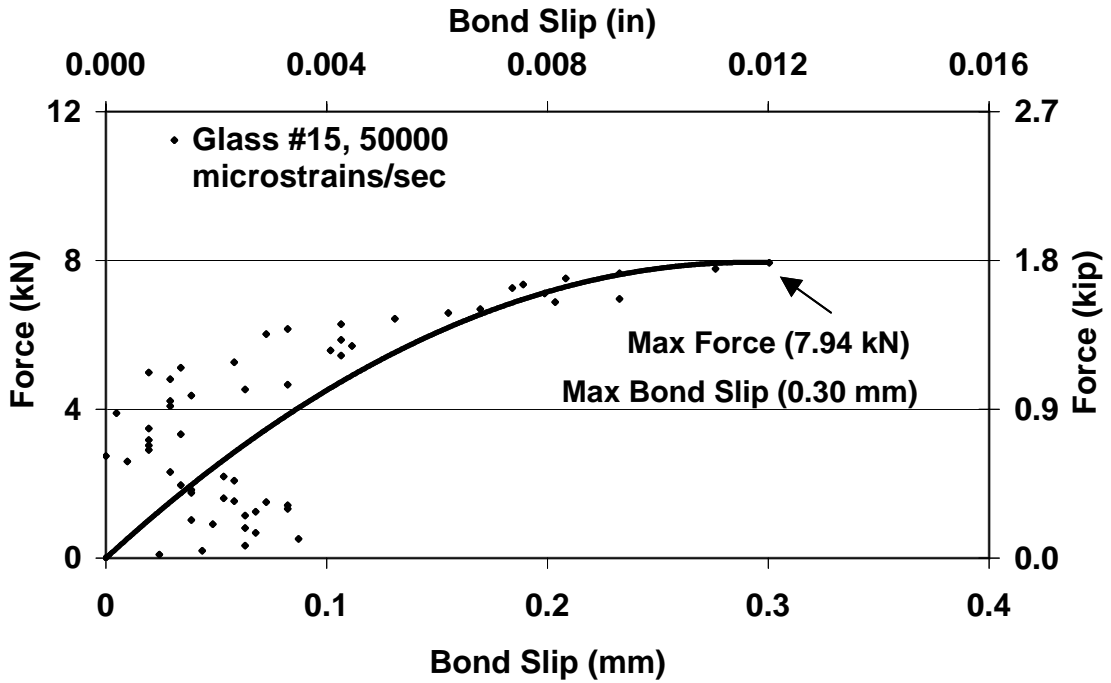


Figure 2-177: Force vs. bond slip for GFRP/concrete bond #15

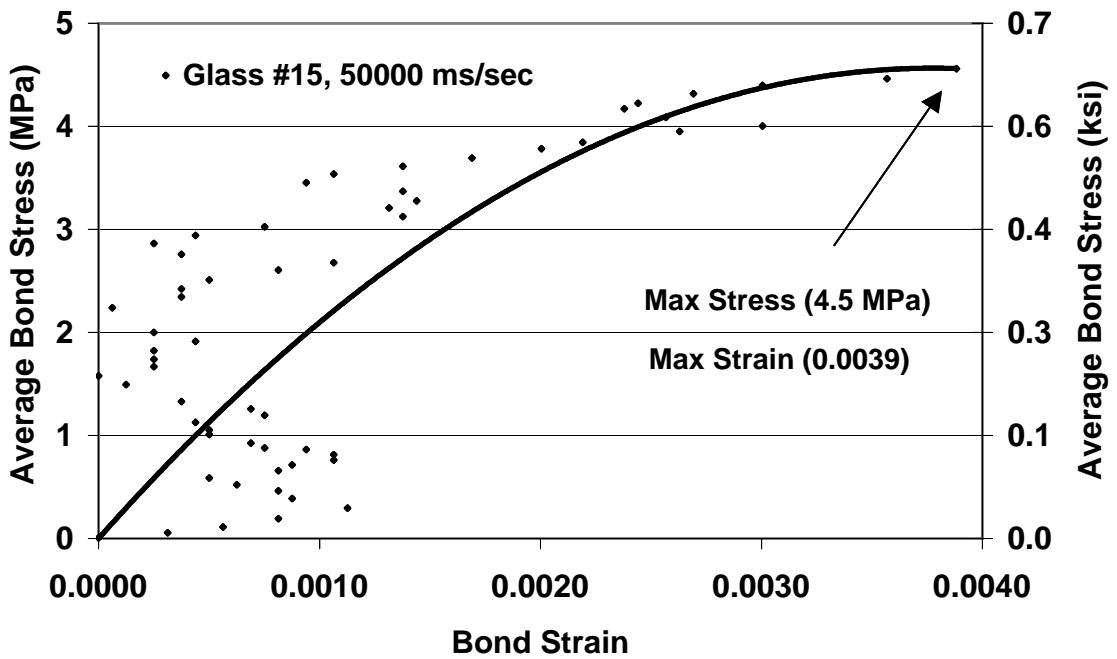


Figure 2-178: Average bond stress vs. bond strain, GFRP/concrete bond #15

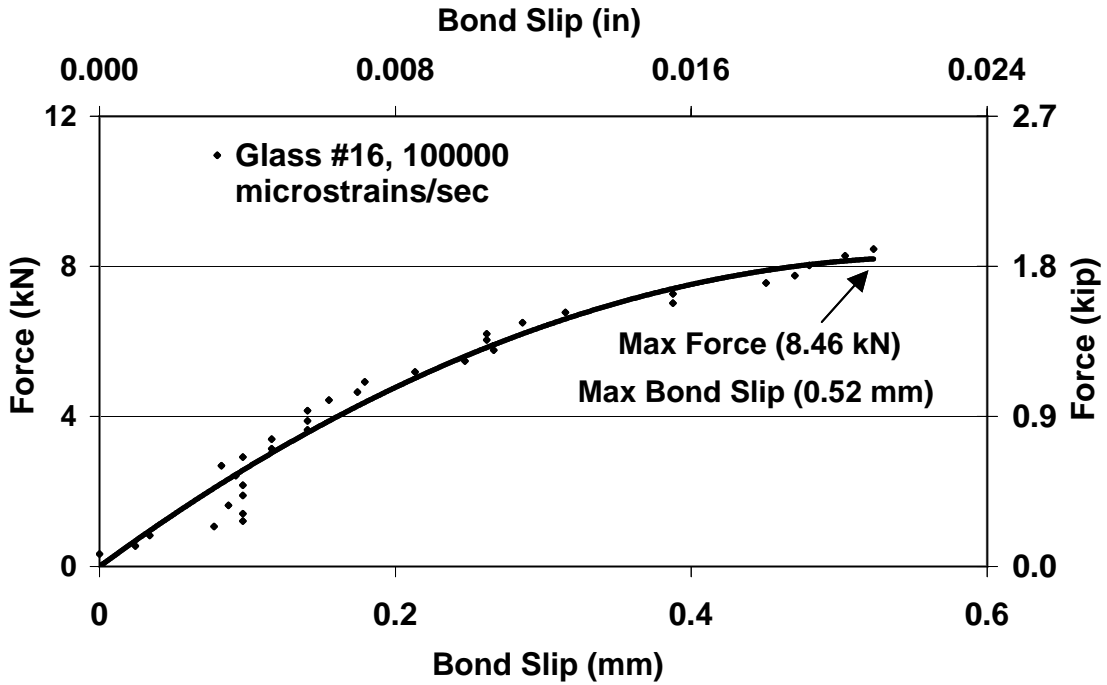


Figure 2-179: Force vs. bond slip for GFRP/concrete bond #16

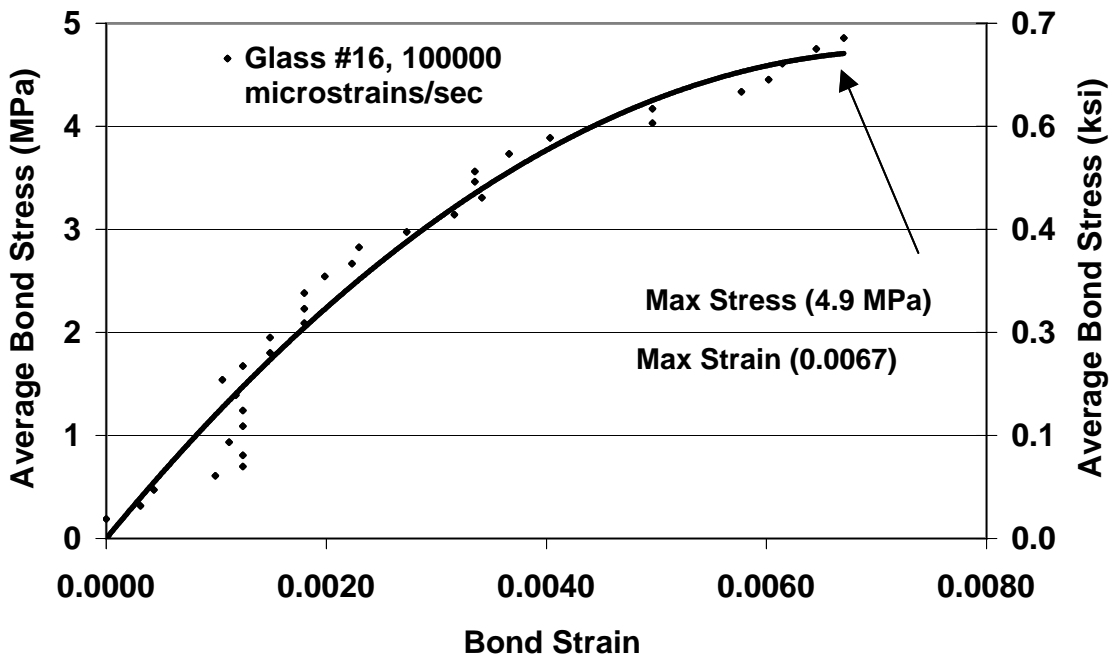


Figure 2-180: Average bond stress vs. bond strain, GFRP/concrete bond #16

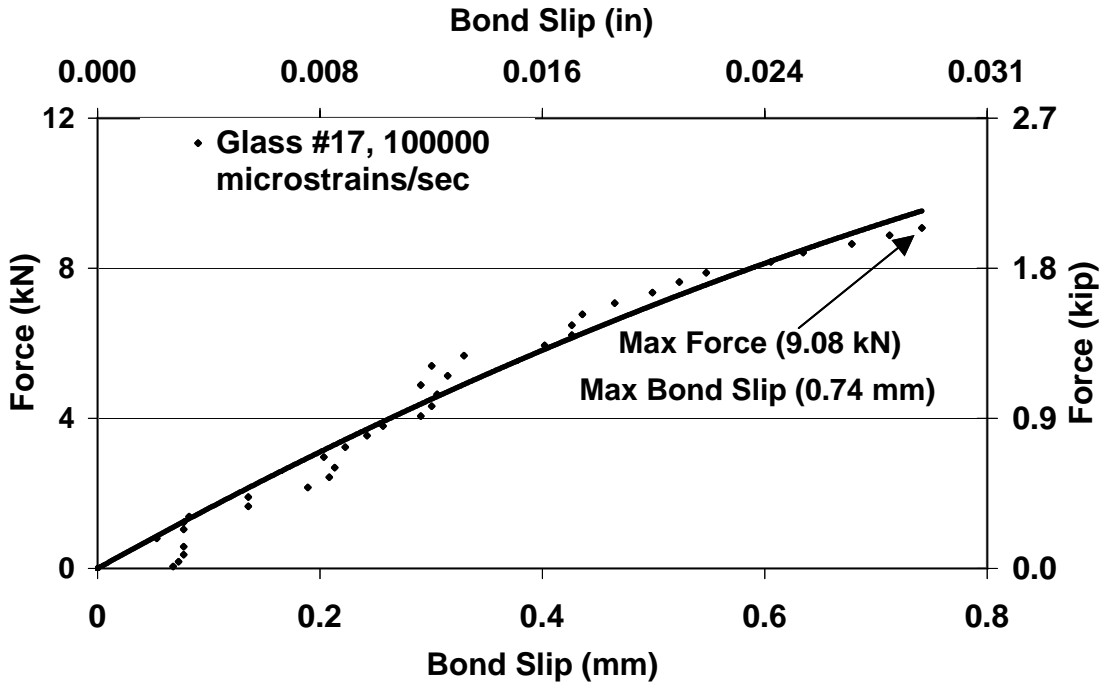


Figure 2-181: Force vs. bond slip for GFRP/concrete bond #17

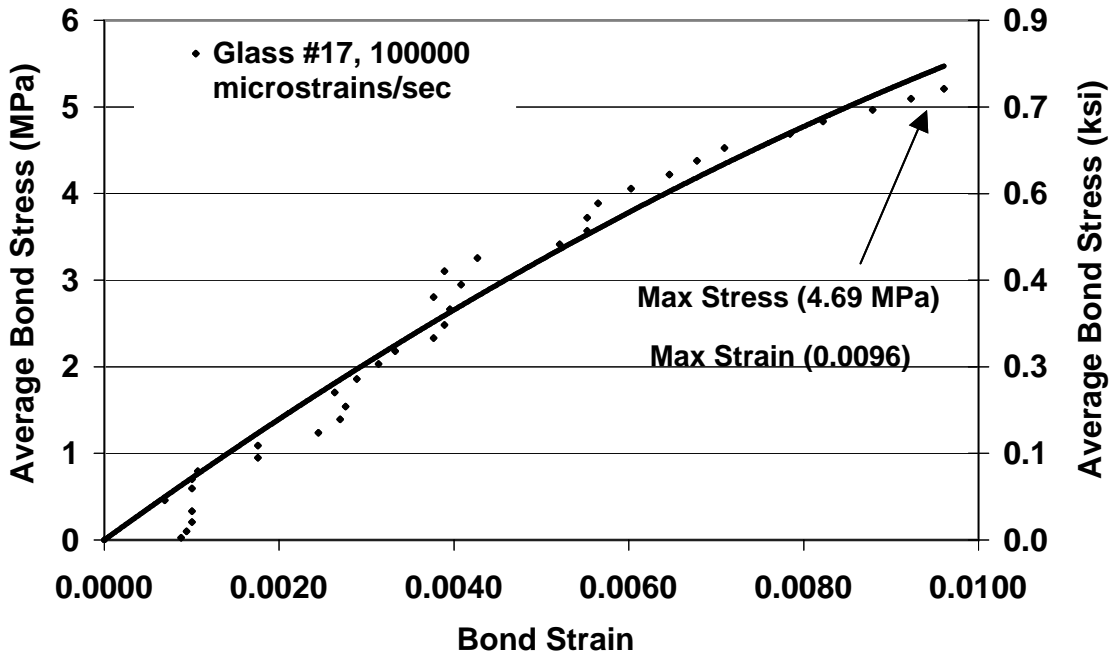


Figure 2-182: Average bond stress vs. bond strain, GFRP/concrete bond #17

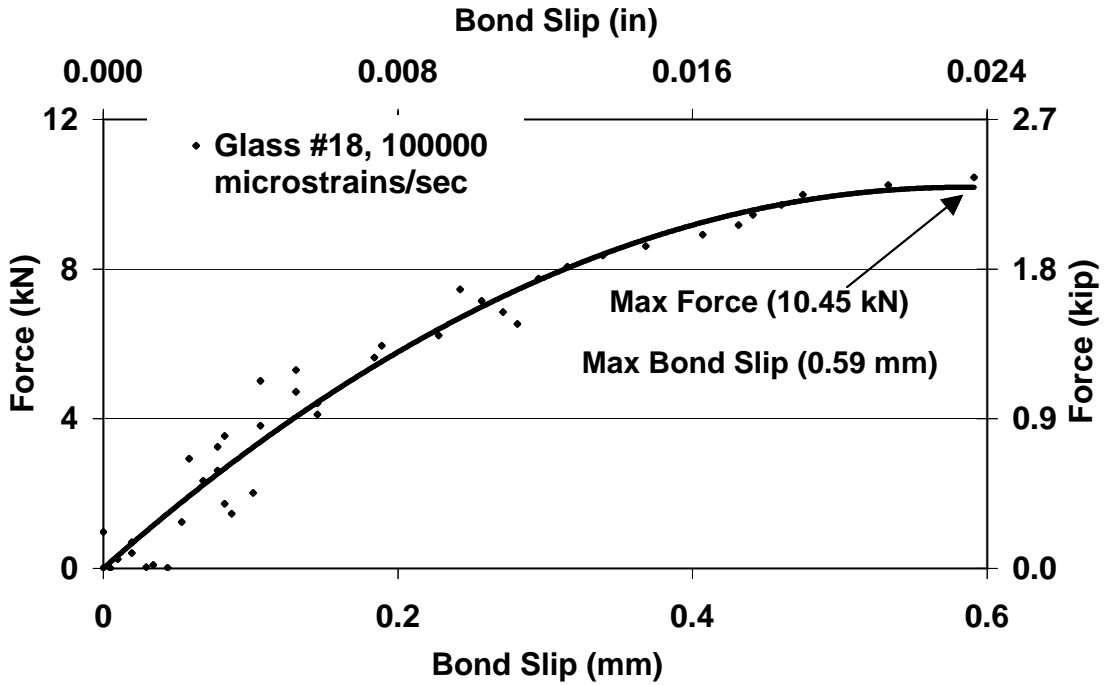


Figure 2-183: Force vs. bond slip for GFRP/concrete bond #18

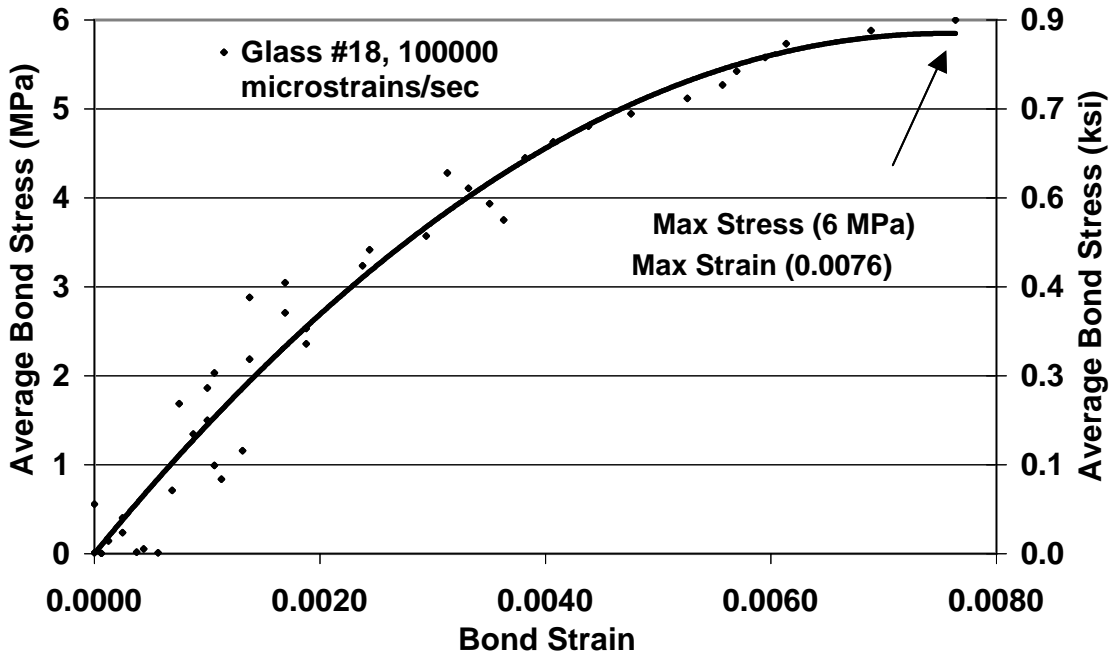


Figure 2-184: Average bond stress vs. bond strain, GFRP/concrete bond #18

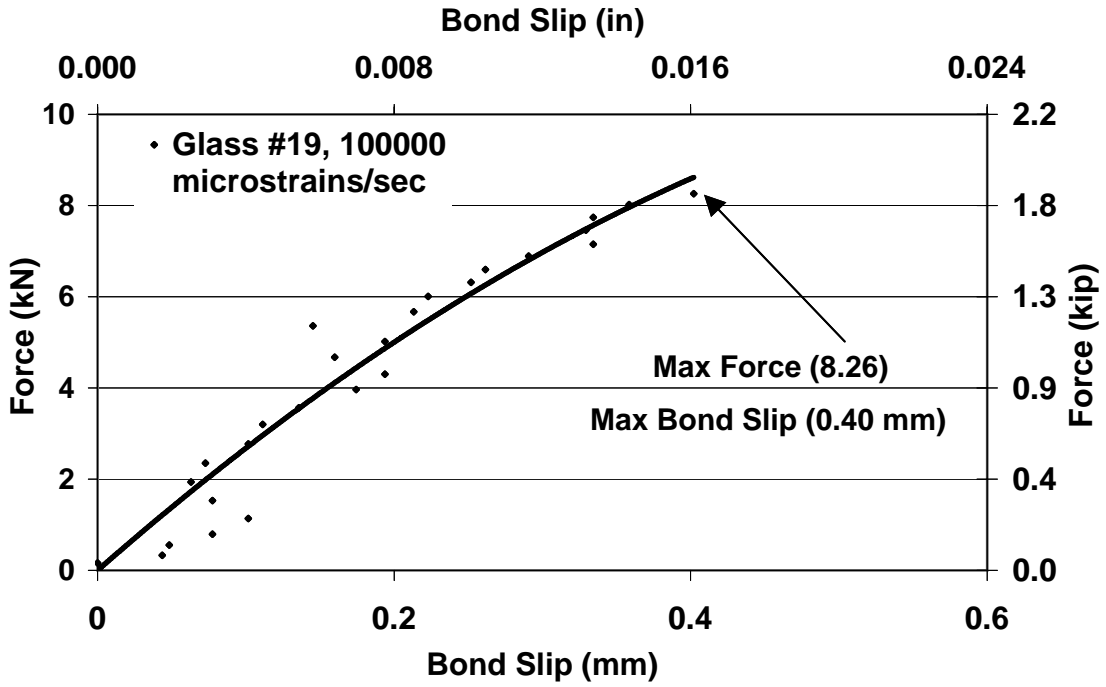


Figure 2-185: Force vs. bond slip for GFRP/concrete bond #19

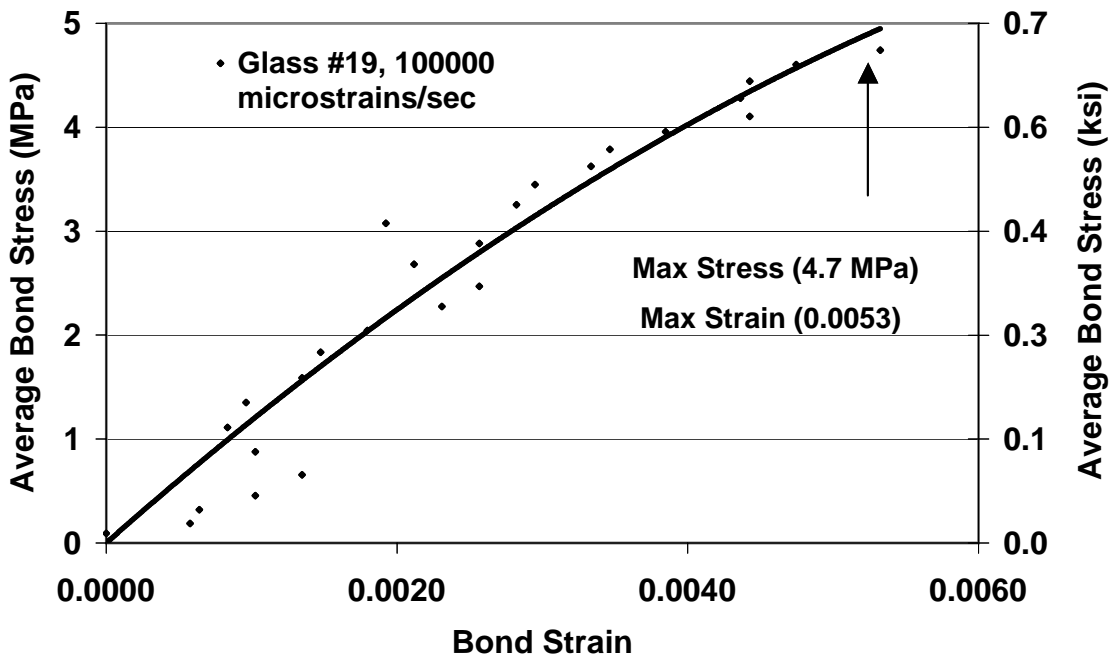


Figure 2-186: Average bond stress vs. bond strain, GFRP/concrete bond #19

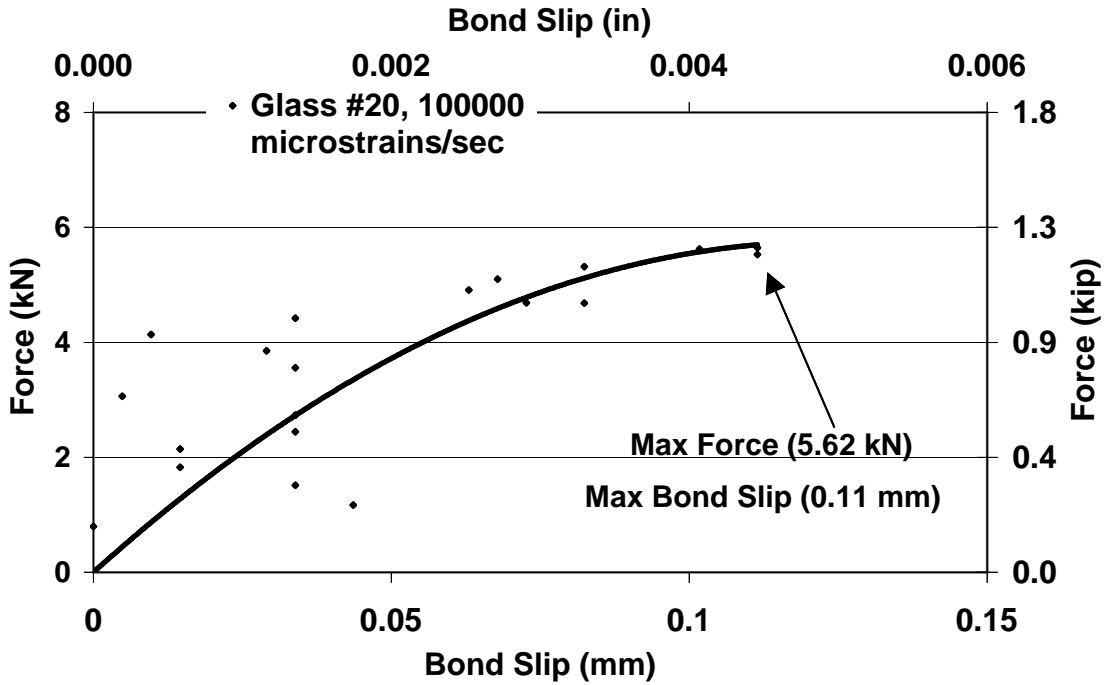


Figure 2-187: Force vs. bond slip for GFRP/concrete bond #20

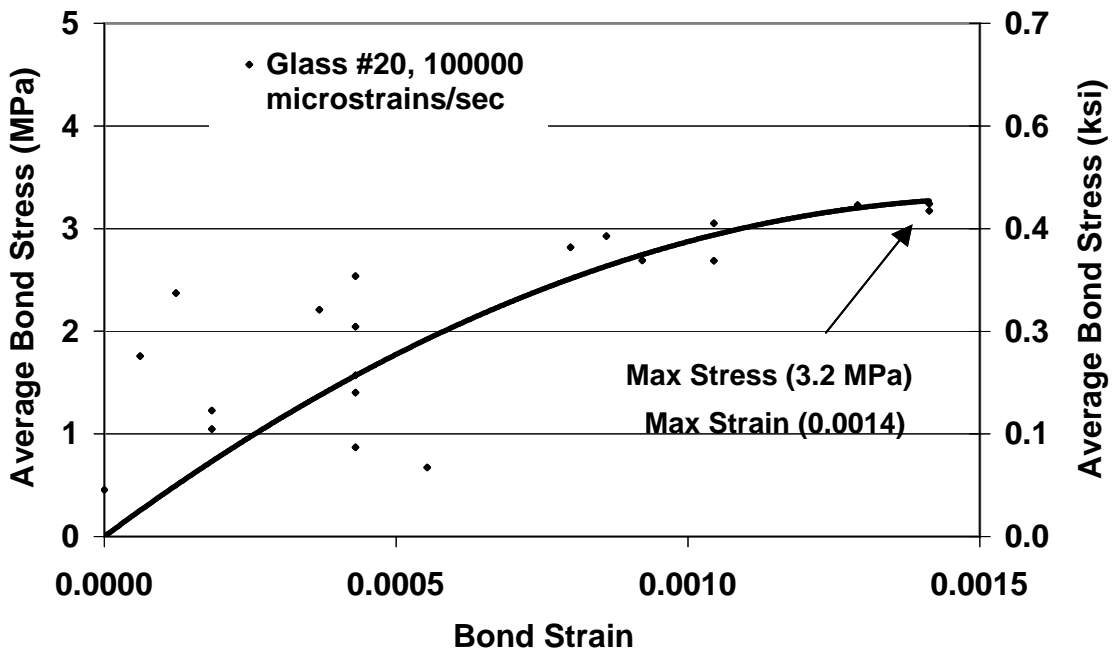


Figure 2-188: Average bond stress vs. bond strain, GFRP/concrete bond #20

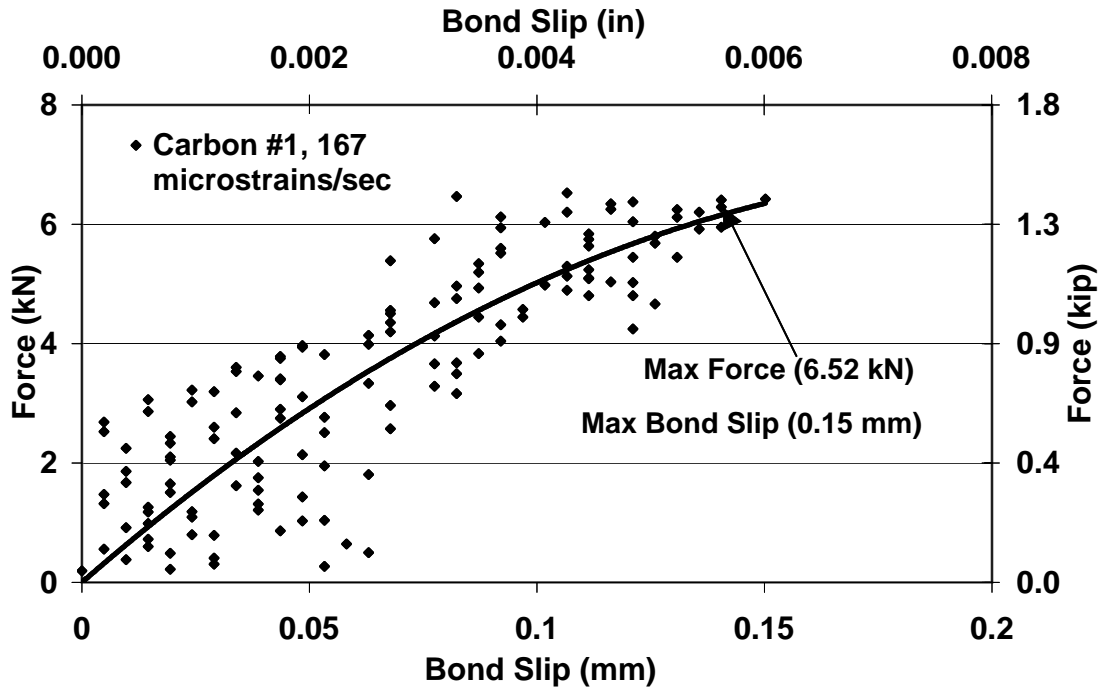


Figure 2-189: Force vs. bond slip for CFRP/concrete bond #1

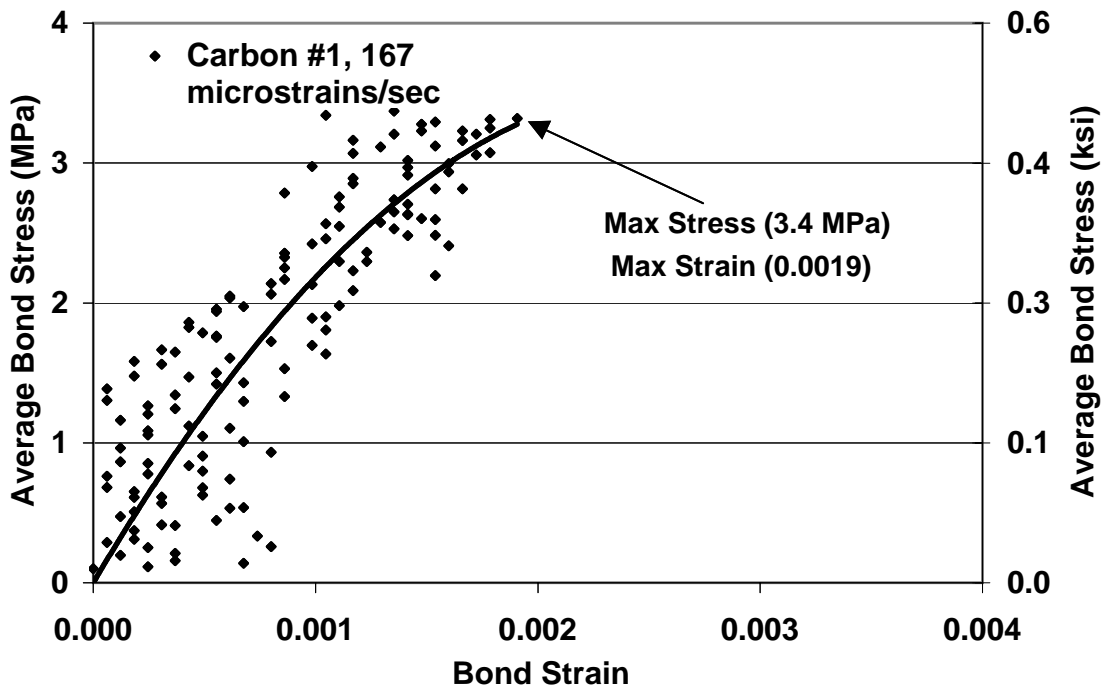


Figure 2-190: Average bond stress vs. bond strain, CFRP/concrete bond #1

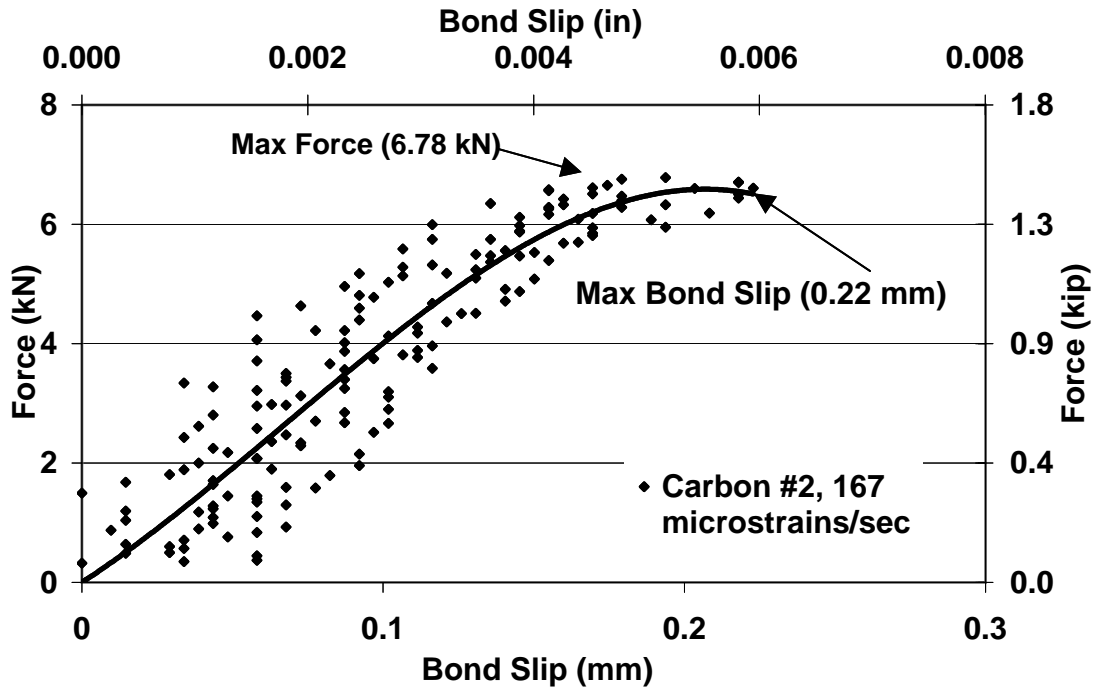


Figure 2-191: Force vs. bond slip for CFRP/concrete bond #2

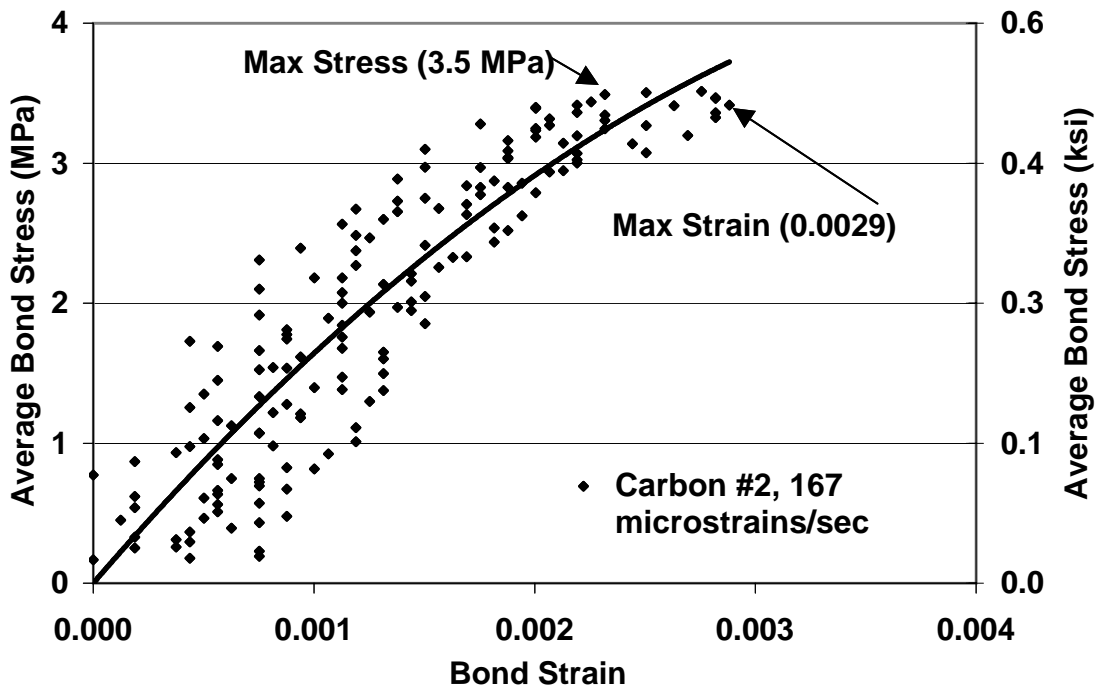


Figure 2-192: Average bond stress vs. bond strain, CFRP/concrete bond #2

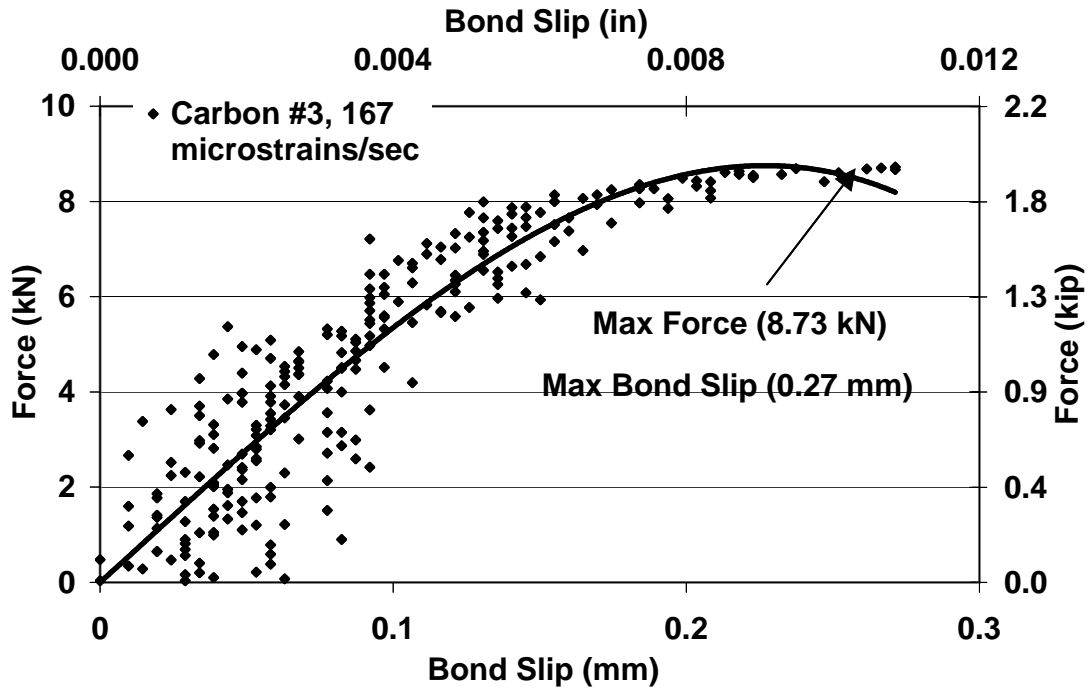


Figure 2-193: Force vs. bond slip for CFRP/concrete bond #3

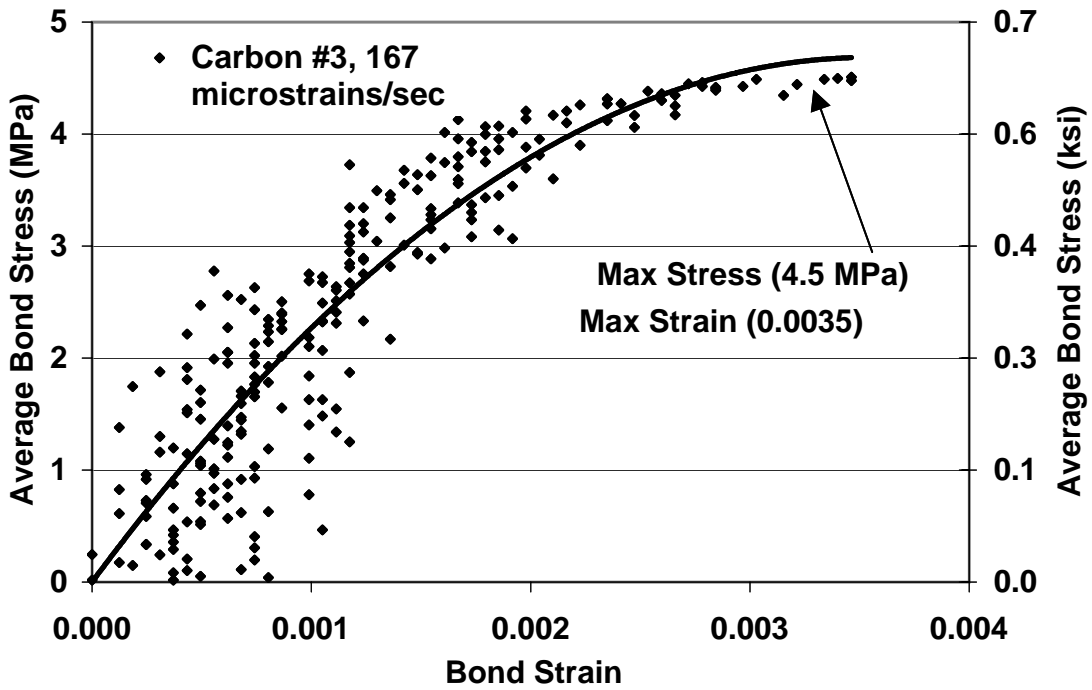


Figure 2-194: Average bond stress vs. bond strain, CFRP/concrete bond #3

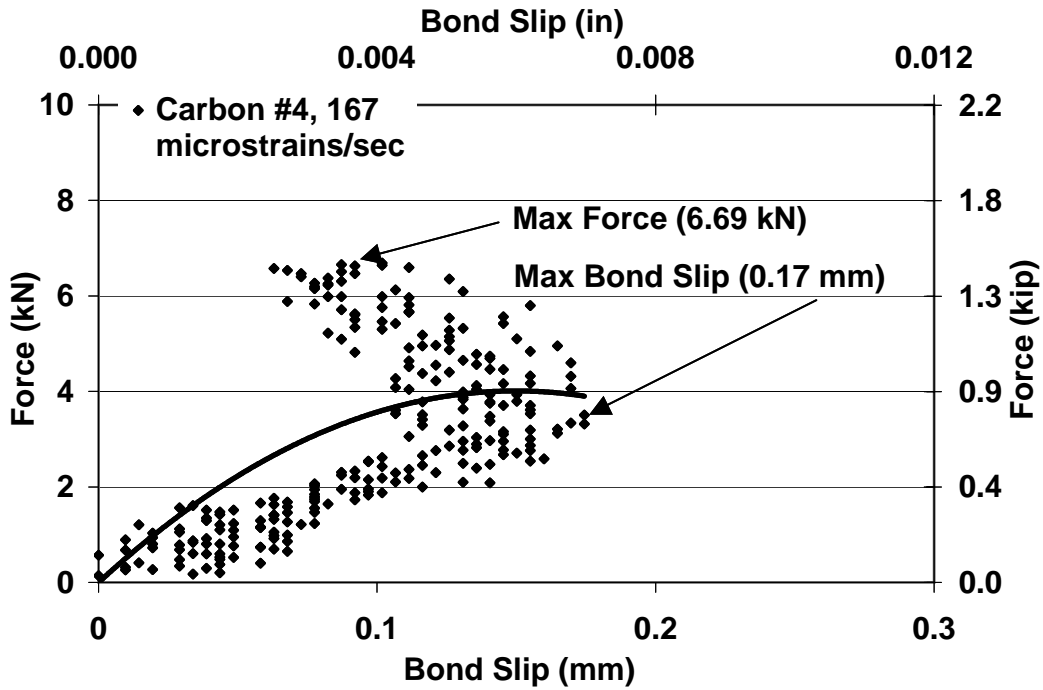


Figure 2-195: Force vs. bond slip for CFRP/concrete bond #4

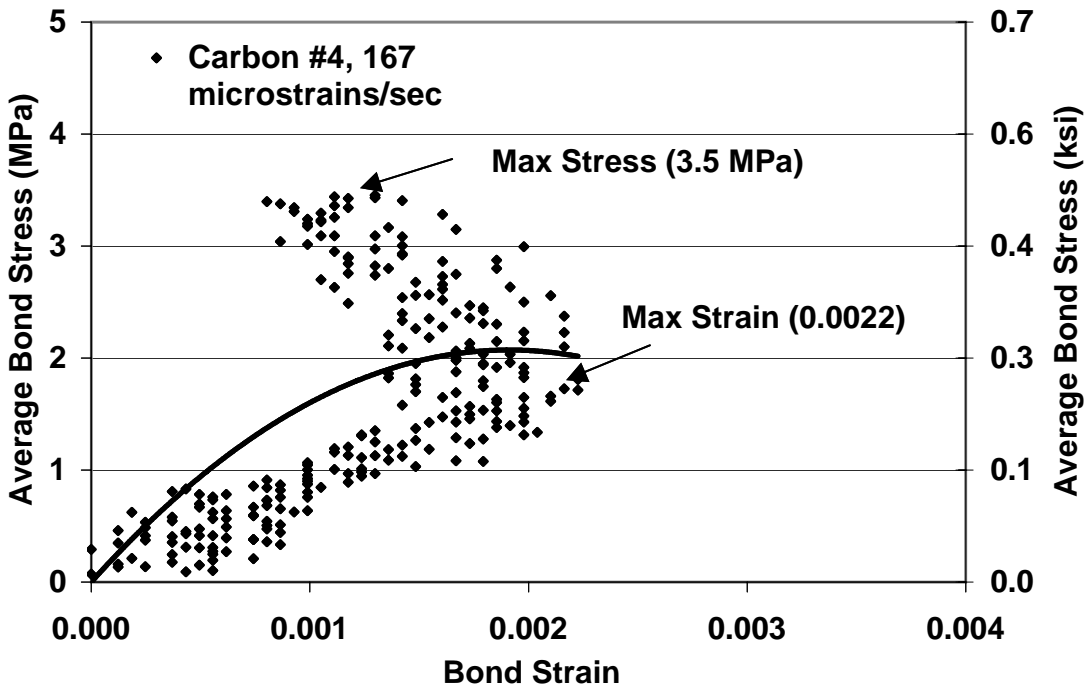


Figure 2-196: Average bond stress vs. bond strain, CFRP/concrete bond #4

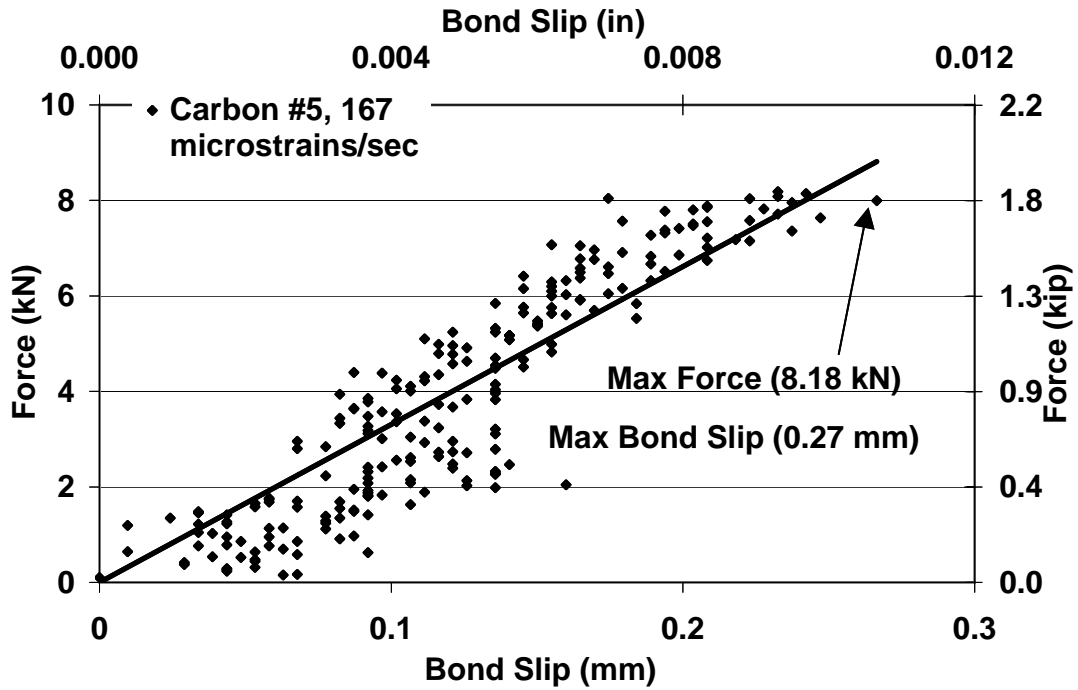


Figure 2-197: Force vs. bond slip for CFRP/concrete bond #5

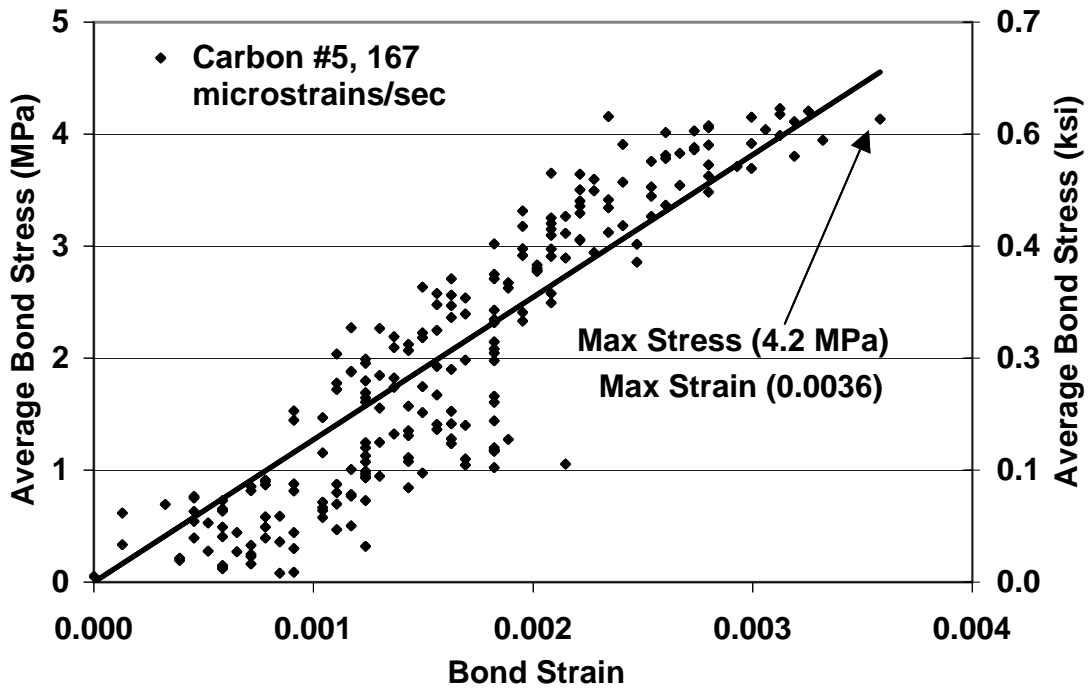


Figure 2-198: Average bond stress vs. bond strain, CFRP/concrete bond #5

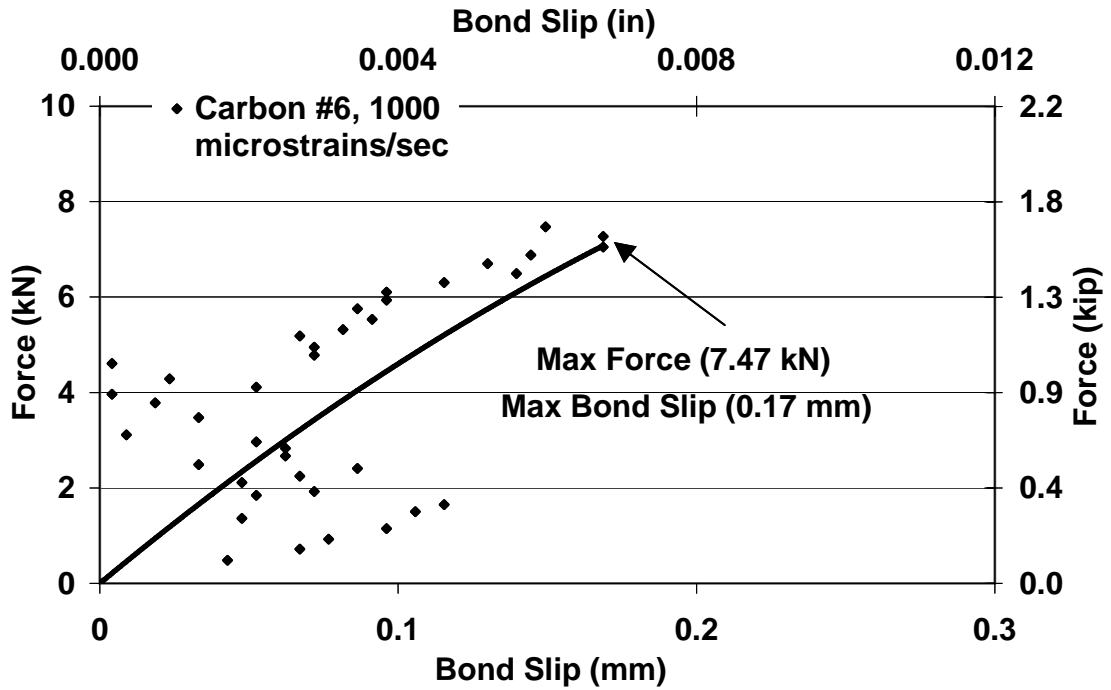


Figure 2-199: Force vs. bond slip for CFRP/concrete bond #6

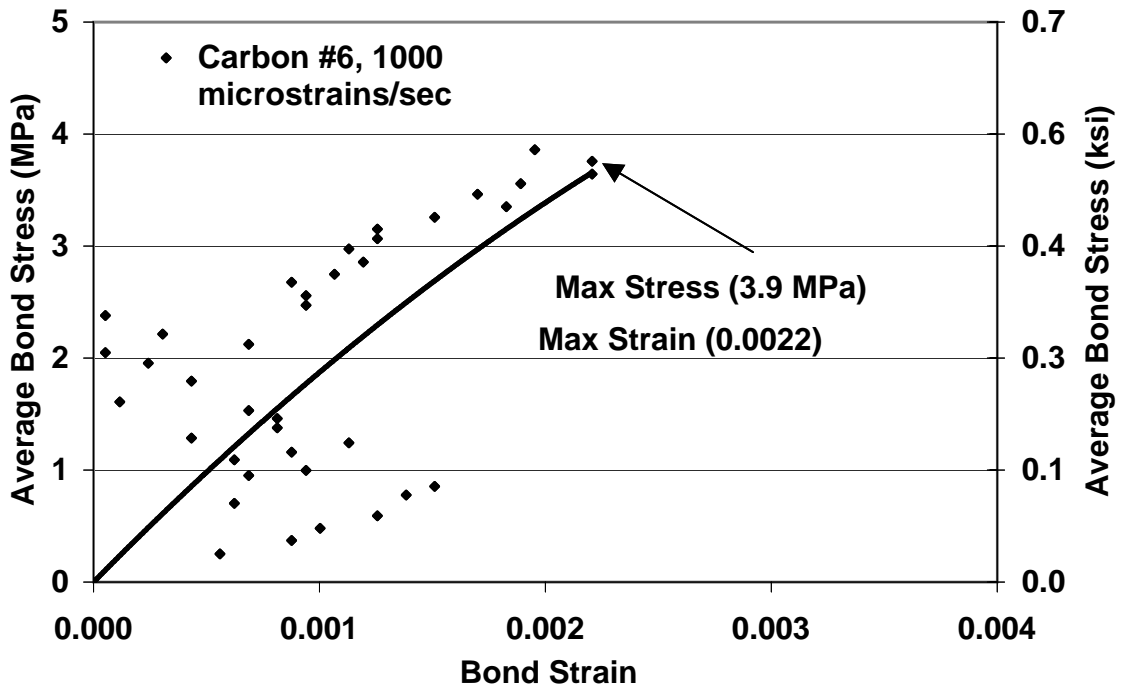


Figure 2-200: Average bond stress vs. bond strain, CFRP/concrete bond #6

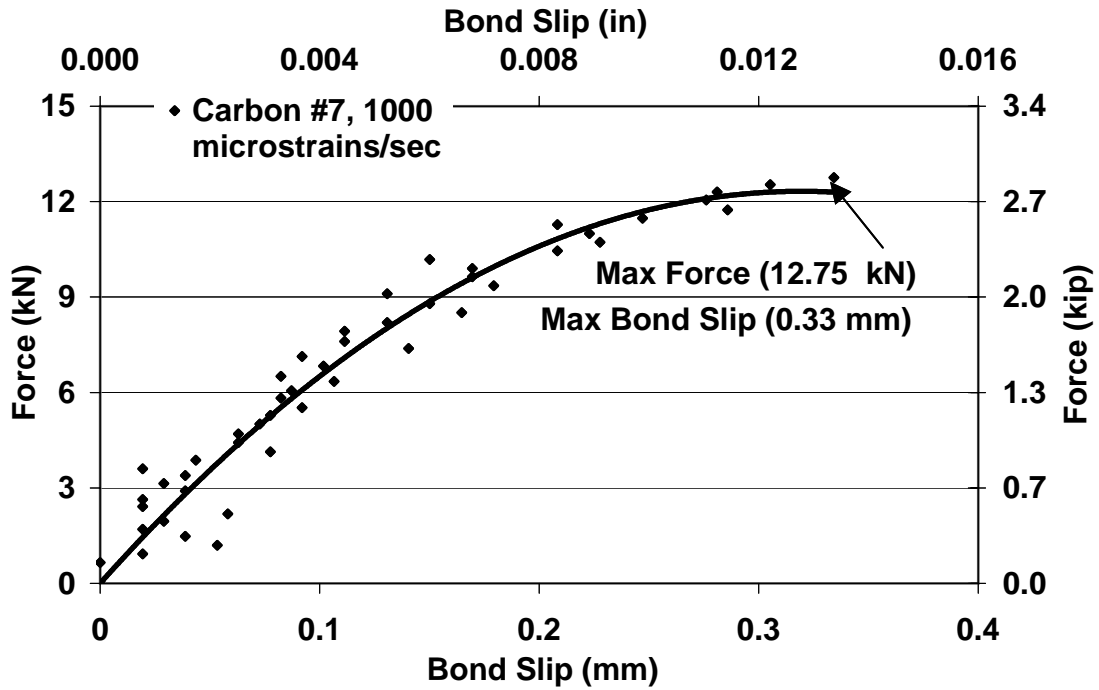


Figure 2-201: Force vs. bond slip for CFRP/concrete bond #7

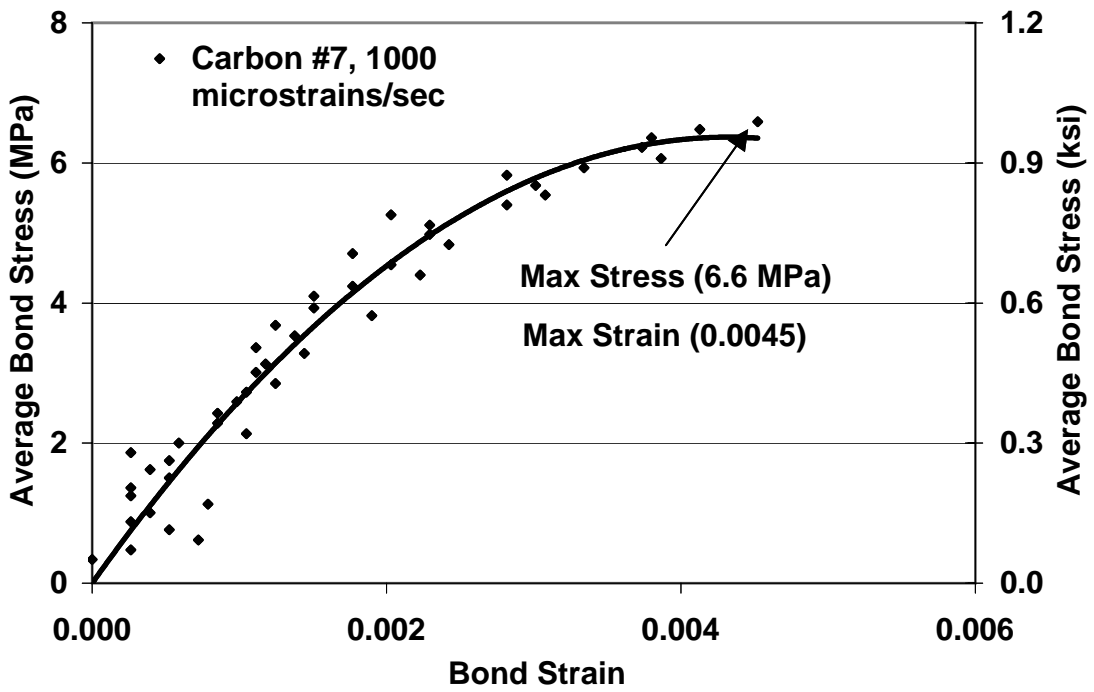


Figure 2-202: Average bond stress vs. bond strain, CFRP/concrete bond #7

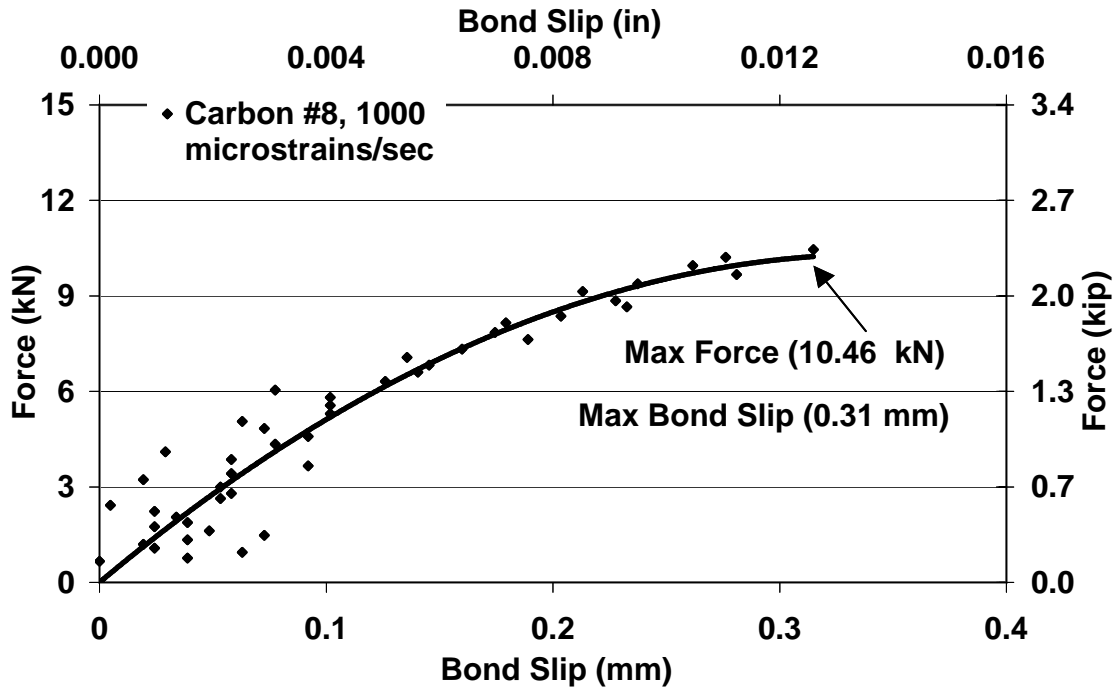


Figure 2-203: Force vs. bond slip for CFRP/concrete bond #8

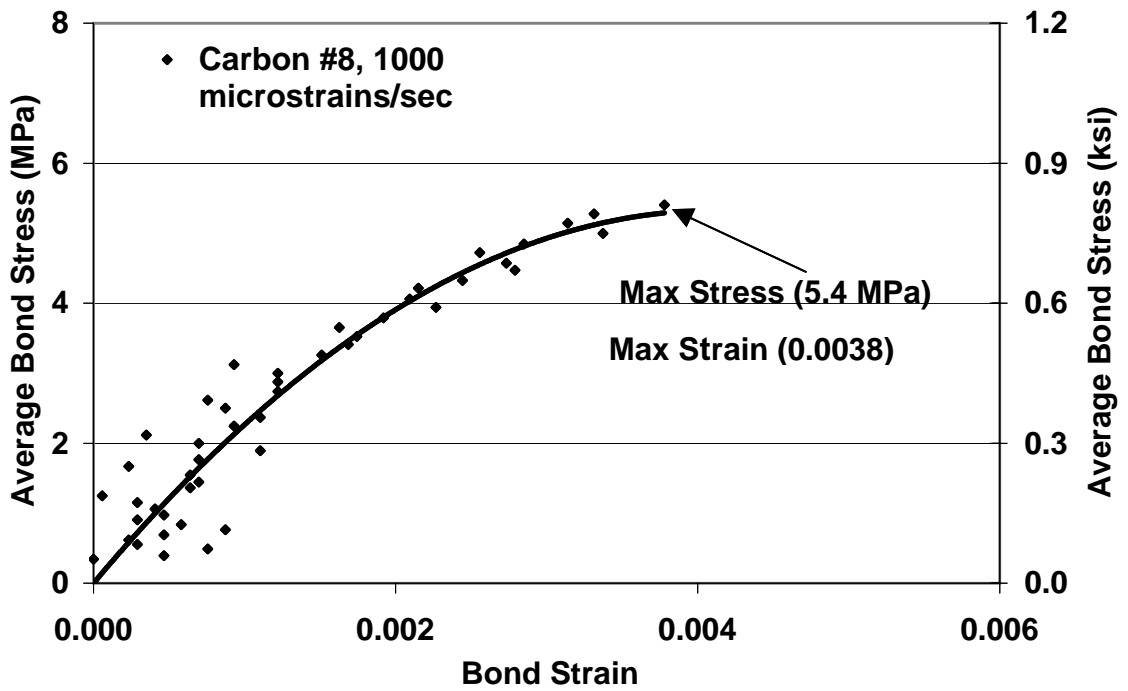


Figure 2-204: Average bond stress vs. bond strain, CFRP/concrete bond #8

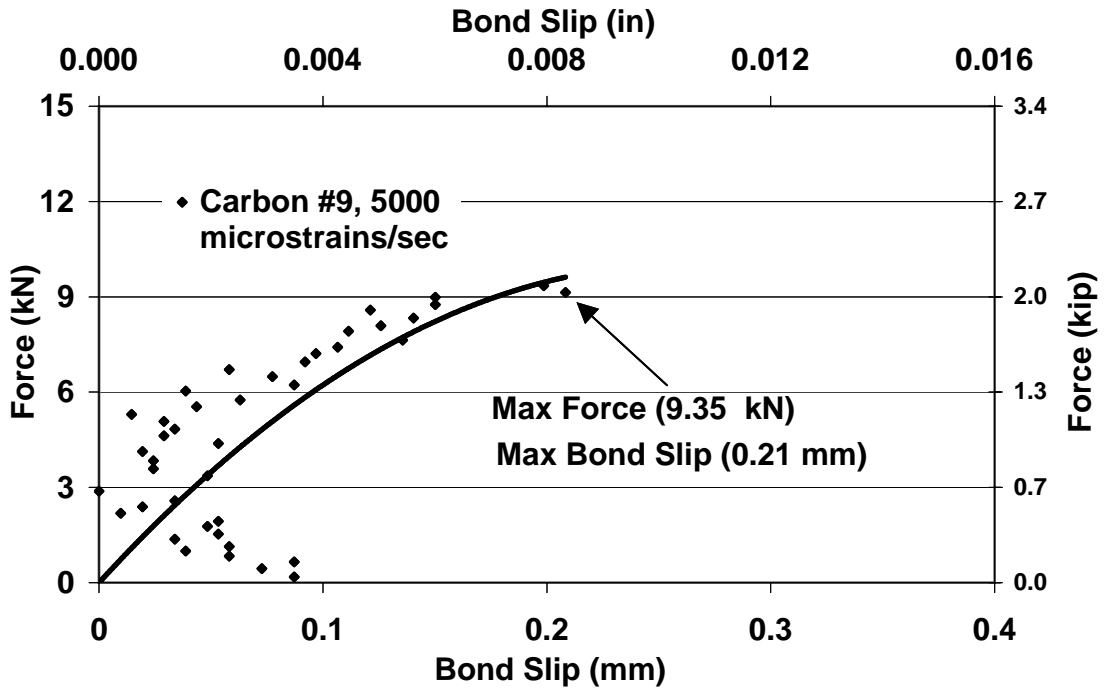


Figure 2-205: Force vs. bond slip for CFRP/concrete bond #9

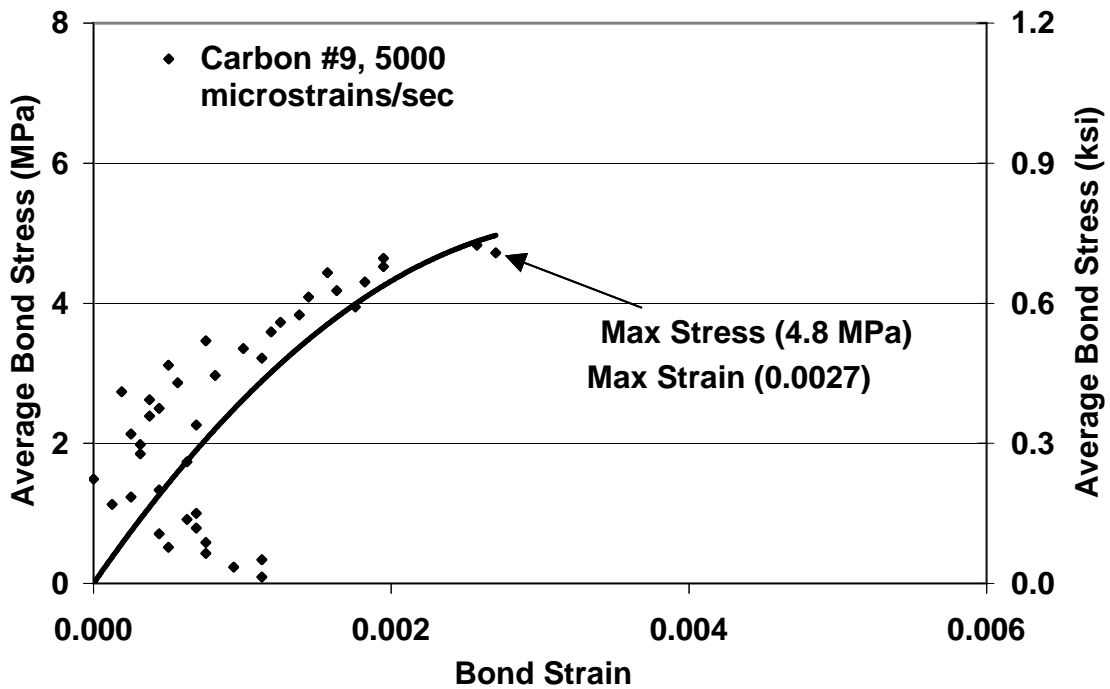


Figure 2-206: Average bond stress vs. bond strain, CFRP/concrete bond #9

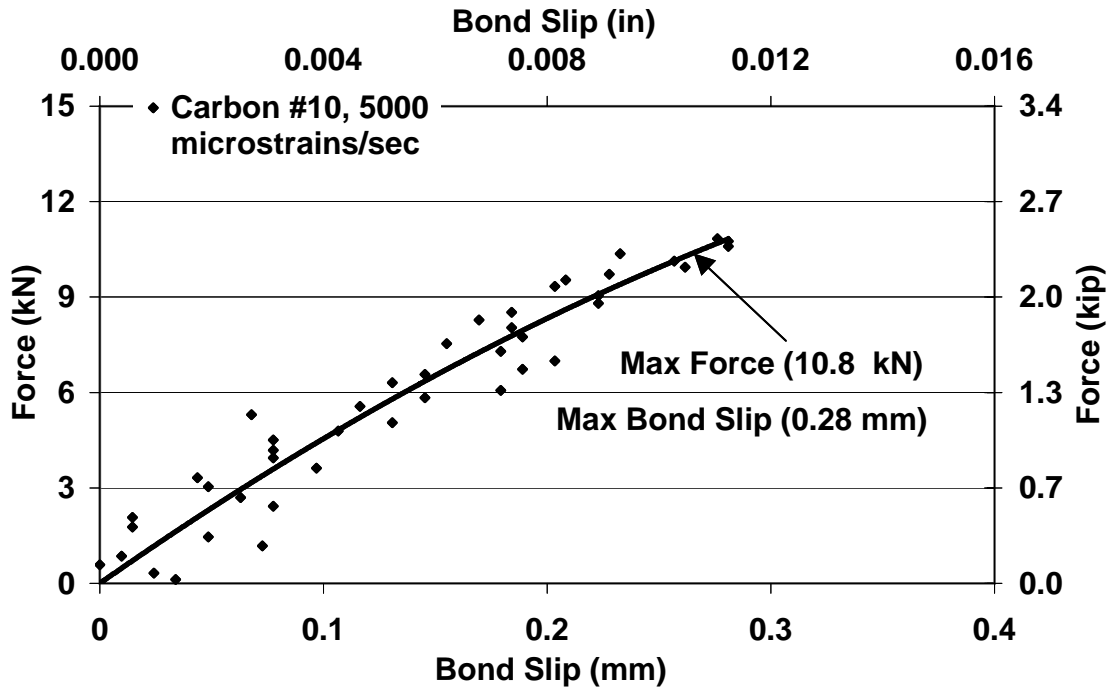


Figure 2-207: Force vs. bond slip for CFRP/concrete bond #10

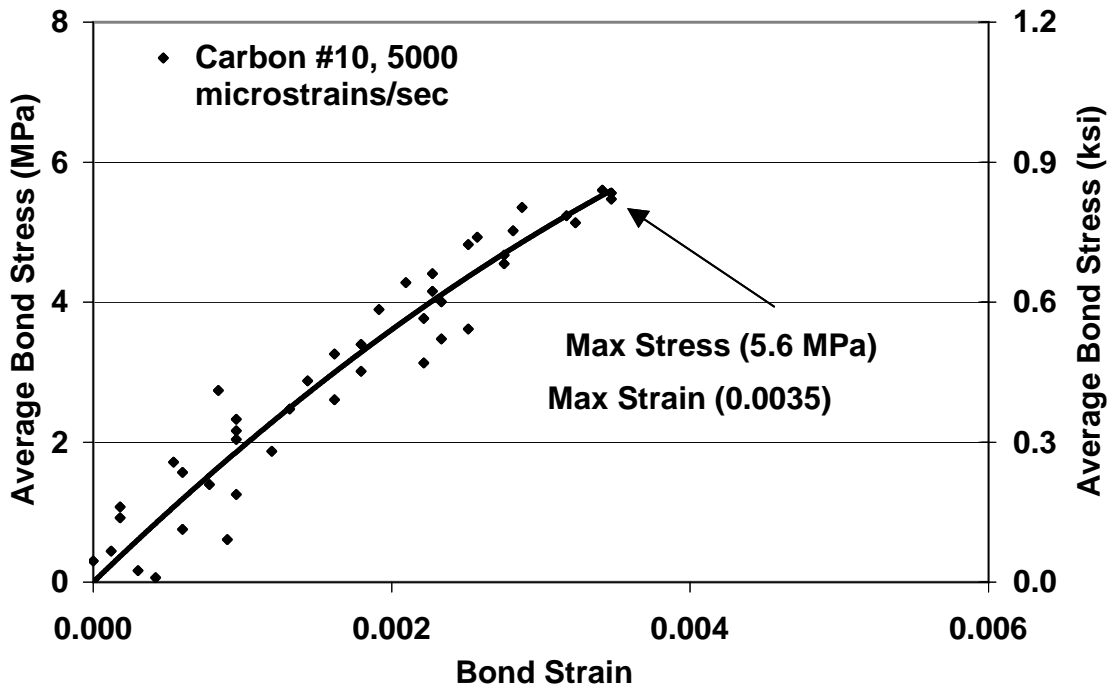


Figure 2-208: Average bond stress vs. bond strain, CFRP/concrete bond #10

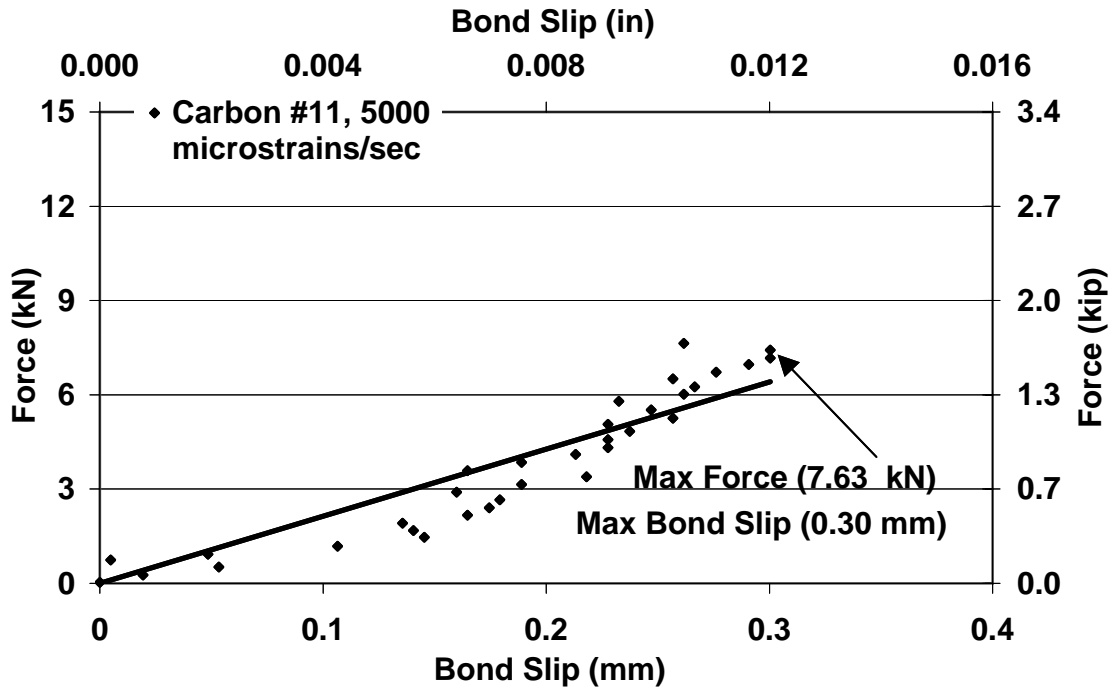


Figure 2-209: Force vs. bond slip for CFRP/concrete bond #11

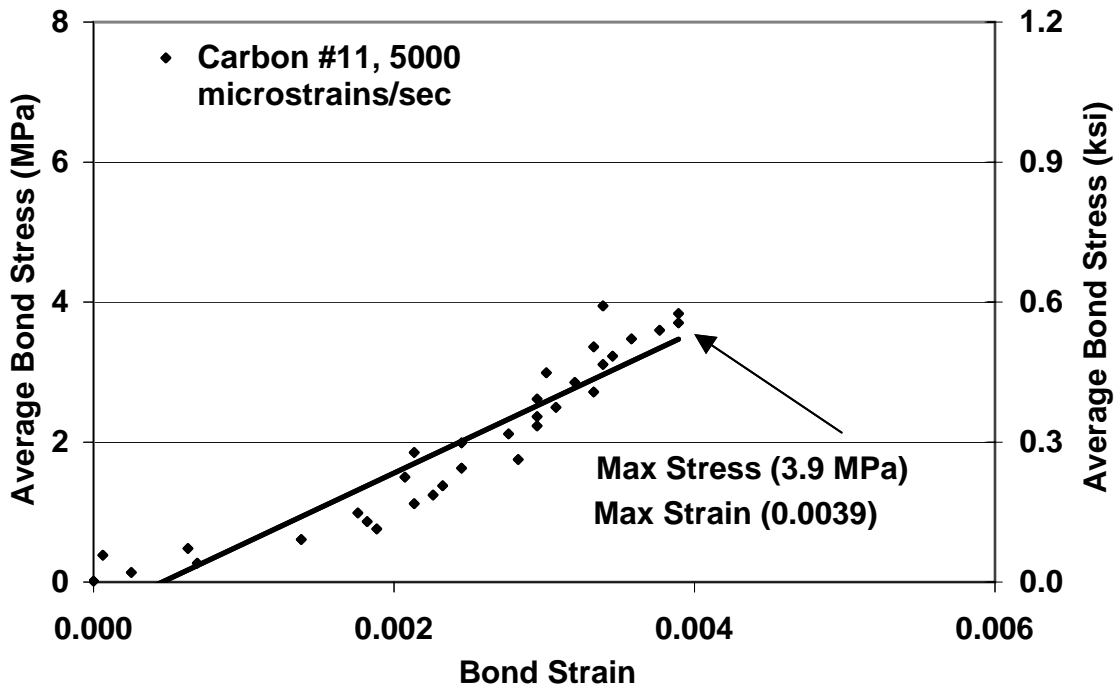


Figure 2-210: Average bond stress vs. bond strain, CFRP/concrete bond #11

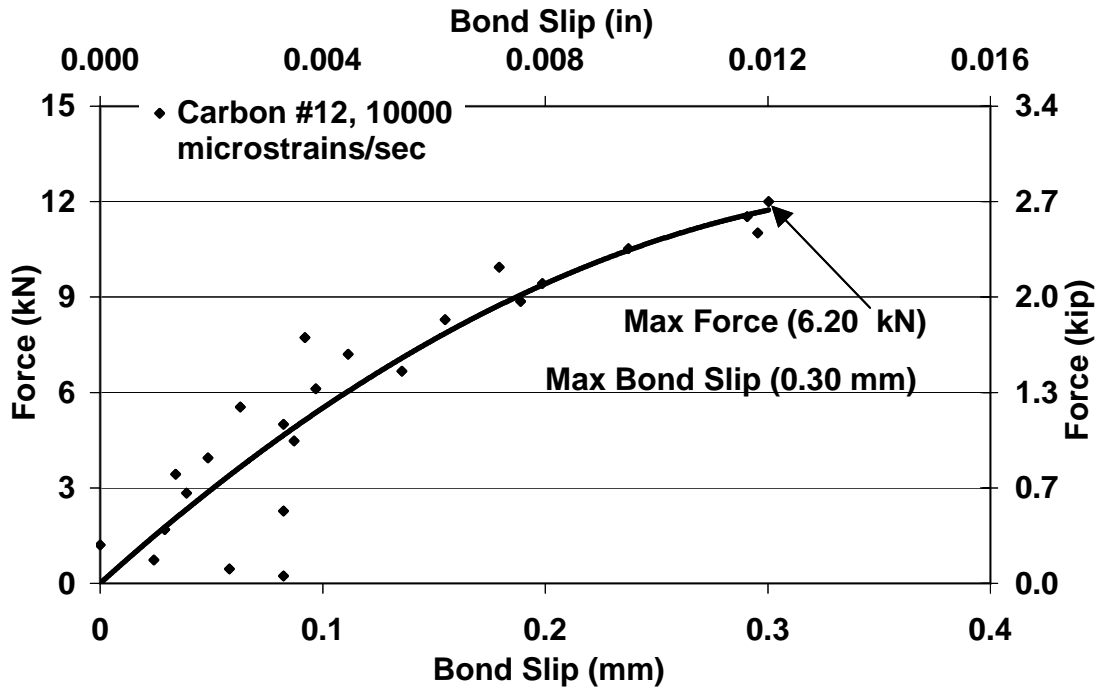


Figure 2-211: Force vs. bond slip for CFRP/concrete bond #12

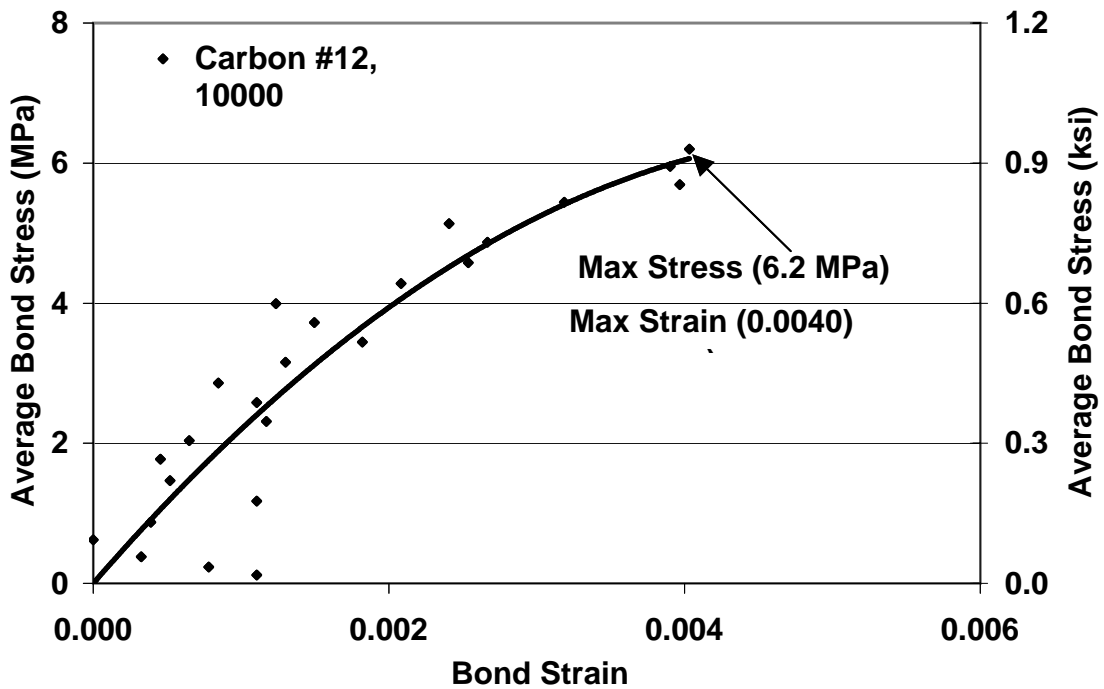


Figure 2-212: Average bond stress vs. bond strain, CFRP/concrete bond #12

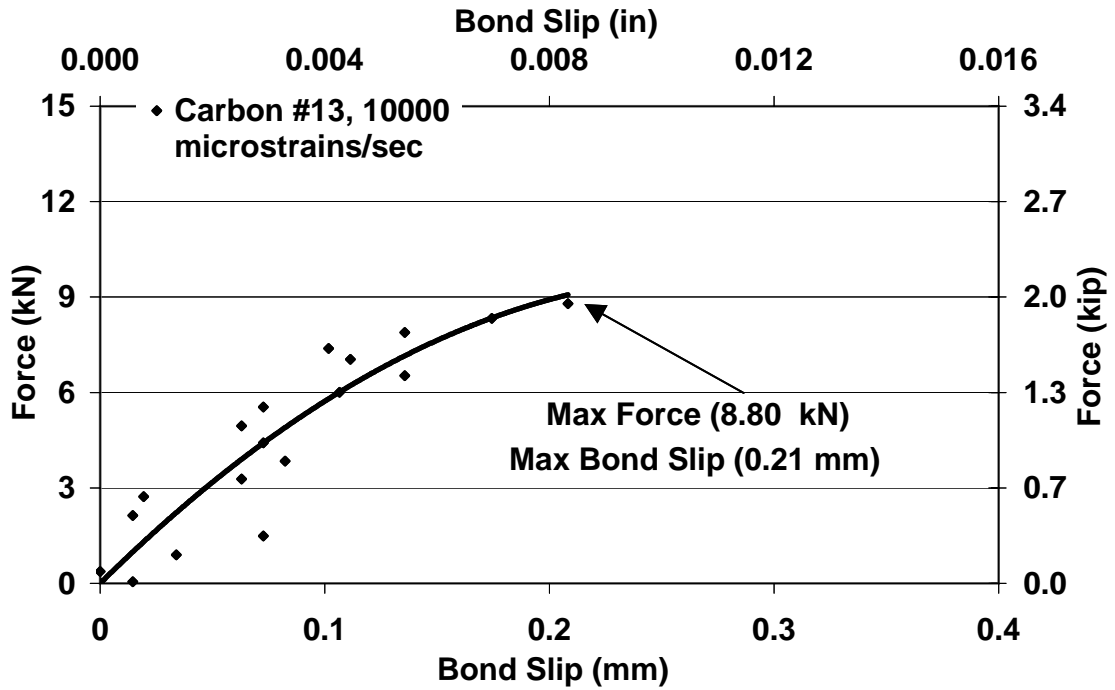


Figure 2-213: Force vs. bond slip for CFRP/concrete bond #13

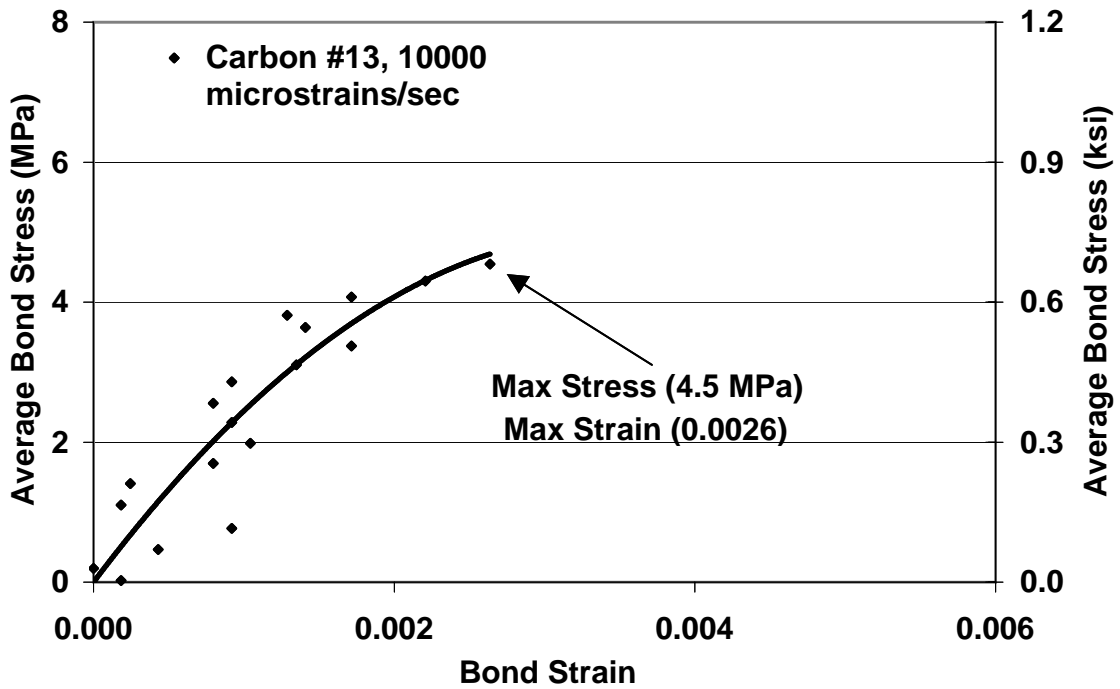


Figure 2-214: Average bond stress vs. bond strain, CFRP/concrete bond #13

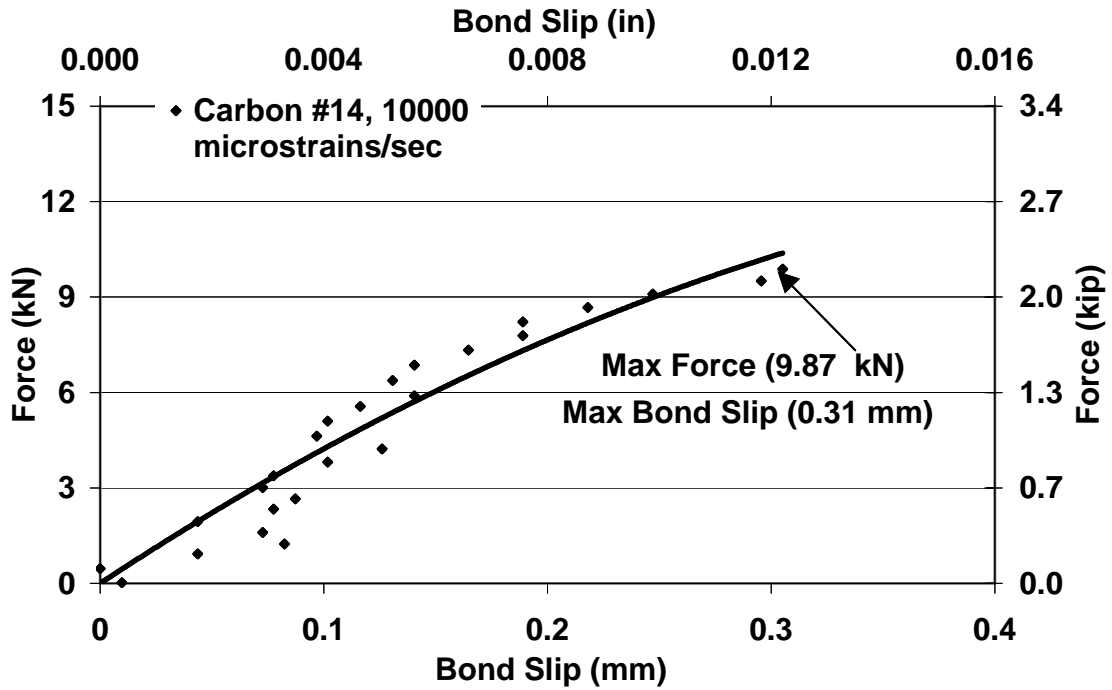


Figure 2-215: Force vs. bond slip for CFRP/concrete bond #14

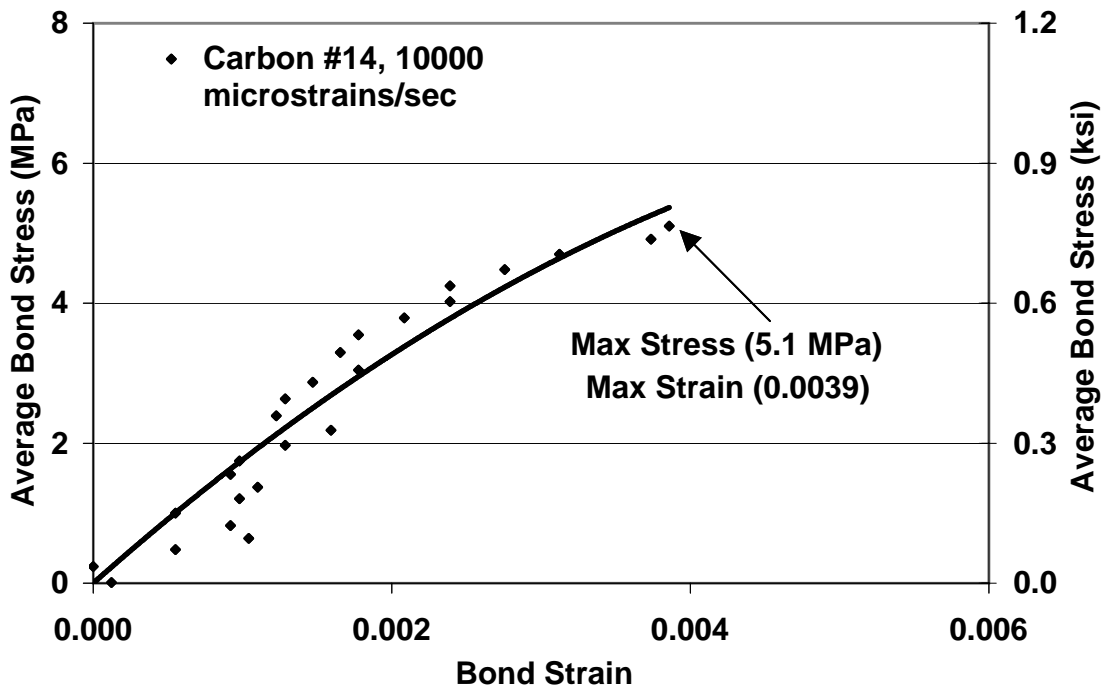


Figure 2-216: Average bond stress vs. bond strain, CFRP/concrete bond #14

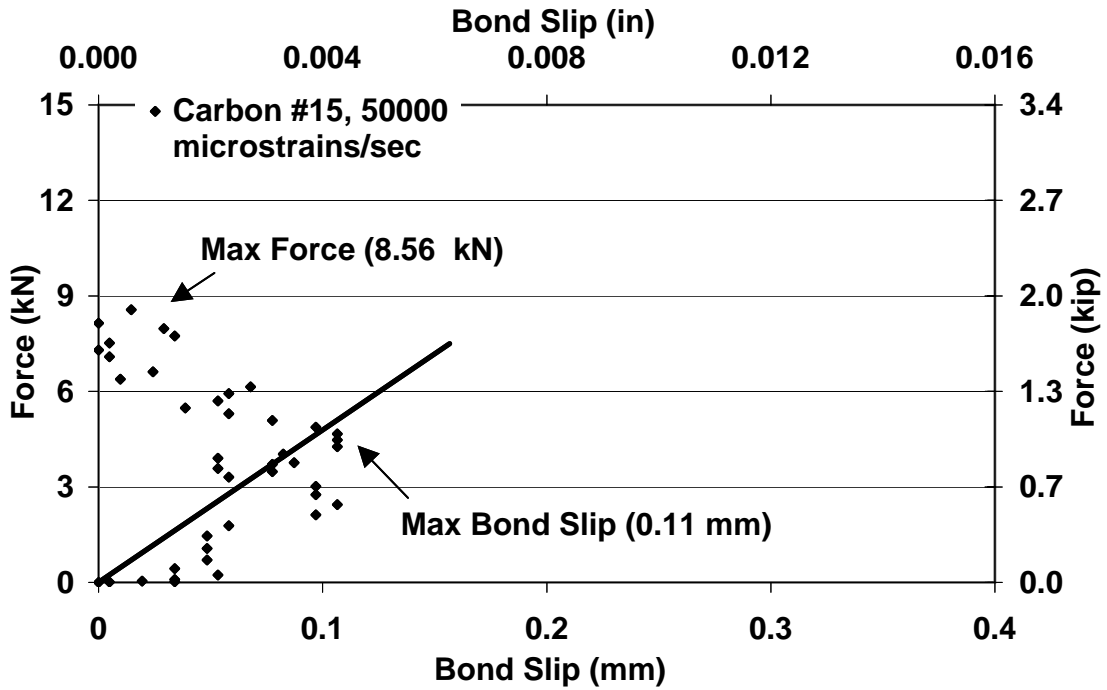


Figure 2-217: Force vs. bond slip for CFRP/concrete bond #15

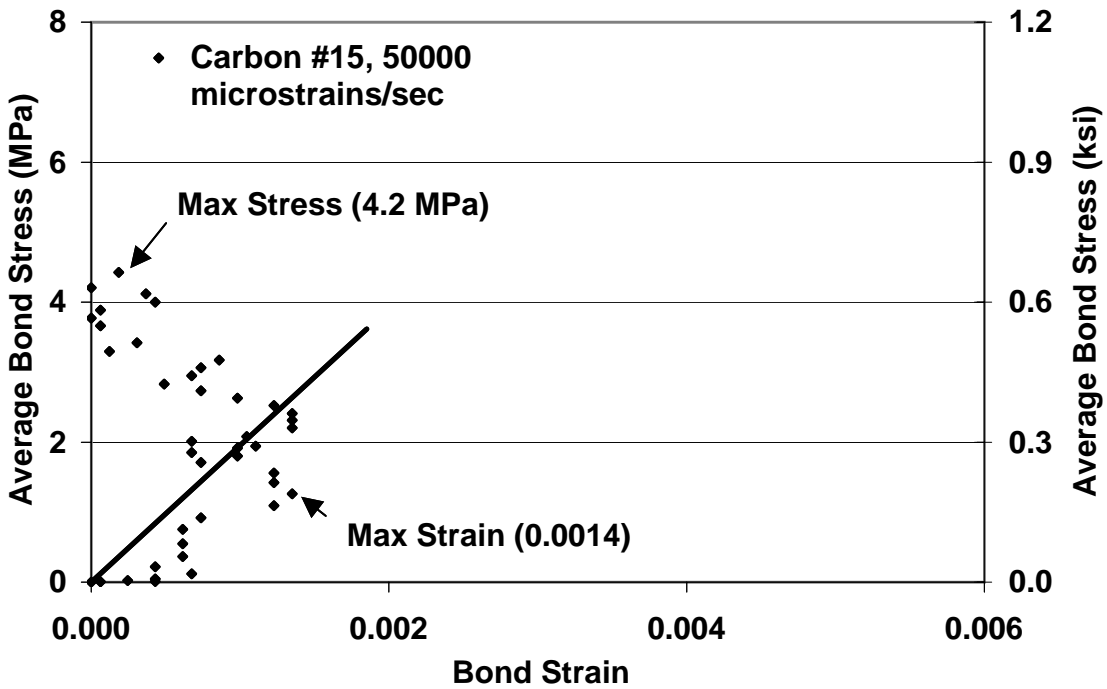


Figure 2-218: Average bond stress vs. bond strain, CFRP/concrete bond #15

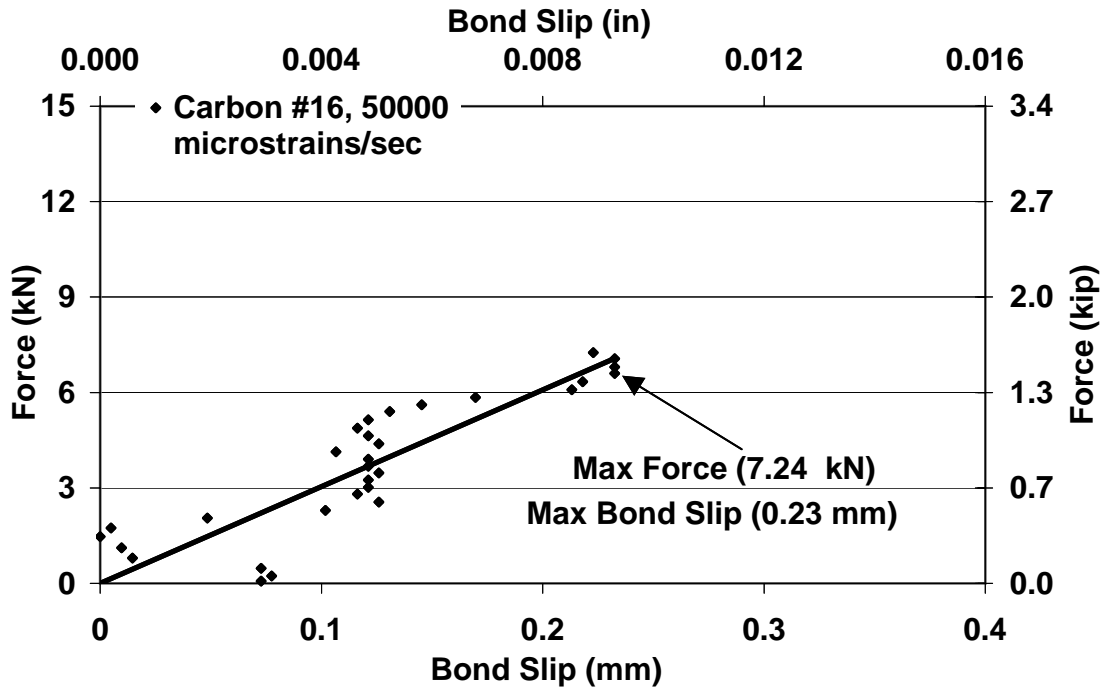


Figure 2-219: Force vs. bond slip for CFRP/concrete bond #16

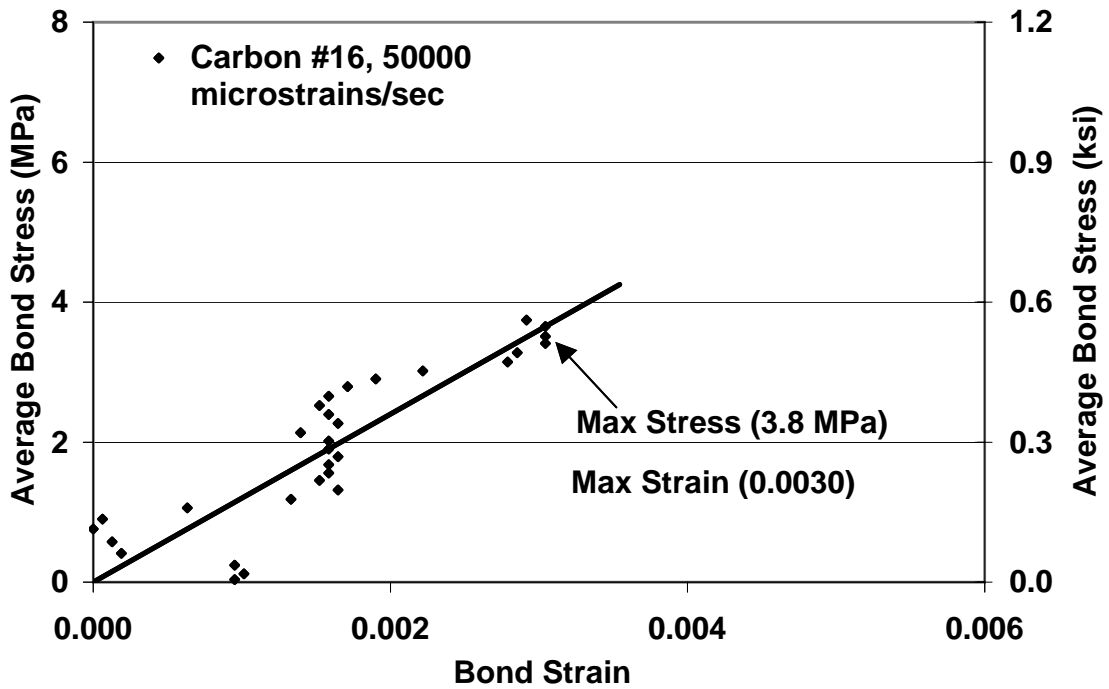


Figure 2-220: Average bond stress vs. bond strain, CFRP/concrete bond #16

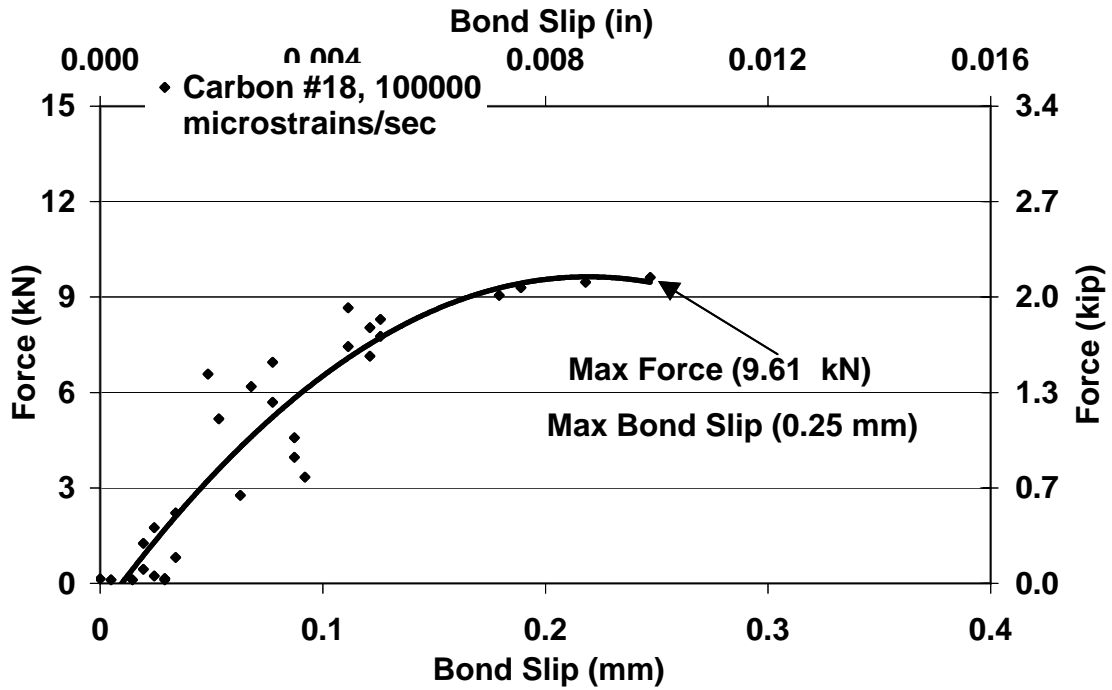


Figure 2-221: Force vs. bond slip for CFRP/concrete bond #18

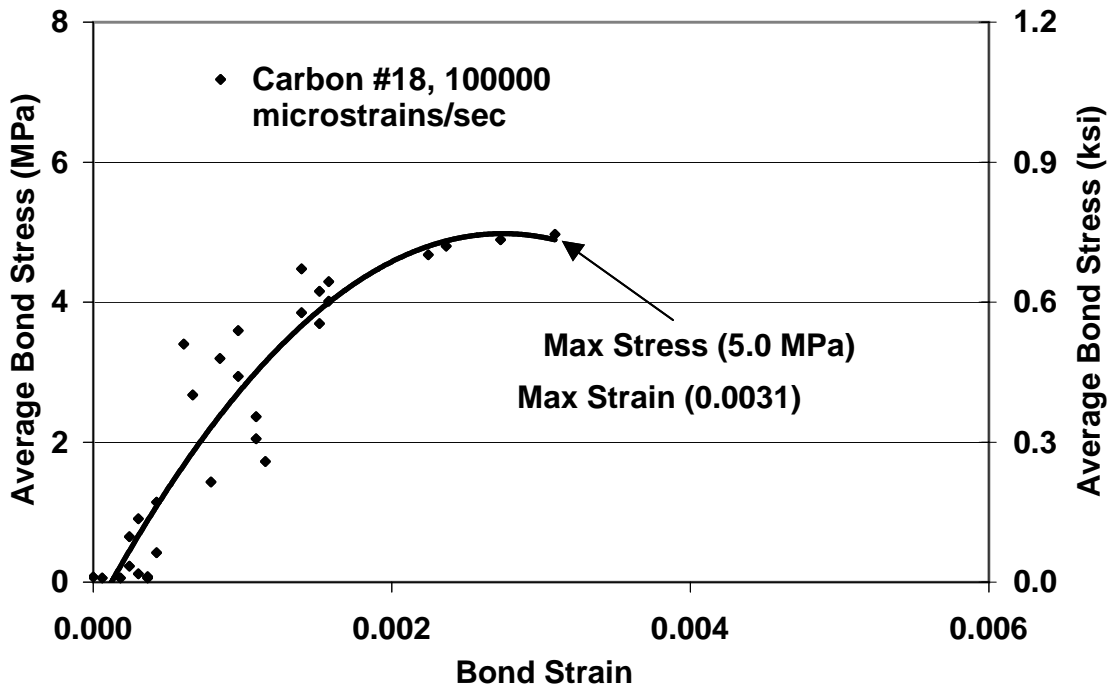


Figure 2-222: Average bond stress vs. bond strain, CFRP/concrete bond #18

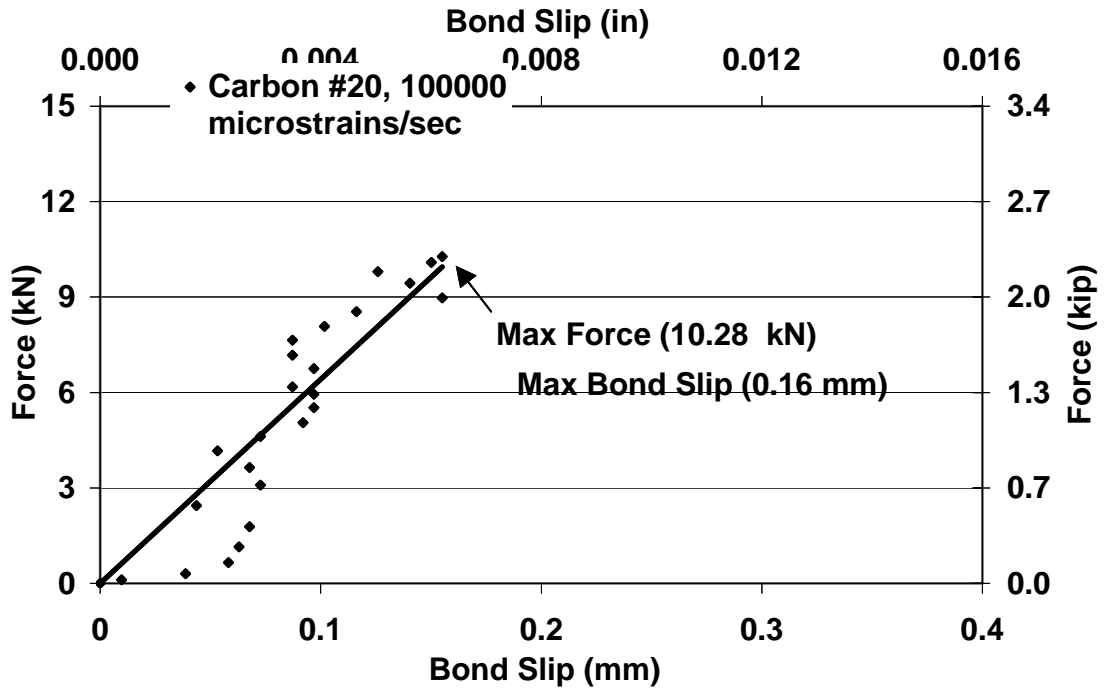


Figure 2-225: Force vs. bond slip for CFRP/concrete bond #20

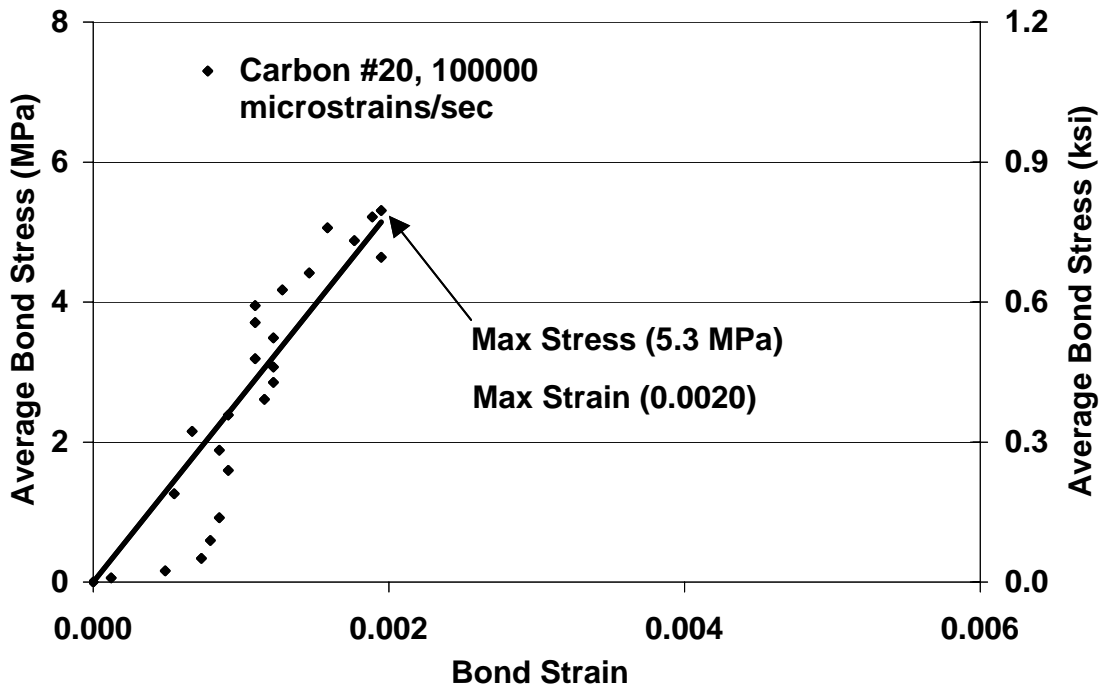


Figure 2-226: Average bond stress vs. bond strain, CFRP/concrete bond #20

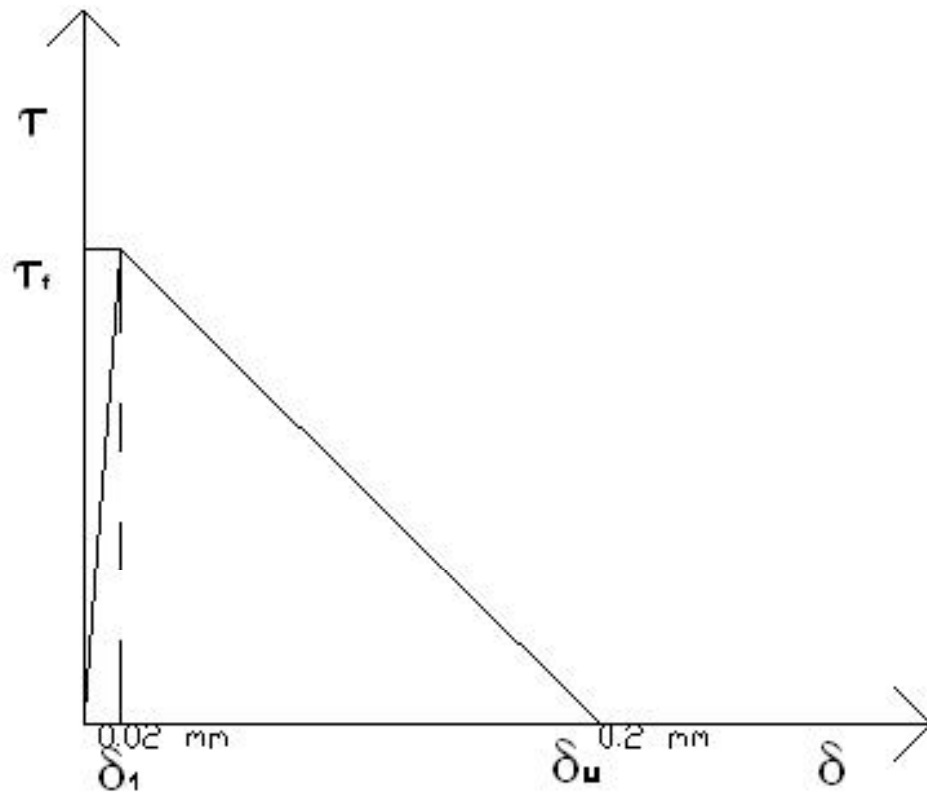


Figure 3-1: Chen and Teng's bond strength model for plate to concrete.

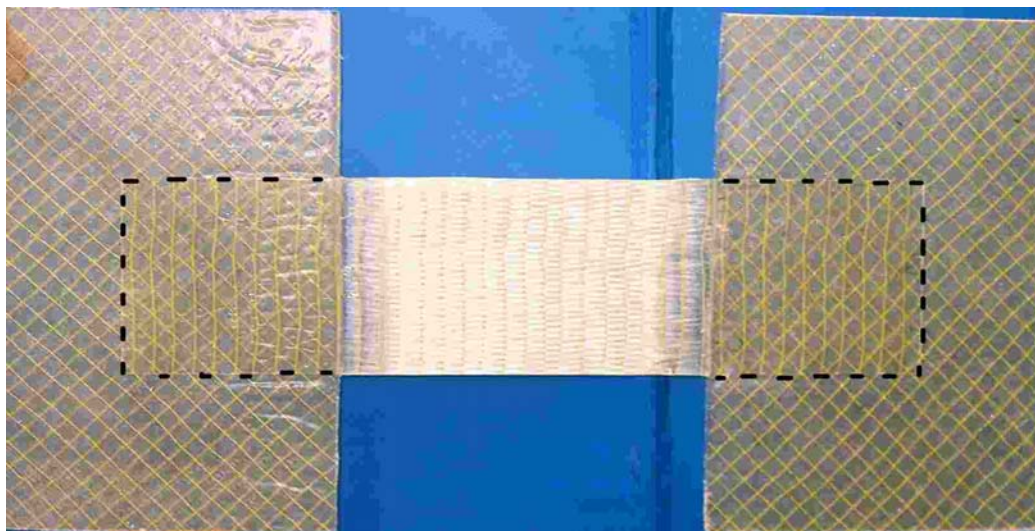


Figure 3-2: Illustration of unidirectional section of the FRP restrainer

Glass		
$L_e = (E_p * t_p / (f'_c)^{0.5})^{0.5}$		
γ_b	1.25	
E_p	20900 MPa	
t_p	1.3 mm	
f'_c	44.8 MPa	
b_c	750 mm	
$\beta_L = 1$	because $L > L_e$	
β_p	$((2-b_p/b_c)/(1+b_p/b_c))^{0.5}$	
$P_u = 0.315\beta_p\beta_L(f'_c)^{0.5}b_pL_e/\gamma_b$		
$\sigma_{db} = 0.315\beta_p\beta_L/\gamma_b(E_p(f'_c)^{0.5}/t_p)^{0.5}$		
$L_e =$	64 mm	2.7 in
Using b_p of 152 mm (6 in), calculated above		
P_u	26771.0 N	
	6.0 kips	<10 kips NG

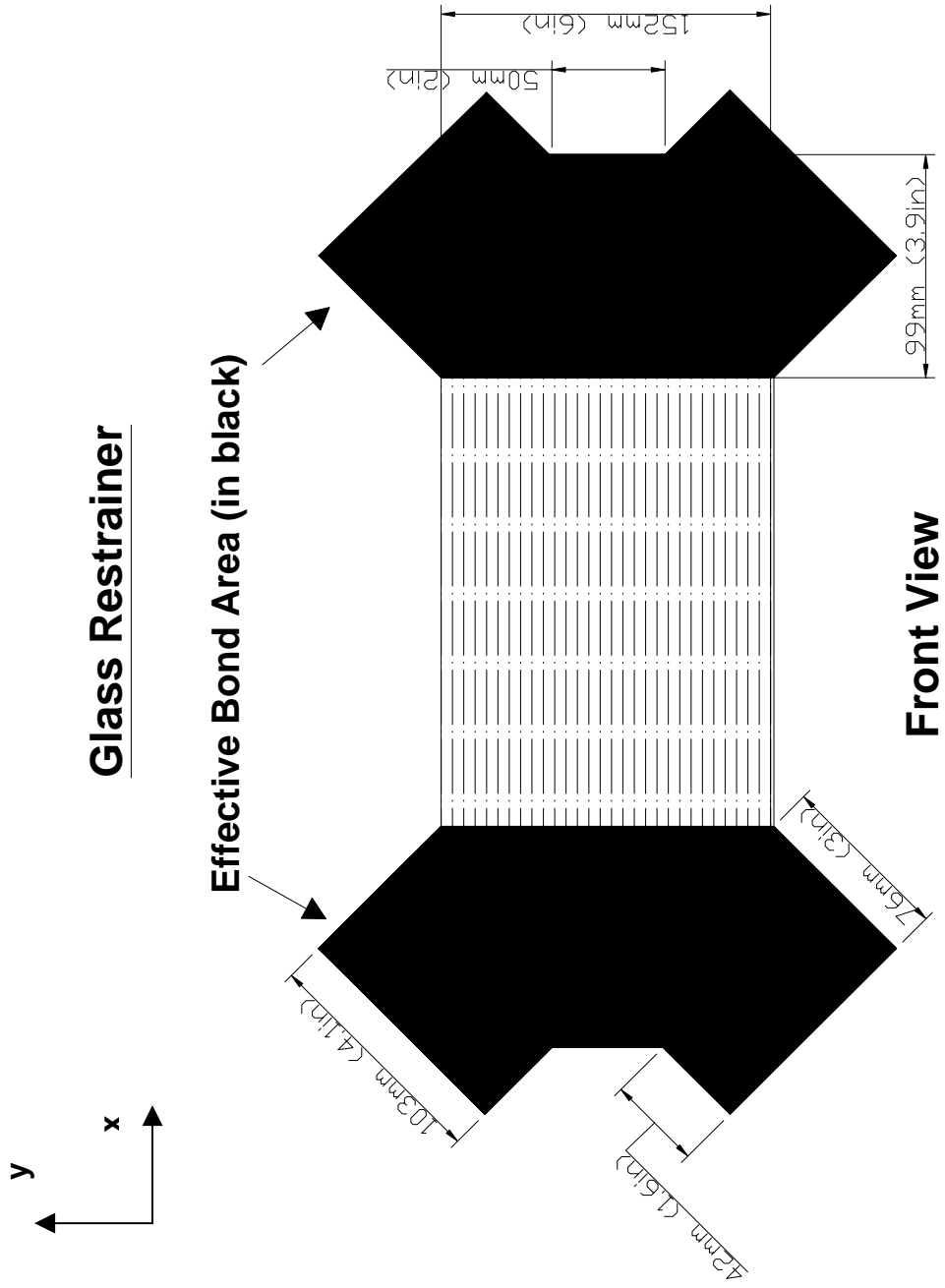
Figure 3-3: Calculation of effective length and bond capacity for GFRP prior to increase in plate size

Glass			
$Le = (E_p * t_p / (f'_c)^{0.5})^{0.5}$			
γ_b	1.25		
E_p	20900 MPa		
t_p	3.13 mm	2.41*1.3	
f'_c	44.8 MPa		
b_c	750 mm		
β_L	= 1 because $L > L_e$		
β_p	$((2-b_p/b_c)/(1+b_p/b_c))^{0.5}$		
P_u	$= 0.315\beta_p\beta_L(f'_c)^{0.5}b_pL_e/\gamma_b$		
σ_{db}	$= 0.315\beta_p\beta_L/\gamma_b(E_p(f'_c)^{0.5}/t_p)^{0.5}$		
L_e	99 mm	3.9 in	
Using b_p of 152 mm (6 in), calculated above			
P_u	41539.9 N	9.3 kips	<10 kips NG

Figure 3-4: Calculation of effective length and bond capacity of 3 layers of GFRP (unidirectional and 45° and 135°)

Glass			
$Le = (E_p * t_p / (f'_c)^{0.5})^{0.5}$			
γ_b	1.25		
E_p	20900 MPa		
t_p	1.83 mm	1.41*1.3	
f'_c	44.8 MPa		
b_c	750 mm		
β_L	= 1 because $L > L_e$		
β_p	$((2-b_p/b_c)/(1+b_p/b_c))^{0.5}$		
P_u	$= 0.315\beta_p\beta_L(f'_c)^{0.5}b_pL_e/\gamma_b$		
σ_{db}	$= 0.315\beta_p\beta_L/\gamma_b(E_p(f'_c)^{0.5}/t_p)^{0.5}$		
L_e	76 mm	3.0 in	

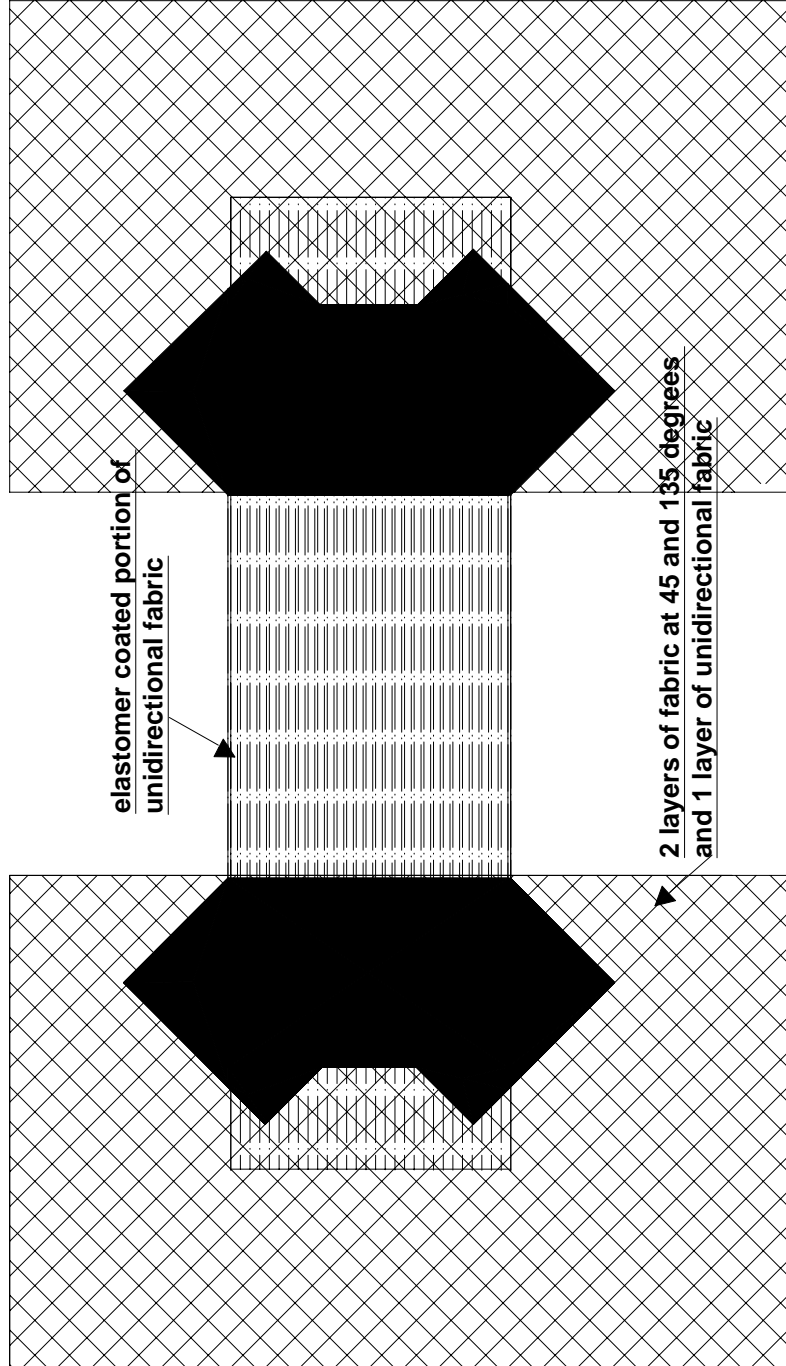
Figure 3-5: Calculation of effective length and bond capacity of FRP plate with two layers of angled laminate (45° and 135°)



Effective bond area = 30200mm² (47in²) in the primary direction + 22000 mm² (34in²) in perpendicular
Strength in perpendicular direction is 0.707 (cos 45) times strength in primary direction
Effective area = (30200 + 0.707*22000) mm² = 45800 mm² (71 in²)

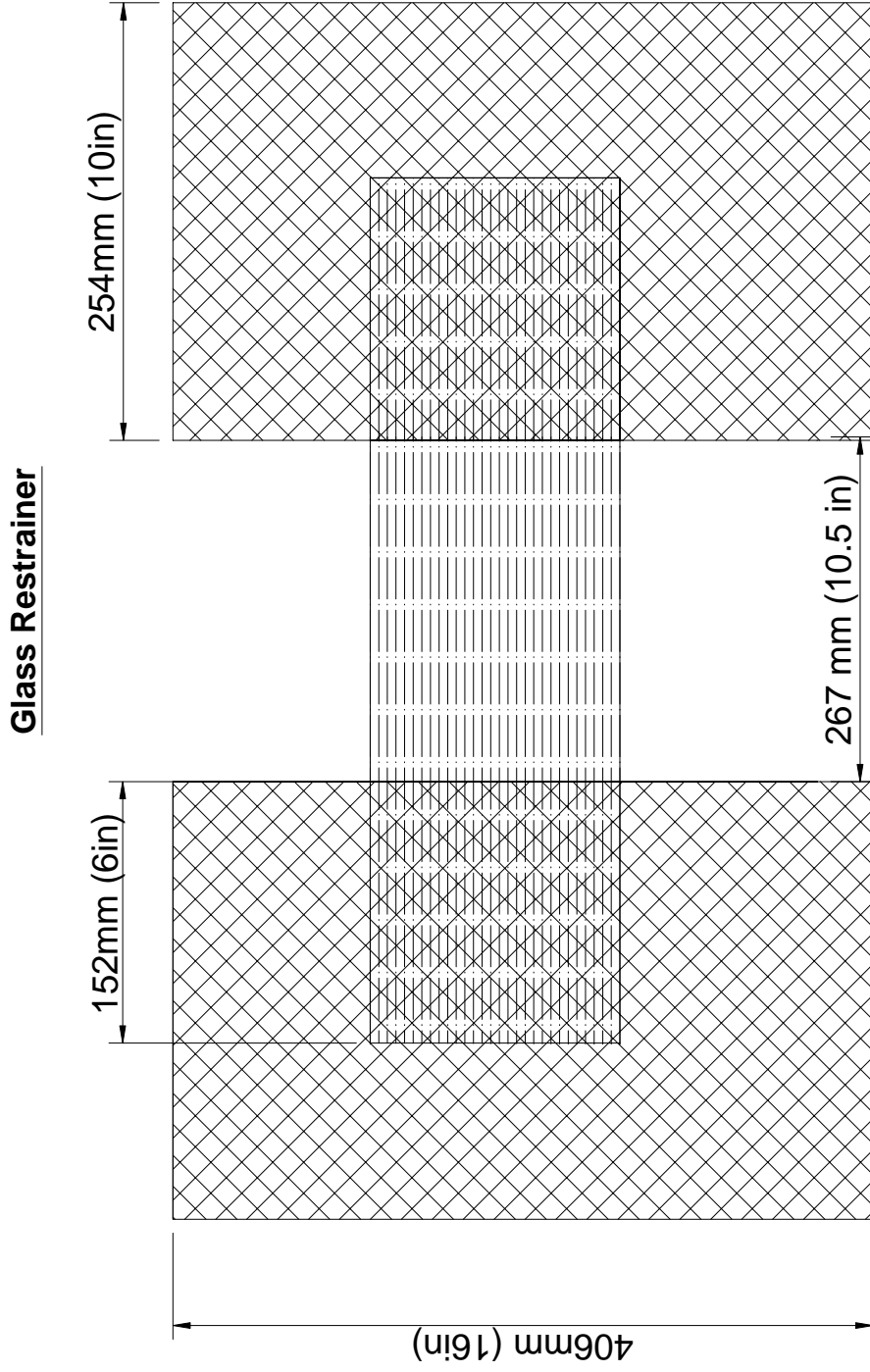
Figure 3-6 Effective Bond Areas for GFRP Restrainer

Glass Restrainer



Front View

Figure 3-7: Area of GFRP restrainer bonded to blocks is double the effective bond area.



Front View

Demand (4 kips) < Flexible GFRP capacity (10 kips/FOS) < Bond Capacity (21 kips/FOS)

Figure 3-8 Dimensions of GFRP restrainer

Carbon		
$L_e = (E_p * t_p / (f'_c)^{0.5})^{0.5}$		
γ_b	1.25	
E_p	61500 MPa	
t_p	1 mm	
f'_c	38 MPa	
b_c	750 mm	
$\beta_L = 1$ because $L > L_e$		
β_p	$((2-b_p/b_c)/(1+b_p/b_c))^{0.5}$	
P_u	$= 0.315\beta_p\beta_L(f'_c)^{0.5}b_pL_e/\gamma_b$	
σ_{db}	$= 0.315\beta_p\beta_L/\gamma_b(E_p(f'_c)^{0.5}/t_p)^{0.5}$	
$L_e =$	100 mm	3.932402 in
Using b_p of 76 mm (3 in), calculated above		
P_u	21686.7 N	
	4.9 kips	<8 kips NG

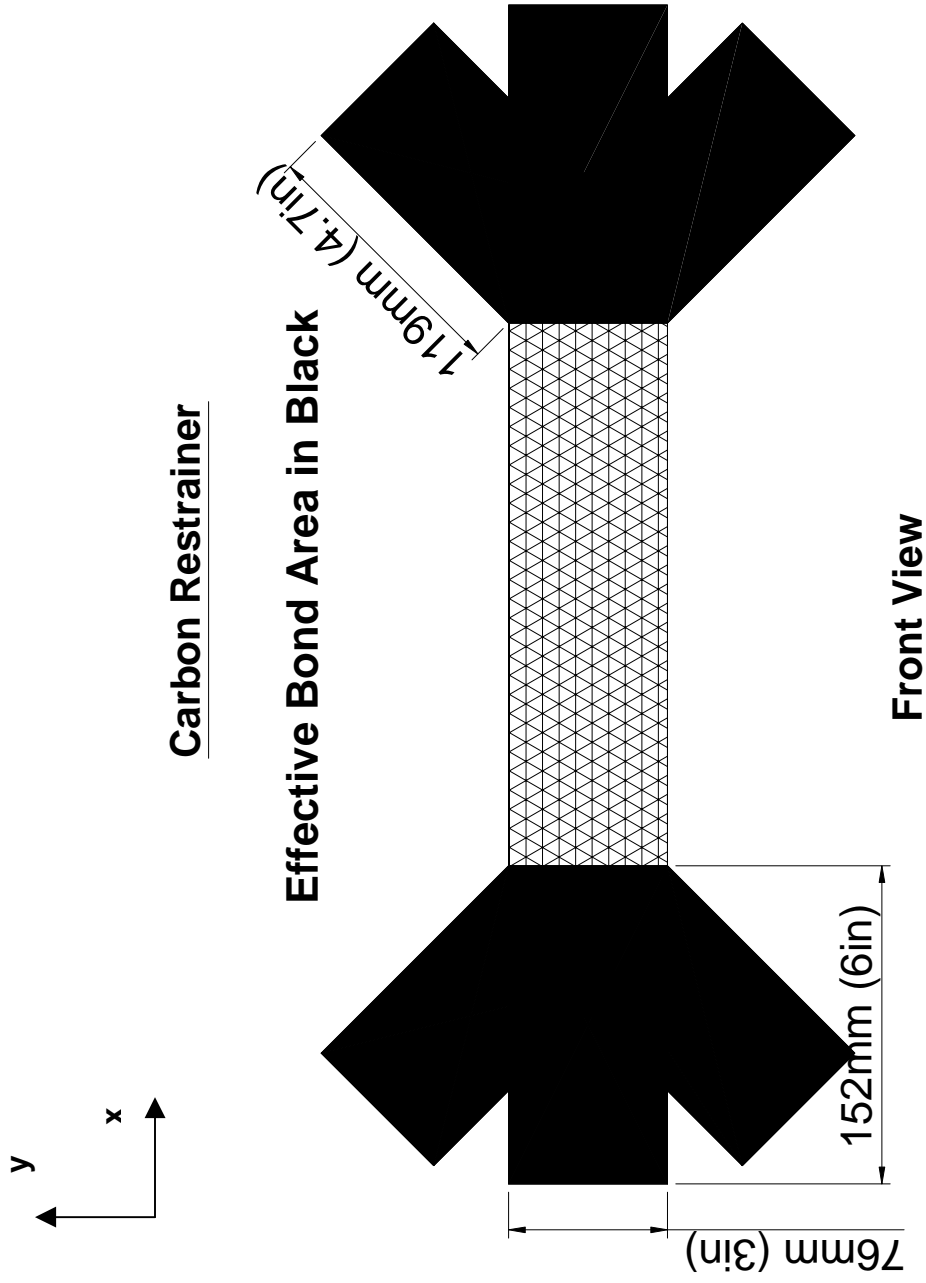
Figure 3-9: Calculation of effective length and bond capacity for CFRP prior to increase in plate size

Carbon		
$Le = (E_p * t_p / (f'_c)^{0.5})^{0.5}$		
γ_b	1.25	
E_p	61500 MPa	
t_p	2.41 mm	2.41*1
f'_c	38 MPa	
b_c	750 mm	
$\beta_L = 1$	because $L > L_e$	
β_p	$((2-b_p/b_c)/(1+b_p/b_c))^{0.5}$	
$Pu = 0.315\beta_p\beta_L(f'_c)^{0.5}b_pL_e/\gamma_b$		
$\sigma_{db} = 0.315\beta_p\beta_L/\gamma_b(E_p(f'_c)^{0.5}/t_p)^{0.5}$		
$L_e =$	155 mm	6.1 in

Figure 3-10: Calculation of effective length and bond capacity of 3 layers of CFRP (unidirectional and 45° and 135°)

Carbon		
$Le = (E_p * t_p / (f'_c)^{0.5})^{0.5}$		
γ_b	1.25	
E_p	61500 MPa	
t_p	1.41 mm	1.41*1
f'_c	38 MPa	
b_c	750 mm	
$\beta_L = 1$	because $L > L_e$	
β_p	$((2-b_p/b_c)/(1+b_p/b_c))^{0.5}$	
$Pu = 0.315\beta_p\beta_L(f'_c)^{0.5}b_pL_e/\gamma_b$		
$\sigma_{db} = 0.315\beta_p\beta_L/\gamma_b(E_p(f'_c)^{0.5}/t_p)^{0.5}$		
$L_e =$	119 mm	4.7 in

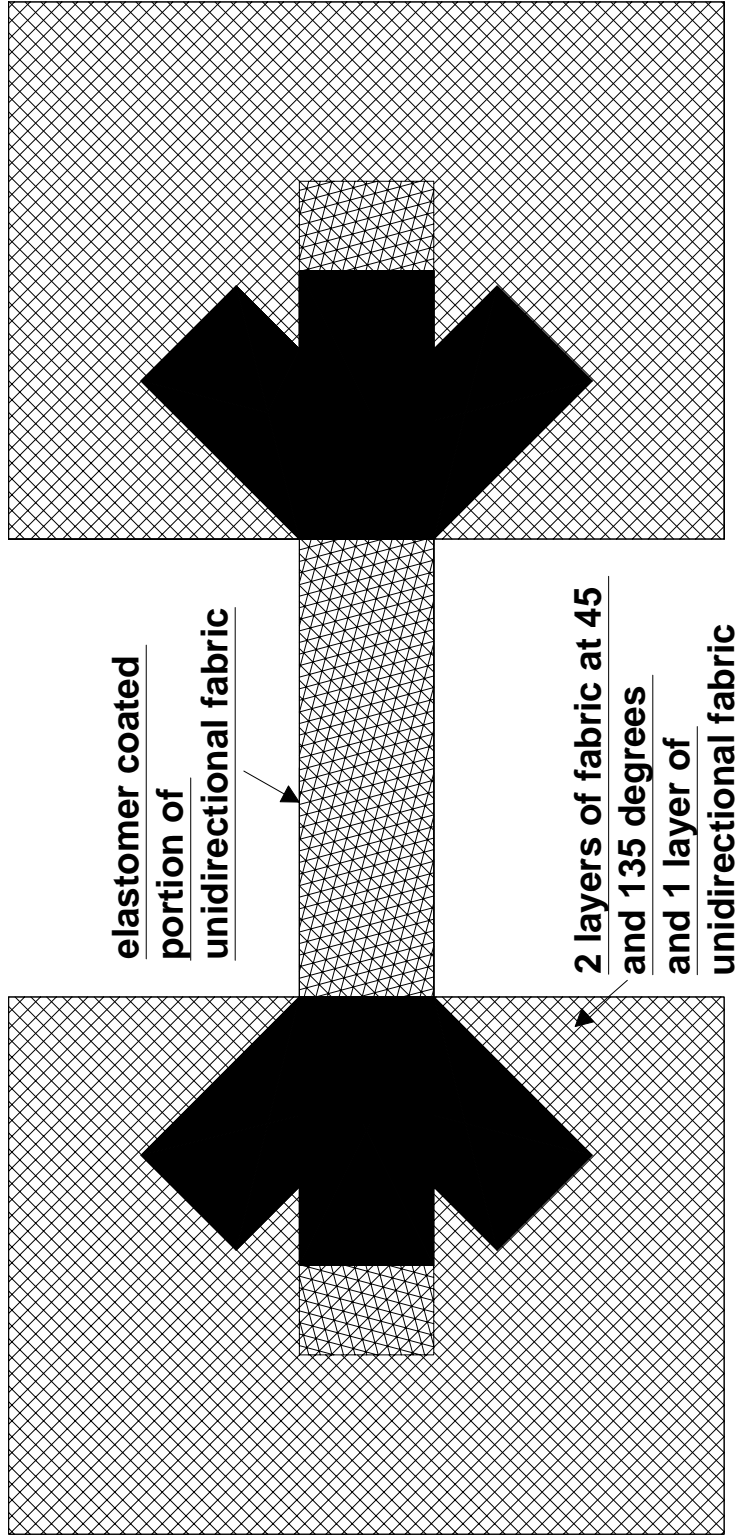
Figure 3-11: Calculation of effective length and bond capacity of CFRP plate with two layers of angled laminate (45° and 135°)



Effective bond area = 23200mm² (36in²) in the primary direction + 27100 mm² (42in²) in perpendicular
Strength in perpendicular direction is 0.707 (cos 45) times strength in primary direction
Effective area = (23200 + 0.707*27100) mm² = 42400 mm² (66 in²)

Figure 3-12 Effective Bond Areas for CFRP Restrainer

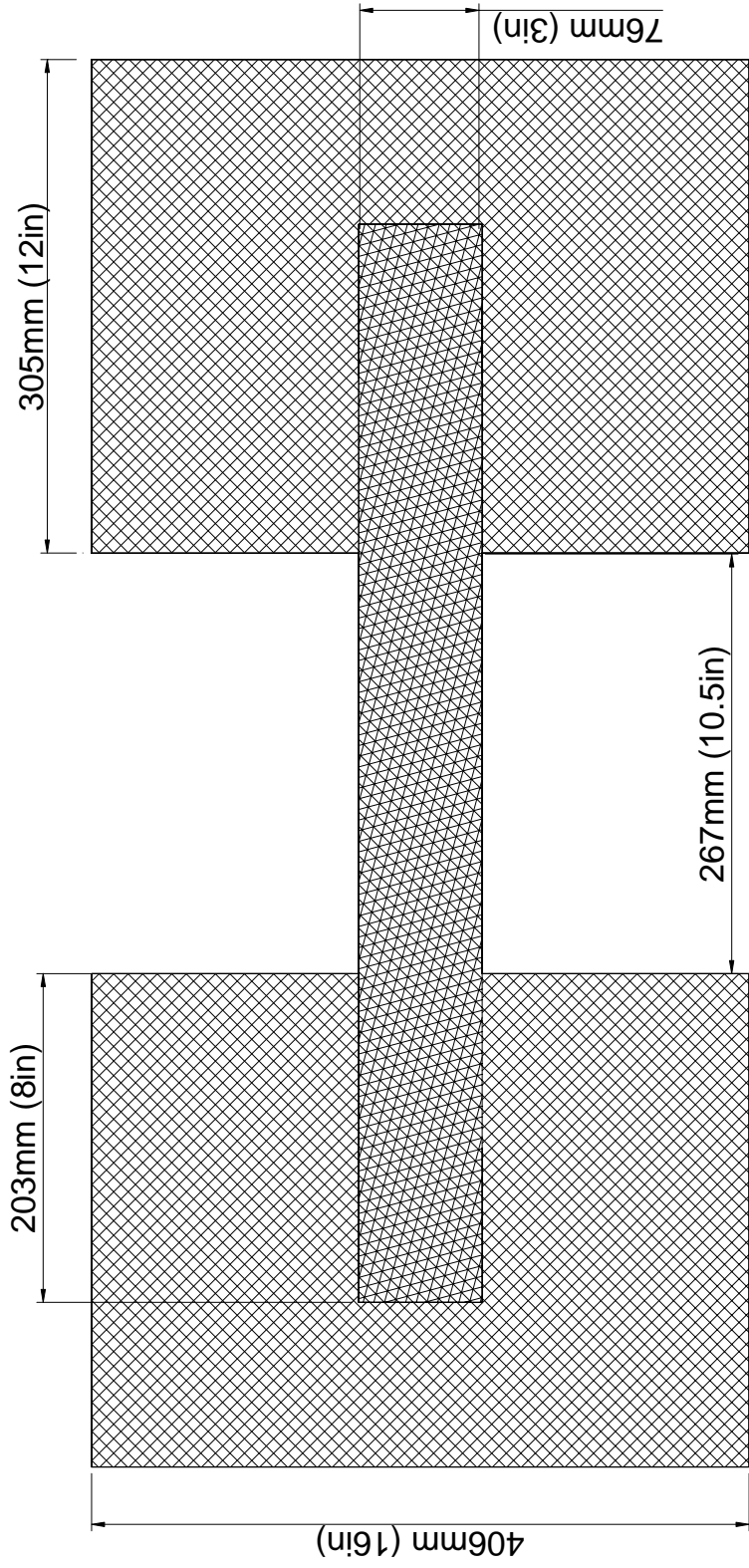
Carbon Restrainer



Front View

Figure 3-13: Area of CFRP Restrainer Bonded to Blocks is Double the Effective Bond

Carbon Restrainer



Front View

Demand (4 kips) < Flexible CFRP capacity (12.5 kips/FOS) < Bond Capacity (18 kips/FOS)

Figure 3-14 Dimensions of CFRP restrainer

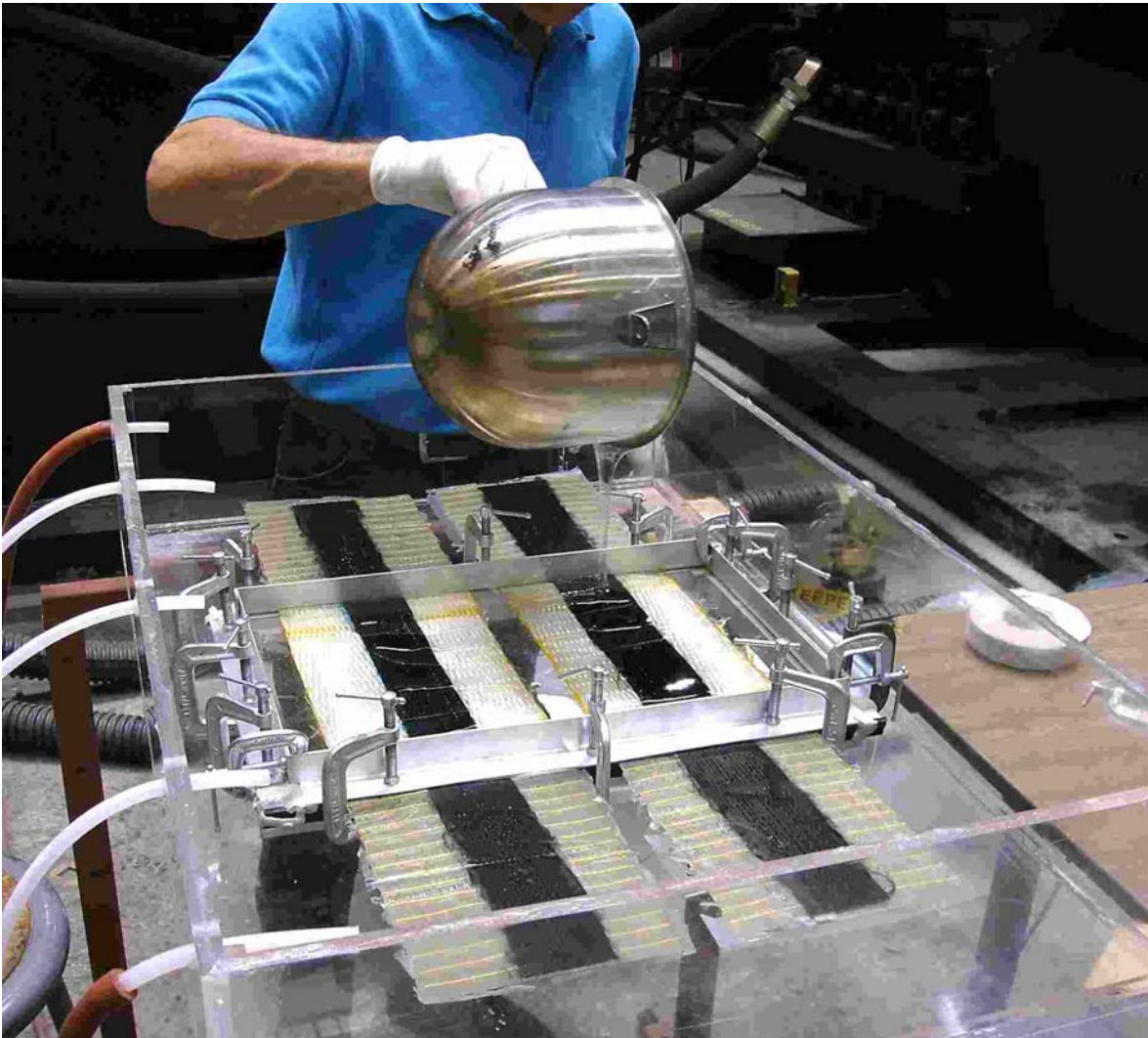


Figure 3-15: Coating unidirectional segment of hybrid restrainer with SYLGARD 184 silicone elastomer.

Glass		
$Le = (E_p * t_p / (f_c)^{(0.5)})^{(0.5)}$		
E_p	20900 MPa	
t_p	1.83 mm	1.41*1.3
f_c	38 MPa	
$L_e =$	79 mm	3.1 in

Figure 3-16: Bond Length Formulation for Angled Glass Epoxy Laminate Portion of FRP Plate

Glass		
$Le = (E_p * t_p / (f_c)^{(0.5)})^{(0.5)}$		
E_p	20900 MPa	
t_p	3.13 mm	2.41*1.3
f_c	38 MPa	
$L_e =$	103 mm	4.1 in

Figure 3-17: Bond Length Formulation for Angled and Unidirectional Glass Epoxy Laminate Portion of FRP plate

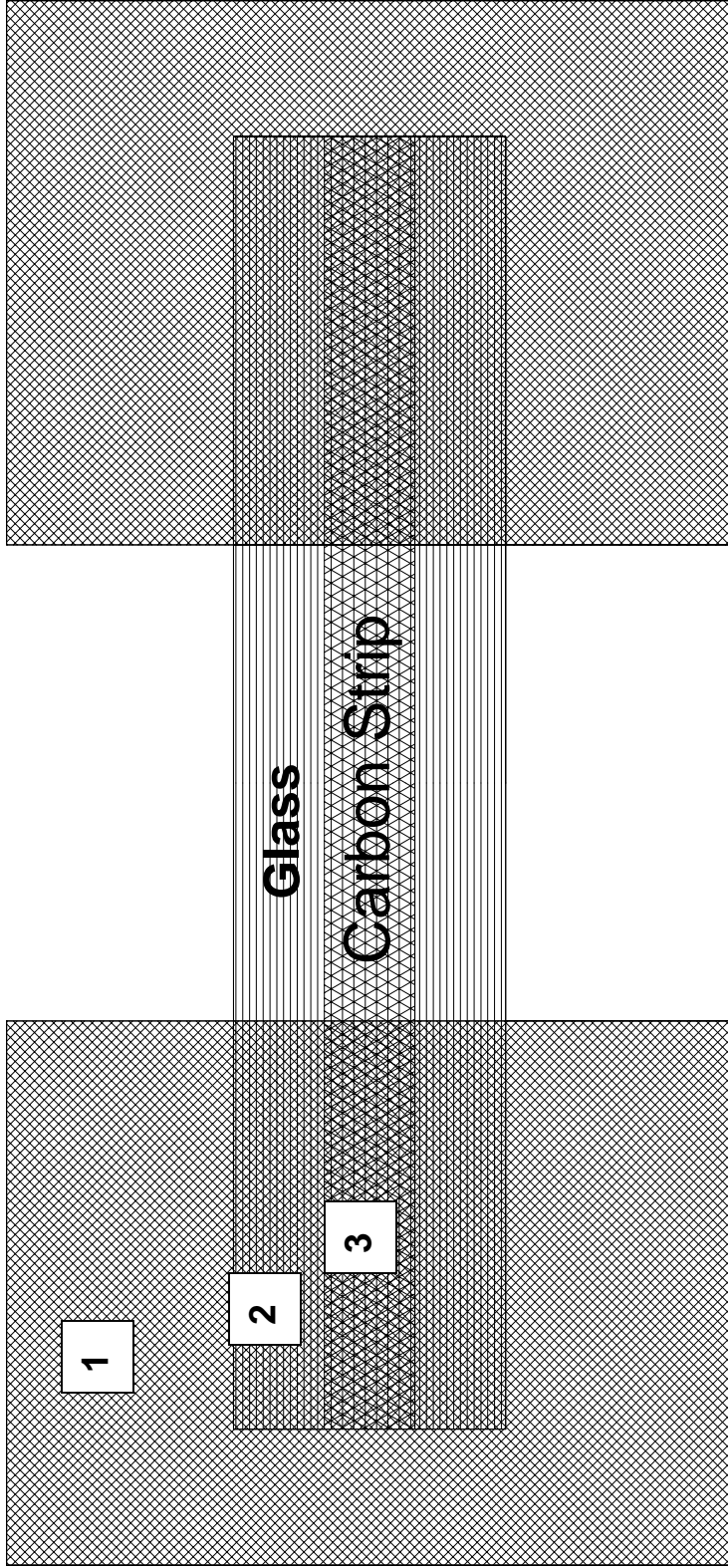
$$t_p = 1.3 + 1 + (1.3*1.41) = 4.13 \text{ mm}$$

$$E_p = (20900*3 + 615000)/4 = 31050 \text{ MPa}$$

Carbon and Glass		
$Le = (E_p * t_p / (f_c)^{(0.5)})^{(0.5)}$		
E_p	31050 MPa	
t_p	4.13 mm	
f_c	38 MPa	
$L_e =$	144 mm	5.7 in

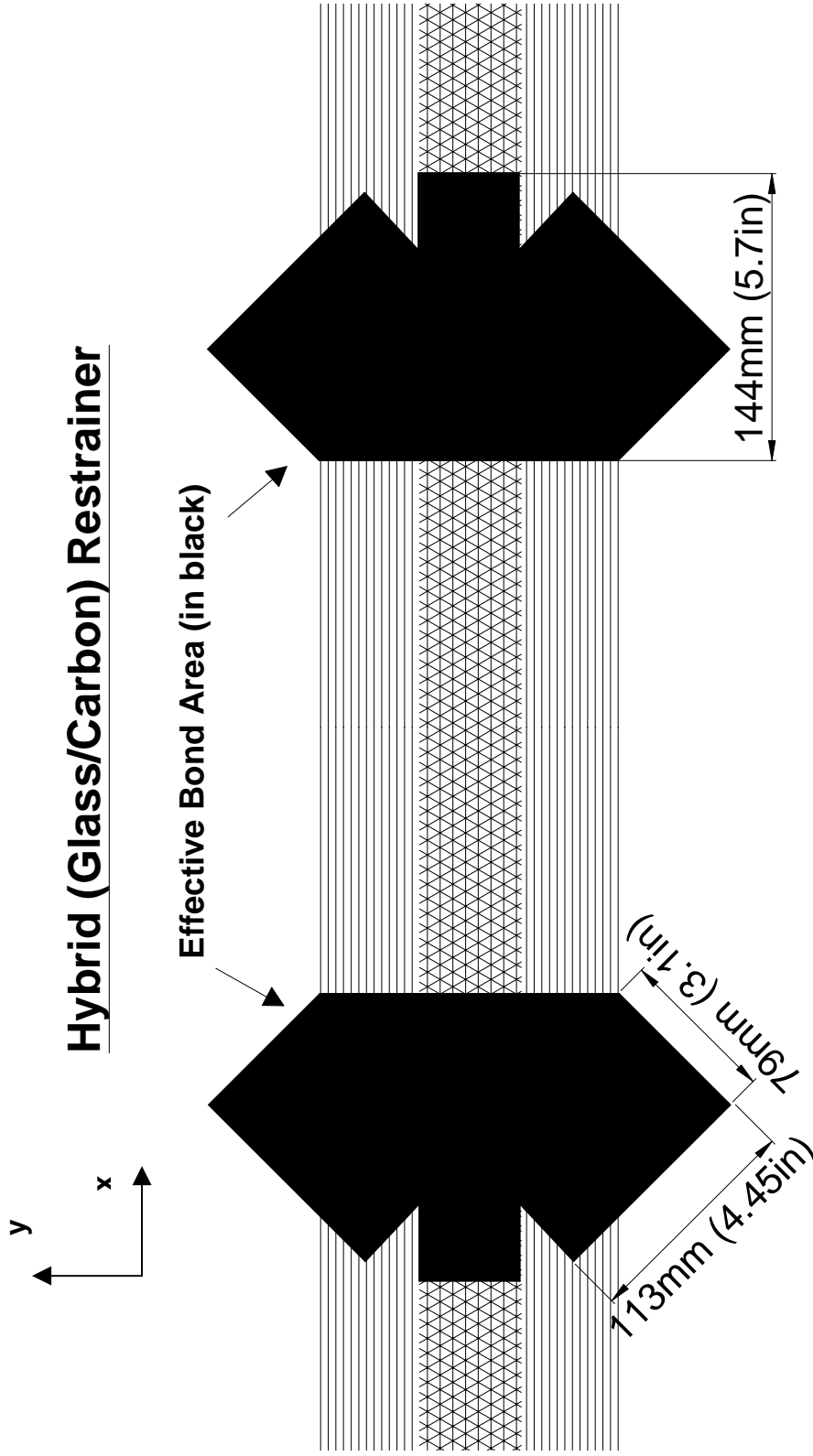
Figure 3-18: Bond Length Formulation for Angled Glass and Unidirectional Carbon Epoxy Laminate Portion of FRP

Hybrid (Glass/Carbon) Restrainer



Front View

Figure 3-19: Components of Hybrid Restrainer Plate, (1) Angled Glass, (2) Unidirectional and Angled Glass, (3) Unidirectional Carbon and Angled Glass



Front View

Effective bond area 35900mm^2 (55.6in^2) in the primary direction + 14200mm^2 (22in^2) in perpendicular
Strength in perpendicular direction is 0.707 ($\cos 45$) times strength in primary direction
Effective area = $(35900 + 0.707 \cdot 14200)\text{mm}^2 = 45900\text{mm}^2$ (71in^2)

Figure 3-20 Effective Bond Areas for Hybrid Restrainer

Hybrid (Glass/Carbon) Restrainer

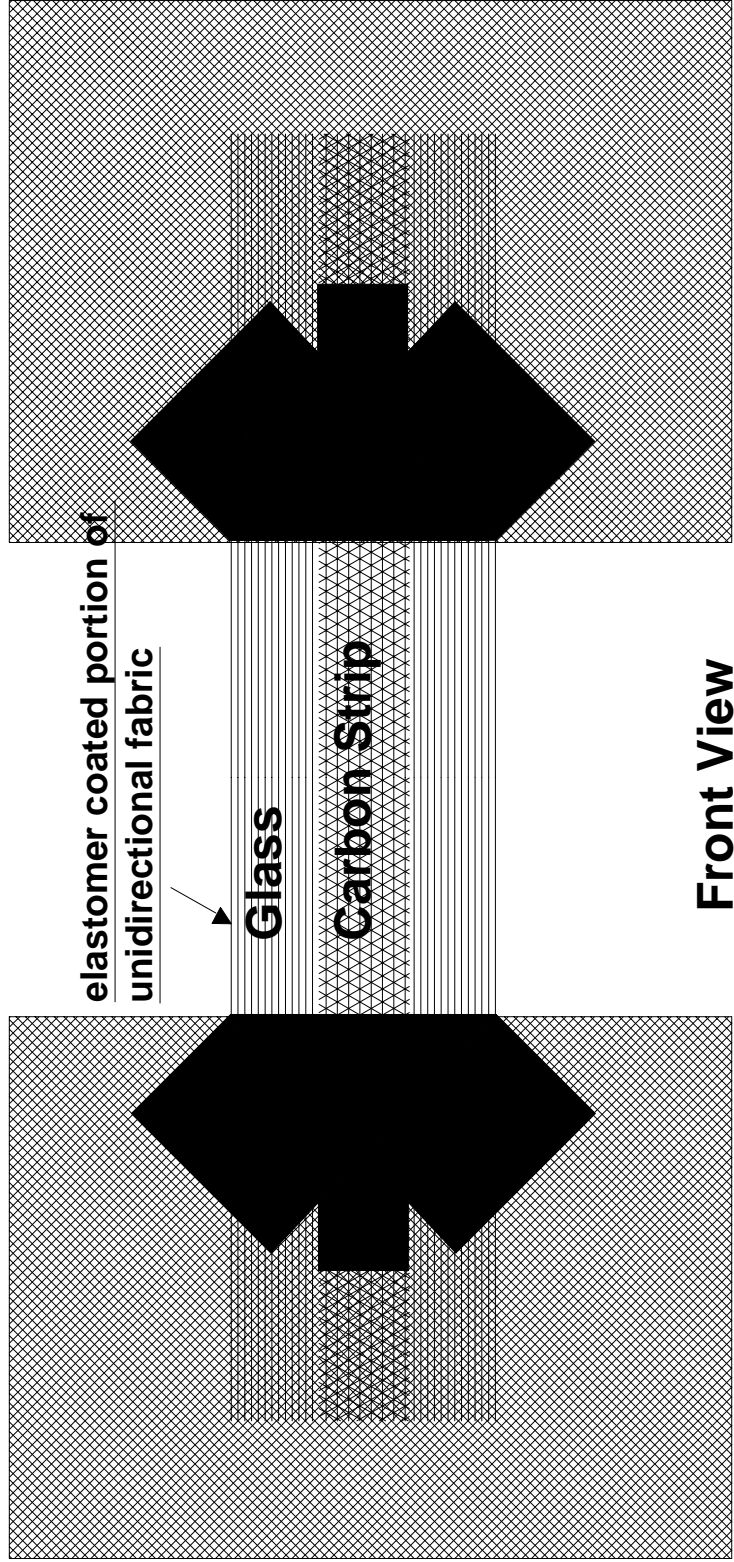
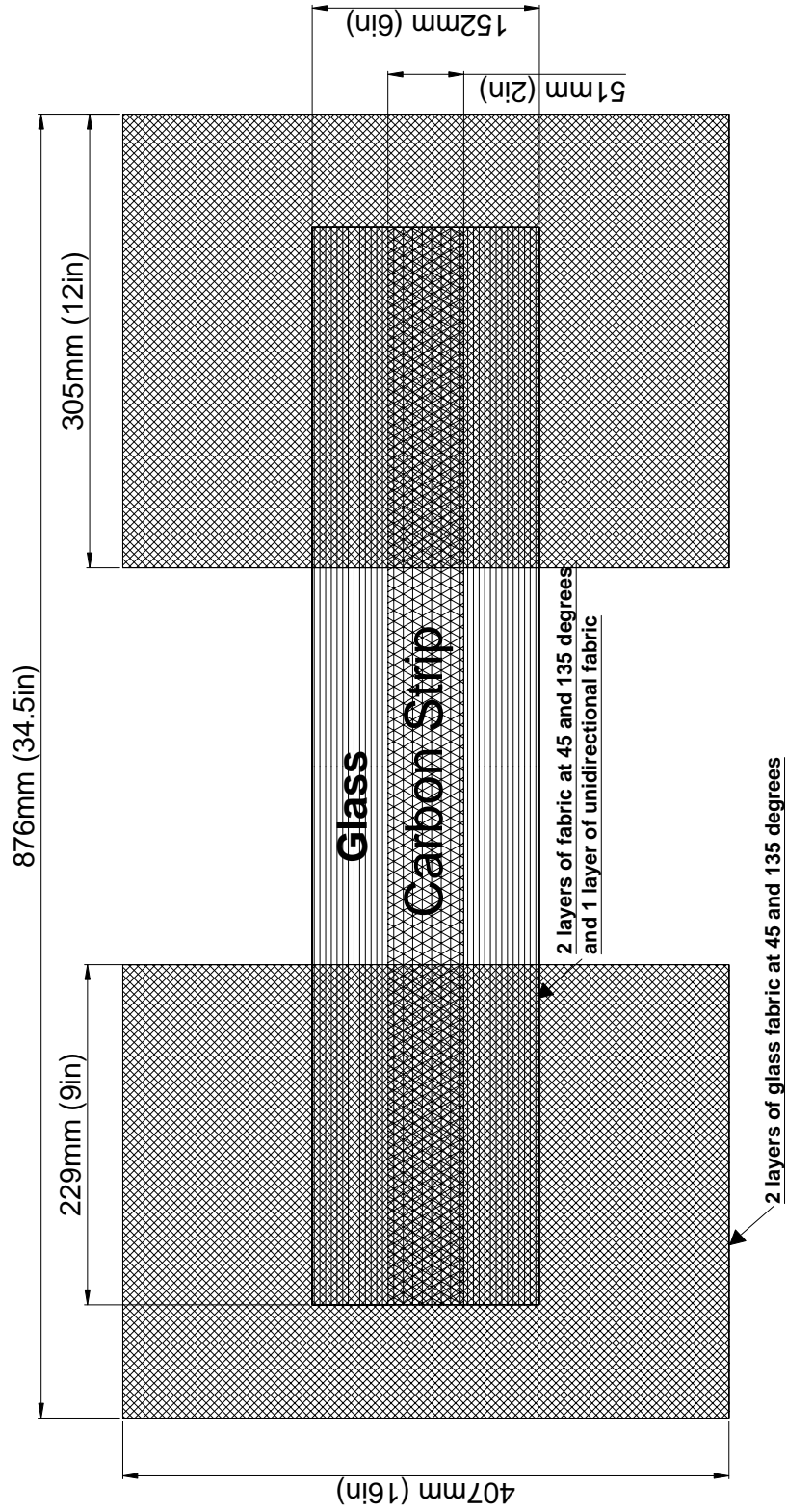


Figure 3-21: Area of hybrid restrainer bonded to blocks is double the effective bond area.

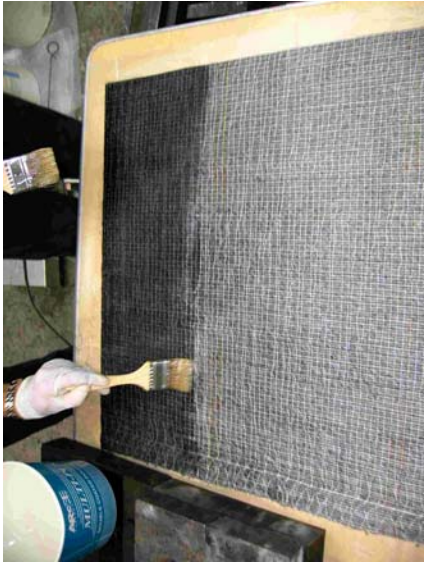
Hybrid (Glass/Carbon) Restrainer



Front View

Demand (4 kips) < Hybrid flexible composite capacity (18 kips/FOS) < Bond Capacity (20 kips/FOS)

Figure 3-22 Dimensions of Hybrid Restrainer



(a) Painting epoxy onto fabric



(b) Pressing excess epoxy from fabric

Figure 3-23: Epoxy Coating Process



(a) Pouring elastomer over fabric

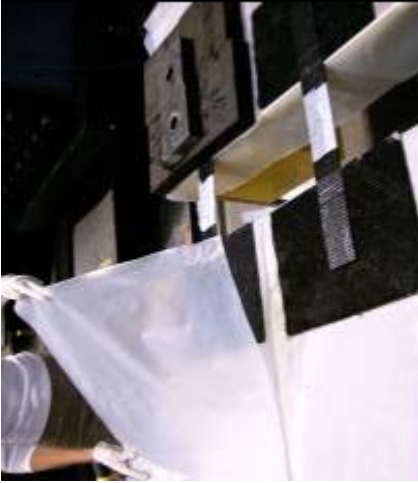


(b) Vacuuming air from elastomer coated fabric

Figure 3-24: Elastomer Coating Process



(a) Arranging fabric prior to epoxy application



(b) Covering with polyurethane



(c) Trimming excess epoxy from FRP plate



(d) Thickening epoxy with cab-o-sil prior to vertical application to blocks



(e) Completed CFRP restrainer

Figure 3-25: Assembling FRP Restrainers



(a) Sanding Blocks



(b) Air-blasting prior to restrainer attachment



(c) Restrainer attachment



(d) Securing FRP plates onto blocks until cure



(e) Second coating of epoxy

Figure 3-26: Attaching FRP restrainers to shake table specimen



Figure 4-1: Test set-up for FRP bridge restrainer shake table experiments.

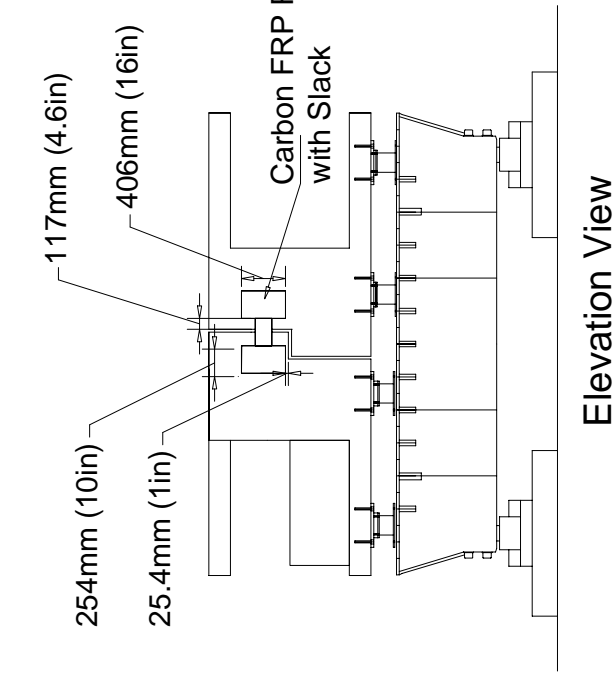
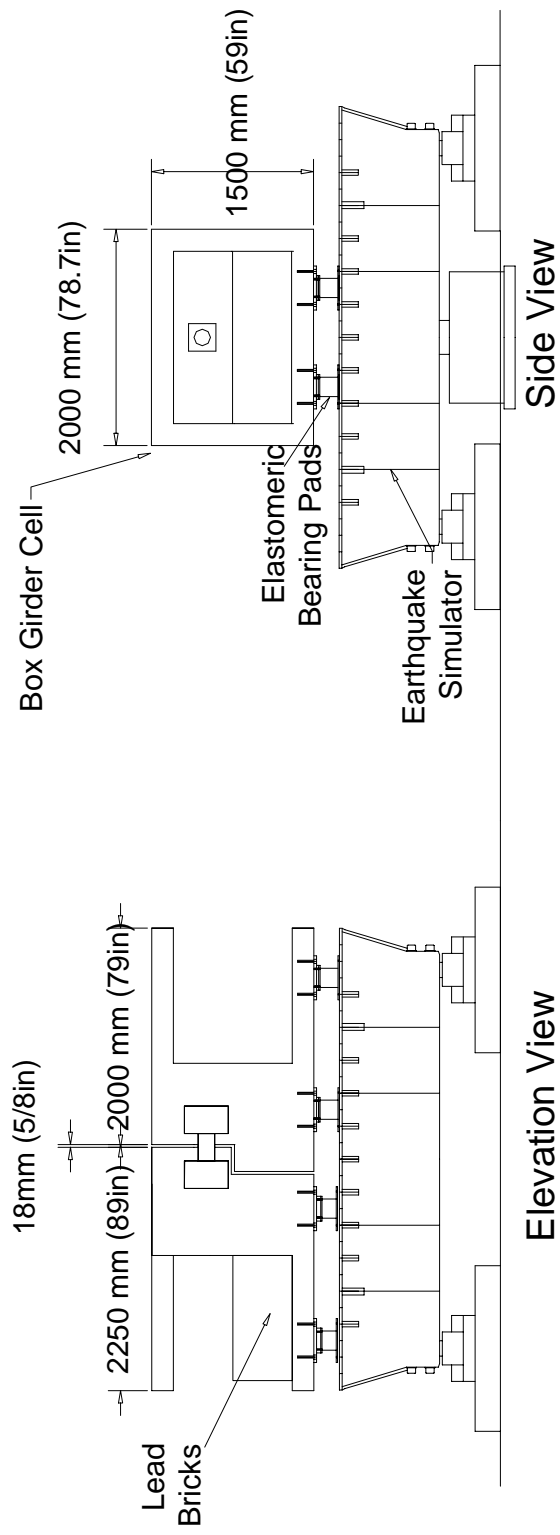


Figure 4-2: FRP restrainer test set-up

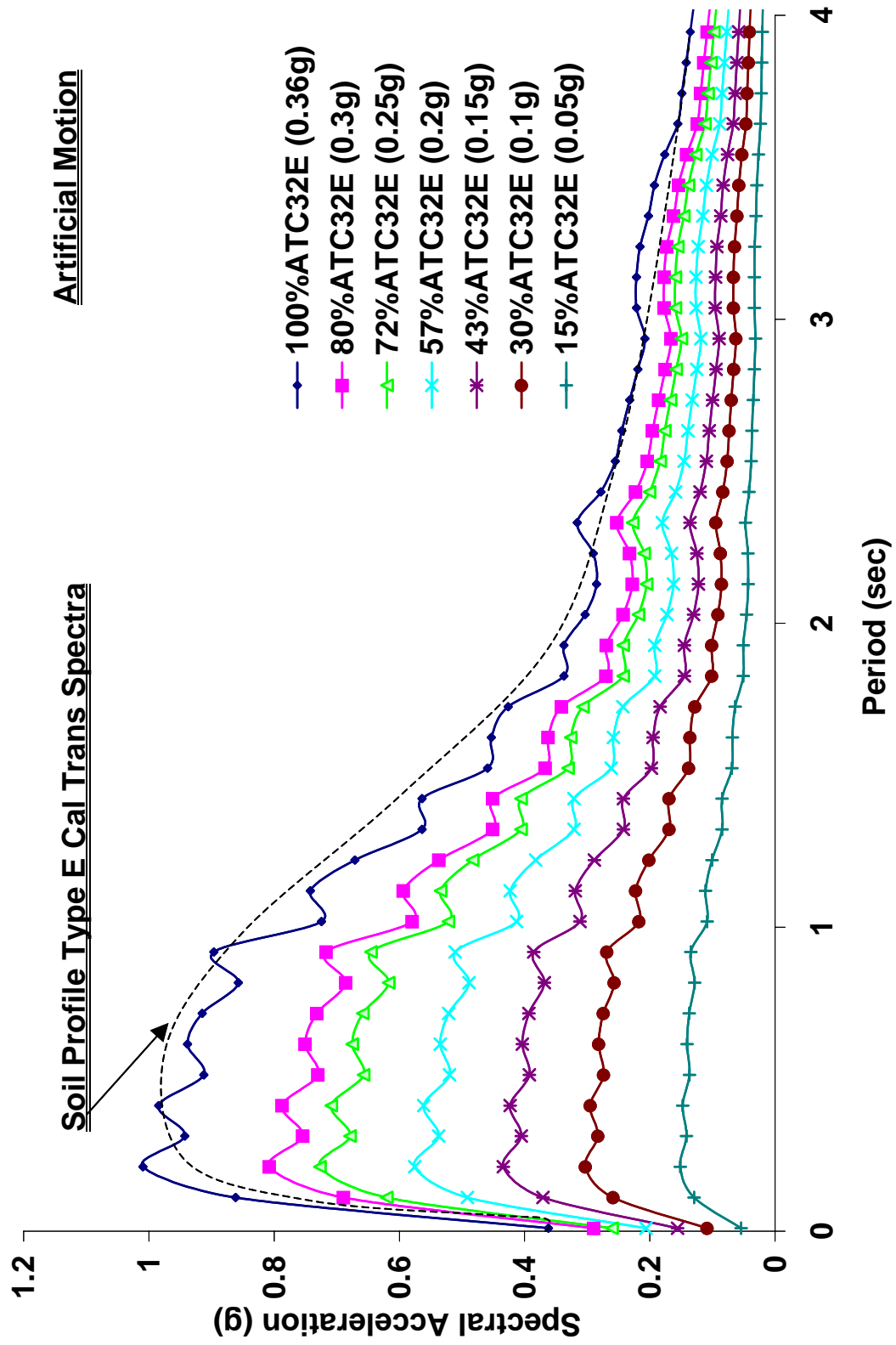
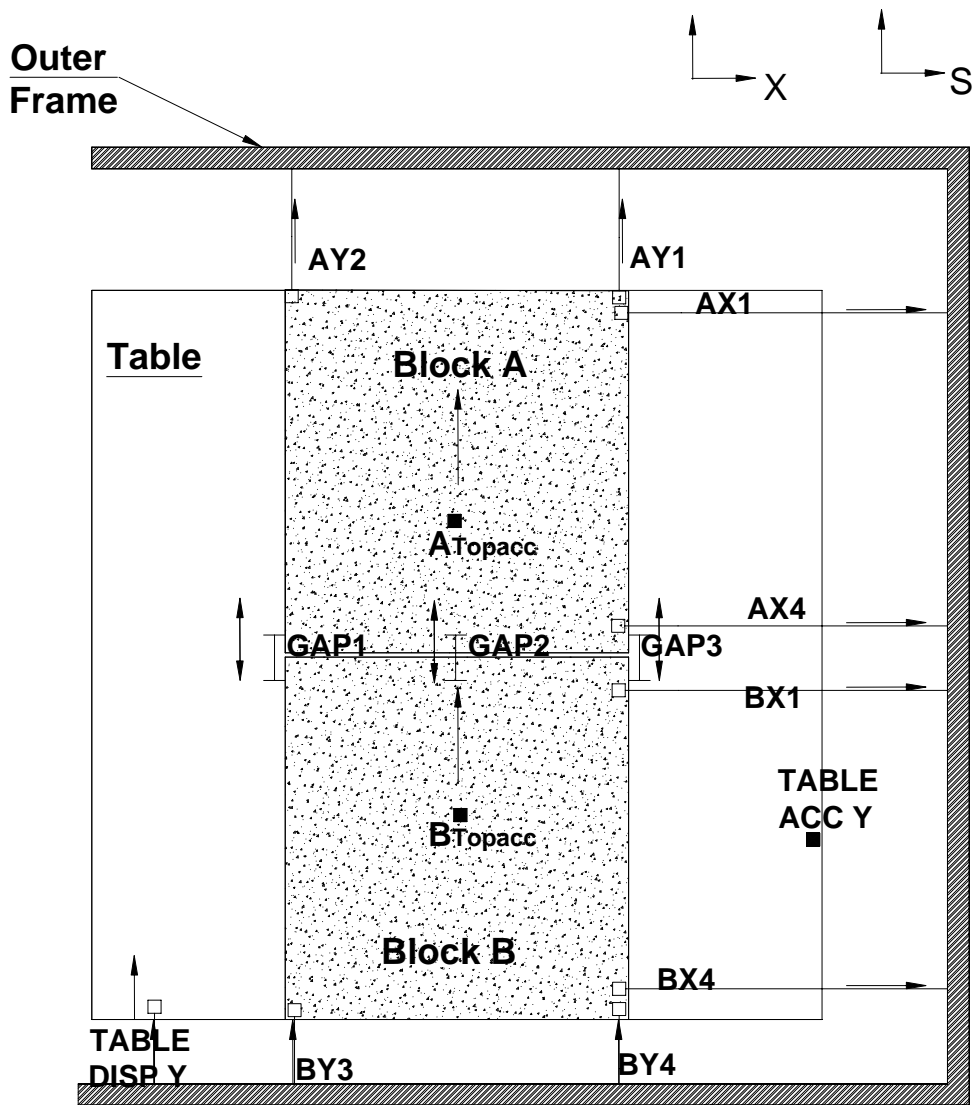





Figure 4-3: CALTRANS ATC32E vs. artificial motion input into shake table

June 29, 2004 GFRP Shake Table Test

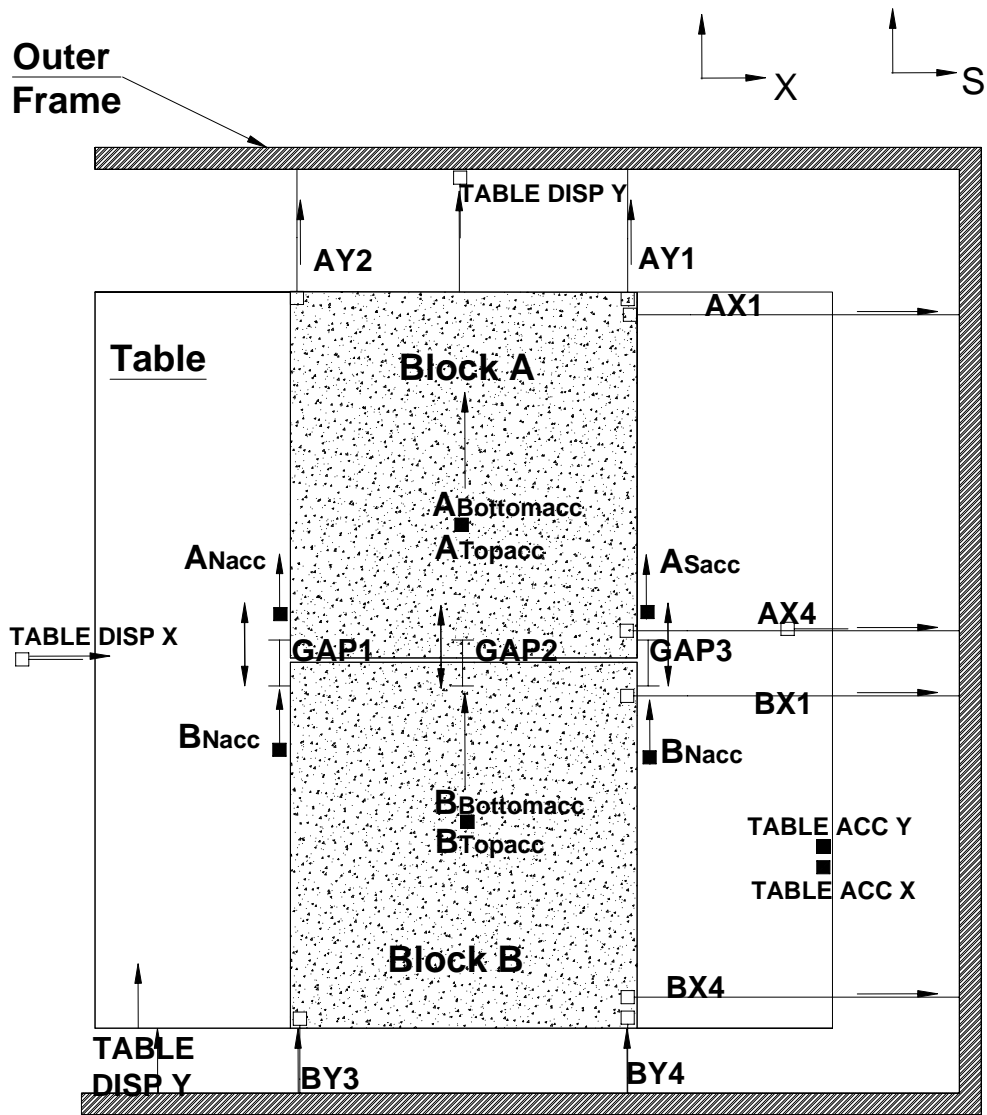





-  Linear Displacement Transducers (measures relative displacement)
-  Accelerometers (measures magnitude of acceleration)
-  Unimeasure String Potentiometers (measures absolute displacement)

TOP VIEW

Figure 4-4: Instrumentation for GFRP restrainer tests

July 20,2004 CFRP Shake Table Test

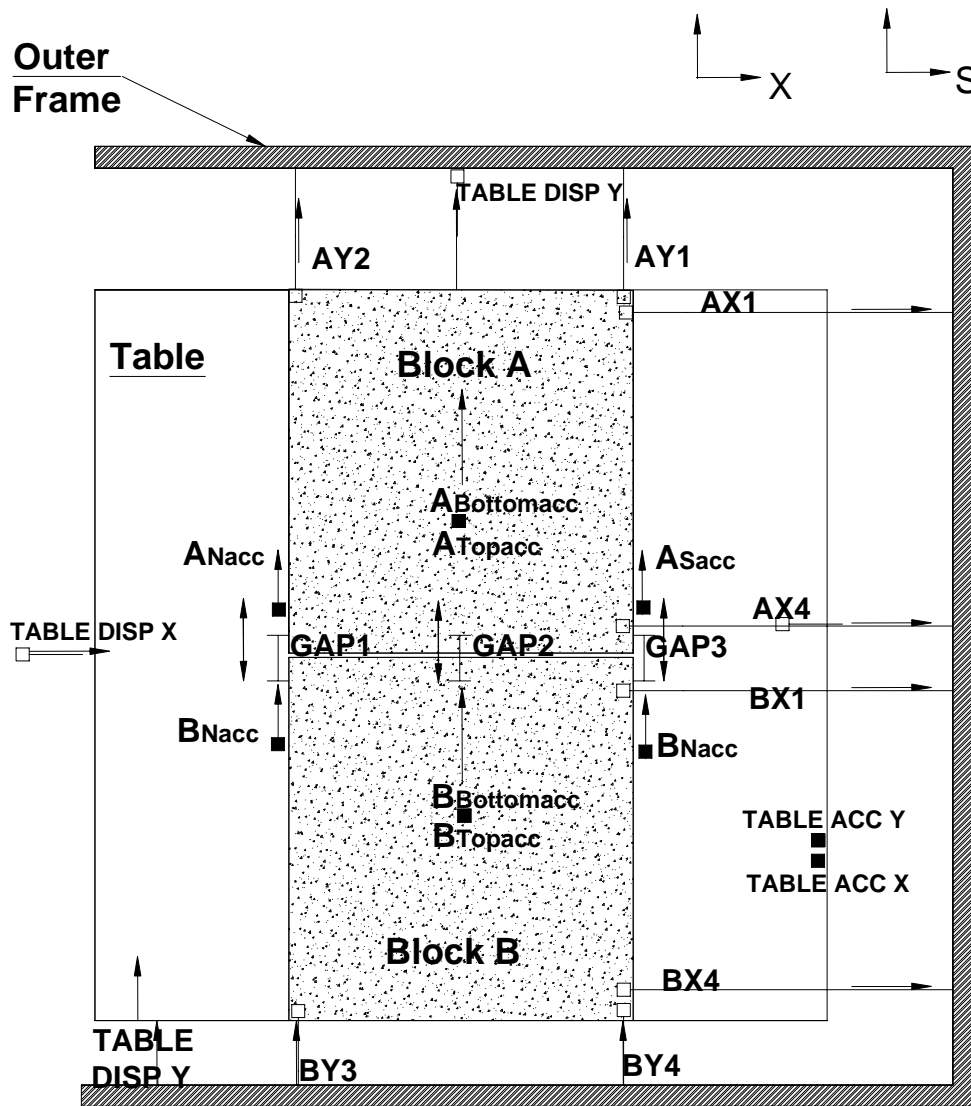





-  Linear Displacement Transducers (measures relative displacement)
-  Accelerometers (measures magnitude of acceleration)
-  Unimeasure String Potentiometers (measures absolute displacement)

TOP VIEW

Figure 4-5: Instrumentation for CFRP restrainer tests

August 11, 2004 Hybrid Shake Table Test



-  Linear Displacement Transducers (measures relative displacement)
-  Accelerometers (measures magnitude of acceleration)
-  Unimeasure String Potentiometers (measures absolute displacement)

TOP VIEW

Figure 4-6: Instrumentation for hybrid FRP restrainer tests



Figure 5-1: GFRP restrainer shake table tests



Figure 5-2: CFRP restrainer shake table tests



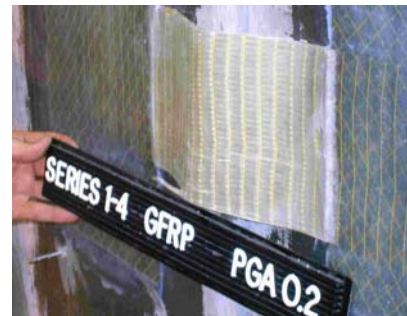
Figure 5-3: CGFRP restrainer shake table tests



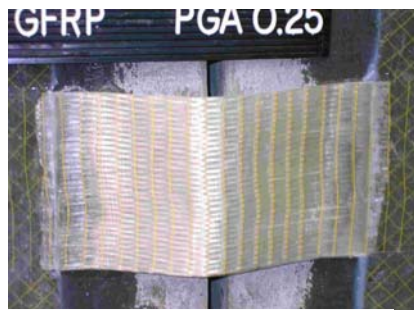
(a) PGA of 0.15g, north-side restrainer



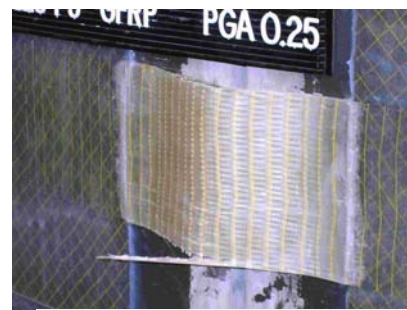
(b) PGA of 0.2g, north



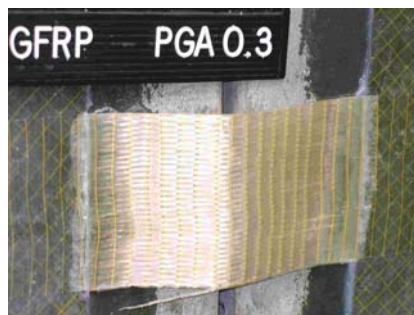
(e) PGA of 0.2g, south



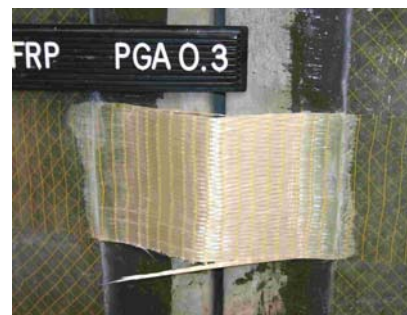
(c) PGA of 0.25g, north



(f) PGA of 0.25g, south



(d) PGA of 0.3g, north



(g) PGA of 0.3g, south

Figure 5-4: Effect of Earthquake Motion on GFRP Restrainers

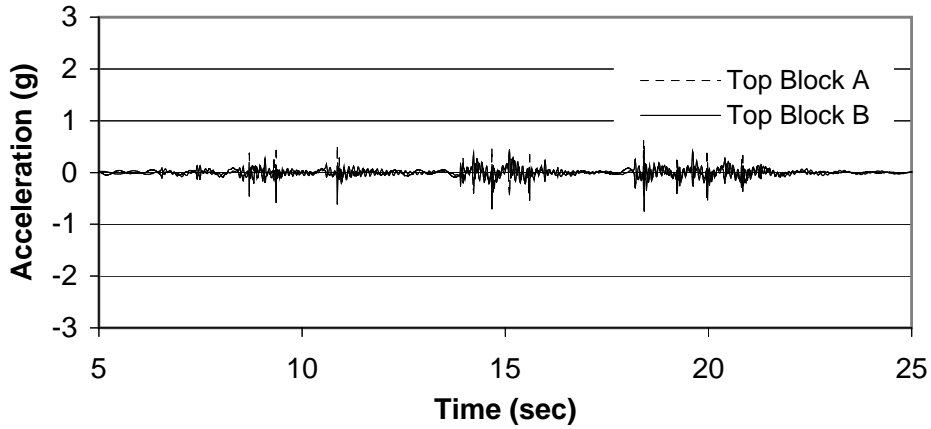


Figure 5-5(a): Acceleration History GFRP Restrainer Test, PGA = 0.05g, ATC32E

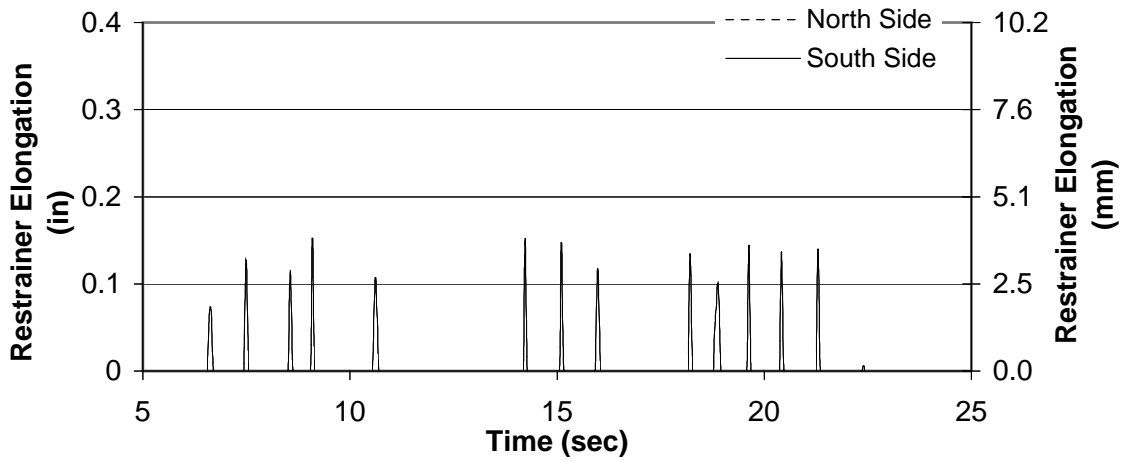


Figure 5-5(b): Displacement History GFRP Restrainer Test, PGA = 0.05g, ATC32E

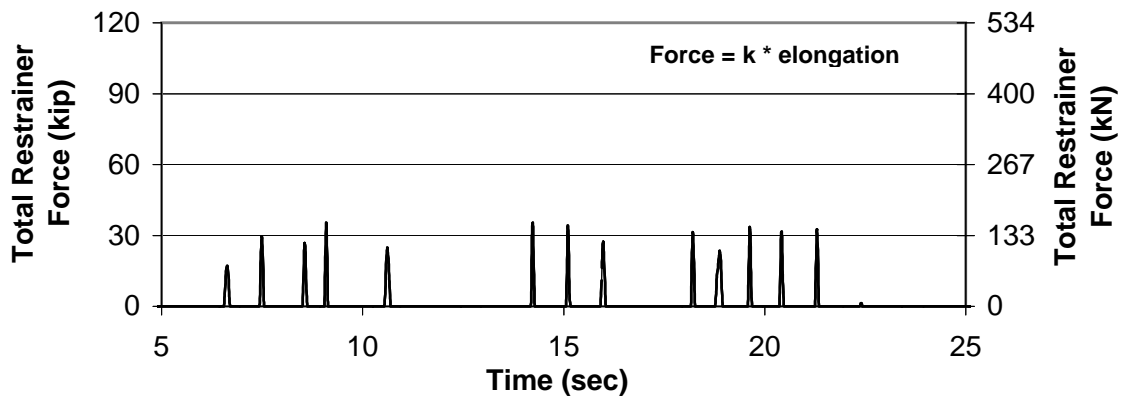


Figure 5-5(c): Force History GFRP Restrainer Test, PGA = 0.05g, ATC32E

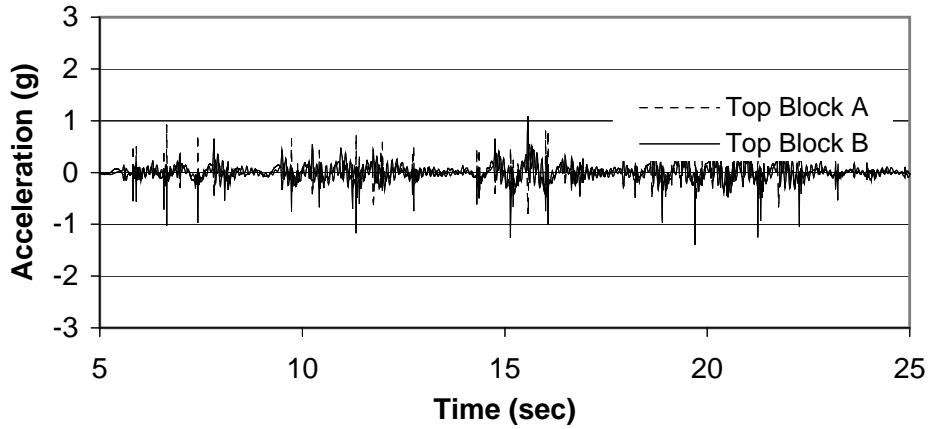


Figure 5-6(a): Acceleration History GFRP Restrainer Test, PGA = 0.1g, ATC32E

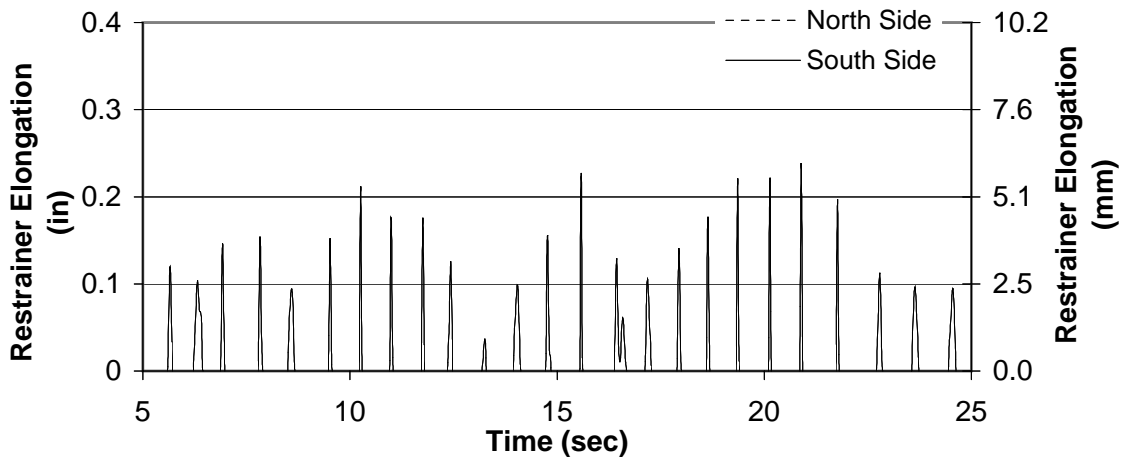


Figure 5-6(b): Displacement History GFRP Restrainer Test, PGA = 0.1g, ATC32E

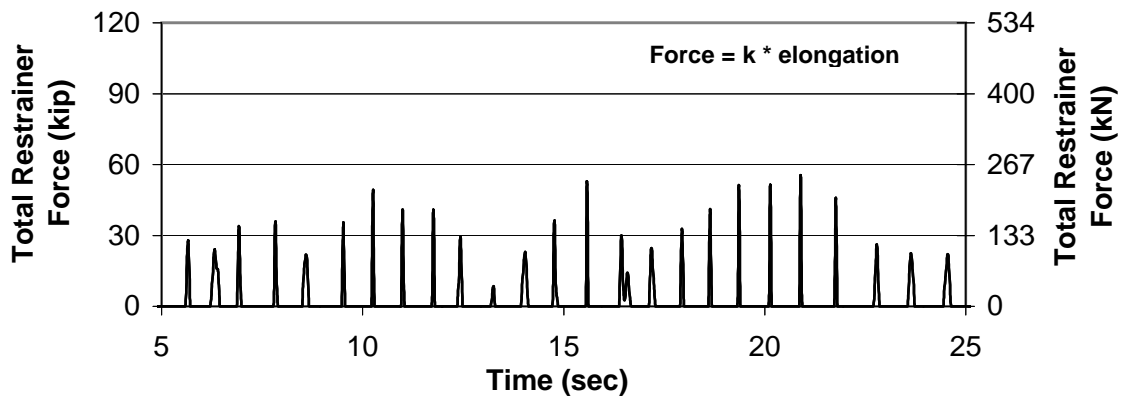


Figure 5-6(c): Force History GFRP Restrainer Test, PGA = 0.1g, ATC32E

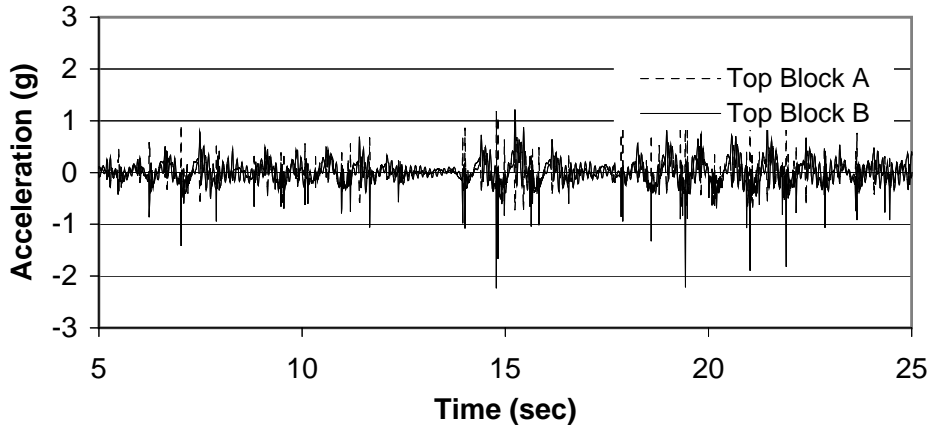


Figure 5-7(a): Acceleration History GFRP Restrainer Test, PGA = 0.15g, ATC32E

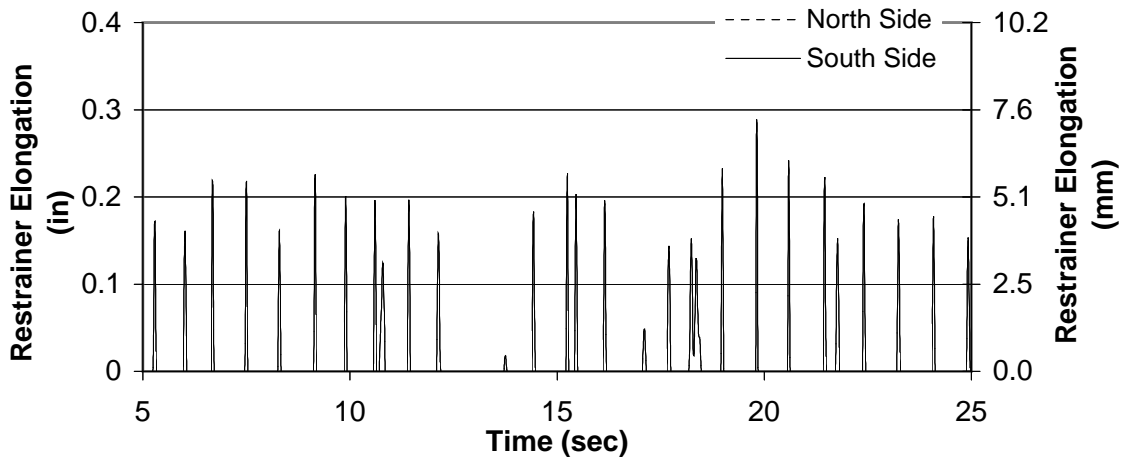


Figure 5-7(b): Displacement History GFRP Restrainer Test, PGA = 0.15g, ATC32E

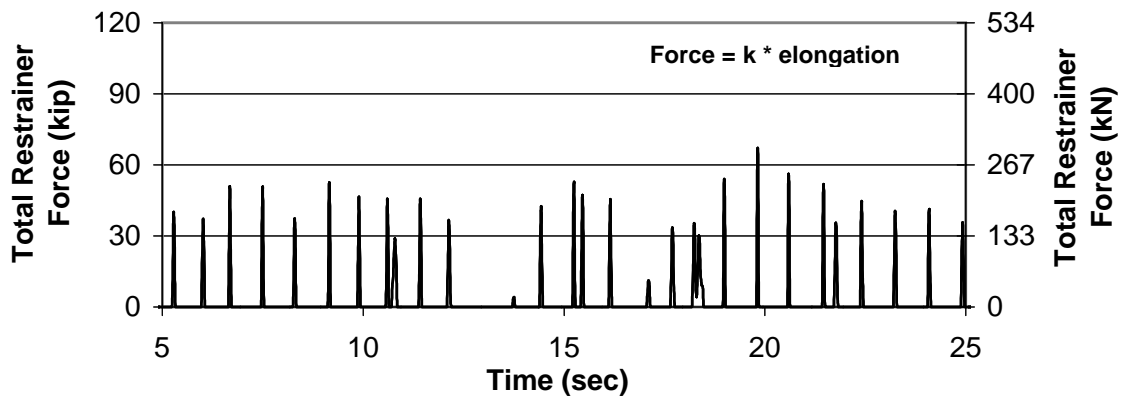


Figure 5-7(c): Force History GFRP Restrainer Test, PGA = 0.15g, ATC32E

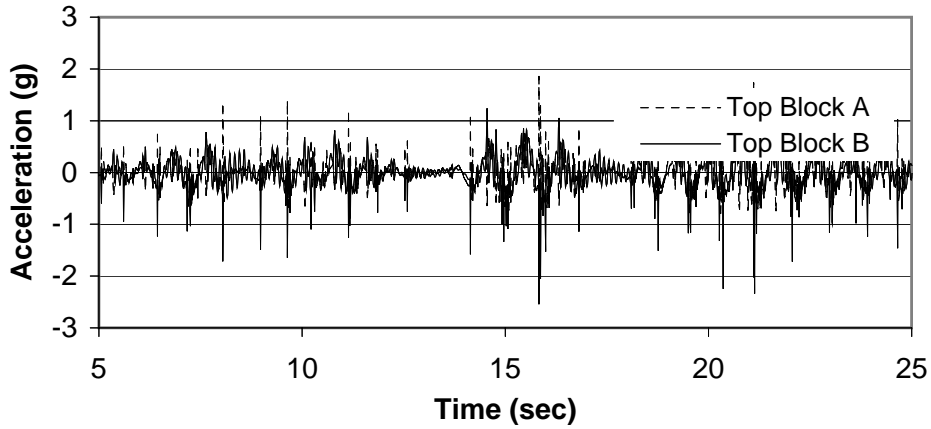


Figure 5-8(a): Acceleration History GFRP Restrainer Test, PGA = 0.2g, ATC32E

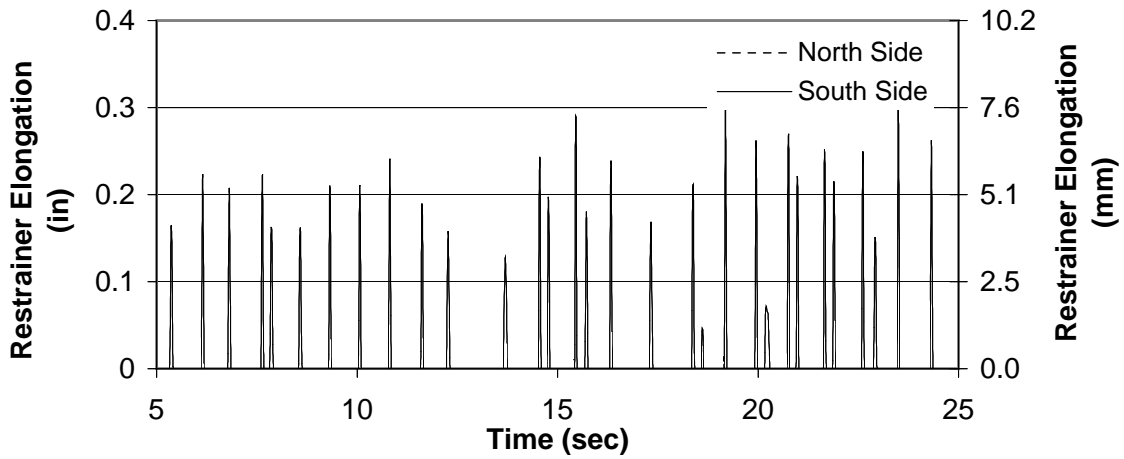


Figure 5-8(b): Displacement History GFRP Restrainer Test, PGA = 0.2g, ATC32E

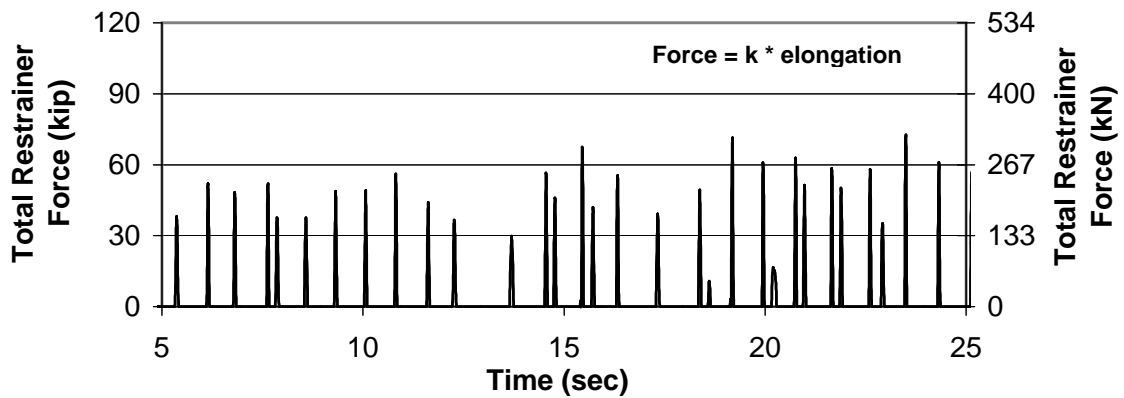


Figure 5-8(c): Force History GFRP Restrainer Test, PGA = 0.2g, ATC32E

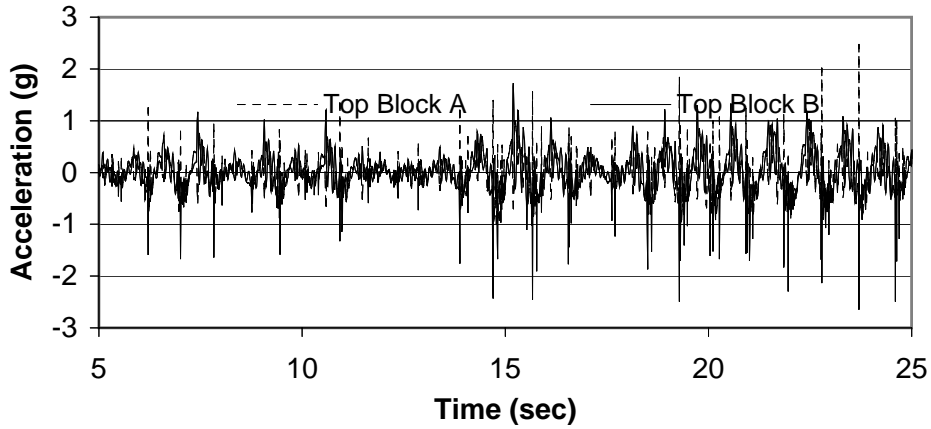


Figure 5-9(a): Acceleration History GFRP Restrainer Test, PGA = 0.25g, ATC32E

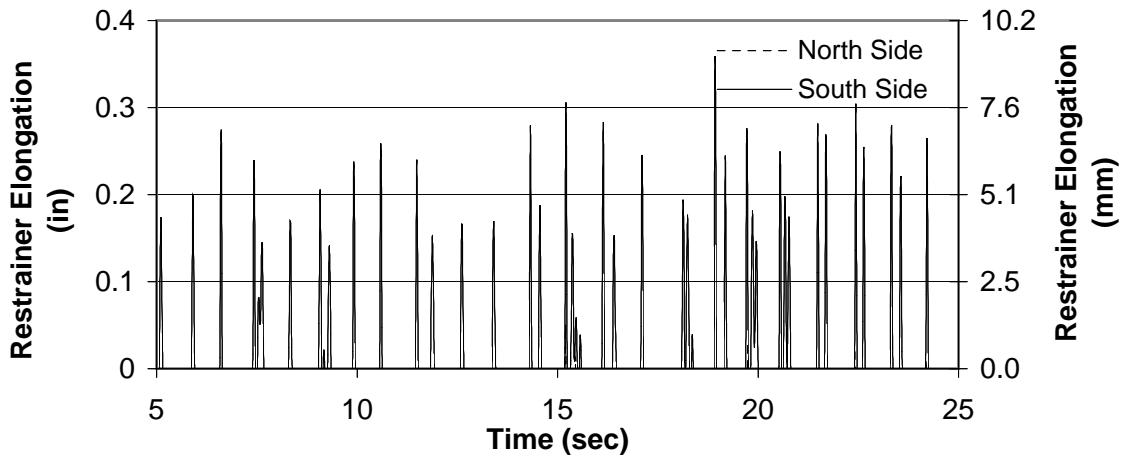


Figure 5-9(b): Displacement History GFRP Restrainer Test, PGA = 0.25g, ATC32E

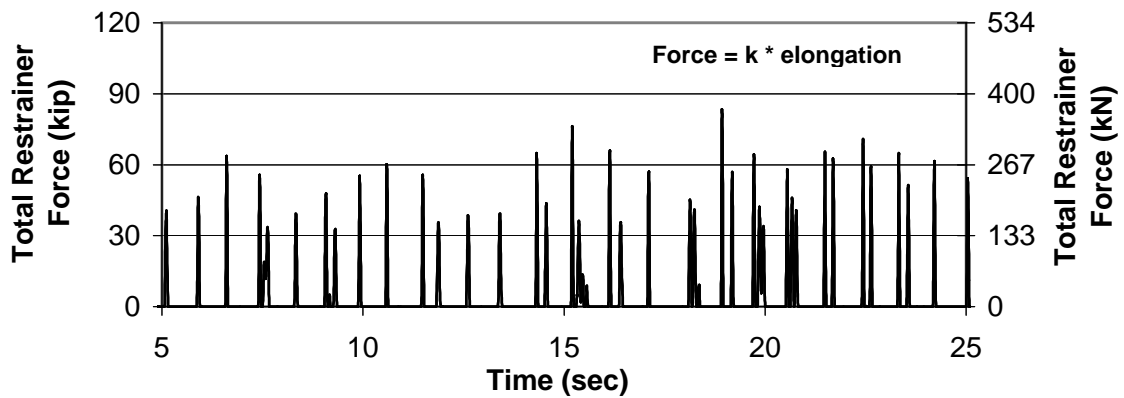


Figure 5-9(c): Force History GFRP Restrainer Test, PGA = 0.25g, ATC32E

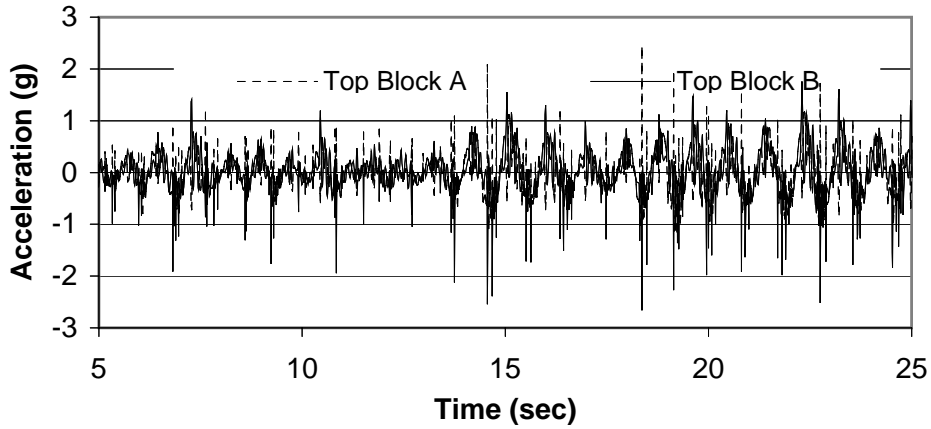


Figure 5-10(a): Acceleration History GFRP Restrainer Test, PGA = 0.3g, ATC32E

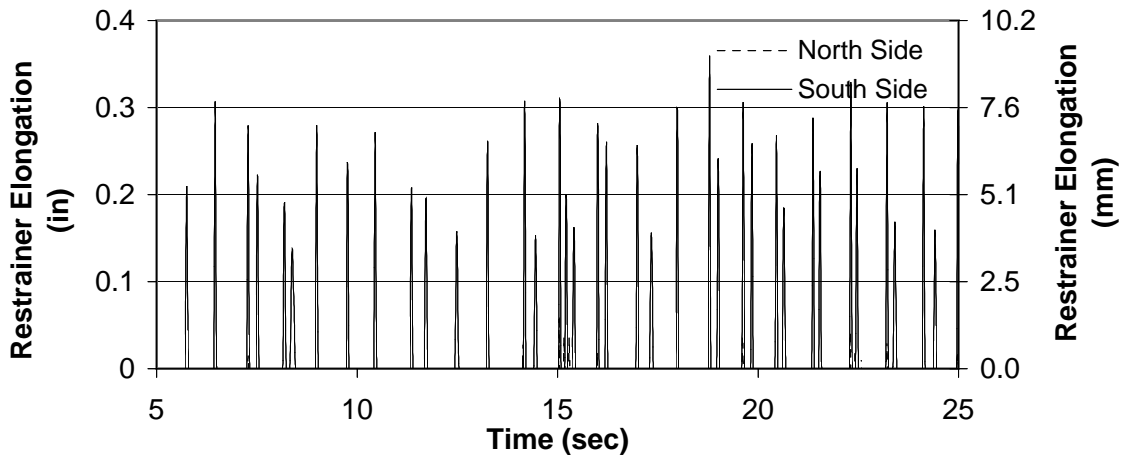


Figure 5-10(b): Displacement History GFRP Restrainer Test, PGA = 0.3g, ATC32E

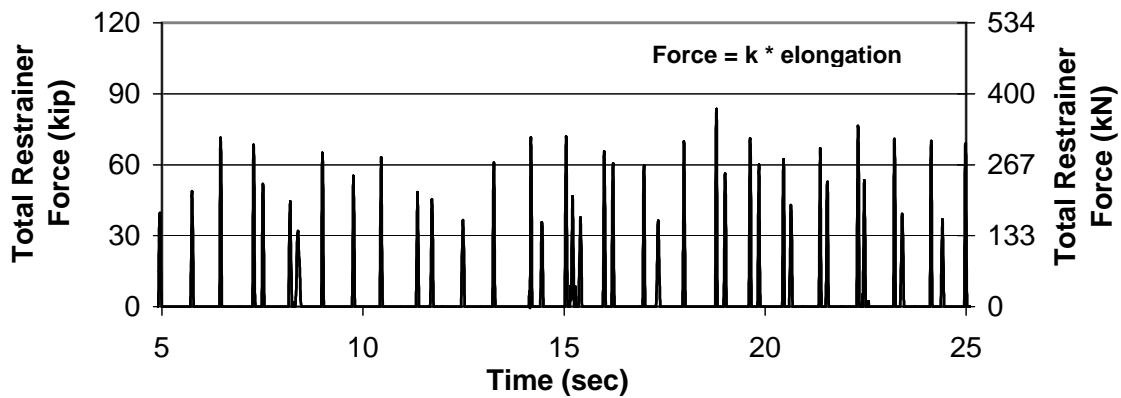


Figure 5-10(c): Force History GFRP Restrainer Test, PGA = 0.3g, ATC32E

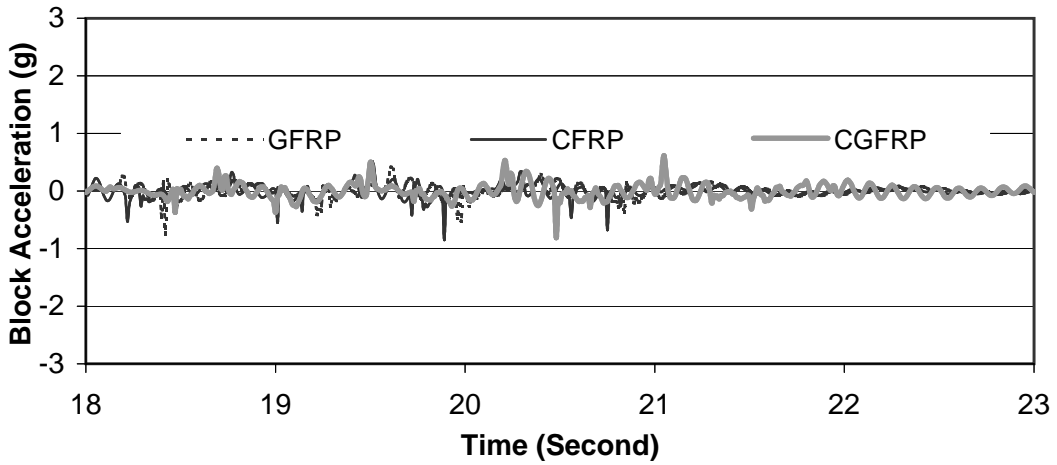


Figure 6-1(a): Block Acceleration Histories, ATC32E, PGA = 0.05g

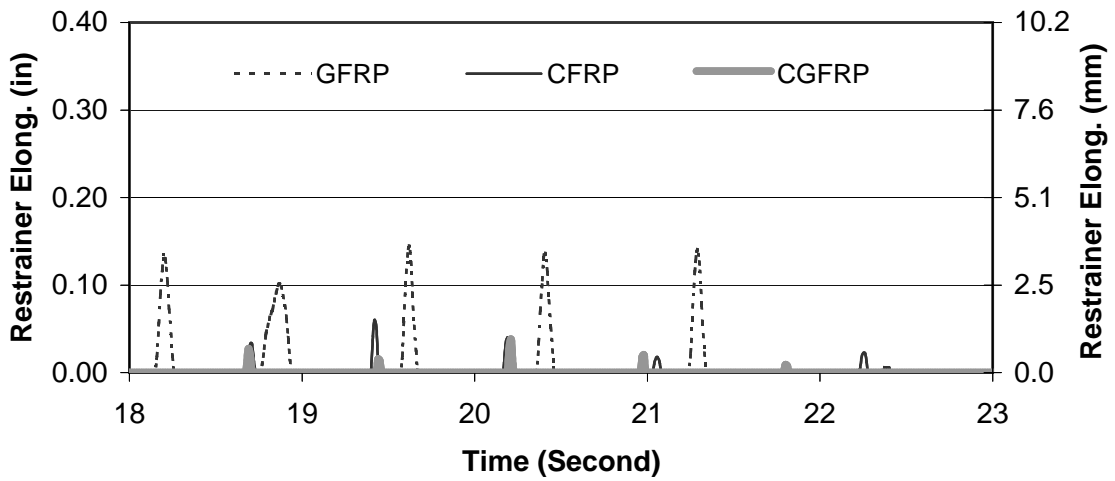


Figure 6-1(b): FRP Restrainer Elongation Histories, ATC32E, PGA = 0.05g

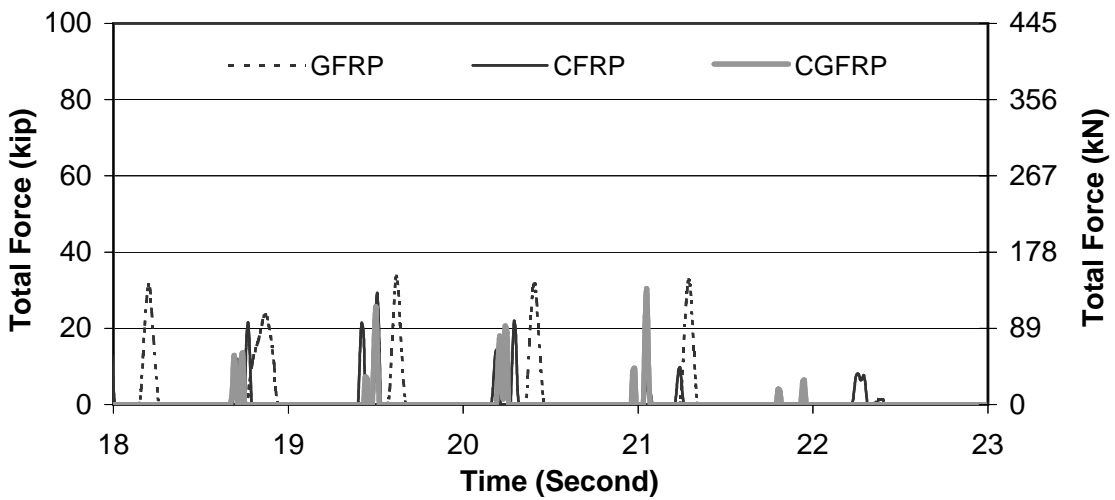


Figure 6-1(c): FRP Total Restrainer Force Histories, ATC32E, PGA = 0.05g

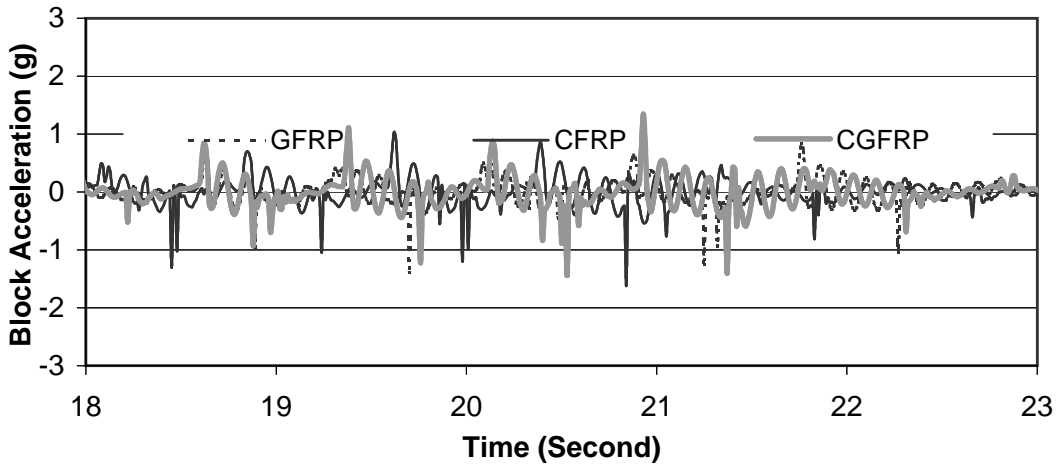


Figure 6-2(a): Block Acceleration Histories, ATC32E, PGA = 0.1g

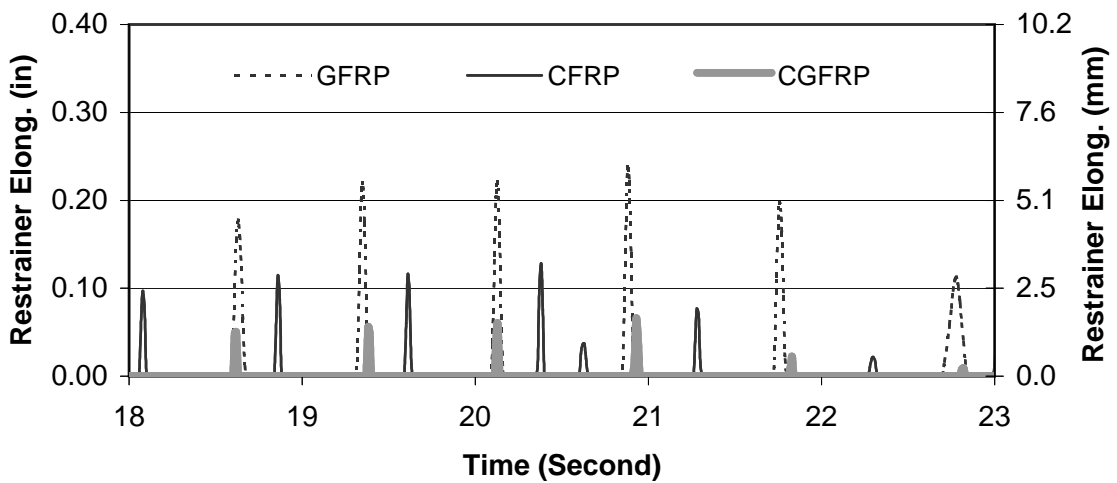


Figure 6-2(b): FRP Restrainer Elongation Histories, ATC32E, PGA = 0.1g

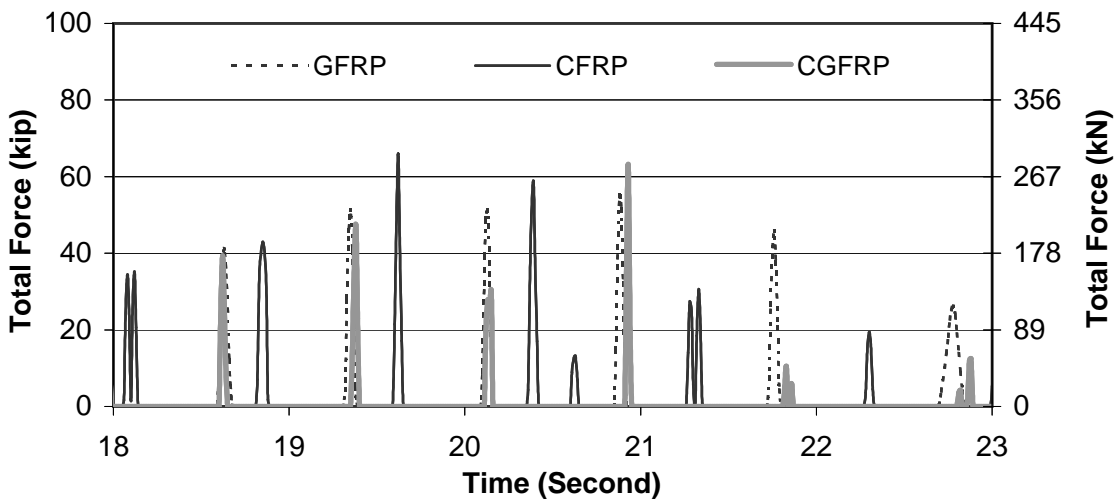


Figure 6-2(c): FRP Total Restrainer Force Histories, ATC32E, PGA = 0.1g

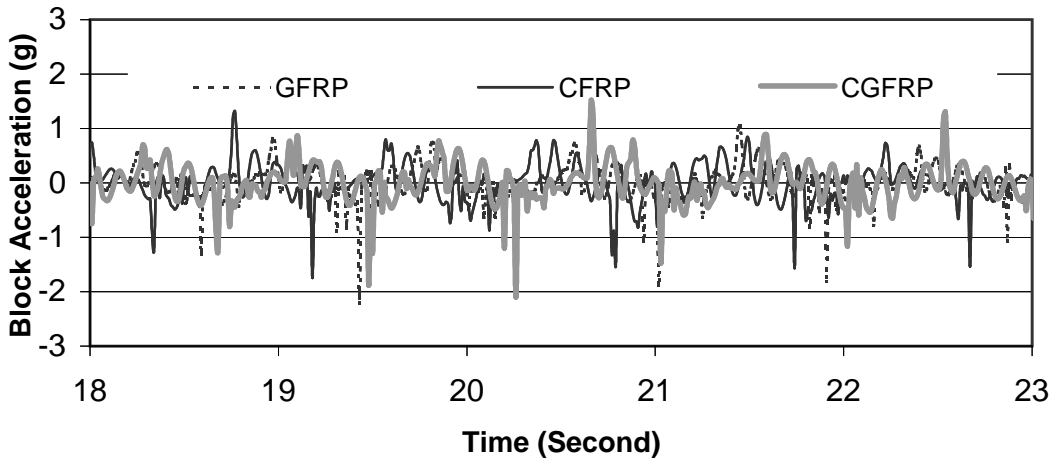


Figure 6-3(a): Block Acceleration Histories, Case 1, PGA = 0.15g

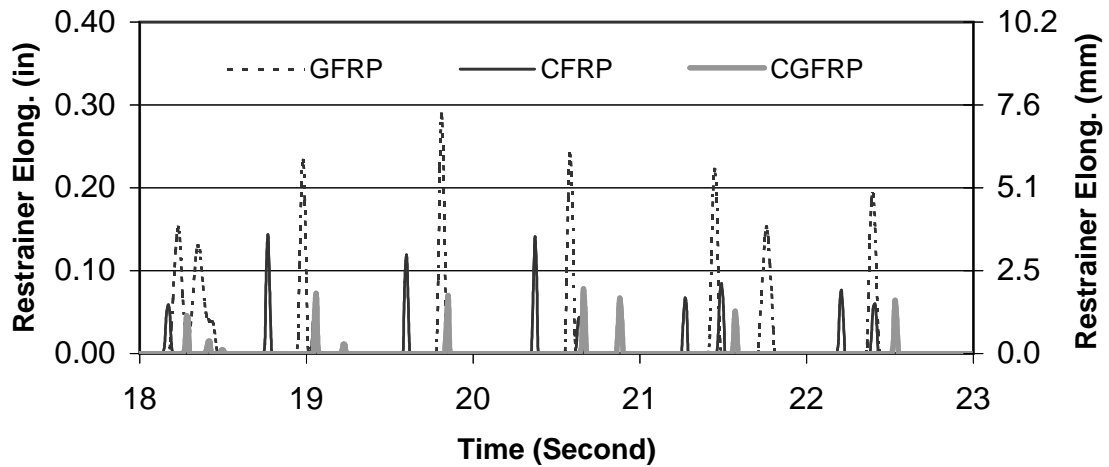


Figure 6-3(b): FRP Restrainer Elongation Histories, Case 1, PGA = 0.15g

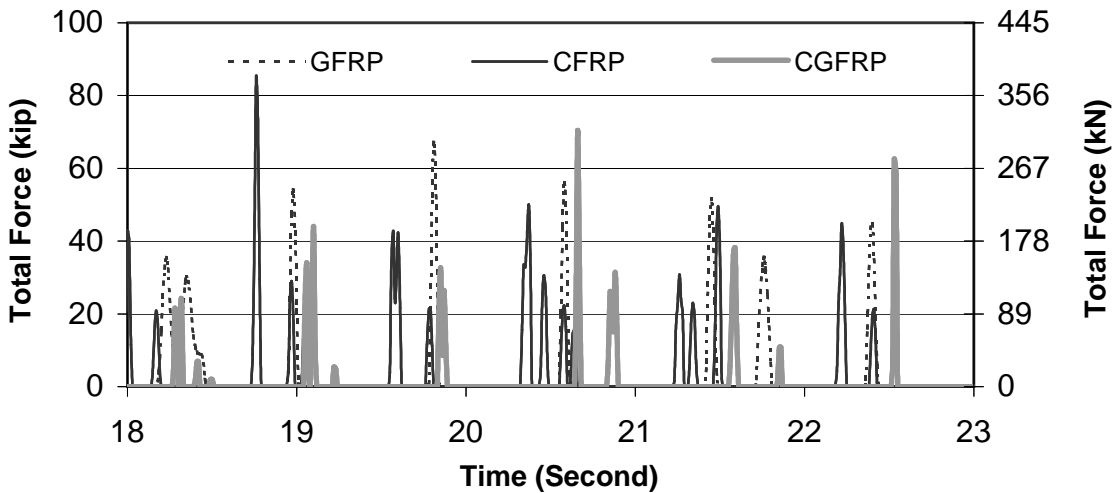


Figure 6-3(c): FRP Total Restrainer Force Histories, Case 1, PGA = 0.15g

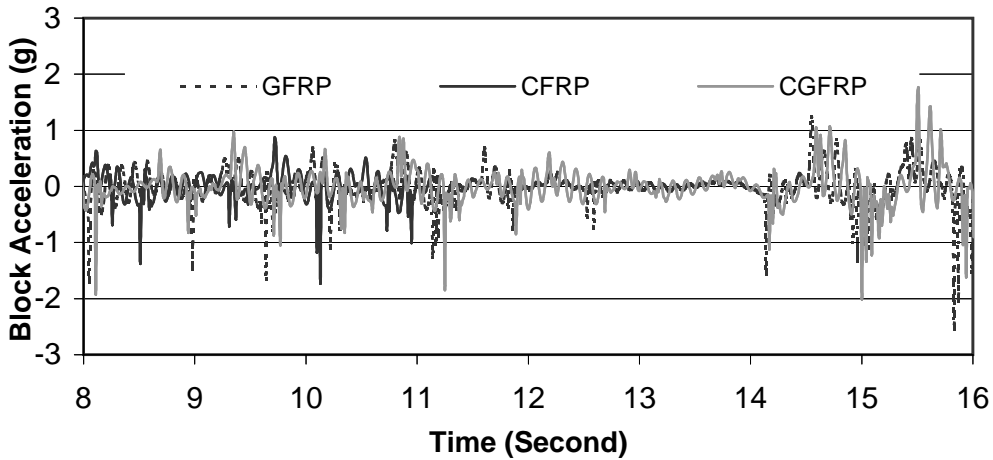


Figure 6-4(a): Block Acceleration Histories, Case 2, PGA = 0.2g

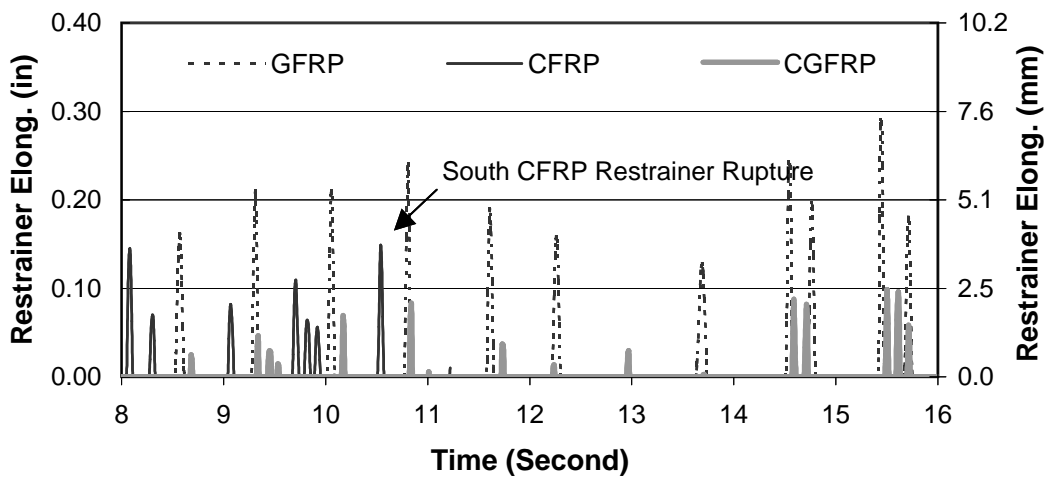


Figure 6-4(b): FRP Restrainer Elongation Histories, Case 2, PGA = 0.2g

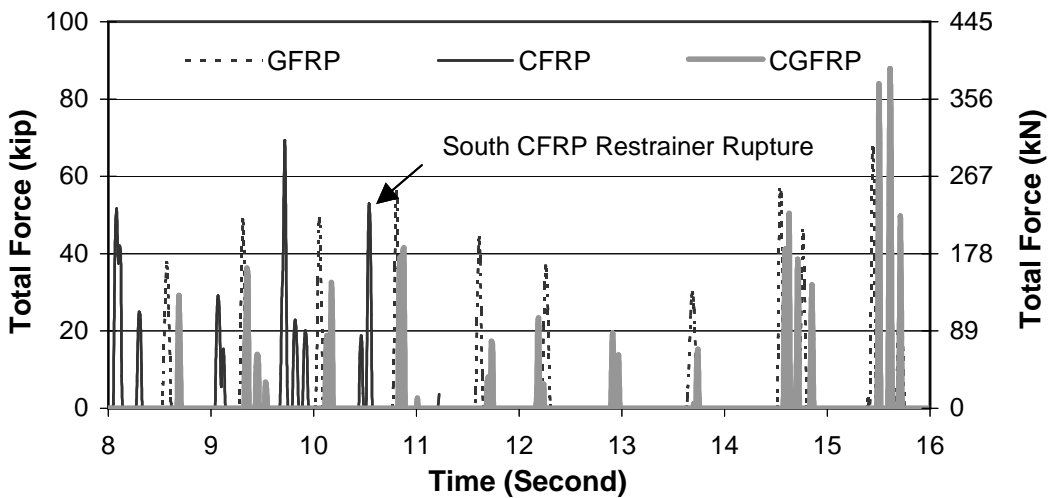


Figure 6-4(c): FRP Total Restrainer Force Histories, Case 2, PGA = 0.2g

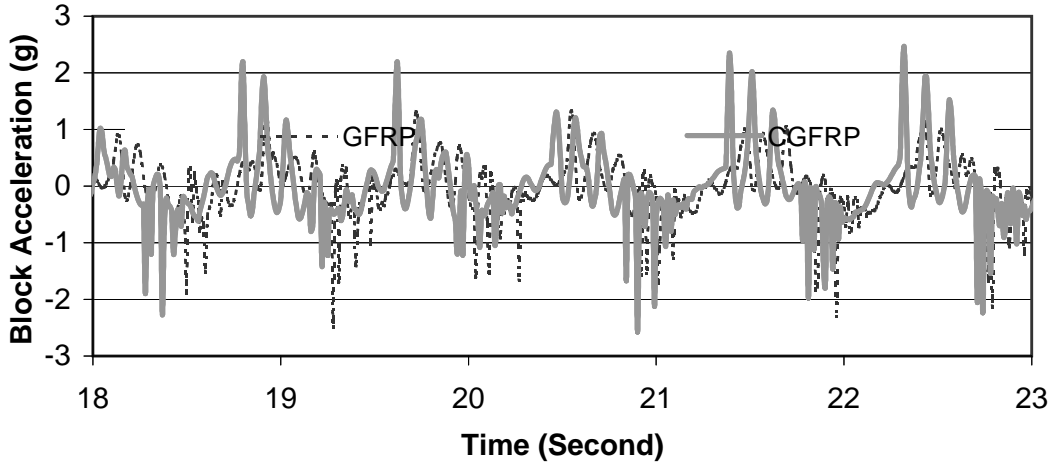


Figure 6-5(a): Block Acceleration Histories, ATC32E, PGA = 0.25g

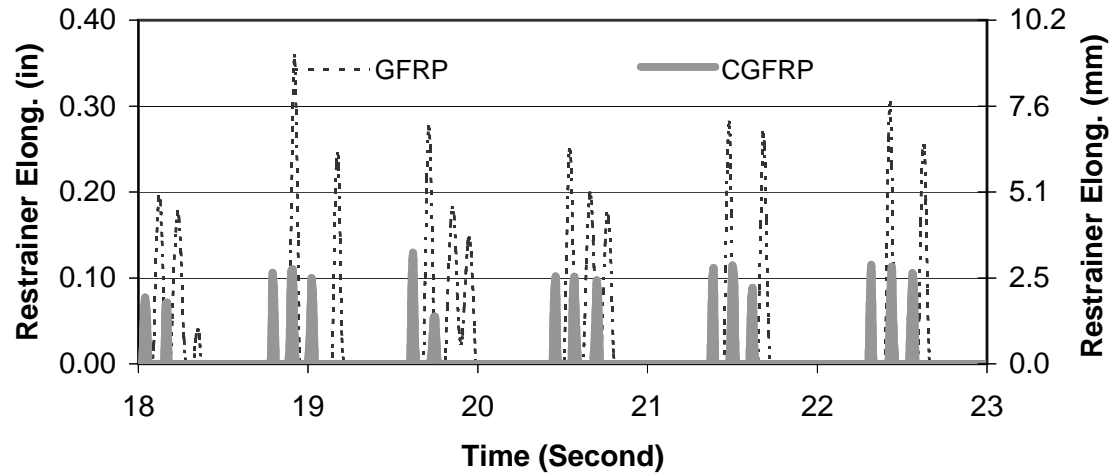


Figure 6-5(b): FRP Restrainer Elongation Histories, ATC32E, PGA = 0.25g

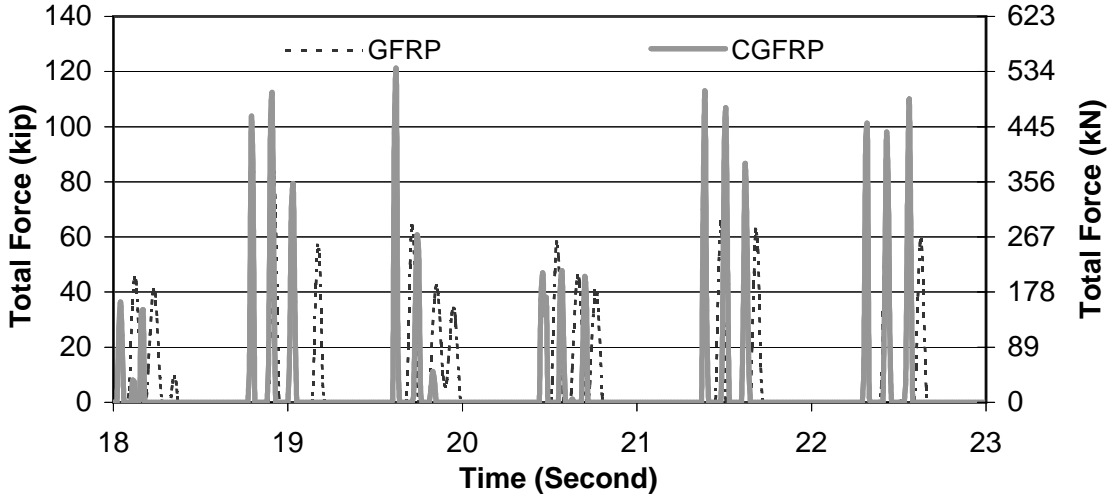


Figure 6-5(c): FRP Total Restrainer Force Histories, ATC32E, PGA = 0.25g

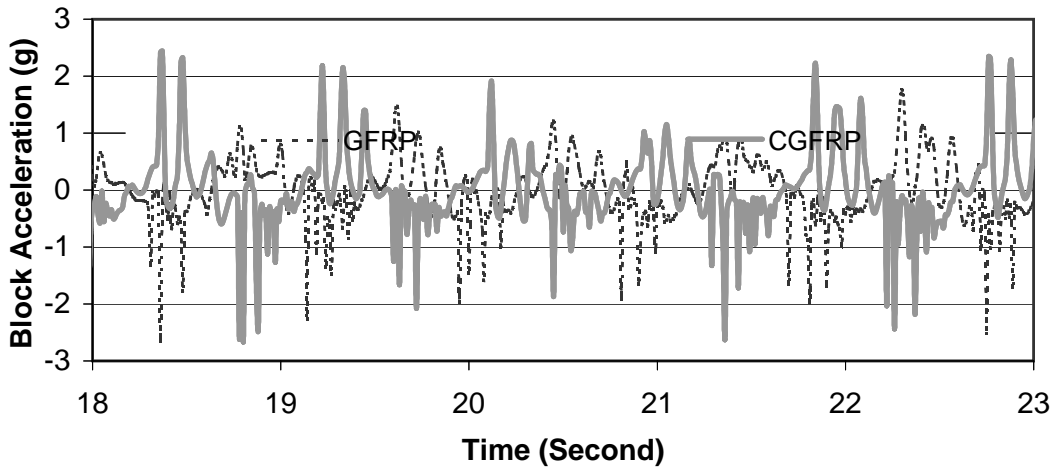


Figure 6-6(a): Block Acceleration Histories, ATC32E, PGA = 0.3g

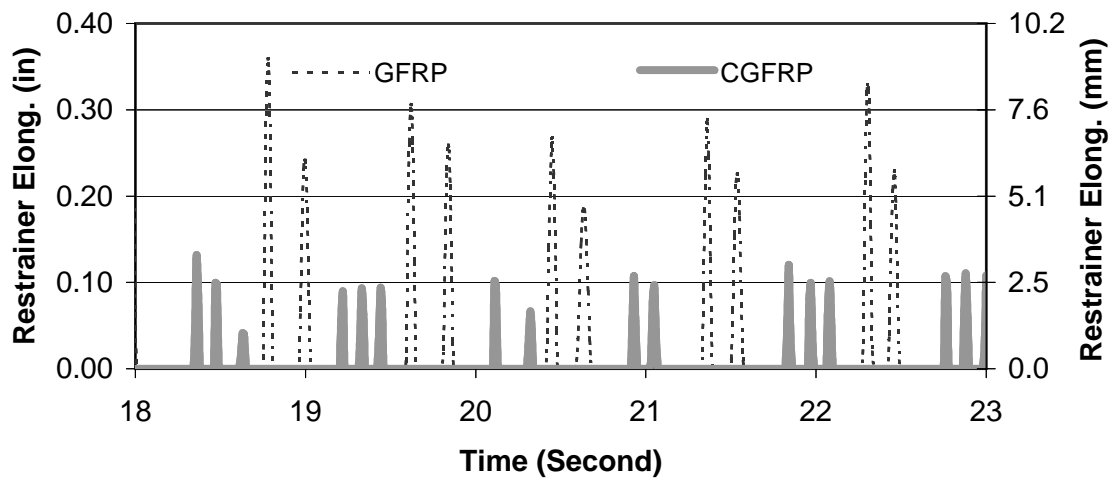


Figure 6-6(b): FRP Restrainer Elongation Histories, ATC32E, PGA = 0.3g

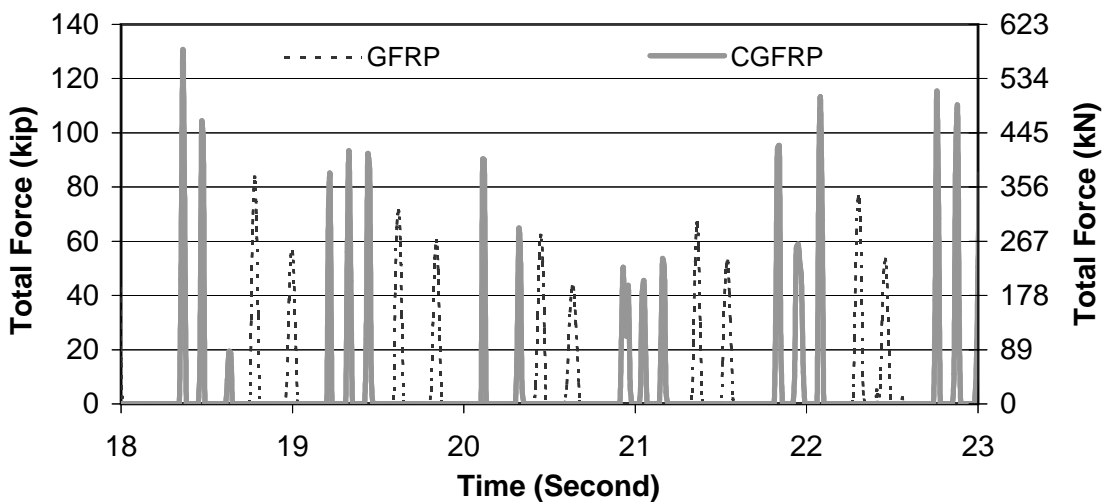


Figure 6-6(c): FRP Total Restrainer Force Histories, ATC32E, PGA = 0.3g

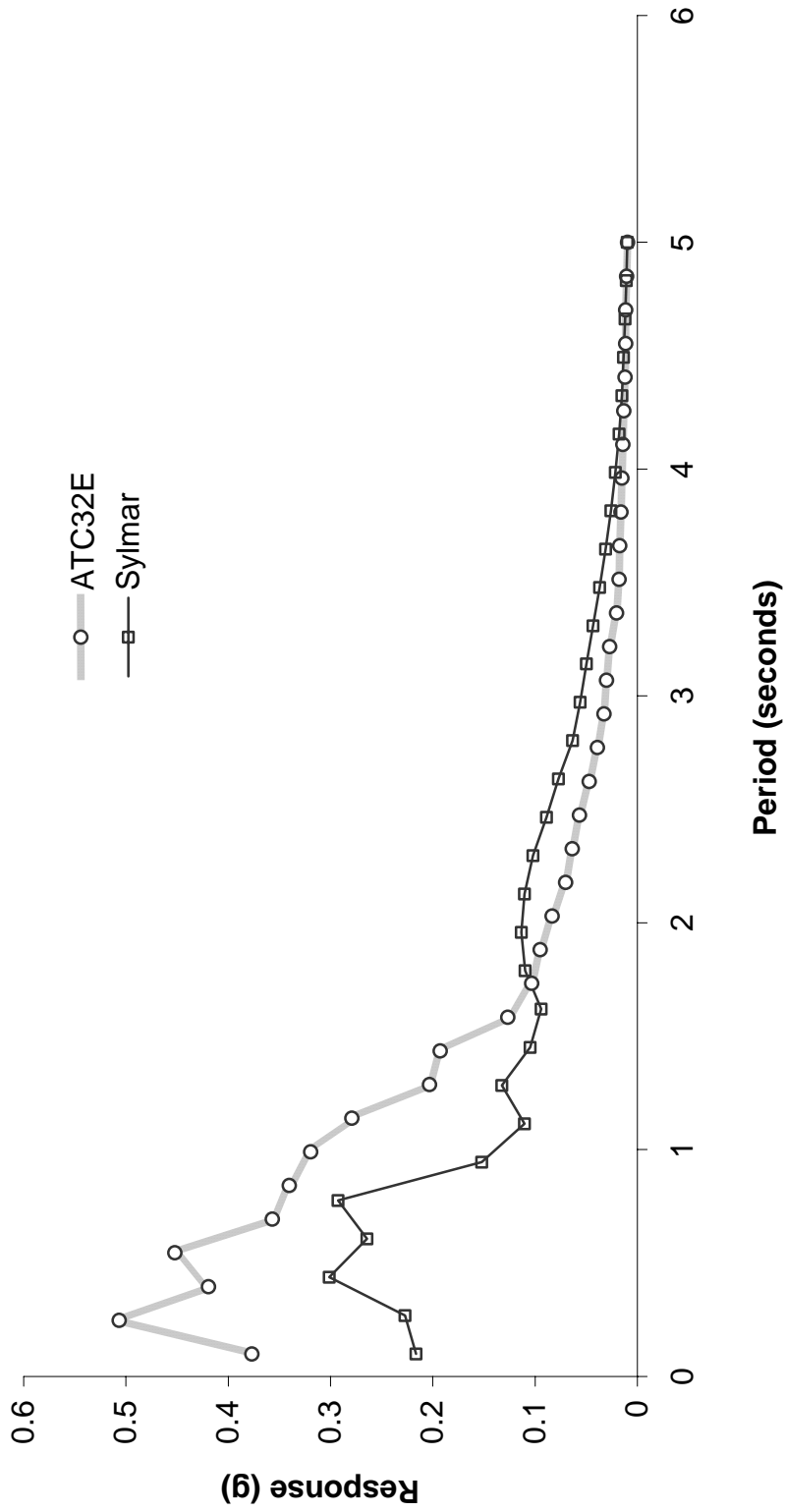


Figure 6-7: Earthquake Spectras from CGFRP Restrainer Shake Table Tests, ATC32E vs. Sylmar, Case 1

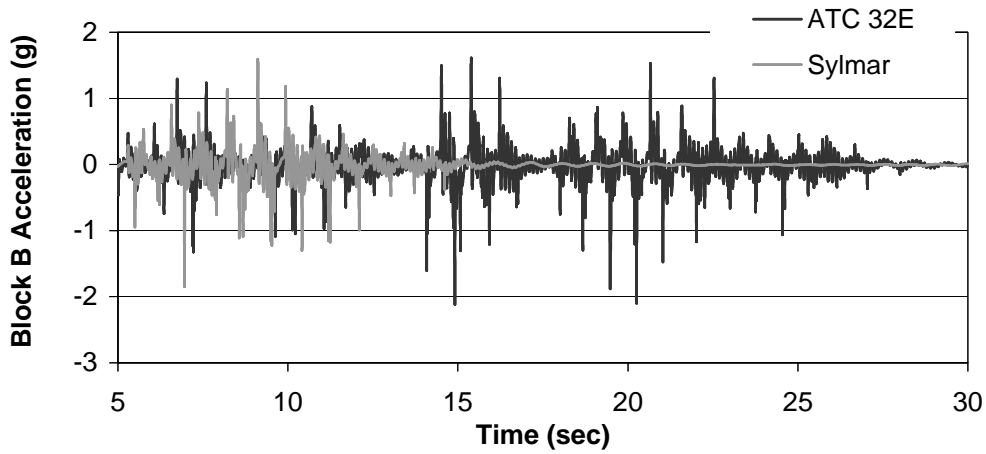


Figure 6-8(a): Acceleration History, CGFRP Restrainer Tests, PGA = 0.15g

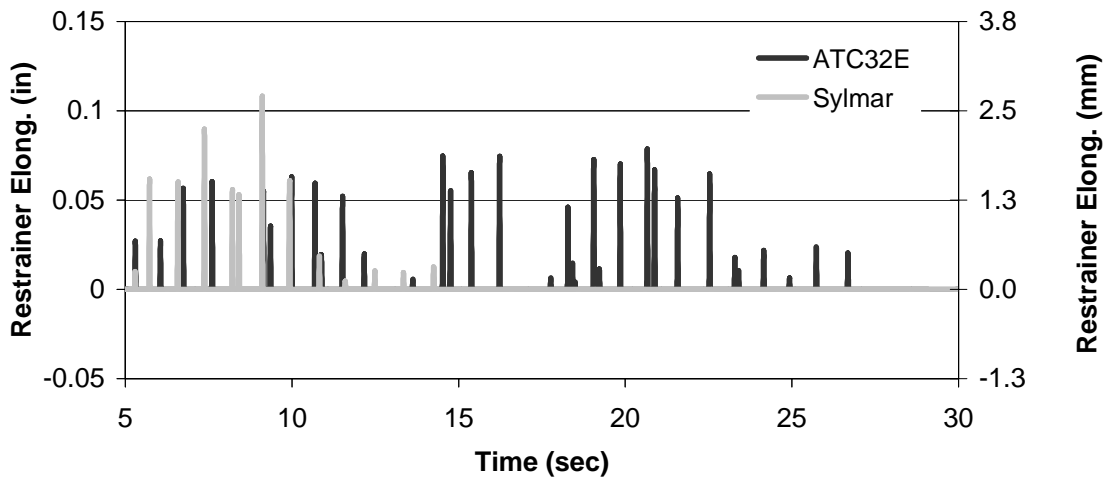


Figure 6-8(b): Restrainer Elongation History, CGFRP Restrainer Tests, PGA = 0.15g

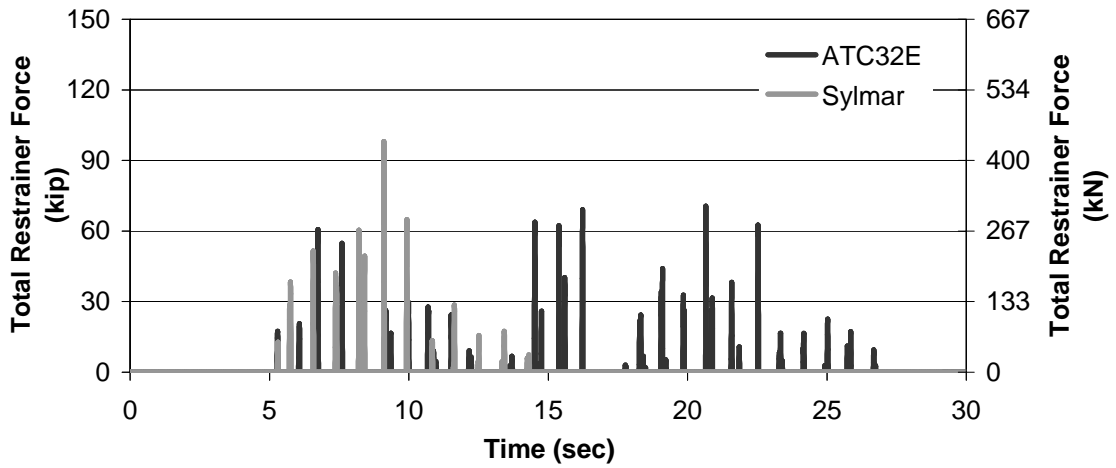


Figure 6-8(c): Total Restrainer Force History, CGFRP Restrainer Tests, PGA = 0.15g

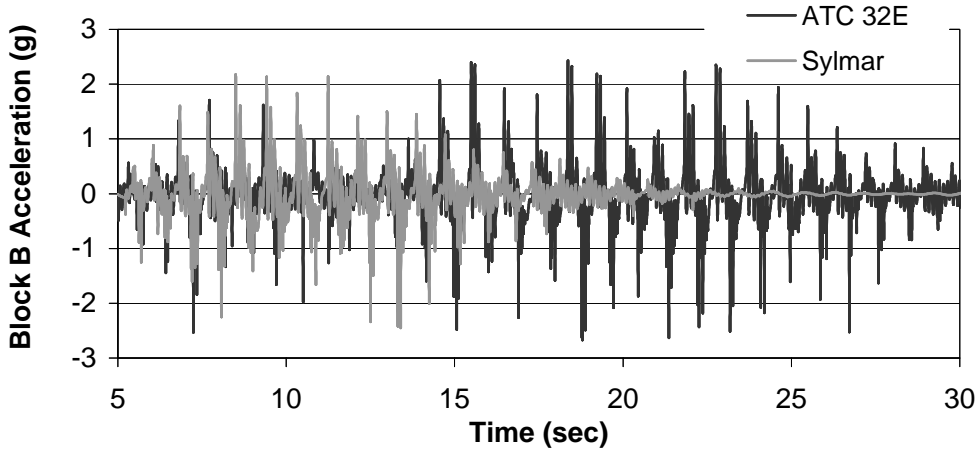


Figure 6-9(a): Acceleration History, CGFRP Restrainer Tests, PGA = 0.3g

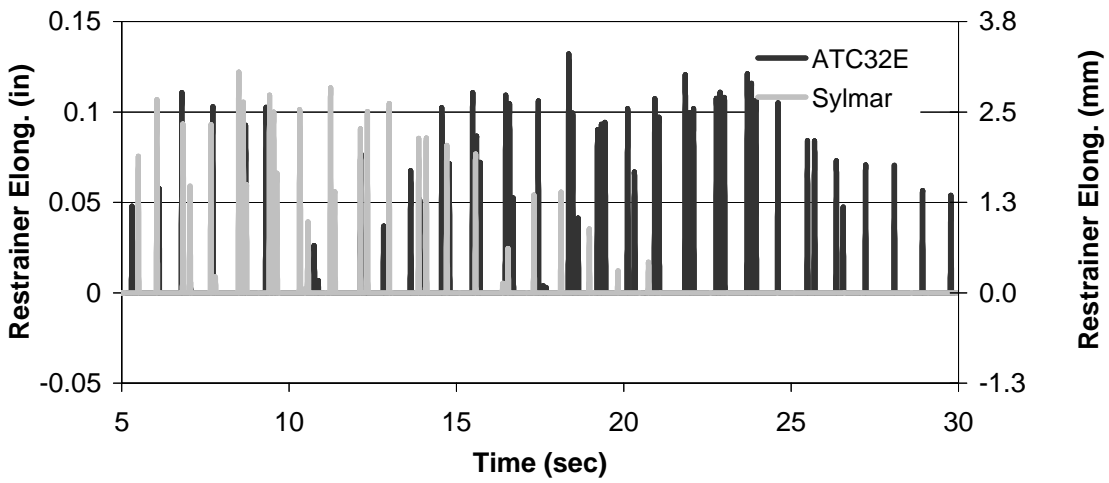


Figure 6-9(b): Restrainer Elongation History, CGFRP Restrainer Tests, PGA = 0.3g

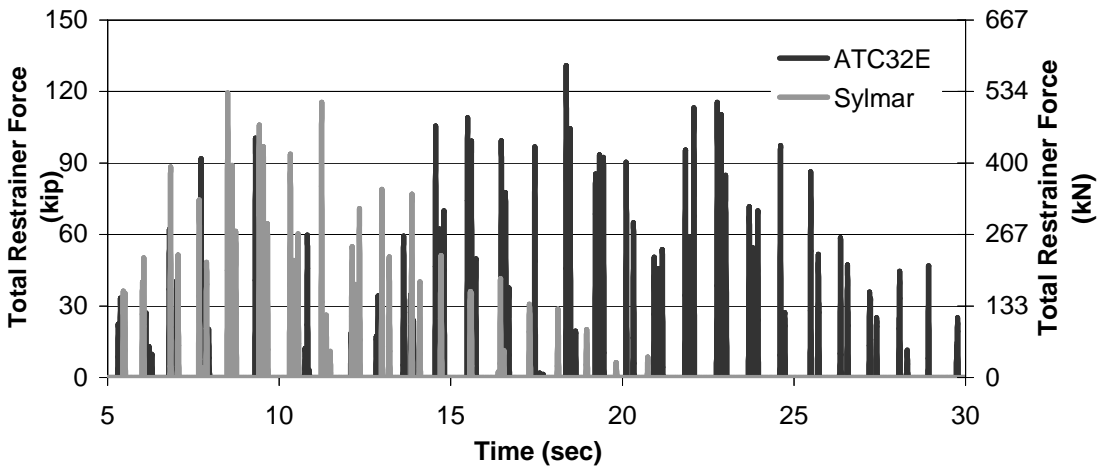


Figure 6-9(c): Total Restrainer Force History, CGFRP Restrainer Tests, PGA = 0.3g

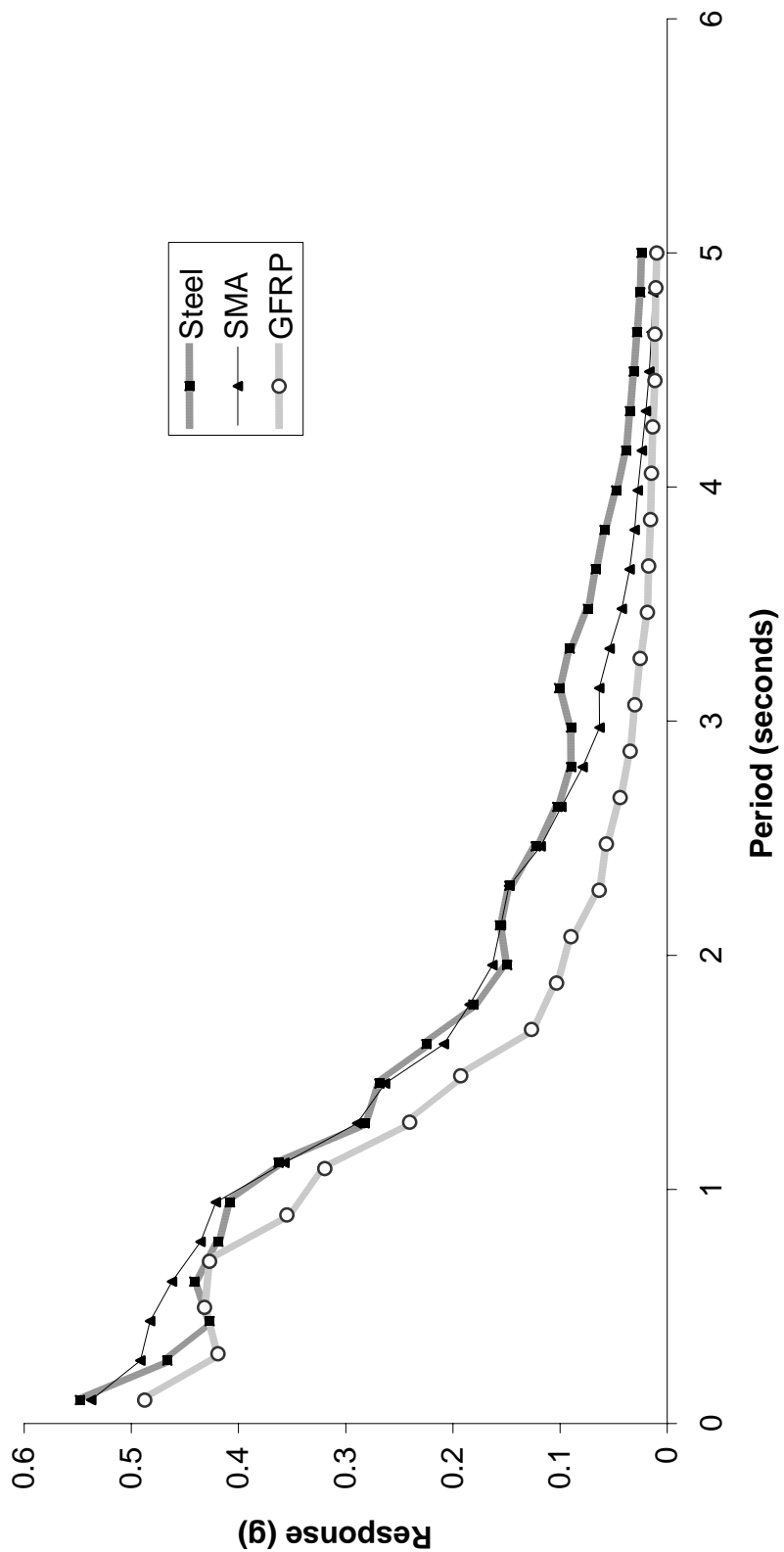


Figure 6-10: Earthquake Spectras from Steel, SMA and GFRP Restrainer Shake Table Tests, Case 1

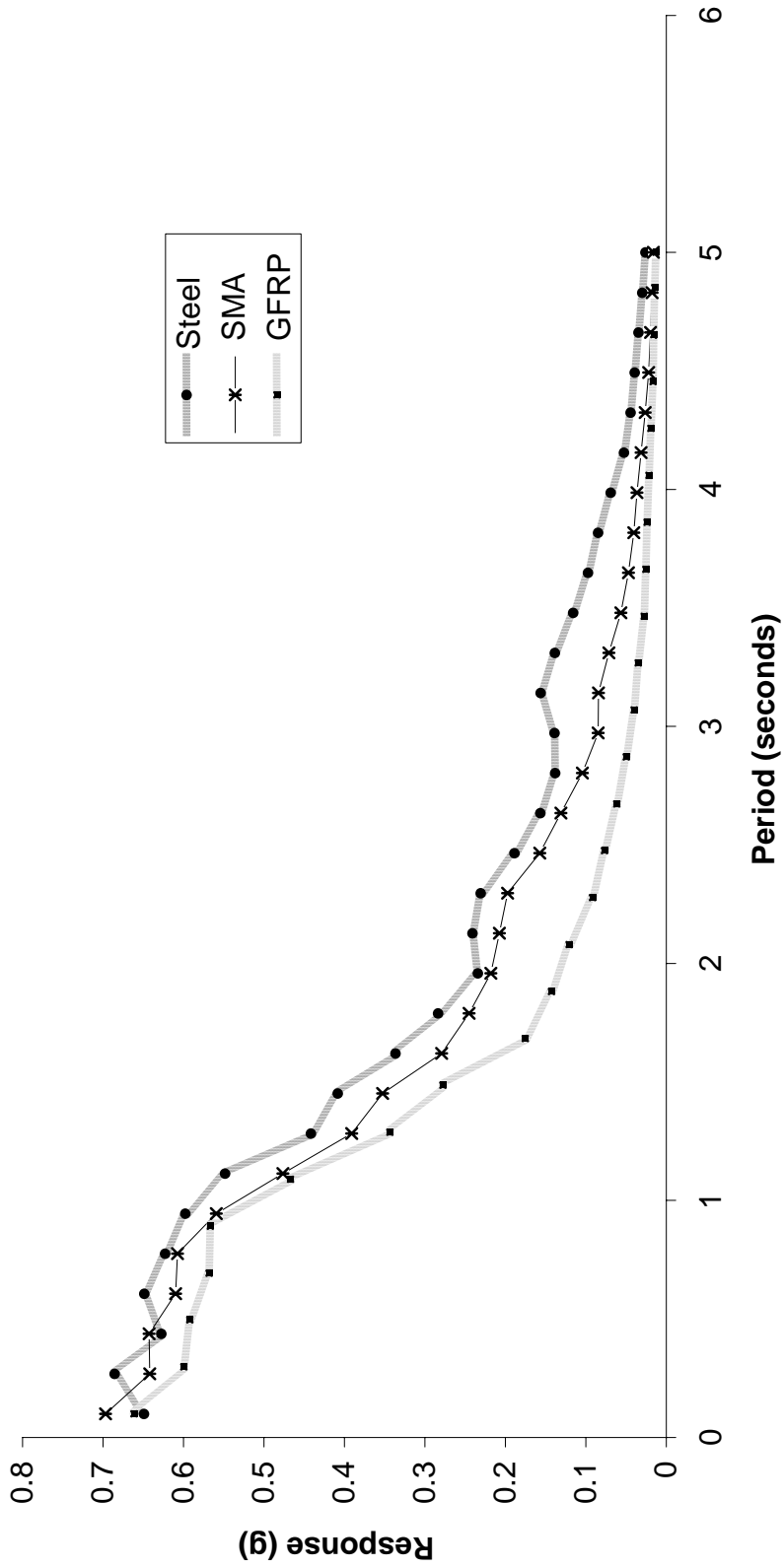


Figure 6-11: Earthquake Spectras from Steel, SMA and GFRP Restrainer Shake Table Tests, Case 2

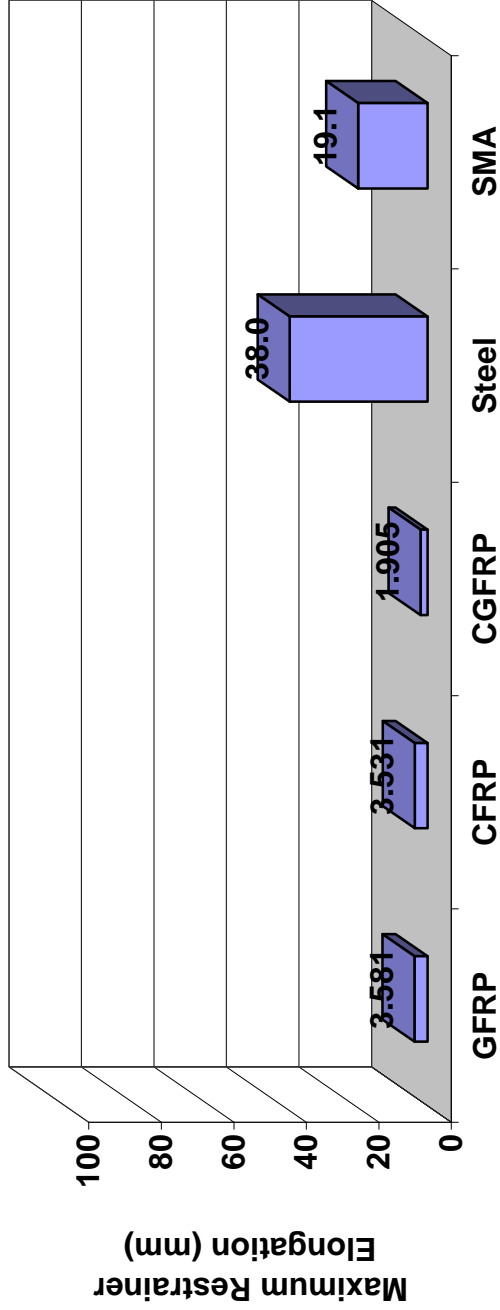


Figure 6-12: Maximum Elongation of Different Restrainer Types, Case 1

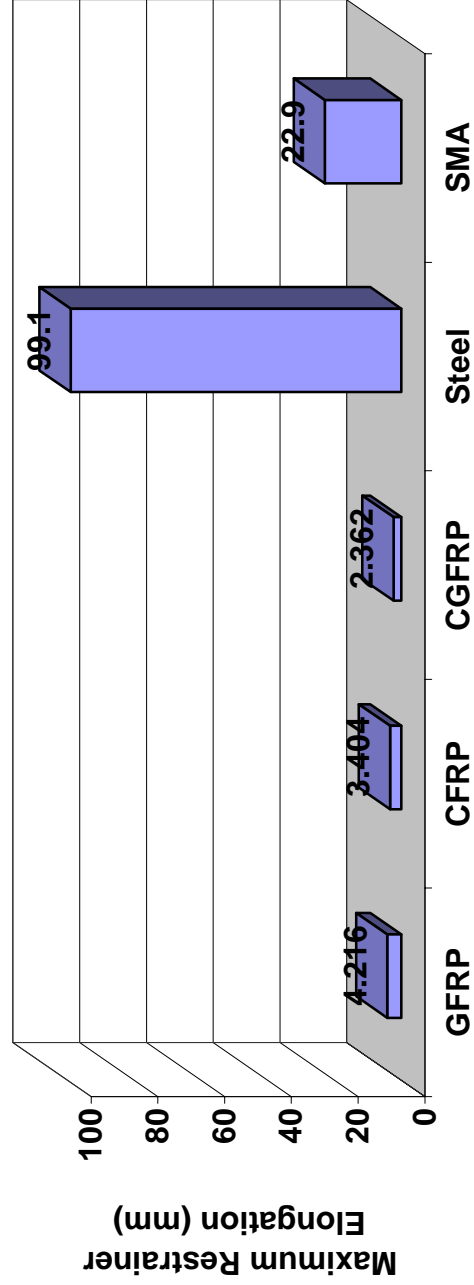


Figure 6-13: Maximum Elongation of Different Restrainer Types, Case 2

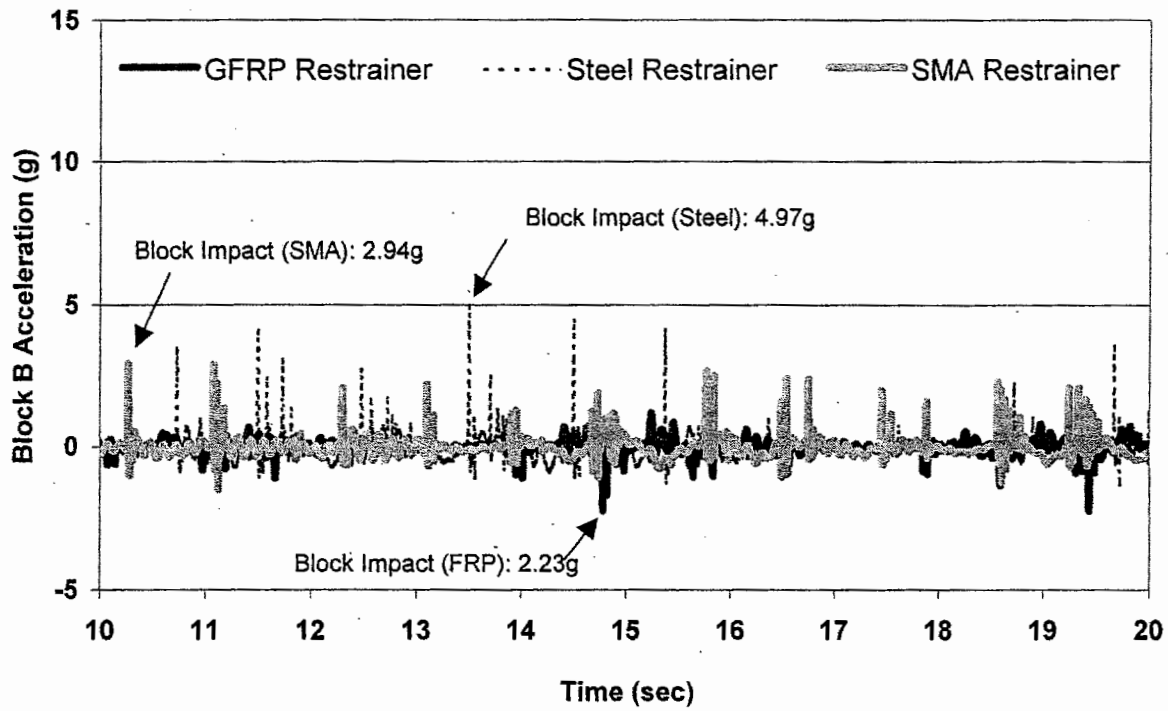


Figure 6-14(a): Block Acceleration Histories from Comparable GFRP, Steel, and SMA Restrainer Tests, Case 1

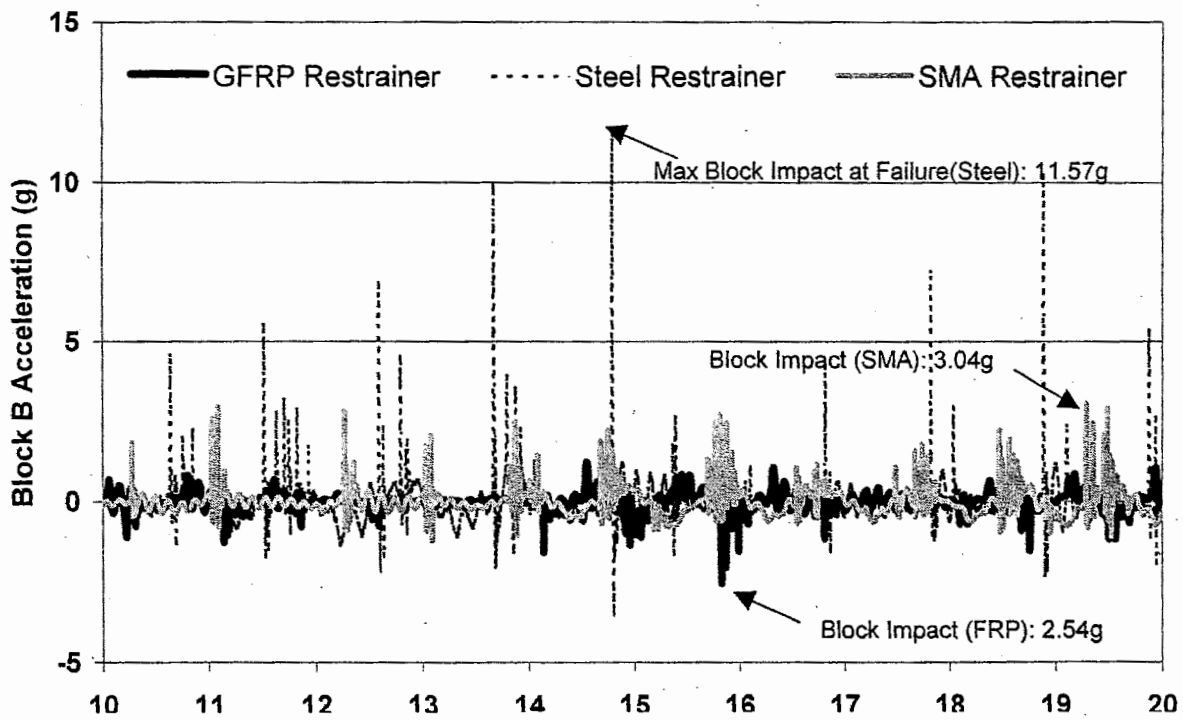


Figure 6-14(b): Block Acceleration Histories from Comparable GFRP, Steel, and SMA Restrainer Tests, Case 2

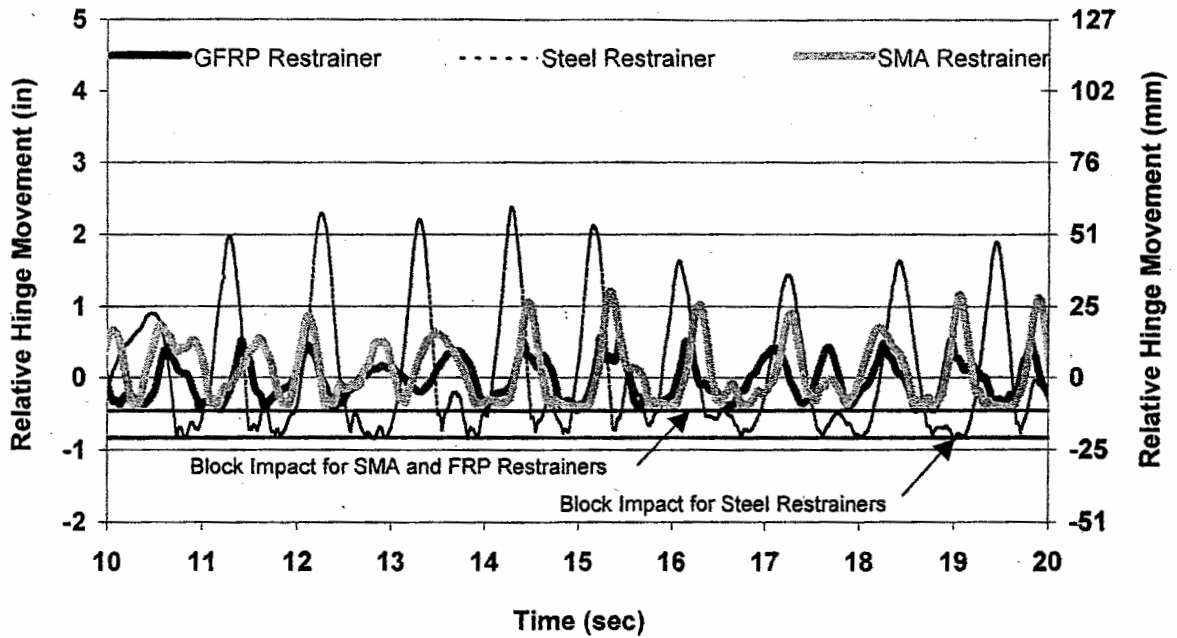


Figure 6-15(a): Relative Hinge Movement Histories from Comparable GFRP, Steel, and SMA Restrainer Tests, Case 1

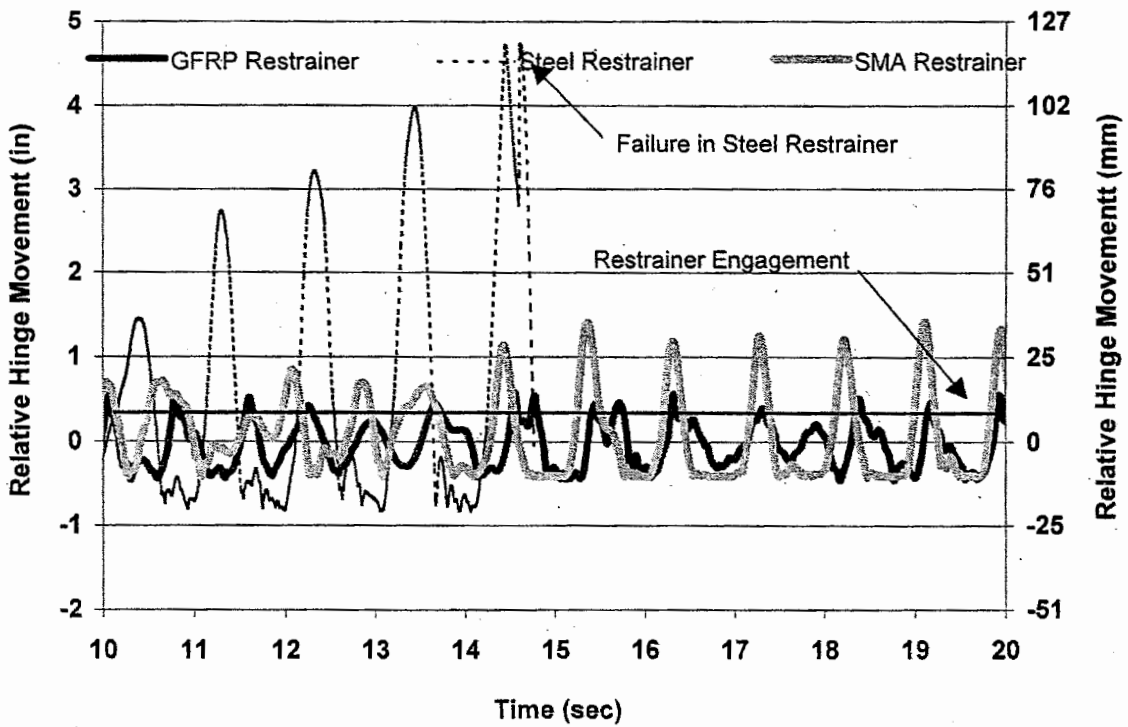


Figure 6-15(b): Relative Hinge Movement Histories from Comparable GFRP, Steel, and SMA Restrainer Tests, Case 2

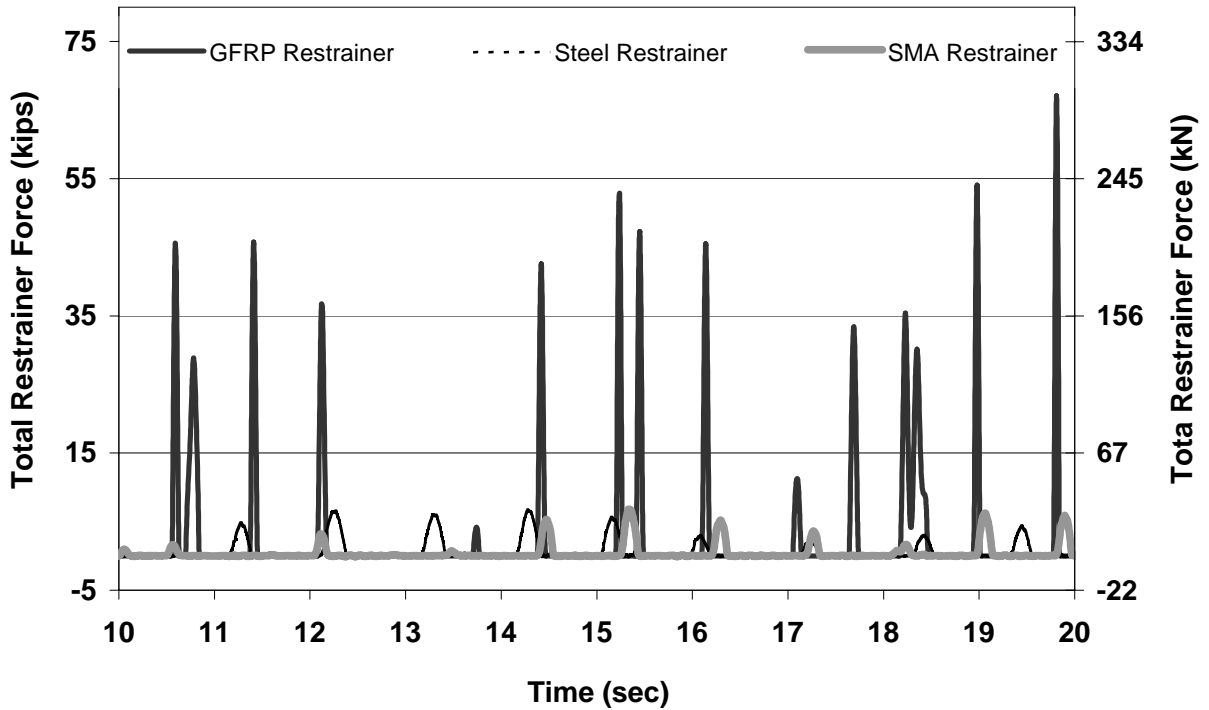


Figure 6-16(a): Total Restrainer Force Histories from Comparable GFRP, Steel, and SMA Restrainer Tests, Case 1

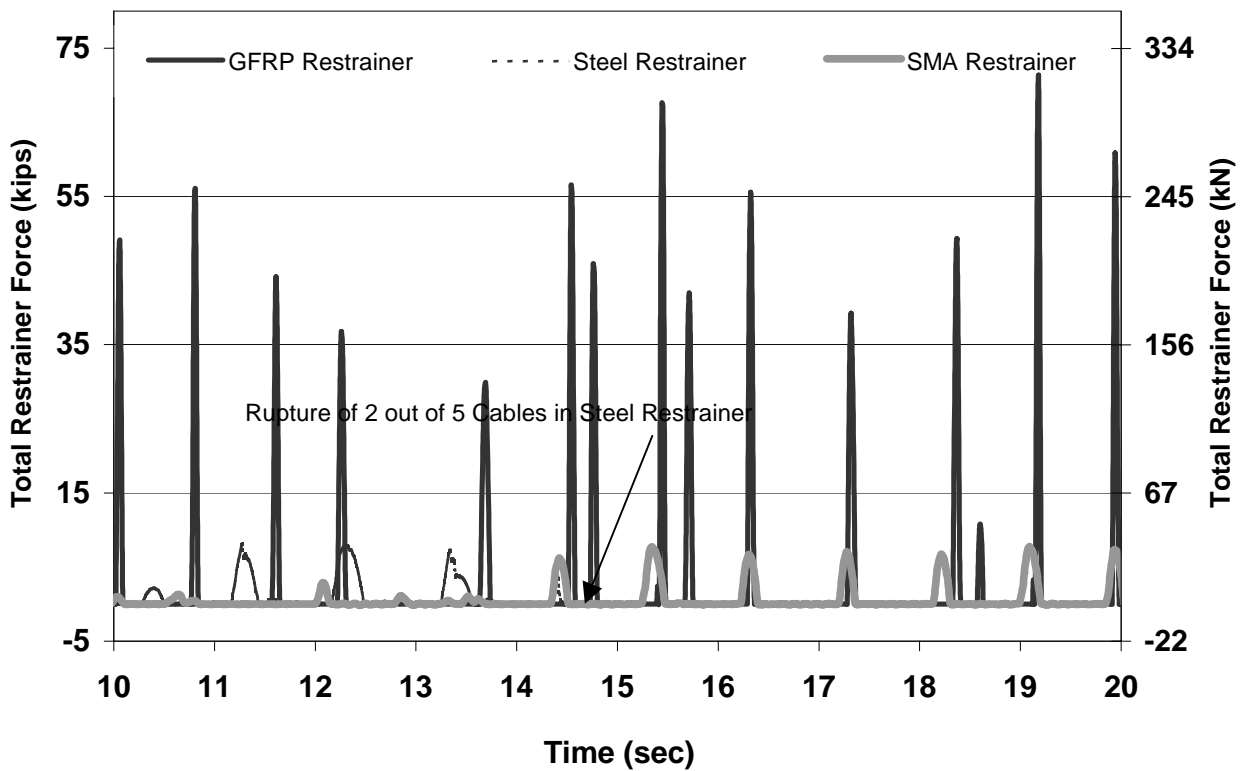


Figure 6-16(b): Total Restrainer Force Histories from Comparable GFRP, Steel, and SMA Restrainer Tests, Case 2

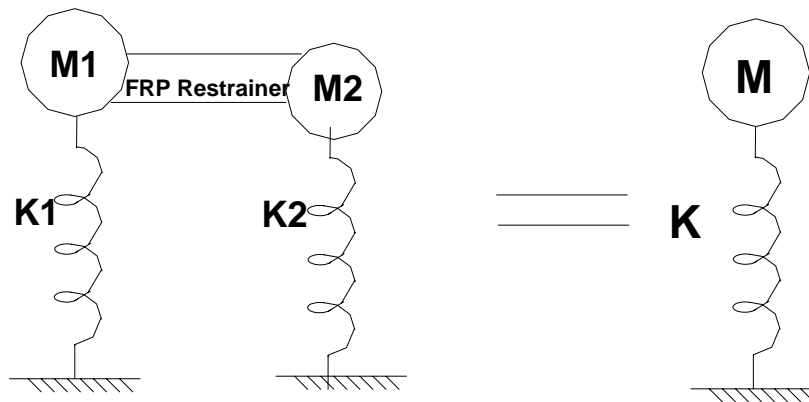


Figure 7-1: 2 DOF of System Converted to Single DOF System with FRP Restrainer

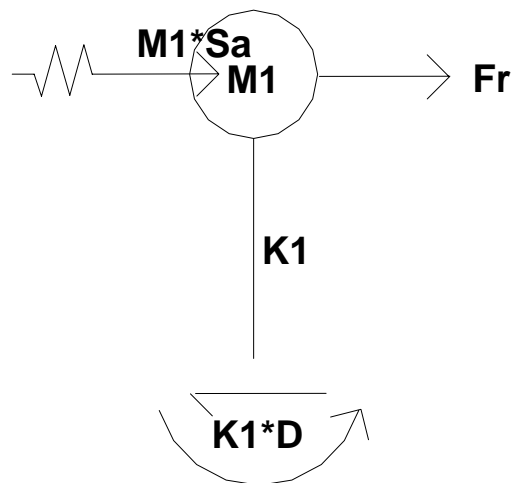
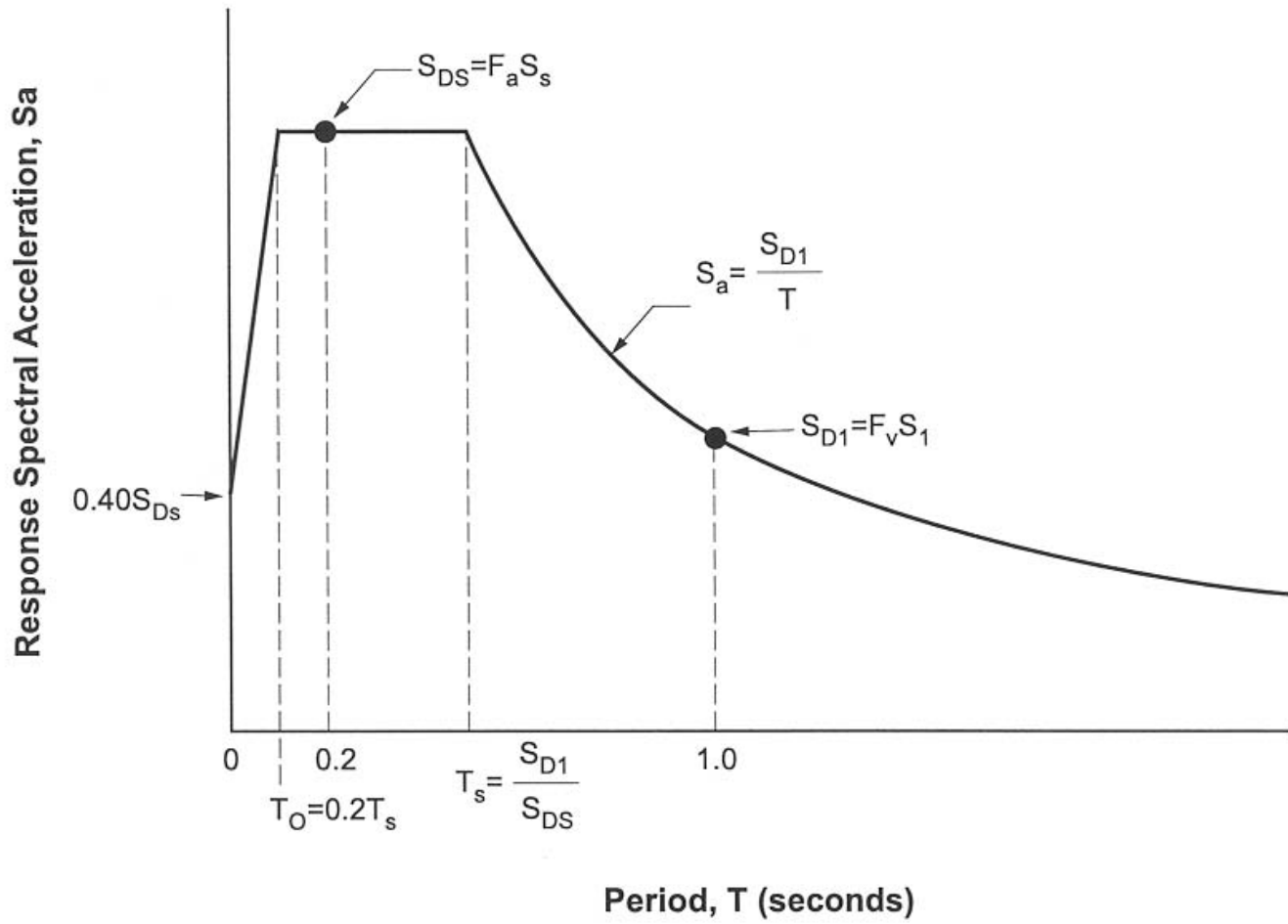


Figure 7-2: Equilibrium of Forces for System with FRP Restrainer



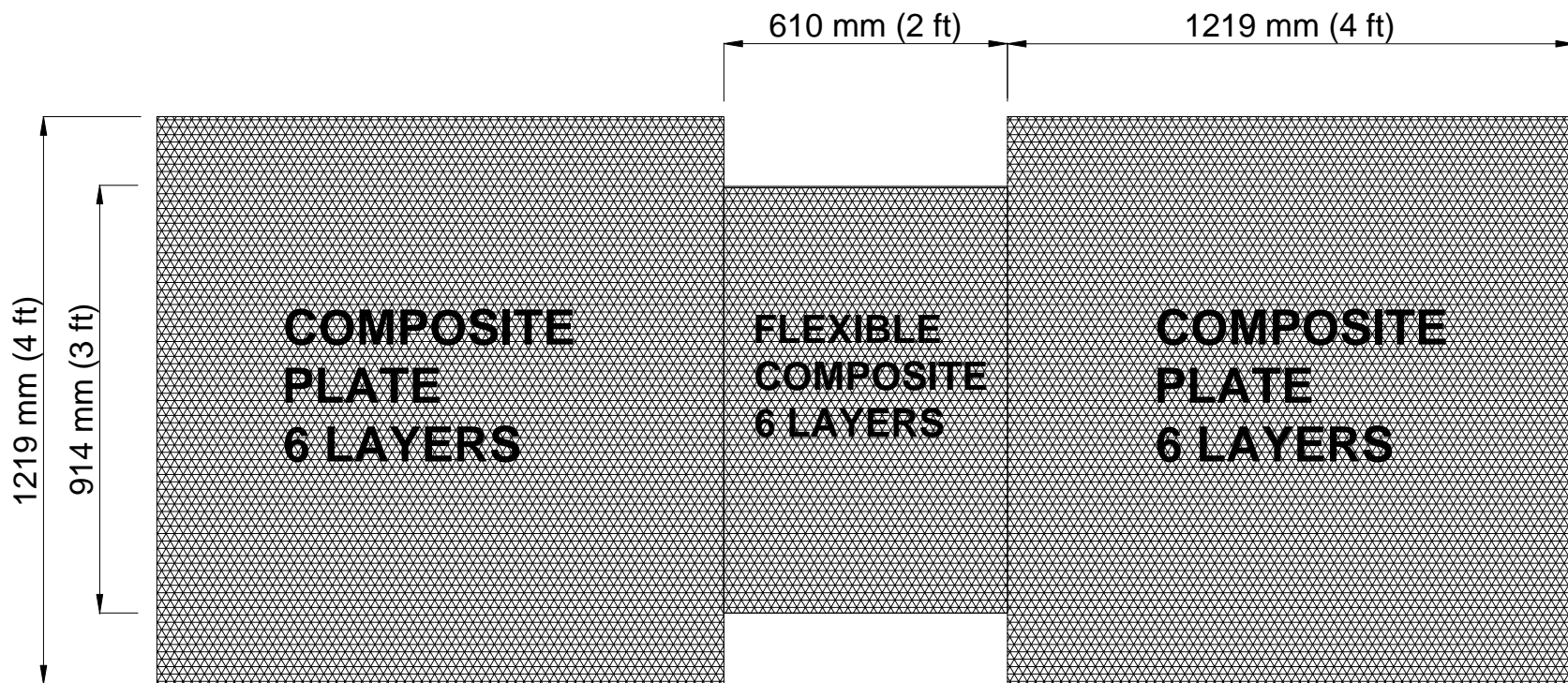


Figure 7-4: Design Dimensions for CFRP Restrainer

LIST OF CCEER PUBLICATIONS

Report No.	Publication
CCEER-84-1	Saiidi, M., and R. Lawver, "User's Manual for LZAK-C64, A Computer Program to Implement the Q-Model on Commodore 64," Civil Engineering Department, Report No. CCEER-84-1, University of Nevada, Reno, January 1984.
CCEER-84-2	Douglas, B. and T. Iwasaki, "Proceedings of the First USA-Japan Bridge Engineering Workshop," held at the Public Works Research Institute, Tsukuba, Japan, Civil Engineering Department, Report No. CCEER-84-2, University of Nevada, Reno, April 1984.
CCEER-84-3	Saiidi, M., J. Hart, and B. Douglas, "Inelastic Static and Dynamic Analysis of Short R/C Bridges Subjected to Lateral Loads," Civil Engineering Department, Report No. CCEER-84-3, University of Nevada, Reno, July 1984.
CCEER-84-4	Douglas, B., "A Proposed Plan for a National Bridge Engineering Laboratory," Civil Engineering Department, Report No. CCEER-84-4, University of Nevada, Reno, December 1984.
CCEER-85-1	Norris, G. and P. Abdollaholiae, "Laterally Loaded Pile Response: Studies with the Strain Wedge Model," Civil Engineering Department, Report No. CCEER-85-1, University of Nevada, Reno, April 1985.
CCEER-86-1	Ghusn, G. and M. Saiidi, "A Simple Hysteretic Element for Biaxial Bending of R/C in NEABS-86," Civil Engineering Department, Report No. CCEER-86-1, University of Nevada, Reno, July 1986.
CCEER-86-2	Saiidi, M., R. Lawver, and J. Hart, "User's Manual of ISADAB and SIBA, Computer Programs for Nonlinear Transverse Analysis of Highway Bridges Subjected to Static and Dynamic Lateral Loads," Civil Engineering Department, Report No. CCEER-86-2, University of Nevada, Reno, September 1986.
CCEER-87-1	Siddharthan, R., "Dynamic Effective Stress Response of Surface and Embedded Footings in Sand," Civil engineering Department, Report No. CCEER-86-2, University of Nevada, Reno, June 1987.
CCEER-87-2	Norris, G. and R. Sack, "Lateral and Rotational Stiffness of Pile Groups for Seismic Analysis of Highway Bridges," Civil Engineering Department, Report No. CCEER-87-2, University of Nevada, Reno, June 1987.
CCEER-88-1	Orie, J. and M. Saiidi, "A Preliminary Study of One-Way Reinforced Concrete Pier Hinges Subjected to Shear and Flexure," Civil Engineering Department, Report No. CCEER-88-1, University of Nevada, Reno, January 1988.
CCEER-88-2	Orie, D., M. Saiidi, and B. Douglas, "A Micro-CAD System for Seismic Design of Regular Highway Bridges," Civil Engineering Department, Report No. CCEER-88-2, University of Nevada, Reno, June 1988.
CCEER-88-3	Orie, D. and M. Saiidi, "User's Manual for Micro-SARB, a Microcomputer Program for Seismic Analysis of Regular Highway Bridges," Civil Engineering Department, Report No. CCEER-88-3, University of Nevada, Reno, October 1988.
CCEER-89-1	Douglas, B., M. Saiidi, R. Hayes, and G. Holcomb, "A Comprehensive Study of the Loads and Pressures Exerted on Wall Forms by the Placement of Concrete," Civil Engineering Department, Report No. CCEER-89-1, University of Nevada, Reno, February 1989.

- CCEER-89-2 Richardson, J. and B. Douglas, "Dynamic Response Analysis of the Dominion Road Bridge Test Data," Civil Engineering Department, Report No. CCEER-89-2, University of Nevada, Reno, March 1989.
- CCEER-89-2 Vrontinos, S., M. Saiidi, and B. Douglas, "A Simple Model to Predict the Ultimate Response of R/C Beams with Concrete Overlays," Civil Engineering Department, Report NO. CCEER-89-2, University of Nevada, Reno, June 1989.
- CCEER-89-3 Ebrahimpour, A. and P. Jagadish, "Statistical Modeling of Bridge Traffic Loads - A Case Study," Civil Engineering Department, Report No. CCEER-89-3, University of Nevada, Reno, December 1989.
- CCEER-89-4 Shields, J. and M. Saiidi, "Direct Field Measurement of Prestress Losses in Box Girder Bridges," Civil Engineering Department, Report No. CCEER-89-4, University of Nevada, Reno, December 1989.
- CCEER-90-1 Saiidi, M., E. Maragakis, G. Ghush, Y. Jiang, and D. Schwartz, "Survey and Evaluation of Nevada's Transportation Infrastructure, Task 7.2 - Highway Bridges, Final Report," Civil Engineering Department, Report No. CCEER 90-1, University of Nevada, Reno, October 1990.
- CCEER-90-2 Abdel-Ghaffar, S., E. Maragakis, and M. Saiidi, "Analysis of the Response of Reinforced Concrete Structures During the Whittier Earthquake 1987," Civil Engineering Department, Report No. CCEER 90-2, University of Nevada, Reno, October 1990.
- CCEER-91-1 Saiidi, M., E. Hwang, E. Maragakis, and B. Douglas, "Dynamic Testing and the Analysis of the Flamingo Road Interchange," Civil Engineering Department, Report No. CCEER-91-1, University of Nevada, Reno, February 1991.
- CCEER-91-2 Norris, G., R. Siddharthan, Z. Zafir, S. Abdel-Ghaffar, and P. Gowda, "Soil-Foundation-Structure Behavior at the Oakland Outer Harbor Wharf," Civil Engineering Department, Report No. CCEER-91-2, University of Nevada, Reno, July 1991.
- CCEER-91-3 Norris, G., "Seismic Lateral and Rotational Pile Foundation Stiffnesses at Cypress," Civil Engineering Department, Report No. CCEER-91-3, University of Nevada, Reno, August 1991.
- CCEER-91-4 O'Connor, D. and M. Saiidi, "A Study of Protective Overlays for Highway Bridge Decks in Nevada, with Emphasis on Polyester-Styrene Polymer Concrete," Civil Engineering Department, Report No. CCEER-91-4, University of Nevada, Reno, October 1991.
- CCEER-91-5 O'Connor, D.N. and M. Saiidi, "Laboratory Studies of Polyester-Styrene Polymer Concrete Engineering Properties," Civil Engineering Department, Report No. CCEER-91-5, University of Nevada, Reno, November 1991.
- CCEER-92-1 Straw, D.L. and M. Saiidi, "Scale Model Testing of One-Way Reinforced Concrete Pier Hinges Subject to Combined Axial Force, Shear and Flexure," edited by D.N. O'Connor, Civil Engineering Department, Report No. CCEER-92-1, University of Nevada, Reno, March 1992.
- CCEER-92-2 Wehbe, N., M. Saiidi, and F. Gordaninejad, "Basic Behavior of Composite Sections Made of Concrete Slabs and Graphite Epoxy Beams," Civil Engineering Department, Report No. CCEER-92-2, University of Nevada, Reno, August 1992.
- CCEER-92-3 Saiidi, M. and E. Hutchens, "A Study of Prestress Changes in A Post-Tensioned Bridge During the First 30 Months," Civil Engineering Department, Report No. CCEER-92-3, University of Nevada, Reno, April 1992.

- CCEER-92-4 Saiidi, M., B. Douglas, S. Feng, E. Hwang, and E. Maragakis, "Effects of Axial Force on Frequency of Prestressed Concrete Bridges," Civil Engineering Department, Report No. CCEER-92-4, University of Nevada, Reno, August 1992.
- CCEER-92-5 Siddharthan, R., and Z. Zafir, "Response of Layered Deposits to Traveling Surface Pressure Waves," Civil Engineering Department, Report No. CCEER-92-5, University of Nevada, Reno, September 1992.
- CCEER-92-6 Norris, G., and Z. Zafir, "Liquefaction and Residual Strength of Loose Sands from Drained Triaxial Tests," Civil Engineering Department, Report No. CCEER-92-6, University of Nevada, Reno, September 1992.
- CCEER-92-7 Douglas, B., "Some Thoughts Regarding the Improvement of the University of Nevada, Reno's National Academic Standing," Civil Engineering Department, Report No. CCEER-92-7, University of Nevada, Reno, September 1992.
- CCEER-92-8 Saiidi, M., E. Maragakis, and S. Feng, "An Evaluation of the Current Caltrans Seismic Restrainer Design Method," Civil Engineering Department, Report No. CCEER-92-8, University of Nevada, Reno, October 1992.
- CCEER-92-9 O'Connor, D., M. Saiidi, and E. Maragakis, "Effect of Hinge Restrainers on the Response of the Madrone Drive Undercrossing During the Loma Prieta Earthquake," Civil Engineering Department, Report No. CCEER-92-9, University of Nevada, Reno, February 1993.
- CCEER-92-10 O'Connor, D., and M. Saiidi, "Laboratory Studies of Polyester Concrete: Compressive Strength at Elevated Temperatures and Following Temperature Cycling, Bond Strength to Portland Cement Concrete, and Modulus of Elasticity," Civil Engineering Department, Report No. CCEER-92-10, University of Nevada, Reno, February 1993.
- CCEER-92-11 Wehbe, N., M. Saiidi, and D. O'Connor, "Economic Impact of Passage of Spent Fuel Traffic on Two Bridges in Northeast Nevada," Civil Engineering Department, Report No. CCEER-92-11, University of Nevada, Reno, December 1992.
- CCEER-93-1 Jiang, Y., and M. Saiidi, "Behavior, Design, and Retrofit of Reinforced Concrete One-way Bridge Column Hinges," edited by D. O'Connor, Civil Engineering Department, Report No. CCEER-93-1, University of Nevada, Reno, March 1993.
- CCEER-93-2 Abdel-Ghaffar, S., E. Maragakis, and M. Saiidi, "Evaluation of the Response of the Aptos Creek Bridge During the 1989 Loma Prieta Earthquake," Civil Engineering Department, Report No. CCEER-93-2, University of Nevada, Reno, June 1993.
- CCEER-93-3 Sanders, D.H., B.M. Douglas, and T.L. Martin, "Seismic Retrofit Prioritization of Nevada Bridges," Civil Engineering Department, Report No. CCEER-93-3, University of Nevada, Reno, July 1993.
- CCEER-93-4 Abdel-Ghaffar, S., E. Maragakis, and M. Saiidi, "Performance of Hinge Restrainers in the Huntington Avenue Overhead During the 1989 Loma Prieta Earthquake," Civil Engineering Department, Report No. CCEER-93-4, University of Nevada, Reno, June 1993 (in final preparation).
- CCEER-93-5 Maragakis, E., M. Saiidi, S. Feng, and L. Flournoy, "Effects of Hinge Restrainers on the Response of the San Gregorio Bridge During the Loma Prieta Earthquake," (in final preparation) Civil Engineering Department, Report No. CCEER-93-5, University of Nevada, Reno.
- CCEER-93-6 Saiidi, M., E. Maragakis, S. Abdel-Ghaffar, S. Feng, and D. O'Connor, "Response of

- Bridge Hinge Restrainers During Earthquakes -Field Performance, Analysis, and Design," Civil Engineering Department, Report No. CCEER-93-6, University of Nevada, Reno, May 1993.
- CCEER-93-7 Wehbe, N., Saiidi, M., Maragakis, E., and Sanders, D., "Adequacy of Three Highway Structures in Southern Nevada for Spent Fuel Transportation, Civil Engineering Department, Report No. CCEER-93-7, University of Nevada, Reno, August 1993.
- CCEER-93-8 Roybal, J., Sanders, D.H., and Maragakis, E., "Vulnerability Assessment of Masonry in the Reno-Carson City Urban Corridor," Civil Engineering Department, Report No. CCEER-93-8, University of Nevada, Reno, May 1993.
- CCEER-93-9 Zafir, Z. and Siddharthan, R., "MOVLOAD: A Program to Determine the Behavior of Nonlinear Horizontally Layered Medium Under Moving Load," Civil Engineering Department, Report No. CCEER-93-9, University of Nevada, Reno, August 1993.
- CCEER-93-10 O'Connor, D.N., Saiidi, M., and Maragakis, E.A., "A Study of Bridge Column Seismic Damage Susceptibility at the Interstate 80/U.S. 395 Interchange in Reno, Nevada," Civil Engineering Department, Report No. CCEER-93-10, University of Nevada, Reno, October 1993.
- CCEER-94-1 Maragakis, E., B. Douglas, and E. Abdelwahed, "Preliminary Dynamic Analysis of a Railroad Bridge," Report CCEER-94-1, January 1994.
- CCEER-94-2 Douglas, B.M., Maragakis, E.A., and Feng, S., "Stiffness Evaluation of Pile Foundation of Cazenovia Creek Overpass," Civil Engineering Department, Report No. CCEER-94-2, University of Nevada, Reno, March 1994.
- CCEER-94-3 Douglas, B.M., Maragakis, E.A., and Feng, S., "Summary of Pretest Analysis of Cazenovia Creek Bridge," Civil Engineering Department, Report No. CCEER-94-3, University of Nevada, Reno, April 1994.
- CCEER-94-4 Norris, G.M. and Madhu, R., "Liquefaction and Residual Strength of Sands from Drained Triaxial Tests, Report 2," Civil Engineering Department, CCEER-94-4, University of Nevada, Reno, August 1994.
- CCEER-94-5 Saiidi, M., Hutchens, E., and Gardella, D., "Prestress Losses in a Post-Tensioned R/C Box Girder Bridge in Southern Nevada," Civil Engineering Department, CCEER-94-5, University of Nevada, Reno, August 1994.
- CCEER-95-1 Siddharthan, R., El-Gamal, M., and Maragakis, E.A., "Nonlinear Bridge Abutment , Verification, and Design Curves," Civil Engineering Department, CCEER-95-1, University of Nevada, Reno, January 1995.
- CCEER-95-2 Norris, G.M., Madhu, R., Valceschini, R., and Ashour, M., "Liquefaction and Residual Strength of Loose Sands from Drained Triaxial Tests," Report 2, Civil Engineering Department, Report No. CCEER-95-2, University of Nevada, Reno, February 1995.
- CCEER-95-3 Wehbe, N., Saiidi, M., Sanders, D., and Douglas, B., "Ductility of Rectangular Reinforced Concrete Bridge Columns with Moderate Confinement," Civil Engineering Department, Report No. CCEER-95-3, University of Nevada, Reno, July 1995.
- CCEER-95-4 Martin, T., Saiidi, M., and Sanders, D., "Seismic Retrofit of Column-Pier Cap Connections in Bridges in Northern Nevada," Civil Engineering Department, Report No. CCEER-95-4, University of Nevada, Reno, August 1995.
- CCEER-95-5 Darwish, I., Saiidi, M., and Sanders, D., "Experimental Study of Seismic Susceptibility

- Column-Footing Connections,” Civil Engineering Department, Report No. CCEER-95-5, University of Nevada, Reno, September 1995.
- CCEER-95-6 Griffin, G., Saiidi, M., and Maragakis, E., “Nonlinear Seismic Response of Isolated Bridges and Effects of Pier Ductility Demand,” Civil Engineering Department, Report No. CCEER-95-6, University of Nevada, Reno, November 1995.
- CCEER-95-7 Acharya, S., Saiidi, M., and Sanders, D., “Seismic Retrofit of Bridge Footings and Column-Footing Connections,” Report for the Nevada Department of Transportation, Civil Engineering Department, Report No. CCEER-95-7, University of Nevada, Reno, November 1995.
- CCEER-95-8 Maragakis, E., Douglas, B., and Sandirasegaram, U., “Full-Scale Field Resonance Tests of a Railway Bridge,” A Report to the Association of American Railroads, Civil Engineering Department, Report No. CCEER-95-8, University of Nevada, Reno, December 1995.
- CCEER-95-9 Douglas, B., Maragakis, E., and Feng, S., “System Identification Studies on Cazenovia Creek Overpass,” Report for the National Center for Earthquake Engineering Research, Civil Engineering Department, Report No. CCEER-95-9, University of Nevada, Reno, October 1995.
- CCEER-96-1 El-Gamal, M.E. and Siddharthan, R.V., “Programs to Computer Translational Stiffness of Seat-Type Bridge Abutment,” Civil Engineering Department, Report No. CCEER-96-1, University of Nevada, Reno, March 1996.
- CCEER-96-2 Labia, Y., Saiidi, M., and Douglas, B., “Evaluation and Repair of Full-Scale Prestressed Concrete Box Girders,” A Report to the National Science Foundation, Research Grant CMS-9201908, Civil Engineering Department, Report No. CCEER-96-2, University of Nevada, Reno, May 1996.
- CCEER-96-3 Darwish, I., Saiidi, M., and Sanders, D., “Seismic Retrofit of R/C Oblong Tapered Bridge Columns with Inadequate Bar Anchorage in Columns and Footings,” A Report to the Nevada Department of Transportation, Civil Engineering Department, Report No. CCEER-96-3, University of Nevada, Reno, May 1996.
- CCEER-96-4 Ashour, M., Pilling, P., Norris, G., and Perez, H., “The Prediction of Lateral Load Behavior of Single Piles and Pile Groups Using the Strain Wedge Model,” A Report to the California Department of Transportation, Civil Engineering Department, Report No. CCEER-96-4, University of Nevada, Reno, June, 1996.
- CCEER-97-1-A Rimal, P. and Itani, A. “Sensitivity Analysis of Fatigue Evaluations of Steel Bridges”, Center for Earthquake Research, Department of Civil Engineering, University of Nevada, Reno, Nevada Report No. CCEER-97-1-A, September, 1997.
- CCEER-97-1-B Maragakis, E., Douglas, B., and Sandirasegaram, U. “Full-Scale Field Resonance Tests of a Railway Bridge,” A Report to the Association of American Railroads, Civil Engineering Department, University of Nevada, Reno, May, 1996.
- CCEER-97-2 Wehbe, N., Saiidi, M., and D. Sanders, "Effect of Confinement and Flares on the Seismic Performance of Reinforced Concrete Bridge Columns," Civil Engineering Department, Report No. CCEER-97-2, University of Nevada, Reno, September 1997.
- CCEER-97-3 Darwish, I., M. Saiidi, G. Norris, and E. Maragakis, “Determination of In-Situ Footing Stiffness Using Full-Scale Dynamic Field Testing,” A Report to the Nevada Department of Transportation, Structural Design Division, Carson City, Nevada, Report No. CCEER-97-3, University of Nevada, Reno, October 1997.

- CCEER-97-4 Wehbe, N., and M. Saiidi, "User's manual for RCMC v. 1.2 : A Computer Program for Moment-Curvature Analysis of Confined and Unconfined Reinforced Concrete Sections," Center for Civil Engineering Earthquake Research, Department of Civil Engineering, University of Nevada, Reno, Nevada, Report No. CCEER-97-4, November, 1997.
- CCEER-97-5 Isakovic, T., M. Saiidi, and A. Itani, "Influence of new Bridge Configurations on Seismic Performance," Department of Civil Engineering, University of Nevada, Reno, Report No. CCEER-97-5, September, 1997.
- CCEER-98-1 Itani, A., Vesco, T. and Dietrich, A., "Cyclic Behavior of "as Built" Laced Members With End Gusset Plates on the San Francisco Bay Bridge" Center for Civil Engineering Earthquake Research, Department of Civil Engineering, University of Nevada, Reno, Nevada Report No. CCEER-98-1, March, 1998.
- CCEER-98-2 G. Norris and M. Ashour, "Liqueficiaion and Undraned response evaluation of Sands from Drained Formulation." Center for Civil Engineering Earthquake Research, Department of Civil Engineering, University of Nevada, Reno, Nevada, Report No. CCEER-98-2, May, 1998.
- CCEER-98-3 Qingbin, Chen, B. M. Douglas, E. Maragakis, and I. G. Buckle, "Extraction of Nonlinear Hysteretic Properties of Seismically Isolated Bridges from Quick-Release Field Tests", Center for Civil Engineering Earthquake Research, Department of Civil Engineering, University of Nevada, Reno, Nevada, Report No. CCEER-98-3, June, 1998.
- CCEER-98-4 Maragakis, E., B. M. Douglas, and C. Qingbin, "Full-Scale Field Capacity Tests of a Railway Bridge", Center for Civil Engineering Earthquake Research, Department of Civil Engineering, University of Nevada, Reno, Nevada, Report No. CCEER-98-4, June, 1998.
- CCEER-98-5 Itani, A., Douglas, B., and Woodgate, J., "Cyclic Behavior of Richmond-San Rafael Retrofitted Tower Leg". Center for Civil Engineering Earthquake Research, Department of Civil Engineering, University of Nevada, Reno. Report No. CCEER-98-5, June 1998
- CCEER-98-6 Moore, R., Saiidi, M., and Itani, A., "Seismic Behavior of New Bridges with Skew and Curvature". Center for Civil Engineering Earthquake Research, Department of Civil Engineering, University of Nevada, Reno. Report No. CCEER-98-6, October, 1998.
- CCEER-98-7 Itani, A and Dietrich, A, "Cyclic Behavior of Double Gusset Plate Connections", Center for Civil Engineering Earthquake Research, Department of Civil Engineering, University of Nevada, Reno, Nevada, Report No. CCEER-98-5, December, 1998.
- CCEER-99-1 Caywood, C., M. Saiidi, and D. Sanders, " Seismic Retrofit of Flared Bridge Columns With Steel Jackets," Civil Engineering Department, University of Nevada, Reno, Report No. CCEER-99-1, February 1999.
- CCEER-99-2 Mangoba, N., M. Mayberry, and M. Saiidi, "Prestress Loss in Four Box Girder Bridges in Northern Nevada," Civil Engineering Department, University of Nevada, Reno, Report No. CCEER-99-2, March 1999.
- CCEER-99-3 Abo-Shadi, N., M. Saiidi, and D. Sanders, "Seismic Response of Bridge Pier Walls in the Weak Direction", Civil Engineering Department, University of Nevada, Reno, Report No. CCEER-99-3, April 1999.
- CCEER-99-4 Buzick, A., and M. Saiidi, "Shear Strength and Shear Fatigue Behavior of Full-Scale Prestressed Concrete Box Girders", Civil Engineering Department, University of Nevada, Reno, Report No. CCEER-99-4, April 1999.

- CCEER-99-5 Randall, M., M. Saiidi, E. Maragakis and T. Isakovic, "Restrainer Design Procedures For Multi-Span Simply-Supported Bridges", Civil Engineering Department, University of Nevada, Reno, Report No. CCEER-99-5, April 1999.
- CCEER-99-6 Wehbe, N. and M. Saiidi, "User's Manual for RCMC v. 1.2, A Computer Program for Moment-Curvature Analysis of Confined and Unconfined Reinforced Concrete Sections", Civil Engineering Department, University of Nevada, Reno, Report No. CCEER-99-6, May 1999.
- CCEER-99-7 Burda, J. and A. Itani, "Studies of Seismic Behavior of Steel Base Plates," Civil Engineering Department, University of Nevada, Reno, Report No. CCEER-99-7, May 1999.
- CCEER-99-8 Ashour, M., and G. Norris, "Refinement of the Strain Wedge Model Program," Civil Engineering Department, University of Nevada, Reno, Report No. CCEER-99-8, March 1999.
- CCEER-99-9 Dietrich, A., and A. Itani, "Cyclic Behavior of Laced and Perforated Steel Members on the San Francisco-Oakland Bay Bridge," Civil Engineering Department, University, Reno. December 1999.
- CCEER 99-10 Itani, A., A. Dietrich, "Cyclic Behavior of Built Up Steel Members and their Connections," Civil Engineering Department, University of Nevada, Reno. December 1999.
- CCEER 99-11 Itani, A., J. Woodgate, "Axial and Rotational Ductility of BuiltUp Structural Steel Members," Civil Engineering Department, University of Nevada, Reno December 1999.
- CCEER-99-12 Sgambelluri, M., Sanders, D.H., and Saiidi, M.S., Behavior of One-Way Reinforced Concrete Bridge Column Hinges in the Weak Direction, Report No. Department of Civil Engineering, University of Nevada, Reno, December 1999.
- CCEER-99-13 Laplace, P., Sanders, D.H., Douglas, B, and Saiidi, M, Shake Table Testing of Flexure Dominated Reinforced Concrete Bridge Columns, Report No. Department of Civil Engineering, University of Nevada, Reno, December 1999.
- CCEER-99-14 Ahmad M. Itani, Jose A. Zepeda, and Elizabeth A. Ware "Cyclic Behavior of Steel Moment Frame Connections for the Moscone Center Expansion," December 1999.
- CCEER 00-1 Ashour, M., and Norris, G. "Undrained Lateral Pile and Pile Group Response in Saturated Sand", Civil Engineering Department, University of Nevada, Reno, Report No. CCEER-00-1, May 1999. January 2000.
- CCEER 00-2 Saiidi, M. and Wehbe, N., "A Comparison of Confinement Requirements in Different Codes for Rectangular, Circular, and Double-Spiral RC Bridge Columns," Civil Engineering Department, University of Nevada, Reno, Report No. CCEER-00-2, January 2000.
- CCEER 00-3 McElhaney, B., M. Saiidi, and D. Sanders, "Shake Table Testing of Flared Bridge Columns With Steel Jacket Retrofit," Civil Engineering Department, University of Nevada, Reno, Report No. CCEER-00-3, January 2000.
- CCEER 00-4 Martinovic, F., M. Saiidi, D. Sanders, and F. Gordaninejad, "Dynamic Testing of Non-Prismatic Reinforced Concrete Bridge Columns Retrofitted with FRP Jackets," Civil Engineering Department, University of Nevada, Reno, Report No. CCEER-00-4, January 2000.

- CCEER 00-5 Itani, A., and M. Saiidi, "Seismic Evaluation of Steel Joints for UCLA Center for Health Science Westwood Replacement Hospital," Civil Engineering Department, University of Nevada, Reno, Report No. CCEER-00-5, February 2000.
- CCEER 00-6 Will, J. and D. Sanders, "High Performance Concrete Using Nevada Aggregates," Civil Engineering Department, University of Nevada, Reno, Report No. CCEER-00-6, May 2000.
- CCEER 00-7 French, C., and M. Saiidi, "A Comparison of Static and Dynamic Performance of Models of Flared Bridge Columns," Civil Engineering Department, University of Nevada, Reno, Report No. CCEER-00-7, October 2000.
- CCEER 00-8 Itani, A., H. Sedarat, "Seismic Analysis of the AISI LRFD Design Example of Steel Highway Bridges," Civil Engineering Department, University of Nevada, Reno, Report No. CCEER 00-08, November 2000.
- CCEER 00-9 Moore, J., D. Sanders, and M. Saiidi, "Shake Table Testing of 1960's Two Column Bent with Hinges Bases," Civil Engineering Department, University of Nevada, Reno, Report No. CCEER 00-09, December 2000.
- CCEER 00-10 Asthana, M., D. Sanders, and M. Saiidi, "One-Way Reinforced Concrete Bridge Column Hinges in the Weak Direction," Civil Engineering Department, University of Nevada, Reno, Report No. CCEER 00-10, April 2001.
- CCEER 01-1 Ah Sha, H., D. Sanders, M. Saiidi, "Early Age Shrinkage and Cracking of Nevada Concrete Bridge Decks," Civil Engineering Department, University of Nevada, Reno, Report No. CCEER 01-01, May 2001.
- CCEER 01-2 Ashour, M. and G. Norris, "Pile Group program for Full Material Modeling an Progressive Failure," Civil Engineering Department, University of Nevada, Reno, Report No. CCEER 01-02, July 2001.
- CCEER 01-3 Itani, A., C. Lanaud, and P. Dusicka, "Non-Linear Finite Element Analysis of Built-Up Shear Links," Civil Engineering Department, University of Nevada, Reno, Report No. CCEER 01-03, July 2001.
- CCEER 01-4 Saiidi, M., J. Mortensen, and F. Martinovic, "Analysis and Retrofit of Fixed Flared Columns with Glass Fiber-Reinforced Plastic Jacketing," Civil Engineering Department, University of Nevada, Reno, Report No. CCEER 01-4, August 2001
- CCEER 01-5 Saiidi, M., A. Itani, I. Buckle, and Z. Cheng," Performance of A Full-Scale Two-Story Wood Frame Structure Supported on Ever-Level Isolators," Civil Engineering Department, University of Nevada, Reno, Report No. CCEER 01-5, October 2001
- CCEER 01-6 Laplace, P., D. Sanders, and M. Saiidi, "Experimental Study and Analysis of Retrofitted Flexure and Shear Dominated Circular Reinforced Concrete Bridge Columns Subjected to Shake Table Excitation," Civil Engineering Department, University of Nevada, Reno, Report No. CCEER 01-6, June 2001.
- CCEER 01-7 Reppi, F., and D. Sanders, "Removal and Replacement of Cast-in-Place, Post-tensioned, Box Girder Bridge," Civil Engineering Department, University of Nevada, Reno, Report No. CCEER 01-7, December 2001.
- CCEER 02-1 Pulido, C., M. Saiidi, D. Sanders, and A. Itani, "Seismic Performance and Retrofitting of Reinforced Concrete Bridge Bents," Civil Engineering Department, University of Nevada, Reno, Report No. CCEER 02-1, January 2002.

- CCEER 02-2 Yang, Q., M. Saiidi, H. Wang, and A. Itani, "Influence of Ground Motion Incoherency on Earthquake Response of Multi-Support Structures," Civil Engineering Department, University of Nevada, Reno, Report No. CCEER 02-2, May 2002.
- CCEER 02-3 M. Saiidi, B. Gopalakrishnan, E. Reinhardt, and R. Siddharthan, A Preliminary Study of Shake Table Response of A Two-Column Bridge Bent on Flexible Footings Civil Engineering Department, University of Nevada, Reno, Report No. CCEER 02-03, June 2002.
- CCEER 02-4 Not Published
- CCEER 02-5 Banghart, A., Sanders, D., Saiidi, M., "Evaluation of Concrete Mixes for Filling the Steel Arches in the Galena Creek Bridge," Civil Engineering Department, University of Nevada, Reno, Report No. CCEER 02-05, June 2002.
- CCEER 02-6 Dusicka, P., Itani, A., Buckle, I. G., "Cyclic Behavior of Shear Links and Tower Shaft Assembly of San Francisco – Oakland Bay Bridge Tower" Civil Engineering Department, University of Nevada, Reno, Report No. CCEER 02-06, July 2002.
- CCEER 02-7 Mortensen, J., and M. Saiidi, " A Performance-Based Design Method for Confinement in Circular Columns," Civil Engineering Department, University of Nevada, Reno, Report No. CCEER 02-07, November 2002.
- CCEER 03-1 Wehbe, N., and M. Saiidi, "User's manual for SPMC v. 1.0 : A Computer Program for Moment-Curvature Analysis of Reinforced Concrete Sections with Interlocking Spirals," Center for Civil Engineering Earthquake Research, Department of Civil Engineering, University of Nevada, Reno, Nevada, Report No. CCEER-03-1, May, 2003.
- CCEER 03-2 Wehbe, N., and M. Saiidi, "User's manual for RCMC v. 2.0 : A Computer Program for Moment-Curvature Analysis of Confined and Unconfined Reinforced Concrete Sections," Center for Civil Engineering Earthquake Research, Department of Civil Engineering, University of Nevada, Reno, Nevada, Report No. CCEER-03-2, June, 2003.
- CCEER 03-3 Nada, H., D. Sanders, and M. Saiidi, " Seismic Performance of RC Bridge Frames with Architectural-Flared Columns," Civil Engineering Department, University of Nevada, Reno, Report No. CCEER 03-3, January 2003.
- CCEER 03-4 Reinhardt, E., M. Saiidi, and R. Siddharthan, " Seismic Performance of a CFRP/ Concrete Bridge Bent on Flexible Footings." Civil Engineering Department, University of Nevada, Reno. Report No. CCEER 03-4, August 2003.
- CCEER 03-5 Johnson, N., M. Saiidi, A. Itani, and S. Ladkany, "Seismic Retrofit of Octagonal Columns with Pedestal and One-Way Hinge at the Base," Center for Civil Engineering Earthquake Research, Department of Civil Engineering, University of Nevada, Reno, Nevada, Report No. CCEER-03-5, August 2003.
- CCEER 03-6 Mortensen, C., M. Saiidi, and S. Ladkany, "Creep and Shrinkage Losses in Highly Variable Climates," Center for Civil Engineering Earthquake Research, Department of Civil Engineering, University of Nevada, Reno, Nevada, Report No. CCEER-03-6, September 2003.
- CCEER 03-7 Ayoub, C., M. Saiidi, and A. Itani, "A Study of Shape-Memory-Alloy-Reinforced Beams and Cubes," Center for Civil Engineering Earthquake Research, Department of Civil Engineering, University of Nevada, Reno, Nevada, Report No. CCEER-03-7, October 2003.

- CCEER 03-8 Chandane, S., D. Sanders, and M. Saiidi, "Static and Dynamic Performance of RC Bridge Bents with Architectural-Flared Columns," Center for Civil Engineering Earthquake Research, Department of Civil Engineering, University of Nevada, Reno, Nevada, Report No. CCEER-03-8, November 2003.
- CCEER 04-1 Olaegbe, C., and Saiidi, M., "Effect of Loading History on Shake Table Performance of A Two-Column Bent with Infill Wall," Center for Civil Engineering Earthquake Research, Department of Civil Engineering, University of Nevada, Reno, Nevada, Report No. CCEER-04-1, January 2004.
- CCEER 04-2 Johnson, R., Maragakis, E., Saiidi, M., and DesRoches, R., "Experimental Evaluation of Seismic Performance of SMA Bridge Restrainers," Center for Civil Engineering Earthquake Research, Department of Civil Engineering, University of Nevada, Reno, Nevada, Report No. CCEER-04-2, February 2004.
- CCEER 04-3 Moustafa, K., Sanders, D., and Saiidi, M., "Impact of Aspect Ratio on Two-Column Bent Seismic Performance," Center for Civil Engineering Earthquake Research, Department of Civil Engineering, University of Nevada, Reno, Nevada, Report No. CCEER-04-3, February 2004.
- CCEER 04-4 Maragakis, E., Saiidi, M., Sanchez-Camargo, F., and Elfass, S., "Seismic Performance of Bridge Restrainers At In-Span Hinges," Center for Civil Engineering Earthquake Research, Department of Civil Engineering, University of Nevada, Reno, Nevada, Report No. CCEER-04-4, March 2004.
- CCEER 04-5 Ashour, M., Norris, G. and Elfass, S., "Analysis of Laterally Loaded Long or Intermediate Drilled Shafts of Small or Large Diameter in Layered Soil," Center for Civil Engineering Earthquake Research, Department of Civil Engineering, University of Nevada, Reno, Nevada, Report No. CCEER-04-5, June 2004.
- CCEER 04-6 Correal, J., Saiidi, M. and Sanders, D., "Seismic Performance of RC Bridge Columns Reinforced with Two Interlocking Spirals," Center for Civil Engineering Earthquake Research, Department of Civil Engineering, University of Nevada, Reno, Nevada, Report No. CCEER-04-6, August 2004.
- CCEER 04-7 Dusicka, P., Itani, A. and Buckle, I., "Cyclic Response and Low Cycle Fatigue Characteristics of Plate Steels," Center for Civil Engineering Earthquake Research, Department of Civil Engineering, University of Nevada, Reno, Nevada, Report No. CCEER-04-7, November 2004.
- CCEER 04-8 Dusicka, P., Itani, A. and Buckle, I., "Built-up Shear Links as Energy Dissipaters for Seismic Protection of Bridges," Center for Civil Engineering Earthquake Research, Department of Civil Engineering, University of Nevada, Reno, Nevada, Report No. CCEER-04-8, November 2004.
- CCEER 04-9 Sureshkumar, K., Saiidi, S., Itani, A. and Ladkany, S., "Seismic Retrofit of Two-Column Bents with Diamond Shape Columns," Center for Civil Engineering Earthquake Research, Department of Civil Engineering, University of Nevada, Reno, Nevada, Report No. CCEER-04-9, November 2004.
- CCEER 05-1 Wang, H. and Saiidi, S., "A Study of RC Columns with Shape Memory Alloy and Engineered Cementitious Composites," Center for Civil Engineering Earthquake Research, Department of Civil Engineering, University of Nevada, Reno, Nevada, Report No. CCEER-05-1, January 2005.

- CCEER 05-2 Johnson, R., Saiidi, S. and Maragakis, E., "A Study of Fiber Reinforced Plastics for Seismic Bridge Restrainers," Center for Civil Engineering Earthquake Research, Department of Civil Engineering, University of Nevada, Reno, Nevada, Report No. CCEER-05-2, January 2005.
- CCEER 05-3 Carden, L.P., Itani, A.M., Buckle, I.G., "Seismic Load Path in Steel Girder Bridge Superstructures," Center for Civil Engineering Earthquake Research, Department of Civil Engineering, University of Nevada, Reno, Nevada, Report No. CCEER-05-3, January 2005.
- CCEER 05-4 Carden, L.P., Itani, A.M., Buckle, I.G., "Seismic Performance of Steel Girder Bridge Superstructures with Ductile End Cross Frames and Seismic Isolation," Center for Civil Engineering Earthquake Research, Department of Civil Engineering, University of Nevada, Reno, Nevada, Report No. CCEER-05-4, January 2005.
- CCEER 05-5 Goodwin, E., Maragakis, M., Itani, A. and Luo, S., "Experimental Evaluation of the Seismic Performance of Hospital Piping Subassemblies," Center for Civil Engineering Earthquake Research, Department of Civil Engineering, University of Nevada, Reno, Nevada, Report No. CCEER-05-5, February 2005.
- CCEER 05-6 Zadeh M. S., Saiidi, S, Itani, A. and Ladkany, S., "Seismic Vulnerability Evaluation and Retrofit Design of Las Vegas Downtown Viaduct," Center for Civil Engineering Earthquake Research, Department of Civil Engineering, University of Nevada, Reno, Nevada, Report No. CCEER-05-6, February 2005.
- CCEER 05-7 Phan, V., Saiidi, S. and Anderson, J., "Near Fault (Near Field) Ground Motion Effects on Reinforced Concrete Bridge Columns" Center for Civil Engineering Earthquake Research, Department of Civil Engineering, University of Nevada, Reno, Nevada, Report No. CCEER-05-7, August 2005.
- CCEER 05-8 Carden, L., Itani, A. and Laplace, P., "Performance of Steel Props at the UNR Fire Science Academy subjected to Repeated Fire" Center for Civil Engineering Earthquake Research, Department of Civil Engineering, University of Nevada, Reno, Nevada, Report No. CCEER-05-8, August 2005.
- CCEER 05-9 Yamashita, R. and Sanders, D., "Shake Table Testing and an Analytical Study of Unbonded Prestressed Hollow Concrete Column Constructed with Precast Segments" Center for Civil Engineering Earthquake Research, Department of Civil Engineering, University of Nevada, Reno, Nevada, Report No. CCEER-05-9, August 2005.
- CCEER 05-10 Moustafa, K. Sanders, D., and Saiidi, M., "Seismic Behavior of R/C Bridge Bents with Architectural-Flared Columns Including both Horizontal and Vertical Gaps," Center for Civil Engineering Earthquake Research, Department of Civil Engineering, University of Nevada, Reno, Nevada, Report No. CCEER-05-10, February 2005.
- CCEER 05-11 Carden, L., Itani, A., and Peckan, G., "Recommendations for the Design of Beams and Posts in Bridge Falsework," Center for Civil Engineering Earthquake Research, Department of Civil Engineering, University of Nevada, Reno, Nevada, Report No. CCEER-05-11, October 2005.
- CCEER 06-01 Cheng, Z., Saiidi, M., and Sanders, D., "Development of a Seismic Design Method for Reinforced Concrete Two-Way Bridge Column Hinges," Center for Civil Engineering Earthquake Research, Department of Civil Engineering, University of Nevada, Reno, Nevada, Report No. CCEER-06-01, February 2006.



Kenny C. Guinn, Governor

Jeff Fontaine, P.E. Director
Prepared by Research Division
Tie He, Research Division Chief
(775) 888-7803
the@dot.state.nv.us
1263 South Stewart Street
Carson City, Nevada 89712